Synthesis, Characterization, *In-silico* Study and Antidiabetic Evaluation of Nitrogen and Sulphur Containing Heterocyclic Analogues

Thesis submitted to

KLE ACADEMY OF HIGHER EDUCATION AND RESEARCH
(Deemed-to-be-University)
BELAGAVI

[Declared as Deemed-to-be-University u/s 3 &12 B of the UGC Act, 1956 vide Govt. of India Notification No.F.9-19/2000-U.3 (A)]
(Accredited 'A^{+}' Grade by NAAC) (3rd Cycle)
[Placed in Category 'A' by MoE (GoI)]

For the award of the degree of
Doctor of Philosophy
In the Faculty of
Pharmacy

By

SHRIRAM D. RANADE **M. Pharm**
(Registration No: KLEU/Ph.D./21-22/DO1221033)

Under the Guidance of

Guide:
Prof. (Dr.) Shankar G. Alegaon **M. Pharm., Ph.D.**
Professor
Department of Pharmaceutical Chemistry
KLE College of Pharmacy,
Belagavi

Co-guide:
Prof. (Dr.) Nayeem. A. Khatib **M. Pharm., Ph.D.**
Professor and Head
Department of Pharmacology
KLE College of Pharmacy,
Belagavi.

2025

UNDERTAKING

I, Mr. **Shriram D. Ranade** hereby declare that the information and the data mentioned in my thesis entitled "**Synthesis, Characterization, *In-silico* Study and Antidiabetic Evaluation of Nitrogen and Sulphur Containing Heterocyclic Analogues**" belongs to me and is original.

I am aware of definition of plagiarism as detailed below:

- An act or instance of using or closely imitating the language and thoughts of another author without authorization and the representation of that author's work as one's own, as by not crediting the original author.
- A piece of writing or other work reflecting such unauthorized use or imitation.
- The deliberate or reckless representation of another's words, thoughts or ideas as one's own without attribution in connection with submission of academic work, whether graded or otherwise.

I hereby declare that the thesis prepared by me is original-one and does not involve plagiarism anywhere. In case at a later stage it is found that I have indulged in plagiarism, then I am solely responsible for the same and the Institution is at liberty to take any disciplinary action against me including cancellation of dissertation or any other penalties imposed by the University.

Signature of the Research Scholar

Date:

Place: Belagavi

Ref. No. KAHER/AA/24-25/D-653

24th January 2025

Sir,

The soft copy of Ph.D. research thesis of **Mr. Shriram D. Ranade, Faculty of Pharmacy** of KAHER, Belagavi has been submitted for anti-plagiarism check at the office of the undersigned through "Turn-it-in" package. The scan has been carried out and the scanned output reveals a match percentage of **4%** which is within the acceptable limit of 10%.

To obtain the comprehensive report of the plagiarism test, research scholar can send a mail to **diracademic@kledeemeduniversity.edu.in** along with the Registration Number, Name of the Scholar, Name of Guide/Co-guide and title of the thesis.

DIRECTOR ACADEMIC AFFAIRS Deemed-to-be University

Dr.(Mrs.) Jyoti M. Nagamoti
Director, Academic Affairs

To,

Mr. Shriram D. Ranade
Full-Time Ph.D. Scholar, 2021-22 Batch A
KLE College of Pharmacy,
Faculty of Pharmacy, KAHER
Belagavi.

Cc to :

1) The Principal, KLE College of Pharmacy, Belagavi.
2) Dr. Shankar G. Alegaon, Professor of Pharmaceutical Chemistry, KLE College of Pharmacy, KAHER, Belagavi – **Guide**

KLE ACADEMY OF HIGHER EDUCATION AND RESEARCH,
(KLE DEEMED UNIVERSITY)

[Declared as Deemed-to-be-University u/s 3 & 12 B of the UGC Act, 1956 vide Govt. of India Notification No.F.9-19/2000-U.3 (A)]

(Accredited 'A^{+}' Grade by NAAC) (3rd Cycle)
[Placed in Category 'A' by MoE (GoI)]
BELAGAVI



COPYRIGHT DECLARATION

We hereby declare that **KLE ACADEMY OF HIGHER EDUCATION AND RESEARCH, BELAGAVI, KARNATAKA**, *shall have the rights to preserve, use and disseminate this thesis in print or electronic format for academic/research purpose.*

Mr. Shriram D. Ranade
Full time Ph.D. Research Scholar
Reg. No: DO1221033
KLE College of Pharmacy Belagavi
KAHER, Belagavi-590010, India
Place: Belagavi
Date:

Prof. Dr. Shankar G. Alegaon
Department of Pharmaceutical chemistry
KLE College of Pharmacy Belagavi
KAHER, Belagavi-590010, India
Place: Belagavi
Date:

© KLE ACADEMY OF HIGHER EDUCATION AND RESEARCH, BELAGAVI

KLE ACADEMY OF HIGHER EDUCATION AND RESEARCH,
(KLE DEEMED UNIVERSITY)

[Declared as Deemed-to-be-University u/s 3 & 12 B of the UGC Act, 1956 vide Govt. of India Notification No.F.9-19/2000-U.3 (A)]

(Accredited 'A^{+}' Grade by NAAC) (3rd Cycle)
[Placed in Category 'A' by MoE (GoI)]
BELAGAVI

DECLARATION

I hereby declare that the thesis entitled **"Synthesis, Characterization, *In-silico* Study and Antidiabetic Evaluation of Nitrogen and Sulphur Containing Heterocyclic Analogues"** *is a Bonafide and original research carried out by me under the guidance of* **Dr. Shankar G. Alegaon**, Department of pharmaceutical chemistry, KLE College of pharmacy, Belagavi-590010. *The thesis or any part thereof has not formed the basis for the award of any degree/fellowship or similar title to any candidate of any University.*

Mr. Shriram D. Ranade
Full time Ph.D. Research Scholar
Reg. No: DO1221033
KLE College of Pharmacy Belagavi,
KAHER, Belagavi-590010
Place: Belagavi
Date:

KLE ACADEMY OF HIGHER EDUCATION AND RESEARCH,
(KLE DEEMED UNIVERSITY)

[Declared as Deemed-to-be-University u/s 3 & 12 B of the UGC Act, 1956 vide Govt. of India Notification No.F.9-19/2000-U.3 (A)]

(Accredited 'A^{+}' Grade by NAAC) (3rd Cycle)
[Placed in Category 'A' by MoE (GoI)]
BELAGAVI

KLE
EMPOWERING PROFESSIONALS

CERTIFICATE

This is to certify that the thesis entitled **"Synthesis, Characterization, *In-silico* Study and Antidiabetic Evaluation of Nitrogen and Sulphur Containing Heterocyclic Analogues"** *is a bonafide and genuine research carried out by* **Mr. Shriram D. Ranade** *under the guidance of* **Dr. Shankar G. Alegaon**, Professor, Department of pharmaceutical chemistry, KLE College of pharmacy, Belagavi-590010

Place: Belagavi
Date:

Proff. (Dr.) Vinayak. S. Mastiholimath
Dean, Faculty of Pharmacy
KLE College of pharmacy, Belagavi
KAHER, Belagavi-590010

KLE ACADEMY OF HIGHER EDUCATION AND RESEARCH,
(KLE DEEMED UNIVERSITY)

[Declared as Deemed-to-be-University u/s 3 & 12 B of the UGC Act, 1956 vide Govt. of India Notification No.F.9-19/2000-U.3 (A)]

(Accredited 'A^{+}' Grade by NAAC) (3rd Cycle)
[Placed in Category 'A' by MoE (GoI)]
BELAGAVI



CERTIFICATE

This is to certify that the thesis entitled **"Synthesis, Characterization, *In-silico* Study and Antidiabetic Evaluation of Nitrogen and Sulphur Containing Heterocyclic Analogues"** *is a Bonafide record of original research carried out by* **Mr. Shriram D. Ranade** *for the award of degree of DOCTOR OF PHILOSOPHY in the faculty of* **PHARMACY** *under my supervision and guidance.*

Place: Belagavi
Date:

Prof. Dr. Shankar G. Alegaon
Department of Pharmaceutical chemistry
KLE College of Pharmacy Belagavi
KAHER, Belagavi-590010, India

KLE ACADEMY OF HIGHER EDUCATION AND RESEARCH,
(KLE DEEMED UNIVERSITY)

[Declared as Deemed-to-be-University u/s 3 & 12 B of the UGC Act, 1956 vide Govt. of India Notification No.F.9-19/2000-U.3 (A)]

(Accredited 'A^{+}' Grade by NAAC) (3rd Cycle)
[Placed in Category 'A' by MoE (GoI)]
BELAGAVI

KLE
EMPOWERING PROFESSIONALS

CERTIFICATE

This is to certify that the thesis entitled **"Synthesis, Characterization, *In-silico* Study and Antidiabetic Evaluation of Nitrogen and Sulphur Containing Heterocyclic Analogues"** *is a Bonafide record of original research carried out by* **Mr. Shriram D. Ranade** *for the award of degree of DOCTOR OF PHILOSOPHY in the faculty of* **PHARMACY** *under my supervision and co-guidance.*

Place: Belagavi

Date:

Signature

Prof. Dr. Nayeem A. Khatib
Department of Pharmacology
KLE College of Pharmacy Belagavi
KAHER, Belagavi-590010, India

KLE ACADEMY OF HIGHER EDUCATION AND RESEARCH,
(KLE DEEMED UNIVERSITY)

[Declared as Deemed-to-be-University u/s 3 & 12 B of the UGC Act, 1956 vide Govt. of India Notification No.F.9-19/2000-U.3 (A)]

(Accredited 'A^{+}' Grade by NAAC) (3rd Cycle)
[Placed in Category 'A' by MoE (GoI)]
BELAGAVI

CERTIFICATE

This is to certify that the thesis entitled **"Synthesis, Characterization, *In-silico* Study and Antidiabetic Evaluation of Nitrogen and Sulphur Containing Heterocyclic Analogues"** *is a bonafide and genuine research carried out by* **Mr. Shriram D. Ranade** *under the guidance of* **Dr. Shankar G. Alegaon**, Professor, Department of pharmaceutical chemistry, KLE College of pharmacy, Belagavi-590010

.

Signature

Place: Belagavi

Date:

Prof. Dr. Sunil S. Jalalpure
Principal, KLE College of Pharmacy, Belagavi
KAHER, Belagavi-590010, India

Acknowledgement

First and foremost, I would like to express my deep sense of gratitude to my advisor, ***Prof. Dr. Shankar G. Alegaon****, for his enthusiastic motivation, patience, endless chemistry discussions and immense knowledge during my doctoral research. Having him as my research guide has provided me with a lot of experience and patience throughout the research journey, Thank you, sir, for your invaluable guidance. I am greatly thankful to my co-guide* ***Prof. Dr. Nayeem A. Khatib****, for his constant support and providing his invaluable expertise to my Ph.D. research, helped me gain research experience in pharmacology domain. Thank you sir.*

Apart from my advisors, I would like to extend my heartfelt gratitude to the esteemed members of my Ph.D. committee, ***Dr. P. A. Patil****,* ***Dr. S. Karki****,* ***Dr. S. G. Alegaon****,* ***Dr. J.B.Prasad****,* ***Dr. Jyoti Nagmoti (Director of Academic Affairs, KAHER)*** *and* ***Dr. Roopa Bellad (Former Director of Academic Affairs, KAHER)****. Your invaluable insights, constructive feedback, and constant encouragement have been instrumental in refining my research. I am deeply thankful for your guidance, I am greatly thankful* ***Dr. Sunil S. Jalalpure****, Principal and* ***Dr. M. B. Patil*** *Vice-Principal College of pharmacy, Belagavi, for their constant support throughout the duration of course.*

I am grateful to ***Dr. B. R Prashantha Kumar****, Department of pharmaceutical chemistry, JSS College of pharmacy, Mysuru, for his assistance throughout my research journey.*

I am thankful for the cooperation and affection extended by ***Dr. M. M. Maste****,* ***Dr. M. S Palled****,* ***Dr. B. M. Dinnimath****,* ***Dr. Parixit Bhandurge****,* ***Dr. Preeti Salve****,* ***Dr. Shailendra Suryawanshi****,* ***Ms. Rohini S. Kavalapure ma'am****,* ***Kiran Gaikwad sir****,* ***Nikhil Gawas****,* ***Pooja kagwad and Rohan singadi****, Department of Pharmaceutical chemistry, KLE College of pharmacy, Belagavi.*

I want to appreciate SAIF-KUD, Dharwad for providing spectral data on time.

Throughout my research journey I have enjoyed discussions with my colleagues, seniors, juniors, and friends. I would like to thank ***Manisha****,* ***Saniya****,* ***Shankar****,* ***Rahul****,* ***Sachin****,* ***Prarambh****,* ***Anchal, Jagdish****, and* ***Pukar*** *for constant support, as we worked restless nights, had many laughs and tears together.*

Last but not least, I want to thank my Parents, sister and brother for supporting both mentally and emotionally.

-Shriram Ranade

Table of Contents

Chapter No.	Chapters	Page No.
	Abstract	
	INTRODUCTION	
1	1.1. Background 1.2. Literature review 1.2.1. Chemistry of nitrogen and Sulphur containing heterocycle and its biological relevance 1.2.2. Antidiabetic activity review 1.3. Justification 1.4. Aims and objectives	**1-27**
2	**MATERIALS AND METHODS** *1. Insilico studies* *1.1. Protein preparation* *1.2. Geometric optimization and ligand preparation* *1.3. Grid Generation and macromolecule docking* *1.4. pharmacophore modeling* *1.4.1. Structure based Pharmacophore modeling* *1.4.2. Ligand based pharmacophore modeling* *1.5. 3D Atom based QSAR* *1.6. Molecular Dynamic simulations* *1.7. Pharmacokinetic prediction* *1.8. Network Pharmacology and enrichment analysis* *2. Synthesis and characterization* *3. Invitro study* *3.1. Invitro glucose consumption assay in yeast cells* *3.2. Invitro glucose uptake assay in L6 myotubes* *3.3. Invitro PPAR-γ TF assay* *3.4. Invitro α-glucosidase inhibitory assay* *3.5. Invitro α-amylase inhibitory assay* *3.6. Toxicity assessment* *4. Invivo studies* *4.1. Ethical approval and animal procurement* *4.2. Acute toxicity study and diabetes induction* *4.3. Estimation of physical parameters* *4.4. Estimation of FBGL and OGTT* *4.5. Estimation of Fasting insulin levels and Insulin tolerance test, and HOMA-IR* *4.6. Collection of blood and visceral organs* *4.7. Estimation of lipid profile* *4.8. Glucose consumption by rat hemidiaphragm* *4.9. Glycogen content in liver and skeletal muscles* *4.10. Estimation of oxidative stress markers* *4.11. Histopathology findings* *4.12. Instrumentation and chromatographic conditions* *4.13. Preparation of stock solution and working standard solution* *4.14. Method validation* *4.15. Quantification of drug from plasma* *4.16. Pharmacokinetic analysis* *4.17. Statistical analysis*	**28-42**

Table of Contents

Results & Discussion (Scheme.1)

1. Design of scheme.1
2. Chemistry
3. Experimental
4. Structural elucidation by spectra data
5. Pharmacological evaluation
5.1. Invitro α-amylase inhibition assay
5.2. Glucose Uptake assay in yeast cells **43-90**
5.3. PPAR-γ transcription factor assay
6. Insilico study of scheme.1
3 *6.1. Molecular docking*
6.2. MD simulations and MMPBSA calculations
6.3. DFT and MEP analysis
6.4. ADMET profile prediction
6.5. Target identification, network construction and cluster analysis

Results & Discussion-(Scheme.2)

1. Design of scheme. 2
1.1. Receptor based pharmacophore modeling
2. Chemistry
3. Experimental
4. Structural elucidation by Spectral data
5. Pharmacological evaluation
5.1. Invitro glucose uptake assay in L6 myotubes
5.2. Invitro PPAR-γ TF assay
5.3. Invivo experimental pharmacology
5.3.1. Impact of Compound 5b and 5f on FBGL and OGTT
5.3.2. Impact of compounds 5b and 5f on body weight, food consumption, and water intake
5.3.3. Impact of compound 5b and 5f on insulin levels and ITT
5.3.4. Impact of compound 5b and 5f on HOMA-IR **91-158**
5.3.5. Impact of compound 5b and 5f on glycogen content in skeletal muscles and liver
4 *5.3.6. Impact of compound 5b and 5f on glucose uptake in rat hemidiaphragm*
5.3.7. Impact of compound 5b and 5f on lipid profile
5.3.8. Effect of Compound 5b and 5f on AST and ALT levels
5.3.9. Effect of Compound 5b and 5f on antioxidant biomarkers
5.3.10. Microphotographs of Liver and adipose tissue.
5.3.11. Bio analytical method development
5.3.12. Determination of invivo pharmacokinetic parameters
6. Insilico study of scheme.2
6.1. Molecular docking studies
6.2. Molecular dynamic simulation and MMGBSA
6.3. Geometric optimization by DFT calculations

Table of Contents

	Results & Discussion-(Scheme.3)	
	1. Design of scheme.3	
	2. Structure based pharmacophore and 3D QSAR	
	2.1. Validation of pharmacophore model	
	3. Chemistry	
	4. Experimental	
	5. Structural elucidation by Spectral data	
	6. Pharmacological evaluation	
	6.1. Invitro α-amylase and α-glucosidase inhibition assay	**159-213**
	6.2. Enzyme inhibitory kinetic study	
	6.3. Toxicity evaluation	
5	*7. Insilico study of scheme.3*	
	7.1. Molecular docking	
	7.2. MD simulations	
	7.3. DFT Computations	
	7.4. *ADMET predictions*	
6	**SUMMARY**	**214-216**
7	**CONCLUSION**	**217-219**
8	**REFERENCES**	**220-245**
	Annexure	
	Ethical approval for animal studies	
	Publications and presentation	

ABBREVIATIONS

ADMET*:** Absorption Distribution Metabolism Excretion-toxicity, ***ALA: Alanine ***ALT*:** Alanine transaminase, ***ANOVA*:** Analysis of variance, ***AST*:** Aspartate aminotransferase, ***AUC*:** Area under the curve, ***ARG:*** Arginine, ***ASN:*** Asparagine, ***ASP:*** Aspartic acid, ***B3LYP*:** Becke 3-parameter,Lee-Yang-Parr, ***CADD:*** Computer aided drug design, ***CAT:*** Catalase, ***CYS:*** Cysteine, ***DFT*:** Density functional theory, ***dL*:** Decilitre, ***DM*:** Diabetes mellitus, ***DNS:*** Dinitrosalicylic acid, ***DPP4*:** Dipeptidyl peptidase-4, ***EDTA*:** Ethylenediaminetetraacetic acid, ***ESP:*** electrostatic potential, ***FBGL:*** Fasting blood glucose level, ***FDR:*** False discovery rate, ***FFA:*** Free fatty acids, ***FMO:*** Frontiers molecular orbitals, ***FTIR:*** Fourier transform infrared, ***GPCR's:*** G-protein coupled receptors, ***GLP*:** Glucagon-like peptide, ***GLU:*** Glutamic acid, ***GLN:*** Glutamine, ***GLUT*:** Glucose transporter, ***GLY:*** Glycine, ***GSH*:** Glutathione, ***HBA:*** Hydrogen bond acceptor, ***HBD:*** Hydrogen bond donor ***HDL*:** High-density lipoprotein, ***HIS:*** Histidine, ***HOMA-IR*:** Homeostasis model assessment-estimated insulin resistance, ***HOMO:*** Highest occupied molecular orbital, ***HPLC*:** High-performance liquid chromatography, ***HRMS:*** High resolution mass spectroscopy, ***IAEC*:** Institutional animal ethics committee, ***IC50*:** Inhibitory concentration 50, ***ICH:*** International conference on harmonization, ***IDF*:** International diabetes federation, ***IFD:*** Induced fit docking, ***ILE:*** Isoleucine, ***IR*:** Insulin resistant, ***IRS*:** Insulin receptor substrate, ***ITT*:** Insulin tolerance test, ***KEGG*:** Kyoto encyclopedia of genes and genomes, ***L6 cells:*** Immortalized rat skeletal myoblast cells, ***LBD*:** ligand binding domain, ***LCMS:*** Liquid chromatography-mass spectroscopy, ***LDL*:** Low-density lipoprotein, ***LEU:*** Leucine, ***LOD:*** limit of detection, ***LOQ:*** limit of quantification, ***LUMO:*** Lowest unoccupied molecular orbital, ***LYS:*** Lysine, ***MD:*** Molecular dynamics, ***MDH*:** Malondialdehyde, ***MEP:*** Molecular Electrostatic potential, ***MET:*** Methionine, ***MF*:** Molecular formula, ***mg*:** Milligram, ***mL*:** Milliliter, ***MMGBSA:*** Molecular mechanics generalized Born surface area, ***MMPB/SA:*** Molecular mechanics Poisson-Boltzmann surface area, ***mp:*** Melting point, ***MW*:** Molecular weight, ***NHB*:**Number of hydrogen bonds, ***NMR:*** Nuclear magnetic resonance, ***NO*:** Nitric oxide, ***NPT:*** Normal pressure temperature, ***OECD*:** Organization for economic co-operation and development, ***OGTT*:** Oral glucose tolerance test, ***OPLS***: optimized potential for liquid simulations ***PARP*:** Poly (adp-ribose) polymerase, ***PDB:*** protein databank, ***pH*:** Potential of hydrogen, ***PHE:*** Phenylalanine, ***PI3K*:** Phosphoinositide 3-kinase, ***PNPG:*** p-nitrophenyl- α-D-glucopyranoside, ***PPAR*:** Peroxisome proliferator-activatedreceptors, ***ppm:*** Parts per million, ***PRO:*** Proline, ***PTEN*:** Phosphatase tensin homolog, ***PLS*:** Partial least square, ***PTP1B*:** Protein tyrosine phosphatase 1b, ***QSAR:*** Quantitative structural activity relationship, ***RCSB*:** Research collaboratory for structural bioinformatics, ***RMSD:*** Root mean square deviation, ***RMSF:*** Root mean square fluctuation, ***ROF:*** Rule of five, ***ROT:*** Rule of three, ***RoG:*** Radius of gyration, ***ROS*:** Reactive oxygen species, ***rt:*** room temperature, ***RXR:*** Retinoid X receptor, ***SAR***: Structural activity relationship, ***SASA:*** solvent-accessible surface area, ***SD*:** Standard deviation, ***SEM*:** Standard error of the mean, ***SER:*** Serine, ***SGLT*:** Sodium-glucose co-transporter, ***SOD*:** Superoxide dismutase, ***SUR1:*** Sulfonylurea receptor 1, ***STRING*:** Search tool for the retrieval of interacting genes/proteins, ***T1DM*:** Type 1 diabetes mellitus, ***T2DM*:** Type 2 diabetes mellitus, ***TBARS*:** Thiobarbituric acid reactive

substances, ***TC*****:** Total cholesterol, ***TG*****:** Triglycerides, ***THR:*** Threonine, ***TLC:*** Thin layer chromatography, ***TRP:*** Tryptophan, ***TTD*****:** Therapeutic target database, ***TYR:*** Tyrosine, ***TZD***: thiazolidinedione's ***USA*****:** United States of America, ***USFDA:*** United States food and drug administration, ***VAL:*** valine, ***VLDL*****:** Very low- density lipoprotein.

List of Tables

Table No.	Title	Page No.
1	Animal grouping in antidiabetic model study.....	38
2	IC_{50} values of Compounds (**6a-6h**) for *α-amylase* inhibition…….....	73
3	The Induced fit docking results of (**6a-6h**) compounds in (4W93) *α-amylase* binding pocket ……	78-79
4	Total Energy of Geometry optimized structures (**6a-6h**)……..	82
5	Calculated quantum chemical parameters of synthesized compounds (**6a-6h**)……	82
6	ADEMT parameters of synthesized inhibitors (**6a-6h**)…….....	83
7	KEGG Pathway analysis of compound **6b**…….	88-89
8	Screening results of dataset on the generated hypothesis…….	95
9	Invitro percentage glucose uptake of the synthesized compounds (**5a-5j**) in L6 myotubes…….	124
10	Effect of **5b** and **5f** on lipid profile in fructose induced insulin resistance ……..	131
11	Effect of **5b** and **5f** on hepatic enzyme markers in fructose induced insulin resistance …….	131
12	Effect of **5b** and **5f** on antioxidant biomarkers in fructose induced insulin resistance …….…….....	132
13	Summary of bioanalytical validation parameters.....	134
14	Recovery assay of compounds from rat plasma ……..	136
15	Pharmacokinetic parameters of compound **5b**, **5b** and pioglitazone……	137
16	Binding Affinity of Synthesized Compounds (**5a-5j**) within the LBD of PPAR-γ ……	139
17	Binding free energy of synthesized ligands (**5a-5j**) calculated using MM/GBSA analysis …….	145
18	Calculated quantum chemical descriptors of compounds **5b** and **5f**……..…….....	146
19	Computed ADMET properties of synthesized molecules (**5a-5j**)……..……	148
20	Enrichment analysis of protein regulated by compound **5b** and **5f** by KEGG pathway database…….....	150
21	Total number of pharmacophore hypothesis generated……	162
22	Atom-based 3D QSAR statistics for the selected pharmacophore hypothesis ……	163
23	Top 10 molecules identified through pharmacophore-based screening of designed compounds and decoy set ligands …….	165
24	*Invitro α-glucosidase* and *α-amylase* inhibitory activities of the synthesized derivatives (**6a-6j**)……..	193
25	Toxicity results of compounds (**6a-6j**) on normal mouse fibroblast L929 cell lines ……	197
26	Binding affinity and interactions of compounds (**6a-6j**) in the *α-glucosidase* binding pocket ……	203
27	Binding affinity and interactions of compounds (**6a-6j**) in *α-amylase* binding pocket ……	204
28	MM/GBSA Calculation of synthesized compounds (**6a-6j**)…….	208
29	Final Energy of Geometry optimized structures (**6a-6j**)…….....	209
30	Calculated quantum chemical parameters of synthesized compounds (**6a-6j**)……..	211
31	Computed ADMET properties of synthesized molecules (**6a-6j**)…….	213

List of Figures

Figure No.	Title	Page No.
1	Marketed antidiabetic agents	3
2	A general workflow employed in the present research	4
3	Molecules containing Nitrogen and Sulphur heteroatoms	7
4	Brief outline of study methods used in the identification of antidiabetic agent in present study	28
5	Study plan in scheme. 1	43
6	Design of thiazolidinone-ethanebenzenesulphonamide template	44
7	Glucose uptake capacity of synthesized compounds (**6a-6h**) in yeast cells	74
8	Expression of PPAR-γ TF by compound **6b** and pioglitazone	75
9	2D and 3D Binding orientation of Acarbose in *α-amylase* (4W93) binding pocket	77
10a	2D binding orientation of 6b in *α-amylase* (4W93) binding pocket (Pose-1)	77
10b	2D binding orientation of 6b in *α-amylase* (4W93) binding pocket (Pose-2)	78
11	MD simulation study of **6b** in *α-amylase* (4W93) binding pocket	80
12	Contours of HOMO and LUMO of compound **6b**	82
13	MEP map of compound **6b**	83
14	(**a**) The Venn diagram representation of common genes between test agent and T2DM, and (**b**) The categorical representation of genes modulated by compound identified via SwissTargetPrediction	86
15	(**a**) STRING identified Protein-protein interaction for compound **6b** and (**b**) The cluster analysis where cluster 1: red; cluster 2: green; cluster 3: blue	87
16	The protein-pathway interaction modulated by compound **6b**	87
17	Connections between pathways and its protein enrichment analysis (A) Type II DM, (B) alpha amylase	88
18	Protein-pathway interaction modulated by compound **6b**	88
19	Probable molecular mechanism of compound **6b** in **A**) Glucose uptake (hsa04930, hsa04151, map03320). **B**) *α-amylase* inhibition. (map04973)	90
20	Study plan in scheme. 2	91
21	Evolution of TZD's as Ligands targeting the Binding domain of the PPAR-γ LBD over the Past three decades	92
22	Design of acetylpyrrolidine-2-carbonitrile-based Substituted benzylidenethiazolidine-2, 4-dione derivatives	93
23	Seven-point pharmacophore hypothesis for the PPAR-γ LBD using pioglitazone as the reference ligand	94
24	Enrichment analysis of the dataset	94
25	Alignment of Hypothesis derived Pharmacophore Sites with compound (a) **5b** and (b) **5f**	95
26	Numbering scheme for proton and carbon assignments used in NMR interpretation	97
27	Study plan for antidiabetic evaluation of compound **5b** and **5f**	122
28	PPAR-γ transcription factor expression induced by compounds **5b**, **5f**, and pioglitazone	125
29	Effect of compound **5b** and **5f** on FBGL and OGTT in fructose-induced insulin resistance	126
30	Effect of compound **5b** and **5f** on physical parameters in fructose-induced insulin resistance	127
31	Effect of compound **5b** and **5f** on insulin level in the OGTT in fructose-induced insulin resistance	128
32	Effect of compound **5b** and **5f** on HOMO-IR in fructose-induced insulin resistance	129
33	Effect of Compound **5b** and **5f** on glycogen content in skeletal muscles and liver in fructose-induced insulin resistance	129
34	Effect of FBE on percentage glucose uptake in rat hemidiaphragm in fructose-induced insulin Resistance	130
35	Effects of compounds **5b** and **5f** on: (A) Liver tissue, (B) Adipose tissue, and (C) Adipocyte count	133
36	HPLC Chromatogram of (a) **5b**, (b) **5f**, and (c) Pioglitazone	135
37	HPLC Chromatogram of (a) **5b**, (b) **5f**, and (c) Pioglitazone in rat plasma	135
38	Pharmacokinetic parameters depicting the peak plasma concentrations of pioglitazone, **5b**, and **5f** at various time intervals, illustrating the drug release profiles from the plasma of experimental animals	137
39	Binding conformation of compound 5b within the LBD of PPAR-γ	140
40	Binding conformation of compound 5f within the LBD of PPAR-γ	140
41	Binding conformation of compound pioglitazone within the LBD of PPAR-γ	141
42	MD simulation study of compound **5b** in the PPAR-γ LBD	143
43	MD simulation study of compound **5f** in the PPAR-γ LBD	144
44	Representation of compound **5b** and **5f**, (A) HOMO and LUMO orbitals, (B) MEP map	147
45	Protein-protein interactions for compounds 5b and 5f were identified through STRING analysis	151

List of Figures

46	Significantly enriched Gene ontology 'biological processes' by compound **5b** and **5f**	**151**
47	Interaction of compounds **5b** and **5f** with proteins involved in T2DM and respective pathways.....	**152**
48	Proposed possible molecular mechanism of compound 5b and 5f, via PPAR signaling pathway, Adipocytokine signaling pathway, and insulin signaling pathway, highlighting triggered proteins.....	**157**
49	Study plan in scheme. 3	**159**
50	Design of Quinoline based Schiff's base molecule template	**160**
51	Representation of the AADRR_1 pharmacophore model	**163**
52	3D QSAR contour plot representation	**164**
53	Enrichment analysis plot of pharmacophore based screening	**165**
54	Illustrates the top-screened active compounds mapped onto the pharmacophoric model AADRR_1...	**166**
55	(**a**) Lineweaver-Burk plot in the presence and absence of various concentration of compound **6b**. (**b**) Secondary replot between Km and different concentration of inhibitor **6b**	**194**
56	(**a**) Lineweaver-Burk plot in the presence and absence of various concentration of compound **6c**. (**b**) Secondary replot between Km and different concentrations of inhibitor **6c**.....	**194**
57	SAR and Pharmacophoric features required for *α-glucosidase* inhibitory activity.....	**196**
58	Ramachandran plot of homology modeled α-glucosidase protein	**199**
59	Represents 2D and surface Binding orientation of compound **6b** in the *α-glucosidase* binding pocket...	**200**
60	Represents 2D and surface Binding orientation of compound **6c** in *α-glucosidase* binding pocket.....	**200**
61	Represents 2D and surface Binding orientation of compound acarbose in the *α-glucosidase* binding pocket.....	**201**
62	Represents 2D and surface Binding orientation of compound **6b** in *α-amylase* binding pocket.	**201**
63	Represents 2D and surface Binding orientation of compound **6c** in *α-amylase* binding pocket.....	**202**
64	Represents 2D and surface Binding orientation of compound acarbose in *α-amylase* binding pocket...	**202**
65	MD simulation study of *α-glucosidase*-**6b** complex.....	**206**
66	MD simulation study of *α-glucosidase*-**6c** complex.....	**207**
67	Represents the HOMO and LUMO orbitals with Energy Gap (ΔE_{GAP}) for the compound **6b** and **6c**	**211**
68	Represents the Molecular electrostatic potential map for the compounds **6b** and **6c**.....	**212**
69	Overall summary of the presented work	**214**
70	Outcome of present research work.....	**217**

ABSTRACT

Background: India, often referred to as the diabetic capital of the world, faces limitations in existing oral antidiabetic drug efficacy. Nitrogen and sulphur-containing heterocycles are potential for managing T2DM by targeting specific biological targets.

Objectives: The study employed to design, synthesis and characterize novel nitrogen and sulphur-containing heterocycles, and explore their molecular mechanisms for antidiabetic activity.

Methodology: A Computer aided drug design (CADD) approach employing structure based drug-design (SBDD) led to the design, synthesis, and characterization (FTIR, ^{1}H & ^{13}C NMR, and Mass studies) of molecules targeting PPAR-γ LBD and α-amylase receptors. Thiazolin-4-one-based benzenesulphonamide hybrids (**6a-6h, Scheme 1**) were evaluated for α-amylase inhibition and PPAR-γ agonism through *insilico* and *invitro* methods. Similarly, thiazolidinone-pyrrolidine carbonitrile analogues (**5a-5j**, **Scheme 2**) were assessed (*insilico*, *invitro*, and *invivo*) using a fructose-induced insulin resistance model to investigate their insulin-sensitizing effects on glycolysis, gluconeogenesis, and glucose utilization, integrated with systems biology tools. Additionally, a ligand based drug-design (LBDD) approach guided the pharmacophore-based identification, synthesis, and characterization of quinoline-based Schiff base analogues (**6a-6j, Scheme 3**) for inhibitory effects on postprandial diabetic enzymes (α-amylase and α-glucosidase)

Results: Compound 1-(2-(5-(4-hydroxybenzylidene)-2, 4-dioxothiazolidin-3-yl) acetyl) pyrrolidine-2-carbonitrile **5b (scheme. 2)** was identified to be ameliorating hyperglycemia and hyperinsulinemia. Compound **6b (scheme. 1)** was identified to be the better inhibitor of α-*amylase* enzyme (IC_{50}: 29.51 ± 1.35 µg/mL). Further from the network pharmacology analysis, **6b** was subjected for *via* PPAR-γ TF assay and glucose uptake assay (88.71%). Similarly Further compound **6b** (**scheme. 3**) was identified as competitive inhibitor of *α-glucosidase* enzyme (IC_{50}: 19.37 ± 0.96 µM)

Conclusion: Results from the present study suggest that the designed molecular templates can be consider for further lead optimization in the management of T2DM.

Keywords: Diabetes; Thiazolidinedione's; PPAR-γ; Computer aided drug design; Network pharmacology.

Chapter 1

Introduction…

1.1. Background

Drug Design being a multifaceted field that uncovers the science behind therapeutic compounds through insights from medicinal chemistry, chemical biology and pharmacology. This facilitates the design and creation of molecules with biological interest targeting protein, enzymes, or receptors to produce a therapeutic response with minimal side effect. The goal is to design molecules that are safe, effective and tailored to treat specific disease or condition.[1-3] Traditionally drug design relied on trial and error method, wherein libraries of compounds were synthesized and screened with a hope of finding one molecule with biological interest, which accounted for financial burden, time consuming process and lesser success rates.[4] Whereas the modern drug design, being more rational, utilizes the knowledge of biological targets (SBDD) and molecular structures (LBDD), along with insights from disease mechanism (systems biology), to design drugs, which still face challenges like limited chemical space exploration, time consuming, limited flexibility in molecular modifications, and huge experimental data requirements.[5-6] Further advancements in the application of computational power to simulate and understand the behaviour of molecules interacting with biological targets have been achieved through CADD techniques, such as pharmacophore modeling, QSAR methods, MD simulations, docking studies, fragment-based drug design, system biology tools and the prediction of drug-like properties using ADMET parameters.[7-9] These tools enhance drug design through computational methods, offering significant advantages over traditional rational drug design. Hence we aimed at employing the CADD strategy to optimize, simulate, and predict the molecular mechanism of lead compounds in the present work.

DM being a complex metabolic disorder resulting in surged glycaemic levels either by impaired β-cell functions to release insulin (T1DM) and or by resistance to action of insulin by body tissues (T2DM). However the T1DM is managed by exogenous supplementation of insulin and its analogues.[10-11] Likewise the T2DM is managed by oral antidiabetic agents (**Fig. 1**), which targets various targets

involved in pathogenesis of T2DM like, insulin secretagogues (gliclazide), PTP1B inhibitors (ertiprotafib), DPP4 inhibitors (vildagliptin), SGLT2 inhibitors (empagliflozin), α-glucosidase enzyme inhibitors (acarbose) and PPAR-γ agonists (pioglitazone).[12-17] However, current pharmacotherapy interventions are associated with adverse drug reactions. For example biguanides can cause gastrointestinal side effect and lactic acidosis; Sulfonylureas carry a risk of hypoglycaemic; meglitinides have a short half-life and may also cause hypoglycaemic; gliptins are linked to nasopharyngitis, a potential risk of carcinoma of the medullary thyroid and pancreatitis; inhibitors of SGLT2 may cause infection at to the genitals, reduction in weight and diuretic effects; α-glucosidase inhibitors are associated with flatulence, and bloating; and thiazolidinedione's increased the risk of fluid retention (which can precipitate arrhythmias), obesity and bone fissure.[18-22] Thus to address these limitations, there is a need to identify and develop new molecules that can effectively trigger a therapeutic response in managing T2DM.

We identified molecules, either previously reported or marketed, that possess nitrogen and sulphur containing heterocyclic moieties, such as thaizole, isothiazole, quinoline, Benzothiazole, thiadiazole, thiazolidine, and rhodanine for their antidiabetic effect.[23-28] Thiazolidinedione is a five-membered heterocyclic ring, where nitrogen is placed at 1st and sulphur at the 3rd position, along with two carbonyl groups at the 2nd and 4th position.[29] It has been reported for its antidiabetic, anticancer, antitubercular, anti-inflammatory activity, anticonvulsant, and antioxidant activities.[30-34] These thiazolidinedione's are known to activate the PPAR-γ receptor, a well-known target of interest in pathogenesis of T2DM.[35] Likewise literature reports suggest that the thiazolidinedione's have shown prominent role in managing post-prandial hyperglycemia *via* inhibition of postprandial diabetic enzymes.[36]

Thus, in the present study (**Fig. 2**), we aimed to perform molecular hybridization of thiazolidinedione's using SBDD approach, incorporating synthons such as benzenesulphonamide,

pyrrolidine carbonitrile, and polyhydroxy compounds to design, synthesize, characterize and pharmacologically evaluate their antidiabetic activity. Additionally, LBDD approach was employed to identify, synthesize, characterize and pharmacologically assess quinoline based hits for their antidiabetic activity. Finally the probable molecular mechanisms of the identified lead molecules were proposed.

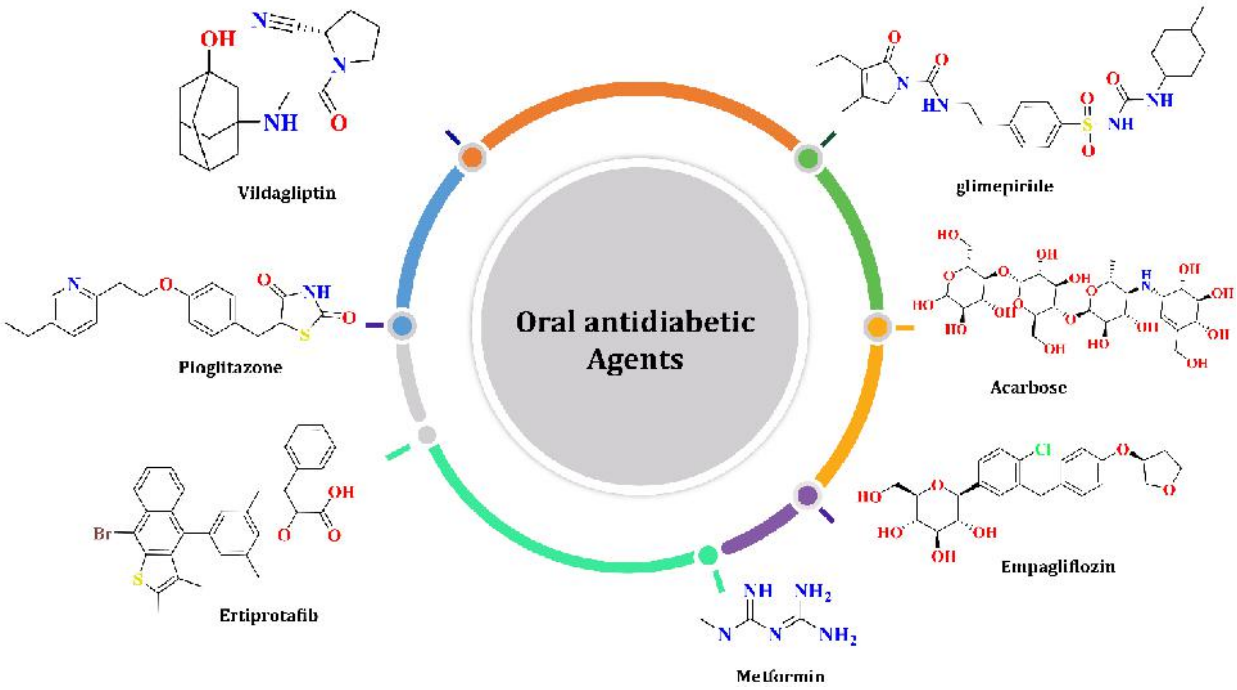


Fig. 1: Marketed antidiabetic agents.

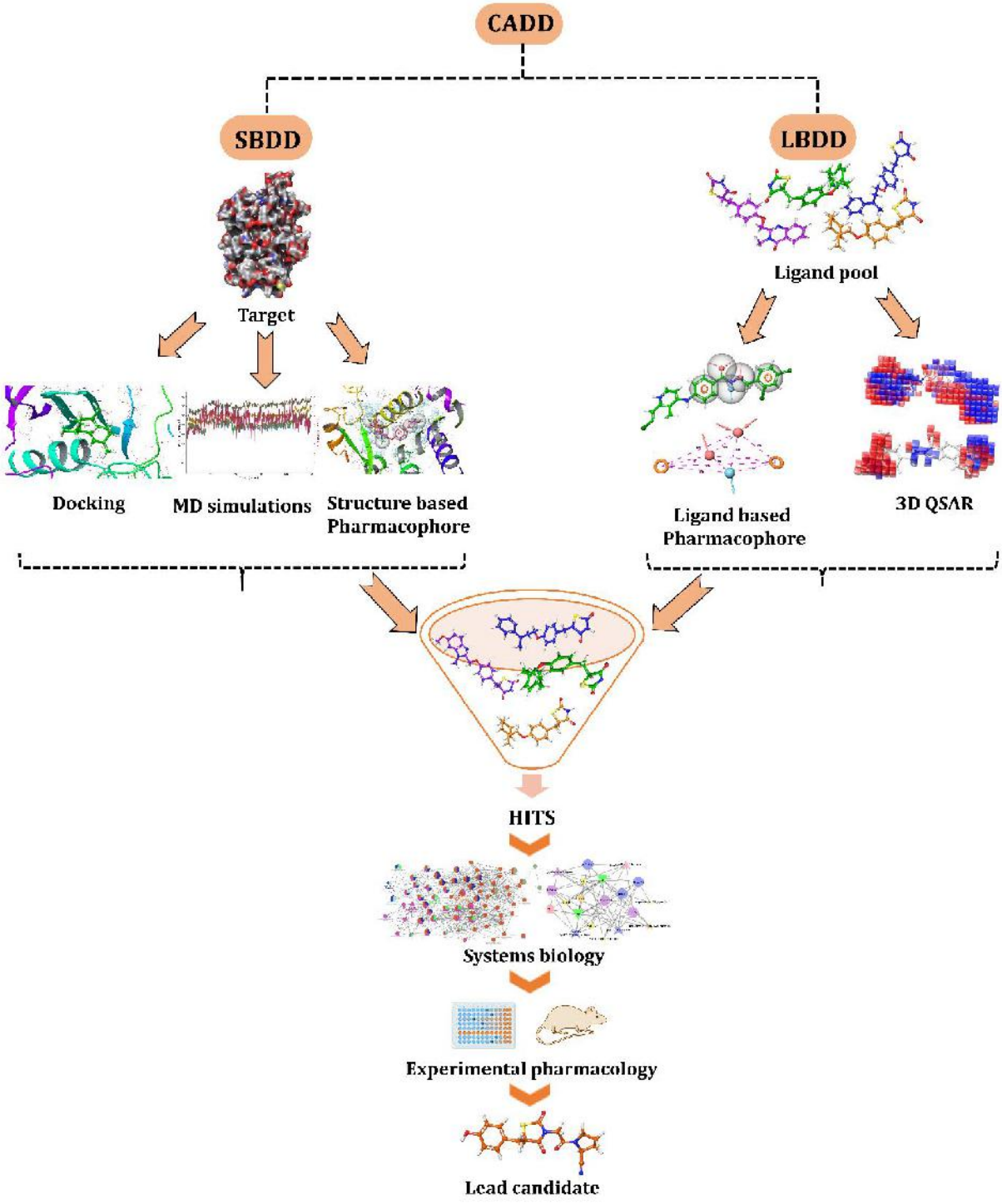


Fig. 2: A general workflow employed in the present study.

1.2. Literature Review

1.2.1. Chemistry of nitrogen and sulphur containing heterocycle and its biological relevance

The presence of nitrogen and sulphur heteroatoms in the molecular framework plays a critical role in the development of molecules targeting enzymes, receptors, and pathways such as insulin signaling, glucose metabolism, and pancreatic functions involved in T2DM. Nitrogen atoms, commonly found in functional groups like amides and amines, contribute to the binding profile of these molecules with biological targets through hydrogen bonding and ionic interactions. Similarly, sulphur atoms, in the form of sulphonamides and sulphides, enhance metabolic stability due to their redox properties. Classes of molecules like TZDs and sulfonylureas, which incorporate nitrogen and sulphur heteroatoms, are effective in managing T2DM owing to their versatile pharmacophores that target various metabolic pathways. This underscores the importance of exploring scaffolds containing nitrogen and sulphur heteroatoms to develop new leads in antidiabetic drug discovery.[37]

TZDs are a distinctive group of synthetic heterocyclic organic compounds that owe their chemical and biological properties to the presence of a thiazolidine-2,4-dione nucleus. The thiazolidine portion is a five-membered heterocyclic ring composed of one nitrogen, one sulphur and three carbon atoms.[29] The presence of sulphur and nitrogen in the ring gives it heterocyclic character, which influences both its reactivity and ability to interact with biological targets, such as enzymes and receptors. The dione in "thiazolidine-2,4-dione" refers to two ketone groups located at the 2^{nd} and 4^{th} positions of the ring. These carbonyl groups, impart polarity, enable resonance stabilization of the ring system and contribute to the molecule's acidic character, as the hydrogen attached to the nitrogen atom can be released as a proton under certain conditions, forming a stabilized anion. The acidic nature of the methylene group at position 5 allows for alkylation and other modifications.[38-39] Substitutions at the nitrogen atom (position 3) are also common and contribute to the diversity of TZD derivatives. This acidic property is essential for the compound's interaction with biological receptors, especially PPAR-γ. The thiazolidine-2,4-dione

ring is largely planar, which aids in receptor binding through π-π stacking or hydrogen bonding. The polar ketone groups and the sulphur atom create a balance between hydrophilic and hydrophobic properties, crucial for biological activity and membrane permeability.[40] Also the TZD core is responsible for (**a**) **ligand binding**: acting as the main interaction site with PPAR-γ receptors. The carbonyl groups engage in hydrogen bonds with the receptor's amino acid residues. (**b**) **Chemical Modifications**: Side chains and substituents attached to this nucleus fine-tune the molecule's pharmacokinetics (absorption, distribution, metabolism, excretion) and pharmacodynamics (activity, potency).[41] All TZDs, such as pioglitazone, rosiglitazone, and earlier drugs like troglitazone (**Fig. 3**), rely on the thiazolidine-2,4-dione nucleus. Modifications to the side chains attached to the nucleus influence the affinity for PPAR-γ receptor, selectivity toward other receptors (e.g., PPAR-α for lipid effects) and reduction in off-target effects.

Sulfonylureas have a common molecular template comprising of (-SO_2-), which relay its lipophilic nature and binding affinity to words the SUR1. Whereas the urea moiety behaves as a linker, most of the marketed drugs like glibenclamide, gliclazide (**Fig. 3**) have the sulfonyl group intact which contributes to its binding nature towards the receptor. Substituting the urea nitrogen significantly affect the molecules affinity towards the SUR1 receptor.[42]

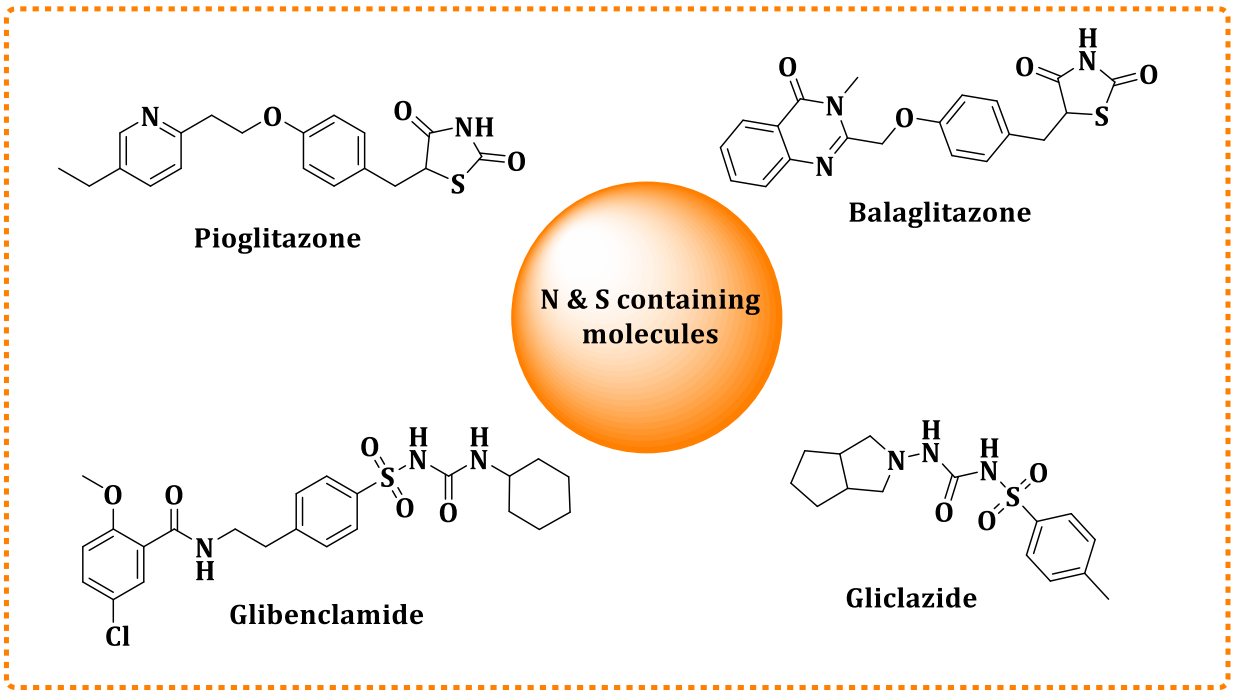
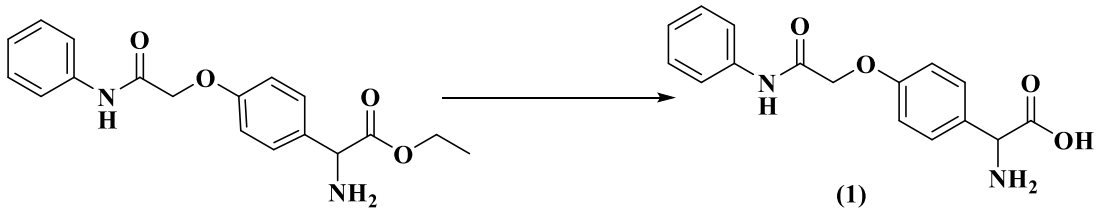


Fig. 3: Molecules containing Nitrogen and sulphur heteroatoms.

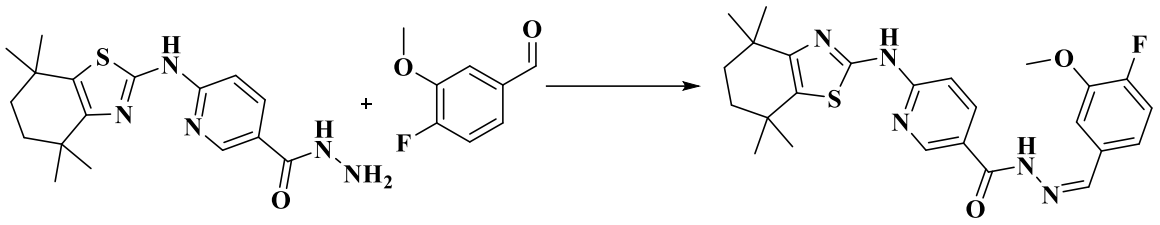
1.2.2. Antidiabetic activity

Mandal S *et al.*, have synthesised novel Nitrogen and Oxygen containing compounds as antidiabetic agents. These compounds were evaluated against PPAR-γ enzyme, among them compound (**1**) showed prominent PPAR-γ agonist activity in protein binding assay via time resolved fluorescence assay (TR-FRET) with IC_{50} value of 5.61µM.[43]



Reagents and condition: NaOH, THF/H_2O, reflux.

Patchipala S.B. *et al.*, have synthesized thiazole pyridine derivatives as antidiabetic agents. These compounds were screened for fasting blood glucose level reduction, among them compound (**2**) showed significant decrease in blood glucose level from **214.3** to **118.8** mg/dL at 10mg/kg dose.[44]



(2)

Reagents and condition: CH_3COOH, EtOH, reflux.

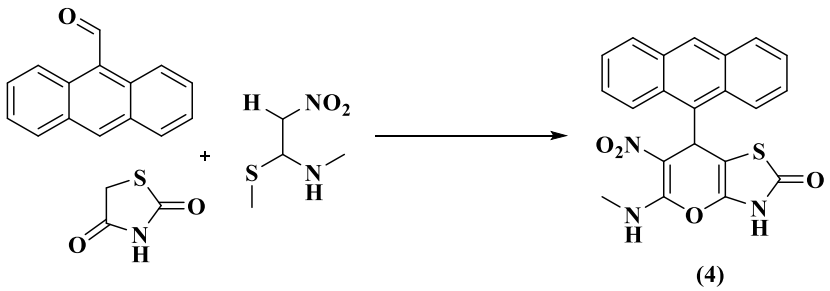
Sameeh Y.M *et al.*, have synthesised newer glitazones as Antihyperglycemic agents. Among the tested compounds against *α-amylase* enzyme, compound (**3**) had the significant inhibitory activity with IC_{50} value 11.8µg/ml.[45]



(3)

Reagents and condition: Piperidine, EtOH, reflux.

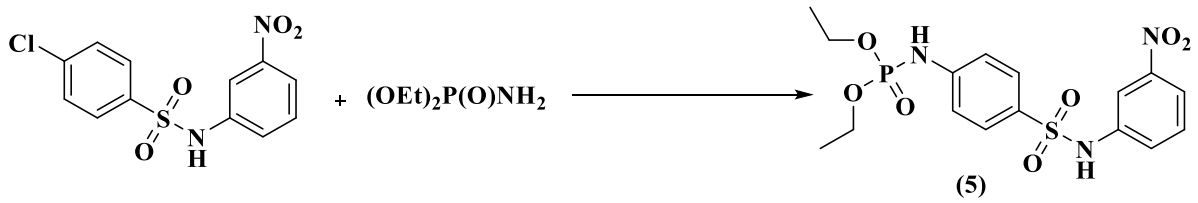
Prabhakaran S. *et al.*, have synthesised multicomponent one pot synthesis of anthracene-3-carboxaldehyde, thiazolidinedione, and substituted methylthiourea giving phenyl-pyrano-thiazole-2-one analogues as antihyperglycemic agents. These compounds were assessed for their *α-glucosidase* enzyme inhibition, among them compound (**4**) displayed good inhibition with IC_{50} value 8.85 µg/ml. [46]



(4)

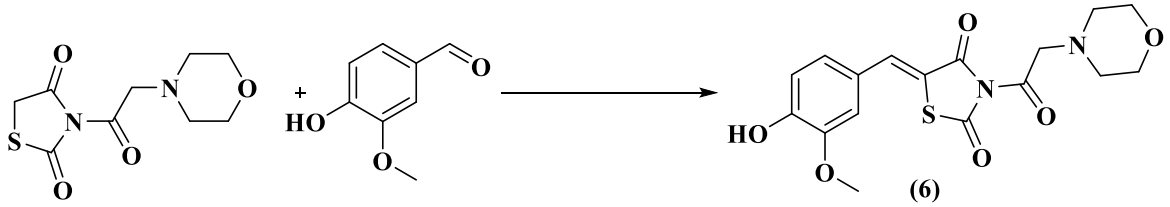
Reagents and conditions: Piperidine, ETOH, reflux.

Ravikumar D. *et al.,* have synthesised new phosphoramidate derivatives as antidiabetic agents. These compounds were examined for their *α-amylase* enzyme inhibition effect, among them compound (**5**) demonstrated inhibitory effect with IC_{50} value 42 µg/ml.[47]



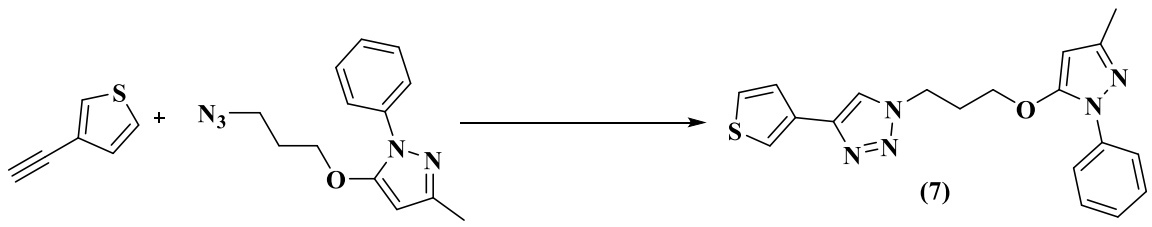
Reagents and condition: THF, Et_3N, r.t.

Huneif A.M *et al.,* have designed and synthesised glitazone-morpholine hybrid as antidiabetic agent. This compound was evaluated for its *α-amylase, α-Glucosidase*, PTP1-B and DPP4 enzyme inhibition effect. This compound (**6**) showed prominent activity against DPP4 enzyme inhibition with IC_{50} value of 0.09µM.[48]



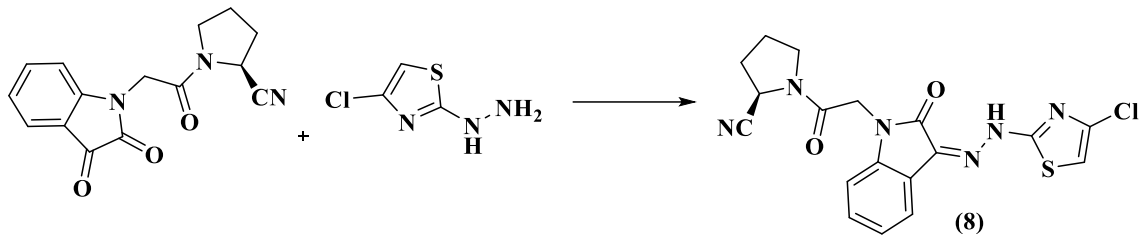
Reagents and condition: Piperidine, EtOH.

Nidhar M. *et al.,* have reported new pyrazole-triazole-persulfonimide derivatives as Antihyperglycemic agents. These compounds were tested for DPP4 enzyme inhibition, among them compound (**7**) demonstrated prominent enzyme repressive activity with IC_{50} value 4.54nM.[49]



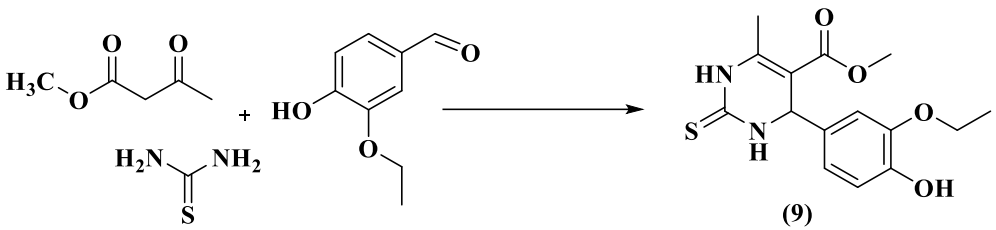
Reagents and condition: CuI/DCM, DIPEA.

Patil. S *et al.,* have synthesised isatin-Schiff's base containing thiazole analogues. These compounds were assessed for *α-glucosidase* enzyme inhibition effect, among them compound (**8**) produced significant enzyme repressive activity with IC_{50} value **28.43 ± 0.33 µg/mL**.[50]



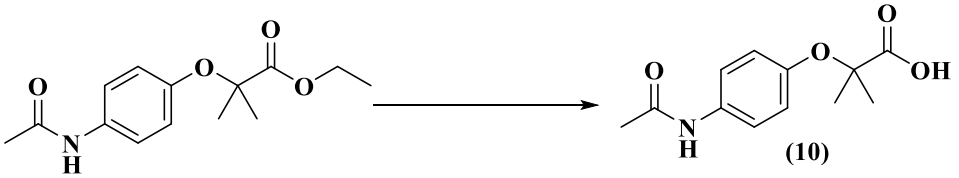
Reagent and condition: CH3COOH, MeOH, reflux.

Bairagi M.K. *et al*., have synthesised dihydropyrimidine based derivatives as antidiabetic agents. These compounds were tested for Antihyperglycemic activity, among them compound (**9**) showed better hypoglycaemic effect with reduction in blood glucose level by 21.76%.[51]



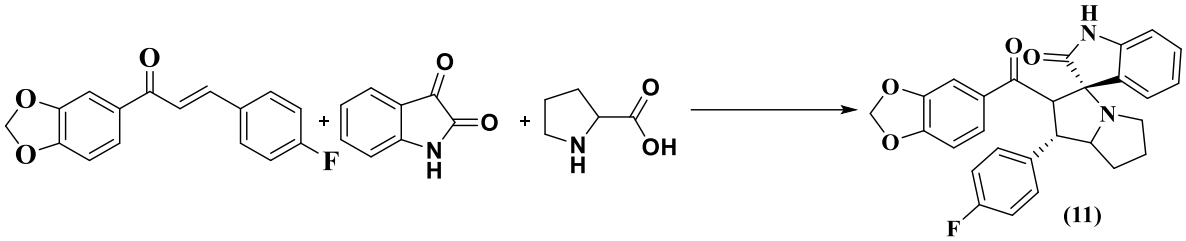
Reagents and condition: CH_3COOH, reflux.

Lozano C. B *et al.,* have synthesised isobutyric acid derivatives as PPAR-γ regulators. These compounds were tested for PPAR- γ and GLUT-4 expression, among them compound (**10**) showed significant glycaemic lowering effect of 50.1% and PPAR- γ expression level fold of 3.89 at 10 µM. [52]



Reagents and condition: LiOH/THF, 10%, HCl.

Nivetha. N *et al*., have synthesised Pyrrolidine and Pyrrolizidine containing spirooxindole hybrids as antihyperglycemic analogues. These compounds were evaluated against *in vitro* post-prandial diabetic enzyme. Among them compound **(11)** showed prominent inhibition effect IC_{50} value **32.40** ± **0.86** and **10.00 ± 0.16 µg/ml** respectively.[53]



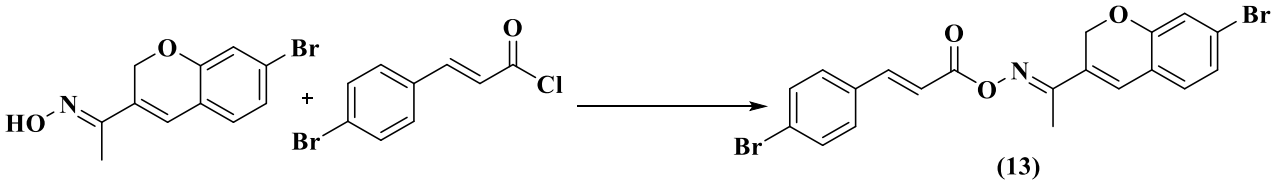
Reagents and condition: MeOH, reflux.

Wahid Sana. *et al.*, have synthesized nitrofurazone as antidiabetic agents. These compounds were screened against *in vitro α-glucosidase* enzyme, among them compound **(12)** showed significant repressive activity with IC_{50} value **0.63 ± 0.25 µg/ml**.[54]



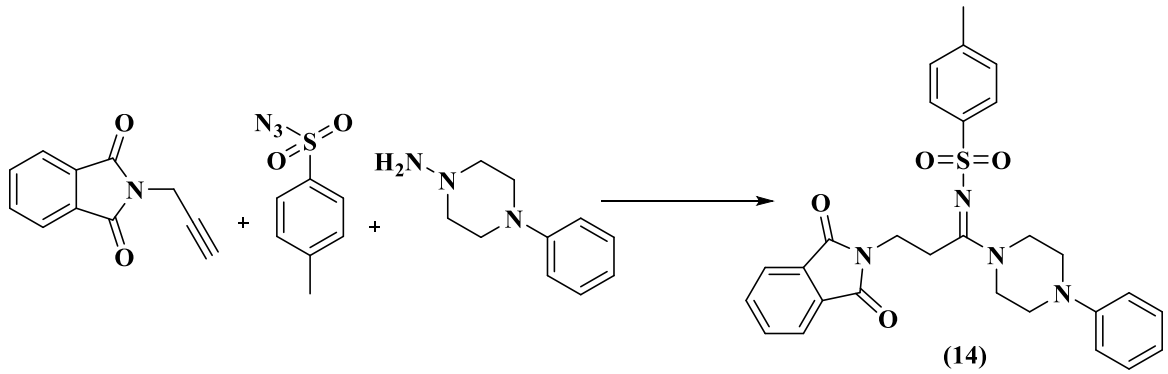
Reagents cand condition: K_2CO_3, DMF, reflux.

Zang kin *et al.*, have synthesised newer Coumarin based oxime esters as Antihyperglycemic agents. These compounds were evaluated against *α-glucosidase* enzyme, among them compound **(13)** showed prominent inhibitory effect with IC_{50} value **2.54 ± 0.25 µg/ml**.[55]



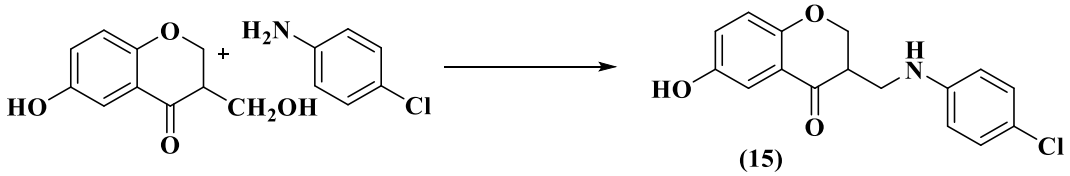
Reagents and condition: DCM, TEA.

Askarzadeh M. *et al.,* have synthesised multicomponent one pot synthesis of phthalimide-benzesulfonamide derivatives. These compounds were screened for their *α-glucosidase* enzyme inhibition effect, among them compound **(14)** displayed prominent inhibitory effect with IC_{50} value **52.2 ± 0.1 µM**.[56]



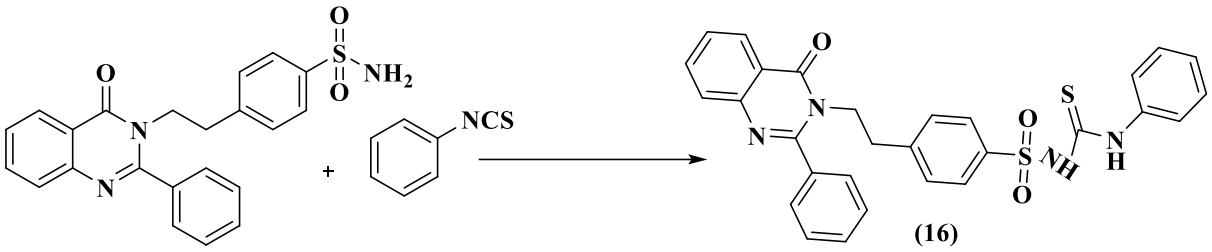
Reagent and condition: TEA, CuI, ACN, rt.

Meyan F. *et al.,* have synthesised new 2-phenyethyl) chromone derivatives as antidiabetic agents. These compounds were examined for *α-glucosidase* enzyme repressive effect, among them compound **(15)** displayed remarkably inhibition of the postprandial diabetic enzyme with IC_{50} value of **11.72 ± 0.1 µg/ml**.[57]



Reagent and condition: $CHCl_3$, Sodiumtriacetoxy borohydride, r.t.

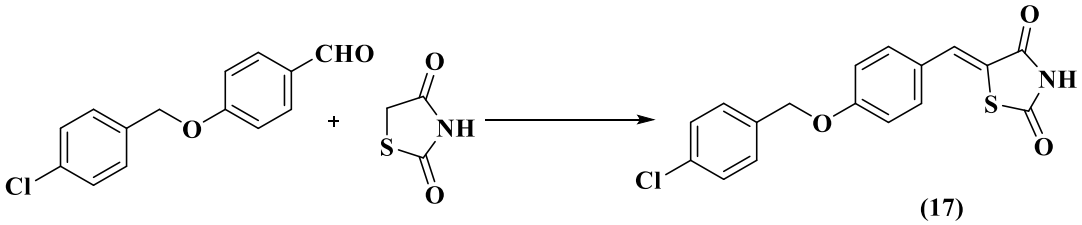
El-Zahabi A.M *et al.,* have designed and synthesised quinazoline-sulfonylurea hybrid as antidiabetic agent. This compound was assessed for its *Invivo* antidiabetic effect. This compound **(16)** displayed prominent activity with significant blood glucose lowering property with **78.2%** at a concentration of **2mg/kg**.[58]



(16)

Reagents and condition: K_2CO_3, acetone.

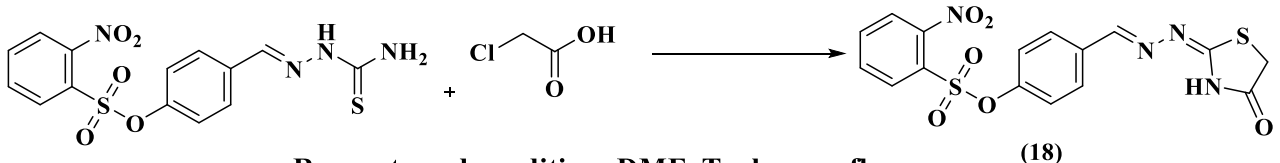
Madrigal-Angulo JL, *et al*., have designed and reported hypoglycaemic and lipid lowering effects of thiazolidine-2, 4-dione clubbed with benzyloxy moiety for modulating PPAR-γ, among them compound **(17)** showed prominent PPAR-γ agonist activity with EC_{50} value **23.01 ± 31** µg/ml.[59]



(17)

Reagents and condition: Piperdine, Toulene, reflux.

Kaur R *et al*., have synthesised hydrazolyl linked sulfonate ester analogues of 4-thiazolidinone analogues by one pot synthesis. These compounds were examined for *α-glucosidase* enzyme repressive activity, among them compound **(18)** displayed significant enzyme inhibition activity with IC_{50} value **42.80 µM**.[60]

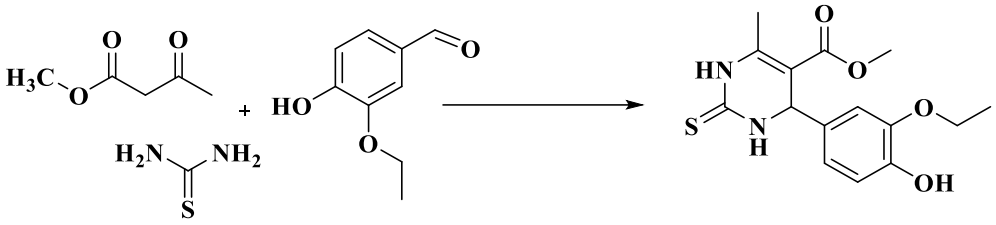


(18)

Reagents and condition: DMF, Toulene, reflux.

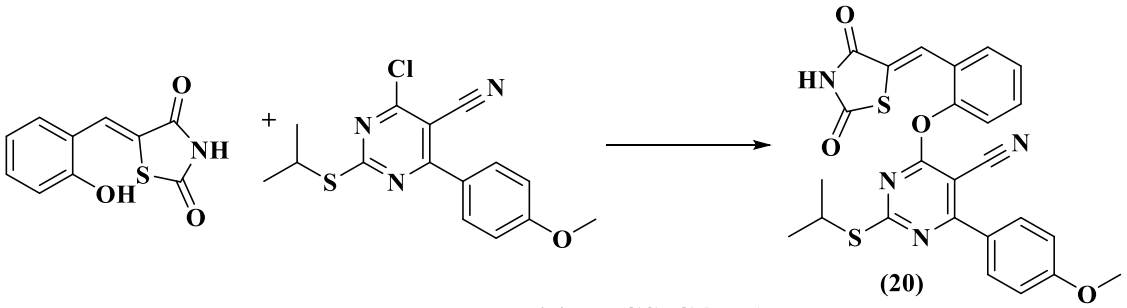
Bairagi M.K. *et al*., have synthesised dihydropyrimidine based derivatives as antidiabetic agents. These compounds were tested for Antihyperglycemic activity, among them compound **(19)**

showed better hypoglycaemic effect with reduction in blood glucose level by **21.76%** at a concentration of **50mg/kg**.[61]



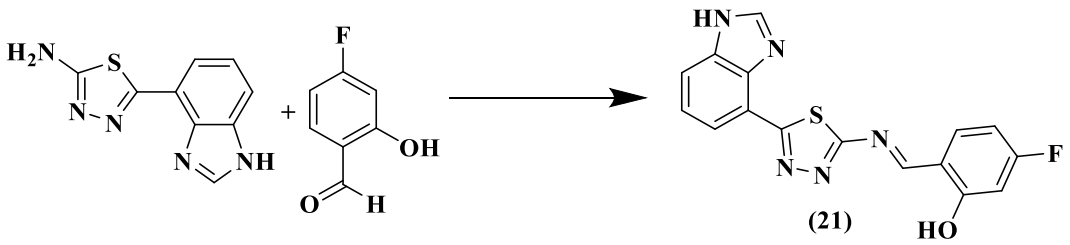
Reagents and condition: CH_3COOH, EtOH, reflux. **(19)**

Shaista Amin *et al*., have reported pharmacological assessment of pyrimidine clubbed thiazolidinedione hybrids as antidiabetic agents. Among the synthesized compounds, the compound **(20)** shown reduced blood glucose concentration at **145.2±1.35** at a concentration of **3mg/kg.**[62]



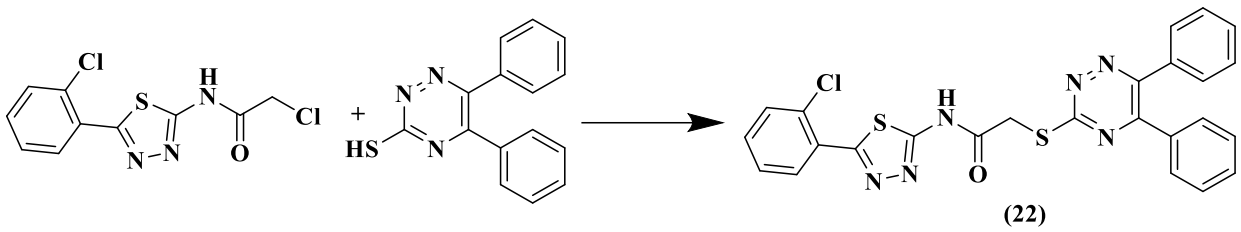
Reagents and condition: CS_2CO_3, Acetone.

Khan S *et al*., revealed series of benzimidazole-thiadiazole hybrids as postprandial antidiabetic agents. Among them, Compound **(21)** showed potent dual inhibitory effect on post-prandial diabetic enzymes with IC_{50} value **1.10±0.10** and **2.10±0.10 µM** respectively.[63]



Reagents and condition: CH_3COOH, MeOH, reflux.

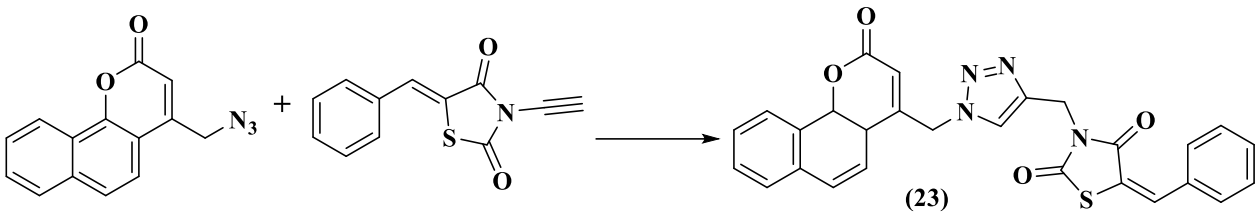
Kumar H *et al*., reported series of thiadiazole-traizine hybrids as new antidiabetic hybrids. These molecules were examined for their postprandial antidiabetic effect. Among them, **(22)** showed prominent *α-glucosidase* inhibition effect with IC_{50} value **14.36 µM**.[64]



(22)

Reagent and condition: K_2CO_3, ACN, reflux

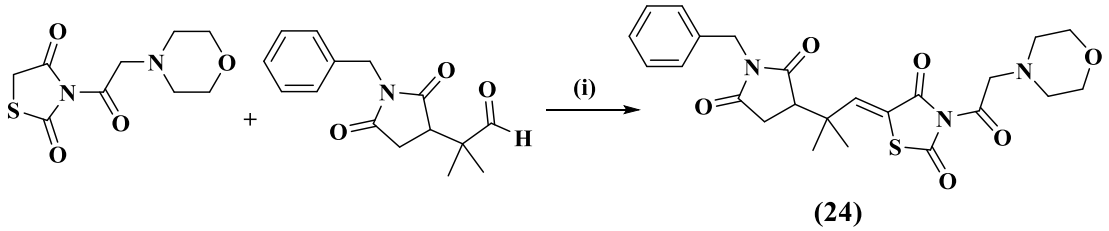
Metre T *et.al*., have reported a series of coumarin-thiazolidine-2,4-diones hybrids against insulin resistance. Among them, compound **(23)** exhibited better Glucose uptake activity with **93.25%** compared with Pioglitazone **94.0%**. Molecular docking was performed on PPAR-gamma receptor.[65]



(23)

Reagents and conditions: THF: H_2O, $CuSO_4$, Sodium Ascorbate, r.t.

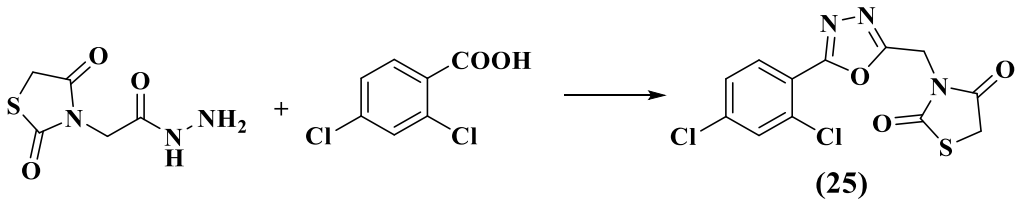
Mohammed A *et al*., reported newer succinimide-thiazolidinedione analogues as antidiabetic agents. The synthesized compounds were further evaluated for DPP-4 inhibition. Among those, compound **(24)** has shown DPP-4 repressive activity with IC_{50} value **4.22 ± 0.36** µM respectively.[66]



(24)

Reagent and Condition: Toulene, Piperdine-acetate, reflux.

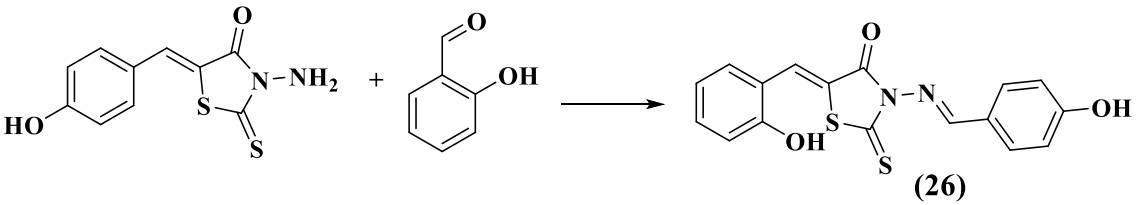
Mahendra. *et al*., has reported newer analogues of thiazolidinedione-oxadiazole as postprandial antidiabetic agents. These compounds were evaluated for postprandial enzyme inhibition. Among them, compound **(25)** displayed *α-amylase* and *α-glucosidase* repressive activity with IC_{50} values **18.42 ± 0.21** and **17.21 ± 0.22 µM** respectively.[67]



(25)

Reagents and Condition: $POCl_3$, reflux.

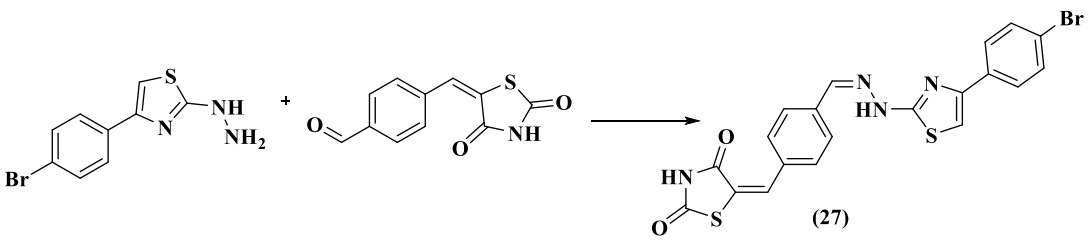
K Martin *et al*., have reported novel rhodanine based inhibitors as antidiabetic agents. These hybrids were studied for their aldose reductase activity. Among them, compound **(26)** showed good aldose reductase repressive effect with IC_{50} value of **22 µM**.[68]



(26)

Reagent and Condition: CH_3COOH, EtOH, reflux

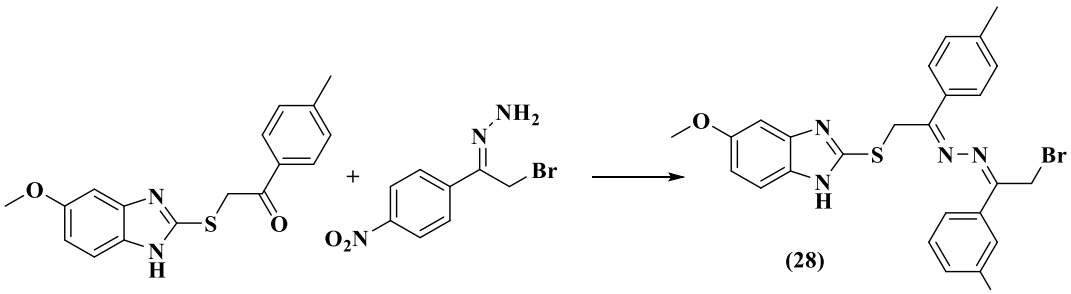
Gharge S *et al*., reported thiazole-rhodanine derivatives as potent antidiabetic agents. These derivatives were examined for their *α-glucosidase* inhibition. Among them, compound **(27)** shows prominent *α-glucosidase* inhibition with IC_{50} value **27.13 ± 1.02 µM** respectively.[69]



(27)

Reagent and conditions: CH_3COOH, MeOH, reflux.

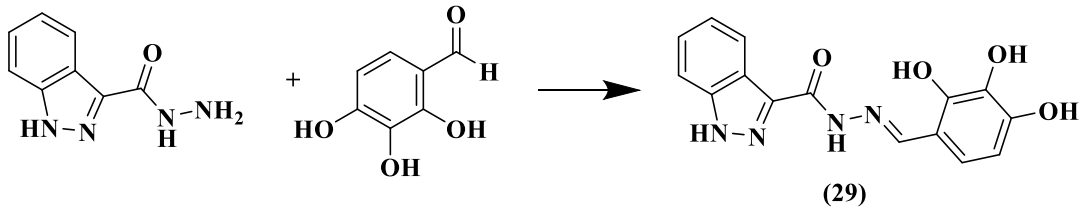
Shawkat Hayat *et al*., have synthesised Schiff's base containing benzimidazole analogues as antidiabetic agents. These molecules were assessed against *α-glucosidase* enzyme. Among them compound **(28)** showed prominent repressive effect with IC_{50} value **38.60 ± 0.20 µM**.[70]



(28)

Reagents and Conditions: CH_3COOH, MeOH, reflux.

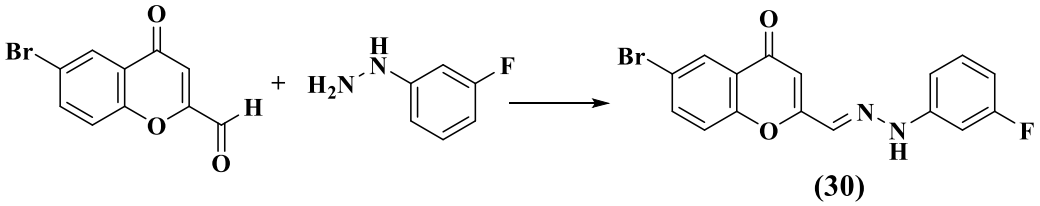
Muhammad Taha. *et al*., have synthesized novel schiff base containing indazole as antidiabetic agents. These compounds were screened against post-prandial inhibitory effect, among them compound **(29)** showed significant *α-glucosidase* and *α-amylase* inhibitory activity with IC_{50} value **0.40 ± 0.01** and **0.70 ± 0.01 µM** respectively.[71]



(29)

Raegent and condition: MeOH /CH_3COOH, reflux

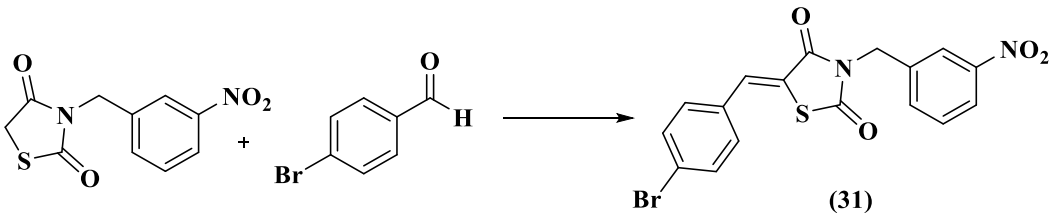
Meiyan Fan *et al*., have synthesised newer chromone-based phenylhydrazone as Antihyperglycemic agents. These compounds were evaluated against *α-glucosidase* enzyme. Among them, molecule **(30)** showed inhibitory activity with IC_{50} value **6.59 ± 0.09 µM**.[72]



(30)

Reagent and condition: EtOH, CH_3COOH, reflux

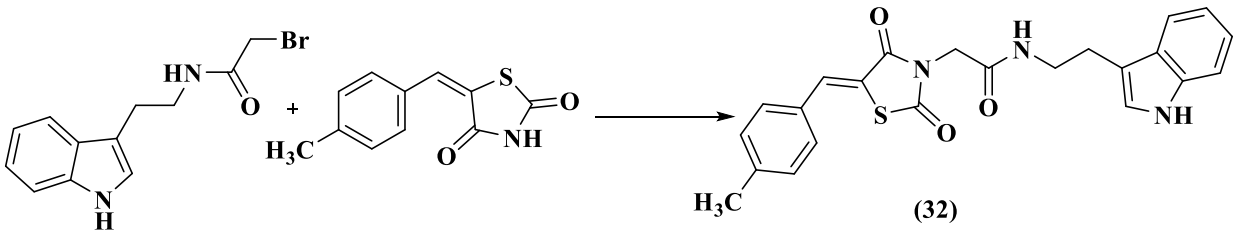
Gurpreet Singh. *et al*., reported novel thiazolidinedione analogues as antidiabetic agents. These compounds were examined for their post-prandial diabetic enzyme inhibitory activity. Among them, compound **(31)** showed *α-amylase* and *α-glucosidase* repressive effect with IC_{50} value **10.33 ± 0.11** and **10.19 ± 0.25 µM** respectively.[73]



(31)

Regents and Condition: EtOH, Piperdine, CH_3COOH, reflux

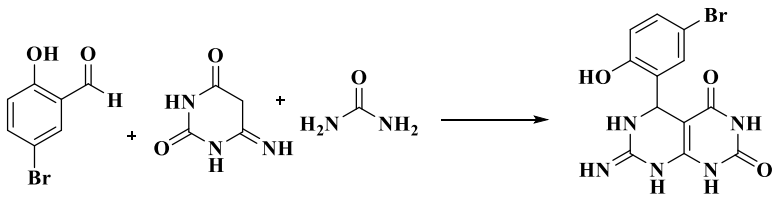
Chunmei Hu *et al*., synthesised newer indole based thiazolidinedione derivatives as antidiabetic agents. These compounds were examined for their *α-glucosidase* enzyme repressive effect, among them compound **(32)** showed inhibition effect with IC_{50} value **11.72 ± 0.1 µg/ml**.[74]



(32)

Regents and Condition: K_2CO_3, DMF, 90°C.

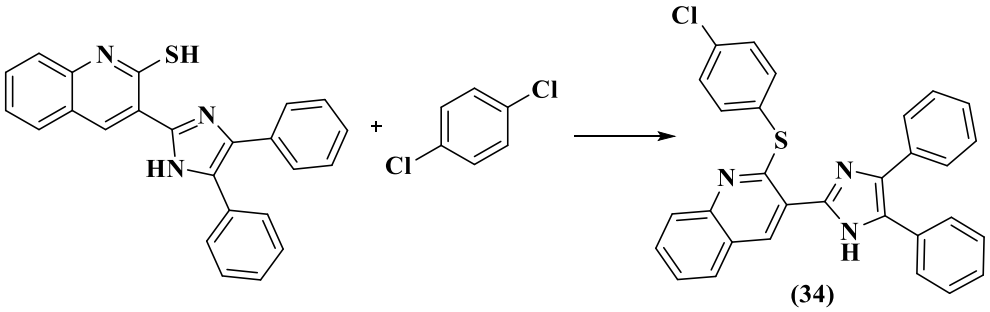
Vinuta Kamat *et al*., have synthesised dihydropyrimidinones analogues *via* one pot Biginelli reaction as antidiabetic agent. These compound was evaluated for its *invitro* dual *α-glucosidase* and *α-amylase* enzyme repressive effect. This compound **(33)** showed prominent effect with IC_{50} value **1.1 ± 0.06** and **1.08 ± 0.42 µg/ml** respectively.[75]



(33)

Reagents and condition: WELPSA (Water Extract of the Lemon Peel-Soaked Ash), EtOH:H_2O (8:2), rt

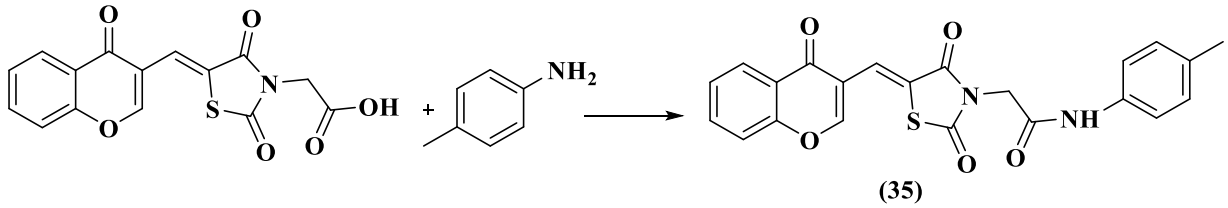
Anita Azmi *et al*., have designed and reported hypoglycaemic effect of imidazole-bearing thioquinoline derivatives mediated by *invitro α-glucosidase* activity, among them compound **(34)** showed *α-glucosidase* repressive effect with EC_{50} value of **12.01 ± 0.2** µg/ml.[76]



(34)

Regents and Conditions: K_2CO_3, DMF; reflux.

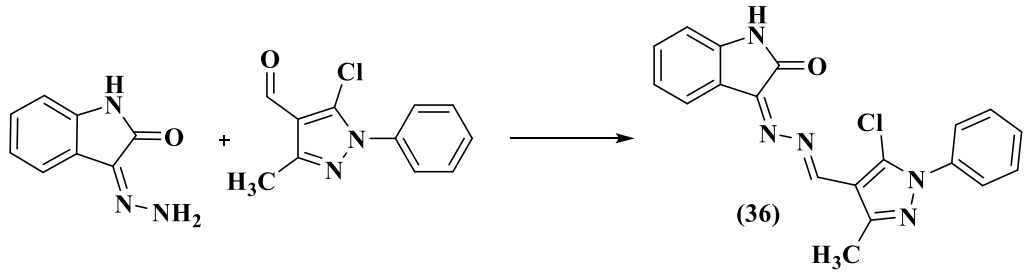
Yingying Zheng *et al*., have synthesised chromone hybrids bearing thiazolidine-2,4-dione nucleus as antidiabetic agents. These compounds were assessed for PTP1B enzyme inhibition activity, among them compound **(35)** showed significant PTP1B enzyme repressive activity with IC_{50} value of **1.40 ± 0.04** µM.[77]



(35)

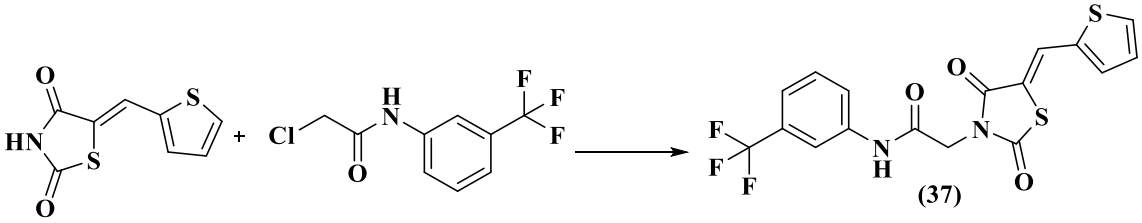
Regents and Condition: EDCI, Pyridine; rt.

Ashraf S. Hassan. *et al*., have synthesised isatin-based Schiff bases derivatives as antidiabetic agents. These compounds were tested against *α-amylase* enzyme. Among them compound **(36)** showed *α-amylase* enzyme inhibition effect with IC_{50} value **57.34 ± 0.13 µM**.[78]



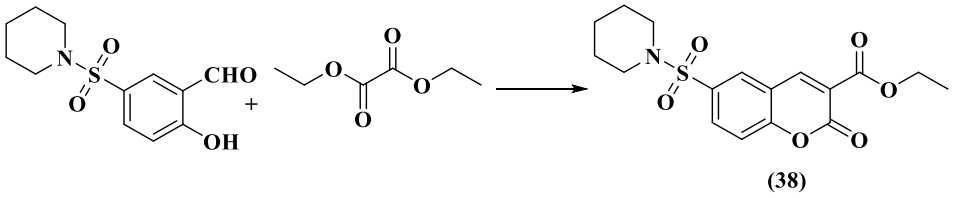
Regents and Condition: EtOH, CH_3COOH, reflux.

Mahendra G. S. *et al*., have synthesised novel thiazolidinedione analogues as PPAR-γ modulators. These compounds were tested for PPAR- γ transcription factor expression *invitro* and *Invivo*, among them compound (**37**) showed significant glycaemic lowering effect of **108.04 ± 4.39** at a concentration of **50mg/kg** .[79]



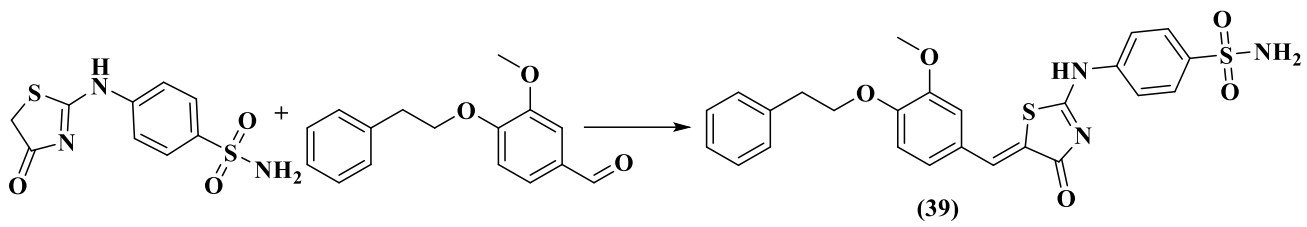
Reagents and Condition: K_2CO_3, DMF, 90°C.

Thabet H. K. *et al*., have synthesised 2H-chromene-based sulphonamide hybrids as antidiabetic agents. These molecules were evaluated against PPAR-γ enzyme. Among them compound **(38)** showed prominent PPAR-γ enzyme agonist activity with IC_{50} value **3.453 ± 0.14 µg/ml**.[80]



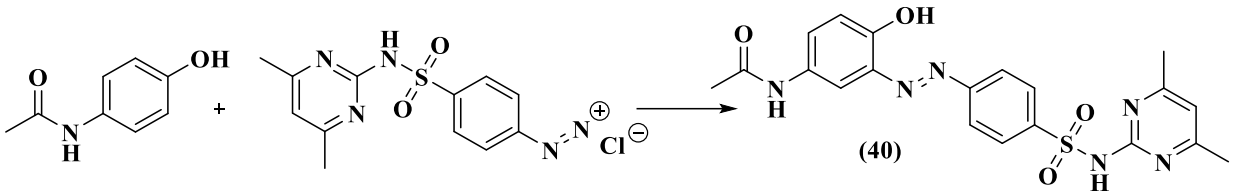
Reagents and Condition: EtOH, Piperdine, reflux.

Ali I. H. *et al.*, have synthesized novel thiazolidinone benzenesulfonamide arylidene analogues as antidiabetic agents. These compounds were screened for *in vitro* PPAR-γ enzyme agonist, among them compound **(39)** showed significant activation of PPAR-γ enzyme with 31.7%.[81]



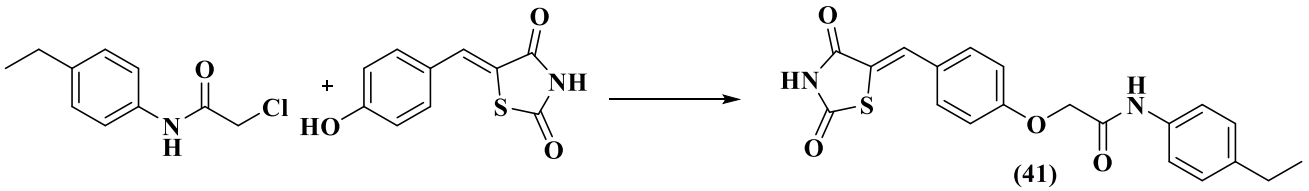
Reagents and condition: CH_3COONa/CH_3COOH, reflux.

Thabet H. K. *et al.*, have synthesised newer paracetamol based sulfa analogues as antidiabetic agents. These compounds were evaluated against *α-glucosidase* enzyme. Among them compound **(40)** showed *α-glucosidase* inhibitory activity with IC_{50} value **5.13 ± 0.082 µM**.[82]



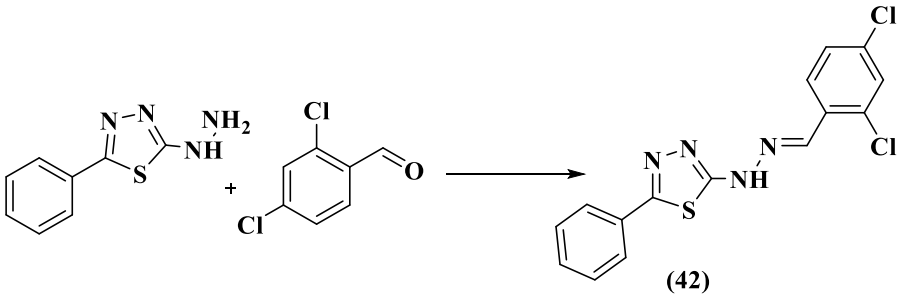
Reagent and condition: Na_2CO_3, NaOH, r.t

Gharge S. *et al*., have reported novel thiazolidinedione derivatives as antidiabetic agents. These compounds were assessed for their GLUT translocation activity, among them compound **(41)** showed good glucose uptake with IC_{50} value of **83.2 %**.[38]



Reagents and Condition: K_2CO_3, ACN, reflux.

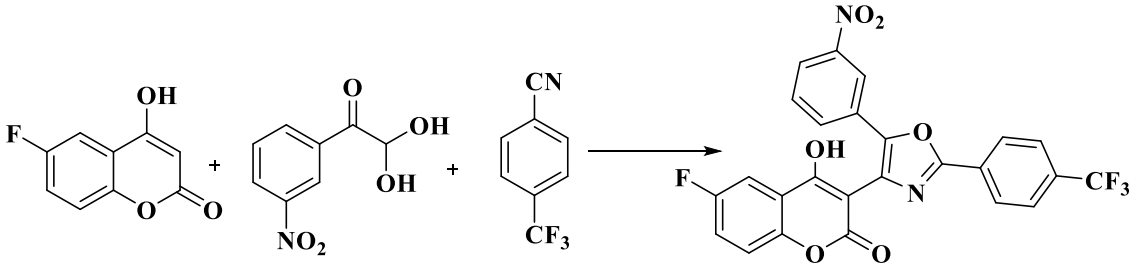
Ali Z. *et al*., have synthesised new 1, 3, 4-thiadiazole-bearing Schiff derivatives as antidiabetic agents. These molecules were assessed against *α-glucosidase* enzyme. Among them compound **(42)** showed inhibitory activity with IC_{50} value **2.02 ± 0.10 µM**.[83]



(42)

Reagents and Condition: MeOH, CH_3COOH, reflux.

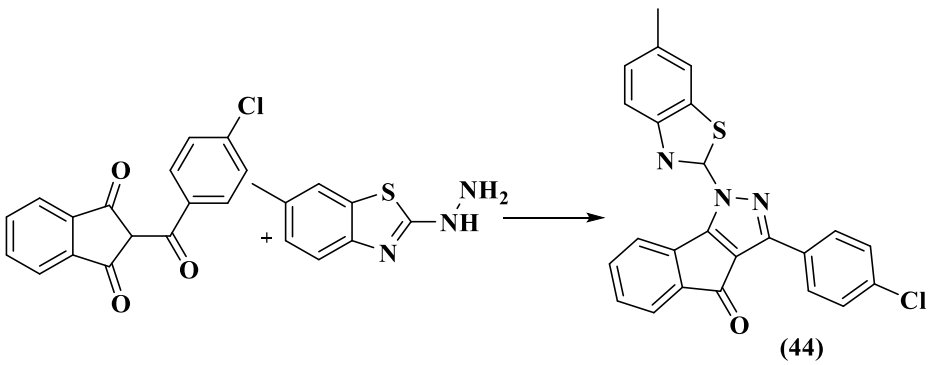
Hussain R. *et al*., have designed and synthesised coumarin-based oxazole derivatives as antidiabetic agent. These molecules were assessed against *α-glucosidase* enzyme. Among synthesized derivatives, compound **(43)** showed prominent inhibitory effect with IC_{50} value **0.70 ± 0.05**.[84]



(43)

Reagent and condition: Trifluroacetic acid, reflux

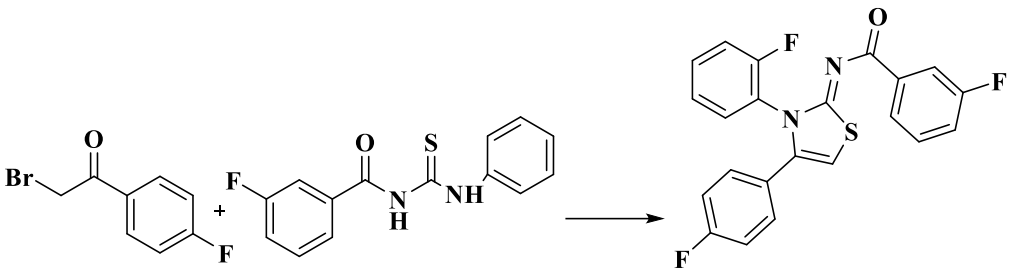
Punia R. *et al.*, have designed and reported antidiabetic effect of indenopyrazolones bearing benzothiazole derivatives mediated by *invitro α-Glucosidase* activity. Among them compound **(44)** showed α-*glucosidase* repressive activity with IC_{50} value **92.99 ± 1.94** µg/ml.[85]



(44)

Reagents and Condition: EtOH, CH_3COOH, reflux.

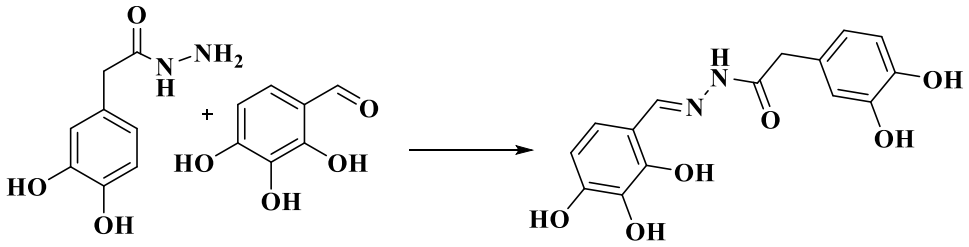
Zahid L. U. *et al*., have synthesised 2-imino-1,3-thiazolines hybrids as antidiabetic agents. These molecules were tested against *α-glucosidase* enzyme. Among them, compound **(45)** displayed significant *α-glucosidase* enzyme repressive effect with IC_{50} value **1.47 ± 0.05** µM.[86]



(45)

Regents and Condition: EtOH, reflux.

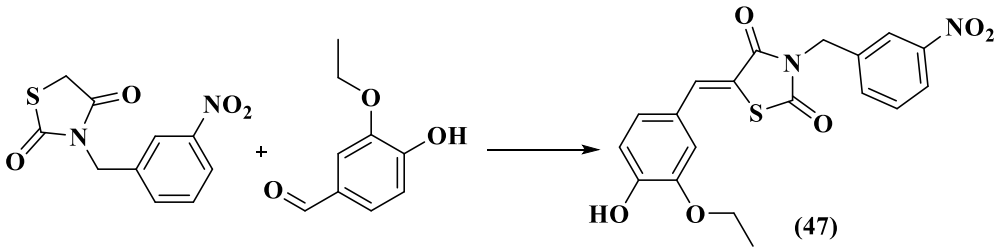
Khan H. *et al*., have synthesised hydrazide–hydrazone analogies of 3, 4-dihydroxyphenylacetic acid as antidiabetic agents. These compounds were tested for postprandial hyperglycemia inhibition, among them compound **(46)** showed *α-glucosidase* enzyme repressive effect with IC_{50} value **12.84 ± 0.52 µM**.[87]



(46)

Reagents and Condition: EtOH, CH_3COOH, reflux.

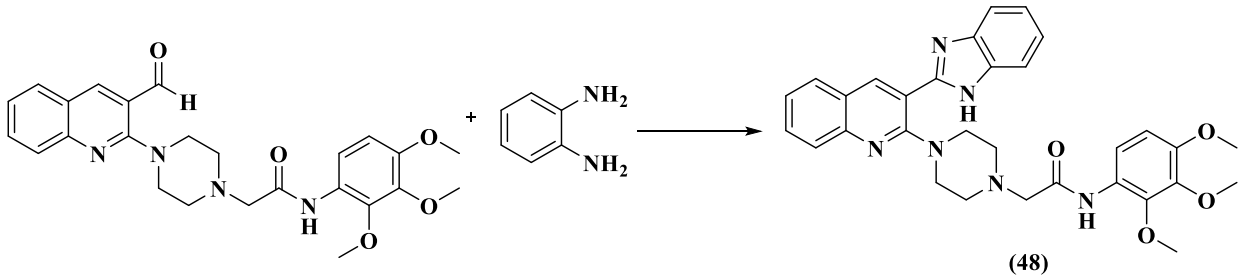
Singh G *et al*., have synthesised novel 3, 5-Disubstituted-thiazolidinedione analogues as antidiabetic agents. These compounds were tested against *α-glucosidase* and *α-amylase* enzyme. Among them, compound (**47**) showed significant repressive effect against *α-glucosidase* and *α-amylase* with IC_{50} value **10.33± 0.11** and **10.19 ± 0.25 µg/mL** respectively.[88]



(47)

Reagents and Condition: MeOH, Pyridine, reflux.

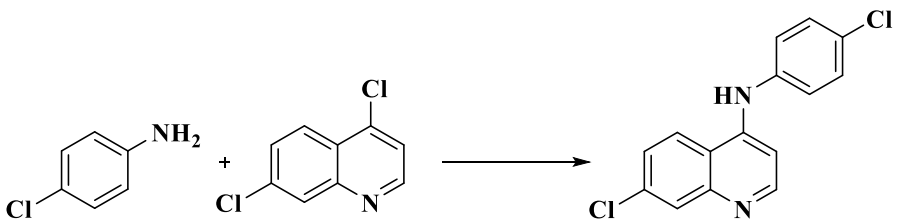
Ghasemi M *et al*, have reported quinoline based benzimidazole hybrids as antidiabetic agents. All the synthesized molecules were screened for inhibition of postprandial diabetic enzyme. Among them, compound (**48**) showed better inhibitory effect against *α-glucosidase* enzyme with IC_{50} value **2.0 ± 0 µM.**[89]



(48)

Reagents and condition: $Na_2S_2O_5$, DMF.

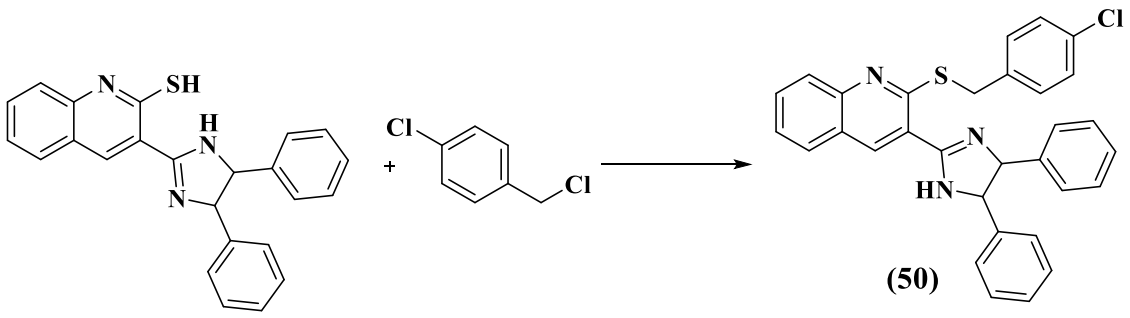
Cele N *et al*, have reported quinoline-arylamine analogues as antidiabetic agents, all the synthesized molecules were screened against *α-glucosidase* enzyme. Among them, compound (**49**) displayed enzyme inhibitory effect with IC_{50} value **41.45 µM.** [90]



(49)

Reagents and condition: *i*PrOH, 80°C

Azmi A *et al,* have reported thioquinoline based imidazole hybrids as postprandial antidiabetic agents, all the synthesized molecules were tested against *α-glucosidase* enzyme. Among them, compound (**50**) displayed enzyme inhibitory effect with IC_{50} value **41.45 µM.**[91]



(50)

Reagents and Condition: K_2CO_3, DMF

1.3. Justification

One of the most widespread 'silent killers' is DM, which has an alarming global prevalence and impact. As per the IDF atlas 2023, Diabetes today affects around 10.5% of adults globally, totalling 537 million people. This figure is projected to surge to 643 million and 783 million by 2030, and 2045 respectively. About deaths reported in 2021 was about 6.7 million, accounting for more than 12% of global mortality by diabetes.[92] The growth in T2DM has been connected to ageing populace, urbanisation, reduced physical activity, and growing obesity epidemic.[93-94] The epidemic of T2DM highlights an urgent need for more effective and targeted therapies. However the current therapies are associated with setbacks such as adverse effects, resistance to drug therapies, secondary failure of drugs, also comorbidities such as obesity and cardiovascular diseases along with metabolic dysfunctioning make it onerous to manage diabetes.[95] Also diabetes with its heterogeneous pathophysiology, involves multiple molecular mechanisms, including defected β-cell functions, resistance to insulin, enhanced gluconeogenesis, and chronic inflammation.[96] Thus medicinal chemistry can aid in designing small molecules and approaches, including SAR studies and CADD, can be leveraged to develop drugs with

fewer adverse effects, enhanced efficacy and better biotherapeutics that specifically target these pathways. The complexity and growing prevalence of T2DM underscore the critical need for ongoing research in diabetic drug discovery, with a particular emphasis on medicinal chemistry.[97-98] This discipline is integral to the rational design of novel agents, optimization of existing therapies, and exploration of innovative strategies to combat this multifaceted disease.

Thus in present research work, we aimed at targeting PPAR-γ receptors along with *α-amylase* and *α-glucosidase* enzyme which presents a promising avenue for T2DM drug discovery. However, the associated challenges, including the need for selectivity and reduced side effects, underscore the importance of advanced medicinal chemistry approaches. Thus by leveraging cutting-edge techniques like CADD and systems biology approach, we have designed novel PPAR-γ modulators, and inhibitors of enzyme involved in postprandial diabetes, that address the unmet needs in T2DM therapy, providing safer and more effective treatment options for patients worldwide.

1.4. Aims and objectives

AIM:

To carry out synthesis, Characterization and Antidiabetic activity of Nitrogen and Sulphur containing Heterocyclic compounds.

OBJECTIVES:

1. To perform synthesis & characterization of nitrogen and Sulphur containing heterocyclic hybrids
2. To perform molecular docking studies and predict possible interactions of ligand and selected protein target.
3. To evaluate antidiabetic activity of newly synthesized compounds.

Chapter 2

Materials and Methods…

The following approaches were used to design, synthesize, and characterize the title compounds *via* Further to predict and validated the antidiabetic activity of these synthesized compounds *via* the execution of *insilico*, *invitro* and *invivo* pharmacology techniques were employed (**Fig.4**)

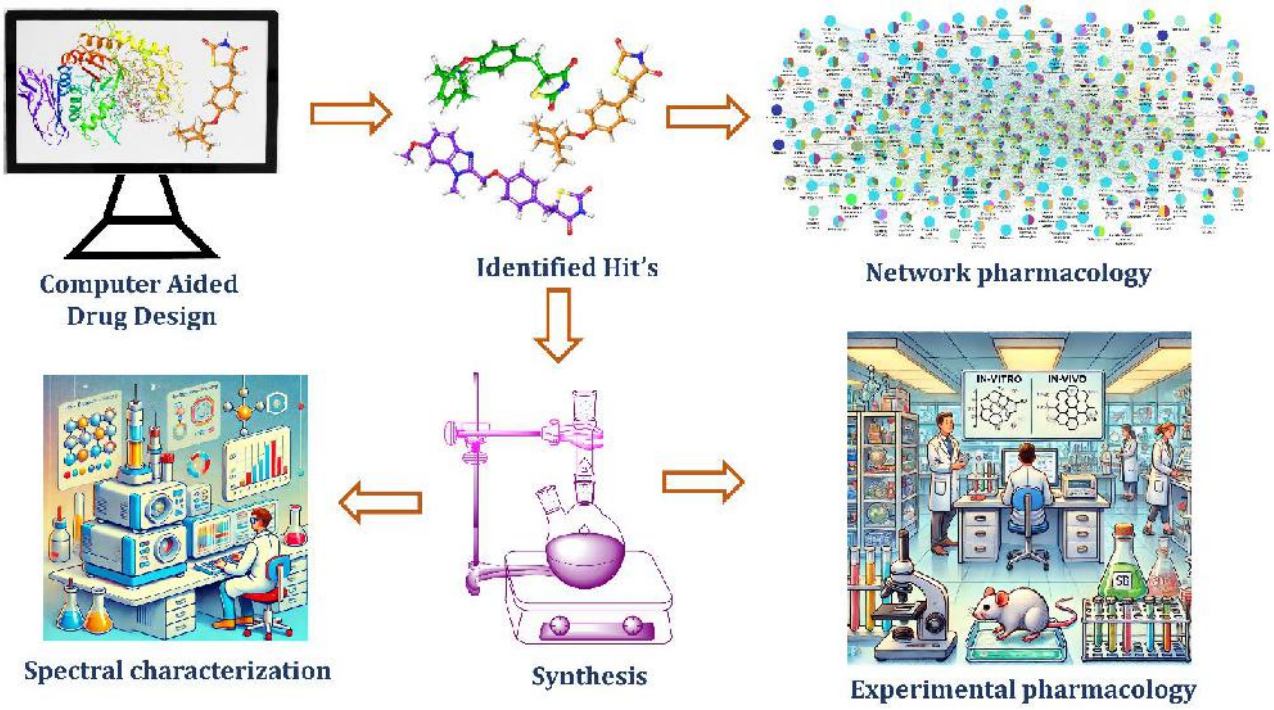


Fig. 4: Brief outline of study methods used in the identification of antidiabetic agent in present study**.**

1. *Insilico* studies

1.1. Protein preparation

In the present work, protein preparation workflow was employed. The crystal structure of macromolecules were retrieved *via* PDB ID corresponding to PPAR-γ receptor (PDB ID: 5U5L)[99], and α-amylase enzyme (PDB ID; 4W93).[100] whereas the *α-glucosidase* enzyme (considered for homology modelling *via* the sequence with accession id: P53341 and template PDB ID: 3A47 in FASTA format). Macromolecules were subjected to addition of polar hydrogen, correcting and assigning the bond orders with respect metals and nonmetals, generating disulphide bonds, terminal oxygen atoms were added to the protein side chains, selenomethionines conversions, filling missing side chain and loops, followed

by generation of ionization states using Epik tool. The macromolecules were optimized for altered hydrogen species using PROPKA mode, finally all the macromolecules were minimized using force field (OPLS4).[101]

1.2. Geometric optimization and Ligand preparation

All the title molecules were sketched using the 2D sketcher followed by generation of 3D structure in maestro interface. The molecules were considered for molecular alignment, followed by optimization of molecular geometry using B3LYP functional and basis set used was 6-31G^{++} (d, p) *via* DFT theory using jaguar tool of Schrodinger's. Moreover, the Quantum chemical parameters, like the energy gap (ΔE_{GAP}), dipole moment (μ), hardness (η), and local softness (σ), were also calculated as per the FMO.[102-103]

$$\Delta EGAP = ELUMO - EHOMO$$

$$\eta = (\mathrm{ELUMO} - E\mathrm{HOMO})\ /2$$

$$\sigma = 1/\eta$$

$$\mu = (EHOMO + ELUMO)/2$$

$$\omega = \mu 2/2\,\eta$$

Further the 3D optimized geometry of all molecules were considered for preparation of ligands *via* Ligprep panel, providing torsional flexibility generating conformers, providing ionization sates followed by energy minimization using OPLS4 force field.[104-105]

1.3. Grid generation and macromolecule docking

All the prepared macromolecules were consider for identification of binding site *via* considering the cocrystal as centroid of binding site and sitemap was performed for apoprotein structures which appropriately identifies the site of binding considering the binding site volume and site score. Finally the grid was created on the preferred site using Schrodinger's grid generation tool.[106-107]

The ligand and macromolecule docking was executed using the glide program of Schrodinger's suit. Where scoring and ranking of ligands was done semi quantitatively to identify the ligand binding to the various conformations of macromolecule and ranked accordingly, XP mode was utilized for docking owing to its extra precision calculations, followed by consideration of penalties like hydrophobic, steric clashes, solvent exposure of ligand to environment of macromolecule. The docking methodology performed was validated using the cocrystal and standard antidiabetic agents.[108-112]

1.4. Pharmacophore modelling

1.4.1. Structure based pharmacophore modeling

The PPAR-γ receptor (PDB ID: 5U5L)-pioglitazone complex, at the LBD was regarded for pharmacophore model generation in receptor binding site, using the 'develop pharmacophore hypothesis' panel of PHASE module of Schrodinger's. Simultaneously the 100 molecules of thiazolidinedione-pyrrolidine carbonitrile ligands were screened on the developed hypothesis, followed by validation using 9820 molecules as decoy set, the enrichment analysis of screened molecules identified the top 10 hits.[113-114]

1.4.2. Ligand based pharmacophore modeling

A dataset comprising 66 α-glucosidase inhibitors was constructed through a literature review and categorized as active or inactive based on their pIC50 values. The hypothesis generation algorithm identified a total of 12 hypotheses derived from pharmacophoric features. The generated model included 4- and 5-point hypotheses characterized by features such as ring aromaticity (R), HBA (A), and HBD (D), represented as (RRAAD). A minimum of 4-point and a maximum of 5-point hypotheses were established as the screening criteria. Ligand alignment was retained based on ligand conformation, and superimposition was made flexible for the ligands using the Phase module. [115-117]

1.5. 3D Atom based QSAR

The 'Phase' tool was employed to validate the top-ranked pharmacophore hypothesis using atom-based 3D QSAR and the PLS approach. An atom-based QSAR technique was used to analyze key aspects such as hydrogen bond donor and acceptor effects, hydrophobic interactions, and positive and negative ionic effects, resulting in contour maps for these parameters. Phase (v4.0) was used to align inhibitors of *α-glucosidase* using the RRAAD_1 hypothesis. The dataset was spontaneously allocated into 70% training and test set containing 30% ligands using the default parameter values. The 3D QSAR model was graded using statistical criteria including (training set correlation coefficient) R^2, (test set correlation coefficient) Q^2, (standard de*via*tion) SD, and (Pearson value) r.[118-120]

1.6. Molecular Dynamics Simulations

The docking complex of Hit molecules was considered for 100-250ns MD run, using Gromacs and Desmond package for the simulations. The OPLS4 force field was considered for minimization of overall system. NPT ensemble was used with temperature set at 310.0 K and pressure of 1 bar. For the pressure control and temperature control the Martyna-tuckerman-kelin coupling chain scheme and nose-hoover coupling scheme was applied respectively. Further the Particle mesh Ewald parameter was considered for the calculation of electrostatic interactions in long range. Moreover cutoff for the columbic interactions was set to 9.0 Å. The solvation using water molecule were explicitly described using the TIP4P model, the boundary conditions were considers as orthorhombic, the dimensions were set to 10.0 Å each. Custom charges were applied as per the partial charges of the complex. An integrator r-RESPA was used to calculate the non-bonded interactions. The overall system was neutralized using the Na^+ and Cl^- ions. The trajectories were captured for the analysis of complex with the interval of every 10 ns. The dynamic changes associated between the protein ligand complexes was evaluated using the simulation interaction diagram. Parameters like RMSD, RMSF for protein-ligand complex and in alone was assessed.[121-123]

1.7. Pharmacokinetic prediction

The ADMET prediction for the synthesized molecules was computed using the Qikprop tool of Schrodinger's.[124]

1.8. Network Pharmacology and enrichment analysis.

The canonical smiles of the lead compounds were queried in the target prediction database like DIGEP-Pred (https://www.way2drug.com/ge/) and Swiss target prediction (http://www.swisstargetprediction.ch/). The gene targets related to the disease were fetched by querying the keywords as T2DM, and postprandial diabetes from the Gene card and DisGeNET database. The targets associated with the lead molecules and those associated with the disease were cross mapped using the venny 2.1.0. The commonly shared genes obtained *via* venny was subjected to the STRING (https://string-db.org/) database, which provided insights into the PPI network and their associated enriched pathways using the KEGG pathway analysis. The obtained proteins, pathways and compounds were merged into the *cytoscape ver.* 3.9.0 to build a compound-protein-pathway network. The topology of the developed network was examined using metrics such as "node degree distribution", and "Betweenness by degree" with parameters like neighborhood connectivity, eccentricity, in-degree and out-degree distribution evaluated. Additionally, molecular functions (MF), cellular components (CC) and biological processes (BP) were identified for the queried compounds using the gene ontology analysis which predicts the response of compounds at cellular levels.[125-128]

2. Synthesis and Characterization

Commercial solvents and chemical reagents were procured from the available vendors (sigma-aldrich, Chemscene) and were used without further purification for the synthetic procedure. The identification and characterization of the synthesized compounds were carried out by the following methods:

- Melting point / Melting range (m.p. / m.r.)

- Thin layer chromatography (TLC)
- FTIR Spectroscopy (FTIR)
- Nuclear Magnetic Resonance Spectroscopy (^{1}H NMR), (^{13}C NMR)
- Mass Spectroscopy (HRMS/LCMS)
- **Melting point:**

  The melting points of the organic compounds were determined by open capillary tube and were uncorrected.

- **Thin layer chromatography:**

  Thin layer chromatography (TLC) was carried out on glass slides, prepared manually with silica gel F 254 using appropriate solvent system. The spot were visualized under iodine vapors' or UV chamber. The progress of reaction was monitored by TLC.

- **Fourier Transformer Infrared Spectroscopy:**

  FTIR can be routinely used to identify the functional groups and for quality control of raw materials/final products. Shimadzu IRAffinity-1using DRS 8000 spectrometer

- **Nuclear Magnetic Resonance Spectroscopy (^{1}H NMR & ^{13}C NMR):**

  ^{1}H NMR spectra was observed with AMX-400, Bruker-400 liquid-state NMR spectrometer, and ECZ 400S, Jeol 400MHz FT-NMR. The basic standard solvent used was tetramethylsilane (TMS). DMSO-d6 was used as a solvent. Chemical shifts were recorded as δ (ppm).

  ^{13}C NMR spectra was observed with Bruker-100 liquid-state NMR spectrometer, and ECZ 400S, Jeol 400MHz FT-NMR. The basic standard solvent used was tetramethylsilane (TMS). DMSO-d6 was used as a solvent. Chemical shifts were recorded as δ (ppm).

- **Mass spectroscopy (LC-MS):**

  The MS spectra of final end product were recorded by using BRUKER compass Data analysis 4.2, Impact HD instrument using following conditions. MS condition: ESI: electron spray ionization to

record M+1 and M-1 values.

3. *Invitro* study

3.1. *Invitro* glucose consumption assay in yeast cells.

As previously reported by the Cirillo, yeast cells were procured which are available commercially, yeast cell were washed with phosphate buffer of 50mM, and then suspension of 1% w/v was prepared, and soaked overnight. Then it was vortexed at rpm of 4200 for 5 mins, then 10mL of supernatant was further mixed with 90 mL of Millipore water. The test compound and pioglitazone at different concentration were added to 500ng/mL solution of glucose and cultured at 37°C for 10 mins, Further to the 2mL of DNS reagent, volume was made up using the Millipore water and again cultured at 37°C for 1h, then vortexed at 3800 rpm for 10 mins, then the obtained liquid layer was estimated for the presence of glucose concentration at 520 nm using the UV spectrometer[129-132] and the % consumption of glucose is calculated using the formula:

$$\% \, Glucose \, uptake = \left(\frac{1-At}{Ac}\right) \times 100 \, ,$$

Where "At" and "Ac" represent the absorbance of the test and control, respectively.

3.2. *Invitro* Glucose uptake in L6 myotubes

DMEM media was used to nurture the L6 cells along with the addition of 10% FBS heat inactivated, 10U/ml penicillin, 25mmol/1D-glucose followed 10mg.mL streptomycin at 37°C with CO_2 supply, the cells were peckish for 24 hours. The residual culture medium was washed with the PBS and further replaced with the RPMI-1640, which comprise of the glucose (11.1mmol) and 0.2% of BSA. Furthermore, the medium was treated with the test samples and standard pioglitazone at equivalent concentration, where DMSO served as blank. The amount of glucose present in the medium was estimated after 24h of incubation of the test and standard into the medium *via* the GOD-POD assay method. 1mL of reagent along with 10µl of the sample were incubated at 37°C for 10 mins and then the

absorbance of the test sample in comparison to the blank was estimated using the colorimetry,[133-135] and % glucose consumption was calculated using the formula

$$Glucose\ consumption = \frac{OD\ of\ blank - OD\ of\ test}{OD\ of\ blank}\ X\ 100$$

3.3. *Invitro* PPAR-γ TF assay

The Raybio PPAR- γ TF assay kit was utilised to assess the levels of PPAR- γ transactivation in the HepG2 cell lines. All the reagents were prepared as per the instruction of the manufacturer, and were brought to room temperature prior to use. 100µL of the prepared sample is added to each well and incubated for 2h at room temperature, followed by the addition of 100µL of prepared antibody to each well and incubate at room temperature for 1h. Similarly add secondary antibody and incubated for 1h at room temperature. Now add 100µL of TMB substrate reagent to each well and incubate the reaction mixture for 30mins at room temperature. Finally stop the reaction by addition of stop solution and immediately read the microplate at 450nm and plot the absorbance verses concentration plot for the test samples.[69,79, 136]

3.4. I*nvitro α-glucosidase* inhibitory assay

As per the previously reported method, with little modifications the inhibitory effect of synthesized compounds was evaluated on *α-glucosidase* enzyme. Potassium phosphate buffer of pH 6.8 was used to prepare the enzyme solution. All the test samples were prepared by adding the synthesized compound in the DMSO, and further 100mL of 100mM potassium phosphate buffer was used to reconstitute the test samples. To 50µL of the *α-glucosidase* solution containing in a well, a 10µL of test sample was added and incubated for 5mins, further the substrate (p-nitrophenyl- α-D-glucopyranoside) with concentration of 5mM was prepared in the potassium phosphate buffer and was added to the above wells and incubated for 10 mins. Finally the released p-nitrophenol was measured at 405 nm using the ELISA plate reader.[137-138] Here DMSO served as blank and acarbose was used as a standard, the % enzyme inhibitory activity was calculated using the formula

$$\%\ \boldsymbol{inhibition}\ =\ [(Abs\ of\ control - Abs\ of\ test)/Abs\ Control]$$

The lead compounds were consider for the *α-glucosidase* enzyme kinetic studies, where the (0-16μM) different concentration of p-nitrophenyl- α-D-glucopyranoside against the enzyme in presence and absence of the test sample at varied concentration was assessed to identify the type of inhibition based on the lineweaver Burk plot and Michael-menten constant (Km) was obtained by the plot of reciprocal of substrate concentration (1/[s]) against reciprocal of rate of enzyme (1/v) for varied concentration of test inhibitor.[139]

3.5. *Invitro α-amylase* inhibitory assay

The inhibitory effect of the synthesized molecules on *α-amylase* enzyme was measured as per the previously reported method. All the test molecules were dissolved in the DMSO, and reconstituted using the methanol. The reaction mixture consist of the equivalent quantity of enzyme solution, and test samples, Acarbose was used as a standard, and methanol as control. At 37°C for 15mins the reaction mixture was pre-incubated followed by addition of (1%) solution of starch as substrate and incubate at 37°C for 25mins. Then DNSA reagent was added to each well and incubated at 100°C for 8-10mins, then the reaction mixture was cooled, and finally the volume was made up using Millipore water, and at 549 nm the absorbance was measured,[140-141] and the % inhibition was calculated using the formula

$$\%\ \boldsymbol{inhibition}\ =\ [(Abs\ of\ control - Abs\ of\ test)/Abs\ Control]$$

3.6. Toxicity assessment

The MTT assay as per the previously reported procedure was performed on the normal mouse fibroblast (L929) cells, to assess the cytotoxic effect of few selected compounds.[142]

4. *Invivo* studies

4.1. Ethical approval and animals procurement

The CPCSEA approved vendor (Invivo Biosciences, Bangalore) provided the Wistar rats of either sex and the IAEC at the KLE College of Pharmacy, Belagavi evaluated the animal study protocol (resolution No. KLECOP/CPCSEA-Reg, No.221/Po/Re/S/2000/CPCSEA, Res.34-03/12/2022). Prior to the initiation of the trial, one week for 12h light/dark cycle animals were acclimatized. Ethical clearance attached in annexure.

4.2. Acute toxicity study and diabetes induction

The Acute oral toxicity of lead molecules was performed as per the OECD #423 guidelines. Overnight starved animal weighing between 180-200 grams, were initially dosed at 5mg/kg of test compounds, and monitored to identify any mortality for the 48h and subsequently signs of toxicity for the next 14 days. This dose group showed no signs of toxicity and mortality, the dose was increased to50mg/kg and assessed for the signs of toxicity and mortality as mentioned above, since no indication of mortality and toxicity was observed, the dose was increased to 300mg/kg, which showed mortality at the 5^{th} and 7^{th} day of administration. The LD_{50} was consider as >300mg/kg, and hence the dose selected for the animal model study was $1/10^{th}$ of the LD_{50}.

The Supplementation of fructose in drinking water for 64 days induced insulin resistance in wistar rats[143-144], here the first 20 days (15%w/v) fructose was provided, which was subsequently increased to (20%w/v) fructose for next 25 days, and finally received (25%w/v) fructose for the last 18 days. A 15 days treatment period was considered for test agents. The OGTT and AUC was evaluated by loading exogenous glucose (2g/kg) load for the fasting body weight, and animals with more than 120mg/dl of fasting blood glucose level were considered as diabetic. Five groups containing six animals each of either sex were grouped as follows.

Sr. No	Group	Dose
I	**Normal**	Normal feed + water (*ad. libitium*)
II	**IR**	Received fructose in drinking water for 63 days
III	**PIO-10**	Received fructose in drinking water for 63 days + (10mg/kg, p.o.) of pioglitazone in 0.5 % CMC for 15 days
IV	**5b**	Received fructose in drinking water for 63 days + (30mg/kg, p.o.) of compound **5b** in 0.5 % CMC for 15 days
V	**5f**	Received fructose in drinking water for 63 days + (30mg/kg, p.o.) of compound **5f** in 0.5 % CMC for 15 days

Where, **IR**: is insulin resistance group; **PIO-10** is pioglitazone treated group, **5b** is compound **5b** treated group; **5f** is compound **5f** treated group.

Table. 1: Animal grouping in antidiabetic model study.

4.3. Estimation of physical parameters

From the 1st day of induction and every 3rd day from the day 1 of induction and 1st day of treatment, the body weight, food and water intake were measure *via* maintaining three animals per cage.

4.4. Estimation of FBGL and OGTT

The FBGL were measured for the overnight starved animals, by tail prick method using the glucometer (Janaushadhi, India), The OGTT and $AUC_{(0\text{-}120mins)}$ was estimated to measure the whole body's insulin sensitivity, by means of exogenous solution of glucose (2g/kg) administration, while blood samples were tested at 0-120mins with 30mins interval using glucometer.[145]

4.5. Estimation of Fasting insulin levels, and insulin tolerance test (ITT), and HOMA-IR index

A commercial kit, GENLISA™ Rat Insulin (INS) ELISA, was used to measure insulin levels in blood. Subcutaneously insulin (0.75 U/kg) was injected, and blood sugar levels (0 to 120 minutes) were determined using a glucometer at 30-minute intervals. The cumulative AUC for glucose was calculated. The HOMA-IR index was computed using the formula,

$$HOMA - IR = \frac{glucose\ mg/dl \times\ insulin(\mu IU/mL)}{405}$$

4.6.Collection of blood and visceral organs

At the completion of the experiment, the animals were euthanized with a high dose of anaesthetic ether, blood was drawn *via* cardiac puncture, centrifuged for and plasm was isolated. The adipose tissue and liver were extracted, cleansed with phosphate buffer to avert clotting, and conserved in 10% v/v formalin.

4.7. Estimation of lipid profile

Plasma from the blood was utilised to determine the TC, TG, and HDL, and the SGPT and SGOT were recorded spectrophotometrically using commercially available kits (GENLISA and AGD clinipark diagnostic kit). The LDL and VLDL quantities were determined as follows,

$$VLDL = TG/5$$

$$LDL = TC - (HDL + VLDL)$$

4.8. Glucose consumption by rat hemidiaphragm

The glucose uptake capacity of rat hemidiaphragm following the treatment period as previously described by (Beloff-Chain., *et al*)[146], isolated hemidiaphragm 1x1cm2 tissue was incubated in (30mM) glucose solution for 10 minutes before being combined with 0.25U insulin under aeration. The percentage Changes in the quantity of glucose in the incubating mixture was then calculated. Thus, the difference in concentration can be calculated as follows:

$$\%\ change\ in\ glucose\ concentration = \frac{Ac - At}{Ac} \times 100$$

Where 'Ac' and 'At' denote the absorbance of the concentration of glucose in the incubating medium prior to the subsequent incubation of hemidiaphragm tissue in the incubating mixture respectively.

4.9. Glycogen content in liver and skeletal muscles

When the experimental animals were dissected, the liver and skeletal muscles were precisely removed, and the blood clots were subsequently eliminated by rinsing them with phosphate buffer and experiment was performed as per the anthrone method.[147] Additionally, 10% v/v phosphate buffer was used to

homogenise the skeletal muscle and liver tissue. After 15 minutes of incubation with 30% w/v KOH (2 ml) in a bath of boiling water, the 1 ml homogenate of liver and skeletal muscle was made up to 25 ml with 30% w/v KOH. Glycogen precipitated after ethanol was added and the container was left to ferment at room temperature for the entire night. After centrifuging the entire mixture for ten minutes at 3000 rpm, the pellet that was left over was dissolved in Millipore water, to which four millilitres of anthrone reagent were added, and the mixture was heated for five minutes. After cooling the liquid, a UV spectrophotometer (Shimazdu UV probe 2.4) was used to measure absorbance.

4.10. Estimation of oxidative stress markers

According to a previously established protocol, the several enzymatic and non-enzymatic oxidative stress measures in liver tissue, such as SOD[148], MDH[149], GSH[150], and CAT[151], were measured.

4.11. Histopathological findings

The organs tissue like liver and adipose tissue were preserved in 10% formalin, and subjected to pathological investigations using (H and E) hematoxylin and eosin stain. The liver samples were assessed for, sinusoidal congestion, venous congestion and ballooning degeneration. The adipocytes count and size were estimated from adipose tissue.

4.12. Instrumentation and chromatographic conditions

The Shimadzu Agilent 1220 Infinity II instrument (LC-20AD, Japan) has a 20 µL loop for injecting value, a CTO-10AS VP column oven, a Quaternary pump with degasser (G7111A), an auto-injector (G7129A), and a PDA detector (G7115A). The analytical data was interpreted using OpenLab CDS software. The chromatographic separation was carried out using a Phenomenex Luna C18 analytical column (4.6 × 150 mm, 5 µm particle size, Phenomenex Inc., USA). Acetonitrile (ACN): 0.1% formic acid (FA) in water with a 60:40 v/v ratio was the ideal mobile phase for the sample analysis, and it eluted at a rate of 1 mL/min. Prior to use, the mobile phase was ultrasonically degassed and filtered using a PVDF membrane filter (0.45µ; Millex HV®, Millipore, USA). The injection volume was maintained at 10 µL for the sample analysis, and the detection wavelength was set.

4.13. Preparation of stock solution and working standard solution

The test compounds were produced as primary stock solutions in acetonitrile at a concentration of 1 mg/mL. The stock solutions were diluted with the mobile phase to reach concentrations between 5 and 30 µg/mL in order to create working standard solutions. All standard solutions were kept in firmly sealed volumetric flasks at 4°C prior to the HPLC analysis.

4.14. Method validation

The precision and dependability of analytical data are guaranteed by HPLC technique validation in compliance with ICH criteria. It includes metrics like accuracy, precision, linearity, LOD, and LOQ. The method's appropriateness for the intended use may be confirmed by validating it, giving assurance regarding the integrity and quality of bio-analytical data produced using the HPLC technology.

4.15. Quantification of drug from plasma

Plasma was collected from fresh rat blood samples by centrifugation at 12,000 rpm for 10 minutes at 4°C. Acetonitrile was used to create stock mixes with concentrations of 10 µg/mL of test compounds. By spiking varied quantity of test compounds into rat plasma, these solutions were utilised to produce a standard calibration curve. In different centrifuge tubes, aliquots of 500 µL of rat plasma were mixed with the standard solutions of test compounds. Following extensive mixing, 200 µL of acetonitrile was added to cause protein precipitation. Finally, the resultant mixture was vortexed and spun for 10 minutes at 15,000 rpm. Using the recommended HPLC procedure, the resulting clear supernatant was separated and examined.[152]

4.16. Pharmacokinetic analysis

Pioglitazone (10 mg/kg) and the synthetic compound **5b** and **5f** (30 mg/kg) were administered orally to three different groups of six mice each. Blood samples were drawn from the retro-orbital sinus every 30 minutes for 1 to 12 hours. A 0.5 mL sample of blood was extracted in EDTA-containing tubes and centrifuged for 10 minutes at -4 °C at 4000 rpm. After being separated, the plasma was put into Eppendorf tubes and kept for up to 24 hours at -4 °C. Acetonitrile is added to 200 µL of plasma from

the Eppendorf tubes to create a 2 mL volume. After 30 seconds of swirling, this combination was spun for 10 minutes at 12,000 rpm. After passing through a microsyringe, the resultant supernatant was transferred to *via*ls for further examination. [152]

4.17. Statistical analysis

The data was represented as Mean ± SEM. One-way or two-way ANOVA was used for statistical analysis, and GraphPad Prism (version 8) was used for posthoc tests such Tukey's or Bonferroni's and Dunn's test for various parameters. The p-value was deemed statistically significant if it was less than 0.05. WinNonlin software was used to analyse pharmacokinetic data when needed (Pharsight Corp., Mountain View, CA). Cmax (µg/mL), Tmax (h), AUC 0-t (h·µg/mL), AUC 0-inf (h·µg/mL), Kel, and T1/2 (h) were among the characteristics that were assessed.

Chapter 3

Results (Scheme. 1)...

The general depiction of research work carried out for **scheme. 1** is briefly summarized in the following **Fig. 5**.

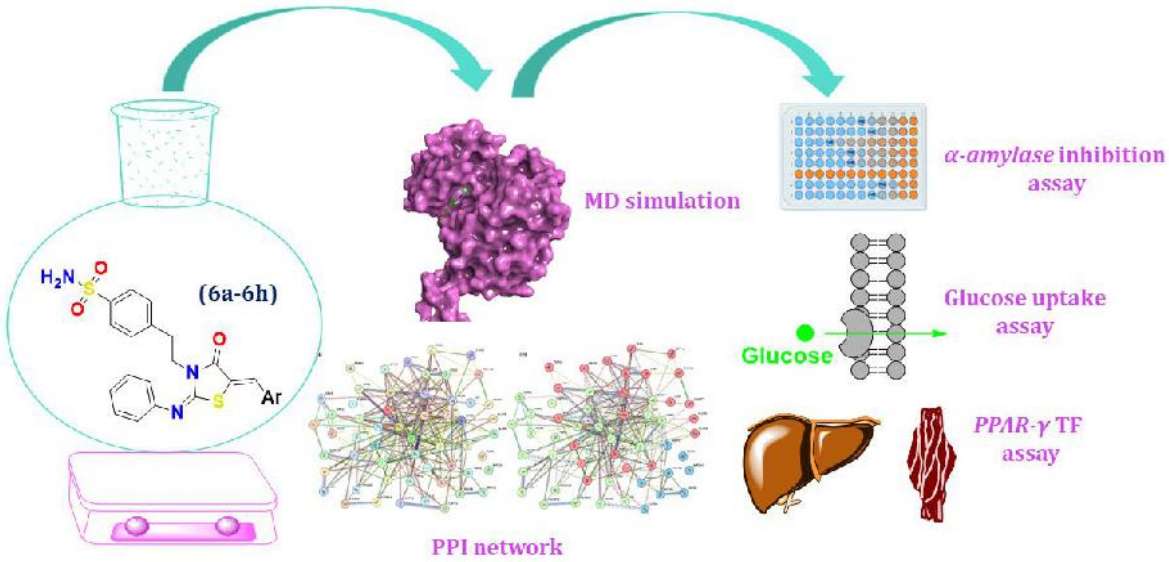
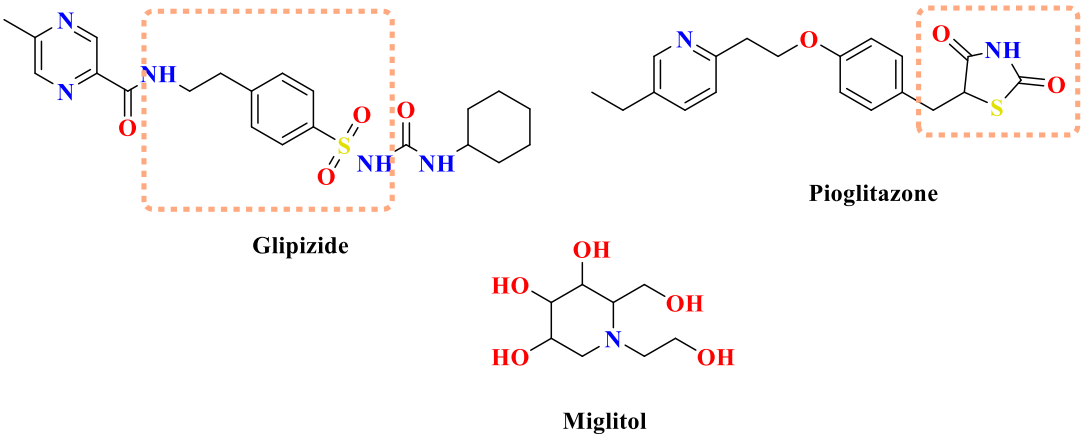
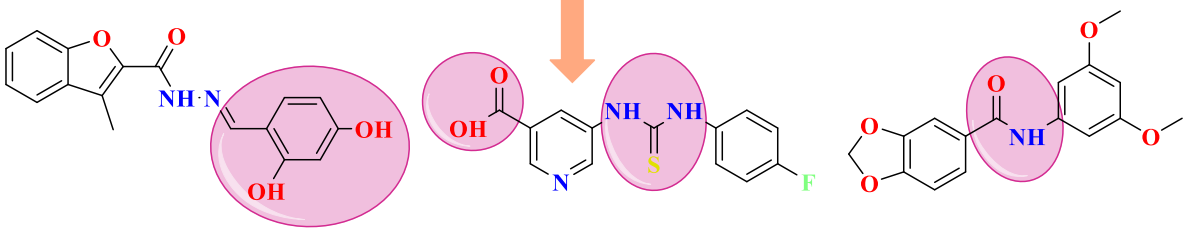


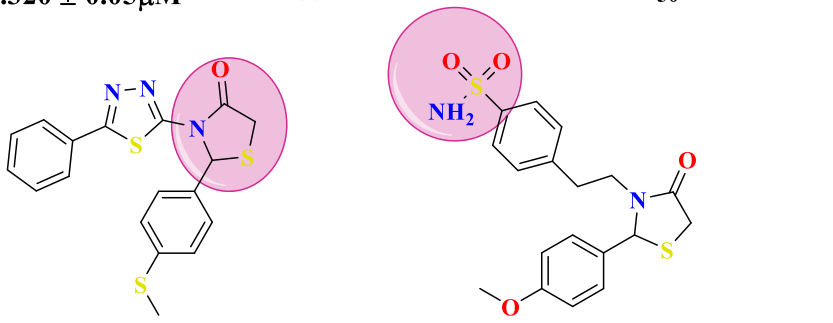
Fig.5: Study plan of scheme. 1

1. Design of scheme. 1

From the literature review, it is evident that the reported inhibitors of the *α-amylase* enzyme, which are studied for their role in postprandial glycemic control, commonly feature hydroxy and polyhydroxy functional groups. In addition to these, thiazolidine analogs have also been identified as inhibitors, apart from their known activity as PPAR-γ activators. Furthermore, molecules containing a benzenesulfonamide nucleus have been reported to exhibit *α-amylase* inhibition. Based on these findings, we designed a template that incorporates the mentioned moieties and functional groups, as illustrated in **Fig. 6.**







Previously reported molecules bearing reactive functions groups inhibiting α-amylase

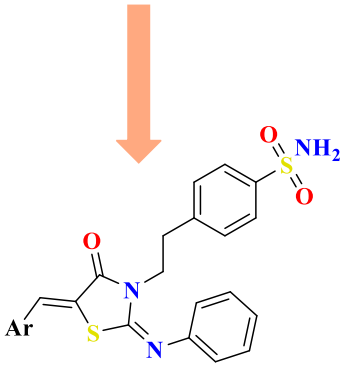
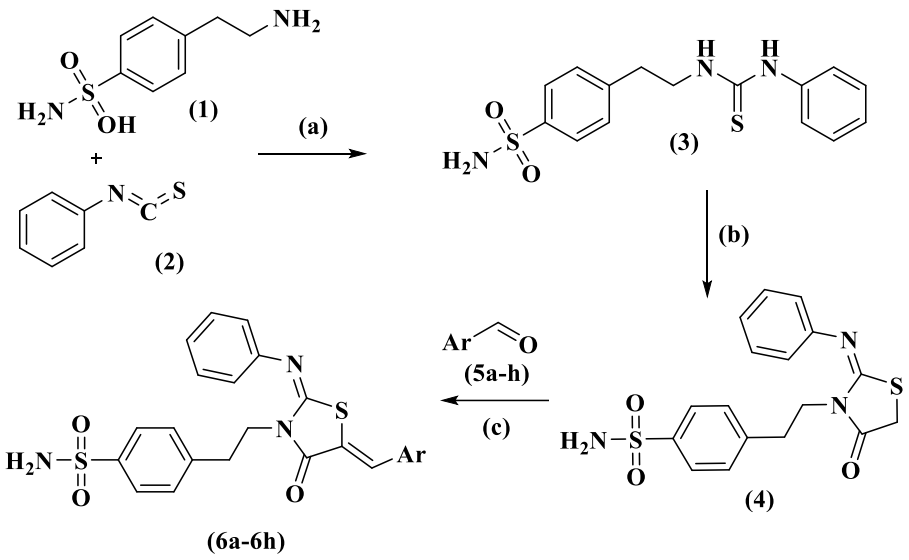


Fig. 6: Design of thiazolidinone-ethanebenzenesulphonamide template. [153-156]

Scheme. 1: Synthesis of thiazolidinone-ethanebenzenesulphonamide hybrids



Reagents and conditions: (a) Dimethylformamide, triethylamine, rt; (b) Chloroacetic acid, sodium acetate, 95% ethanol, reflux; (c) Methanol, piperdine, reflux

2. Chemistry

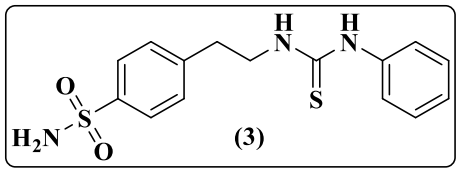
The synthetic route for the preparation of 4-(2-((E)-5-(substituted-benzylidene)-4-oxo-2-(phenylimino) thiazolidin-3-yl) ethyl) benzenesulfonamide derivatives (**6a–6h**) is outlined in **Scheme 1**. The key intermediate, 4-(2-(3-phenylthioureido) ethyl) benzenesulfonamide (**3**), was obtained via the reaction of 4-(2-aminoethyl) benzenesulfonamide (1) with phenyl isothiocyanate in the presence of a catalytic amount of triethylamine. Refluxing the thiourea derivative (**3**) with chloroacetic acid and anhydrous sodium acetate produced 4-(2-(4-oxo-2-(phenylimino) thiazolidin-3-yl) ethyl) benzenesulfonamide (**4**). The target compounds (**6a–6h**) were synthesized via a Knoevenagel condensation between the appropriate aryl aldehydes (5a–5h) and compound (4) in methanol using a catalytic amount of piperidine. The structures of intermediates (**3**) and (**4**) as well as the final compounds (**6a–6h**) were confirmed using FTIR, ^{1}H NMR, ^{13}C NMR, and HRMS spectroscopic techniques. The FTIR spectrum of 4-(2-(3-phenylthioureido) ethyl) benzenesulfonamide (**3**) displayed a primary amine (NH_2) absorption band at 3187 cm^{-1}. The ^{1}H NMR spectrum of (**3)** exhibited a characteristic NH_2 signal at δ

7.32 ppm, two distinct CH_2 signals at δ 2.947 ppm (triplet) and 3.719 ppm, and a secondary amine (NH) signal at δ 9.570 ppm. The HRMS spectrum provided further confirmation of the molecular structure. The FTIR spectrum of 4-(2-(4-oxo-2-(phenylimino) thiazolidin-3-yl) ethyl) benzenesulfonamide (**4**) showed a primary amine (NH_2) absorption band at 3266 cm^{-1}. In the ^1H NMR spectrum, the NH_2 proton appeared as a signal at δ 7.34 ppm, while the characteristic signal for the methylene (CH_2) protons, indicative of cyclization, appeared at δ 3.986 ppm. Additional CH_2 signals were observed at δ 3.019 ppm (triplet) and 3.959 ppm. The FTIR spectra of the target compounds (**6a–6h**) displayed characteristic NH_2 absorption bands within the range of 3100–3400 cm^{-1}. The ^1H NMR spectra of the compounds (**6a–6h**) revealed indicative singlets at approximately δ 7 ppm, attributed to NH_2 protons, as well as signals corresponding to CH_2 protons at around δ 3 ppm and δ 4 ppm. The HRMS spectra of the final compounds (**6a–6h**) confirmed their molecular structures, providing conclusive evidence of the successful synthesis.

3. Experimental

Synthesis of 4-(2-(3-phenylthioureido) ethyl) benzenesulfonamide (3)

To a solution of 4-(2-aminoethyl) benzenesulfonamide (**1**) (9.9 mmol) in 15 mL of dimethylformamide, phenylisothiocyanate (**2**) (9.9 mmol) and a catalytic amount of triethylamine were added. The reaction mixture was stirred at room temperature for 6 h, and the progress of the reaction was monitored by TLC. Upon completion, the reaction mixture was poured onto crushed ice, resulting in the precipitation of a crude product. The solid was collected by filtration, washed with water, and recrystallized from ethanol to afford 4-(2-(3-phenylthioureido) ethyl) benzenesulfonamide (**3**) as a white coloured purified product. Yield: 94%; mp: 179-181°C.



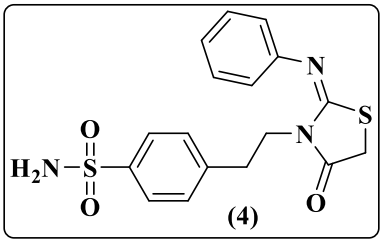
(3)

FTIR (KBr, cm^{-1}): 3187.51 (NH_2), 3038.98 (Ar-CH), 1539.26 (C=C). ^1H NMR [400 MHz, δ ppm, DMSO-d_6]: 2.96-2.92 (t, 2H, CH_2), 3.719-3.710 (t, 2H, CH_2), 7.112-7.082 (m, 1H, *J*=7.2Hz, Ar-H), 7.301-7.291 (m, 5H, Ar-H), 7.320 (s, 2H, NH_2), 7.44-7.42 (m, 2H, *J*=8Hz, Ar-H), 7.77-7.75 (m,

2H, *J*=8Hz, Ar-H), 9.57 (s, 1H, NH). ^{13}C NMR [100 MHz, δ ppm, DMSO-*d6*]: 34.69, 45.46, 123.61, 124.71, 126.30, 129.24, 129.71, 139.48, 142.65, 144.10, 180.77. Chemical formula: $C_{15}H_{17}N_3O_2S_2$; Molecular Mass; calculated: 335.08; Mass (M+1): 336. 08.

Synthesis of 4-(2-(4-oxo-2-(phenylimino) thiazolidin-3-yl) ethyl) benzenesulfonamide (4):

A mixture of compound (**3**) (1.0 equiv), chloroacetic acid (1.0 equiv), and sodium acetate (1.0 equiv) was dissolved in 95% ethanol and refluxed for 12 h. The progress of the reaction was monitored by TLC. Upon completion, the reaction mixture was allowed to cool to room temperature and poured into crushed ice, resulting in the precipitation of a crude solid. The solid was collected by filtration, washed thoroughly with water, and recrystallized from ethanol to afford 4-(2-(4-oxo-2-(phenylimino) thiazolidin-3-yl) ethyl) benzenesulfonamide (**4**) as a white coloured purified product. Yield: 87%; mp: 143-145°C.

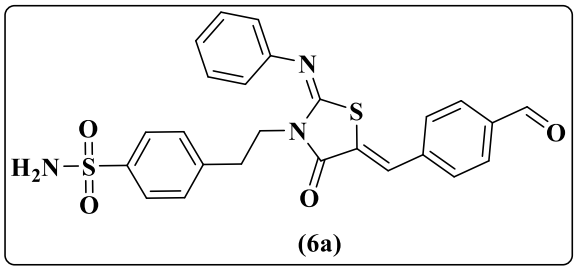


FTIR (KBr, cm^{-1}): 3266.59 (NH_2), 3032.23 (Ar-CH), 1708.04 (C=O), 1592.31 (C=C). ^{1}H NMR [400 MHz, δ ppm, DMSO-*d6*]: 3.03-3.00 (t, 2H, CH2), 3.95 (s, 2H, S-CH_2), 3.98 (t, 2H, CH_2) 6.81-6.79 (m, 2H, *J*=7.6Hz, Ar-H), 7.117-7.083 (m, 1H, Ar-H), 7.325-7304 (s, 2H, *J*=8.4Hz Ar-H), 7.341 (m, 2H, NH_2), 7.42-7.40 (m, 2H, *J*=7.6Hz, Ar-H), 7.75-7.73 (m ,2H, *J*=7.6Hz, Ar-H). ^{13}C NMR [100 MHz, δ ppm, DMSO-*d6*]: 32.71, 32.94, 43.47, 121.35, 124.76, 126.26, 129.79, 129.87, 142.94, 148.59, 155.41, 172.32. Chemical formula: $C_{17}H_{17}N_3O_3S_2$; Molecular Mass; calculated: 375.07; Mass (M+1): 376.07.

General procedure for synthesis of (6a-6h)

A mixture of equimolar amounts of compound (**4**) and the appropriate aryl aldehydes (**5a**–**5h**) was refluxed in methanol (15 mL) for 24 h in the presence of a catalytic amount of piperidine. The progress of the reaction was monitored by TLC. Upon completion, the reaction mixture was cooled to room temperature, and the resulting crude product was collected by filtration. The product was then purified by recrystallization from methanol to afford the desired compounds (**6a**–**6h**)

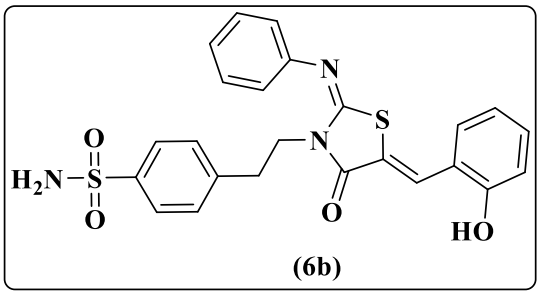
Synthesis of 4-(2-((E)-5-((Z)-4-formylbenzylidene)-4-oxo-2-(phenylimino) thiazolidin-3-yl) ethyl) benzenesulfonamide (6a):



(6a)

Yield: 78.16%; mp: 176-178°C; FTIR (KBr, cm^{-1}): 3409.33 (NH_2), 3093.95 (Ar-CH), 1663.68 (C=O), 1581.70 (C=C). ^{1}H NMR [400 MHz, δ ppm, DMSO-*d6*]: 3.123-3.019 (t, 2H, CH_2), 4.172-4.140 (t, 2H, CH_2), 6.877-6.857 (d, 2H, Ar-H), 7.193-7.156 (m, 1H, Ar-H), 7.433-7.413 (m, 2H, *J*=8 Hz, Ar-H), 7.390-7.352(m, 4H, Ar-H), 7.563 (s, 2H, NH_2), 7.664 (s, 1H, CH), 7.753-7.733 (d, 2H, *J*=8Hz, Ar-H). 9.982 (s, 1H, CHO). ^{13}C NMR [100 MHz, δ ppm, DMSO-*d6*]: 32.910, 44.063, 121.424, 122.986, 125.429, 126.282, 129.578, 129.875, 130.038, 131.063, 134.819, 142.858, 142.983, 148.099, 149.632, 166.017. Chemical formula: $C_{25}H_{21}N_3O_4S_2$; Molecular mass; calculated: 491.10; Mass (M+1): 492.10.

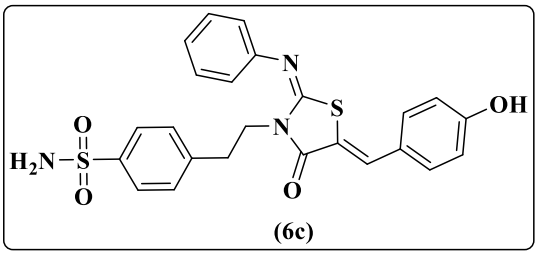
Synthesis of 4-(2-((E)-5-((Z)-2-hydroxybenzylidene)-4-oxo-2-(phenylimino) thiazolidin-3-yl) ethyl) benzenesulfonamide (6b):



(6b)

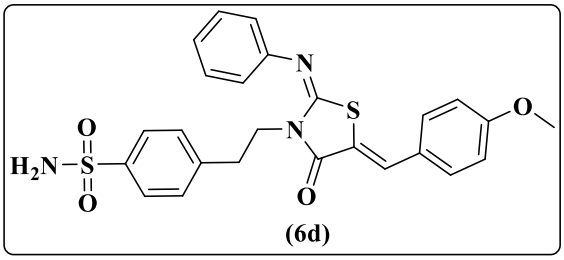
Yield: 78.32%; mp: 143-145°C. FTIR (KBr, cm^{-1}): 3504.81 (OH), 3274.31 (NH_2), 1639.56 (C=O), 3060.55 (Ar-CH). ^{1}H NMR [400 MHz, δ ppm, DMSO-*d6*]: 3.11 (t, 2H, CH_2), 4.15 (s, 2H, CH_2), 6.869-6.854 (d, 2H, *J*=6Hz, Ar-H), 6.926-6.907 (d, 2H, *J*=7.6Hz Ar-H), 7.230-7.156 (m, 2H, Ar-H), 7.34 (s, 2H, NH_2), 7.442-7.426 (m ,4H, *J*=6.4Hz, Ar-H), 7.765-7.748 (m, 2H, *J*=6.8Hz, Ar-H), 7.95 (s, 1H, CH), 10.46 (s, 1H, OH) ^{13}C NMR [100 MHz, δ ppm, DMSO-*d6*]: 32.93, 43.84, 116.52, 119.92, 120.16, 120.70, 121.46, 125.24, 126.06, 126.28, 128.81, 129.89, 129.98, 132.39, 142.95, 148.41, 150.44, 157.47, 166.36. Chemical formula: $C_{24}H_{21}N_3O_4S_2$; Molecular mass; calculated: 479.10; Mass (M+1): 480.10.

Synthesis of 4-(2-((E)-5-((Z)-4-hydroxybenzylidene)-4-oxo-2-(phenylimino) thiazolidin-3-yl) ethyl) benzenesulfonamide (6c):



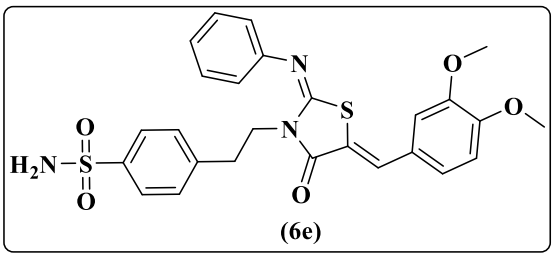
Yield: 81.46%; mp: 163-165°C. FTIR (KBr, cm^{-1}): 3428.54 (O-H), 3018.16 (Ar-CH), 1648.73 (C=O), 1592.31 (C=C). ^{1}H NMR [400 MHz, δ ppm, DMSO-*d6*]: 3.106-3.166 (t, 2H, CH_2), 4.12-4.16 (t, 2H, CH_2), 6.794-6.773 (m, 2H, *J*=8.4Hz Ar-H), 6.883-6.864 (m, 2H, *J*=7.6Hz, Ar-H), 7.176-7.140 (m, 1H, Ar-H), 7.312-7.291 (d, 2H, *J*=8Hz, Ar-H), 7.37 (s, 2H, NH_2), 7.43-7.41 (d, 2H, *J*=8Hz, Ar-H) 7.595 (s, 1H, CH), 7.76-7.74 (m, 2H, *J*=8Hz Ar-H), 9.67 (s, 1H, OH); ^{13}C NMR [100 MHz, δ ppm, DMSO-*d6*]: 32.95, 43.74, 115.67, 117.26, 121.35, 121.50, 123.42, 125.16, 126.27, 129.86, 129.98, 131.65, 132.78, 142.96, 148.54, 150.46, 150.46, 162.12, 166.44. Chemical formula: $C_{24}H_{21}N_3O_4S_2$; Molecular mass; calculated: 479.57; Mass (M+1): 480.10.

Synthesis of 4-(2-((E)-5-((Z)-4-methoxybenzylidene)-4-oxo-2-(phenylimino) thiazolidin-3-yl) ethyl) benzenesulfonamide (6d):



Yield: 75.12%; mp: 149-151°C. FTIR (KBr, cm^{-1}): 3272.38 (NH_2), 1623.17 (C=O), 1590.06 (C=C); ^{1}H NMR [400 MHz, δ ppm, $CDCl_3$-*d6*]: 3.196-3.159 (t, 2H, CH_2), 3.82 (s, 3H, -OCH_3), 4.26-4.23 (t, 2H, CH_2), 4.91 (s, 2H, NH_2), 6.925-6.890 (m, 4H, Ar-H), 7.206-7.170 (m, 1H, Ar-H), 7.401-7.362 (m, 4H, Ar-H.), 7.45-7.43 (m, 2H, *J*=8Hz Ar-H), 7.68 (s, 1H, CH), 7.86-7.84 (d, 2H, *J*=8Hz Ar-H). ^{13}C NMR [100 MHz, δ ppm, $CDCl_3$-*d6*]: 33.47, 43.63, 55.53, 114.66, 118.31, 121.18, 124.98, 126.31, 126.76, 129.50, 129.94, 131.20, 132.04, 140.30, 143.89, 148.13, 150.42, 161.01, 166.94. Chemical formula: $C_{24}H_{21}N_3O_4S_2$; Molecular mass; calculated: 493.11; Mass (M+1): 494.12.

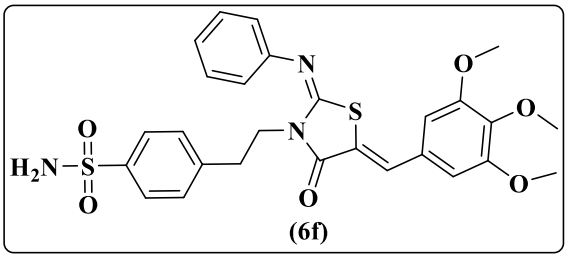
Synthesis of 4-(2-((E)-5-((Z)-3, 4-dimethoxybenzylidene)-4-oxo-2-(phenylimino) thiazolidin-3-yl) ethyl) benzenesulfonamide (6e):



(6e)

Yield: 75.12%; mp: 167-169°C. FTIR (KBr, cm^{-1}): 3247.30 (NH_2), 3068.88 (Ar-CH), 1699.36 (C=O), 1593.27 (C=C). ^{1}H NMR [400 MHz, δ ppm, DMSO-*d6*]: 3.112 (t, 2H, CH_2), 3.754-3.72 (d, 6H, -OCH_3), 4.157 (t, 2H, CH_2), 6.895-6.877 (d, 2H, *J*=7.2Hz, Ar-H), 7.065-6.992 (q, 2H, Ar-H), 7.172 (s, 2H, Ar-H), 7.345 (s, 2H, NH_2) 7.438-7.420 (m, 2H, *J*=7.2Hz, Ar-H), 7.393-7.375 (m, 2H, *J*=7.2Hz, Ar-H), 7.667 (s, 1H, CH), 7.756-7.737 (d, 2H, *J*=7.6Hz Ar-H). ^{13}C NMR [100 MHz, δ ppm, DMSO-*d6*]: 32.929, 43.852, 56.069, 56.117, 112.60, 114.84, 118.59, 121.511, 122.871, 125.305, 126.263, 126.512, 129.894, 129.961, 131.226, 142.935, 148.358, 149.326, 150.246, 150.964, 166.228. Chemical formula: $C_{26}H_{25}N_3O_5S_2$; Molecular mass; calculated: 523.12; Mass (M+1): 524.13.

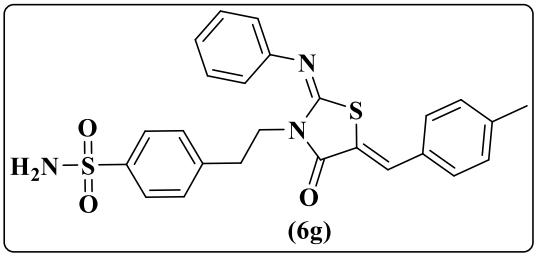
Synthesis of 4-(2-((E)-4-oxo-2-(phenylimino)-5-((Z)-3, 4, 5-trimethoxybenzylidene) thiazolidin-3-yl) ethyl) benzenesulfonamide (6f):



(6f)

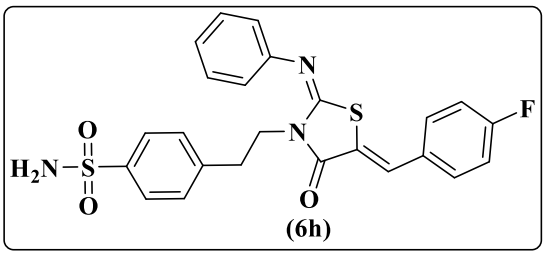
Yield: 83.12%; mp: 173-175°C; FTIR (KBr, cm^{-1}): 3247.30 (NH_2), 3085.27 (Ar-CH), 1701.29, (C=O).^{1}H NMR [400 MHz, δ ppm, DMSO-*d6*]: 3.115 (t, 2H, CH_2), 3.710-3.673 (d, 9H, -OCH_3), 4.162 (t, 2H, CH_2), 6.801 (s, 2H, Ar-H), 6.910-6.892 (d, 2H, *J*=7.2Hz, Ar-H), 7.183-7.166 (m, 1H, *J*=6.8Hz, Ar-H), 7.440-7.421 (m, 2H, *J*=7.6Hz, Ar-H), 7.352 (m 3H, Ar-H, NH_2), 7.657 (s, 1H, CH), 7.758-7.740 (d, 2H, *J*=7.2Hz Ar-H). ^{13}C NMR [100 MHz, δ ppm, DMSO-*d6*]: 32.910, 43.938, 56.509, 60.716, 108.028, 120.485, 121.530, 125.429, 126.273, 129.904, 131.169, 139.725, 142.897, 142.964, 148.032, 149.735, 153.628, 166.017. Chemical formula: $C_{27}H_{27}N_3O_6S_2$; Molecular mass; calculated: 553.13; Mass (M+1): 554.14.

Synthesis of 4-(2-((E)-5-((Z)-4-methylbenzylidene)-4-oxo-2-(phenylimino) thiazolidin-3-yl) ethyl) benzenesulfonamide (6g):



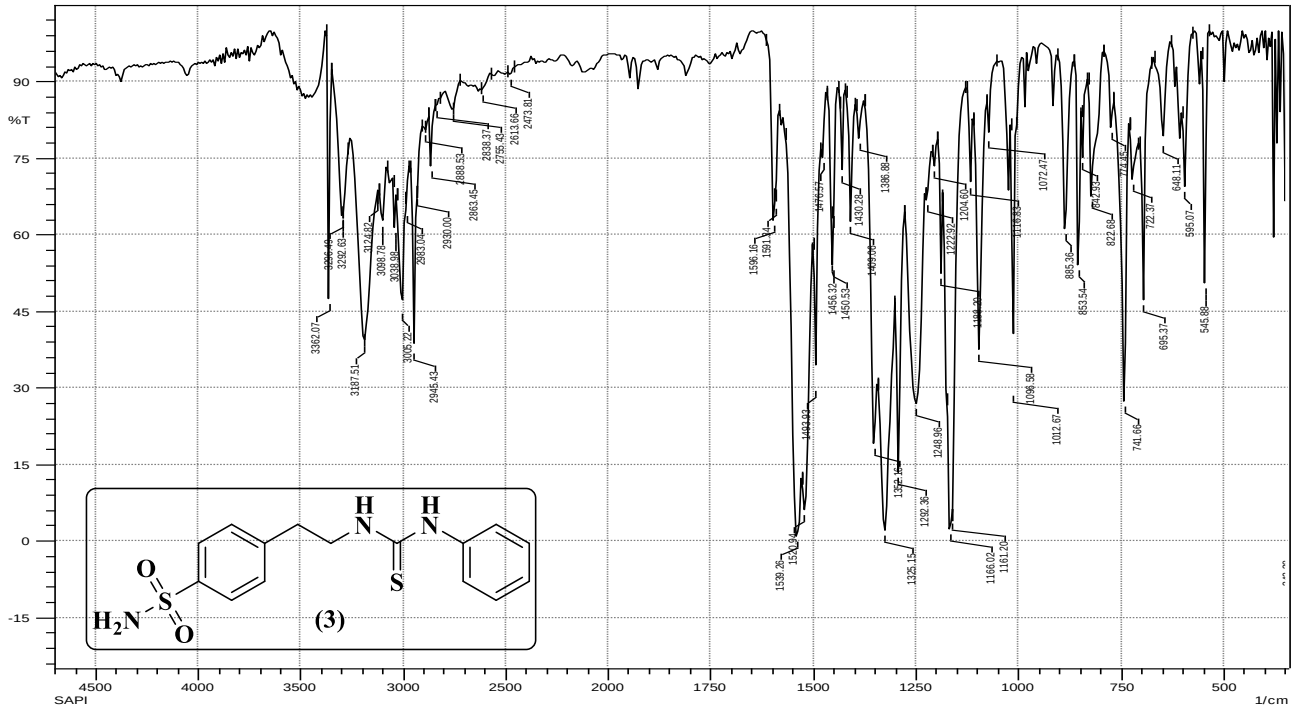
Yield: 80.52%; mp: 151-153°C FTIR (KBr, cm^{-1}): 3273.34 (NH_2), 3124.82 (Ar-CH), 1711.90 (C=O), ^{1}H NMR [400 MHz, δ ppm, $CDCl_3$-*d6*]: 2.363 (s, 3H, -CH_3), 3.203-3.168 (t, 2H, CH_2), 4.277-4.240 (t, 2H, CH_2), 4.814 (s, 2H, -NH_2), 6.910-6.890 (d, 2H, *J*=8Hz, Ar-H), 7.216-7.196 (m, 2H, *J*=8Hz, Ar-H), 7.344-7.324 (m, 2H, *J*=8Hz, Ar-H), 7.405-7.367(m, 2H, Ar-H), 7.462-7.440 (m, 2H, *J*=8.8Hz, Ar-H), 7.711 (s, 1H, CH), 7.872-7.852 (d, 2H, *J*=8Hz, Ar-H). ^{13}C NMR [100 MHz, δ ppm, $CDCl_3$-*d6*]: 21.652, 33.475, 43.651, 120.045, 121.166, 125.037, 126.790, 129.511, 129.894, 129.952, 130.163, 130.862, 131.447, 140.281, 140.769, 143.887, 148.042, 150.313, 166.882. Chemical formula: $C_{25}H_{23}N_3O_3S_2$; Molecular mass; calculated: 477.12; Mass (M+1): 478.12.

Synthesis of 4-(2-((E)-5-((Z)-4-fluorobenzylidene)-4-oxo-2-(phenylimino) thiazolidin-3-yl) ethyl) benzenesulfonamide (6h):

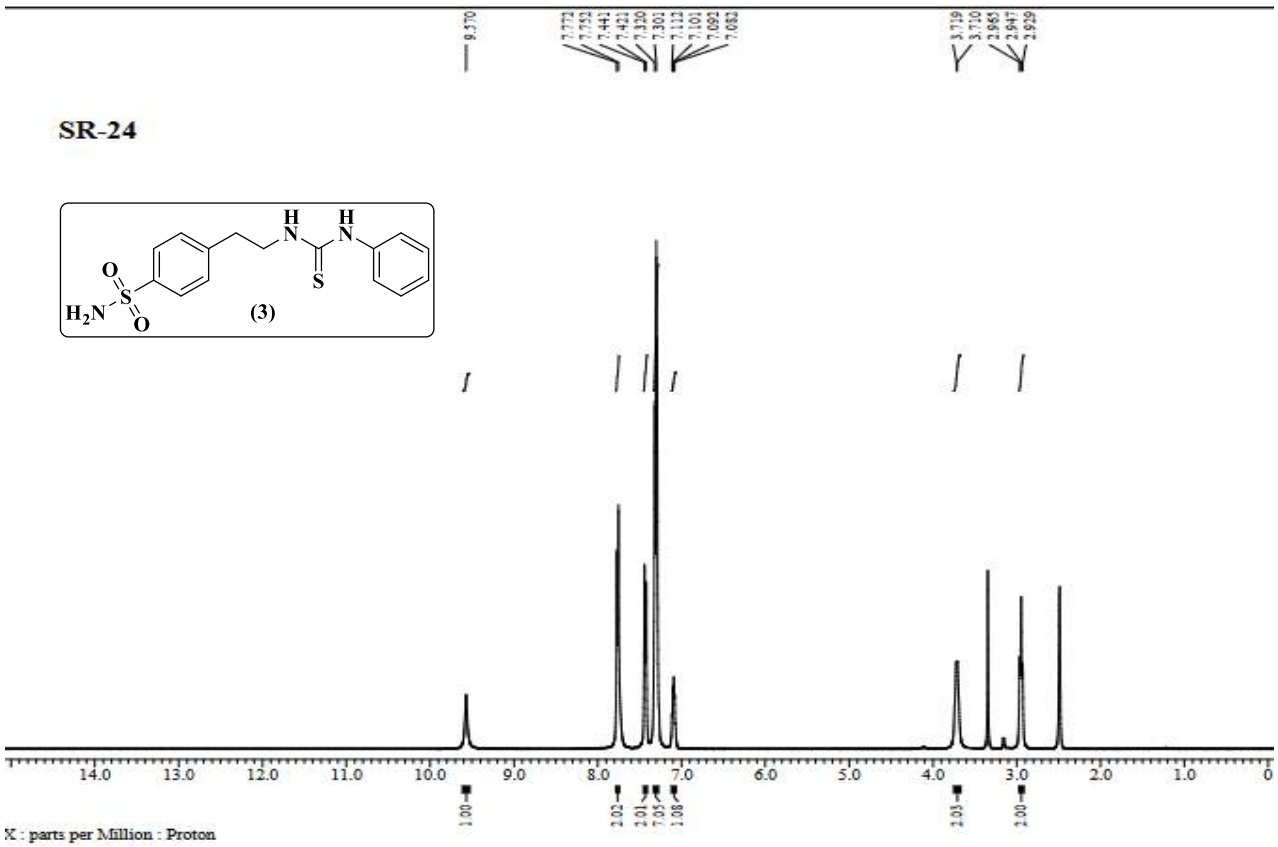


Yield: 78.16%; mp: 147-149°C; FTIR (KBr, cm^{-1}): 3274.31 (NH_2), 2938.69 (Ar-CH), 1710.93 (C=O), 1596.16 (C=C). ^{1}H NMR [400 MHz, δ ppm, DMSO-*d6*]: 3.133-3.100 (t, 2H, CH_2), 4.184-4151 (t, 2H, CH_2), 6.881-6.862 (d, 2H, *J*=7.6Hz, Ar-H), 7.193-7.156 (m, 1H, Ar-H), 7.398-7.7.289 (m, 6H, Ar-H, -NH_2), 7.442-7.422 (d, 2H, *J*=8Hz, Ar-H), 7.584-7.550 (m, 2H, Ar-H), 7.757-7.736 (m, 2H, *J*=8.4Hz, Ar-H), 7.757 (s, 1H, CH). ^{13}C NMR [100 MHz, δ ppm, DMSO-*d6*]: 32.900, 43.996, 116.864, 117.084, 121.166, 121.415, 125.401, 126.273, 129.770, 129.904, 130.038, 130.402, 132.750, 132.836, 142.877, 142.973, 148.253, 149.853, 161.868, 164.350, 166.084. Chemical formula: $C_{24}H_{20}FN_3O_3S_2$; Molecular mass; calculated: 481.09; Mass (M+1): 482.10.

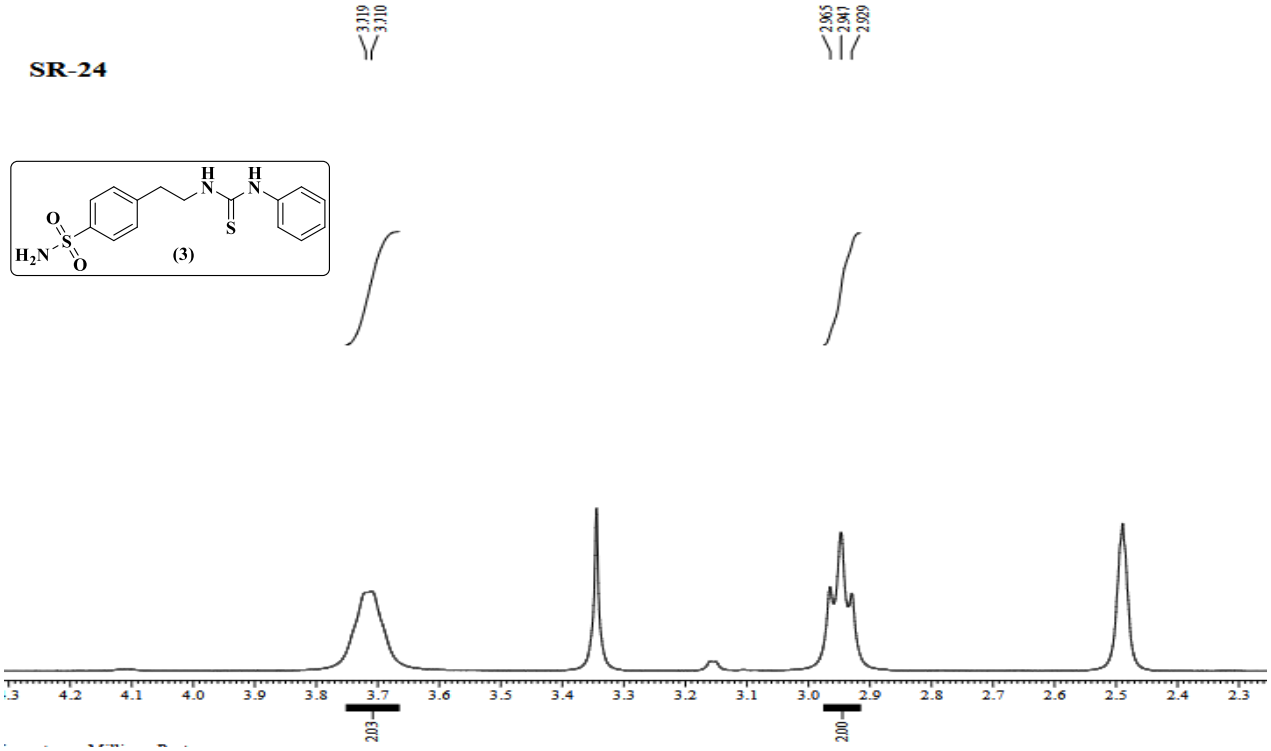
4. Spectral data evaluation



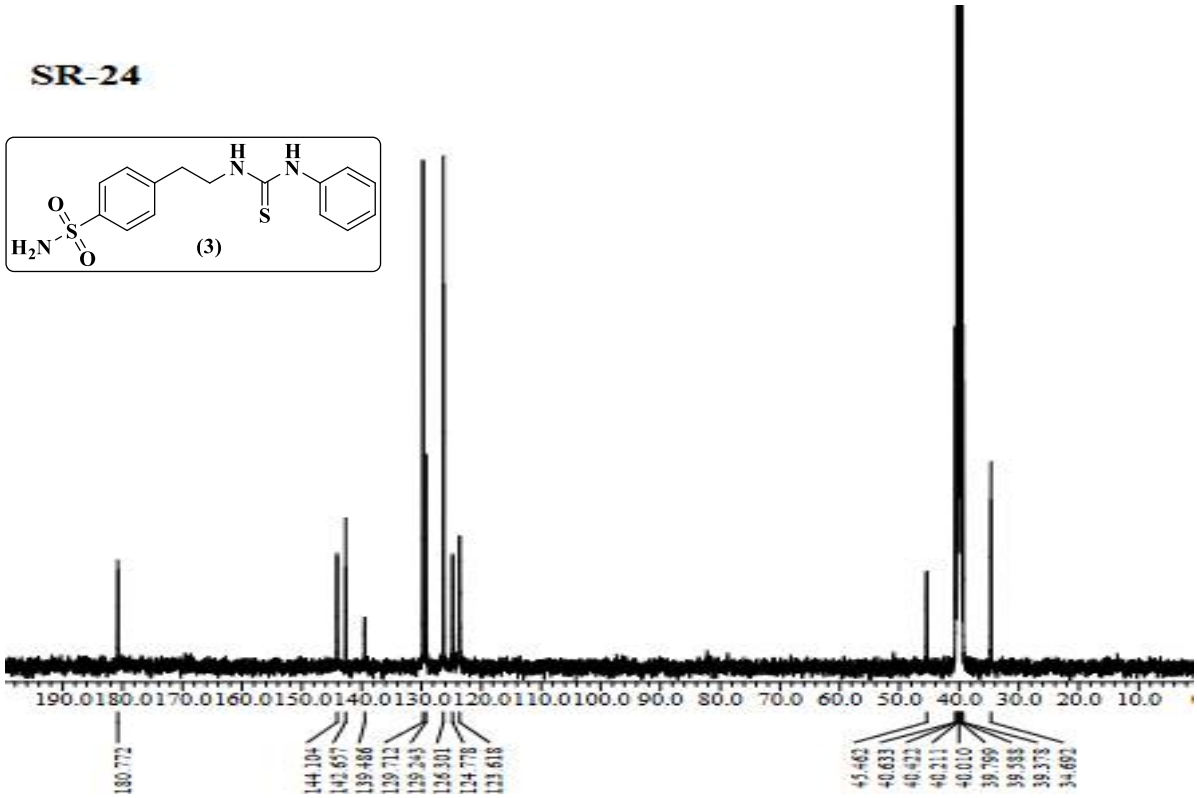
Spectra. 1: FTIR (KBr, cm^{-1}) spectra of compound 3



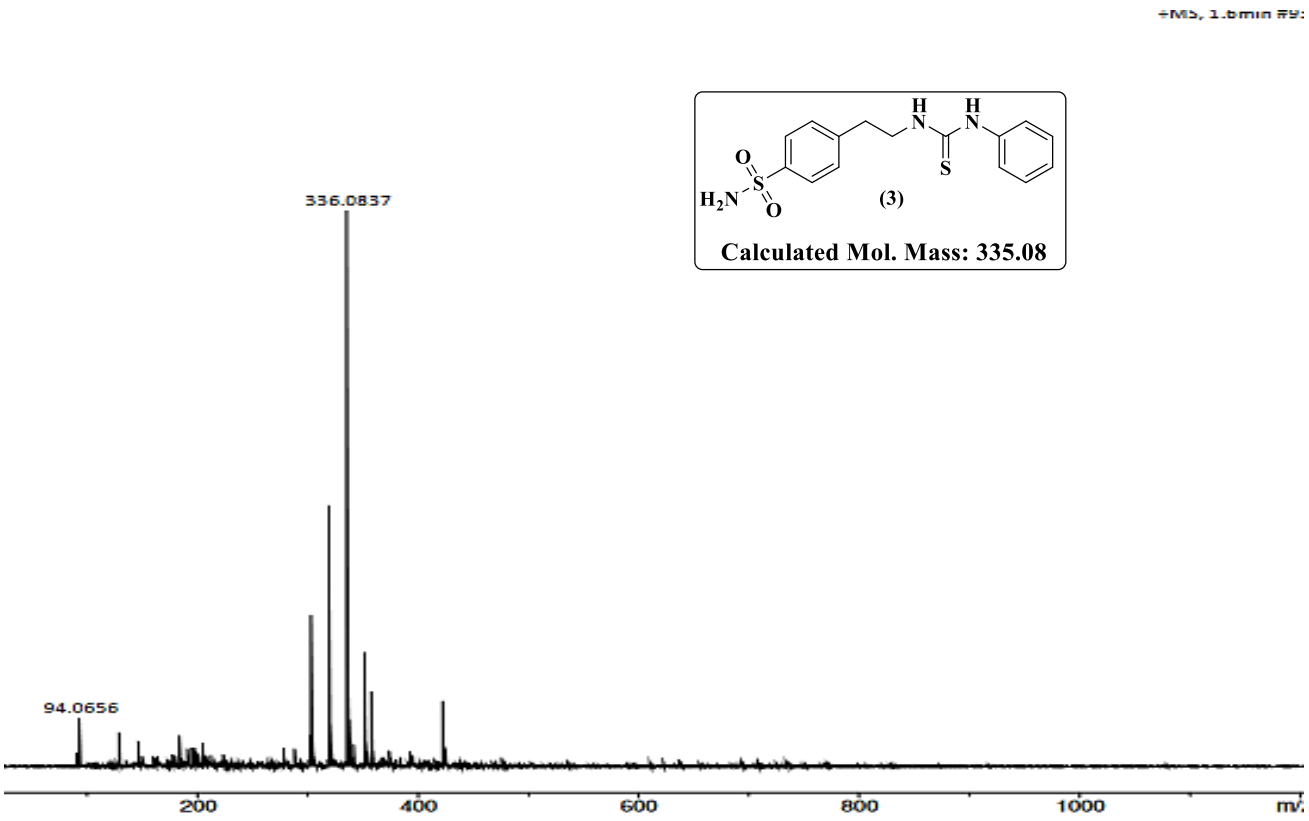
Spectra. 2: ^{1}H NMR (400 MHz, δ, ppm) spectra of compound 3



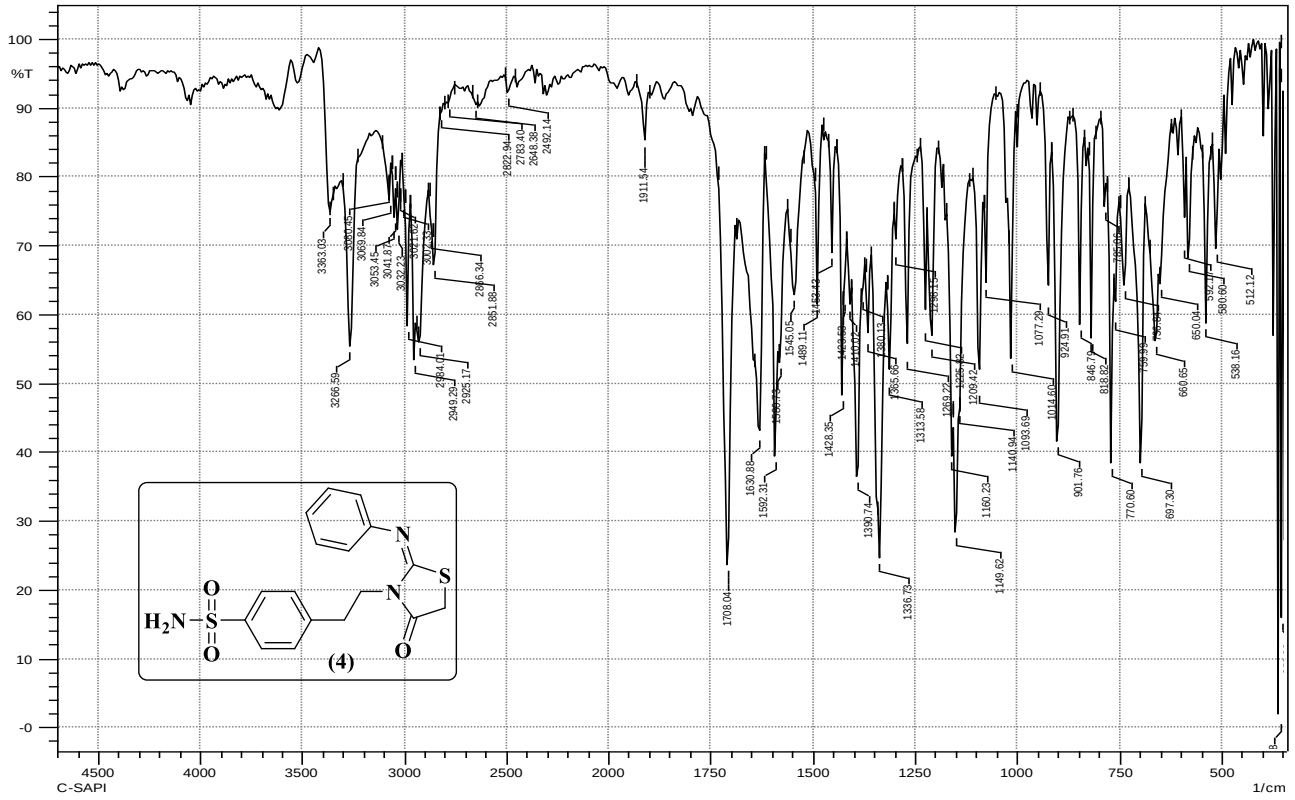
Spectra. 2: ^{1}H NMR Extended form (400 MHz, δ, ppm) spectra of compound 3



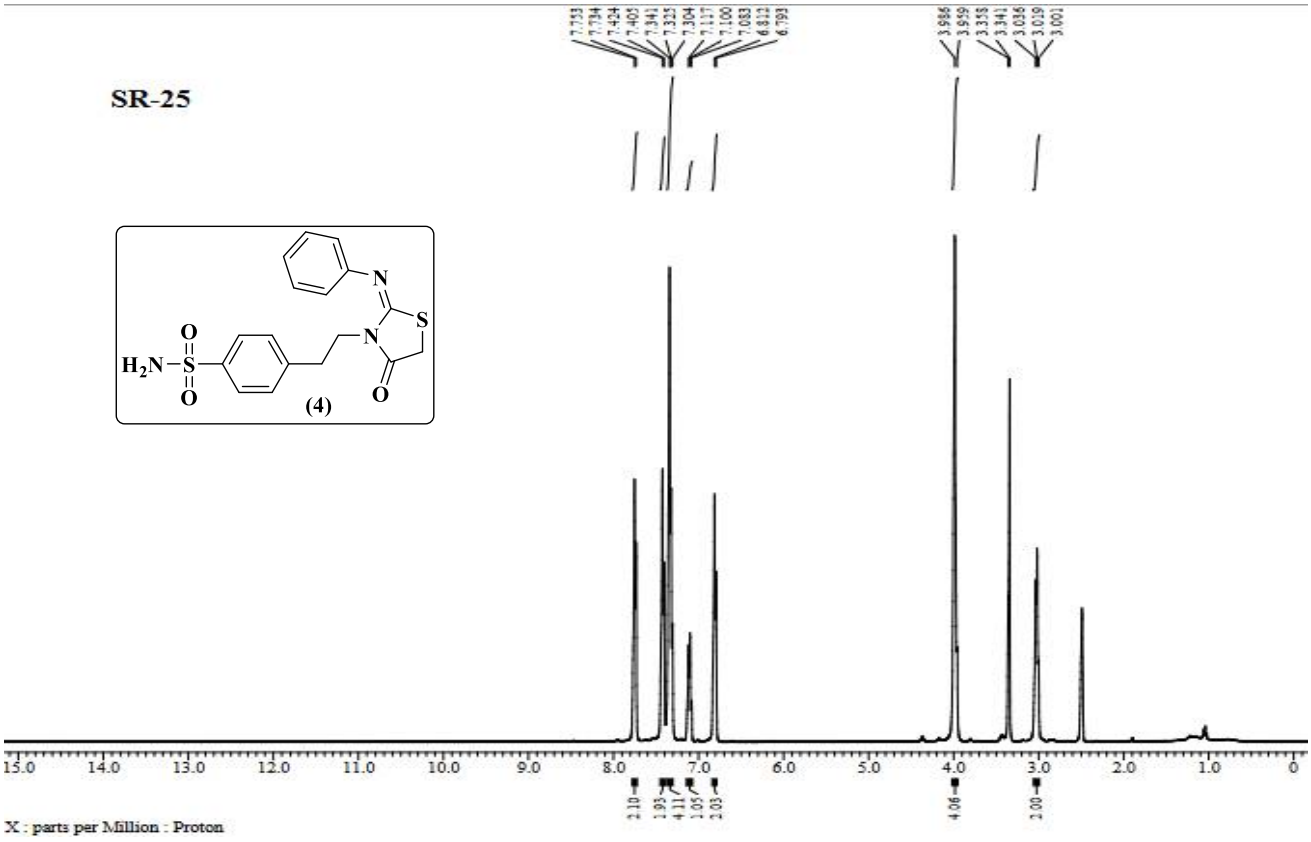
Spectra. 3: ^{13}C NMR (100 MHz, δ, ppm) spectra of compound 3



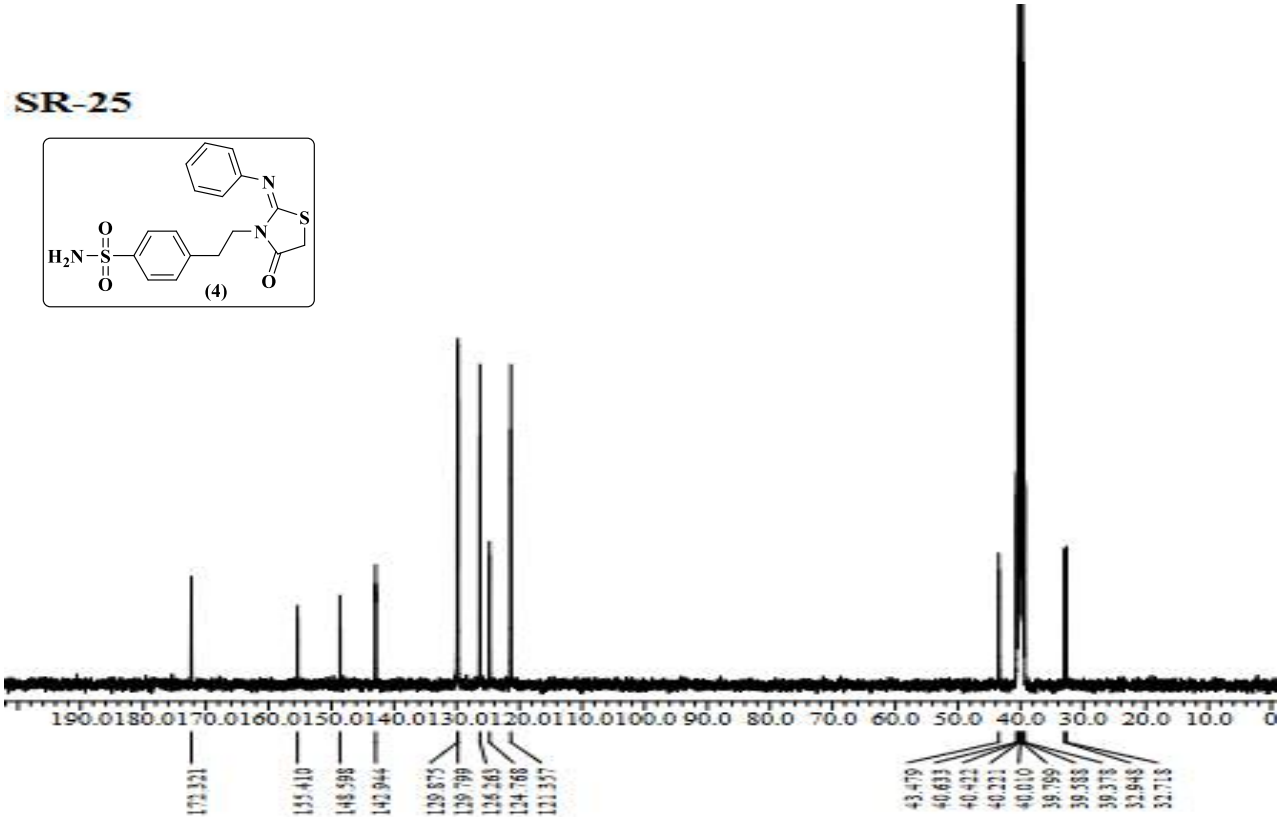
Spectra.4: HRMS spectra of compound 3



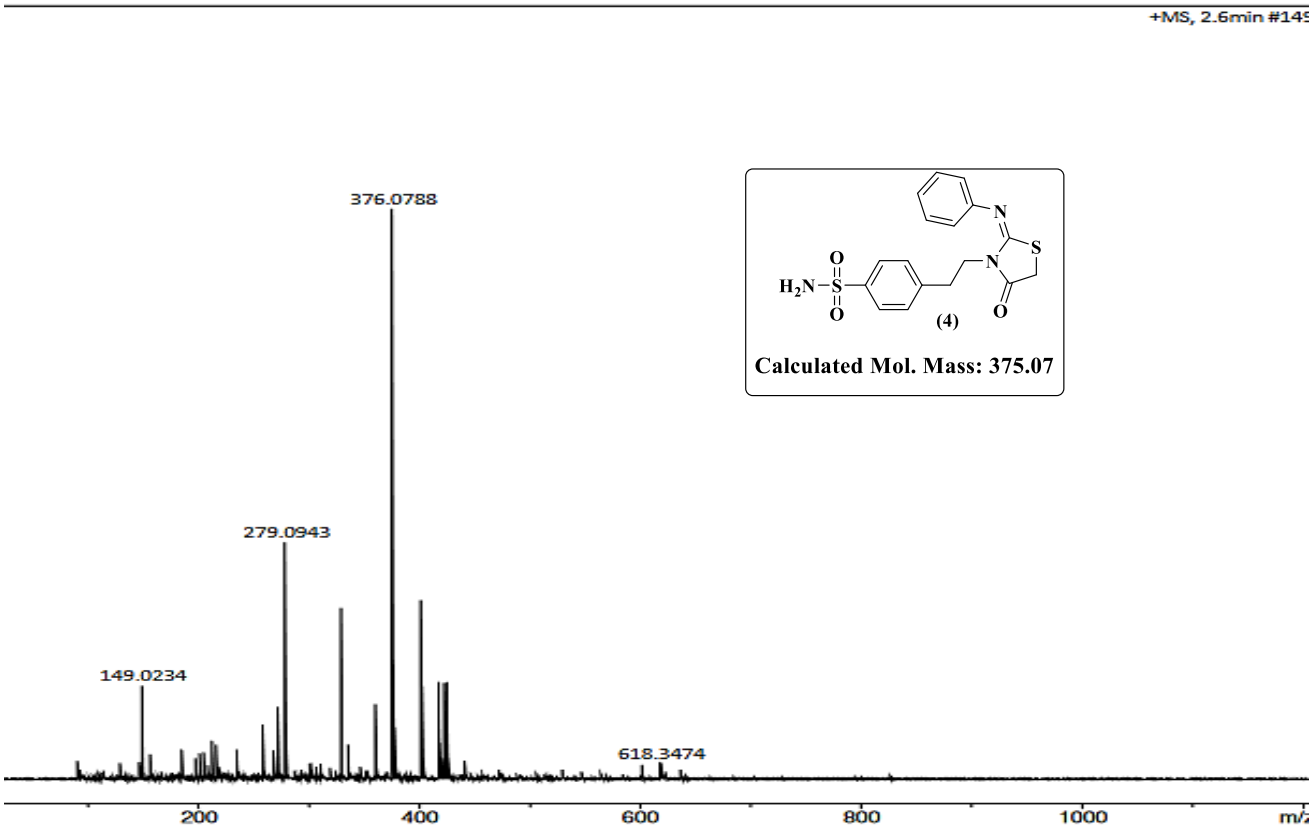
Spectra. 5: FTIR (KBr, cm^{-1}) spectra of compound 4



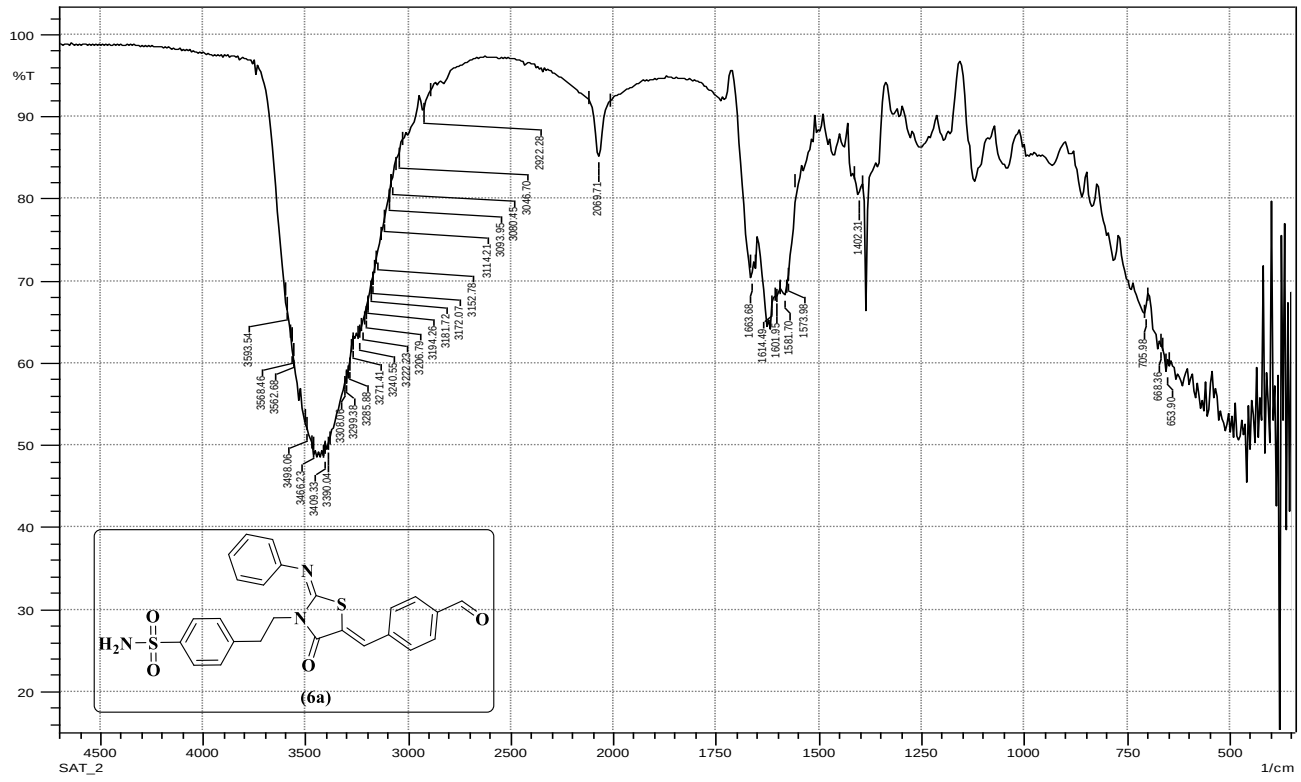
Spectra. 6: ^{1}H NMR (400 MHz, δ, ppm) spectra of compound 4



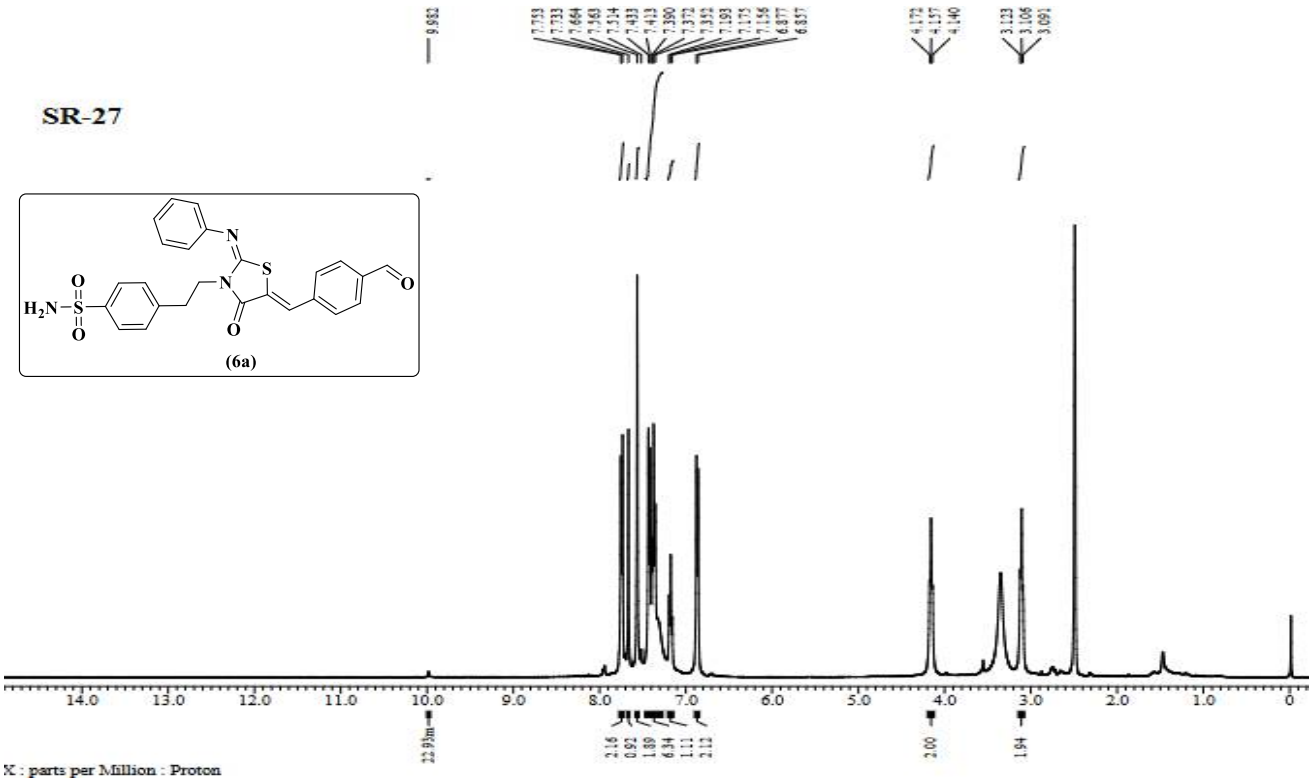
Spectra. 7: ^{13}C NMR (100 MHz, δ, ppm) spectra of compound 4



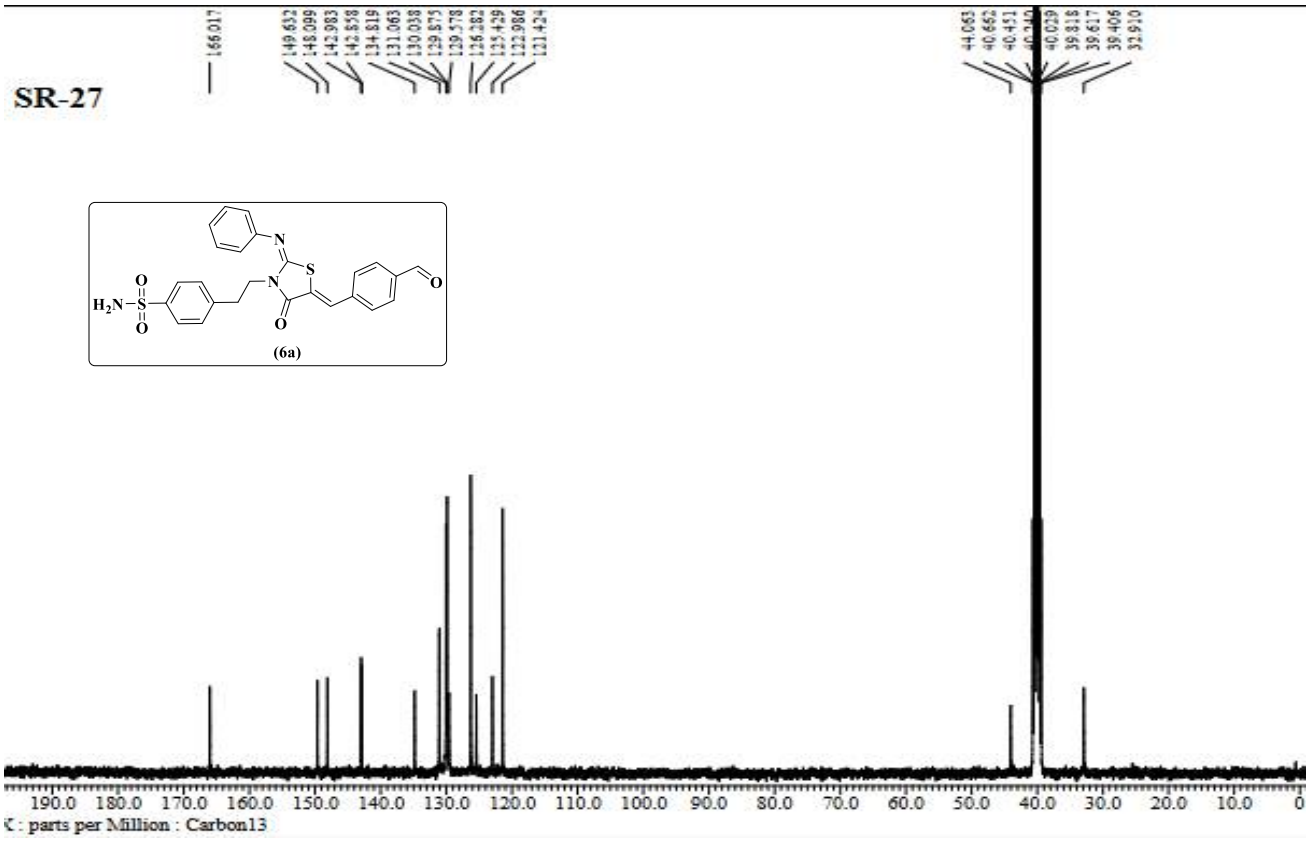
Spectra. 8: HRMS spectra of compound 4



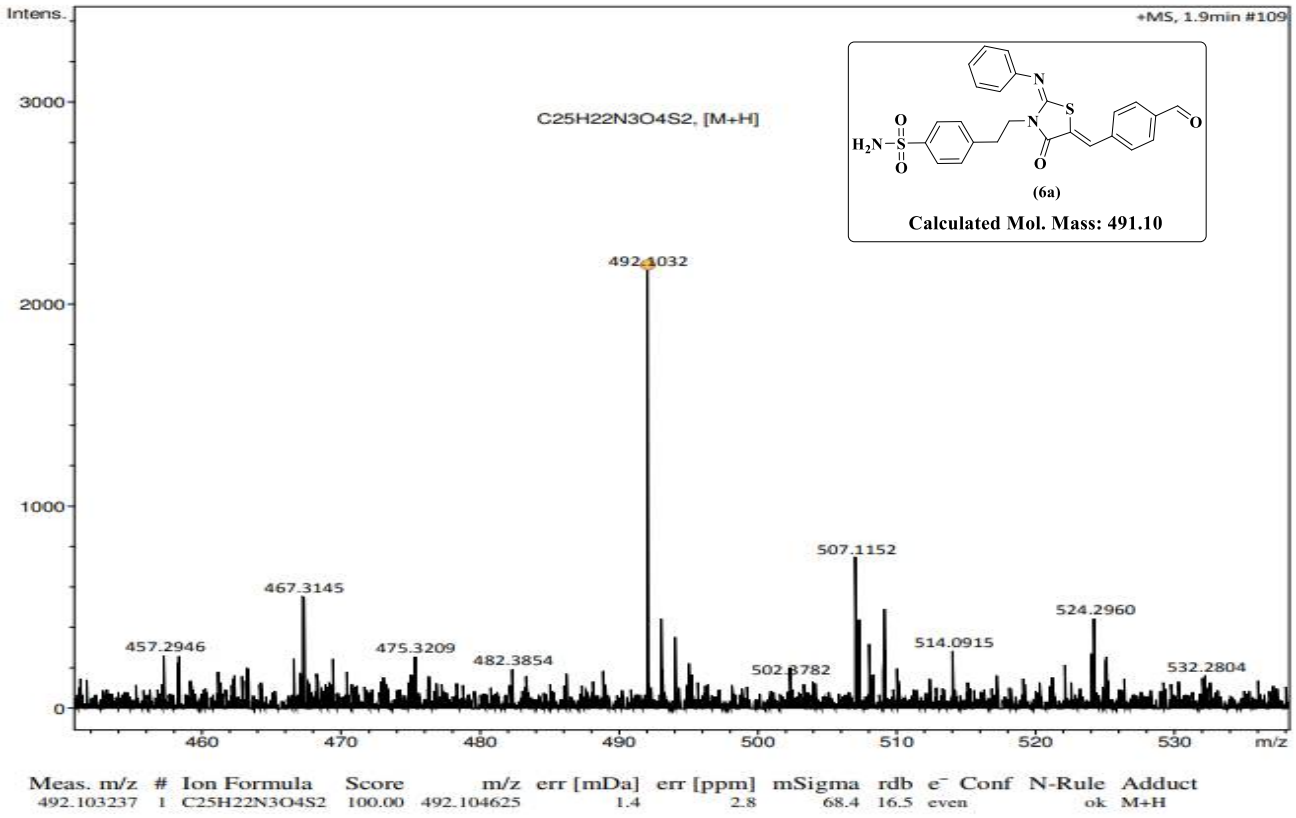
Spectra. 9: FTIR (KBr, cm^{-1}) spectra of compound 6a



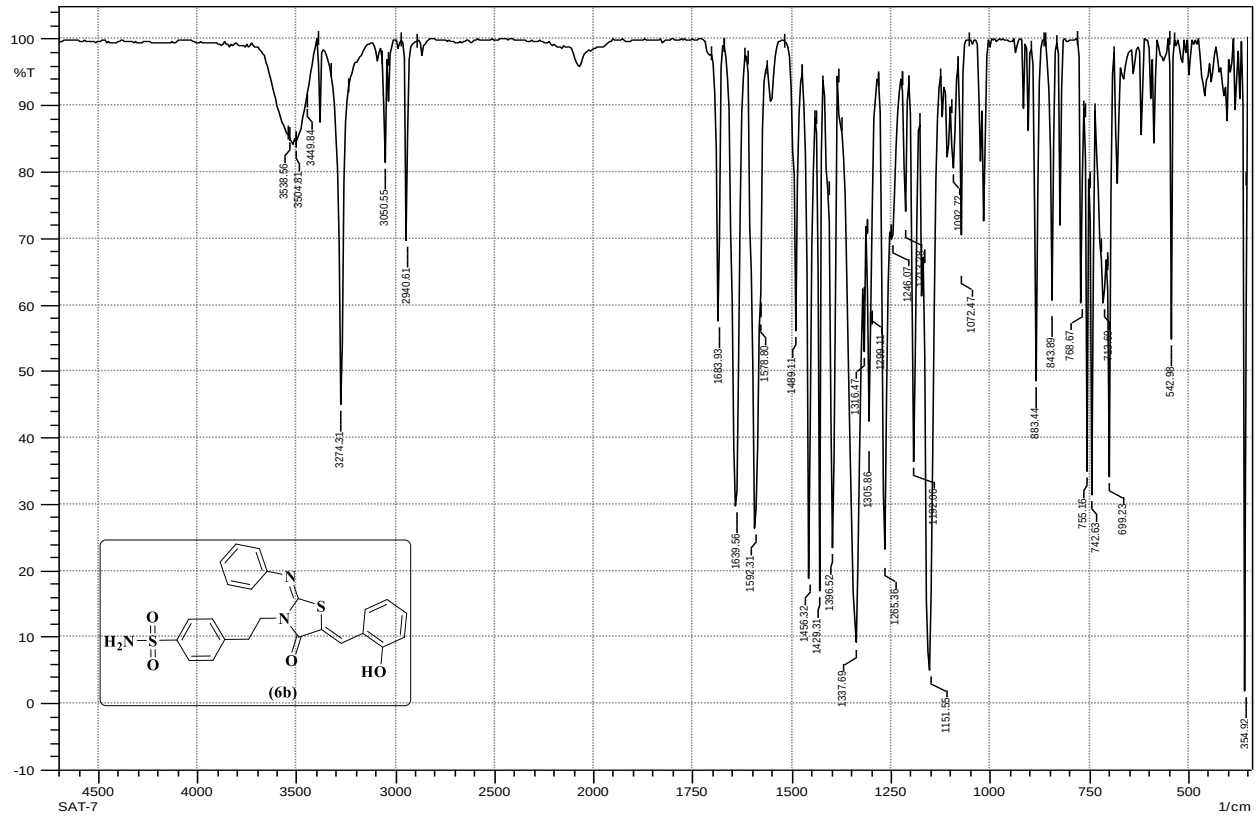
Spectra. 10: ^{1}H NMR (400 MHz, δ, ppm) spectra of compound 6a



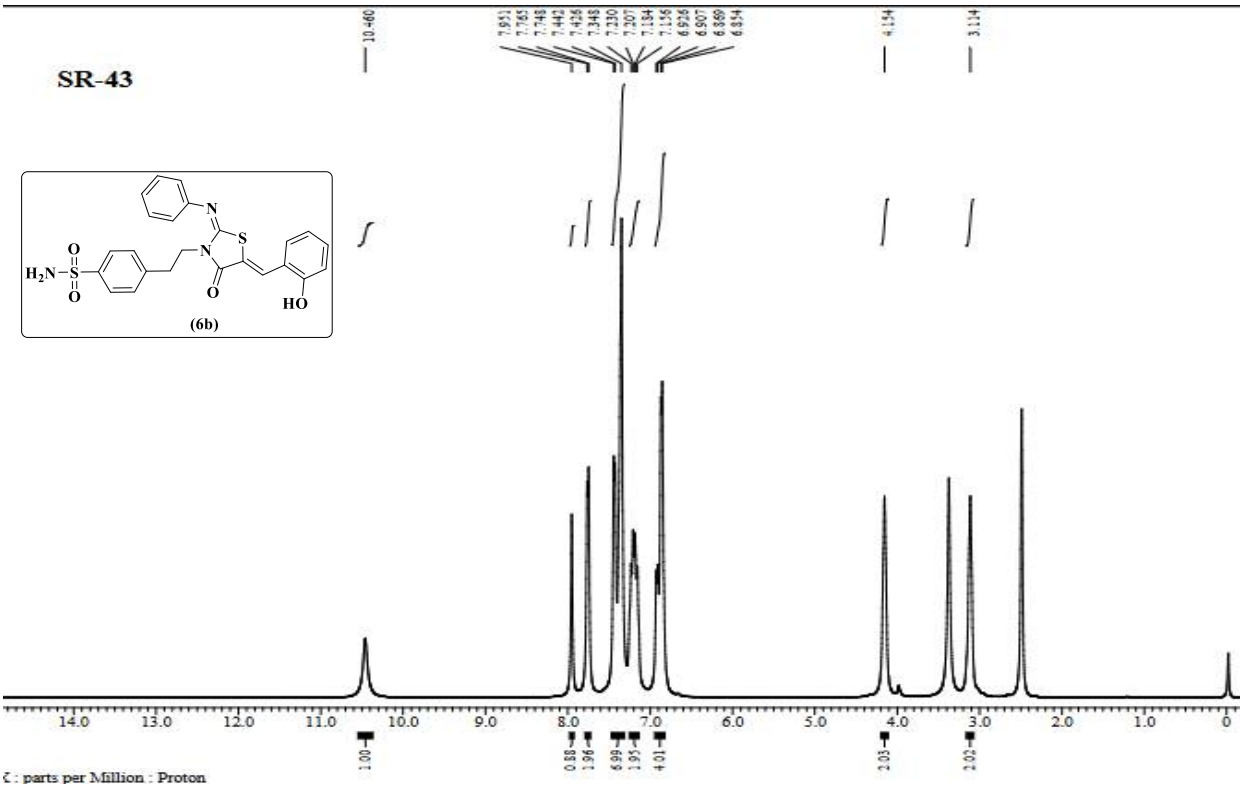
Spectra. 11: ^{13}C NMR (100 MHz, δ, ppm) spectra of compound 6a



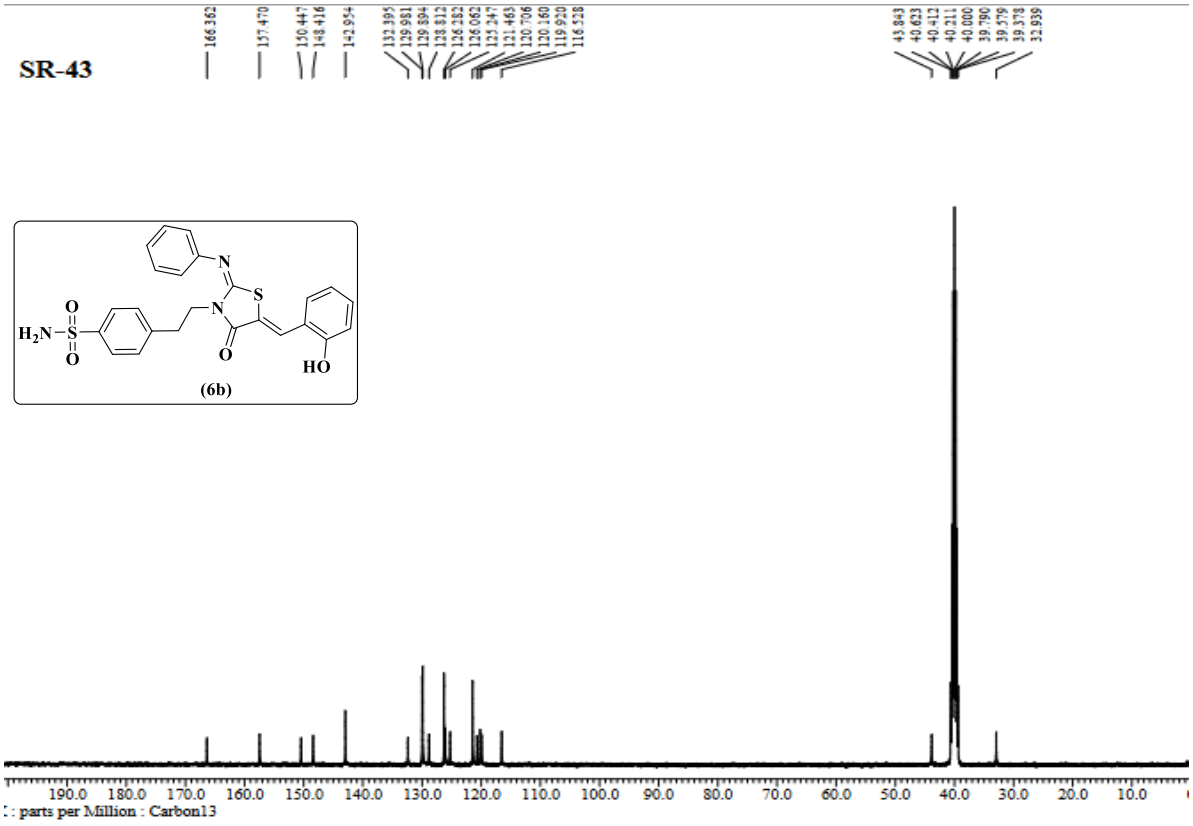
Spectra. 13: HRMS Spectra of compound 6a



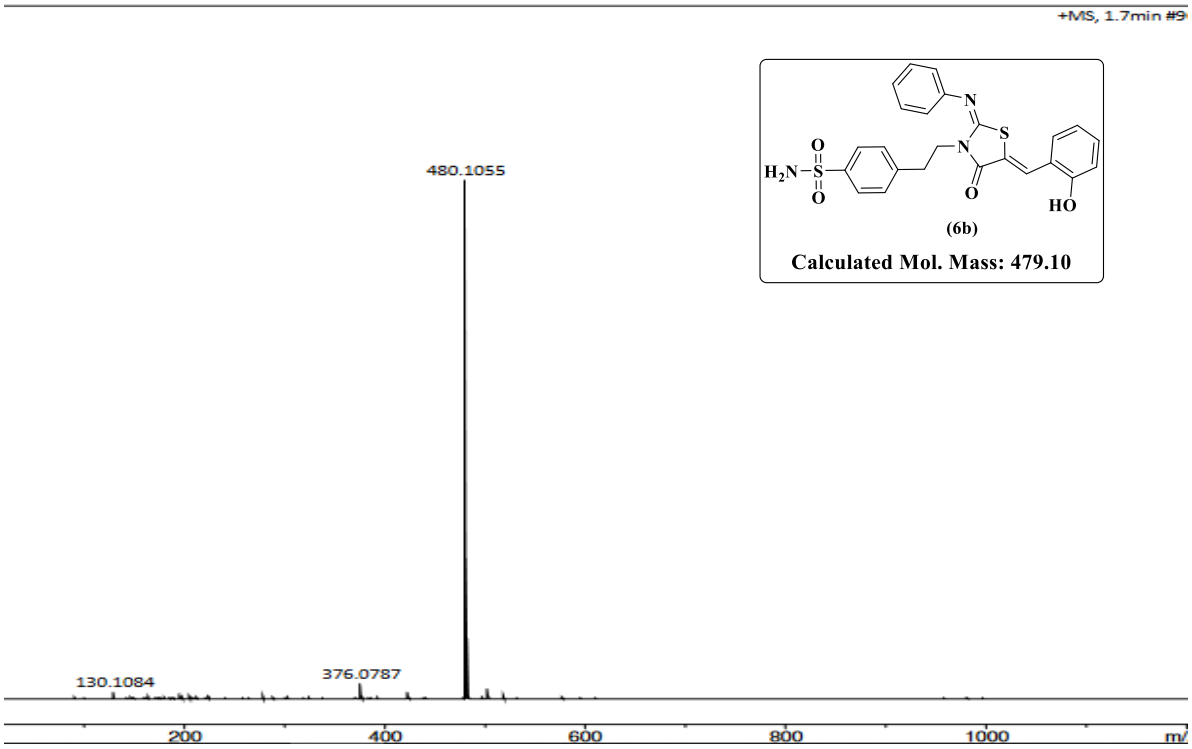
Spectra. 14: FTIR (KBr, cm^{-1}) spectra of compound 6b



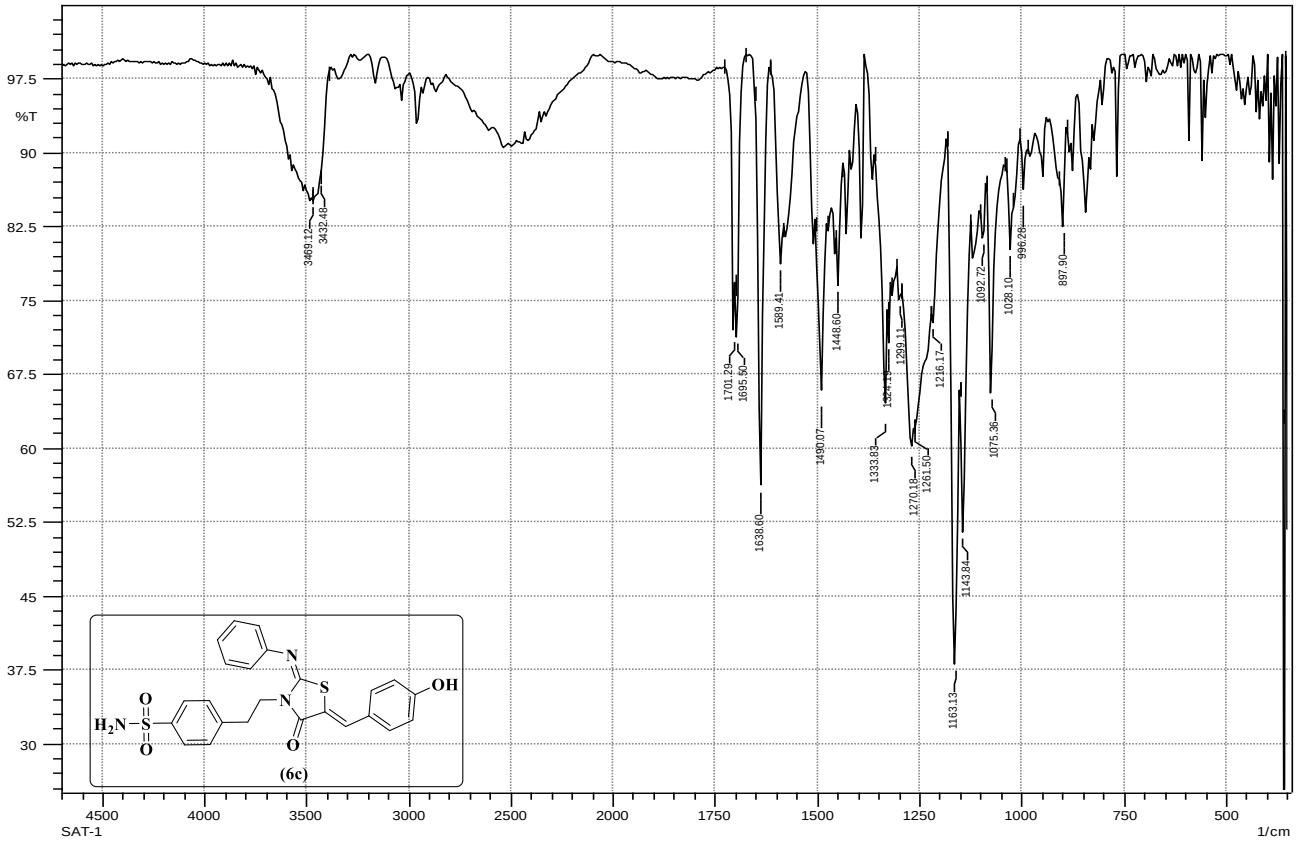
Spectra. 15: ^{1}H NMR (400 MHz, δ, ppm) spectra of compound 6b



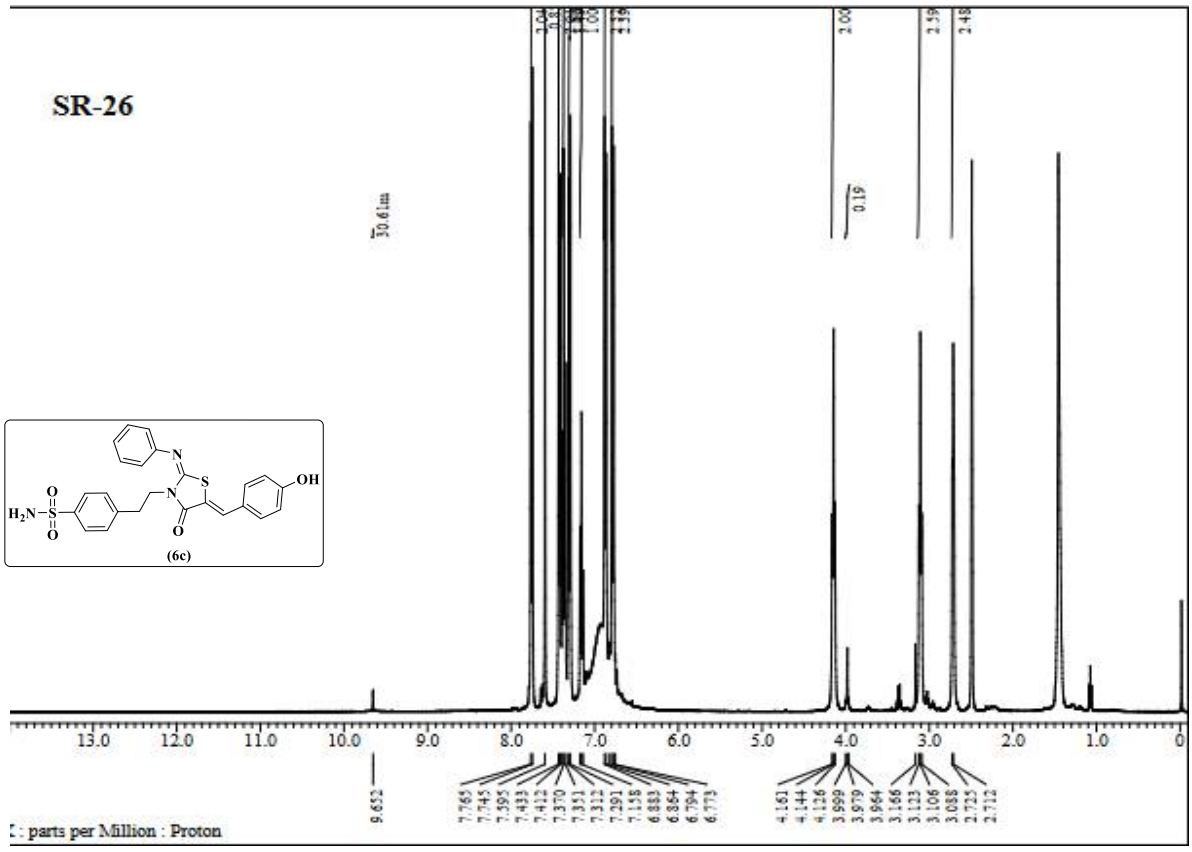
Spectra. 16: ^{13}C NMR (100 MHz, δ, ppm) spectra of compound 6b



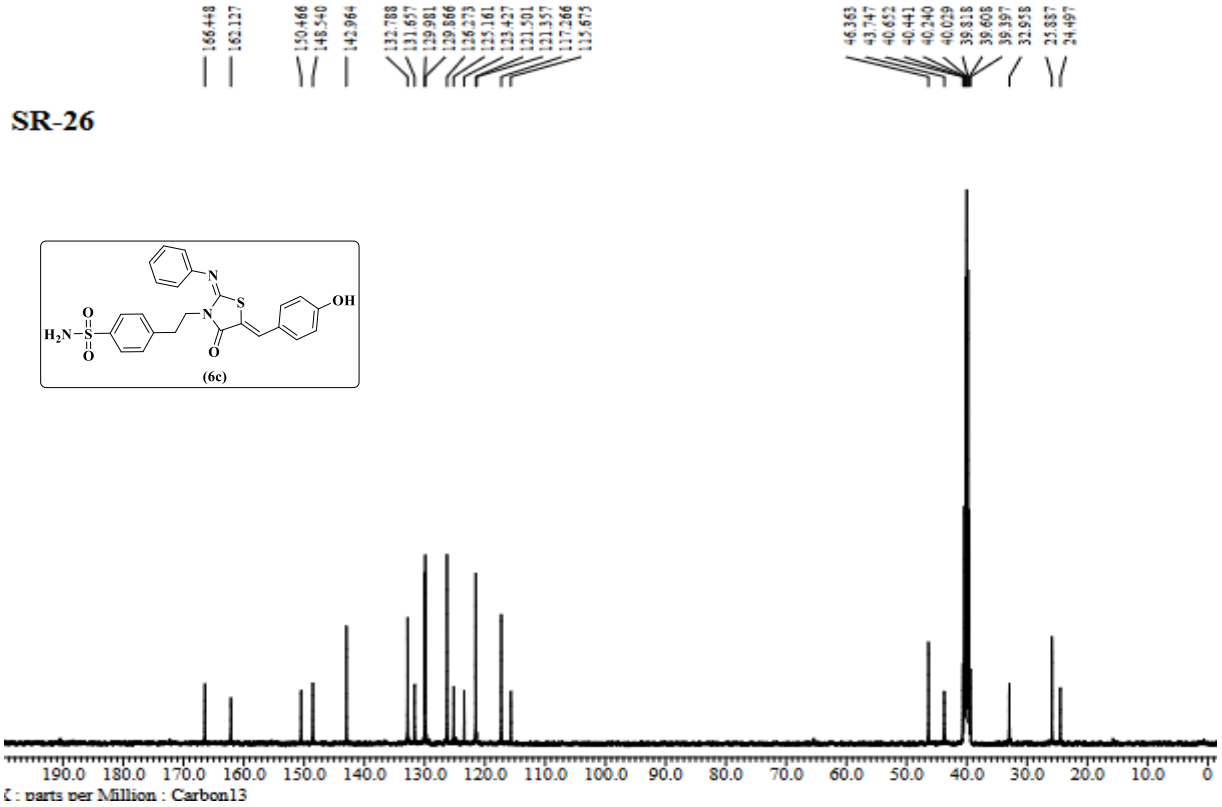
Spectra. 17: HRMS Spectra of compound 6b



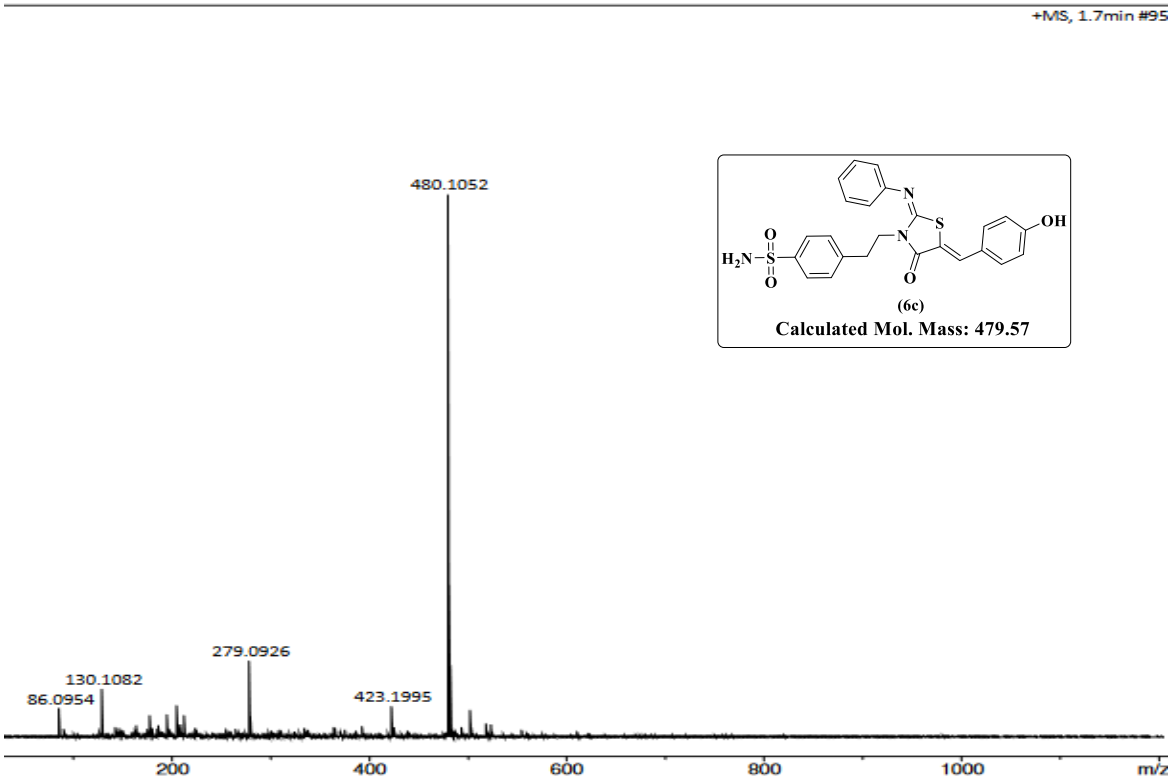
Spectra. 18: FTIR (KBr, cm^{-1}) spectra of compound 6c



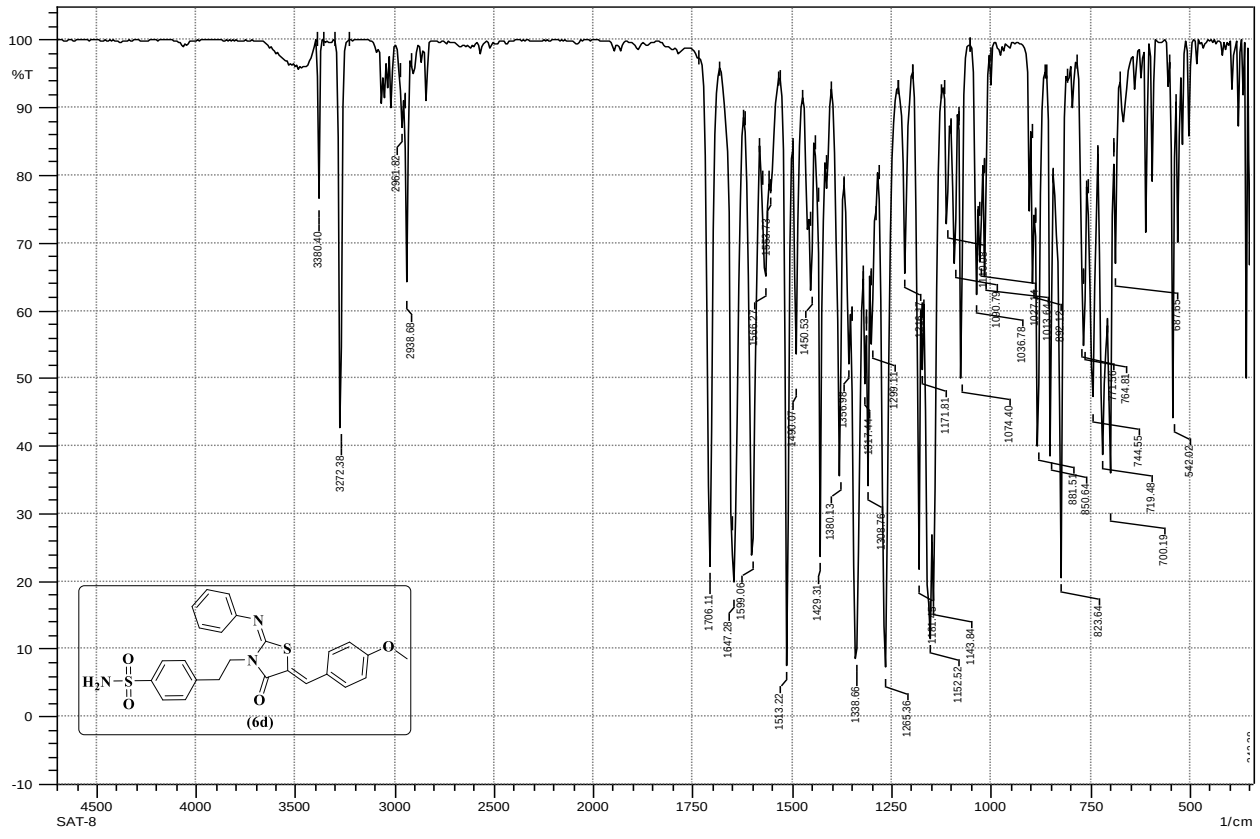
Spectra. 19: ^{1}H NMR (400 MHz, δ, ppm) spectra of compound 6c



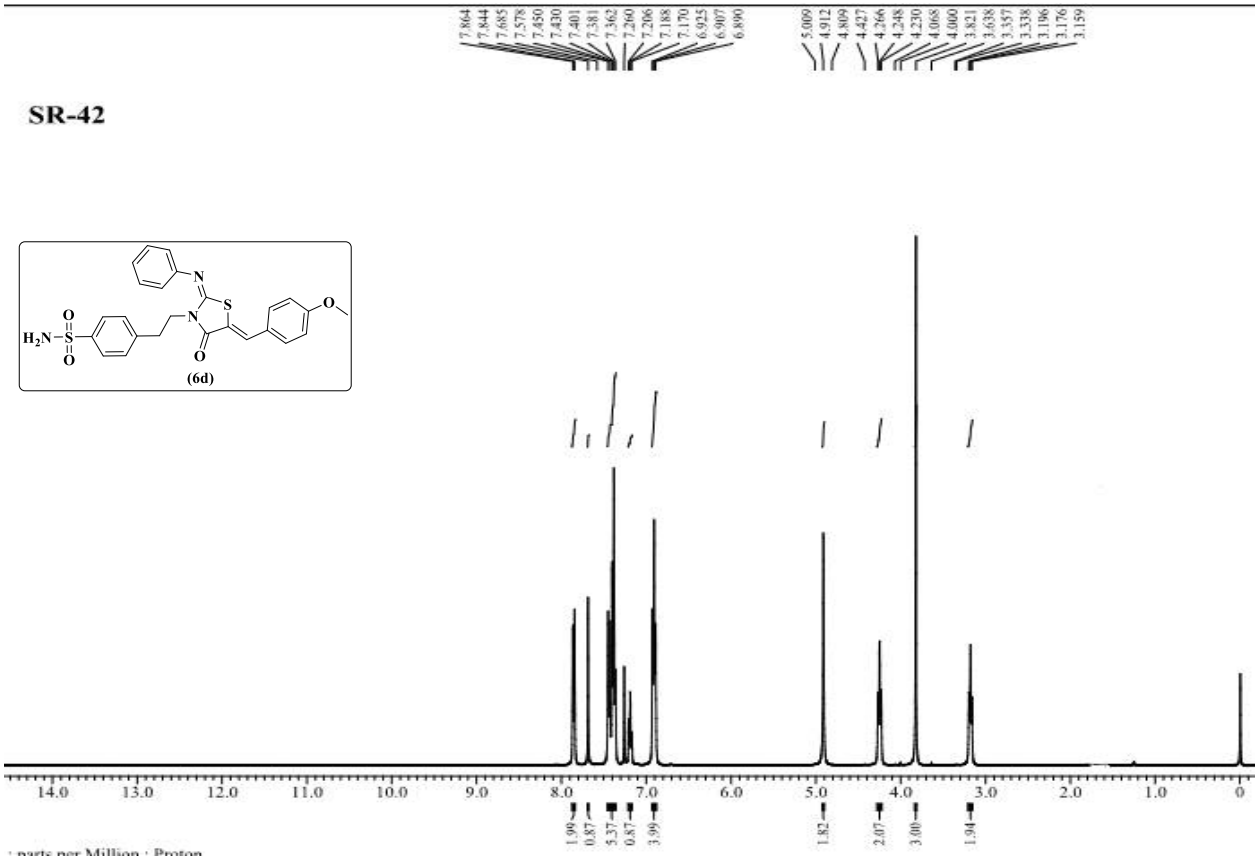
Spectra. 20: ^{13}C NMR (100 MHz, δ, ppm) spectra of compound 6c



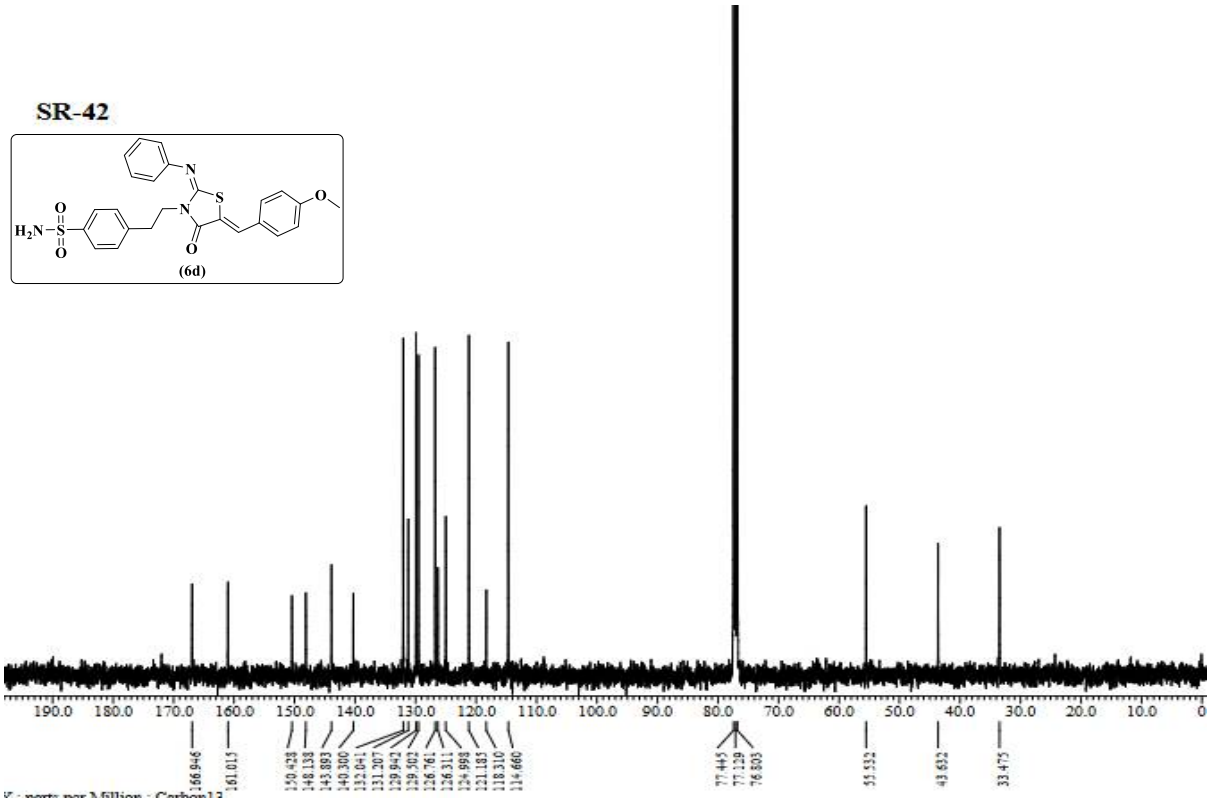
Spectra. 21: HRMS spectra of compound 6c



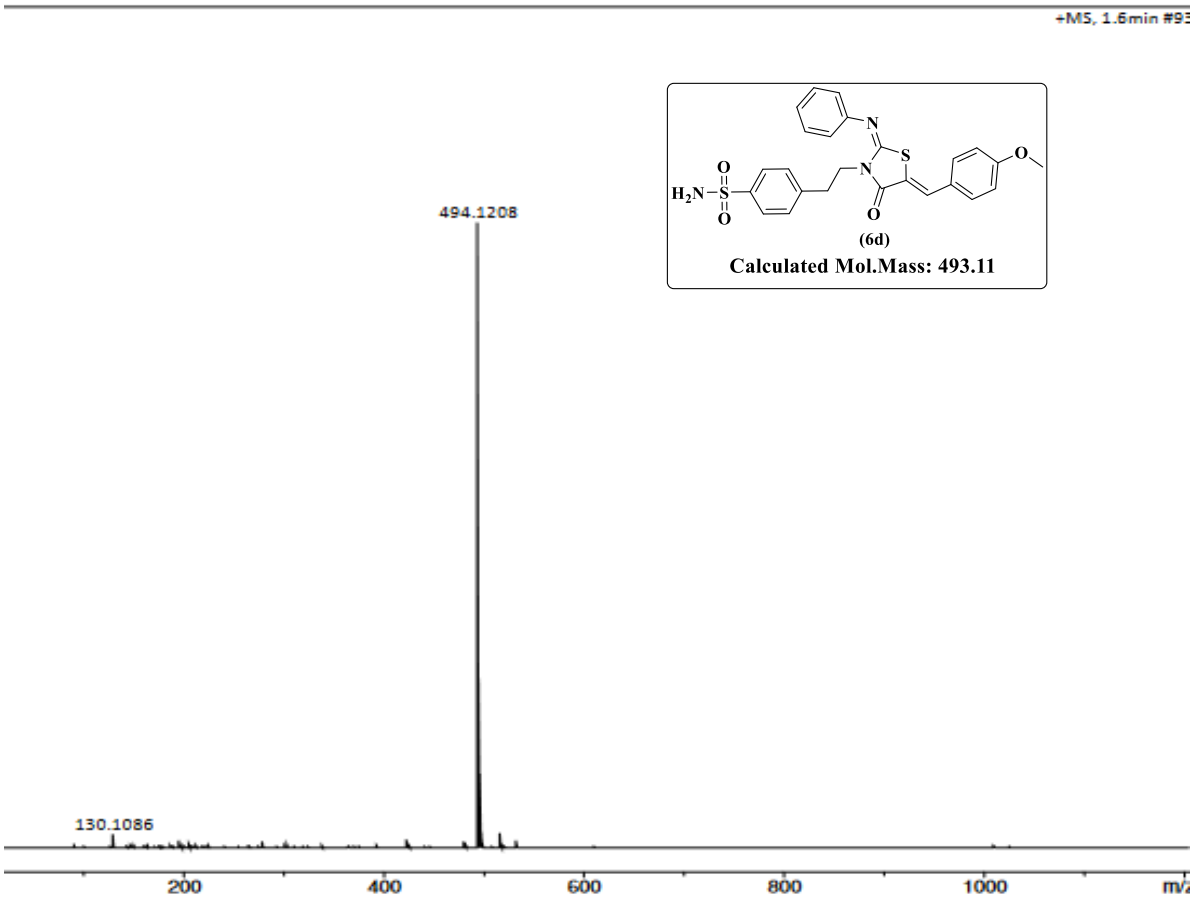
Spectra. 22: FTIR (KBr, cm^{-1}) spectra of compound 6d



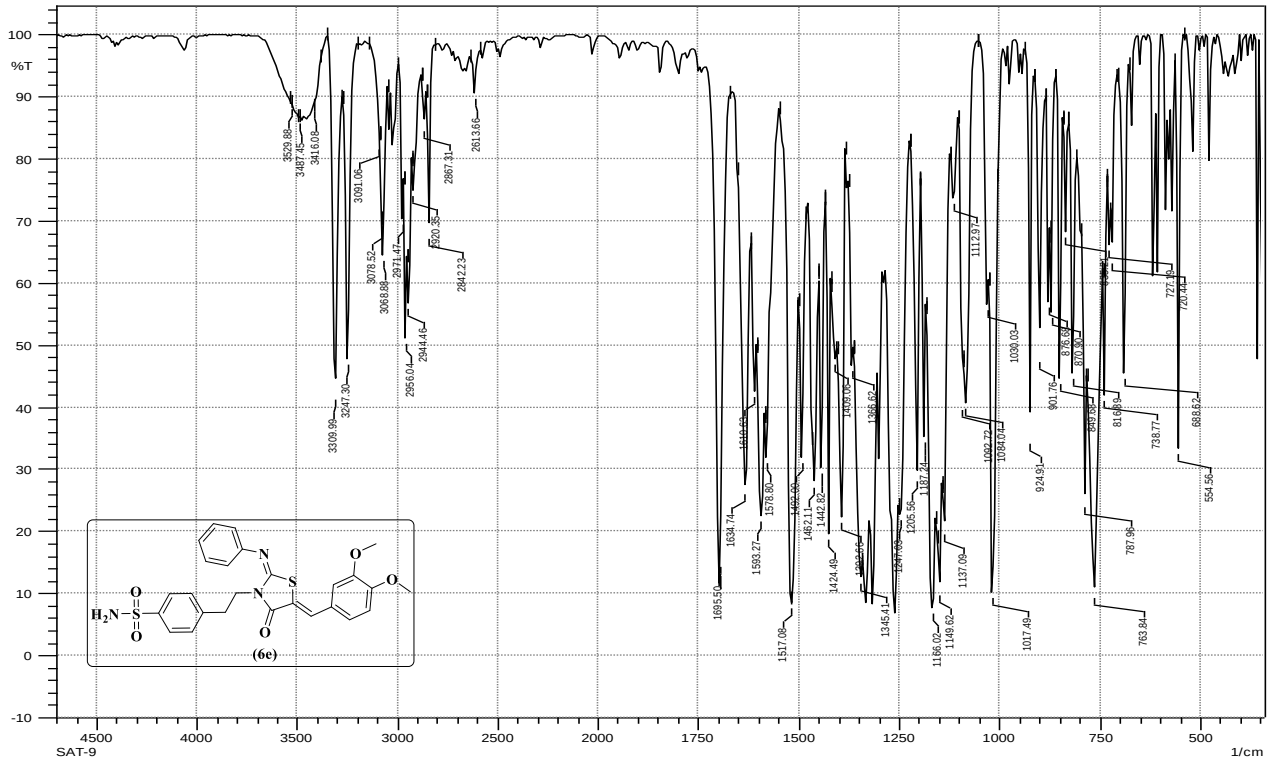
Spectra. 23: ^{1}H NMR (400 MHz, δ, ppm) spectra of compound 6d



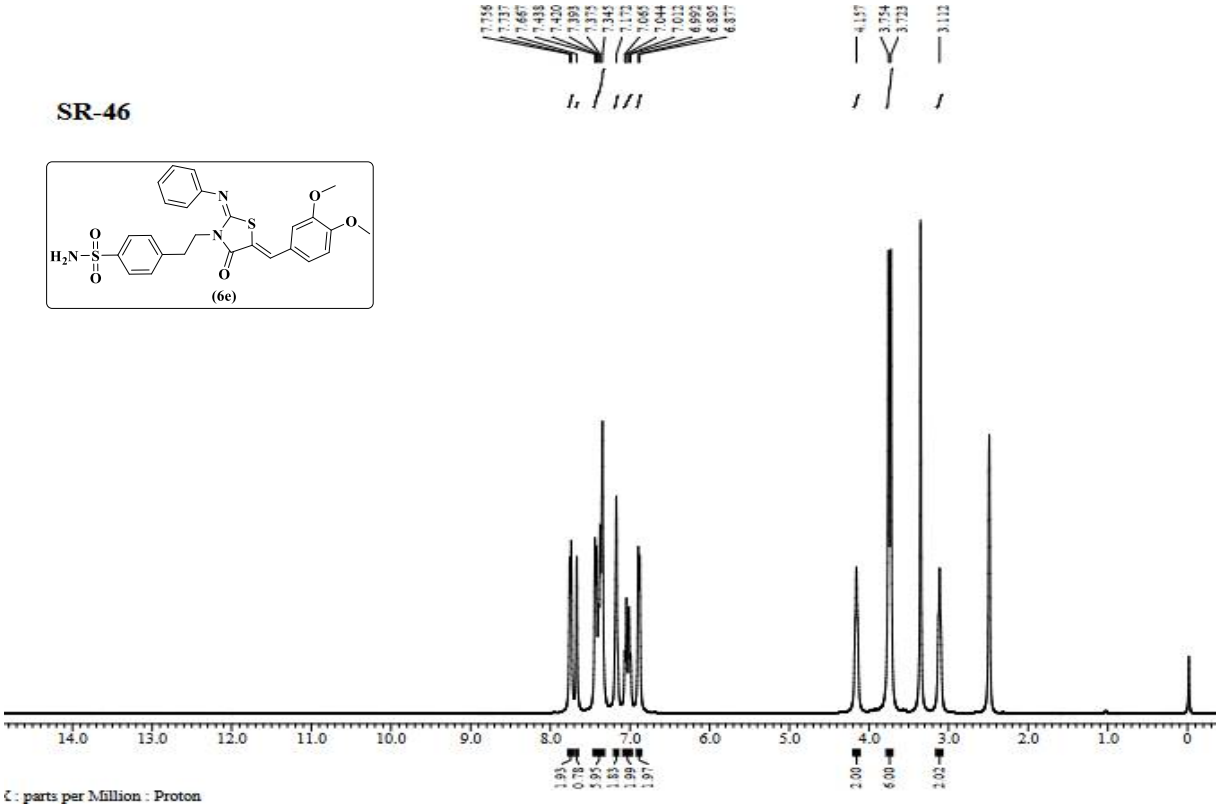
Spectra. 24: ^{13}C NMR (100 MHz, δ, ppm) spectra of compound 6d



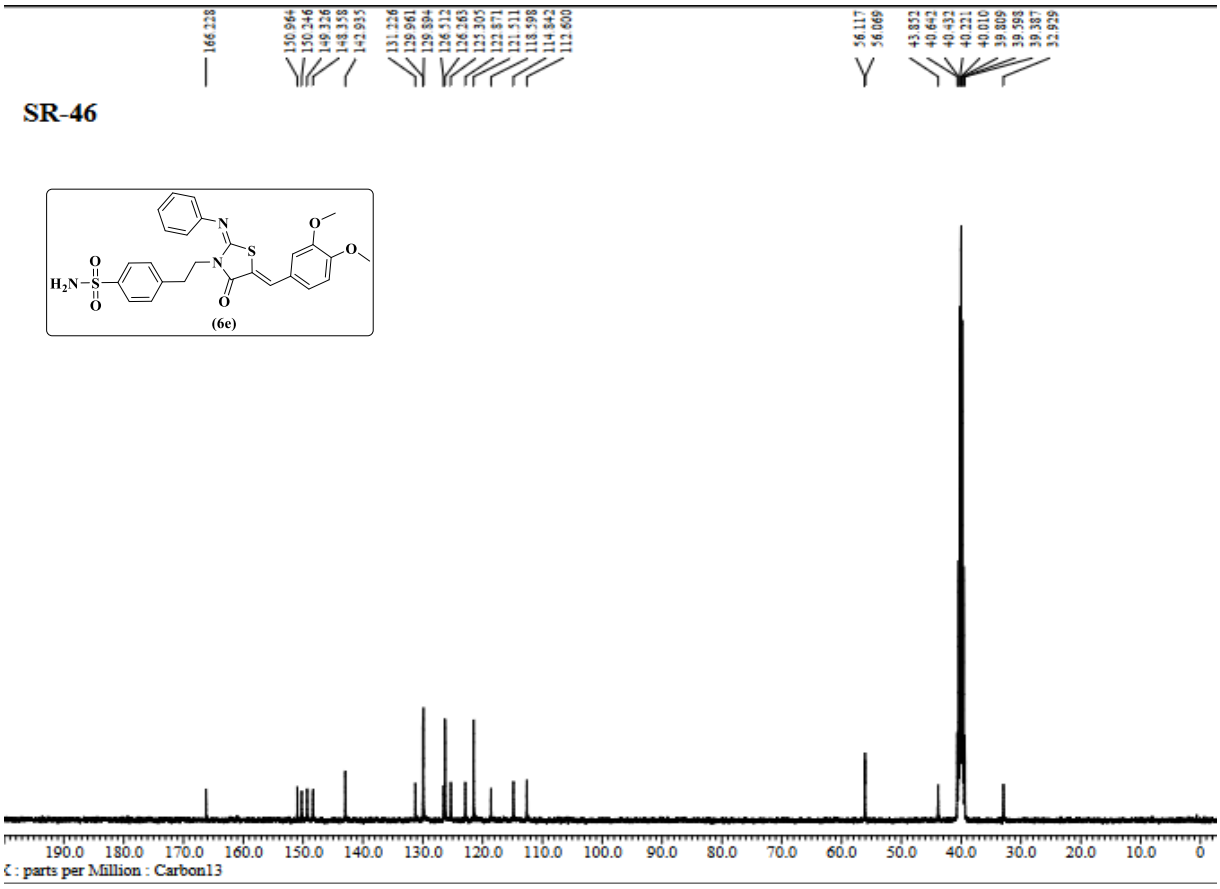
Spectra. 25: HRMS spectra of compound 6d



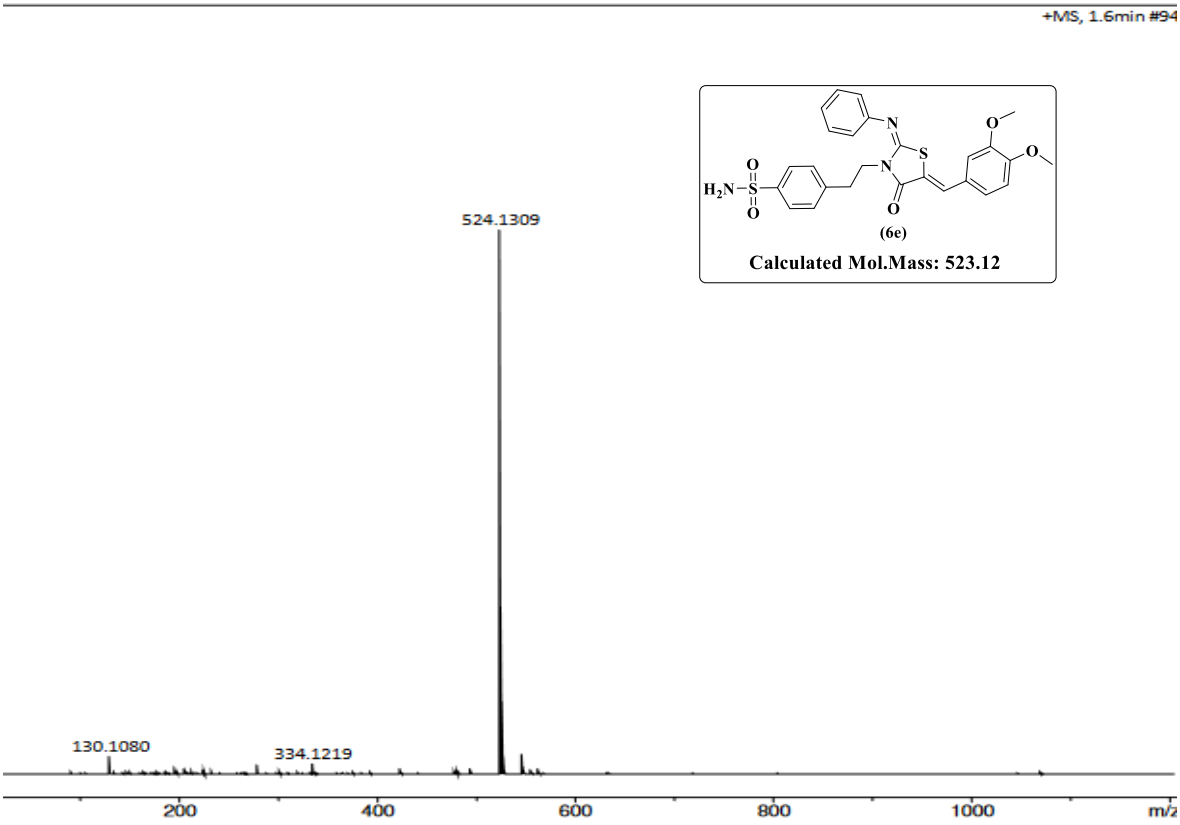
Spectra. 26: FTIR (KBr, cm^{-1}) spectra of compound 6e



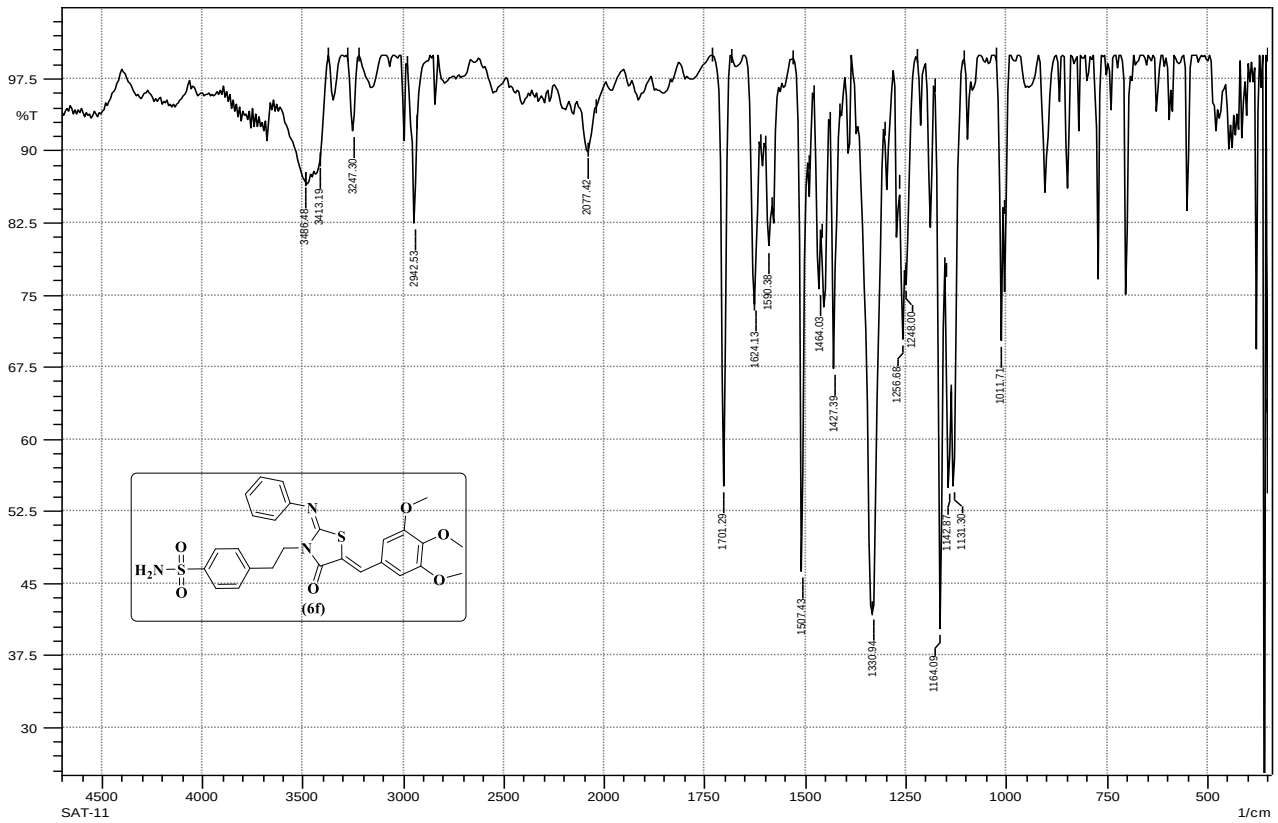
Spectra. 27: ^{1}H NMR (400 MHz, δ, ppm) spectra of compound 6e



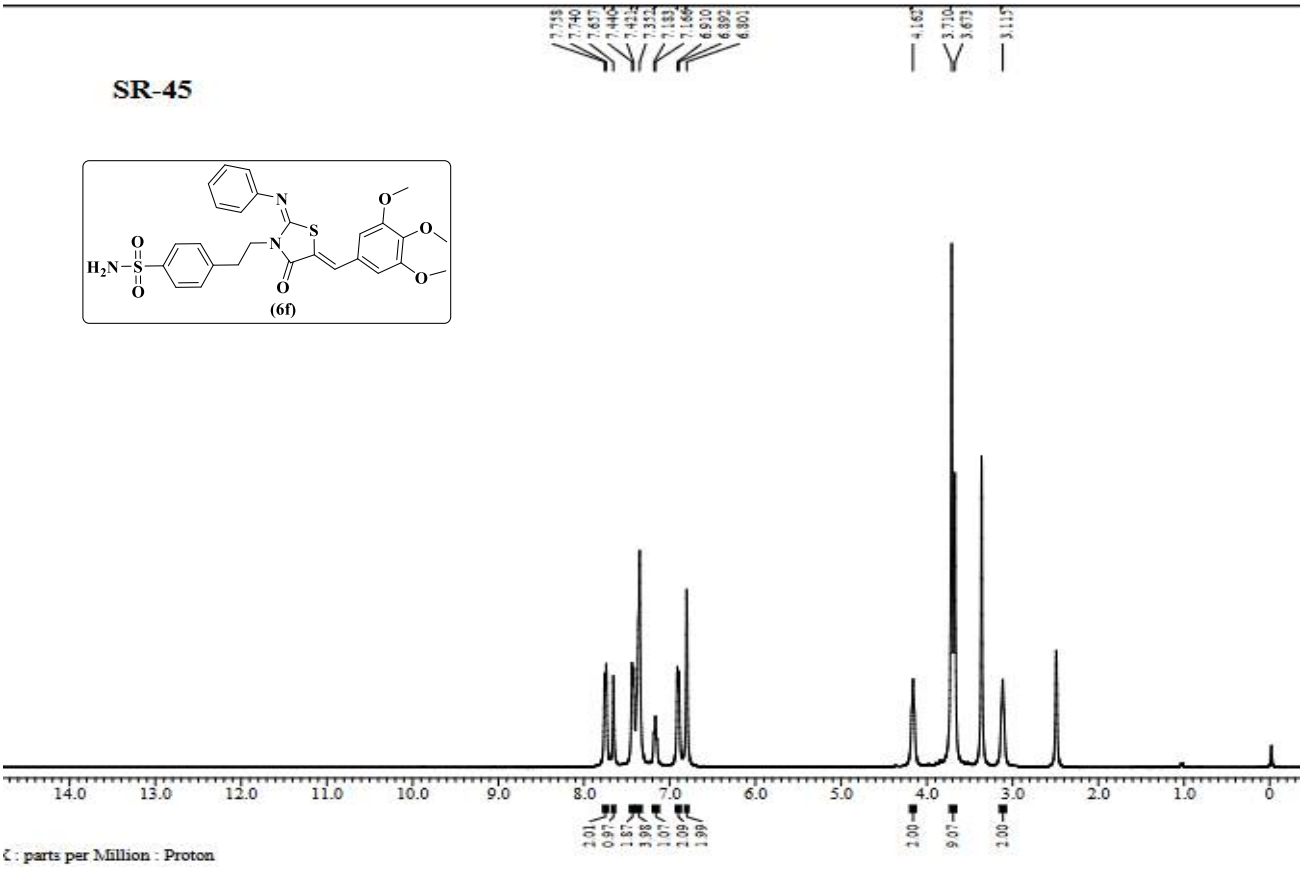
Spectra. 28: ^{13}C NMR (100 MHz, δ, ppm) spectra of compound 6e



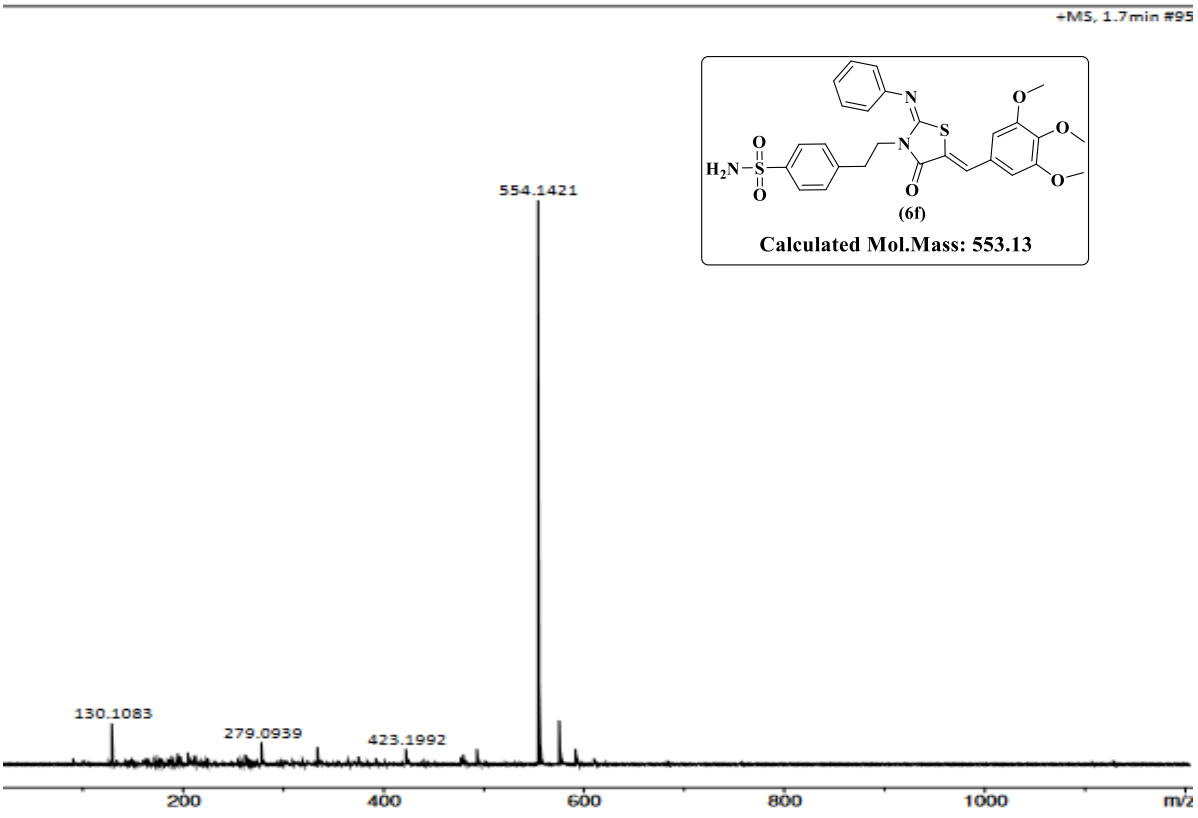
Spectra. 29: HRMS Spectra of compound 6e



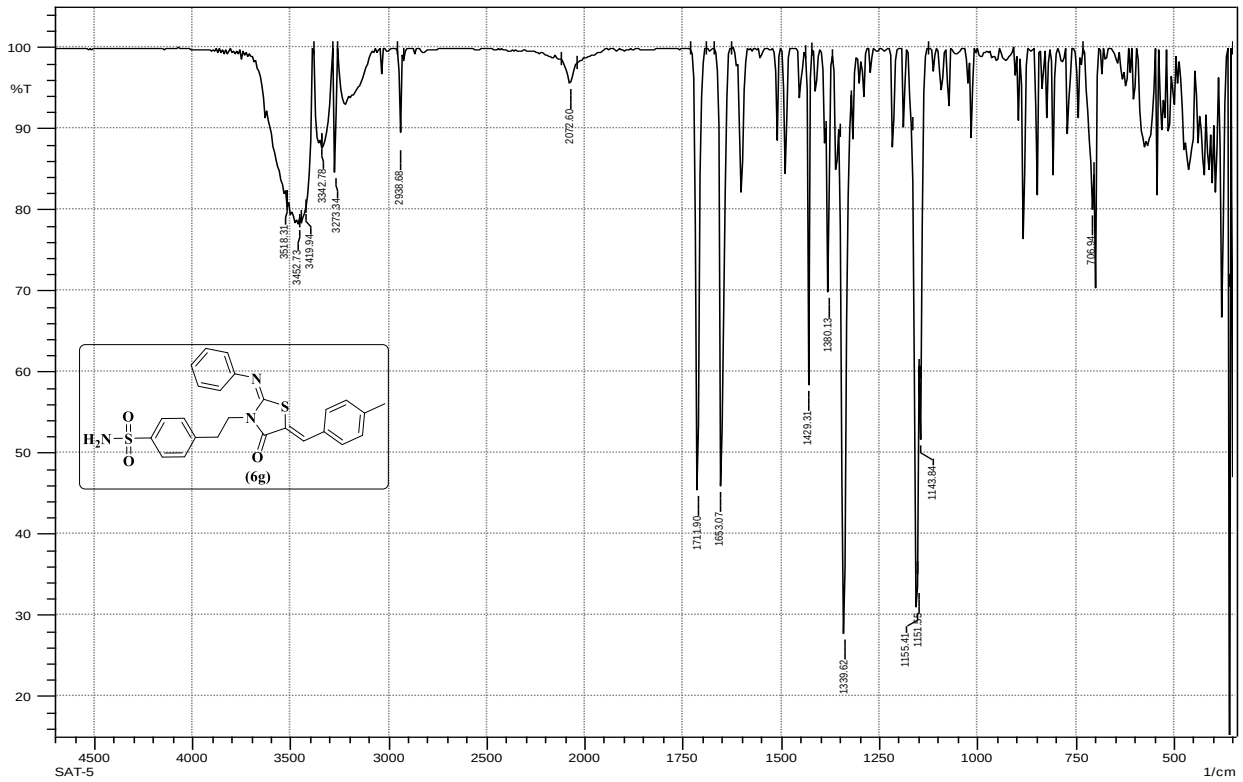
Spectra. 30: FTIR (KBr, cm^{-1}) spectra of compound 6f



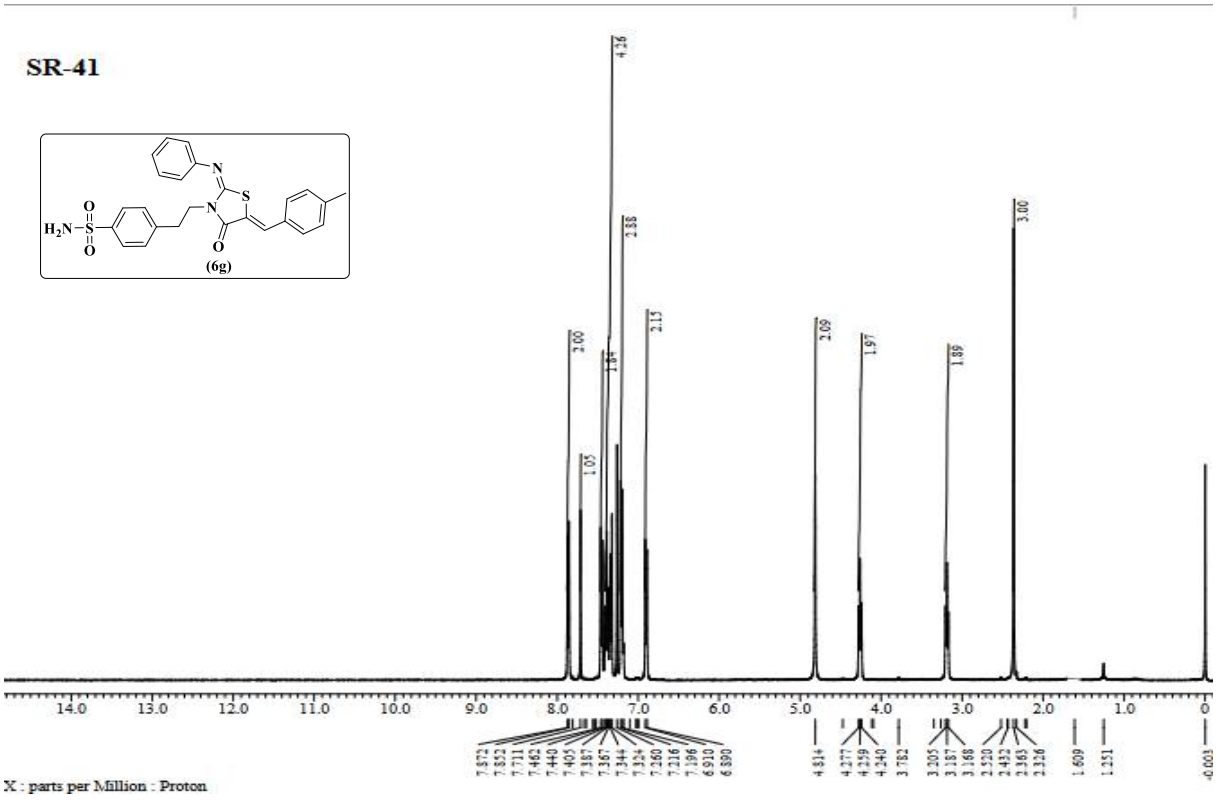
Spectra. 31: ^{1}H NMR (400 MHz, δ, ppm) spectra of compound 6f



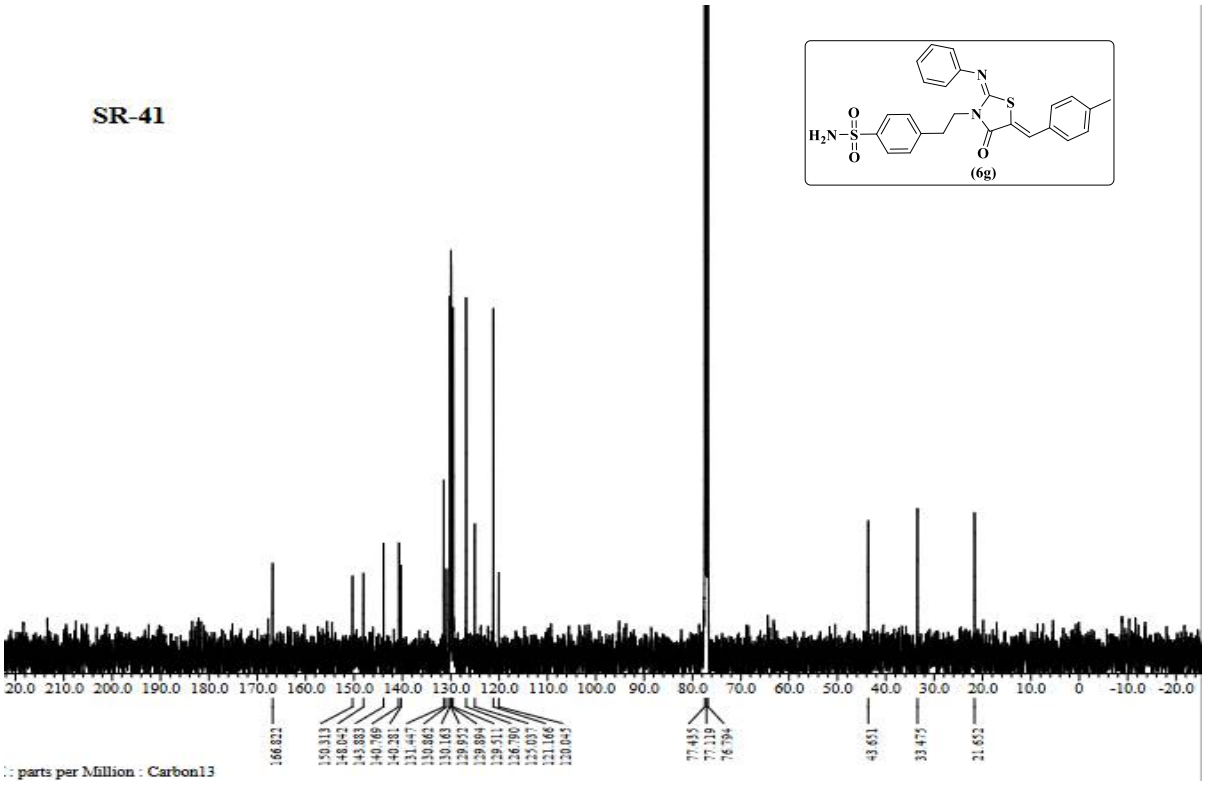
Spectra. 32: HRMS spectra of compound 6f



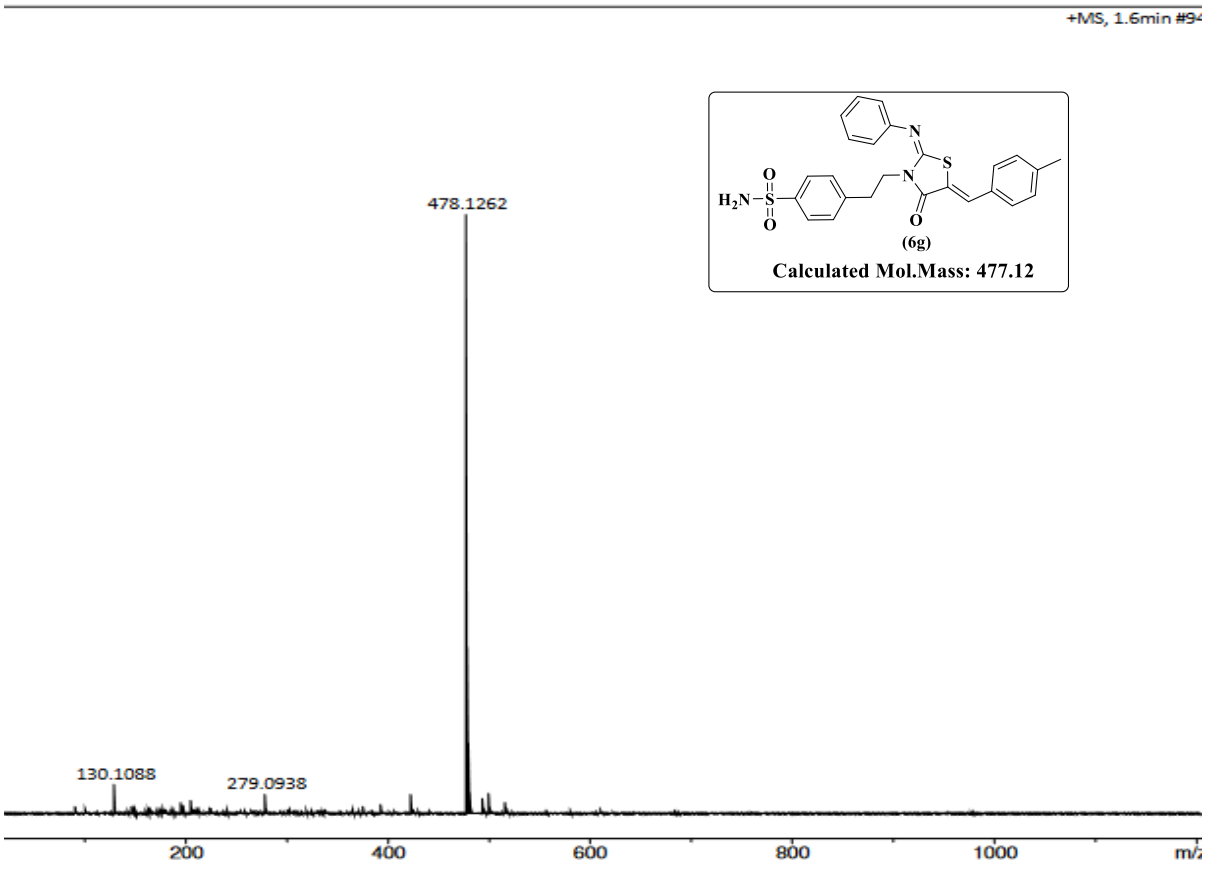
Spectra. 33: FTIR (KBr, cm^{-1}) spectra of compound 6g



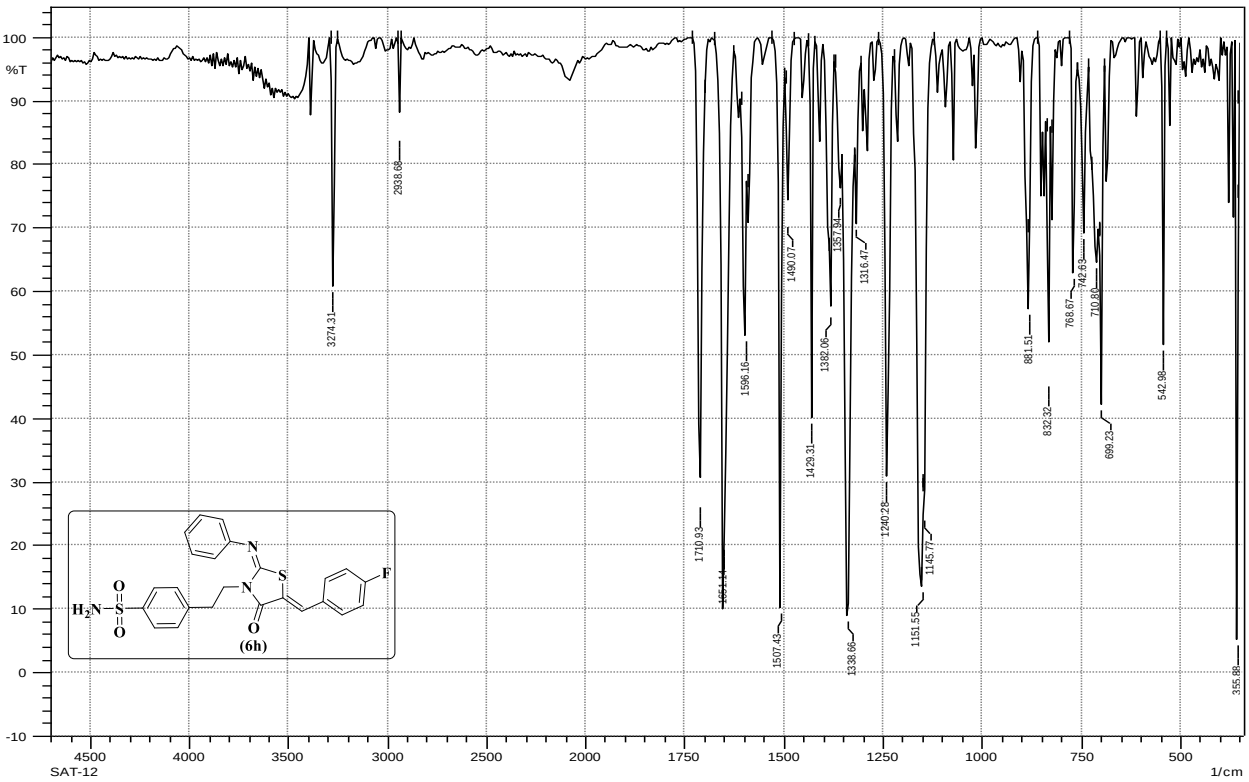
Spectra. 34: ^{1}H NMR (400 MHz, δ, ppm) spectra of compound 6g



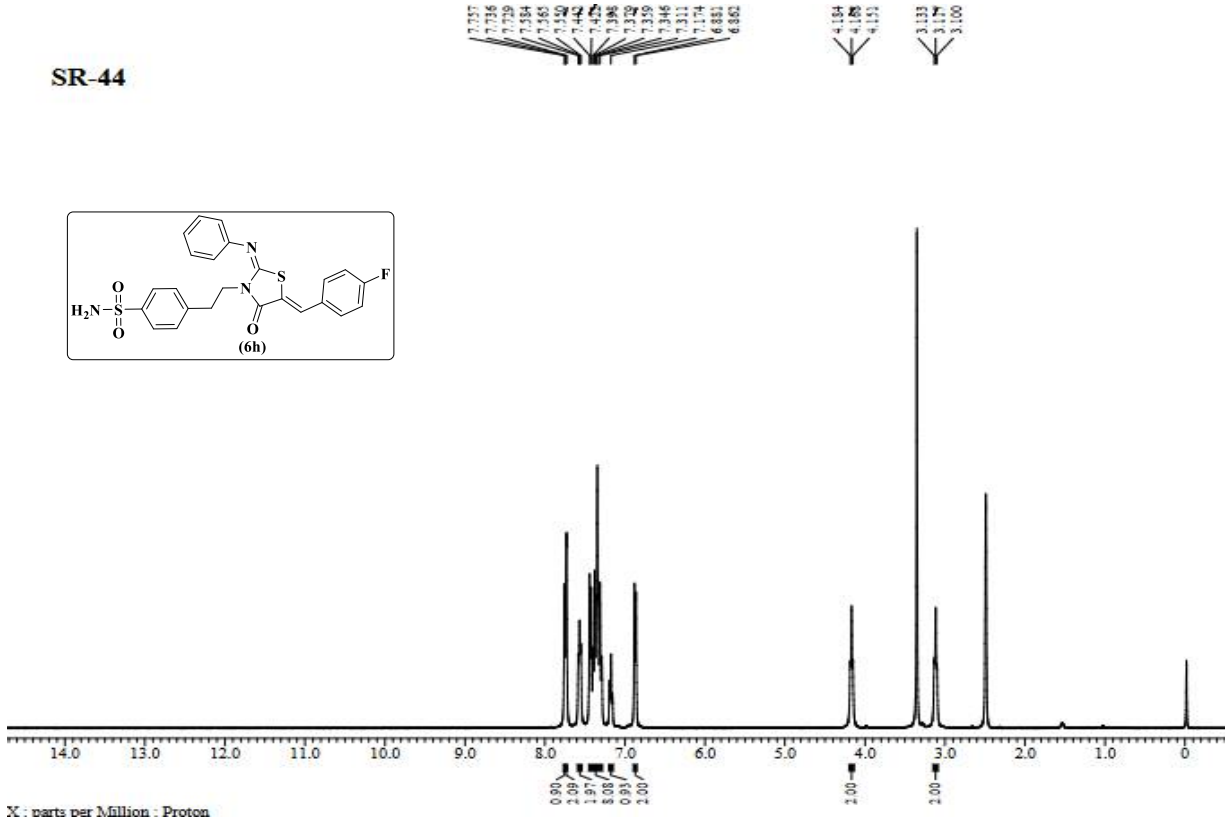
Spectra. 35: ^{13}C NMR (100 MHz, δ, ppm) spectra of compound 6g



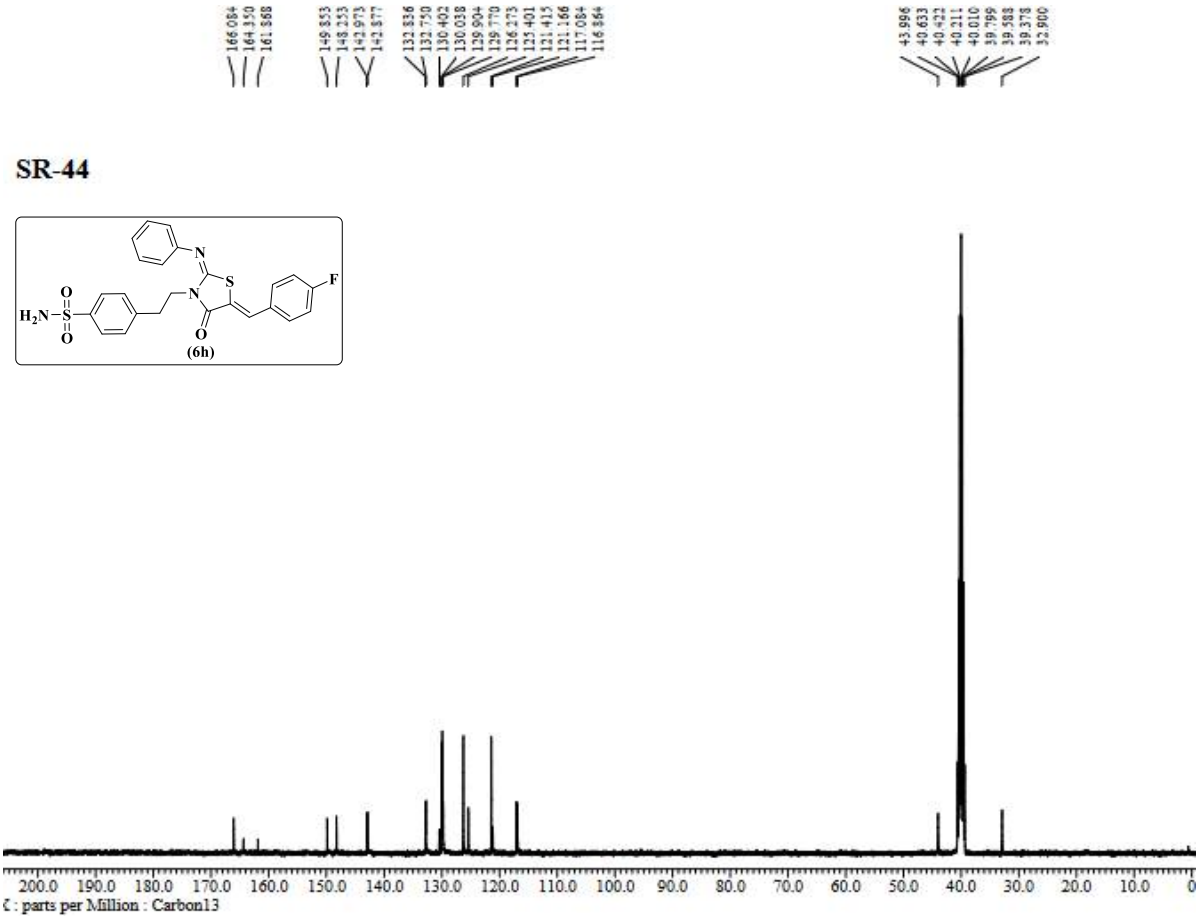
Spectra. 36: HRMS spectra of Compound 6g



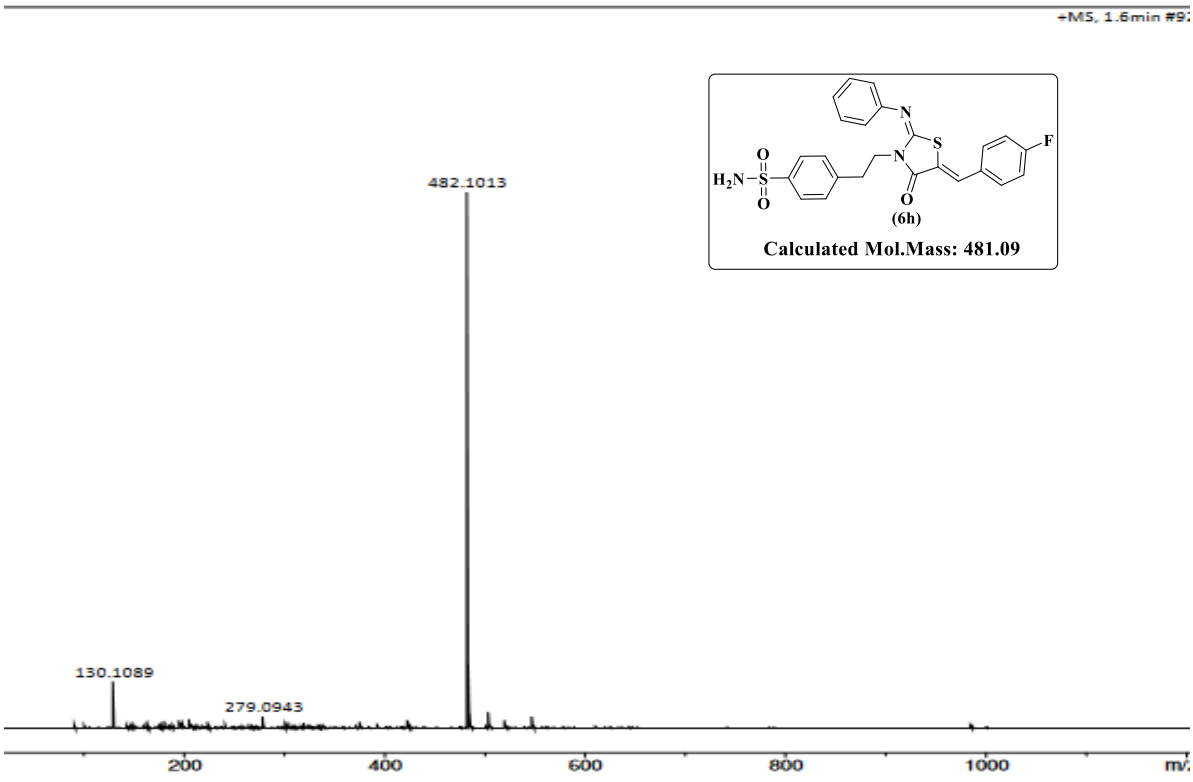
Spectra. 37: FTIR (KBr, cm^{-1}) spectra of compound 6h



Spectra. 38: ^{1}H NMR (400 MHz, δ, ppm) spectra of compound 6h



Spectra. 39: ^{13}C NMR (100 MHz, δ, ppm) spectra of compound 6h

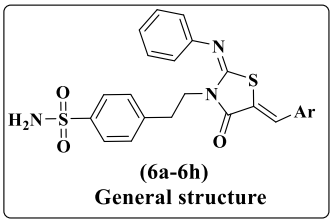


Spectra. 40: HRMS Spectra of compound 6h

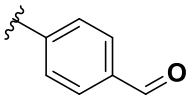
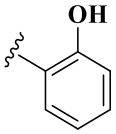
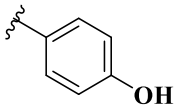
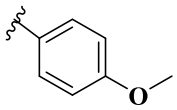
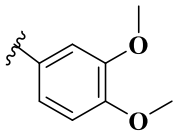
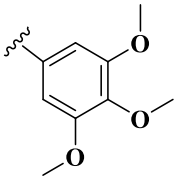
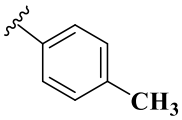
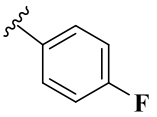
5. Pharmacological evaluation

5.1. *Invitro α-amylase* inhibition assay

The synthesized title compounds were evaluated for their *α-amylase* inhibitory activity, and several compounds exhibited significant enzyme inhibition. The inhibitory activity, expressed as IC_{50} values, ranged from 29.51 ± 1.35 µg/mL to 58.73 ± 0.476 µg/mL (**Table 2**). Among the tested derivatives, compound **6b** demonstrated the most potent inhibitory activity with an IC_{50} of 29.51 ± 1.35 µg/mL, which is comparable to the standard acarbose (IC_{50} = 26.89 ± 0.116 µg/mL). Other active analogs, such as 6c, 6d, and 6e, displayed IC_{50} values of 35.70 ± 0.21 µg/mL, 31.19 ± 0.104 µg/mL, and 36.77 ± 0.263 µg/mL, respectively. Among the series, **6b** emerged as a promising lead compound for *α-amylase* inhibition, attributed to the presence of a polar hydroxyl (-OH) substitution at the ortho position of the phenyl ring. The second most active compound, **6d**, exhibited a para-positioned methoxy ($-OCH_3$) substituent on the phenyl moiety. A decrease in inhibitory activity was observed with the introduction of bulkier non-polar groups, such as 2, 4-dimethoxy and 3, 4, 5-trimethoxy substitutions on the phenyl ring. The superior inhibitory effect of **6b** may be explained by its resemblance to the electron-donating properties of acarbose, a polyhydroxy compound, where the ortho-hydroxyl group on the phenyl ring of **6b** serves as an electron-donating substituent, thereby enhancing the enzyme-binding interactions. The SAR of the synthesized compounds revealed a correlation between the nature of substituents and their *α-amylase* inhibitory activity. Compounds bearing polar, electron-donating substituents exhibited enhanced inhibitory potency, as observed in **6b** and **6c**. This trend is consistent with the reference compound acarbose, a polyhydroxy molecule with strong electron-donating properties. In contrast, the introduction of non-polar, electron-donating groups, as seen in compound **6g**, resulted in a reduction in inhibitory activity. Similarly, compounds **6a**, **6d**, **6e**, **6f**, and **6h**, which contain electron-withdrawing substituents, also showed diminished inhibitory potency. These findings suggest that the presence of polar, electron-donating groups enhances *α-amylase* inhibition, whereas non-polar or electron-withdrawing substituents reduce the activity.



(6a-6h)
General structure

Code	Ar	IC_{50} ± SEM[a] (µg/ml)
6a		47.56 ±0.165
6b		29.51±1.35
6c		35.70±0.21
6d		31.19±0.104
6e		36.77±0.263
6f		47.79±0.05
6g		>50
6h		47.70±0.183
Acarbose		26.89±0.116

[a] Standard Error Mean

Table 2. IC_{50} values of Compounds (**6a-6h**) for *α-amylase* inhibition.

5.2. Glucose Uptake assay in yeast cells

The synthesized compounds (**6a-6h**) were evaluated for their glucose uptake activity using a yeast cell assay. In the human body, approximately 80% of glucose uptake occurs in skeletal muscle, primarily facilitated by insulin. Impairment in insulin secretion or resistance in skeletal muscle and adipose tissue leads to reduced glucose uptake. Glucose uptake is mediated by glucose transporter proteins (GLUTs), predominantly GLUT1 and GLUT4, with GLUT4 playing a key role in promoting glucose uptake into cells.[157] In this context, the ability of compounds (**6a-6h**) to modulate GLUT activity was investigated in yeast cells. Compounds (**6a-6h**) were screened for glucose uptake activity at concentrations of 12.5, 25, 50, 100, and 200 µg/mL (**Fig. 7**). Compounds **6b**, **6e**, and **6f** demonstrated significant glucose uptake, with maximum uptake of 88.71%, 85.79%, and 81.43%, respectively, at 200 µg/mL, compared to the standard pioglitazone (91.64% at 200 µg/mL). Compounds 6a, 6c, 6d, 6g, and 6h exhibited moderate glucose uptake, with uptake values of 70.21%, 73.67%, 69.05%, 71.84%, 72.79%, and 68.63%, respectively, at 200 µg/mL. These findings suggest that compounds **6b**, **6e**, and **6f** may have potential as modulators of GLUT-mediated glucose uptake, similar to pioglitazone, while the other analogs displayed moderate activity.

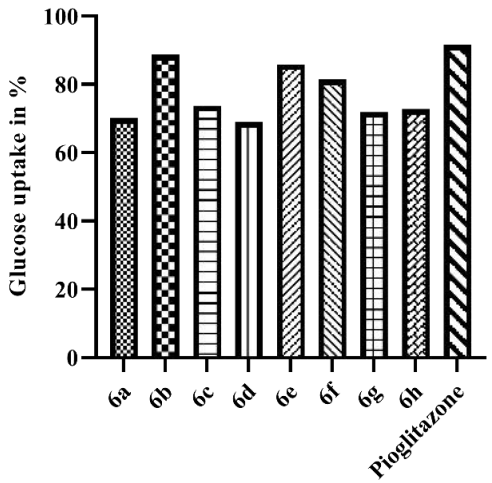


Fig. 7: Glucose uptake capacity of synthesised compounds **(6a-6h)** in yeast cells.

5.3. PPAR-γ transcription factor assay

The PPAR- γ activation is known to be positively associated with the expression of GLUT carriers, also PPAR-γ modulation enhances lipid metabolism in adipose tissue *via* reducing the circulating FFA which results in enhanced translocation of GLUT to cell membrane resulting in glucose uptake in insulin resistance condition associated with DM. Thus the modulation of PPAR-γ TF by the compound **6b** (6.25-100 µM) was studied and compared with standard pioglitazone (1µM), which revealed, compound **6b** demonstrated that there was a dose dependent increase in transactivation of PPAR- γ TF as shown in the **Fig. 8.**

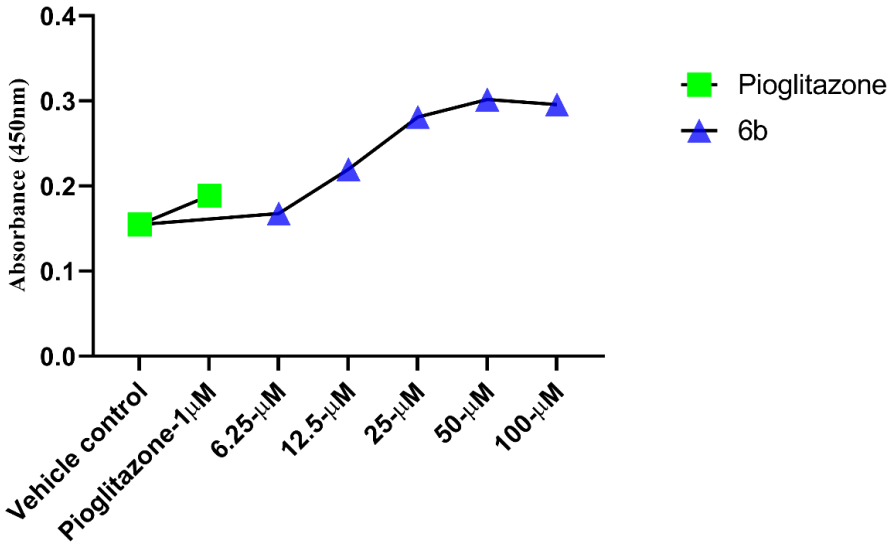


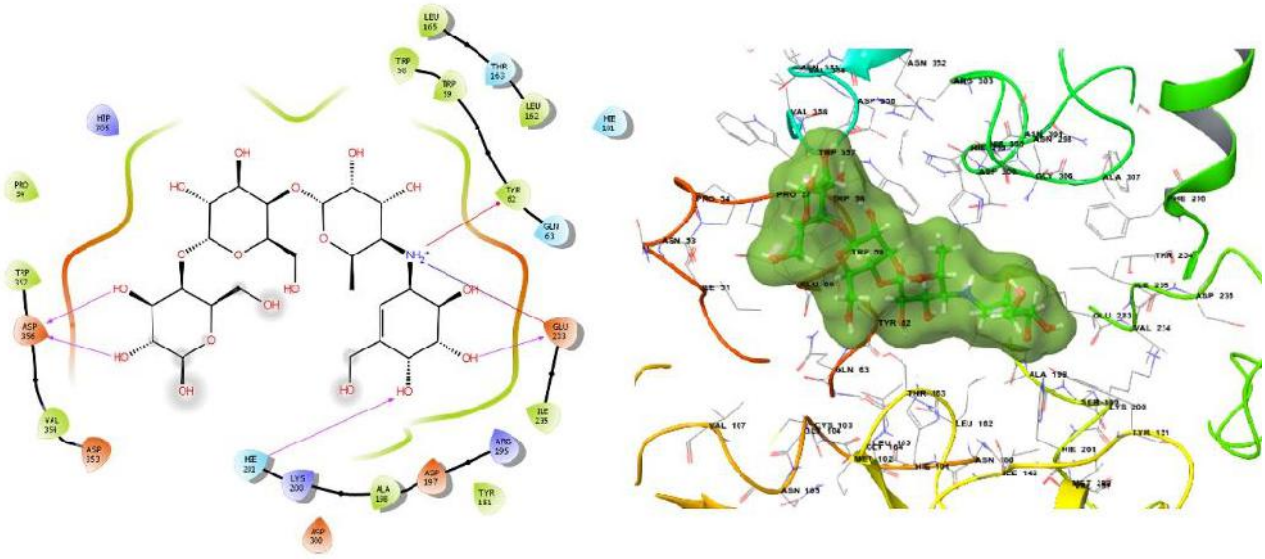
Fig. 8: Expression of PPAR-γ TF by compound **6b** and pioglitazone.

6. *Insilico* study

6.1. Induced fit docking

To support the *α-amylase* inhibition results, molecular docking studies were conducted to explore the binding interactions of the synthesized ligands (**6a-6h**) with the active site of the *α-amylase* enzyme. IFD was performed using the Schrödinger Suite (version 2023-2), allowing for flexibility at the enzyme's binding site and refinement of the ligand–receptor complex poses. This approach provided

insights into the potential binding interactions that contribute to the observed antidiabetic activity of the compounds. The synthesized compounds (**6a–6h**) and the standard acarbose were docked into the binding pocket of human pancreatic *α-amylase* (PDB ID: 4W93). Docking was performed using a standard sampling protocol, which involved simultaneous Prime refinement and Glide docking to accurately predict the ligand–receptor binding modes and interactions within the active site. This approach provided a comprehensive analysis of the binding conformations and interaction patterns of the ligands with the enzyme. As previously described by Brayer, G. D., et al, key amino acid residues within the domain A binding site of the *α-amylase* enzyme, which are responsible for triggering the biological response, include Asp197, Glu233, Asp300, Arg195, His299, Ala198, Tyr62, and Gln63.[158] Acarbose was shown to form three hydrogen bond networks, involving Glu233 and Asp356, with the hydroxy group interacting with Glu233. Additionally, acarbose established a salt bridge between the amino groups in its quaternary state and Glu233, while a π-cation interaction occurred between Tyr62 and the quaternary amino group (**Fig. 9**). Compound **6b** also exhibited favourable binding interactions, where the ortho-hydroxy group formed a hydrogen bond with Ala307 and Asp300. The carbonyl group of the thiazolidin-4-one moiety interacted with Asn289 via hydrogen bonding, while three π-π stacking interactions were observed with Trp58 and Tyr62, as shown in **Fig. 10a** (pose-1). **Fig. 10b** (pose-2) illustrates two hydrogen bonds between the NH_2 group of the ligand and Glu233, along with a hydrogen bond between the oxygen atom of the SO_2 group and His299. Moreover, compound **6b** formed a π-π stacking interaction with Trp59. The docking scores and hydrogen bond interactions of all synthesized compounds (**6a-6h**) are summarized in **Table 3**.



(2D) (3D)

Fig. 9: 2D and 3D Binding orientation of **Acarbose** in *α-amylase* binding pocket.

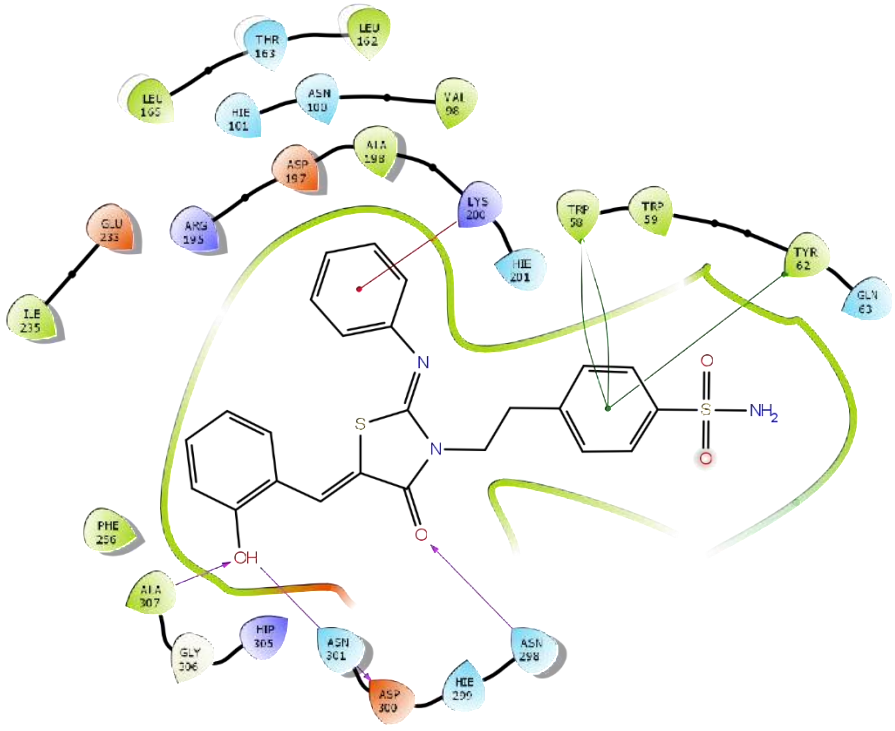


Fig. 10a: 2D binding orientation of **6b** in *α-amylase* binding pocket (Pose-1).

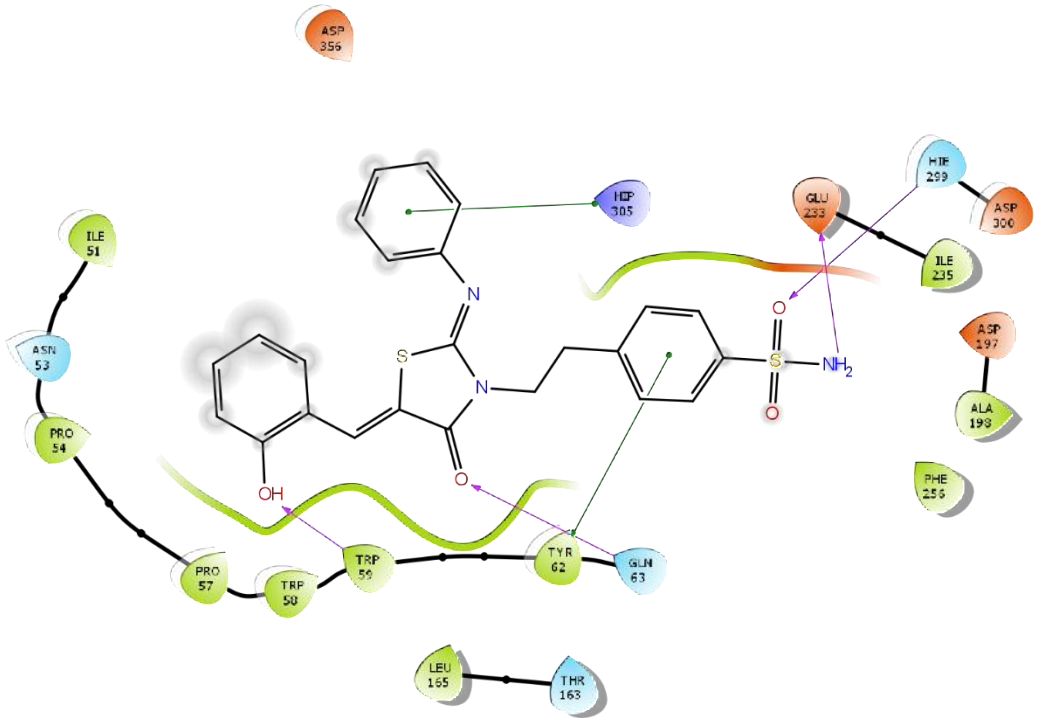


Fig. 10b: 2D binding orientation of **6b** in *α-amylase* binding pocket (Pose-2).

	PDB ID:4W93		H-Bond		
Com.	**IFD Score**	**Glide Energy (kcal/mol)**	**Ligand Atom interactions**	**Amino Acid**	**Bond length**
6a	-1159.02	-53.02	**-NH_2** of ligand to HIP 305	HIP 305	1.92
			-C=O of ligand to SER 43	SER 43	1.83
			-OH, of ligand to ALA 307, ASP 300	ALA 307, ASP300	2.29 2.02
6b	-1162.77	-54.56	**-C=O** of ligand to ASN 298	ASN 298	1.98
			-NH_2 of ligand to GLU233	GLU 233	2.02
			-C=O of ligand to GLN 63	GLN 63	1.08
6c	-1173.41	-69.32	**-OH,** of ligand to GLU 233	GLU 233	1.80
6d	-1165.25	-52.32	**-C=O** of ligand to GLN 63	GLN 63	1.88
6e	-1163.86	-60.99	**-S=O** of ligand to ARG195	ARG195	1.90
				HIE299	2.26

			-S=O of ligand to HIE299	GLU 233	2.02
			-NH_2 of ligand to GLU 233	ASP 197	1.79
			-NH_2 of ligand to ASP 197		
			-S=O of ligand to ASN 352	ASN 352	
			-NH_2 of ligand to VAL 351	VAL 351	1.90
6f	-1160.82	-59.79	**NH_2** of ligand to ASP 356	ASP 356	2.10
			-OCH_3 of ligand to HIE 201	HIE 201	1.62
			-NH_2 of ligand to ASP 197	ASP 197	1.68
6g	-1163.00	-57.44	**-C=O** of ligand to ARD 195	ARG 195	1.68
			-NH_2 of ligand to GLU 233	GLU 233	2.02
			-C=O of ligand to GLN 63	GLN 63	2.07
6h	-1165.10	-58.87	**-S=O** of ligand to HIE299	HIE299	1.97
			-NH_2 of ligand to GLU 233	GLU 233	2.17
			-OH, of ligand to GLU 233	GLU 233	2.16
			-OH, of ligand to ASP 356	ASP 356	1.67
Acarbose	-577.22	-52.034	**-OH**, of ligand to ASP 356	ASP 356	1.73
			-OH, of ligand to HIE 201	HIE 201	2.13

Table. 3: The Induced fit docking results of (**6a-6h**) compounds in 4W93 binding pocket.

6.2. MD simulations and MMPBSA calculations

The stability of the **6b**-4W93 (ligand-protein) complex was evaluated over a 100 ns period using molecular dynamics simulations with the GROMACS package. The complex exhibited RMSD fluctuations of less than 2.5 Å during the first 50 ns of the simulation. Between 56 ns and 58 ns, RMSD fluctuations ranged from 2.5 Å to 2.6 Å, but the complex remained stable throughout the entire 100 ns simulation. The backbone RMSD fluctuation was maintained below 2 Å during the first 50 ns. Further fluctuations were observed at 57 ns, 61 ns, and 67 ns, each showing a value of 2.01 Å; however, both

the backbone and the overall complex retained stability throughout the 100 ns run. RMSF of the complex ranged from 1 Å to 3 Å. Notably, the hydrogen-bonded residues ASN 298, ASP 300, and ALA 307 showed fluctuations of 0.9 Å, 0.9 Å, and 2.0 Å, respectively. Residue 549 exhibited the highest fluctuation at 2.5 Å, although it is located outside the binding pocket. The RoG showed a maximum fluctuation of 2 Å, with notable peaks around 40 ns and 60 ns during the MD run. The SASA fluctuated between 178.813 and 215.411 nm^2 .Hydrogen bond analysis revealed up to 4 hydrogen bonds in total; initially, 1-4 hydrogen bonds were observed until 30 ns, followed by an increase to 6 hydrogen bonds between 31 ns and 46 ns. Afterward, 3 hydrogen bonds were consistently present until 80 ns, and 2 stable hydrogen bonds persisted throughout the 100 ns simulation. Energy contribution analysis via MMPBSA indicated that residue ASN 298 contributed the most significant van der Waals energy (-7.71 kcal/mol), followed by ASP 300 (-5.15 kcal/mol) and ALA 307 (-2.24 kcal/mol), as shown in **Fig. 11**. MMPBSA analysis was performed for a 100 ns simulation of the compound **6b-4w93** complex. The analysis revealed a minimal van der Waals interaction energy of −34.53 ± 0.06 kcal/mol, a non-polar solvation energy contribution of −22.79 ± 0.08 kcal/mol, and a total gas-phase molecular mechanics energy of 18.01 ± 0.13 kcal/mol.

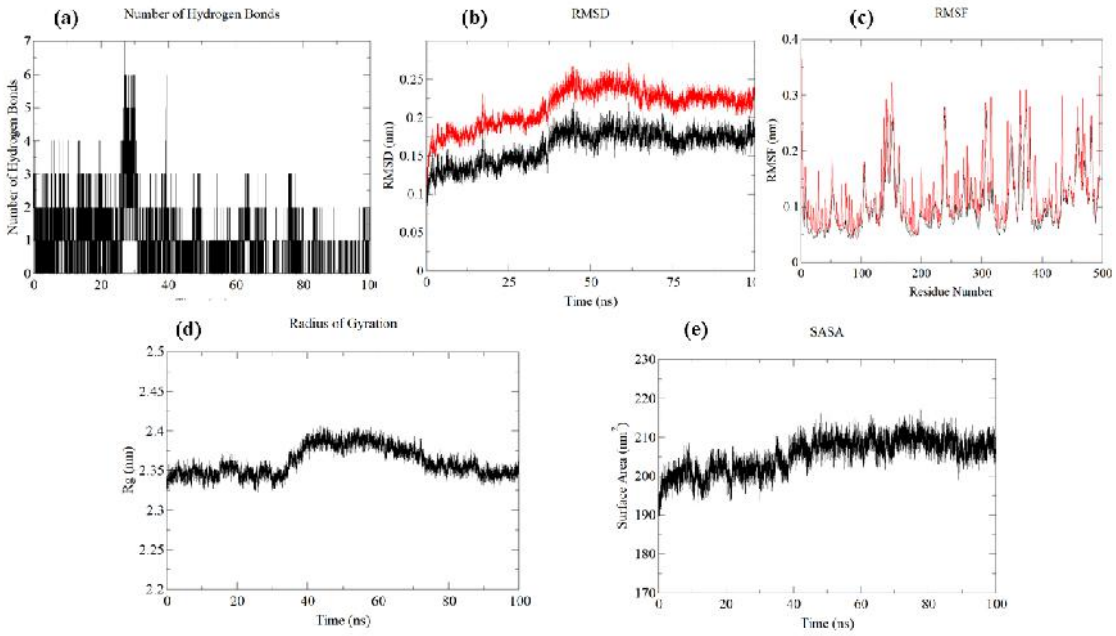
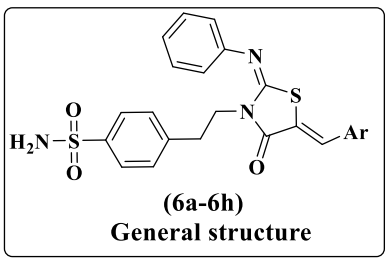


Fig. 11: Parameters describing stability of compound **6b** and **4w93** complex, where **(a)** Number of hydrogen bonds between protein and ligand; **(b)** RMSD of backbone (black) and complex (red); **(c)** RMSF of complex (black) and RMSF of c-alpha atom (red); **(d)** RoG; **(e)** SASA.

6.3. DFT and MEP analysis

All the synthesized title compounds (**6a–6h**) underwent geometric optimization using DFT calculations. The gas-phase energies of the optimized molecular structures are presented in **Table 4**. The FMO primarily consist of the HOMO and the LUMO. The HOMO energy is associated with ionization potential, while the LUMO energy corresponds to electron affinity. FMOs provide insights into the chemical properties of the molecules, including their reactivity, stability, and kinetics. The FMO orbitals for the synthesized compound 6b are illustrated in **Fig 12**. Chemical reactivity descriptors were calculated using the DFT/B3LYP/6-31G (d, p**) method, and the corresponding values are listed in **Table. 5**. The reactivity of a molecule is determined by the HOMO–LUMO energy gap, with a smaller energy gap indicating higher reactivity. The analysis revealed that compound **6b** has a HOMO energy level of −0.19179 eV and a LUMO energy level of −0.054447 eV. The calculated electrochemical potential (μ) is −0.1231185 eV, the chemical hardness (η) is −0.068671 eV, and the chemical softness (σ) is 14.5621 eV. The ESP on a molecular surface is a useful tool for identifying regions of high electron density (negative potential) and low electron density (positive potential). It aids in predicting sites of electrophilic and nucleophilic attack and provides insights into molecular interactions. The MEP were calculated at the optimized geometry using the B3LYP method with a 6-31G (d, p**) basis set. The MEP for compound **6b** is illustrated in **Fig. 13**.



(6a-6h)
General structure

Compound	Gas Phase Energy (eV)
6a	-2226.816209
6b	-2141.384249
6c	-2165.395209
6d	-2228.020846
6e	-2342.540483
6f	-2457.057217
6g	-2152.815555
6h	-2212.725562

Table 4: Total Energy of Geometry optimized structures (**6a-6h**)

Quantum chemical parameters	E_{HOMO} (eV)	E_{LUMO} (eV)	ΔE_{GAP} (eV)	μ (eV)	σ (eV)	η (eV)
6a	-0.230245	-0.101432	-0.128813	-0.1658385	-15.5263832	-0.064406
6b	-0.19179	-0.054447	-0.137343	-0.1231185	-14.5620818	-0.068671
6c	-0.194667	-0.057394	-0.137273	-0.0686365	-14.5695074	-0.126030
6d	-0.210492	-0.072777	-0.137715	-0.1416345	-14.5227462	-0.068857
6e	-0.204323	-0.071377	-0.132946	-0.13785	-15.0437019	-0.066473
6f	-0.208655	-0.075328	-0.133327	-0.0666635	-15.0007125	-0.141991
6g	-0.216732	-0.076572	-0.14016	-0.146652	-14.2694063	-0.07008
6h	-0.220833	-0.080641	-0.140192	-0.150737	-14.2661492	-0.070096

Table. 5: Calculated quantum chemical parameters of synthesized compounds (**6a-6h**).

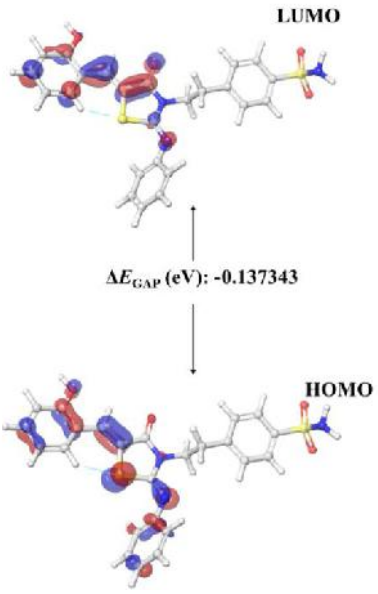


Fig. 12: Contours of HOMO and LUMO of compound **6b.**

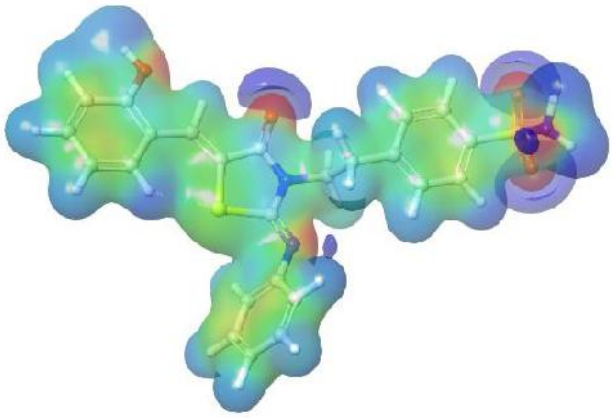


Fig. 13: MEP map of compound **6b**

6.4. ADMET profile prediction

The ADMET properties, including hydrogen bond donors, hydrogen bond acceptors, hydrophilicity, molecular weight, permeability, binding affinity to human serum albumin, and human oral absorption, were predicted using the QikProp module of Schrödinger's software. Deviations from Lipinski's ROF and Jorgensen's ROT were assessed and compared with the recommended thresholds, as presented in **Table 6**.

Comp.	MW	DHB	AHB	QPlog Pw	QPlog Po/w	QP logS	QPlog HERG	QPP Caco
6a	491.579	2	10.5	17.713	2.782	-5.802	-7.705	35.837
6b	479.568	3	9.25	17.809	3.077	-5.688	-7.627	68.105
6c	479.568	3	9.25	17.813	3.018	-5.734	-7.607	55.68
6d	493.594	2	9.25	15.981	3.879	-6.273	-7.708	194.292
6e	523.621	2	10	16.228	3.967	-6.516	-7.612	194.263
6f	553.647	2	10.75	16.459	4.058	-6.313	-7.208	193.624
6g	477.595	2	8.5	15.449	4.091	-6.615	-7.717	193.748
6h	481.559	2	8.5	15.528	4.02	-6.414	-7.696	193.865

Comp.	QPP MDCK	QPlog BB	%HOA	CNS	ROF	ROT
6a	33.49	-2.581	77.77	-2	0	1
6b	26.944	-2.697	75.863	-2	0	0
6c	104.019	-2.092	90.616	-2	0	1
6d	104.009	-2.208	78.174	-2	1	1
6e	100.958	-2.213	78.682	-2	1	1
6f	30.917	-2.77	64.873	-2	1	1
6g	187.455	-1.885	91.423	-2	0	1
6h	16.728	-2.998	71.056	-2	0	1

Table 6. ADEMT parameters of synthesised inhibitors (**6a-6h**).

MW: Molecular weight (<500).
DHB: Number of hydrogen bond donors (<5).
AHB: number of hydrogen bond acceptors (<10).
QPlogPw: water/gas partition coefficient.
QPlogPo/w: Octanol/ water partition coefficient (<5).
QPlogS: Aqueous solubility (-6.5 to0.5).
QPlog HERG: IC_{50} value for blockage of HERG K^+ channels (<-5).
QPP Caco: apparent Caco-2 permeability (nm/sec) (<25poor, >500great).
QPP MDCK: apparent MDCK permeability (nm/sec) (<25poor, >500great).
QPlogBB: Prediction of brain/blood partition coefficient (-3.0 to1.2).
%HOA: Percent Human Oral Absorption (>80% is high <25% is poor).
CNS: predicted Central nervous system activity (-2.0 to +2.0).
ROF: Number of violations of Rule of Five.
ROT: Number of violations of Rule of Three.

6.5. Target identification, network construction and cluster analysis

Network pharmacology is an integrative approach that combines principles from pharmacology and systems biology. It uses network analysis to investigate the intricate relationships between bioactive chemicals and their pathways. A network pharmacology method was used to discover putative targets and molecular mechanisms related with compound **6b**'s consumption of glucose and *α-amylase* inhibition.

A total of 3,134 targets associated with the pathogenesis of T2DM were identified using the DisGeNet database. Similarly, 119 potential targets were predicted to be modulated by compound **6b**. Of these, 46.22% of the targets identified through the DIGEP-Pred and SwissTargetPrediction databases overlapped with T2DM-related targets, indicating modulation of 55 common proteins (**Fig.14a**). Categorical classification of the shared targets revealed that the top three protein classes were kinases (26.7%), enzymes (13.3%), and GPCR's (13.3%) (**Fig.14b**). Protein-protein interactions (PPIs) for the matched targets were analyzed using the STRING database, and the interaction network is shown in **Fig. 15a**. Pathway enrichment analysis identified 18 pathways involved in T2DM, as presented in **Table 7**. A protein-pathway interaction network (**Fig. 16**) was constructed using Cytoscape, which revealed that PI3KCA, MTOR, and BRAF had the highest edge counts of 14, 10, and 6, respectively. The PI3K-Akt signaling pathway (hsa04151) was identified as the key pathway modulated by compound **6b**, with a FDR of 1.65E-06, a strength of 1.01, and a gene ratio of 0.0286 (**fig 15b**).

Cluster analysis revealed the presence of three distinct clusters, with Cluster 2 containing the largest number of genes (n = 25), including ADORA1, ADORA2B, ADORA3, BRAF, CA2, CAPN2, CNR1, CNR2, CYP11B2, EGFR, FGFR1, GABRG2, GCGR, GRK2, GRK5, KDR, MMP2, MMP9, MTOR, PIK3CA, PTPN1, SRC, TACR3, TRPV1, and TSPO. The PI3K-Akt signalling pathway is regulated through the gene NGFR, CDK4, KDR, PIK3CA, CDK2, EGFR, PRL, HSP90AA1, MTOR, and FGFR1. The PI3K-Akt pathway is initiated by IRS protein binding to PI3k subunits. This, in turn, activates Akt kinase, which catalyses the translocation of GLUT present in cytoplasmic vesicles on the surface of the cell membrane, increasing glucose transport across the cell in the presence of insulin. In addition, Akt is involved in a variety of intracellular metabolic processes.[159-160]

IRS is made up of six proteins IRS1-6, the IRS-1 and IRS-2, which are expressed in almost all tissues, including muscle, liver, fat, and pancreatic islets. IRS-1 and IRS-2 are particularly important in adipose tissue and hepatocytes, respectively.[161-162]

The mTOR exists in two distinct complexes, mTOR complex 1 (mTORC1) and mTOR complex 2 (mTORC2), each associated with unique protein components and downstream substrates. In skeletal muscle, activation of mTORC1 promotes the phosphorylation of IRS-1, which subsequently activates the PI3K-Akt signaling cascade. This activation facilitates glycogen accumulation and enhances glucose uptake.[163-165]

Glucose uptake is mediated by the GLUT family of membrane transporters, primarily GLUT1, GLUT2, and GLUT4. GLUT1 facilitates basal glucose uptake, while GLUT4 plays a pivotal role in glucose transport in muscle fibers through vesicles located adjacent to the plasma membrane.[166] The translocation of GLUT4 is regulated by various molecular mechanisms, with key involvement of proteins such as p38 mitogen-activated protein kinase (p38 MAPK). Exercise-induced glucose uptake is predominantly driven by AMP-activated protein kinase (AMPK), which serves as a central energy

sensor in contracting muscles. Upon activation, AMPK triggers a downstream signaling cascade that promotes GLUT4 translocation to the plasma membrane, thereby enhancing glucose uptake.[167-168]

A network was constructed for compound **6b** to identify proteins associated with postprandial hyperglycemia using DIGEP-Pred. Targets related to postprandial hyperglycemia were retrieved from the GeneCards database, and proteins modulated by compound **6b** were screened for their involvement in this condition. Protein enrichment analysis was conducted using the STRING database to identify pathways linked to postprandial hyperglycemia, with pathway annotation performed using the KEGG database. Among the identified pathways, the metabolic pathway was found to be the most significantly modulated.

The analysis revealed that compound **6b** modulates a total of 193 targets, with key proteins such as EGFR, AMY1A, KDR, ITGB1, FLT3, CAT, REN, CSNK2B, and GCK being notably affected. The metabolic pathway was identified as the most enriched pathway, as illustrated in **Fig. 17**. A compound **6b**–protein–pathway interaction network was constructed using Cytoscape, with the resulting network visualized in **Fig. 18**.

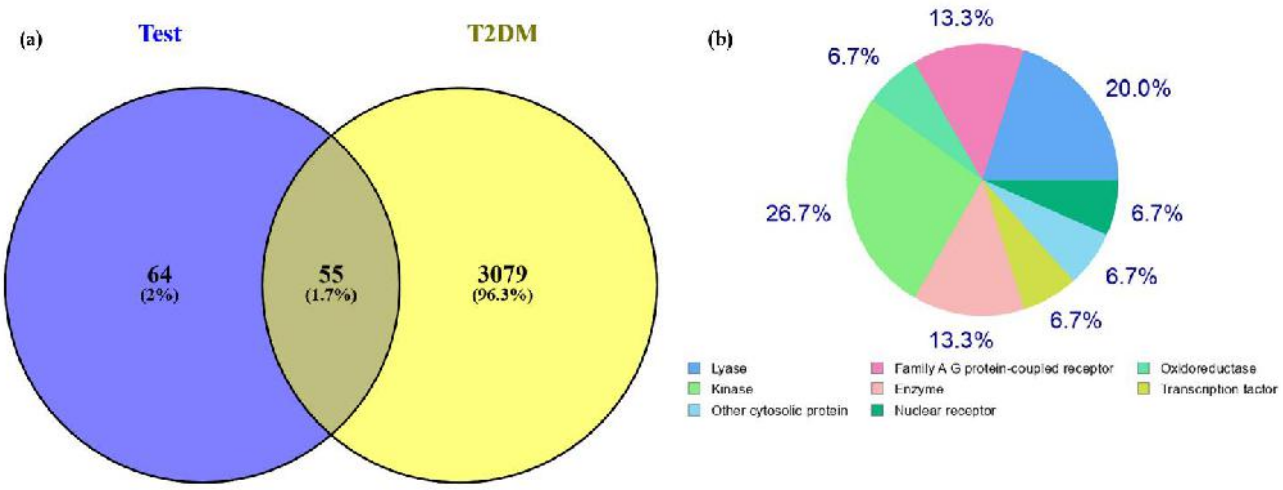


Fig. 14: (a) The Venn diagram representation of common genes between test agent and T2DM; **(b)** The categorical representation of genes modulated by compound identified via SwissTargetPrediction.

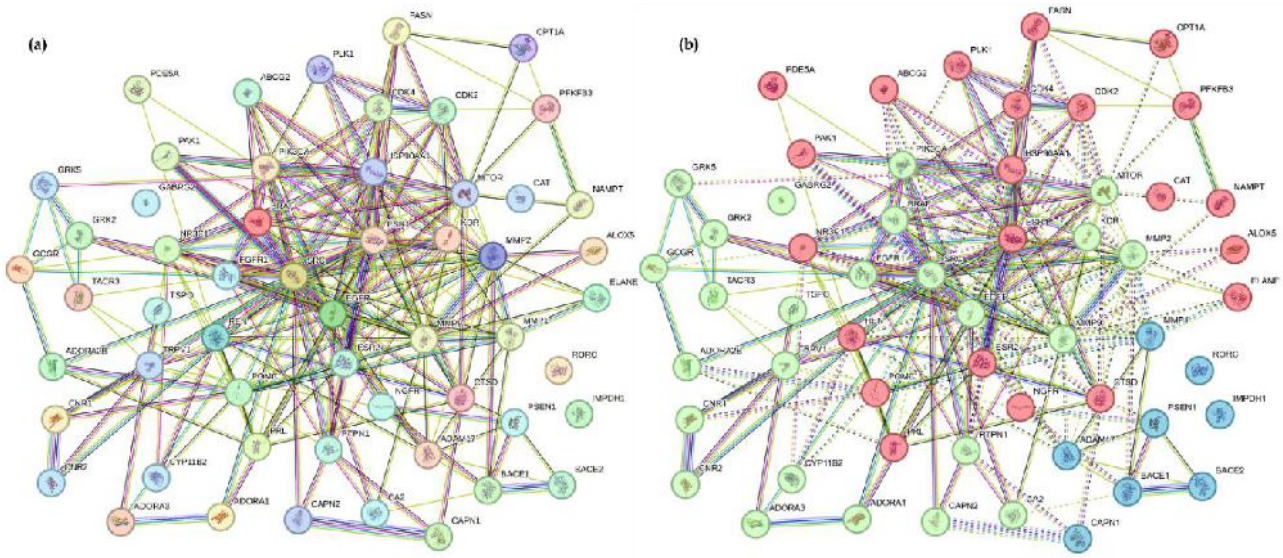


Fig. 15: (a) STRING identified Protein-protein interaction for compound **6b**, and **(b)** The cluster analysis where cluster 1: red; cluster 2: green; cluster 3: blue.

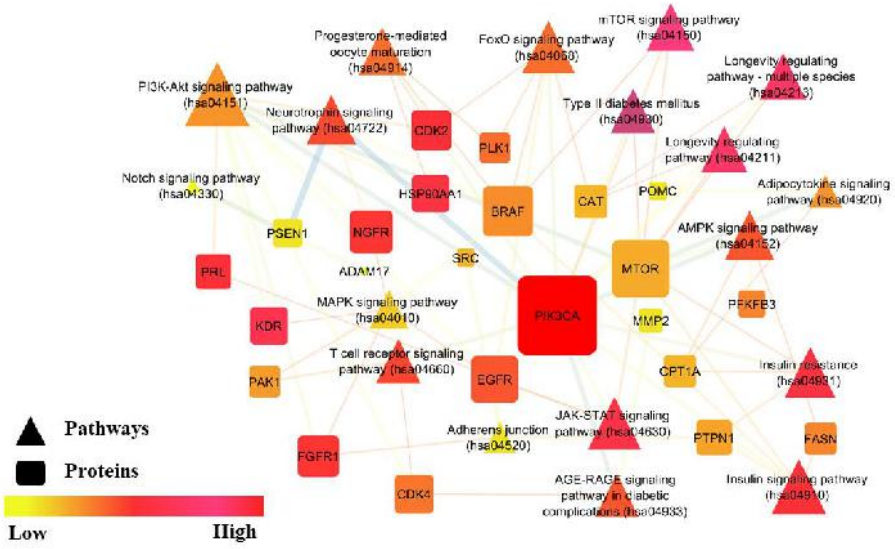


Fig. 16: The protein-pathway interaction modulated by compound **6b**

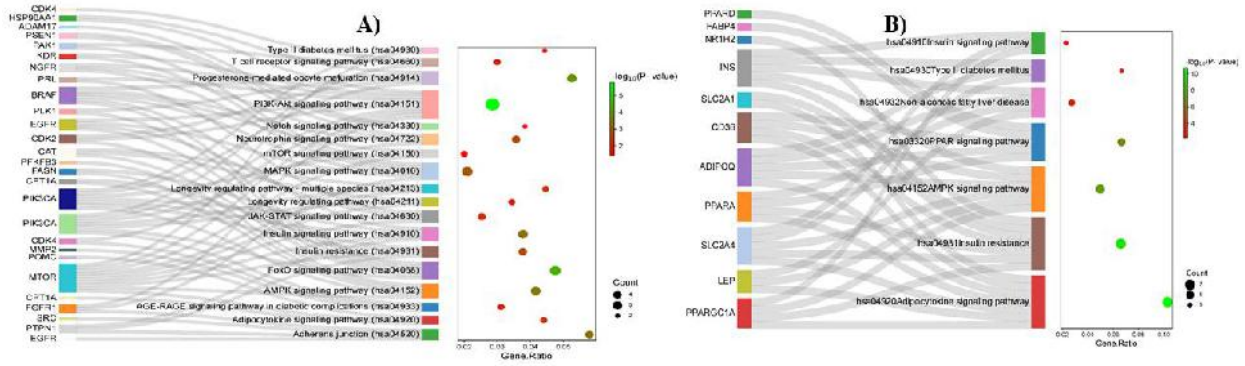


Fig. 17: Connections between pathways and its protein enrichment analysis **A)** Type II DM, **B**) alpha amylase.

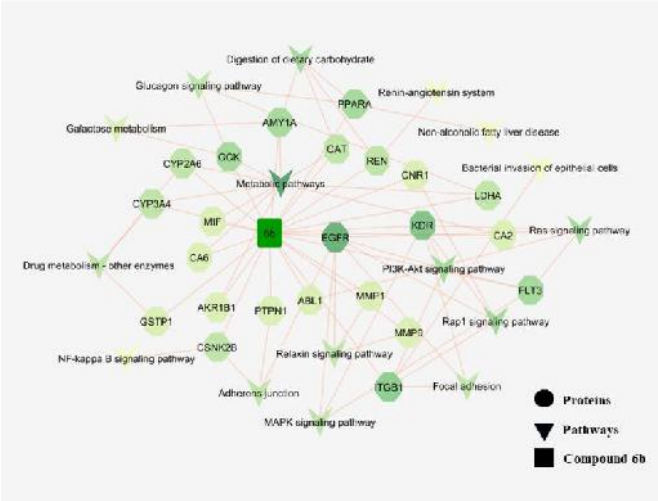


Fig. 18: Protein-pathway interaction modulated by compound **6b**

Pathway (KEGG ID)	OGC/BGC	Strength	FDR	Proteins
Adherens junction (hsa04520)	0.05797	1.32	0.00052	EGFR, PTPN1, SRC, FGFR1
Adipocytokine signaling pathway (hsa04920)	0.0441	1.2	0.0062	CPT1A, MTOR, POMC
AGE-RAGE signaling pathway in diabetic complications (hsa04933)	0.0312	1.05	0.0129	MMP2, CDK4, PIK3CA
AMPK signaling pathway (hsa04152)	0.041667	1.17	0.00034	PIK3CA, CPT1A, FASN, MTOR, PFKFB3
FoxO signaling pathway (hsa04068)	0.0476	1.23	3.94E-05	CAT, PIK3CA, CDK2, EGFR, PLK1, BRAF
Insulin resistance (hsa04931)	0.037736	1.13	0.002	PIK3CA, CPT1A, MTOR, PTPN1
Insulin signaling pathway (hsa04910)	0.0378	1.13	0.00047	PIK3CA, FASN, MTOR, PTPN1, BRAF
JAK-STAT signaling pathway (hsa04630)	0.0253	0.96	0.0064	PIK3CA, EGFR, PRL, MTOR

Longevity regulating pathway (hsa04211)	0.0344	1.09	0.0111	CAT, PIK3CA, MTOR
Longevity regulating pathway - multiple species (hsa04213)	0.0447	1.25	0.0049	CAT, PIK3CA, MTOR
MAPK signaling pathway (hsa04010)	0.0209	0.88	0.0013	NGFR, KDR, EGFR, PAK1, FGFR1, BRAF
mTOR signaling pathway (hsa04150)	0.02	0.86	0.0348	PIK3CA, MTOR, BRAF
Neurotrophin signaling pathway (hsa04722)	0.0357	1.11	0.0024	NGFR, PIK3CA, PSEN1, BRAF
Notch signaling pathway (hsa04330)	0.0384	1.14	0.0383	ADAM17, PSEN1
PI3K-Akt signaling pathway (hsa04151)	0.0286	1.01	1.65E-06	NGFR, CDK4, KDR, PIK3CA, CDK2, EGFR, PRL, HSP90AA1, MTOR, FGFR1
Progesterone-mediated oocyte maturation (hsa04914)	0.0526	1.28	0.00012	PIK3CA, CDK2, PLK1, HSP90AA1, BRAF
T cell receptor signaling pathway (hsa04660)	0.03	1.03	0.014	CDK4, PIK3CA, PAK1
Type II diabetes mellitus (hsa04930)	0.0444	1.2	0.0307	PIK3CA, MTOR



Low **High**

Where, OGC: Observed gene count, BGC: Background gene count, FDR: False discovery rate

Table. 7: KEGG Pathway analysis of compound **6b**.

The in vitro glucose uptake capacity and *α-amylase* inhibition potential of compound **6b** are supported by its predicted interactions with key proteins and pathways implicated in the progression of T2DM and its associated complications. These interactions were identified through network pharmacology and pathway enrichment analysis. **Fig. 19** illustrates the proposed molecular mechanism of action of compound **6b**, highlighting its dual role as (**A**) a GLUT modulator and (**B**) a *α-amylase* inhibitor.

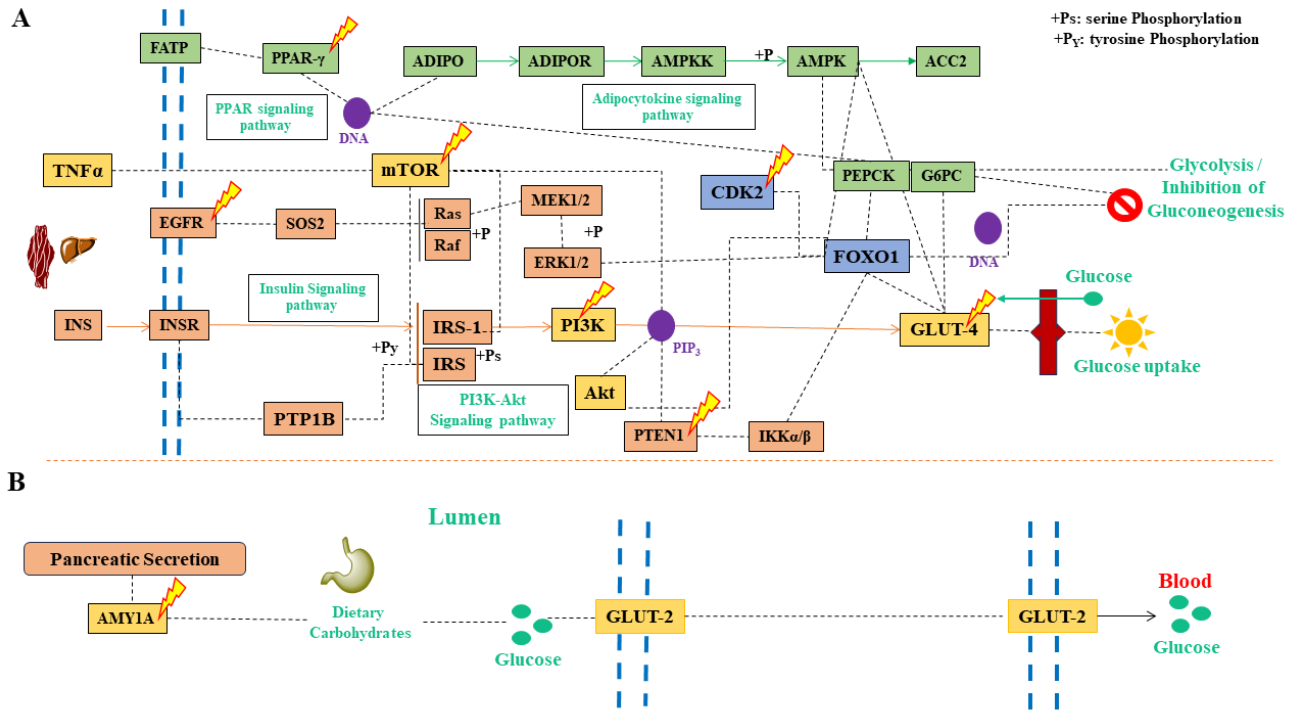
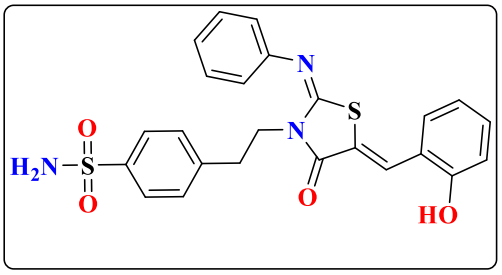


Fig. 19: Probable molecular mechanism of compound **6b** in **A)** Glucose uptake (hsa04930, hsa04151, map03320). **B**) *α-amylase* inhibition. (map04973) represents checkpoints affected by the compound **6b**.

Outcome of scheme. 1

Identified Hit molecules as dual targeting α-amylase inhibitor and PPAR-γ agonist



(6b)

Chapter 4

Results (Scheme. 2)...

The general depiction of research work carried out for **scheme. 2** is briefly summarized in the following **Fig. 20.**

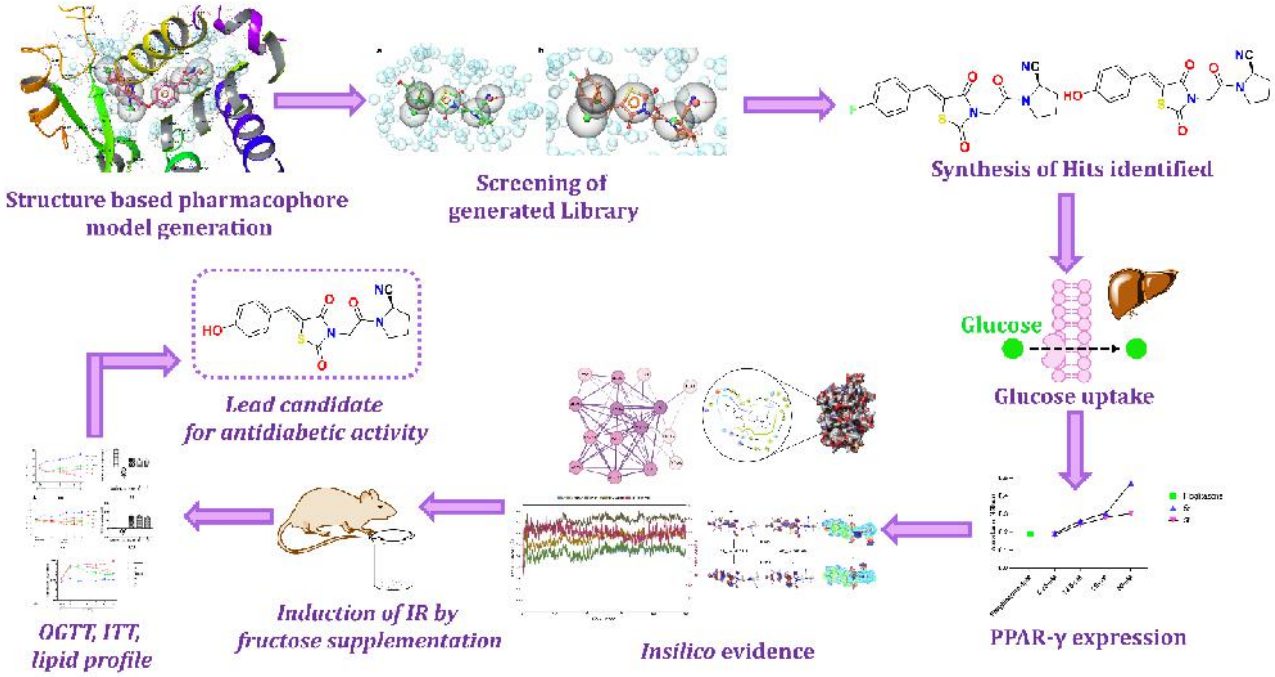


Fig. 20: Study plan of scheme.2

1. Design of scheme. 2

A review of the literature indicates that since the development of ciglitazone in the 1980s, extensive structural modifications have been made to the TZD scaffold. Researchers have focused on introducing branched-chain amino acids (BCAAs) and carbon chain linkers at the fifth position of the TZD core. These modifications aimed to extend the hydrophobic tail region, resembling the structural framework of conventional glitazones, while retaining the free TZD moiety as a polar head.[169] Over the past decade, efforts have shifted toward exploring substitutions at the third position of the TZD head. Specifically, the amino group (NH) has been replaced with functional groups such as substituted acetamides, acid chlorides, and acetyl chlorides to investigate their influence on PPAR-γ activity. This approach is depicted in **Fig. 21**, highlighting the rational design strategy employed to enhance the pharmacological profile of TZD derivatives (**A, B, C,** and **D**).[170-173]

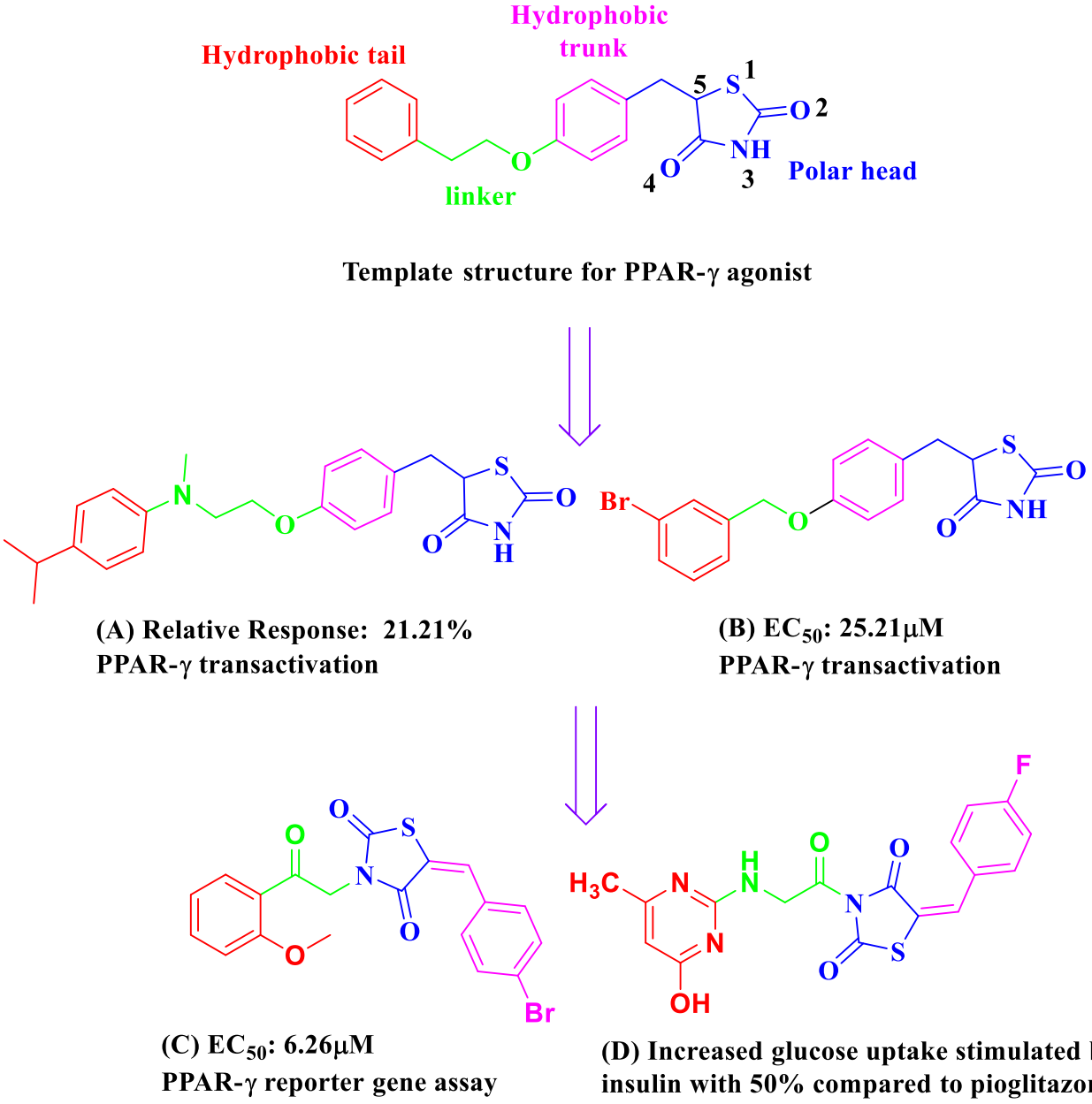


Fig. 21: Evolution of TZD's as Ligands targeting the Binding domain of the PPAR-γ LBD over the Past three decades.

Based on the aforementioned insights and the therapeutic relevance of marketed antidiabetic agents, such as pioglitazone (a PPAR-γ agonist) and vildagliptin (a DPP-4 inhibitor), a rational design approach was adopted. This involved the structural modification and development of a library of acetylpyrrolidine-2-carbonitrile-based substituted benzylidenethiazolidine-2, 4-dione (**Fig. 22**) derivatives aimed at enhancing antidiabetic activity.

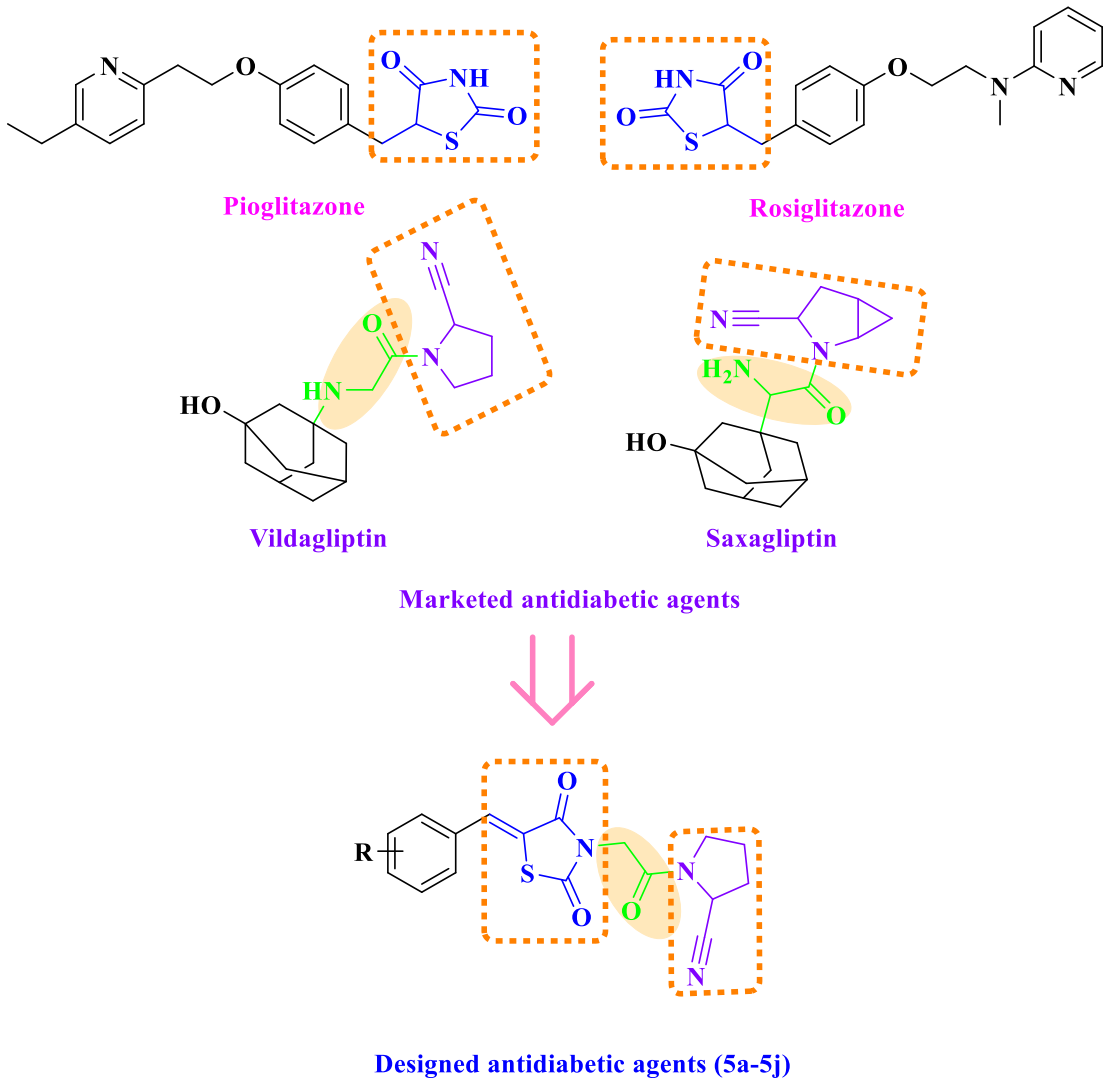


Fig. 22: Design of acetylpyrrolidine-2-carbonitrile-based Substituted benzylidenethiazolidine-2, 4-dione derivatives.

1.1. Receptor based pharmacophore modeling

A structure/receptor-based pharmacophore hypothesis was developed to identify the key structural features and positions required for ligands to elicit a biological response. A seven-point pharmacophore model (AHHHRRR) was generated for the PPAR-γ LBD (PDB ID: 5U5L), using pioglitazone as the reference ligand (**Fig. 23**). The designed compound library was subsequently screened against this pharmacophore model, and enrichment analysis was performed using a decoy set of 1,000 molecules (**Fig. 24**). Based on the fitness score relative to the reference ligand, the top 10 ligands were prioritized for synthesis (**Table. 8**). Pioglitazone exhibited a fitness score of 1.594 with five out of seven site matches and an alignment score of 0.808. Notably, compound **5b** (A12) and compound **5f** (A3)

demonstrated fitness scores of 1.081 and 1.026, respectively, with five out of seven site matches. The alignment scores for compound **5b** and **5f** were 1.126 and 0.085, respectively. The alignment of compounds **5b** and **5f** on the generated pharmacophore hypothesis is illustrated in **Fig. 25**

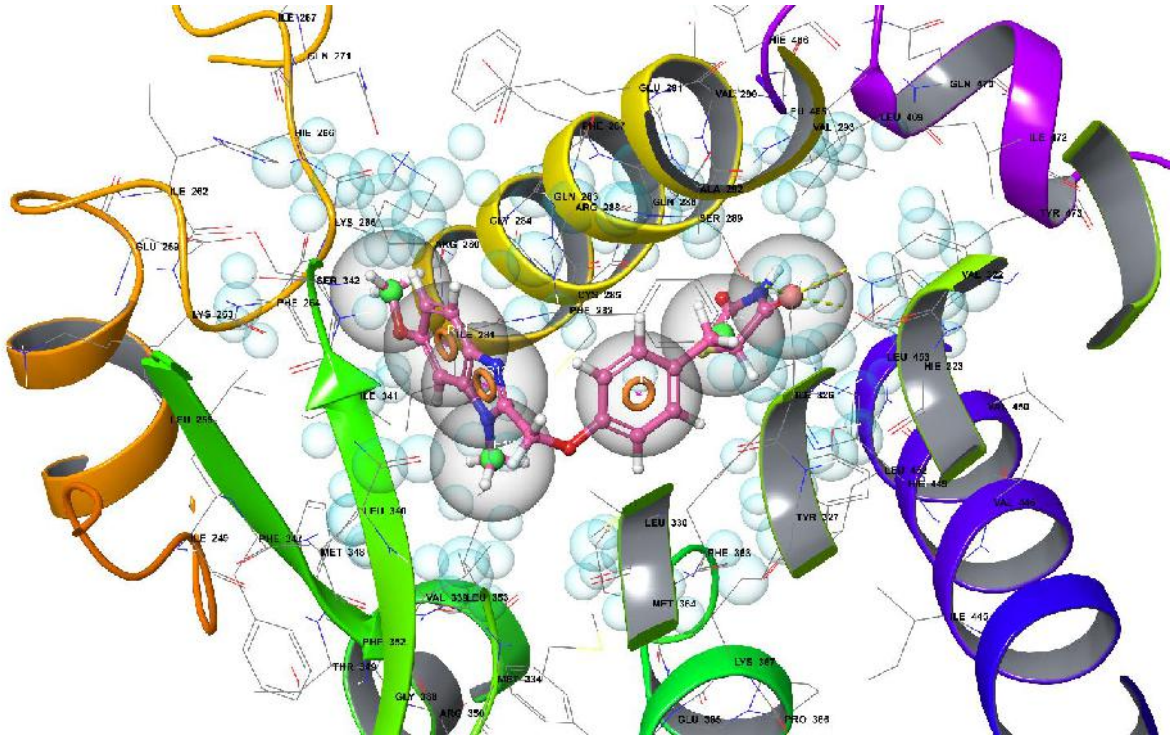


Fig. 23: Seven-point pharmacophore hypothesis for the PPAR-γ LBD using pioglitazone as the reference ligand.

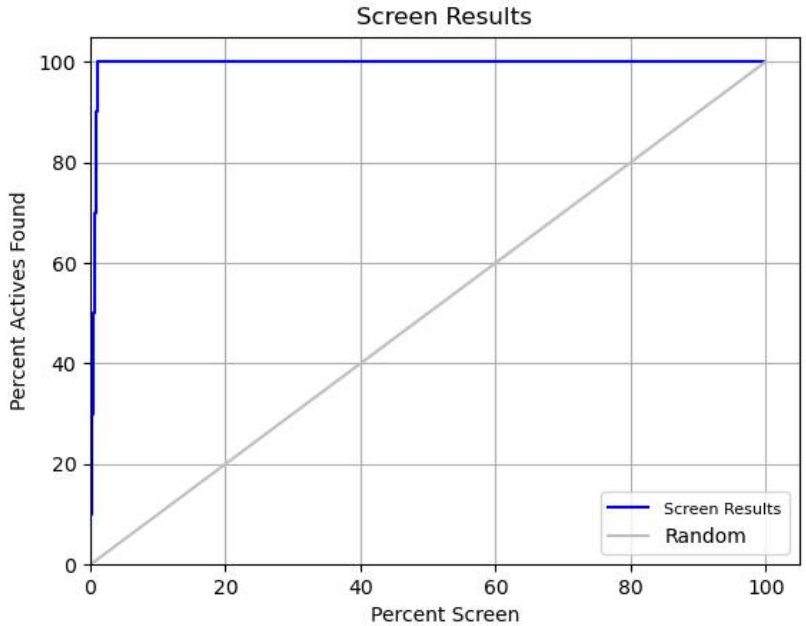


Fig. 24: Enrichment analysis of the dataset

Codes	Ligand Matching sites	Fitness score	Align score	Volume score	Vector score
Pioglitazone	5	1.594	0.808	0.572	0.802
A12 (**5b**)	5	1.081	1.126	0.351	0.704
A3 (**5f**)	5	1.026	0.885	0.36	0.605
A28	3	0.854	0.851	0.271	0.489
A32	3	0.848	0.919	0.264	0.489
A41	3	0.844	0.802	0.264	0.485
A44	4	0.84	0.863	0.263	0.484
A18	3	0.832	0.942	0.257	0.482
A37	3	0.826	0.932	0.247	0.605
A8	3	0.605	0.965	0.24	0.489

Table. 8: screening results of dataset on the generated hypothesis.

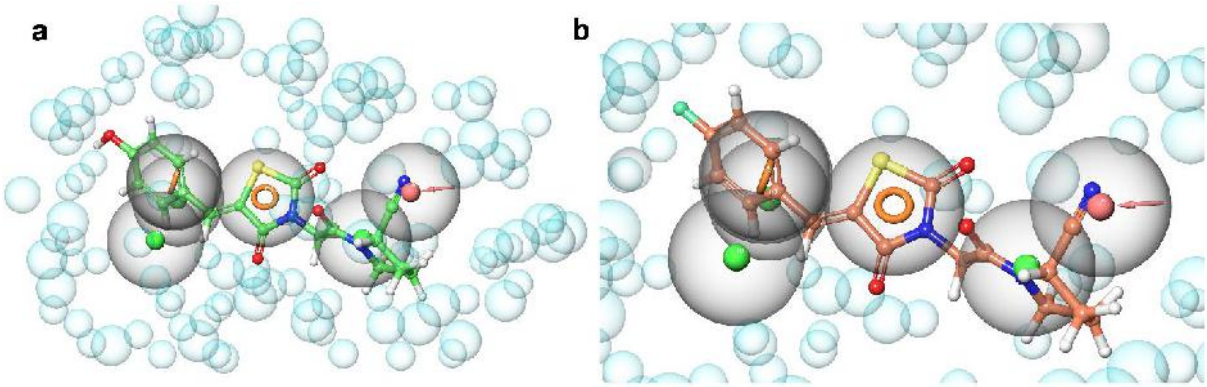
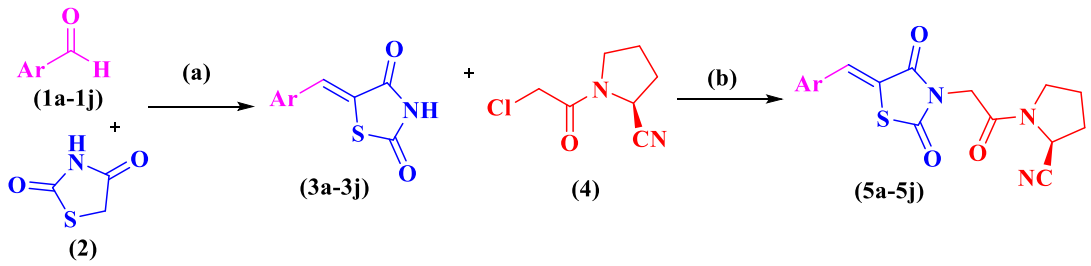


Fig. 25: Alignment of Hypothesis-Derived Pharmacophore Sites with (a) Compound **5b** and (b) Compound **5f.**

2. Chemistry

Scheme. 2: Synthesis of substituted benzylidene-2, 4-thiazolidinedione- pyrrolidine-2-carbonitrile compounds



Reagents and conditions: (a) Piperdine-acetate, toluene, reflux; (b) acetonitrile, triethyamine, reflux

The synthesis of the top hits (**5a–5j**) identified from pharmacophore screening is outlined in **Scheme 2**. The intermediate compounds (**3a–3j**) were synthesized following a previously reported method.[174] In this process, appropriately selected aryl and heteroaryl aldehydes (**1a–1j**) were subjected to a Knoevenagel condensation with TZD in the presence of a catalytic amount of piperidine-acetate in toluene, resulting in the formation of substituted benzylidenethiazolidine-2, 4-dione derivatives (**3a–3j**). Subsequently, an equimolar ratio of intermediates (**3a–3j**) was refluxed with 2-chloroacetylpyrrolidine-2-carbonitrile (**4**) in acetonitrile using triethylamine as a base catalyst. This reaction yielded the final target compounds, 5-(substituted-benzylidene)-2, 4-dioxothiazolidin-3-yl) acetyl) pyrrolidine-2-carbonitrile (**5a–5j**).

The structural characterization of the synthesized hit compounds (**5a–5j**) was performed using FTIR spectroscopy, ^{1}H NMR, ^{13}C NMR, and HRMS. The FTIR spectra of the 1-(2-(5-substituted-benzylidene-2,4-dioxothiazolidin-3-yl) acetyl) pyrrolidine-2-carbonitrile (**5a–5j**) derivatives exhibited characteristic absorption peaks corresponding to the nitrile (CN) group at 2235.59-2251.02 cm^{-1} and the carbonyl (C=O) groups at 1731.19-1749.51 cm^{-1}.

The ^{1}H NMR spectrum of compound **5a** (**Fig. 26**) displayed a distinct upfield multiplet signal at δ 1.90-2.24 ppm, attributed to the methylene protons (4H) at C1 and C2 of the pyrrolidine ring. A set of signals at δ 3.53–3.59 ppm and δ 3.78 ppm corresponded to the diastereotropic methylene protons at C5, consistent with the reported NMR data for the pyrrolidine ring[1]**.** Additionally, a multiplet at δ 4.52-4.78 ppm was assigned to the proton at C3 (CHCN), which was coupled with two protons from (CH_2) at C7. This assignment was further confirmed by a heteronuclear single quantum coherence (HSQC) experiment. Aromatic protons were observed as multiplets at δ 7.56-7.50 ppm (2H) and δ 7.65-7.63 ppm (3H). The characteristic proton of the benzylidene (CH) group was identified as a singlet at δ 7.97 ppm. The ^{13}C NMR spectrum of compound **5a** confirmed the presence of characteristic carbon signals. Peaks corresponding to the pyrrolidine ring carbons were observed at δ 25.34 (C1), 30.00 (C2), 43.59 (C5), 46.01 (C3), and 46.99 (C7) ppm. Signals at δ 164.52 (C15), 165.69 (C14), and 167.53 (C6) were attributed to the carbonyl carbons. Further confirmation of the structure of compound **5a** was provided

by HRMS analysis, which validated its molecular formula. Compounds **5b–5j** were characterized using the same approach, and their structural assignments were made according to the criteria described above.

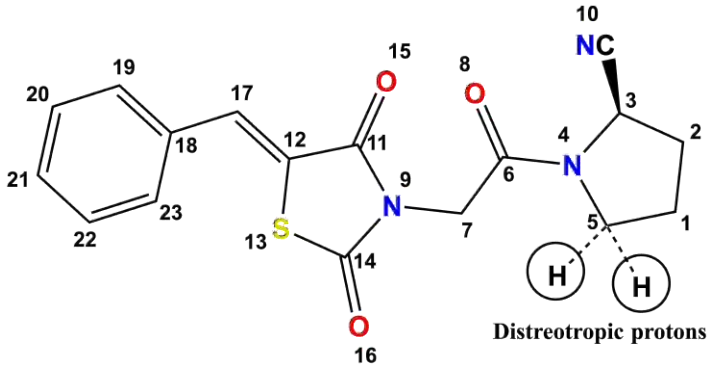
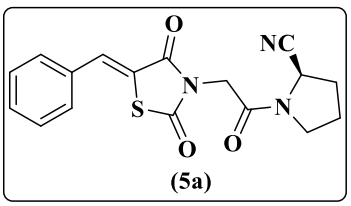


Fig. 26: Numbering scheme for proton and carbon assignments used in NMR interpretation.

3. Experimental

General Procedure For synthesis of 1-(2-(5-substituted-benzylidene-2, 4-dioxothiazolidin-3-yl) acetyl) pyrrolidine-2-carbonitrile (5a-5j): An equimolar mixture of 2-chloroacetylpyrrolidine-2-carbonitrile (**4**) and substituted benzylidenethiazolidine-2, 4-dione (**3a–3j**) was refluxed in acetonitrile in the presence of a catalytic amount of triethylamine for 24 hours. The progress of the reaction was monitored via TLC. Upon completion, the reaction mixture was poured onto crushed ice to precipitate the crude product, which was subsequently filtered, washed with cold water, and recrystallized from methanol to obtain the purified final product

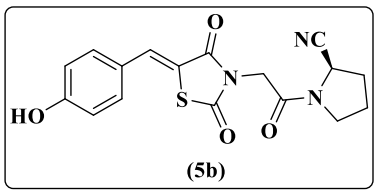
Synthesis of 1-(2-(5-benzylidene-2, 4-dioxothiazolidin-3-yl) acetyl) pyrrolidine-2-carbonitrile (5a):



Yield: 76.21%; mp: 211-213°C; FTIR (KBr, cm^{-1}): 3121.18 (Ar-CH), 2235.59 (CN), 1745.65 (C=O), 1573.02 (C=C). ^{1}H NMR [400 MHz, δ ppm, DMSO-*d6*]: 1.90-2.24 (m, 4H, -CH_2 & CH_2), 3.53-3.59 (m, 1H, CH_2), 3.78 (s, 1H, CH_2), 4.52-4.78 (m, 3H, CH_2 & CHCN), 7.56-7.50 (m, 2H, Ar-H), 7.65-7.63 (m, 3H, Ar-H), 7.97 (s, 1H, CH). ^{13}C NMR [100 MHz, δ ppm, DMSO-*d6*]: 25.34, 30.00, 43.59, 46.01, 46.99,

119.52, 121.33, 129.96, 130.76, 131.38, 133.32, 134.28, 164.52, 165.69, 167.53. Chemical formula: $C_{17}H_{15}N_3O_3S$; Molecular mass; calculated: 341.39; Mass (M+1): 342.09.

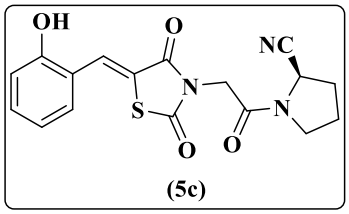
Synthesis of 1-(2-(5-(4-hydroxybenzylidene)-2, 4-dioxothiazolidin-3-yl) acetyl) pyrrolidine-2-carbonitrile (5b):



(5b)

Yield: 76.21%; mp: 168-170°C; FTIR (KBr, cm^{-1}): 3255.02 (OH), 3015.83 (Ar-CH), 2251.02 (CN), 1749.51 (C=O), 1580.73 (C=C). ^{1}H NMR [400 MHz, δ ppm, DMSO-*d6*]: 2.02-2.30 (m, 4H, -CH_2 & CH_2), 3.48-3.60 (m, 1H, CH_2), 3.76-3.80 (m, 1H, CH_2), 4.39-4.86 (m, 3H, CH_2 & CHCN), 6.93-6.95 (m, 2H, Ar-H), 7.51-7.53 (m, 2H, Ar-H), 7.88 (s, 1H, CH), 10.39 (s, 1H, OH). ^{13}C NMR [100 MHz, δ ppm, DMSO-*d6*]: 24.75, 29.44, 42.91, 46.28, 45.44, 116.40, 118.93, 123.71, 132.68, 134.10, 160.27, 164.04, 165.30, 167.12. Chemical formula: $C_{17}H_{15}N_3O_4S$; Molecular mass; calculated: 357.38; Mass (M+1): 358.08.

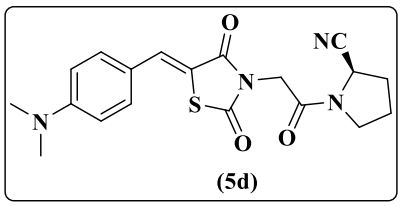
Synthesis of 1-(2-(5-(2-hydroxybenzylidene)-2,4-dioxothiazolidin-3-yl)acetyl)pyrrolidine-2-carbonitrile (5c):



(5c)

Yield: 82.32%; mp: 168-170°C; FTIR (KBr, cm^{-1}): 3252.12 (OH), 3043.80 (Ar-CH), 2246.20 (CN), 1740.83 (C=O), 1599.06 (C=C). ^{1}H NMR [400 MHz, δ ppm, DMSO-*d6*]: 2.01-2.21 (m, 4H, -CH_2 & CH_2), 3.48-3.59 (m, 1H, CH_2), 3.75-3.80 (m, 1H, CH_2), 4.38-4.78 (m, 3H, CH_2 & CHCN), 6.94-6.99 (m, 2H, Ar-H), 7.39-7.32 (m, 2H, Ar-H), 8.15 (s, 1H, CH), 10.64 (s, 1H, OH). ^{13}C NMR [100 MHz, δ ppm, DMSO-*d6*]: 25.31, 30.00, 43.50, 46.00, 46.97, 116.76, 119.52, 119.84, 120.23, 120.35, 129.21, 129.56, 133.30, 157.94, 164.59, 165.92, 167.85; Chemical formula: $C_{17}H_{15}N_3O_4S$; Molecular mass; calculated: 357.38; Mass (M+1): 358.08

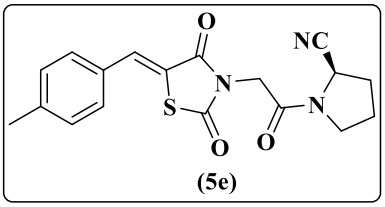
Synthesis of 1-(2-(5-(4-(dimethylamino) benzylidene)-2, 4-dioxothiazolidin-3-yl) acetyl) pyrrolidine-2-carbonitrile (5d):



(5d)

Yield: 79.63%; mp: 173-175°C; FTIR (KBr, cm^{-1}): 3006.39 (Ar-CH), 2249.17 (CN), 1731.19 (C=O), 1569.16 (C=C). ^{1}H NMR [400 MHz, δ ppm, $CDCl_3$-*d6*]: 2.06-2.31 (m, 4H, -CH_2 & CH_2), 3.05 (s, 6H, $N(CH_3)_2$), 3.54-3.60 (m, 1H, CH_2), 3.66-3.74 (m, 1H, CH_2), 4.37-4.81 (m, 3H, CH_2 & CHCN), 6.70-6.72 (m, 2H, Ar-H), 7.40-7.38 (m, 2H, Ar-H), 7.83 (s, 1H, CH). ^{13}C NMR [100 MHz, δ ppm, $CDCl_3$-d_6]: 25.29, 29.98, 40.13, 42.63, 45.82, 46.89, 111.99, 113.77, 117.99, 120.53, 132.75, 135.77, 151.78, 164.16, 166.23, 168.47. Chemical formula: $C_{19}H_{20}N_4O_3S$; Molecular mass; calculated: 384.13; Mass (M+1): 385.13.

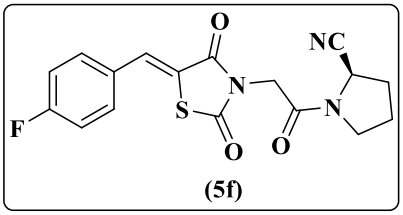
Synthesis of 1-(2-(5-(4-methylbenzylidene)-2,4-dioxothiazolidin-3-yl)acetyl)pyrrolidine-2-carbonitrile (5e):



(5e)

Yield: 84.17%; mp: 170-172°C; FTIR (KBr, cm^{-1}): 3036.09 (Ar-CH), 2251.16 (CN), 1738.90 (C=O), 1512.26 (C=C). ^{1}H NMR [400 MHz, δ ppm, $CDCl_3$-d_6]: 1.97-2.29 (m, 4H, -CH_2 & CH_2), 2.37 (s, 3H, CH_3), 3.51-3.57 (m, 1H, CH_2), 3.64-3.73 (m, 1H, CH_2), 4.33-4.74 (m, 3H, CH_2 & CHCN), 7.24-7.26 (m, 2H, Ar-H), 7.36-7.38 (m, 2H, Ar-H), 7.86 (s, 1H, CH). ^{13}C NMR [100 MHz, δ ppm, $CDCl_3$-d_6]: 21.72, 25.28, 29.98, 42.81, 45.84, 46.91, 117.89, 119.87, 130.13, 130.40, 130.46, 134.98, 141.65, 163.85, 165.94, 167.95; Chemical formula: $C_{18}H_{17}N_3O_3S$; Molecular mass; calculated 355.10; Mass (M+1): 356.10.

Synthesis of 1-(2-(5-(4-fluorobenzylidene)-2,4-dioxothiazolidin-3-yl)acetyl)pyrrolidine-2-carbonitrile (5f):



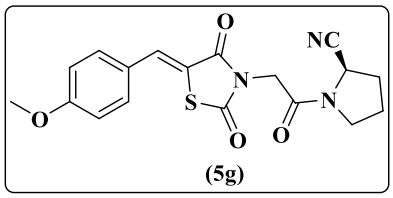
(5f)

Yield: 85.32%; mp: 160-162°C; FTIR (KBr, cm^{-1}): 2241.38 (CN), 1741.80 (C=O), 1596.16 (C=C). ^{1}H NMR [400 MHz, δ ppm, DMSO-*d6*]: 2.05-2.32 (m, 4H, -CH_2 & CH_2), 3.49-3.61 (m, 1H, CH_2), 3.77-

3.82 (m, 1H, CH_2), 4.41-4.90 (m, 3H, CH_2 & CHCN), 7.38-7.43 (m, 2H, Ar-H), 7.21-7.55 (m, 2H, Ar-H), 8.00 (s, 1H, CH). ^{13}C NMR

[100 MHz, δ ppm, DMSO-*d6*]: 24.73, 29.40, 43.10, 45.44, 46.30, 116.45, 118.90, 120.52, 129.44, 132.64, 161.81, 163.91, 164.31, 164.90, 164.99, 165.05, 166.80. Chemical formula: $C_{17}H_{14}FN_3O_3S$; Molecular mass; calculated: 359.08; Mass (M+1): 360.08.

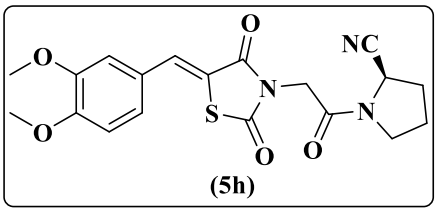
Synthesis of 1-(2-(5-(4-methoxybenzylidene)-2, 4-dioxothiazolidin-3-yl) acetyl) pyrrolidine-2-carbonitrile (5g):



(5g)

Yield: 85.32%; mp: 167-169°C; FTIR (KBr, cm^{-1}): 3071.77 (Ar-CH), 2241.38 (CN), 1738.90 (C=O), 1586.52 (C=C). ^{1}H NMR [400 MHz, δ ppm, DMSO-*d6*]: 2.02-2.30 (m, 4H, -CH_2 & CH_2), 3.48-3.60 (m, 1H, CH_2), 3.75-3.81 (m, 1H, CH_2), 3.83 (s, 3H, OCH_3), 4.50-4.78 (m, 3H, CH_2 & CHCN), 7.10-7.12 (m, 2H, Ar-H), 7.60-7.62 (m, 2H, Ar-H), 7.92 (s, 1H, CH). ^{13}C NMR [100 MHz, δ ppm, DMSO-*d6*]: 25.32, 30.03, 43.53, 46.03, 46.98, 56.07, 115.45, 118.10, 119.47, 125.85, 132.91, 134.24, 161.88, 164.58, 165.78, 167.57. Chemical formula: $C_{18}H_{17}N_3O_4S$; Molecular mass; calculated: 371.41; Mass (M+1): 372.10.

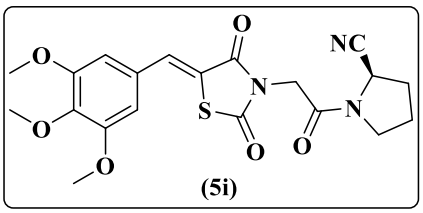
Synthesis of 1-(2-(5-(3, 4-dimethoxybenzylidene)-2, 4-dioxothiazolidin-3-yl) acetyl) pyrrolidine-2-carbonitrile (5h):



(5h)

Yield: 85.32%; mp: 171-173°C; FTIR (KBr, cm^{-1}): 3011.98 (Ar-CH), 2242.34 (CN), 1738.90 (C=O), 1575.91 (C=C). ^{1}H NMR [400 MHz, δ ppm, DMSO-*d6*]: 1.90-2.24 (m, 4H, -CH_2 & CH_2), 3.50-3.59 (m, 1H, CH_2), 3.75-3.81 (m, 1H, CH_2), 3.80-3.82 (d, 6H, OCH_3), 4.38-4.88 (m, 3H, CH_2 & CHCN), 7.12-7.14 (m, 2H, Ar-H), 7.22-7.24 (m, 2H, Ar-H), 7.91 (s, 1H, CH). ^{13}C NMR [100 MHz, δ ppm, DMSO-*d6*]: 25.34, 30.00, 43.51, 46.00, 46.97, 56.06, 56.23, 112.63, 114.04, 118.16, 119.53, 124.46, 125.97, 134.61, 149.47, 151.65, 164.58, 165.78, 167.62. Chemical formula: $C_{19}H_{19}N_3O_5S$; Molecular mass; calculated: 401.44; Mass (M+1): 402.12.

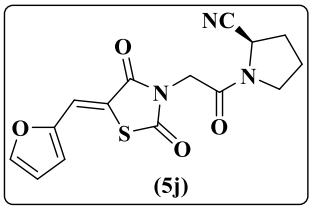
Synthesis of 1-(2-(2, 4-dioxo-5-(3, 4, 5-trimethoxybenzylidene) thiazolidin-3-yl) acetyl) pyrrolidine-2-carbonitrile (5i):



(5i)

Yield: 80.07%; mp: 164-166°C; FTIR (KBr, cm^{-1}): 3004.26 (Ar-CH), 2243.31 (CN), 1738.90 (C=O), 1575.91 (C=C). ^{1}H NMR [400 MHz, δ ppm, DMSO-*d6*]: 2.01-2.34 (m, 4H, -CH_2 & CH_2), 3.48-3.59 (m, 1H, CH_2), 3.72 (S, 3H, OCH_3), 3.76-3.80 (m, 1H, CH_2), 3.83 (d, 6H, OCH_3), 4.39-4.89 (m, 3H, CH_2 & CHCN), 6.97 (s, 2H, Ar-H), 7.92 (s, 1H, CH). ^{13}C NMR [100 MHz, δ ppm, DMSO-*d6*]: 25.34, 30.01, 43.57, 46.00, 46.98, 56.54, 60.75, 108.20, 119.53, 120.30, 128.85, 134.51, 140.17, 153.77, 164.53, 165.64, 167.52. Chemical formula: $C_{20}H_{21}N_3O_6S$; Molecular mass; calculated: 431.46; Mass (M+1): 432.12.

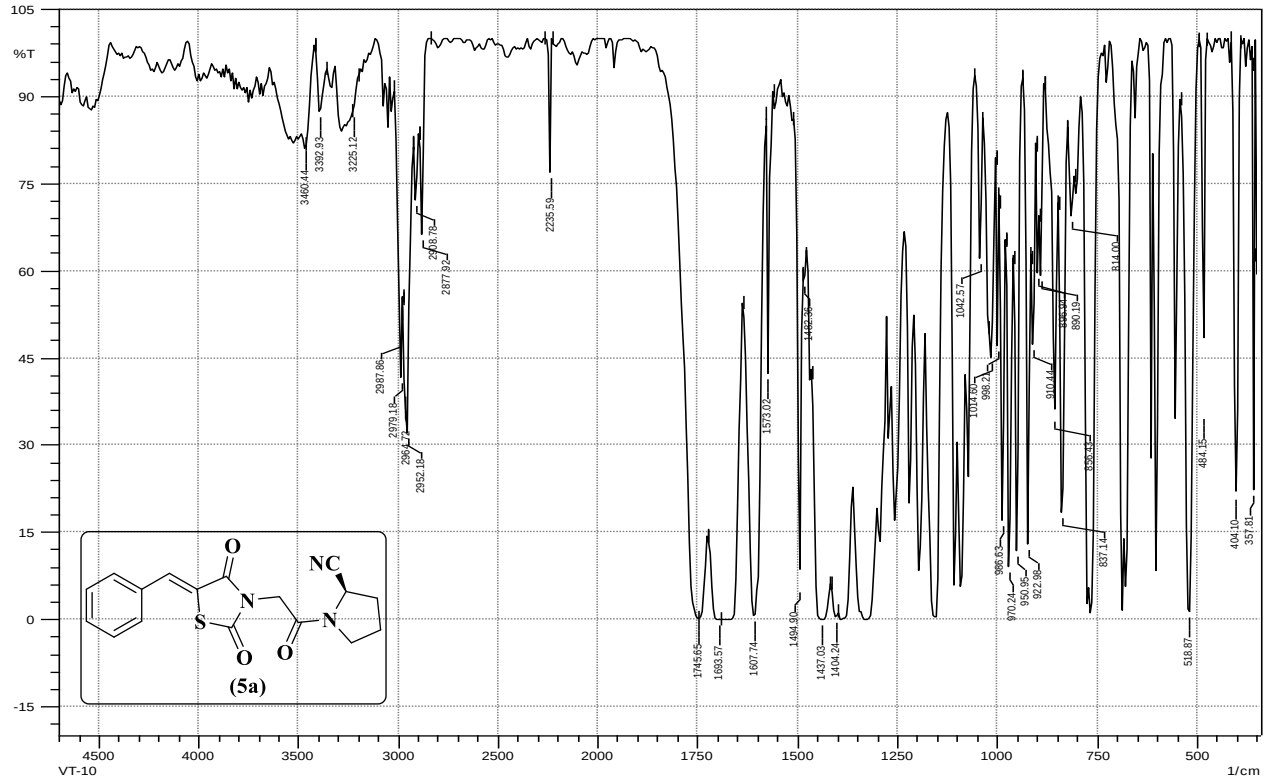
Synthesis of 1-(2-(5-(furan-2-ylmethylene)-2, 4-dioxothiazolidin-3-yl) acetyl) pyrrolidine-2-carbonitrile (5j):



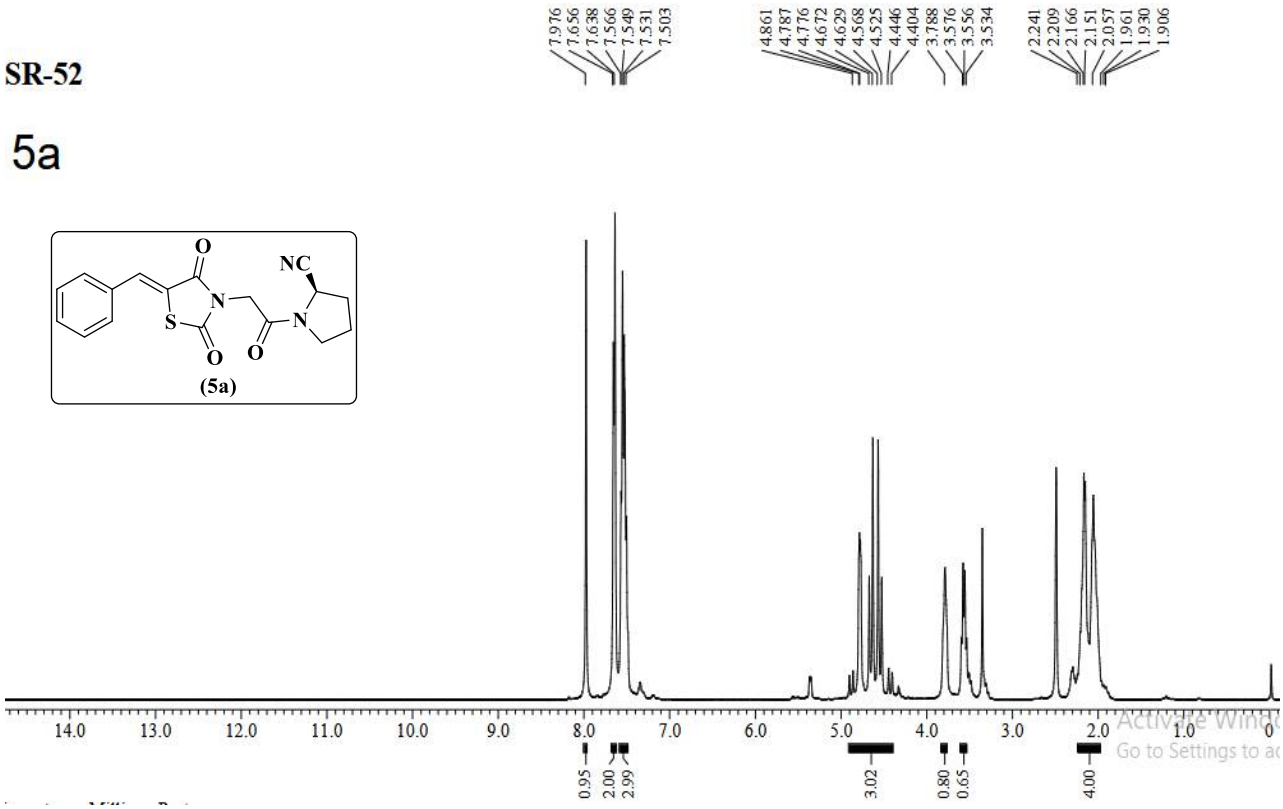
(5j)

Yield: 80.07%; mp: 178-180°C; FTIR (KBr, cm^{-1}): 3078.52 (Ar-CH), 2244.27 (CN), 1747.58 (C=O), 1545.05 (C=C). ^{1}H NMR [400 MHz, δ ppm, DMSO-*d6*]: 2.06-2.29 (m, 4H, -CH_2 & CH_2), 3.47-3.58 (m, 1H, CH_2), 3.77 (m, 1H, CH_2), 4.37-4.86 (m, 3H, CH_2 & CHCN), 6.76 (s, 1H, Ar-H), 7.16-7.17 (d, 1H, Ar-H), 7.80 (s, 1H, Ar-H), 8.09 (s, 1H, CH). ^{13}C NMR [100 MHz, δ ppm, DMSO-*d6*]: 25.34, 29.99, 43.43, 45.99, 46.97, 114.23, 117.84, 119.53, 120.28, 120.61, 148.61, 149.65, 164.11, 164.58, 165.49, 168.26. Chemical formula: $C_{20}H_{21}N_3O_6S$; Molecular mass; calculated: 330.07; Mass (M+1): 332.06.

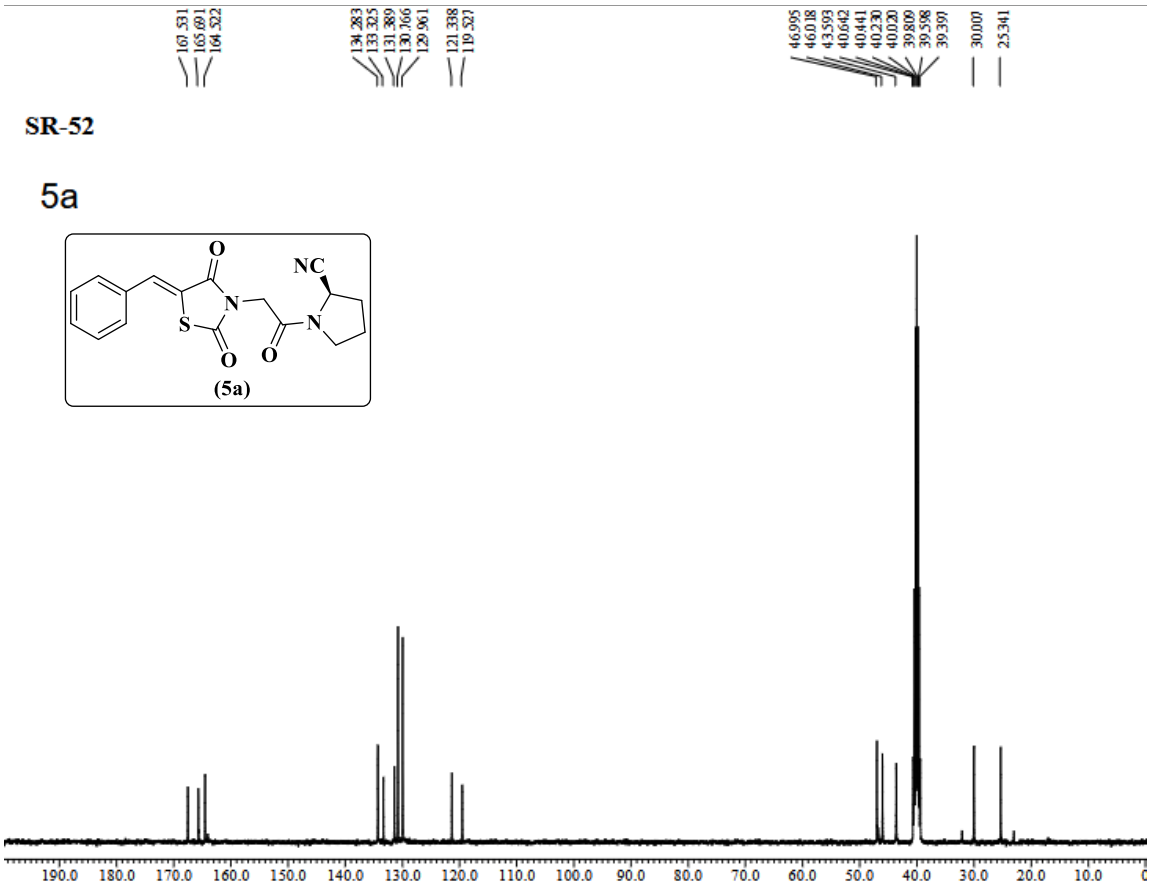
4. Spectral data evaluation



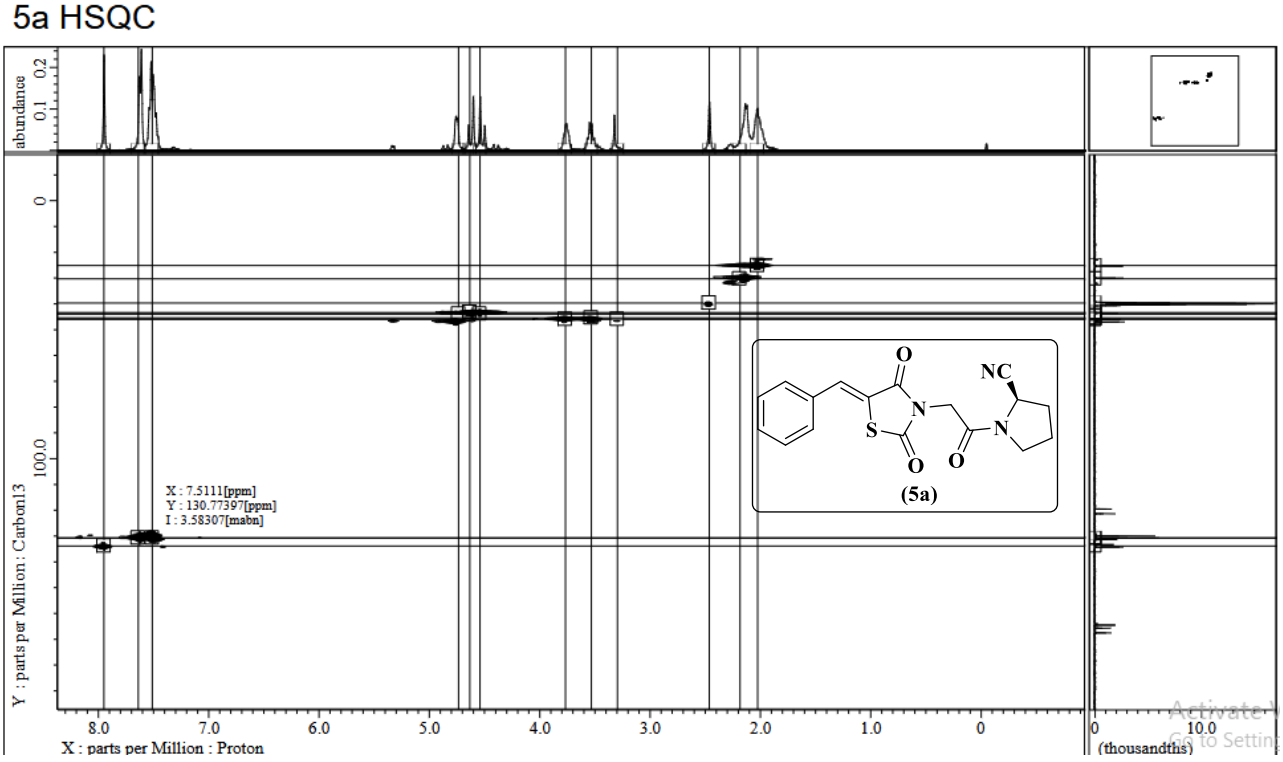
Spectra. 41: FTIR (KBr, cm^{-1}) spectra of compound 5a



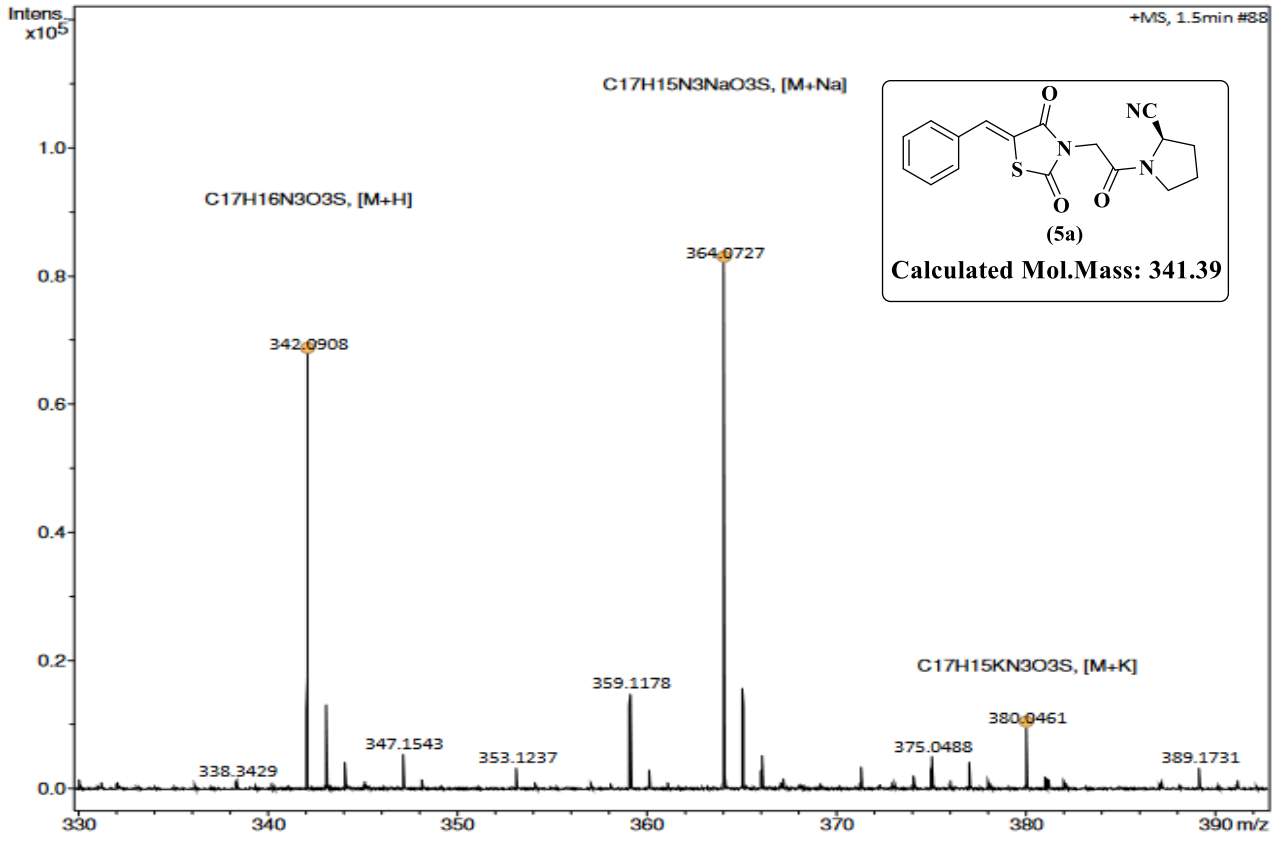
Spectra. 42: ^{1}H NMR (400 MHz, δ, ppm) spectra of compound 5a



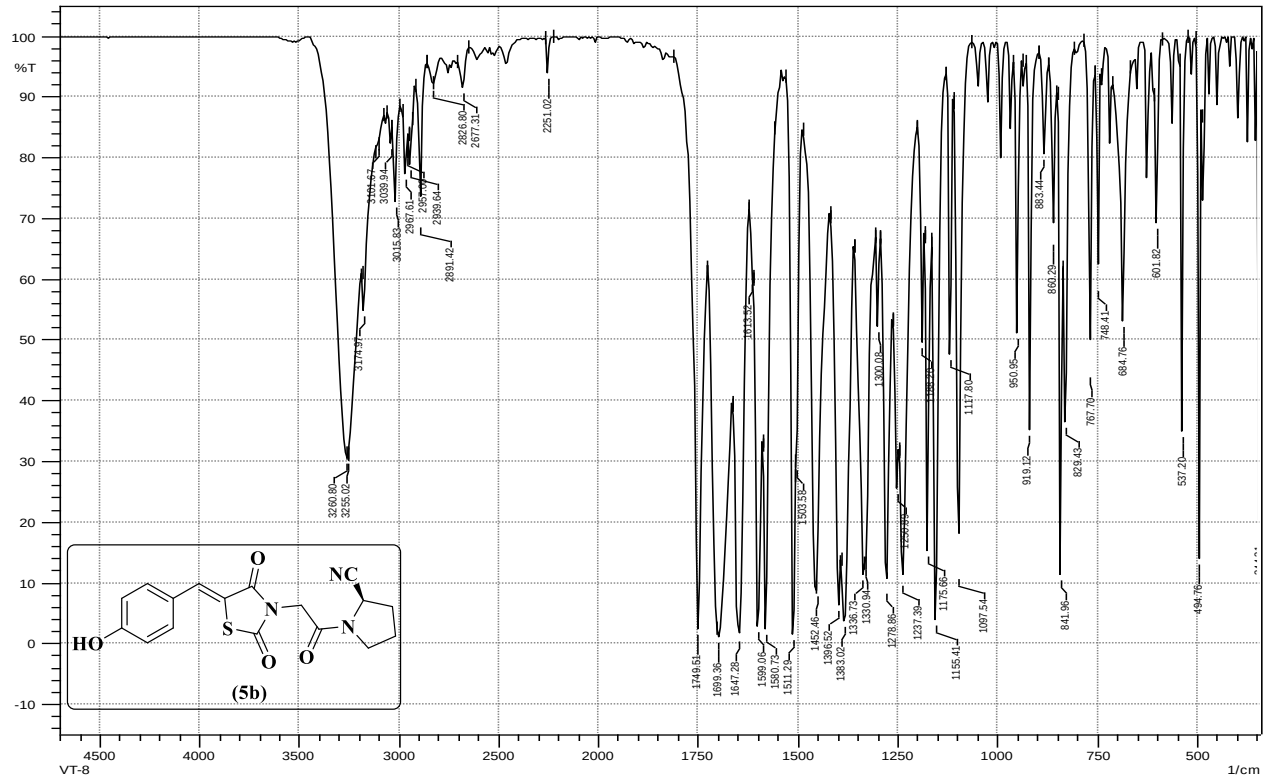
Spectra. 43: ^{13}C NMR (100 MHz, δ, ppm) spectra of compound 5a



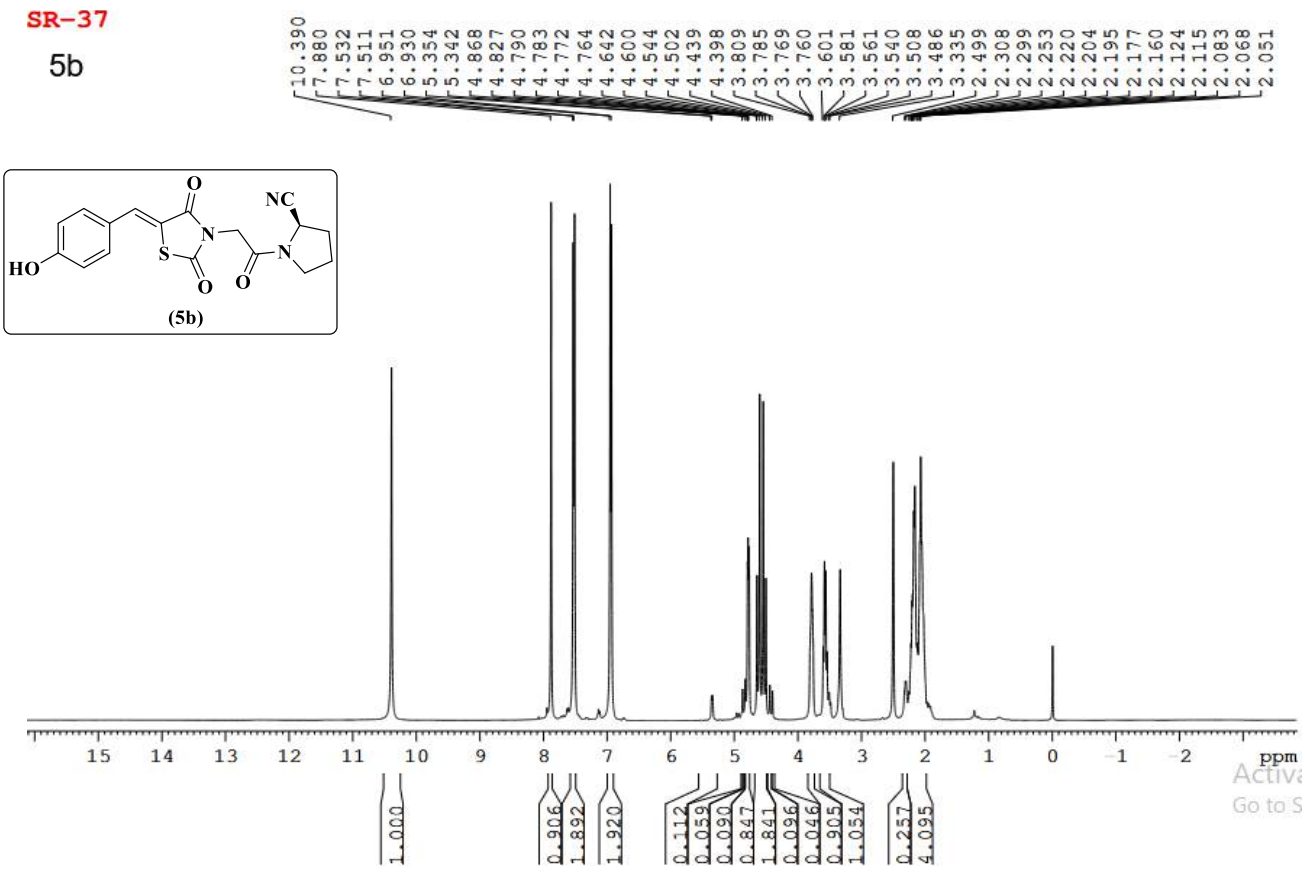
Spectra. 44: ^{1}H-^{13}C NMR (HSQC) spectrum of compound 5a



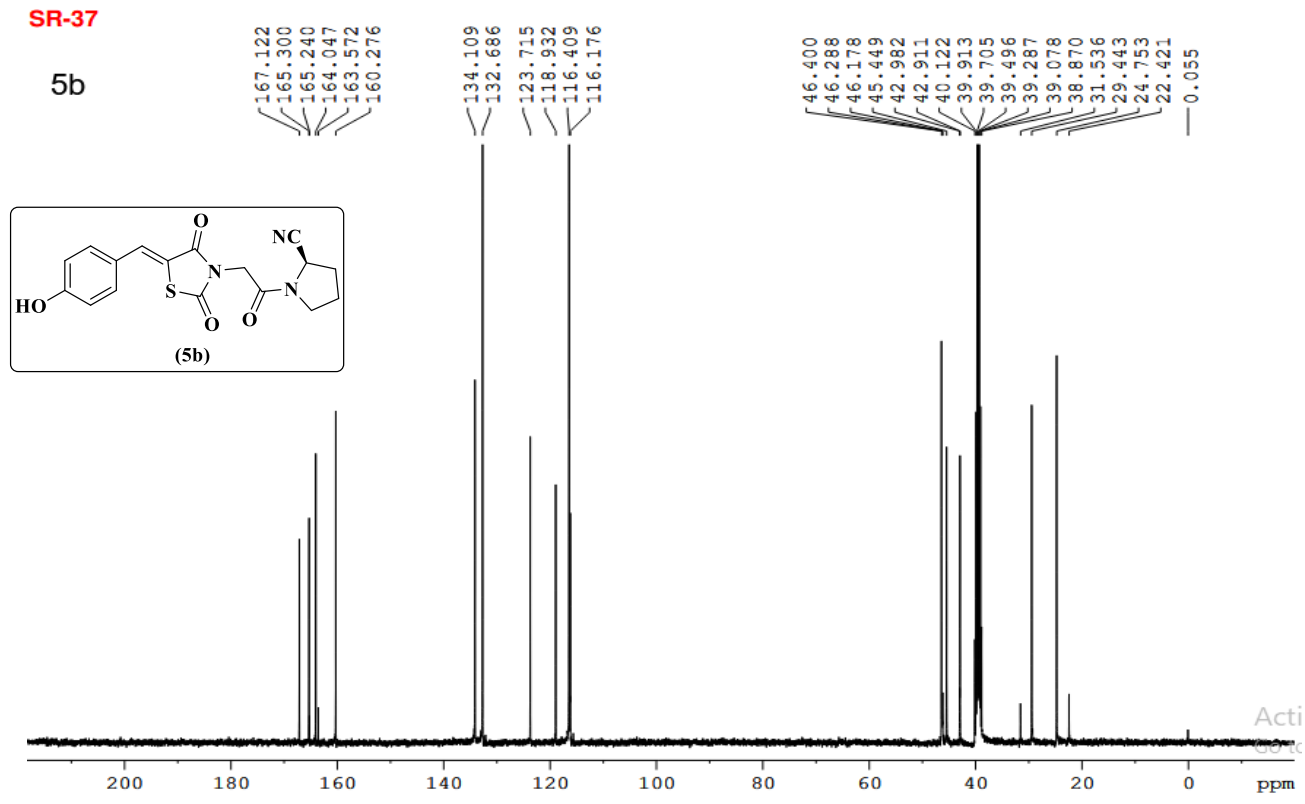
Spectra. 45: HRMS spectra of compound 5a



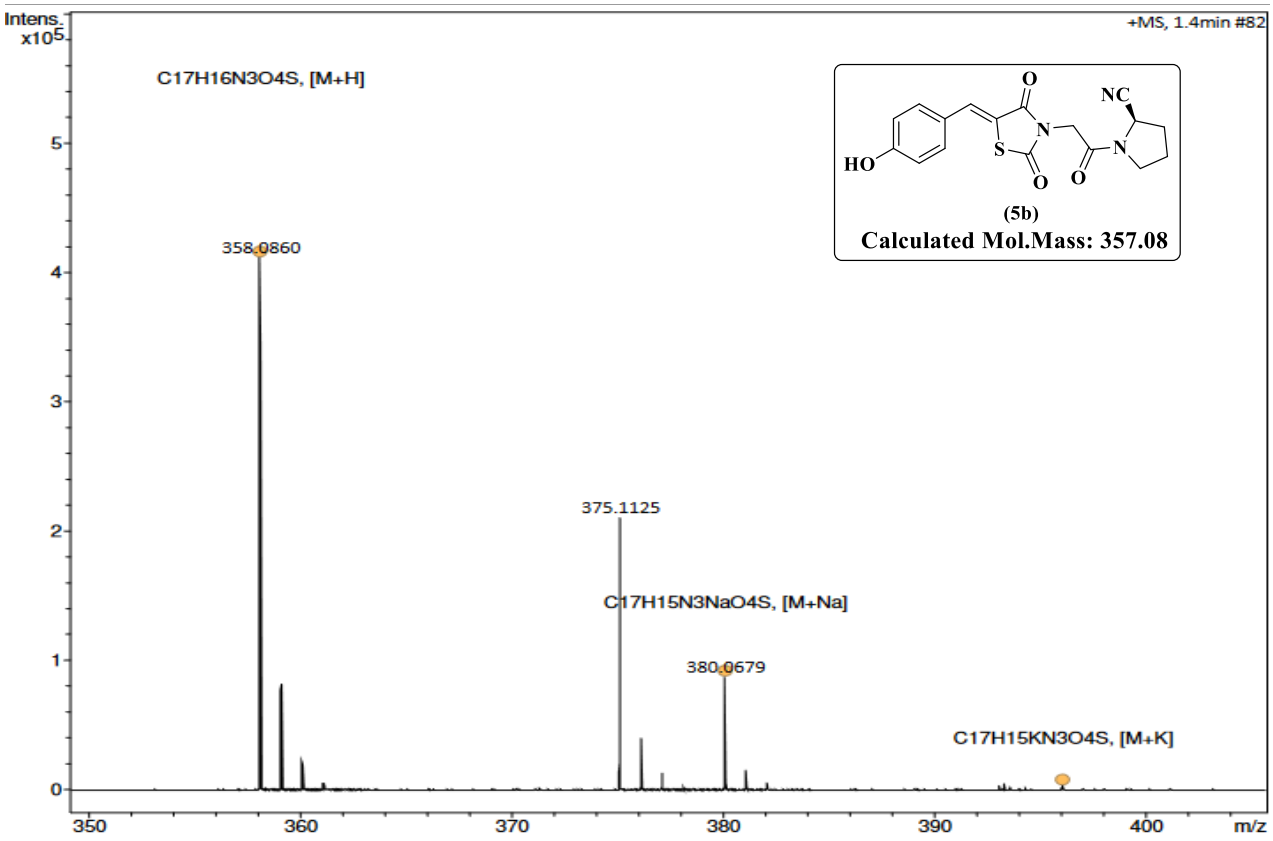
Spectra. 46: FTIR (KBr, cm^{-1}) spectra of compound 5b



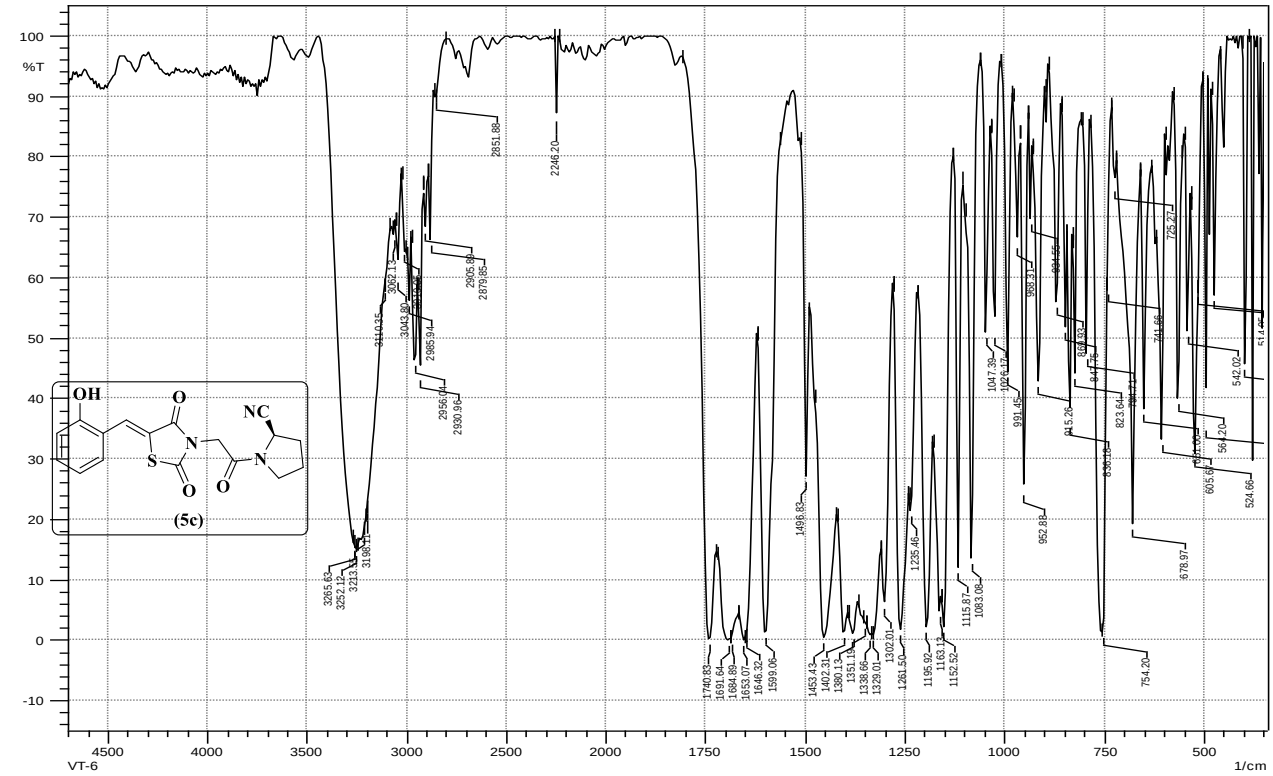
Spectra. 47: ^{1}H NMR (400 MHz, δ, ppm) spectra of compound 5b



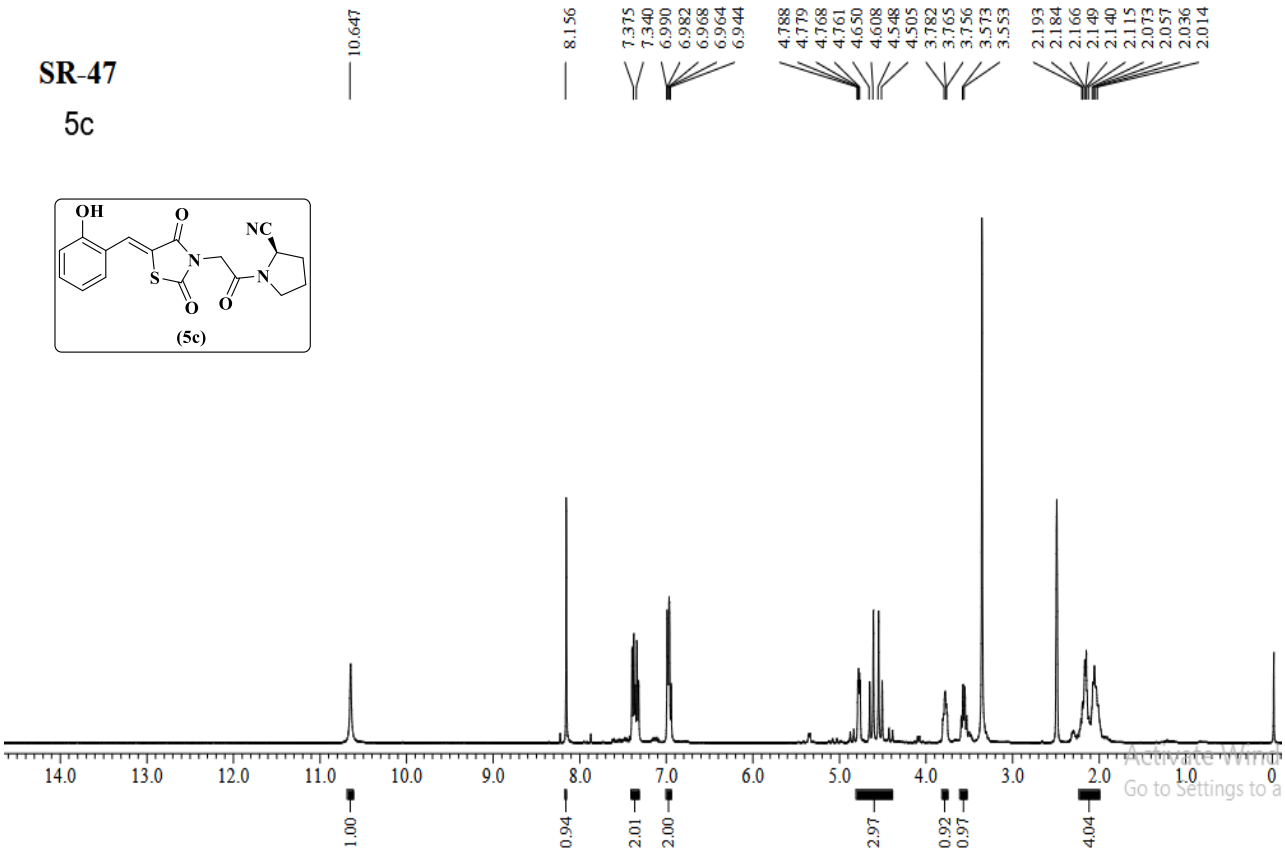
Spectra. 48: ^{13}C NMR (100 MHz, δ, ppm) spectra of compound 5b



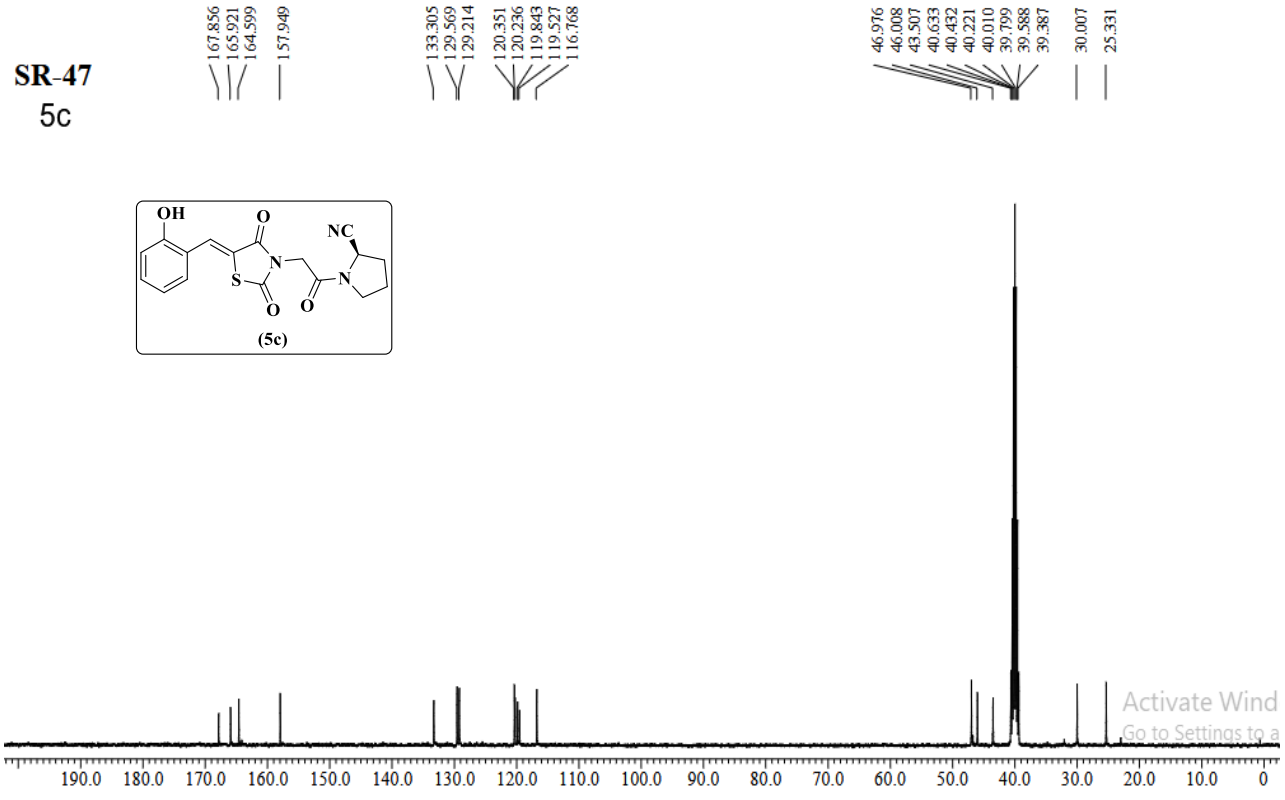
Spectra. 49: HRMS spectra of compound 5b



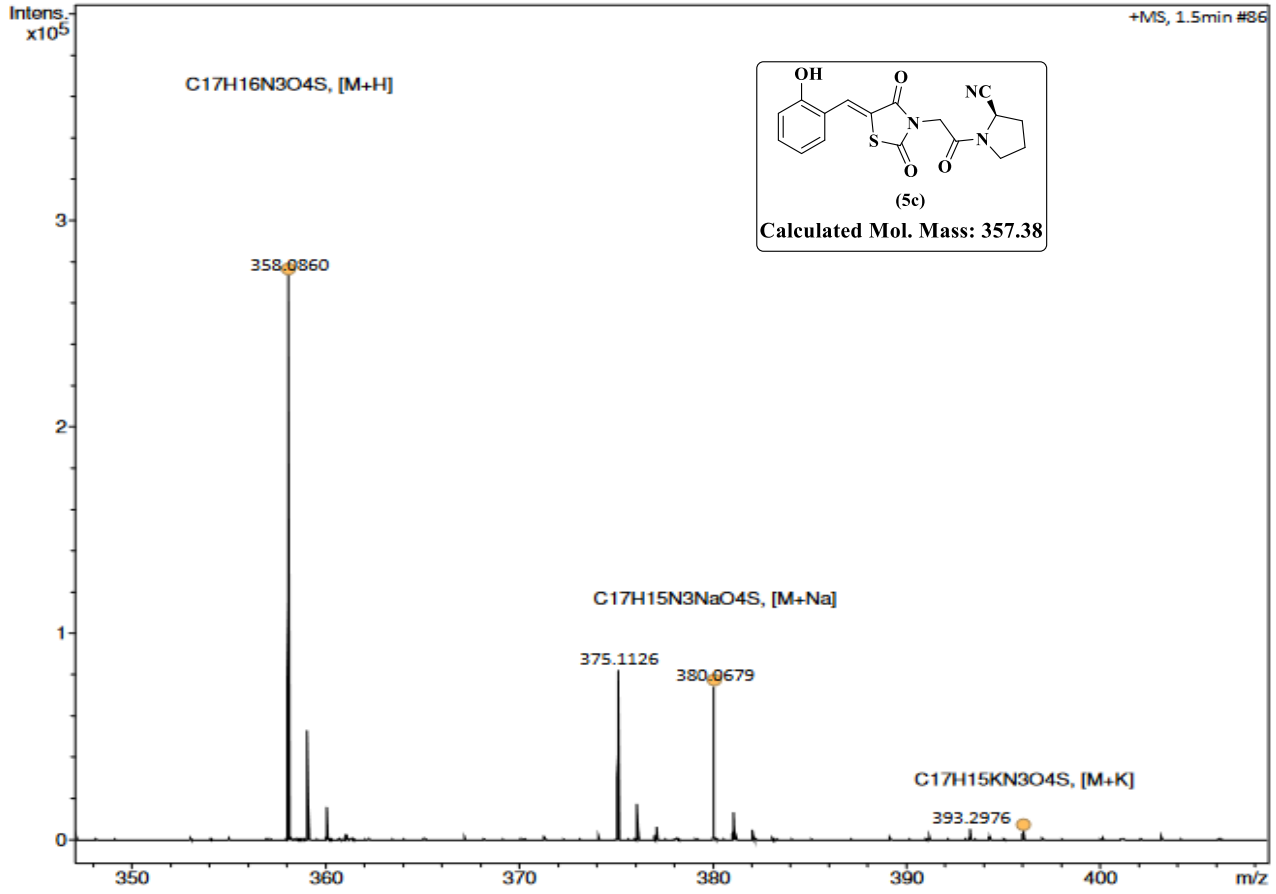
Spectra. 50: FTIR (KBr, cm^{-1}) spectra of compound 5c



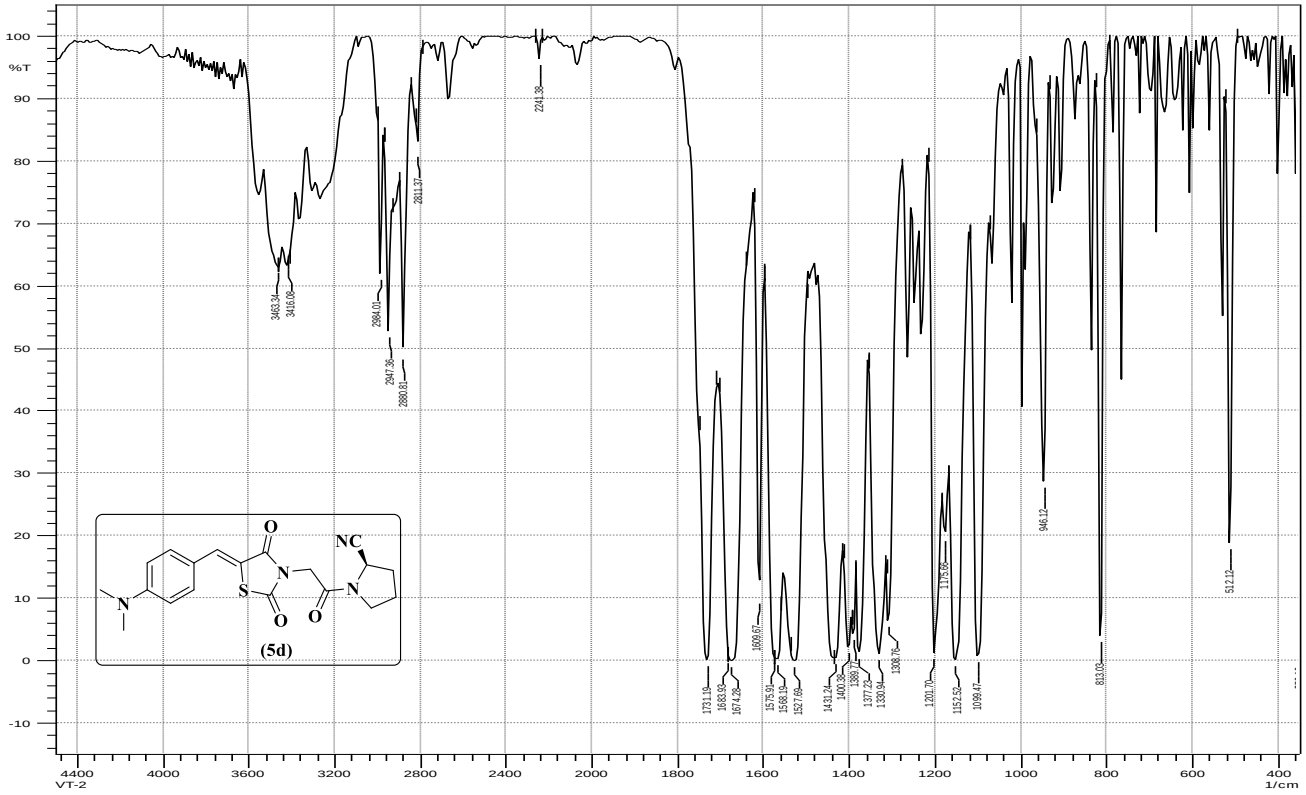
Spectra. 51: ^{1}H NMR (400 MHz, δ, ppm) spectra of compound 5c



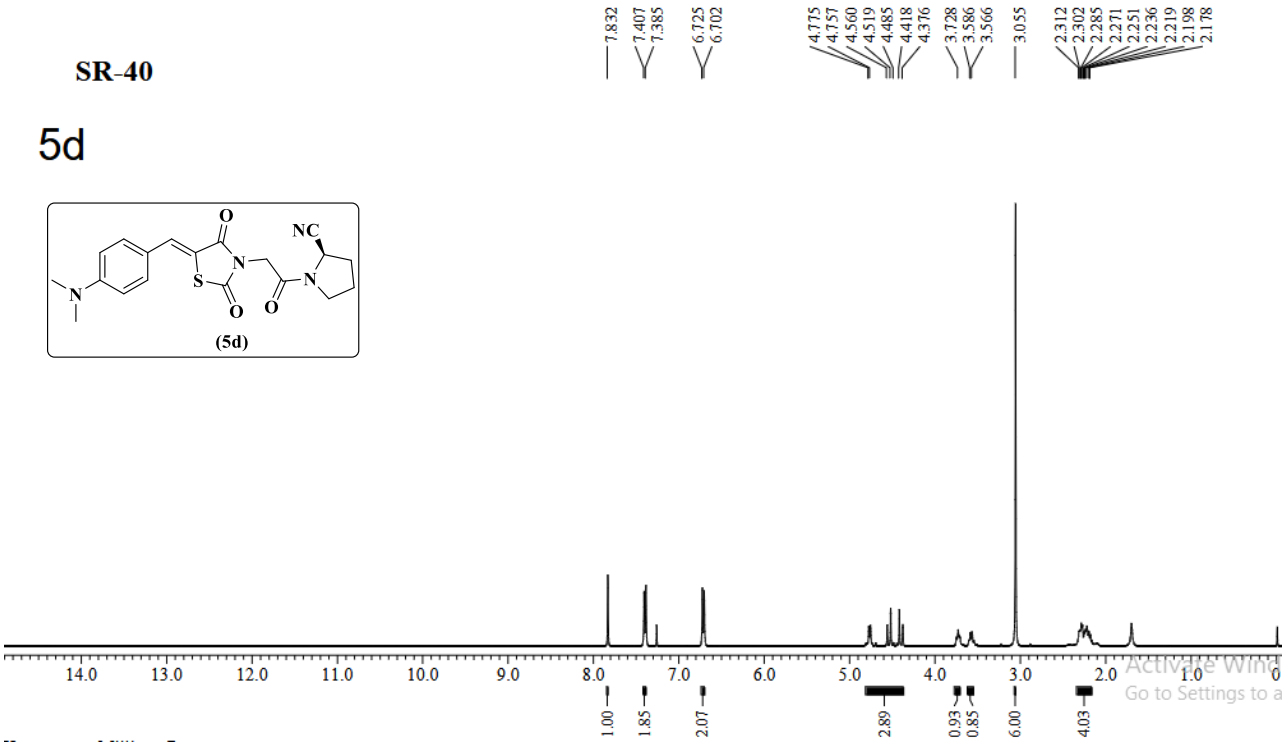
Spectra. 52: ^{13}C NMR (100 MHz, δ, ppm) spectra of compound 5c



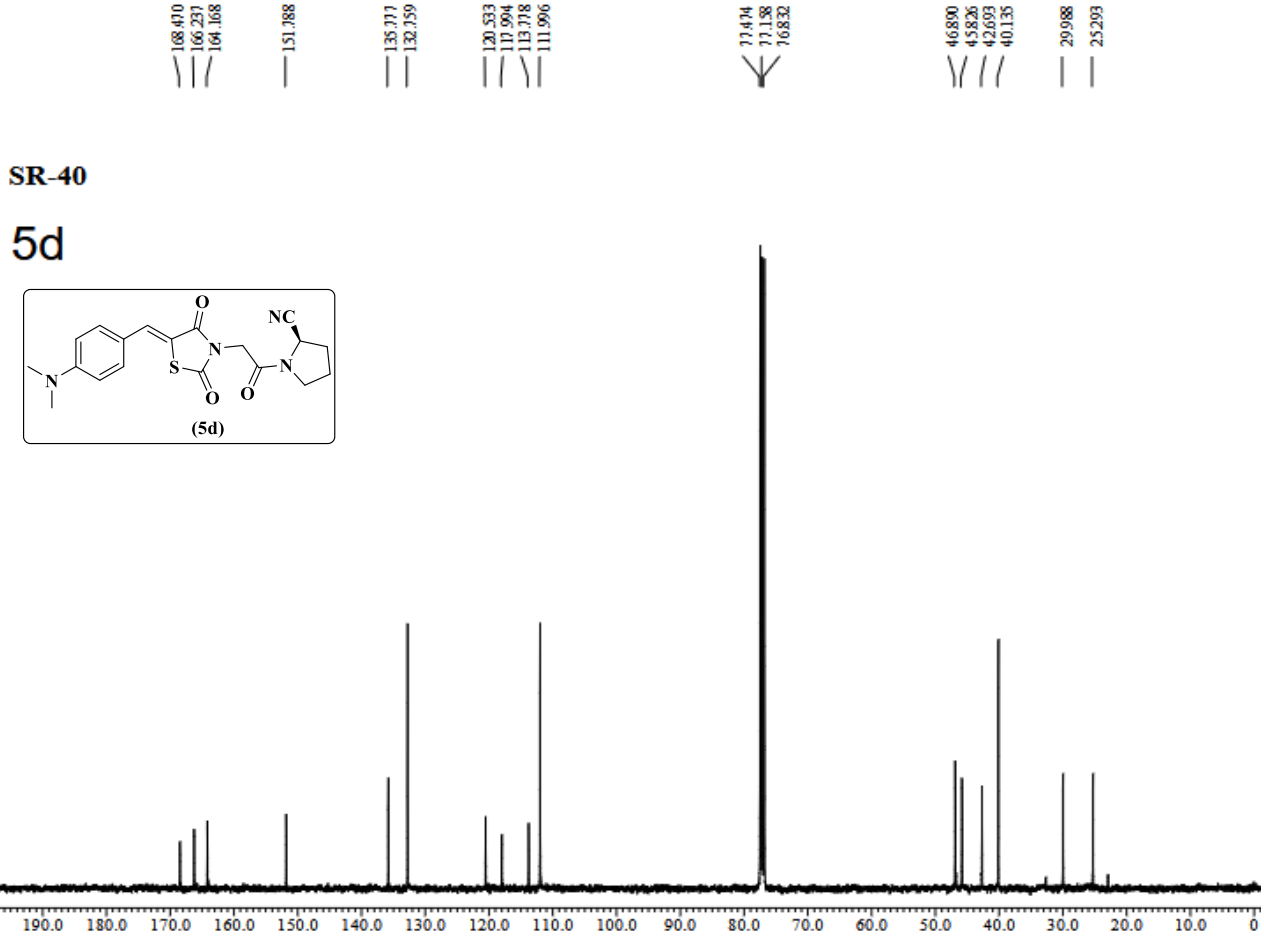
Spectra. 53: HRMS Spectra of compound 5c



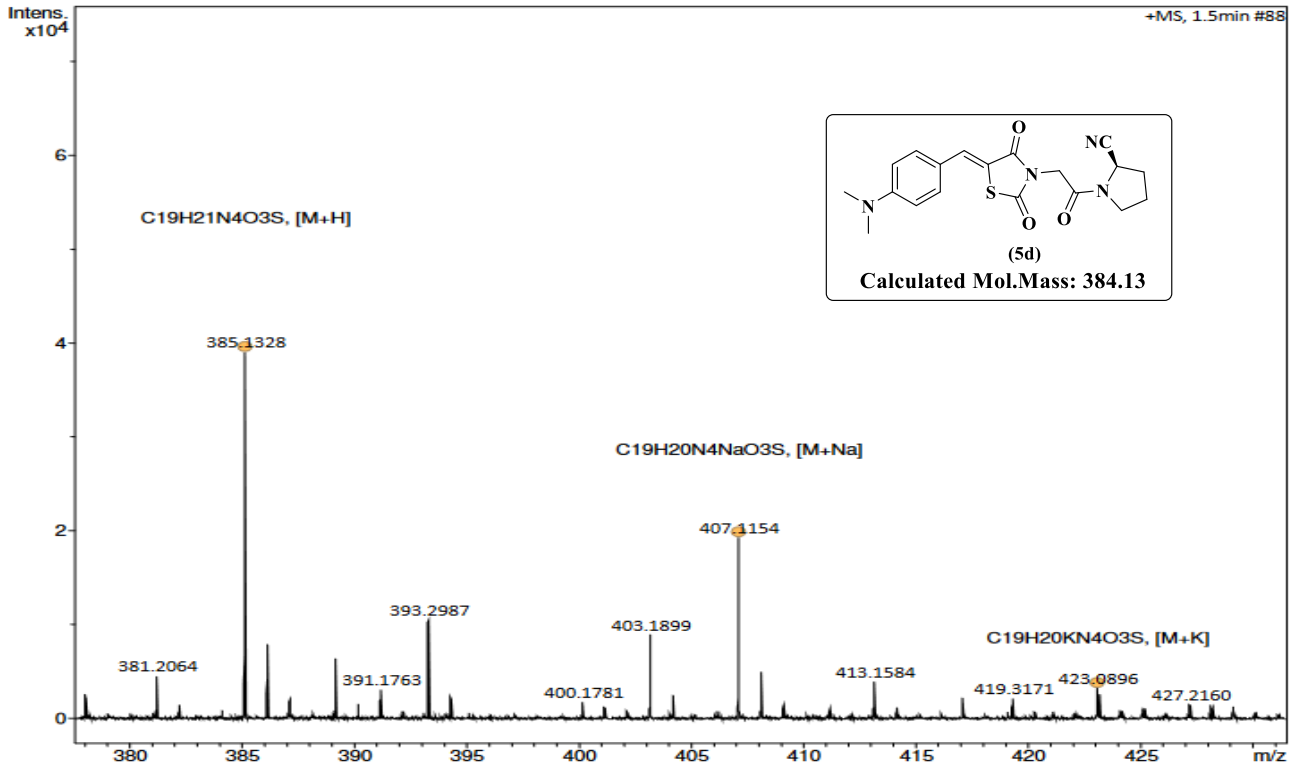
Spectra. 54: FTIR (KBr, cm^{-1}) spectra of compound 5d



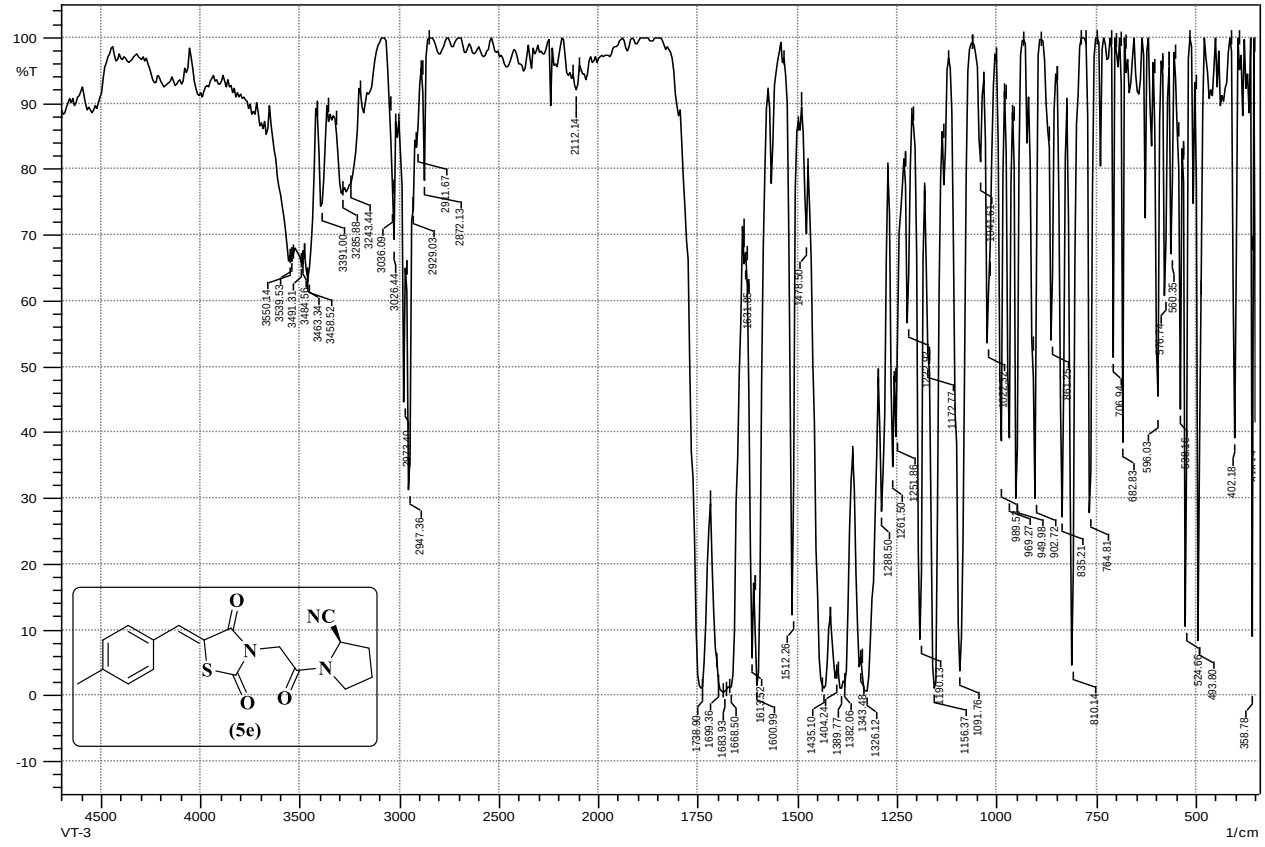
Spectra. 55: ^{1}H NMR (400 MHz, δ, ppm) spectra of compound 5d



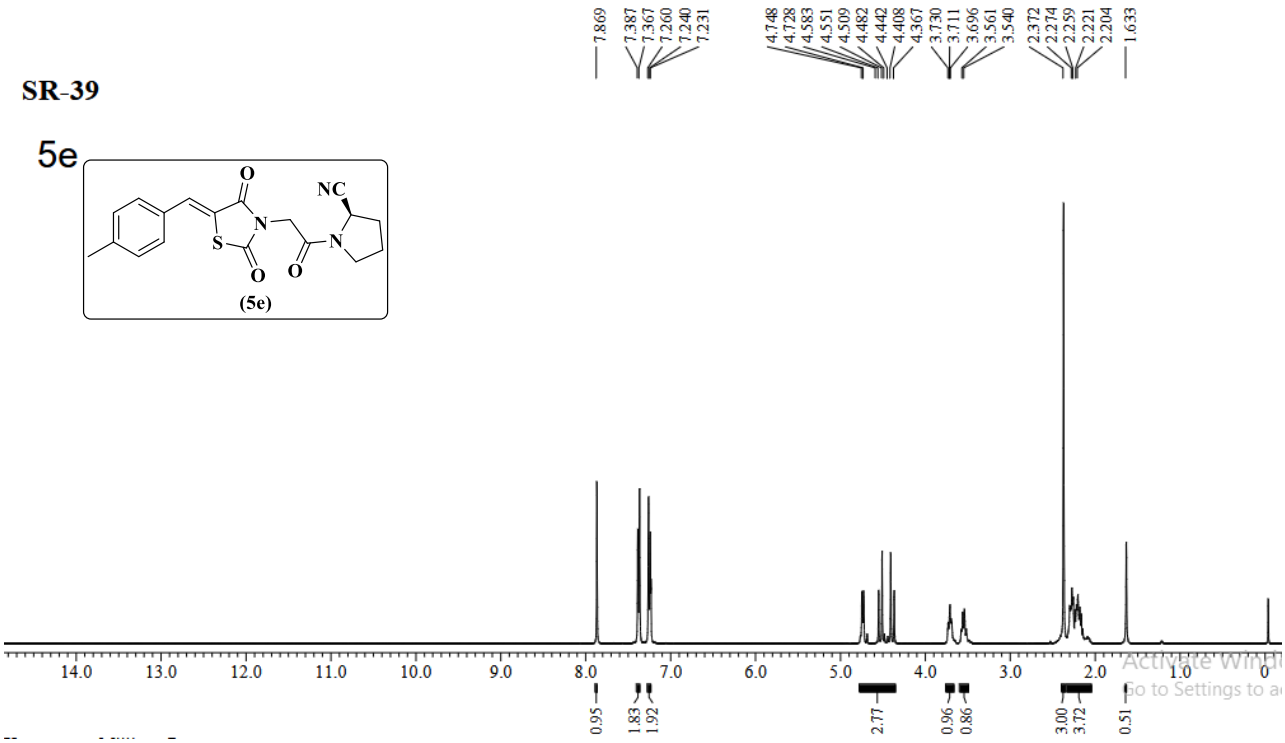
Spectra. 56: ^{13}C NMR (100 MHz, δ, ppm) spectra of compound 5d



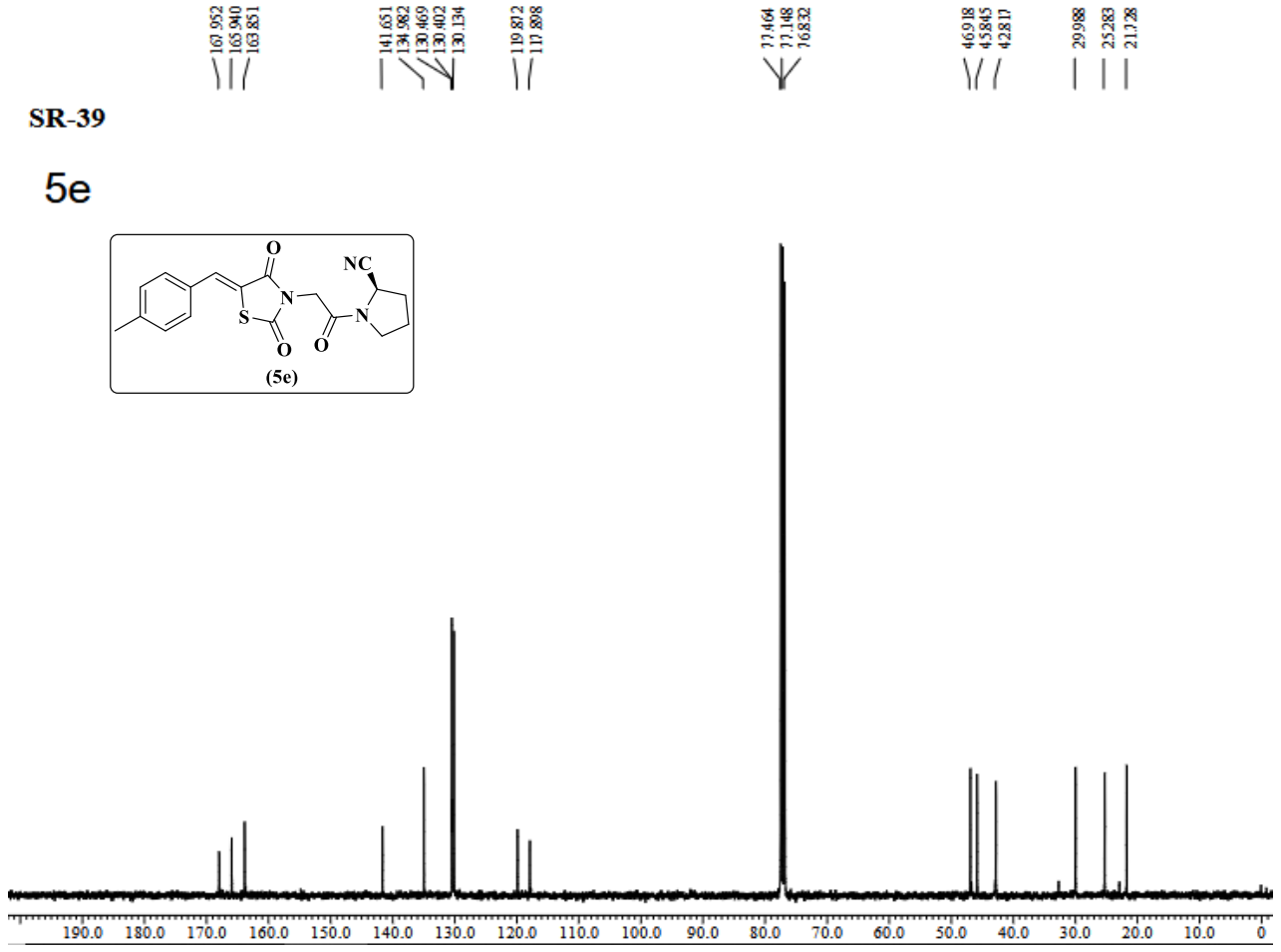
Spectra. 57: HRMS Spectra of compound 5d



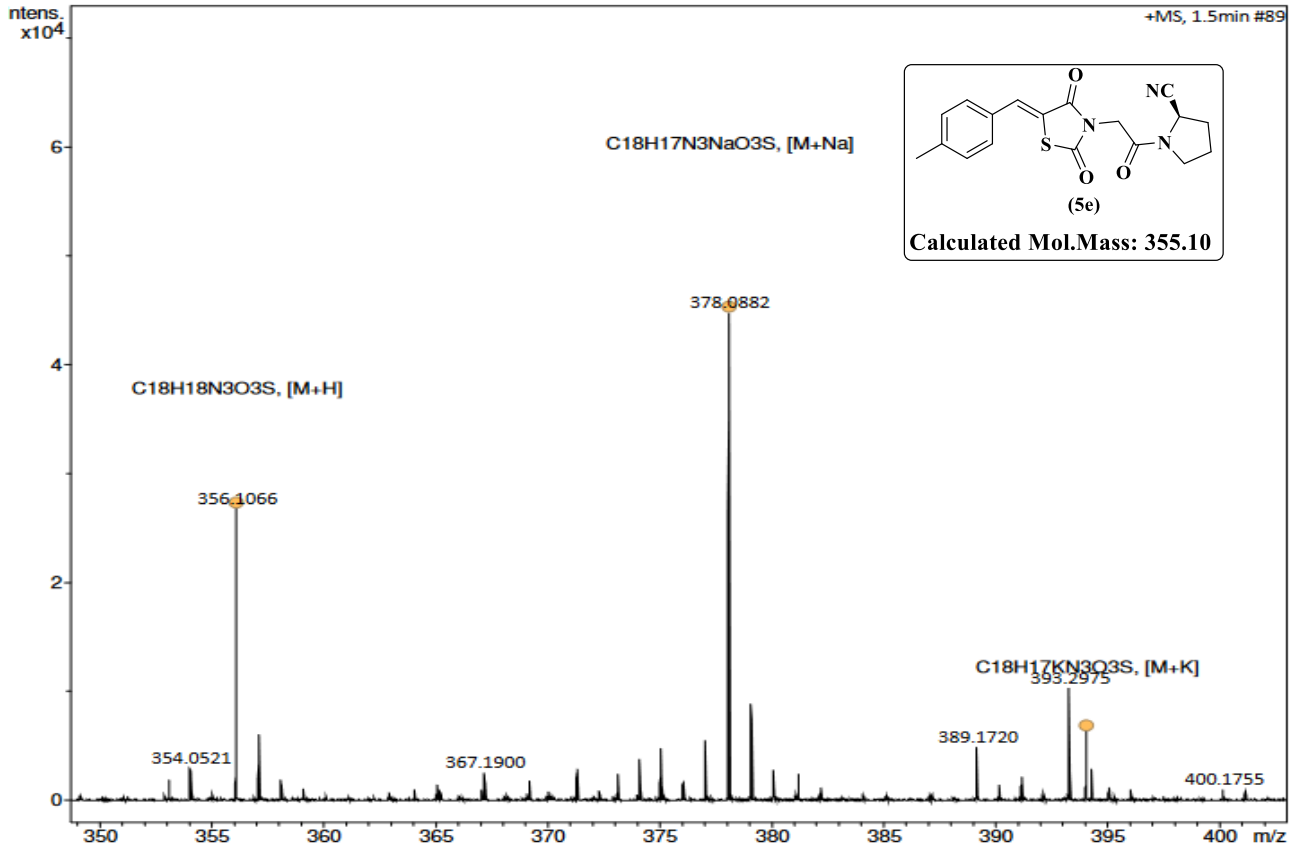
Spectra. 58: FTIR (KBr, cm^{-1}) spectra of compound 5e



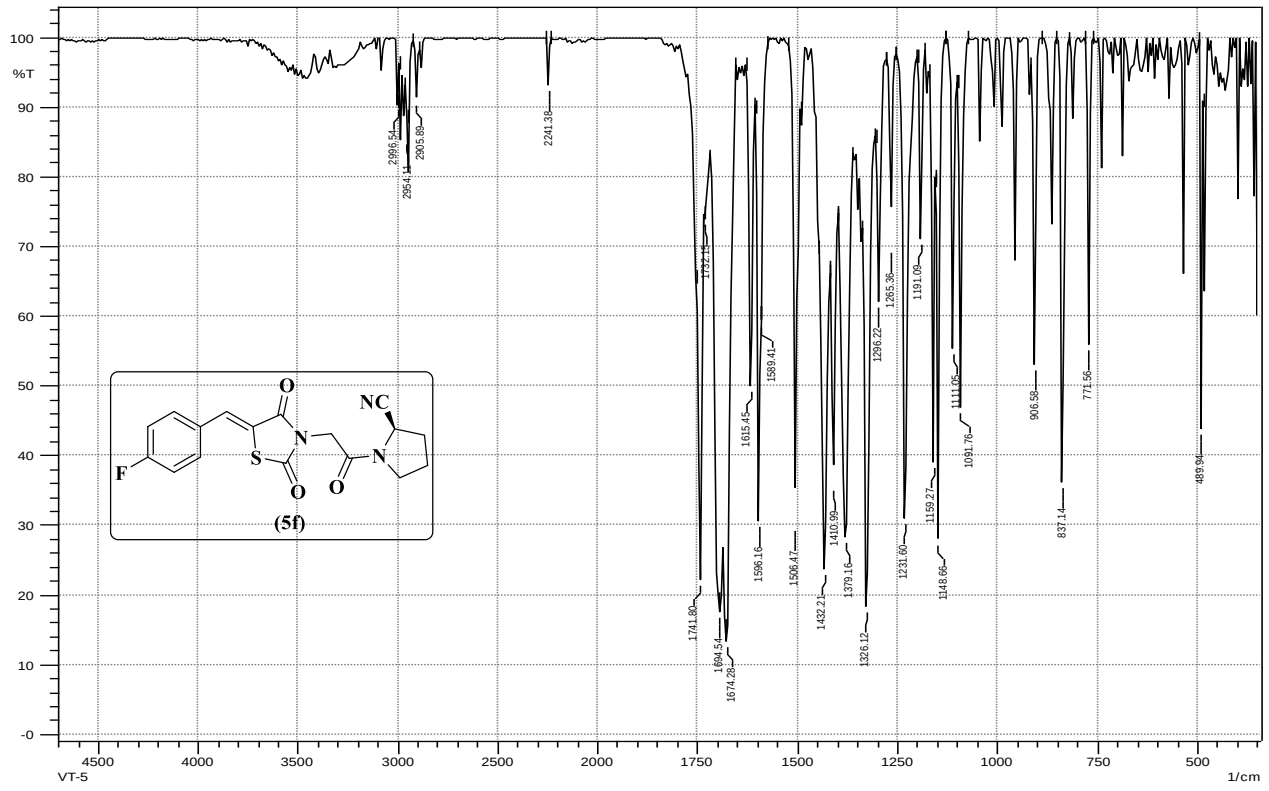
Spectra. 59: ^{1}H NMR (400 MHz, δ, ppm) spectra of compound 5e



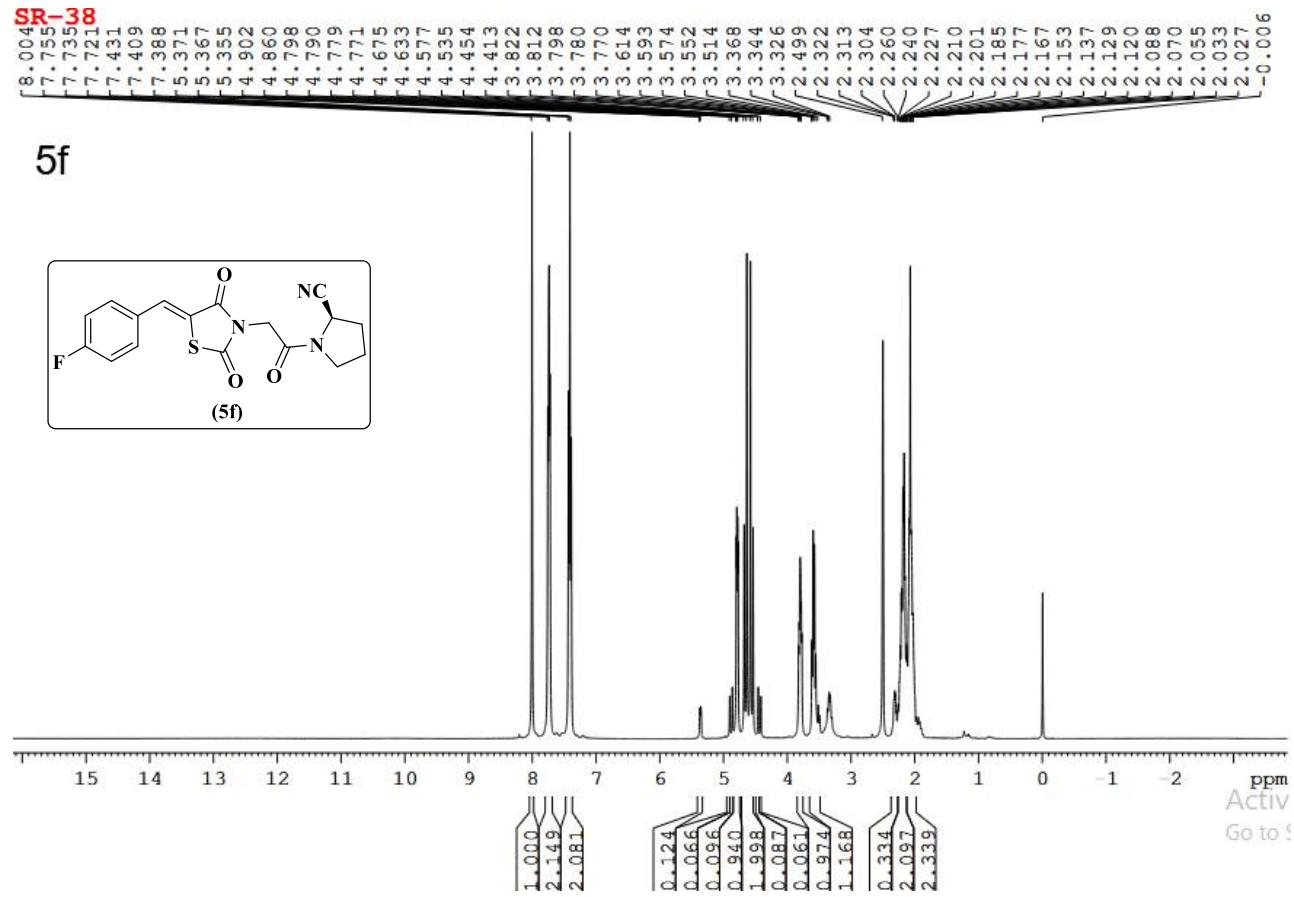
Spectra. 60: ^{13}C NMR (100 MHz, δ, ppm) spectra of compound 5e



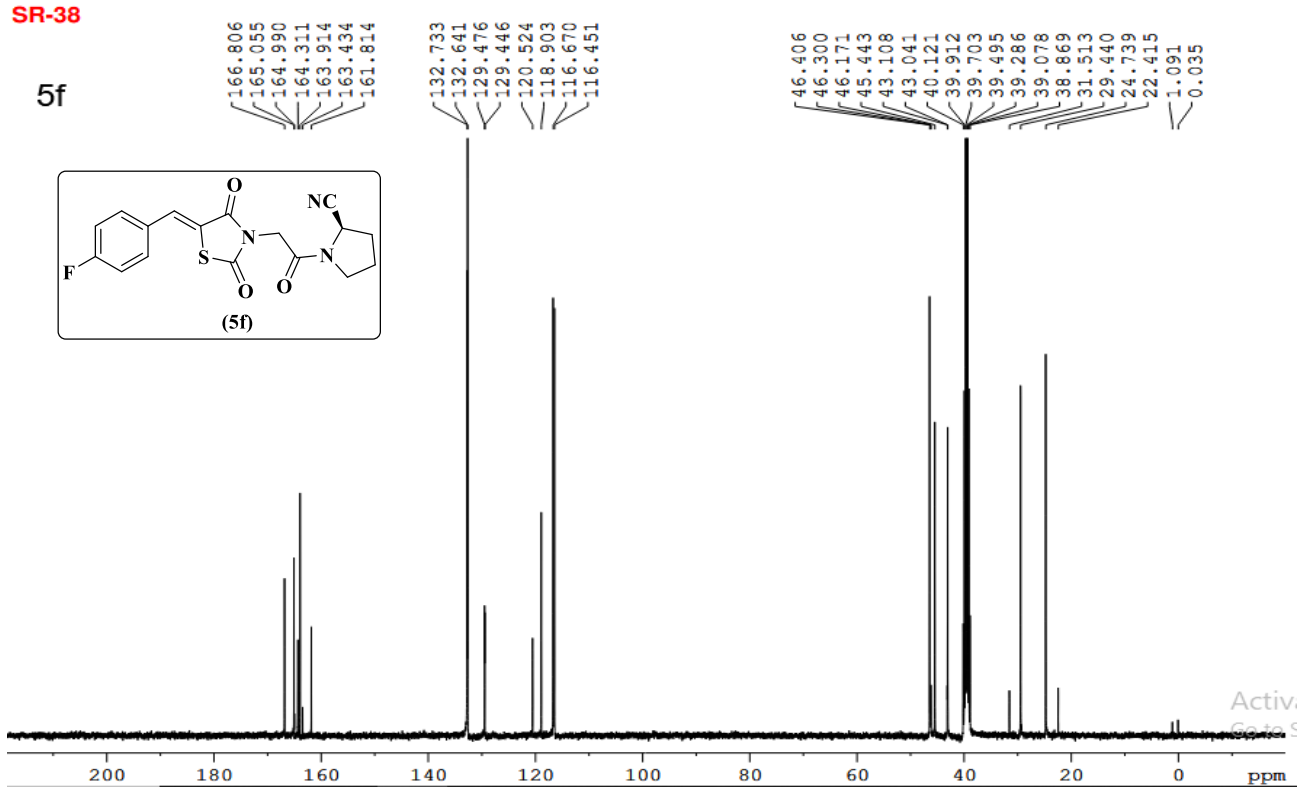
Spectra. 61: HRMS spectra of compound 5e



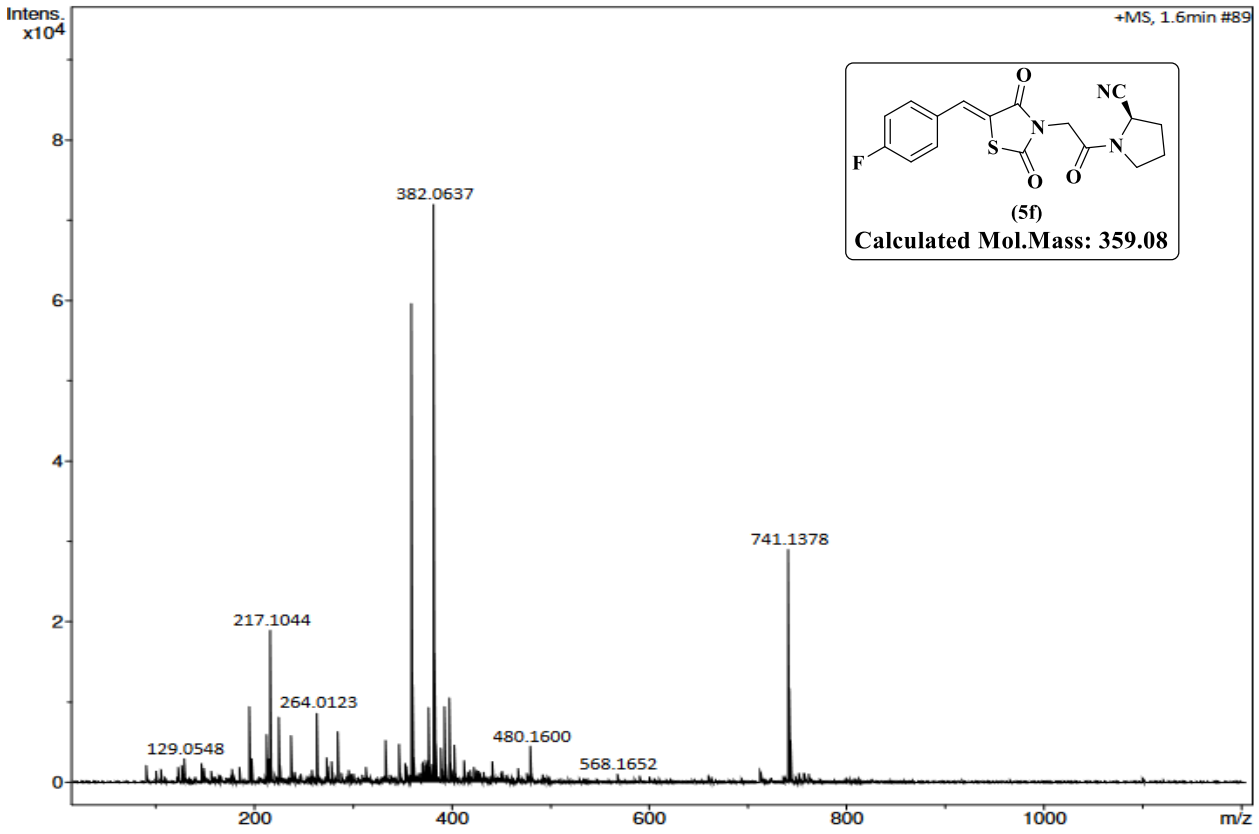
Spectra. 62: FTIR (KBr, cm^{-1}) spectra of compound 5f



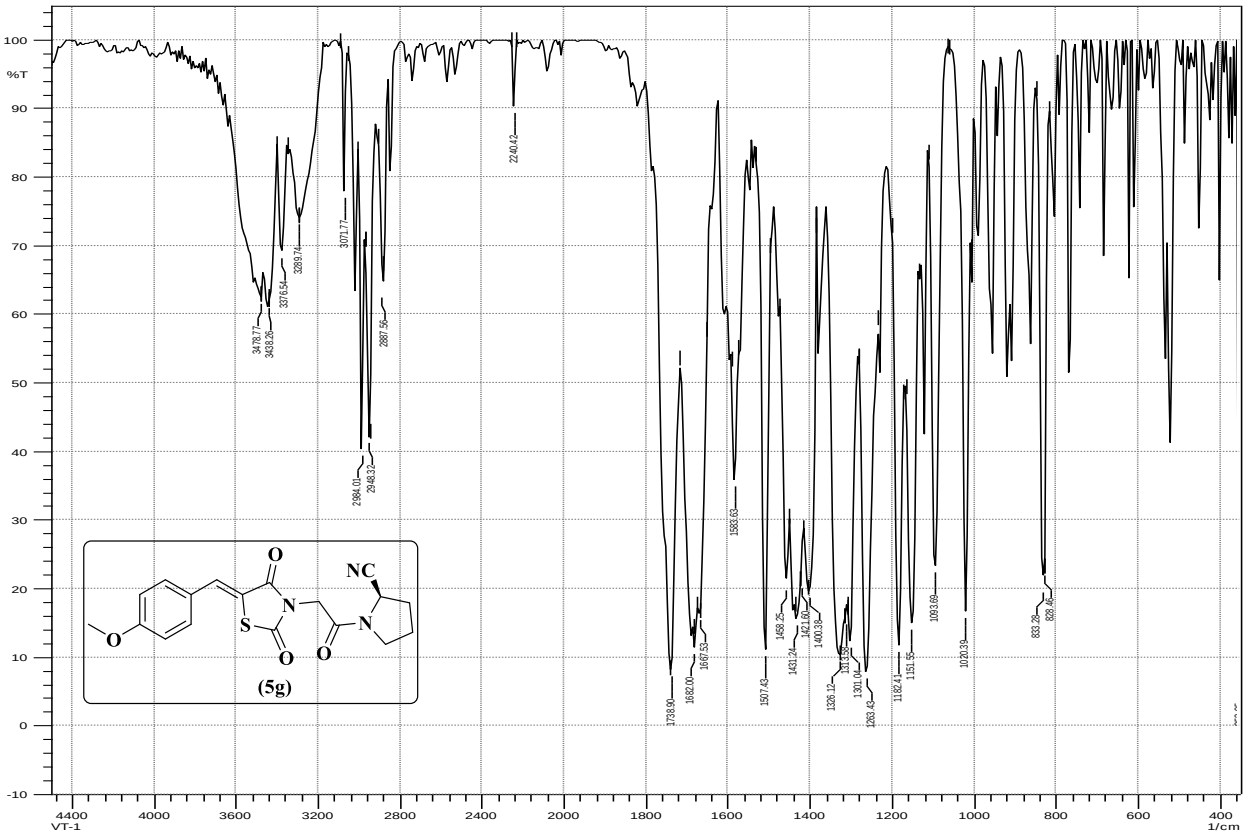
Spectra. 63: ^{1}H NMR (400 MHz, δ, ppm) spectra of compound 5f



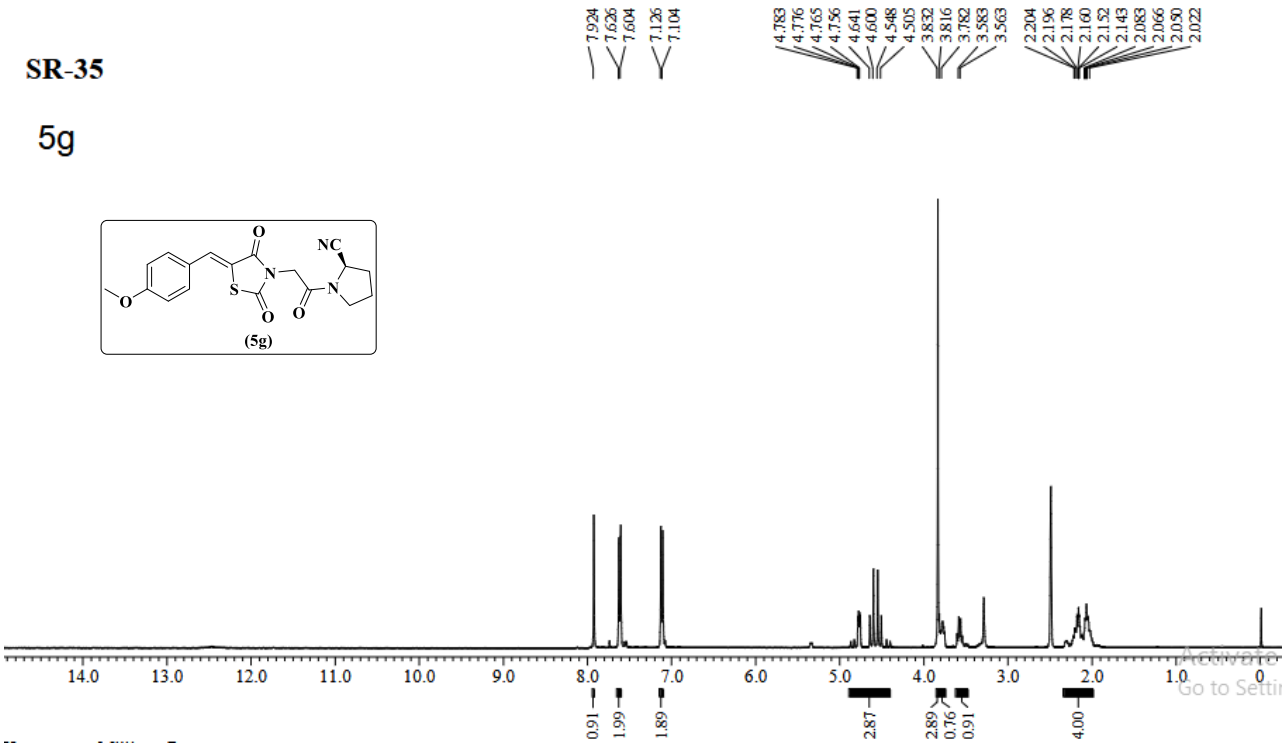
Spectra. 64: ^{13}C NMR (100 MHz, δ, ppm) spectra of compound 5f



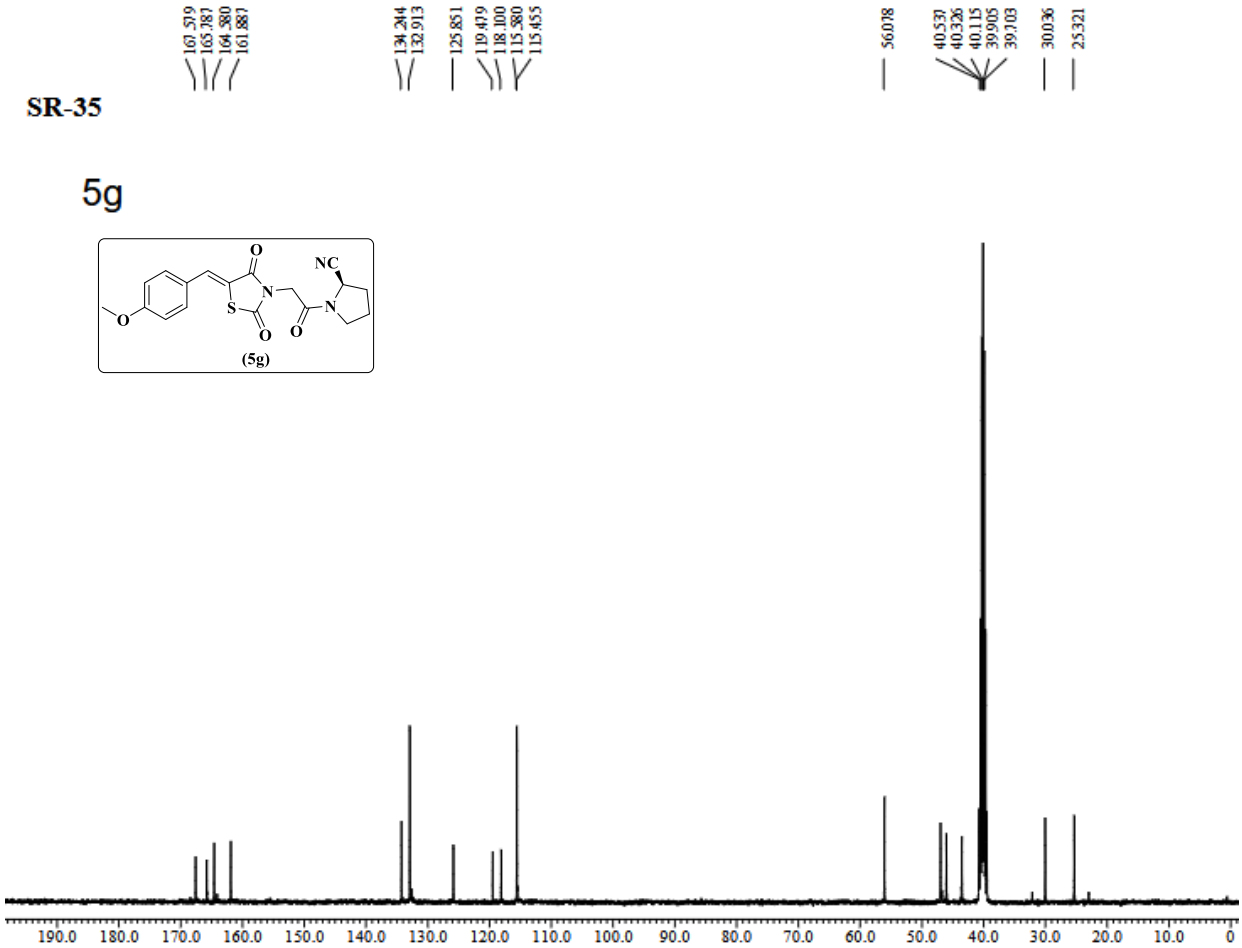
Spectra. 65: HRMS spectra of compound 5f



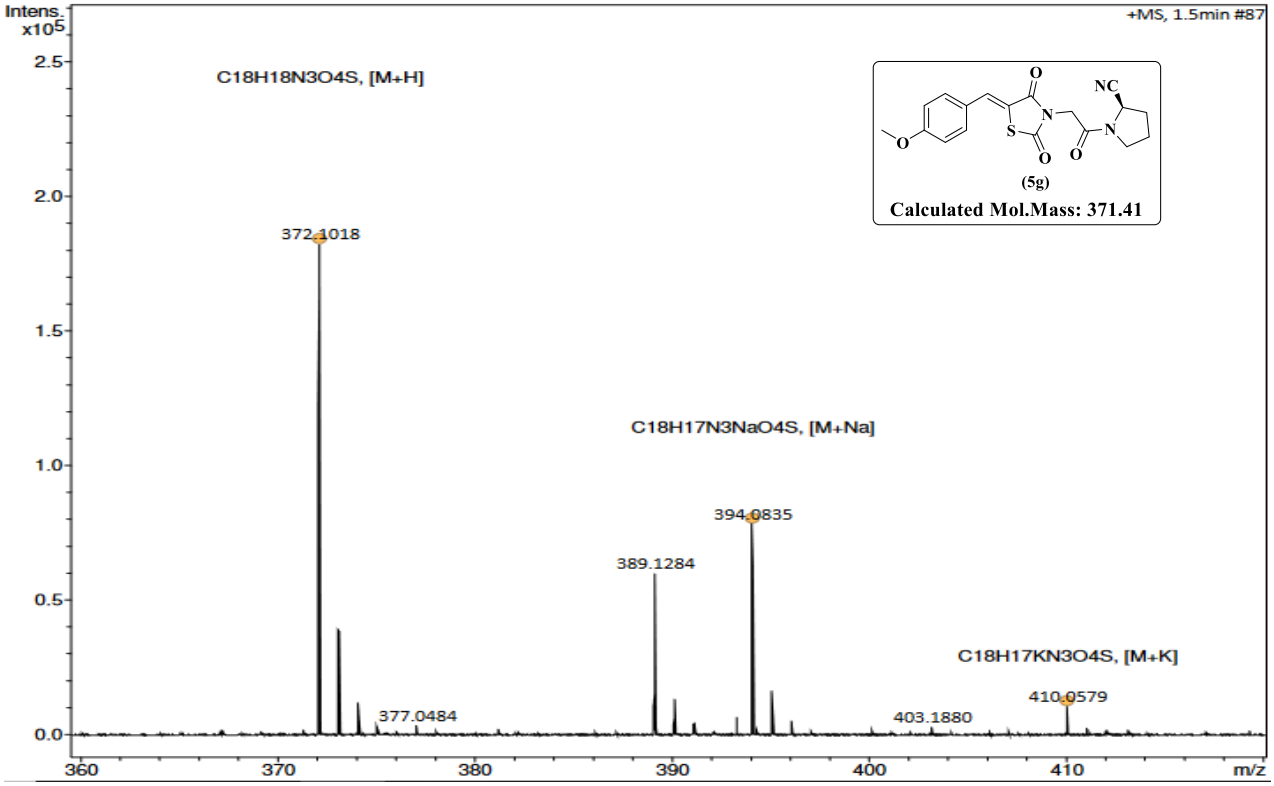
Spectra. 66: FTIR (KBr, cm^{-1}) spectra of compound 5g



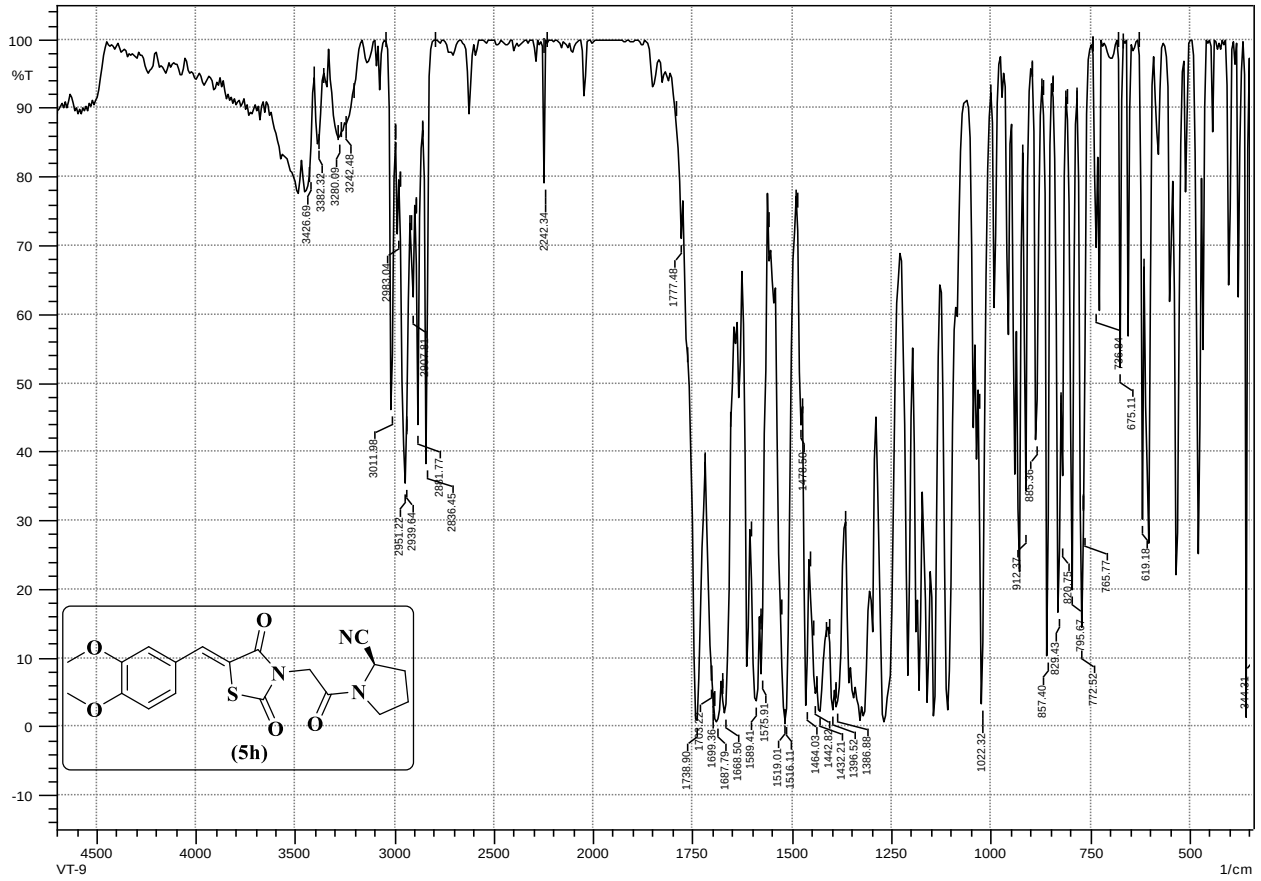
Spectra. 67: ^{1}H NMR (400 MHz, δ, ppm) spectra of compound 5g



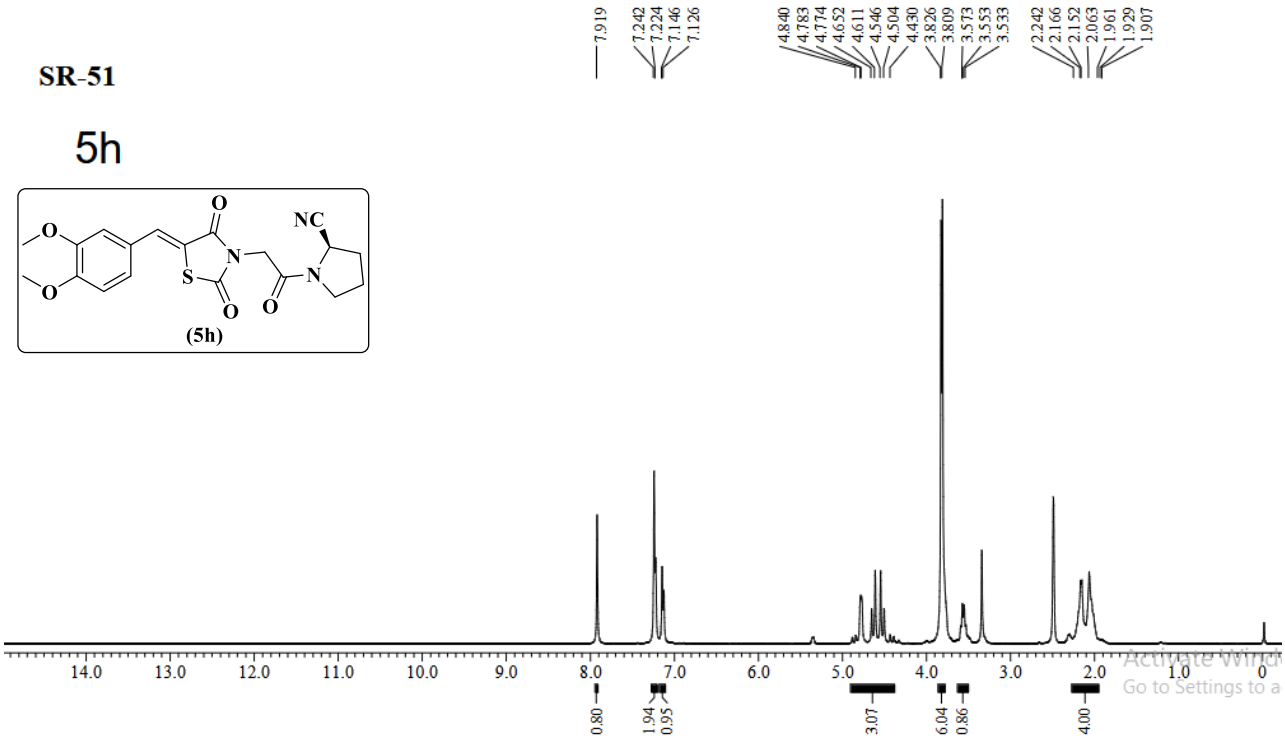
Spectra. 68: ^{13}C NMR (100 MHz, δ, ppm) spectra of compound 5g



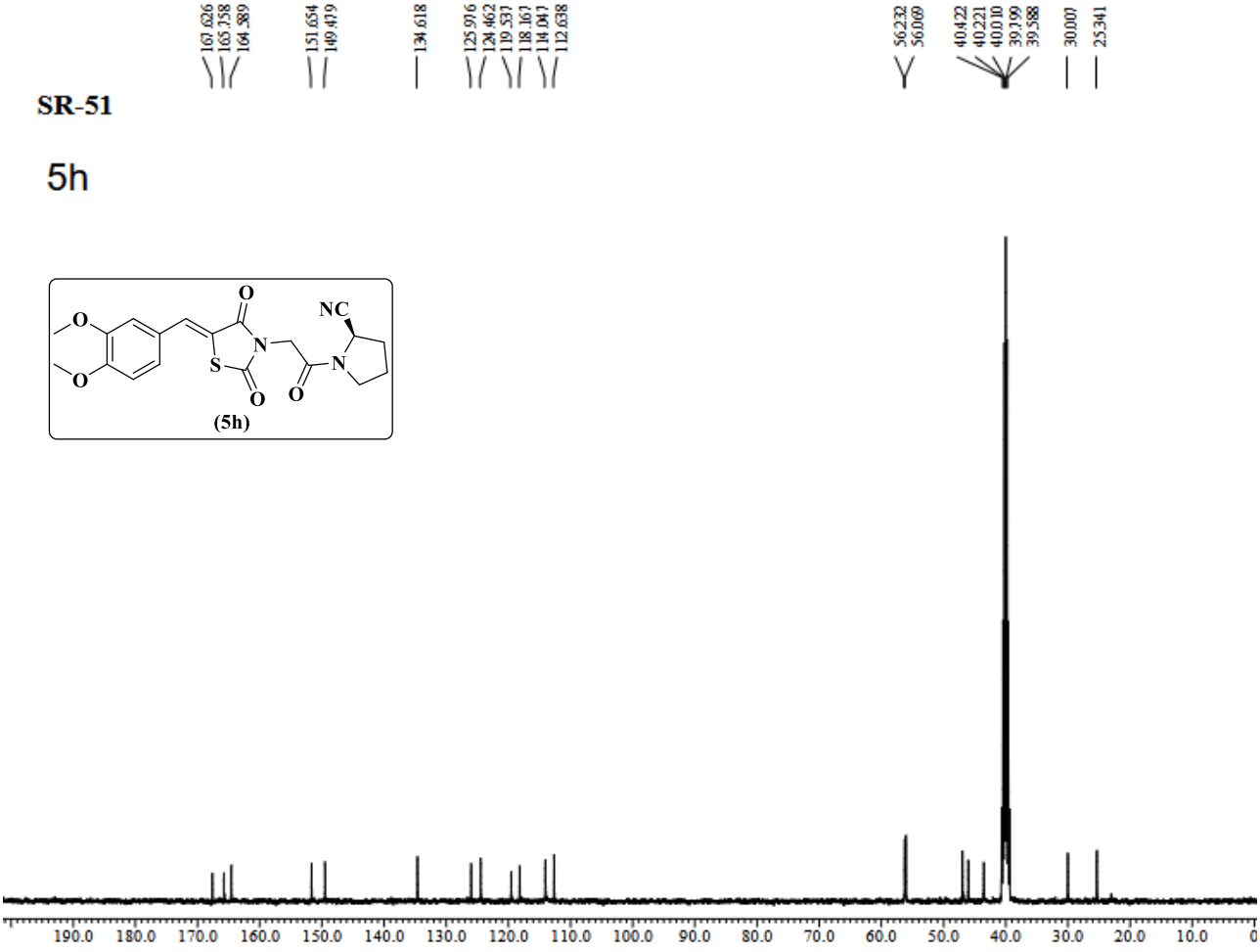
Spectra. 69: HRMS Spectra of compound 6g



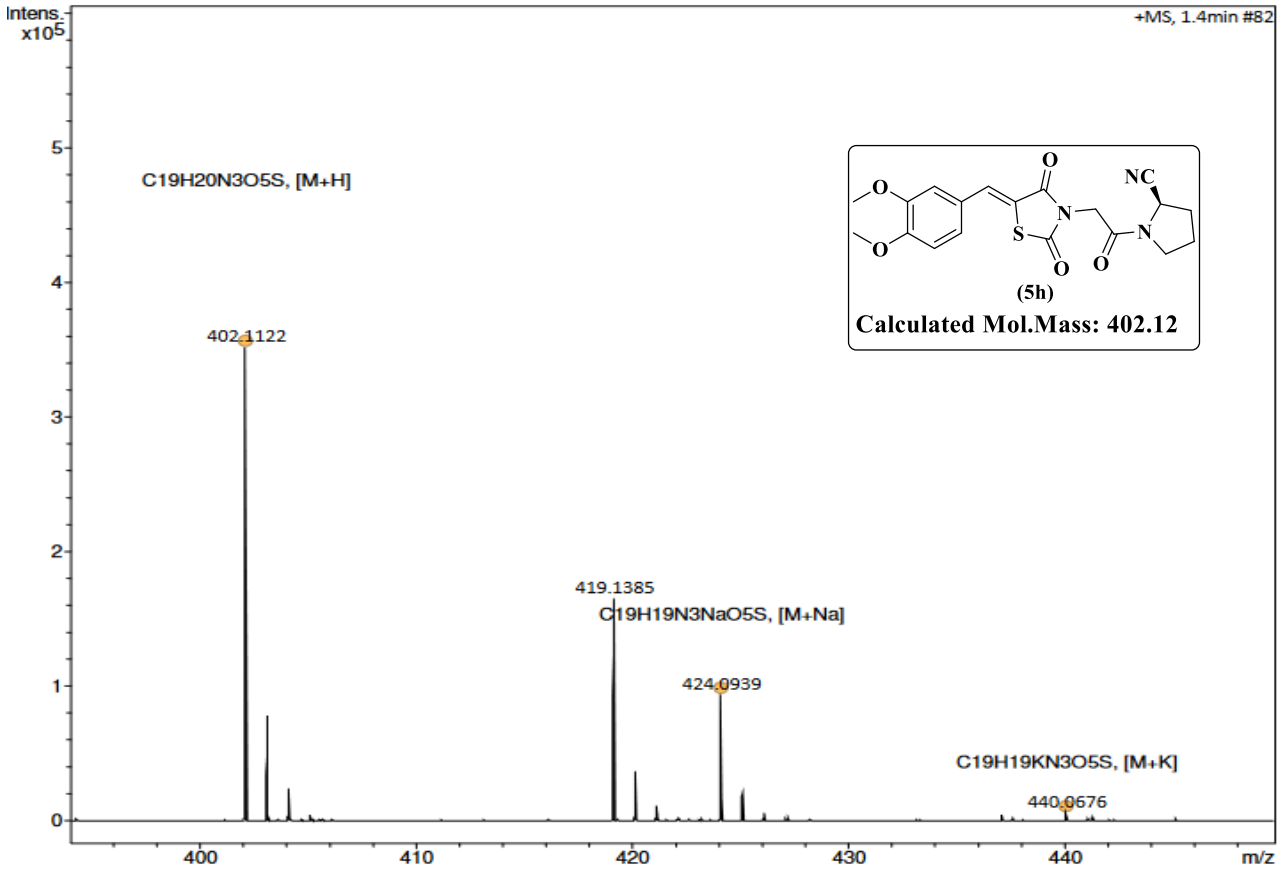
Spectra. 70: FTIR (KBr, cm^{-1}) spectra of compound 5h



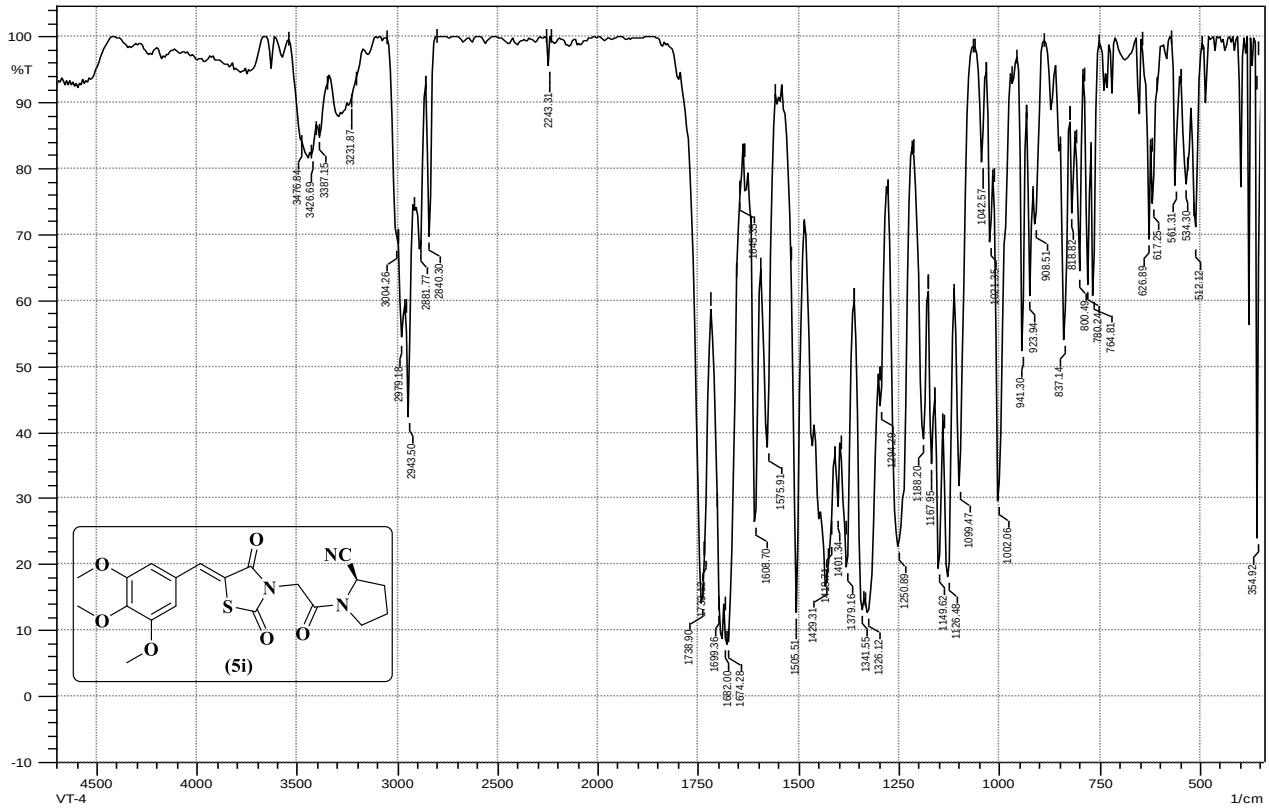
Spectra. 71: ^{1}H NMR (400 MHz, δ, ppm) spectra of compound 5h



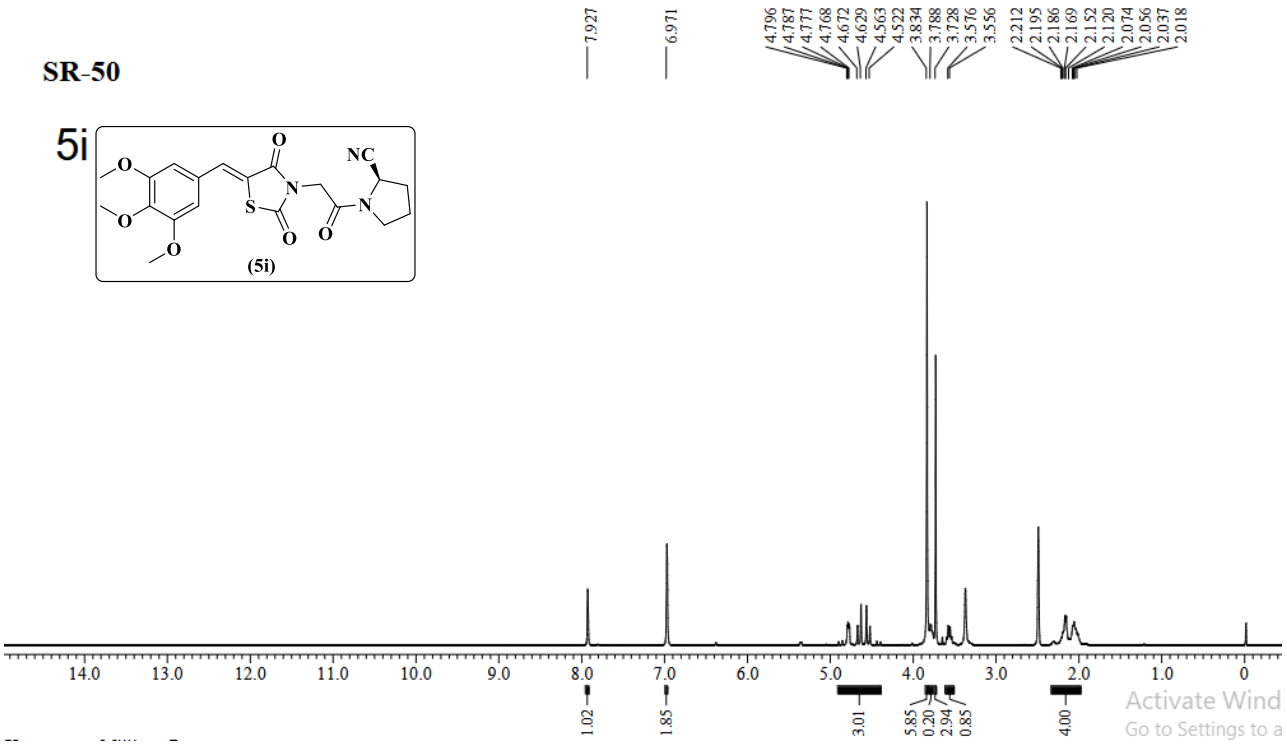
Spectra. 72: ^{13}C NMR (100 MHz, δ, ppm) spectra of compound 5h



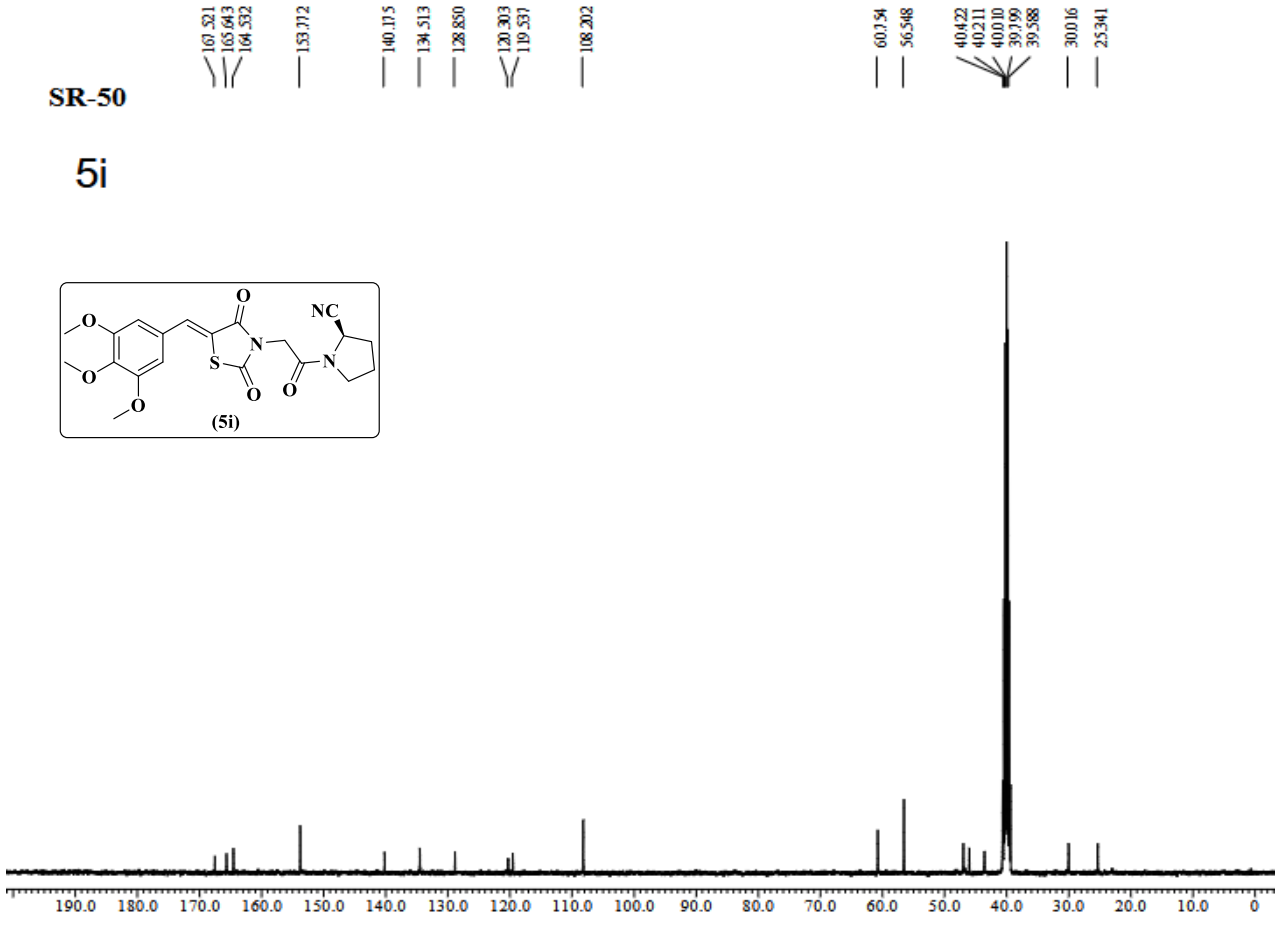
Spectra. 73: HRMS spectra of compound 5h



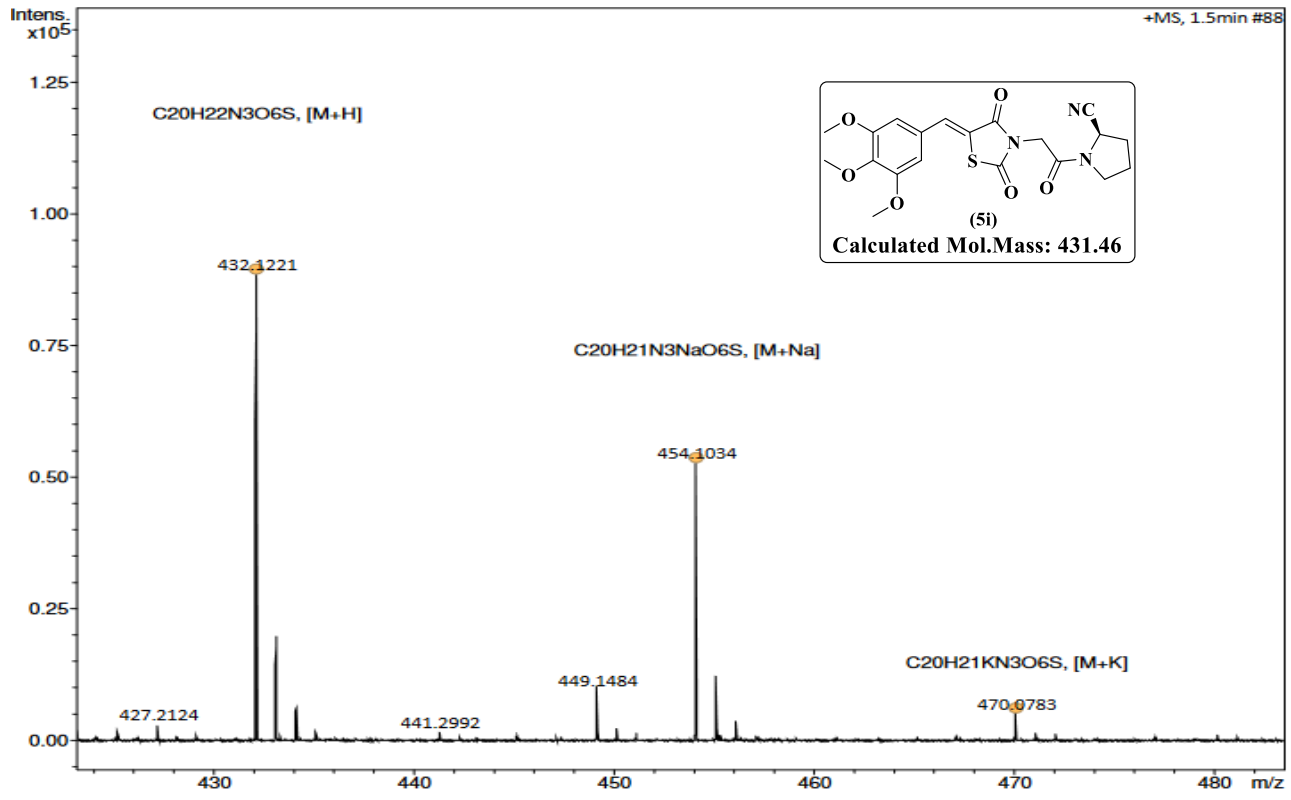
Spectra. 74: FTIR (KBr, cm^{-1}) spectra of compound 5i



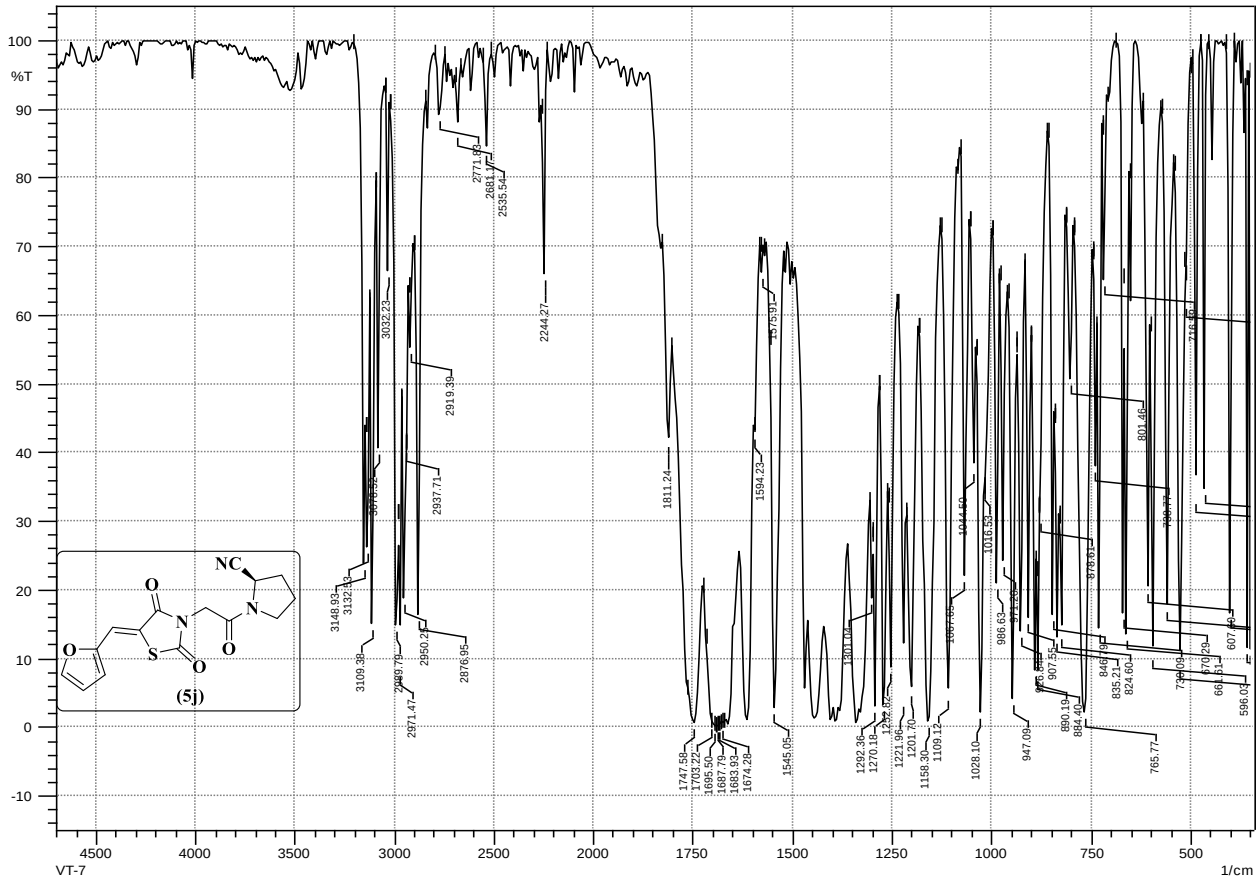
Spectra. 75: ^{1}H NMR (400 MHz, δ, ppm) spectra of compound 5i



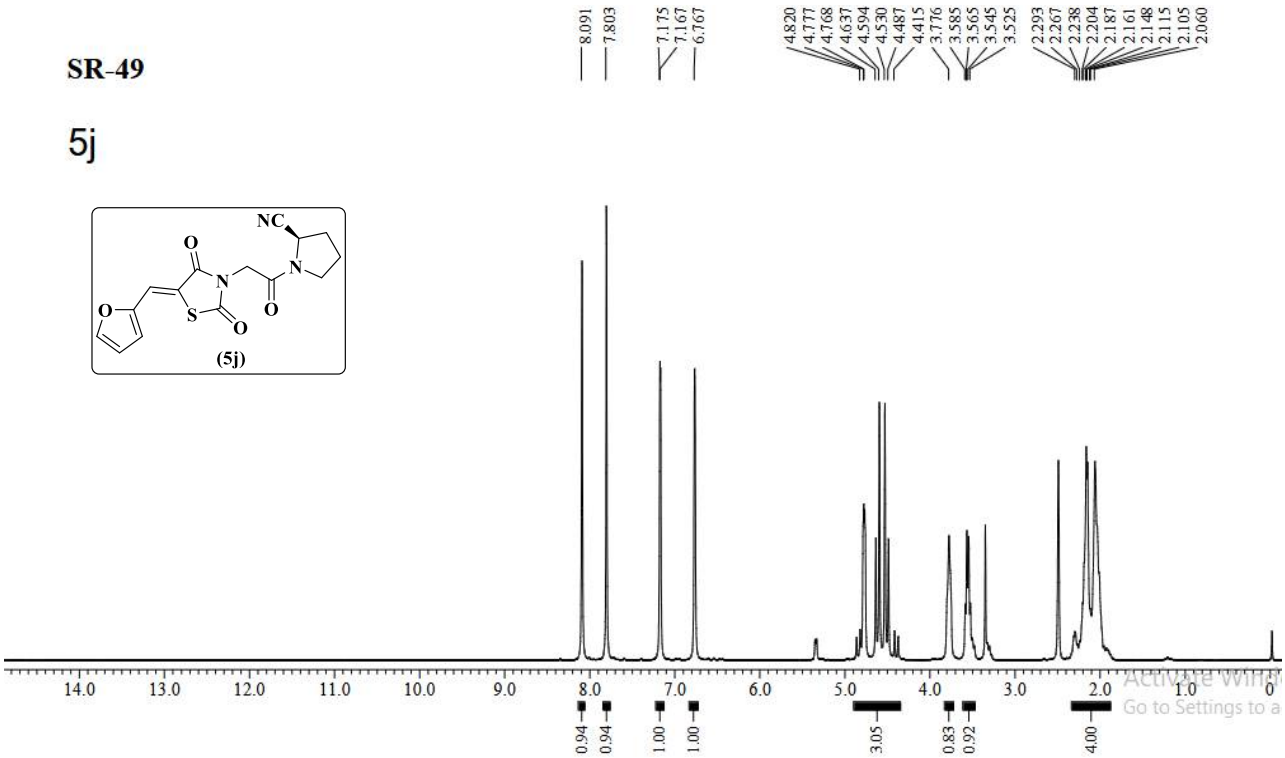
Spectra. 76: ^{13}C NMR (100 MHz, δ, ppm) spectra of compound 5i



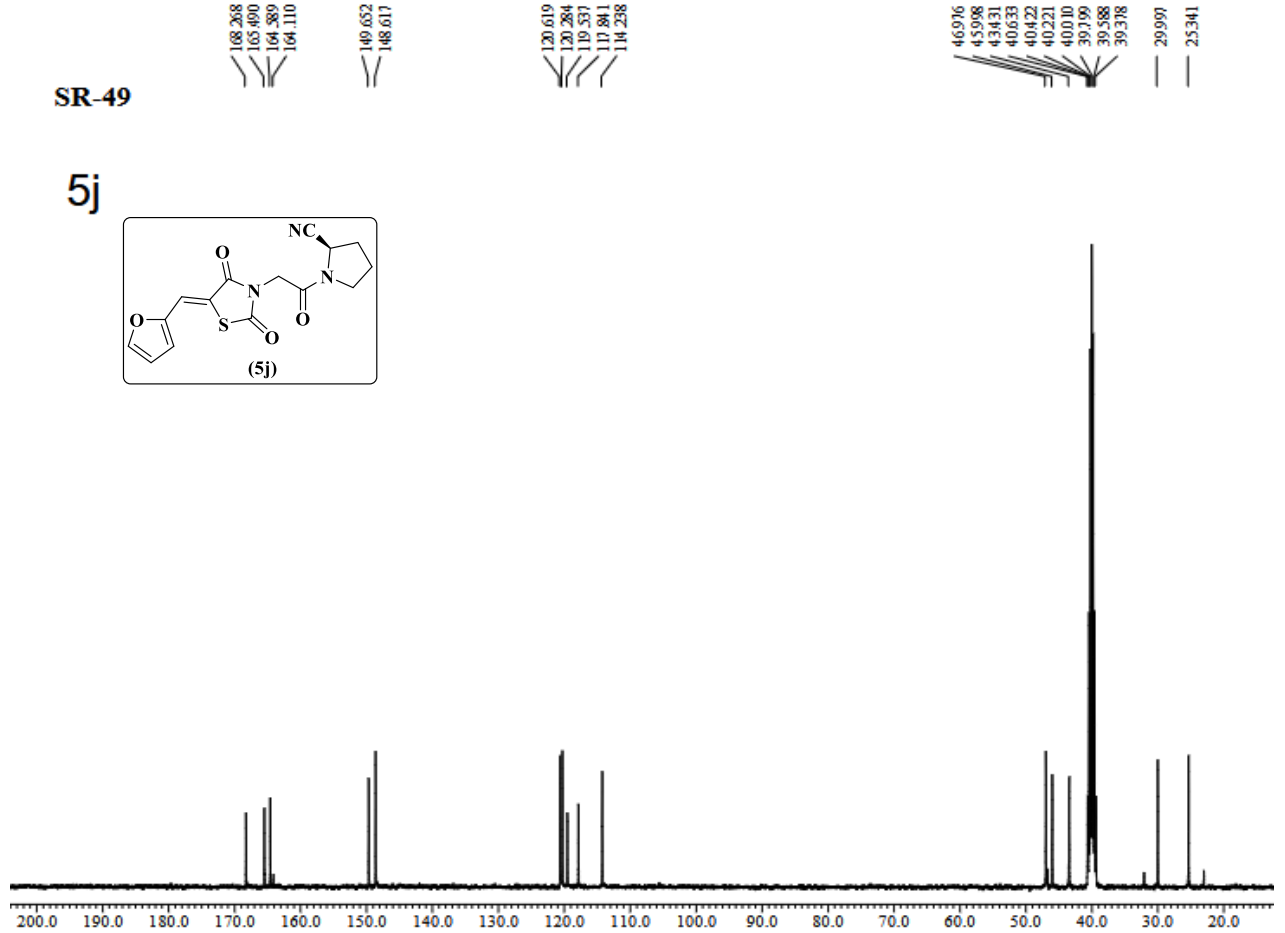
Spectra. 77: HRMS spectra of Compound 5i



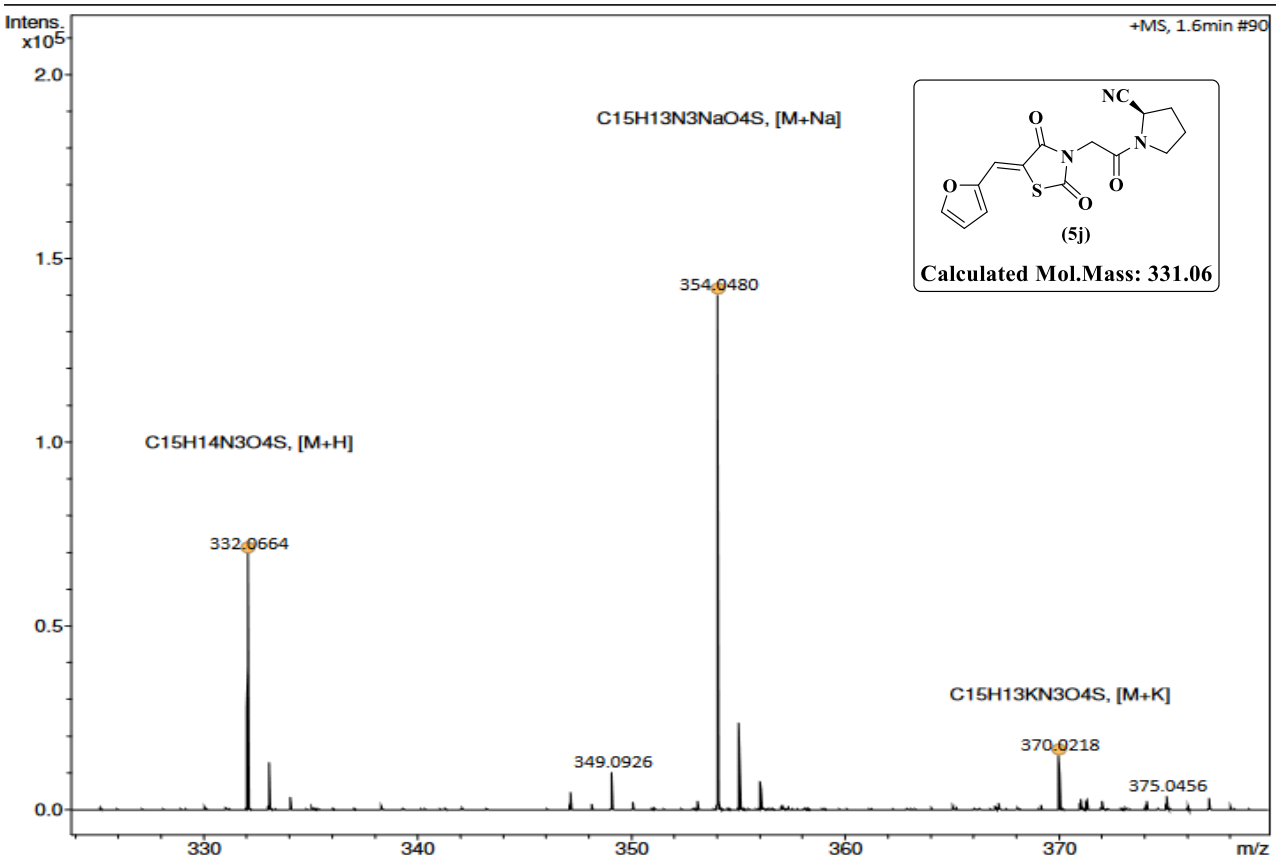
Spectra. 78: FTIR (KBr, cm^{-1}) spectra of compound 5j



Spectra. 79: ^{1}H NMR (400 MHz, δ, ppm) spectra of compound 5j



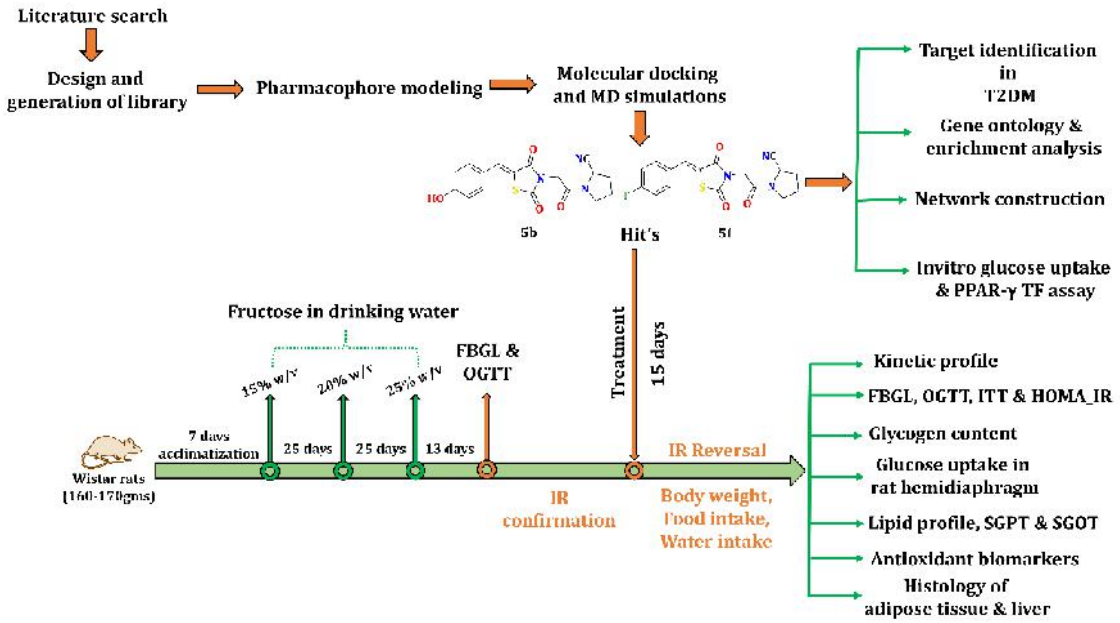
Spectra. 80: ^{13}C NMR (100 MHz, δ, ppm) spectra of compound 5j



Spectra. 81: HRMS Spectra of compound 5j

5. Pharmacological evaluation

Fig. 27: Antidiabetic evaluation was carried out as per the following study plan as illustrated in the following



5.1. *Invitro* glucose uptake assay in L6 myotubes

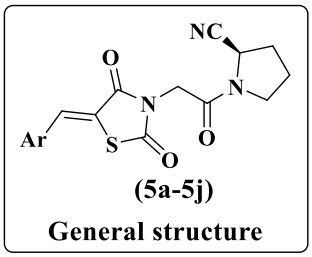
Skeletal muscles play a pivotal role in the regulation of glucose homeostasis and metabolism, serving as the primary site for the utilization of postprandial glucose from circulation. This process is facilitated by GLUTs, particularly GLUT4 and GLUT1. Among these, GLUT4 is the most abundant in skeletal muscle and is primarily responsible for glucose uptake in response to insulin and other exogenous stimuli.[175] To evaluate the glucose uptake potential of the synthesized compounds (**5a-5j**), a glucose consumption assay was conducted using L6 myotubes (rat skeletal muscle cells). The results revealed that the compounds exhibited glucose uptake in the range of 57.40 ± 0.07% to 79.29 ± 1.02%. Notably, compounds **5b**, **5c**, and **5f** demonstrated moderate to high glucose uptake of 79.29 ± 1.02%, 72.86 ± 1.03%, and 74.58 ± 0.54%, respectively, when compared to the standard pioglitazone, which exhibited an uptake of 82.36 ± 0.98% (**Table. 9**). These findings suggest that the synthesized compounds may promote the translocation of GLUT4 to the plasma membrane, thereby facilitating glucose uptake. Alternatively, the compounds might influence the transcriptional activity of PPAR-γ, which is also expressed in skeletal muscle and plays a critical role in glucose metabolism.

5.2. *Invitro* PPAR-γ TF assay

The PPAR-γ, a nuclear receptor, plays a crucial role in regulating lipid metabolism and enhancing insulin sensitivity. PPAR-γ functions as a transcription factor that forms a heterodimer with the RXR to regulate the expression of genes involved in lipid metabolism and glucose homeostasis. Additionally, PPAR-γ activation has been shown to modulate leptin and TNF-α levels, both of which contribute to improved insulin sensitivity. These effects are mediated through the stimulation of the PPAR-γ ligand-binding domain.[176]

To assess the potential PPAR-γ agonist activity of the hit compounds **5b** and **5f**, a PPAR-γ transcription factor assay was conducted using pioglitazone (1 µM) as the reference control. The results indicated a dose-dependent increase in PPAR-γ transcriptional activity for compounds **5b** and

5f within a concentration range of 6.25–50 µM **Fig. 28**. The observed increase in PPAR-γ expression suggests that compounds 5b and 5f may act as effective PPAR-γ agonists, comparable to the standard control pioglitazone.



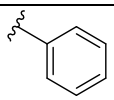
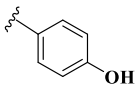
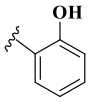
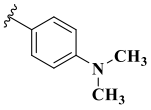
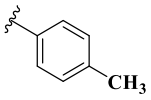
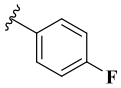
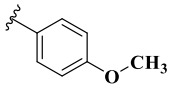
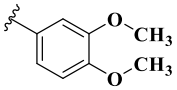
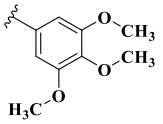
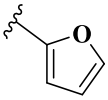
Sr. No	Ar	% glucose uptake in L6 myotubes
5a		63.23 ± 0.02
5b		79.29 ± 1.02
5c		72.86 ± 1.03
5d		64.18 ± 0.31
5e		64.57 ± 0.76
5f		74.58 ± 0.54
5g		58.66 ± 0.31
5h		64.56 ± 0.73
5i		69.74 ± 0.10
5j		57.40 ± 0.07
Pioglitazone		82.36 ±0.98

Table. 9: *Invitro* percentage glucose uptake of the synthesized compounds (**5a-5j**) in L6 myotubes.

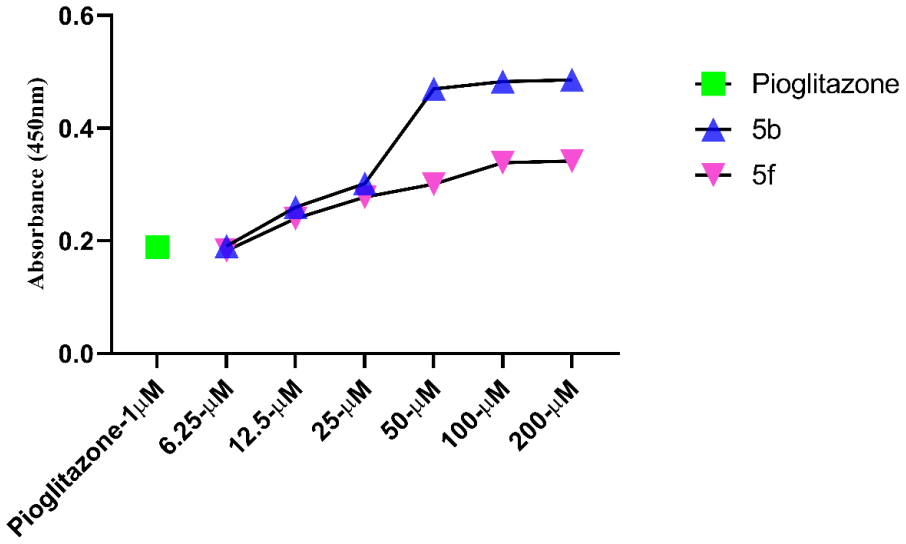


Fig. 28: PPAR-γ transcription factor expression induced by compounds **5b**, **5f**, and pioglitazone

5.3. *Invivo* experimental pharmacology

5.3.1. Impact of Compound 5b and 5f on FBGL and OGTT

Following 15 days of treatment with compound **5b** and **5f**, the IR group exhibited a significant increase ($p<0.001$) in FBGL compared to the normal group. In contrast, the groups treated with PIO-10, compound **5b**, and compound **5f** demonstrated a significant reduction ($p<0.001$) in FBGL relative to the IR group. Notably, no significant difference in FBGL was observed between the PIO-10 and 5b-treated groups.

For the OGTT, the AUC was significantly higher ($p<0.001$) in the IR group compared to the normal group. Treatment with PIO-10 resulted in a significantly lower AUC ($p < 0.001$) relative to the IR group. While the AUC values for the **5b**-treated group were comparable to those of the PIO-10 group, the **5f**-treated group exhibited a significant increase ($p<0.01$) in AUC compared to the **5b**-treated group. (**Fig. 29**)

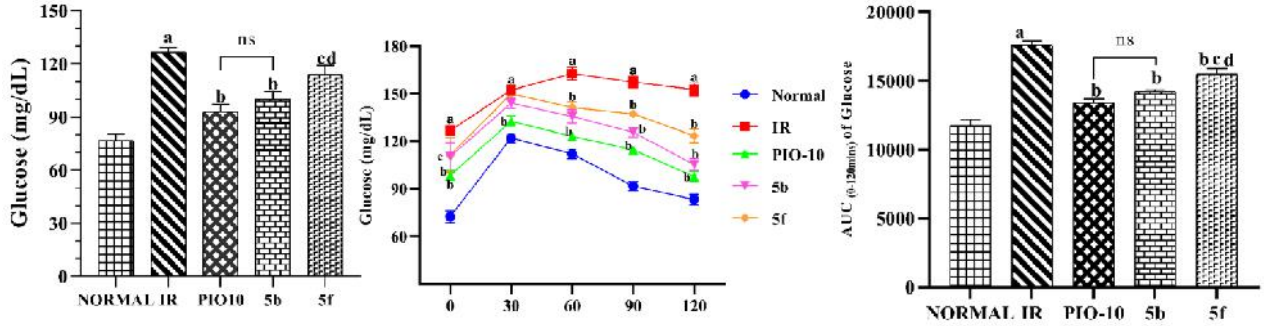


Fig. 29: Effect of compound **5b** and **5f** on FBGL and OGTT. Where, insulin resistance group is IR; PIO-10 is pioglitazone (10mg/kg) treated group; **5b** is compound **5b** treated group; **5f** is compound **5f** treated group. Data is expressed in Mean ± SEM (n=6); one-way ANOVA was used to analyze FBGL and AUC for glucose and two-way ANOVA followed by Bonferroni's post hoc test was used to analyze OGTT. $^{a}P < 0.001$ compared to normal; $^{b}P < 0.001$ compared to IR; $^{c}P < 0.05$ compared to PIO-10; $^{d}P < 0.001$ compared to **5b** treated group.

5.3.2. Impact of compounds 5b and 5f on body weight, food consumption, and water intake

Induction of insulin resistance resulted in a significant increase in body weight compared to the normal group. Administration of pioglitazone (**10 mg/kg**) for 15 days led to a notable increase in body weight relative to the IR group. Similarly, treatment with compounds **5b** and **5f** showed a significant increase in body weight compared to the IR group. The percentage change in body weight was significantly reduced in the IR group ($p < 0.001$) compared to the normal group. In contrast, the treatment groups, including those receiving pioglitazone, **5b**, and **5f**, exhibited a marked increase in percentage change in body weight, except for the normal group (**Fig. 30**).

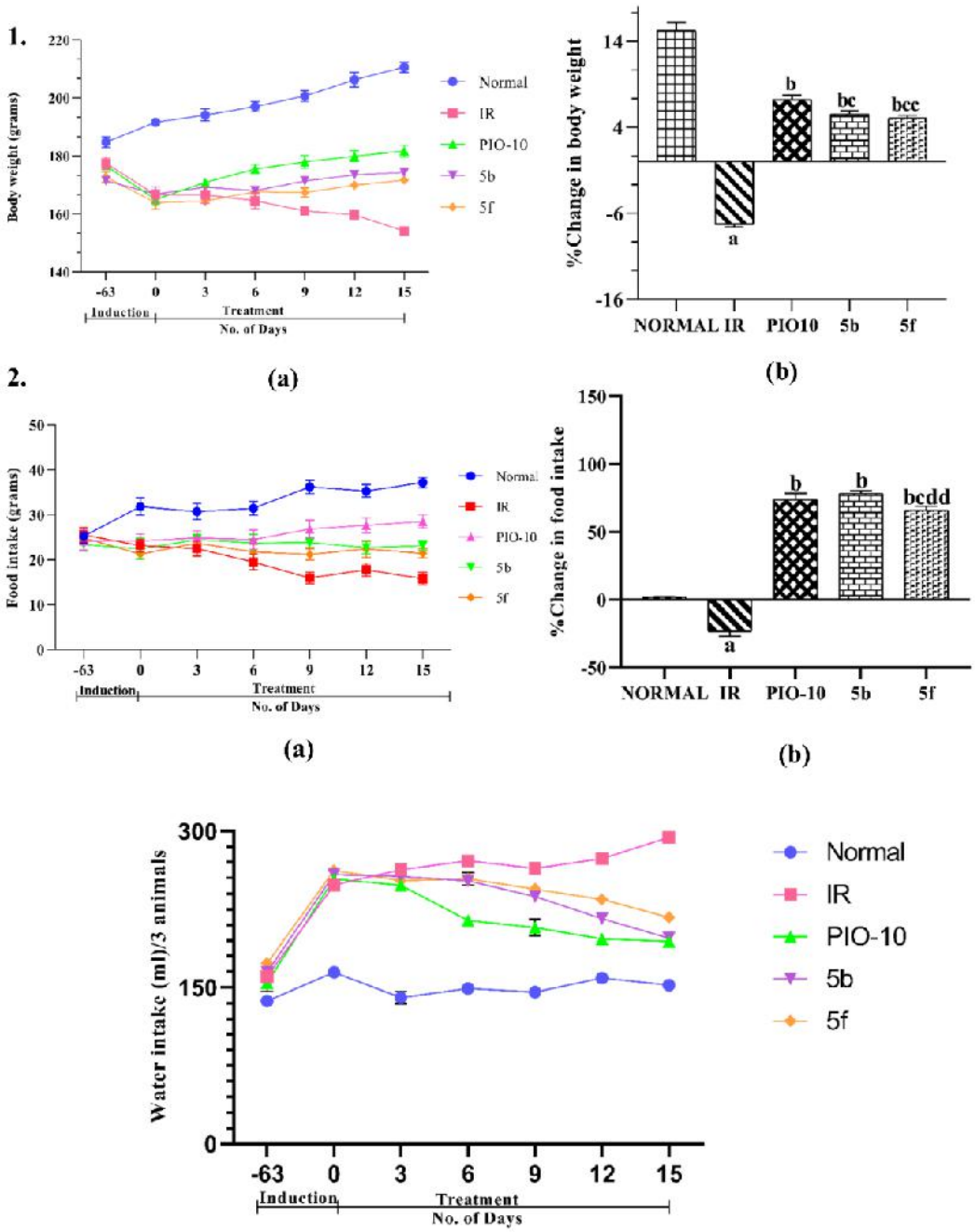


Fig. 30: Effect of compound **5b** and **5f** on food intake, body weight, and water intake. Where, insulin resistance group is **IR**; **PIO-10** is pioglitazone (10mg/kg) treated group; **5b** is compound **5b** treated group; **5f** is compound **5f** treated group. Data is expressed in Mean ± SEM (n=6); one-way ANOVA Followed by post Hoc tukey's test was used to analyze percent change in body weight, food intake and water intake; **1.** Body weight: $^{a}P < 0.001$ compared to normal group; $^{b}P < 0.001$ compared to IR; $^{c}P < 0.05$, $^{cc}P < 0.01$ as compared to PIO-10; **2.** Food intake: $^{a}P < 0.001$ compared to normal group; $^{b}P < 0.001$ compared to IR; $^{c}P < 0.05$, as compared to PIO-10; $^{dd}P < 0.01$ as compared to **5b** treated group. **3.** Water intake representation.

5.3.3. Impact of compound 5b and 5f on insulin levels and ITT

Fasting insulin levels were significantly elevated ($p<0.001$) in the IR group compared to the normal group. Treatment with PIO-10 led to a significant reduction in insulin levels ($p<0.001$) relative to the IR group. Similarly, both compound **5b** and compound **5f** treatments resulted in a significant decrease ($p<0.001$) in insulin levels compared to the IR group. No significant difference in insulin levels was observed between the PIO-10 and **5b**-treated groups. However, a significant difference ($p<0.01$) was noted between the PIO-10 and **5f**-treated groups. Furthermore, compound **5b** showed a significant difference ($p<0.05$) when compared to the **5f**-treated group. These results were consistent with the findings from the AUC analysis for glucose. (**Fig. 31**)

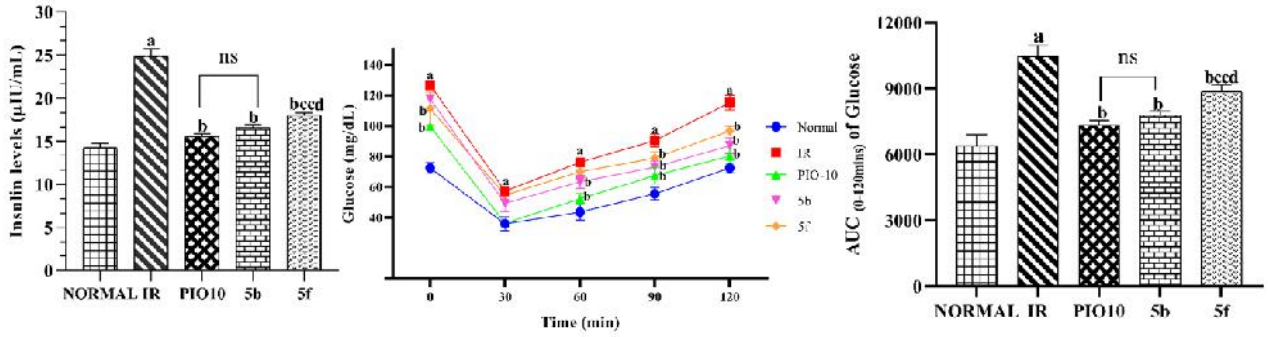


Fig. 31: Effect of compound **5b** and **5f** on insulin levels and OGTT. Where, insulin resistance group is IR; PIO-10 is pioglitazone (10mg/kg) treated group; **5b** is compound **5b** treated group; **5f** is compound **5f** treated group. Data is expressed in Mean ± SEM (n=6); one-way ANOVA followed by post Hoc tukeys test was used to analyze insulin levels and AUC for glucose and two-way ANOVA followed by Bonferroni's post hoc test was used to analyze OGTT. $^{a}P < 0.001$ compared to normal; $^{b}P < 0.001$ compared to IR; $^{c}P < 0.05$ compared to PIO-10; $^{d}P < 0.001$ compared to **5b** treated group.

5.3.4. Impact of compound 5b and 5f on HOMA-IR

HOMO-IR levels were significantly elevated ($p<0.001$) in the IR group compared to the normal group. However, treatment with PIO-10 led to a significant decrease ($p<0.001$) in HOMO-IR levels. The **5f**-treated group exhibited a significant increase ($p<0.01$) in HOMO-IR levels compared to the PIO-10 group, while no significant difference was observed between the **5b** and PIO-10 groups. (**Fig. 32**)

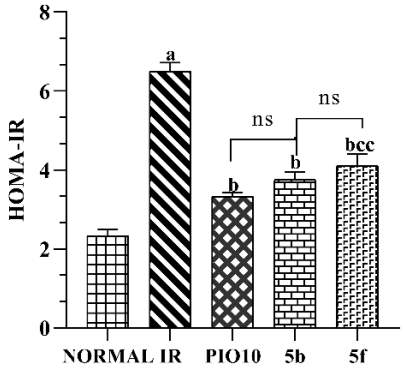


Fig. 32: Effect of compound **5b** and **5f** on HOMO-IR. Where, insulin resistance group is IR; PIO-10 is pioglitazone (10mg/kg) treated group; **5b** is compound **5b** treated group; **5f** is compound **5f** treated group. Data is expressed in Mean ± SEM (n=6); HOMA-IR was analysed by one-way ANOVA followed by post Hoc tukeys test. $^{a}P < 0.001$ compared to normal; $^{b}P < 0.001$ compared to IR; $^{cc}P < 0.01$ compared to PIO-10.

5.3.5. Impact of compound 5b and 5f on glycogen content in skeletal muscles and liver

The IR group exhibited a significant reduction ($p<0.001$) in glycogen content in both skeletal muscles and liver compared to the normal group. Treatment with PIO-10 significantly restored glycogen content ($p<0.001$) relative to the IR group. Similarly, treatment with compounds **5b** and **5f** led to a significant increase in glycogen content ($p<0.01$ and $p<0.05$, respectively) compared to the IR group. No significant difference was observed between the glycogen content of the **5b** and **5f** treated groups. (**Fig. 33**)

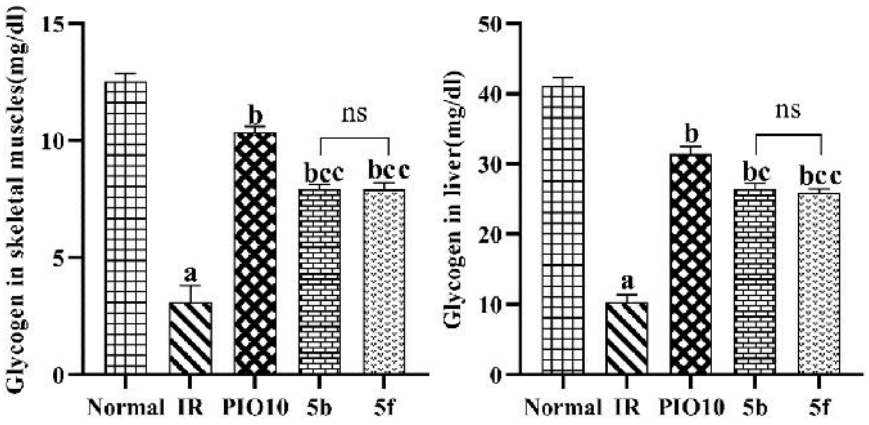


Fig. 33: Effect of Compound **5b** and **5f** on glycogen content in skeletal muscles and liver. Where, IR is insulin resistance group; PIO-10 is pioglitazone (10mg/kg) treated group; **5b** is compound **5b** treated group; **5f** is compound **5f** treated group. Data is expressed in Mean ± SEM (n=6); one-way ANOVA followed by post Hoc tukeys test was used to analyze glycogen content in skeletal muscles and liver. $^{a}P < 0.001$ compared to normal; $^{b}P < 0.001$ compared to IR; $^{c}P < 0.05$; $^{cc}P < 0.01$ compared to PIO-10.

5.3.6. Impact of compound 5b and 5f on glucose uptake in rat hemidiaphragm.

The IR group exhibited a significant reduction ($p<0.001$) in glucose uptake compared to the normal group. Treatment with PIO-10, as well as compounds **5b** and **5f**, significantly increased glucose uptake ($p<0.001$) relative to the IR group. However, the percentage of glucose uptake in the **5b** and **5f** treatment groups was significantly lower ($p<0.05$ and $p<0.01$, respectively) compared to the PIO-10 group. Additionally, the **5f** treatment group demonstrated a significant reduction ($p < 0.001$) in glucose uptake relative to the **5b** treated group. (**Fig. 34**)

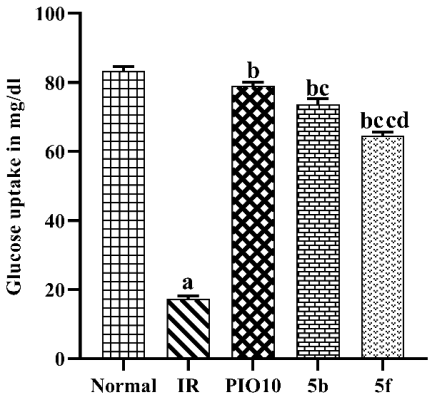


Fig. 34: Effect of Compound **5b** and **5f** on glucose uptake in rat hemidiaphragm. Where, IR is insulin resistance group; PIO-10 is pioglitazone (10mg/kg) treated group; **5b** is compound **5b** treated group; **5f** is compound **5f** treated group. Data is expressed in Mean ± SEM (n=6); one-way ANOVA followed by post Hoc tukeys test was used to analyse glucose uptake. $^{a}P < 0.001$ compared to normal; $^{b}P < 0.001$ compared to IR; $^{c}P < 0.05$ and $^{cc}P < 0.01$ compared to PIO-10; $^{d}P < 0.001$ compared to **5b** group.

5.3.7. Impact of compound 5b and 5f on lipid profile

The IR group exhibited significantly reduced levels of HDL cholesterol and LDL cholesterol ($p<0.001$) alongside markedly elevated levels of triglycerides and VLDL ($p<0.001$) in comparison to

the normal group. Treatment with pioglitazone, compounds **5b**, and **5f** resulted in a significant increase ($p<0.001$) in total cholesterol and HDL cholesterol levels, while LDL cholesterol levels remained unaffected by **5f** relative to the IR group. Additionally, treatment with PIO-10, **5b**, and **5f** was associated with a pronounced reduction in triglyceride and VLDL levels (**Table 10**).

Group	Triglycerides (mg/dL)	Total cholesterol (mg/dL)	HDL (mg/dL)	VLDL (mg/dL)	LDL (mg/dL)
Normal	54.97±1.82	127.98±1.71	65.21±1.01	10.99±0.4	55.77±2.10
IR	140.03±3.55^{a}	93.68±1.68 ^{a}	25.35±2.03 ^{a}	28.00±0.28 ^{a}	40.32±1.08 ^{a}
PIO-10	63.57±1.83^{b}	122.79±1.83 ^{b}	60.72±1.20 ^{b}	12.71±0.24 ^{b}	49.35±1.12 ^{b}
5b	76.18±2.24^{bc}	114.79±1.75 ^{bc}	53.25±2.54 ^{bc}	15.23±0.18 ^{bc}	47.81±1.83 ^{b}
5f	86.15±1.23^{bcc}	112.30±1.83 ^{bc}	51.39±1.34 ^{bcc}	17.23±0.25 ^{bcd}	42.74±1.01

Table. 10: Effect of **5b** and **5f** on lipid profile. Where, IR is insulin resistance group; PIO-10 is pioglitazone (10mg/kg) treated group; **5b** is compound **5b** treated group; **5f** is compound **5f** treated group. HDL: High Density Lipoproteins, VLDL: Very Low-density Lipoproteins, LDL: Low Density Lipoproteins. Data is expressed in Mean ± SEM (n=6); one-way ANOVA followed by post Hoc tukeys test was used to analyze the lipid profile. $^{a}P < 0.001$ compared to normal; $^{b}P < 0.001$ compared to IR; $^{c}P < 0.05$ & $^{cc}P < 0.01$ compared to PIO-10 in triglycerides levels, HDL, LDL and total cholesterol levels; $^{c}P < 0.001$ compared to PIO-10 & $^{d}P < 0.001$ compared to **5b** treated group for VLDL levels.

5.3.8. Effect of Compound 5b and 5f on AST and ALT levels

The IR group exhibited significantly elevated levels of AST and ALT ($p<0.001$) compared to the normal group. However, treatment with PIO-10, **5b**, and **5f** significantly restored AST and ALT levels ($p<0.001$). Notably, AST and ALT levels showed a significant increase ($p<0.05$ and $p<0.01$, respectively) in the **5b** and **5f** treatment groups. No significant difference in AST or ALT levels was observed between the **5b** and **5f** treatment groups as shown in **Table.11.**

Group	AST (U/L)	ALT (U/L)
Normal	27.35±1.28	24.19±1.38
IR	59.32±2.09^{a}	56.41±2.09 ^{a}
PIO-10	32.45±1.83^{b}	29.73±1.33 ^{b}
5b	41.32±1.23^{bc}	37.12±1.29 ^{bc}
5f	46.36±1.36^{bc}	39.72±1.82 ^{bcc}

Table. 11: Effect of **5b** and **5f** on hepatic markers. Where, IR is insulin resistance group; PIO-10 is pioglitazone (10mg/kg) treated group; **5b** is compound **5b** treated group; **5f** is compound **5f** treated group. Data is expressed in Mean ± SEM (n=6); one-way ANOVA followed by post Hoc tukeys test was used to analyze ALT and AST levels. $^{a}P < 0.001$ compared to normal; $^{b}P < 0.001$ compared to IR; $^{c}P < 0.05$ & $^{cc}P < 0.01$ as compared to PIO-10.

5.3.9. Effect of Compound 5b and 5f on antioxidant biomarkers

Levels of catalase, GSH, and SOD were significantly reduced ($p<0.001$) in the IR group compared to the normal group. However, treatment with Pio-10, as well as compounds **5b** and **5f**, significantly restored ($p<0.001$) the levels of these antioxidant enzymes. Conversely, MDA levels were significantly elevated in the IR group relative to the normal group but were significantly reduced ($p<0.001$) following treatment with Pio-10, **5b**, and **5f** as shown in **Table 12**.

Group	SOD (U/ml)	CAT (U/min/mg of protein)	MDA(nM/mg of protein)	GSH (µM/mg of protein)
Normal	29.87±0.98	77.65±0.98	142.65±10.98	110.35±0.86
IR	13.25±1.35^{a}	27.65±1.02^{a}	294.65±11.78 ^{a}	39.98±1.21^{a}
PIO-10	27.65±1.98^{b}	55.63±0.98^{b}	178.35±8.6^{b}	77.65±1.07^{b}
5b	24.68±1.73^{bc}	52.36±1.32^{b}	197.32±11.74 ^{b}	61.35±.230^{bccc}
5f	20.36±0.98^{bcc}	48.65±1.06^{bcc}	224.65±9.73^{bc}	58.63±1.47^{bccc}

Table. 12: Effect of **5b** and **5f** on antioxidant biomarkers. Where, IR is insulin resistance group; PIO-10 is pioglitazone (10mg/kg) treated group; **5b** is compound **5b** treated group; **5f** is compound **5f** treated group. Data is expressed in Mean ± SEM (n=6); one-way ANOVA followed by post Hoc tukeys test was used to analyze the antioxidant biomarkers. $^{a}P < 0.001$ compared to normal; $^{b}P < 0.001$ compared to IR; $^{c}P < 0.05$ & $^{cc}P < 0.01$ as compared to PIO-10.

5.3.10. Microphotographs of Liver and adipose tissue.

Histopathological evaluation of adipose and liver tissues confirmed the presence of insulin resistance in the IR group and its reversal following treatment with compounds **5b** and **5f**. This was evidenced by key pathological features, including sinusoidal congestion, ballooning degeneration, steatosis, Kupffer cell hyperplasia, and lymphocyte infiltration. The IR group exhibited prominent macrovesicular steatosis, characterized by fat vacuoles within hepatocytes and peripheral displacement

of the nucleus. Ballooning degeneration indicated hepatocyte injury, while lymphocyte infiltration reflected an inflammatory response. Sinusoidal congestion suggested elevated intravascular pressure, collectively pointing to insulin resistance as the underlying pathology. These pathological alterations were markedly ameliorated in the treatment groups (**Fig. 35**).

Similarly, histological analysis of adipose tissue revealed a reduction in adipocyte count in the IR group compared to the normal group. This reduction was reversed in all treatment groups, as demonstrated in **Fig. 35**.

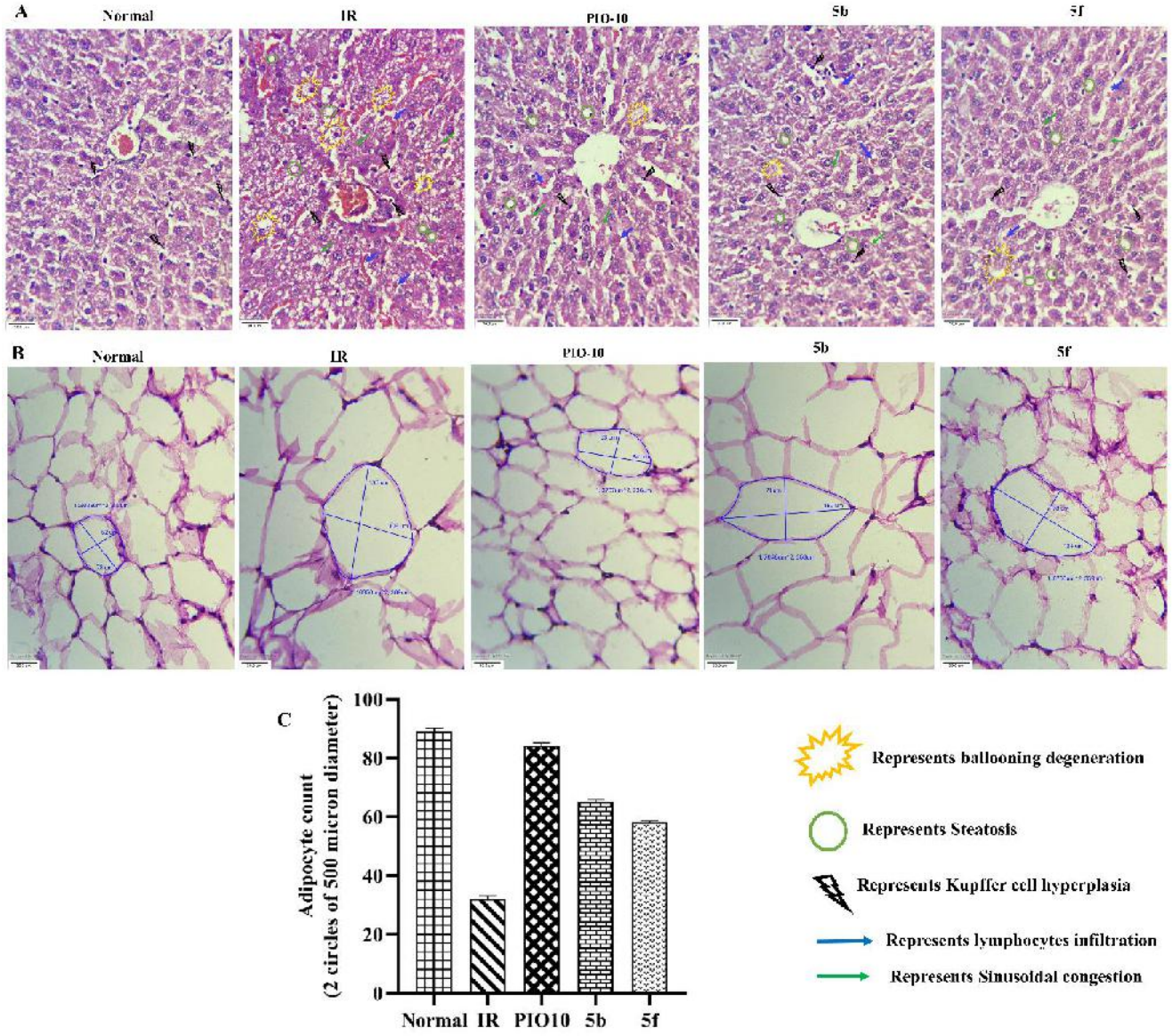


Fig. 35: Effects of compounds 5b and 5f on: (A) Liver tissue, (B) Adipose tissue, and (C) Adipocyte count**.**

5.3.11. Bio analytical method development

The retention times (RT) for compounds **5b**, **5f**, and pioglitazone were determined using HPLC with a C-18 column. The analytical method was rigorously validated following the USFDA guidelines for bioanalytical method development and validation, ensuring compliance with key parameters such as linearity, sensitivity, precision, and accuracy, as detailed in **Table 13**. The retention times were recorded as 6.7 minutes for compound **5f**, 4.4 minutes for compound **5b**, and 2.4 minutes for pioglitazone, as illustrated in **Fig. 36**.

This validated method was subsequently employed to identify and quantify compounds **5b**, **5f**, and pioglitazone in rat plasma, with six replicate measurements performed. The results, presented in **Table 14**, demonstrated high recovery rates ranging from 96.1% to 98.6%. Distinct chromatographic peaks corresponding to **5b**, **5f**, and PIO-10 were observed in rat plasma, underscoring the method's superior sensitivity, precision, and accuracy. These findings confirm the robustness and reliability of the analytical approach, as depicted in **Fig. 37.**

Sr. no	Validation parameters	5f	5b	PIO
1	Linearity			
	Linearity range (µg/mL)	5-30	5-30	5.-30
	Slope	24.406x	18.396x	
	Intercept	4.53	8.48	
	Correlation-coefficient	0.9997	0.998	
2	LOD (µg/mL)	0.51	1.33	1.52
	LOQ(µg/mL)	1.57	4.05	4.592
3	Precision			
	Intra-day (%RSD)	0.25	0.71	0.17
	Inter-day (%RSD)	0.39	0.96	0.63
4	Accuracy			
	50% recovery	97.2	98.5	96.12
	100% recovery	98.6	99.7	97.87
	150% recovery	98.1	97.4	99.04

Table. 13: Summary of validation parameters.

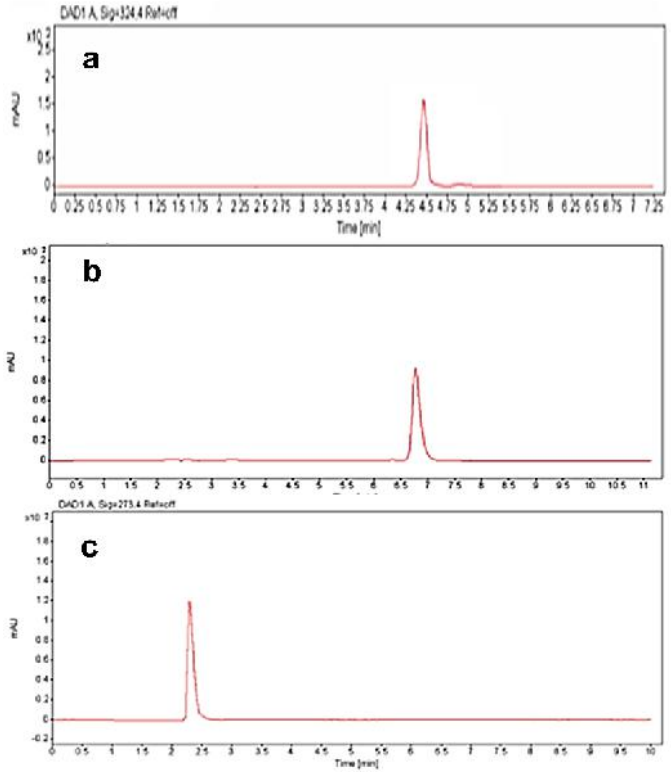


Fig. 36: HPLC Chromatogram of (a) **5b**, (b) **5f**, and (c) Pioglitazone.

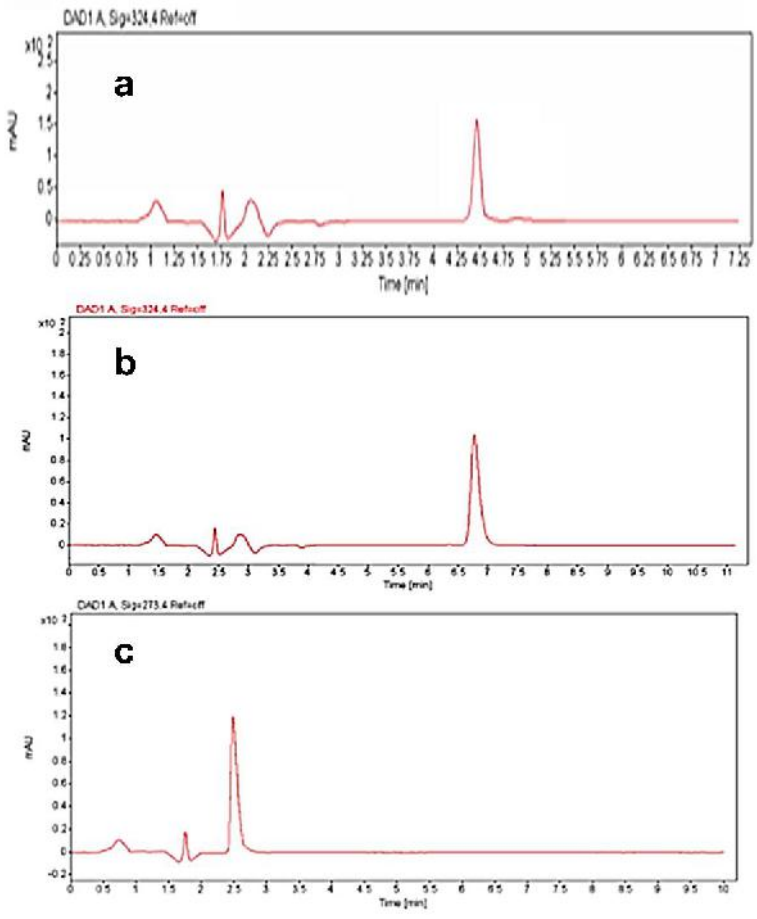


Fig. 37: HPLC Chromatogram of (a) **5b**, (b) **5f**, and (c) Pioglitazone

Sample	Drug	Excess drug added to analytes (%)	Spiked (µg/ml)	Found (µg/ml)	Recovery (%)
Blood plasma	**5b**	50	15	14.56±0.47	97.1
		100	20	20.20±0.15	101.0
		150	25	24.02±0.74	96.1
	5f	50	15	14.99±0.21	99.96
		100	20	19.91±0.27	99.58
		150	25	24.59±0.34	98.36
	PIO	50	15	14.57±0.54	97.1
		100	20	19.48±0.63	97.4
		150	25	24.51±0.98	98.0

Table. 14: Recovery assay of compounds **5b**, **5f** and PIO from rat plasma

5.3.12. Determination of *invivo* pharmacokinetic parameters

The plasma concentrations of pioglitazone, **5b,** and **5f** at various time intervals were quantified using a validated HPLC method. The retention times (RT) observed in the bioanalytical analysis were consistent with those of plasma eluents, thereby confirming the presence of the respective compounds. Pharmacokinetic profiling was performed using Phoenix WinNonlin 8.1 software and the Agilent Infinity II system to characterize the plasma concentration-time profiles of the three compounds. Pioglitazone exhibited rapid absorption, achieving a mean peak plasma concentration (C_{max}) of 3.12 µg/mL at 2.69 hours (T_{max}). In comparison, compound **5f** reached a C_{max} of 0.9261 µg/mL at 2.0 hours, while compound **5b** reached a C_{max} of 1.0261 µg/mL at 2.21 hours. The elimination half-lives (t1/2) of **5f**, **5b**, and pioglitazone were 3.96, 4.21, and 4.92 hours, respectively. The area under the plasma concentration-time curve for pioglitazone was significantly greater than that of **5b** and **5f**, indicating higher systemic exposure. Despite these differences, the analysis revealed comparable absorption patterns for **5b** and **5f**, as evidenced by similar distribution volumes and elimination rate constants. The rate of clearance from the body was calculated as 0.361 µg/mL for 5f, 0.387 µg/mL for 5b, and 0.21 µg/mL for pioglitazone. Furthermore, the relative bioavailability of **5b** and **5f** was assessed in comparison to the reference compound pioglitazone using the standard bioavailability calculation formula,

$$Frel = \frac{\text{AUC Test}}{\text{AUC Reference}} \times 100$$

Compounds **5b** and **5f** demonstrated relative bioavailability of 13.73% and 13.54%, respectively. Here, the AUC test represents the area under the plasma concentration-time curve for the compounds (**5b** and **5f**), while the AUC reference corresponds to the AUC of the pioglitazone. The complete kinetic profile, including detailed pharmacokinetic parameters, is presented in **Table 15** and illustrated in **Fig. 38**.

Parameters	5f	5b	PIO
C_{max} (µg/mL)	0.9261	1.0261	3.1261
T_{max} (h)	2.0	2.21	2.69
AUC 0-t (h. µg/mL)	5.62	5.98	41.52
AUC 0-inf (h. µg/mL)	6.24	6.62	43.62
K_{el}	0.361	0.387	0.21
$T_{1/2}$ (h)	3.96	4.21	4.92
AUC 0-t (h. µg/mL)	5.62	5.98	41.52

Table. 15: Pharmacokinetic parameters of compound **5b**, **5b** and pioglitazone.

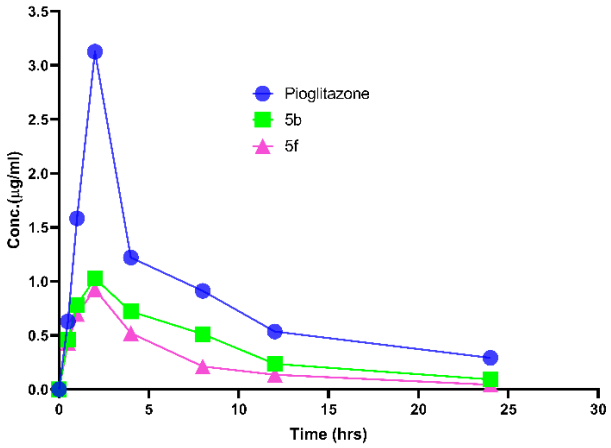
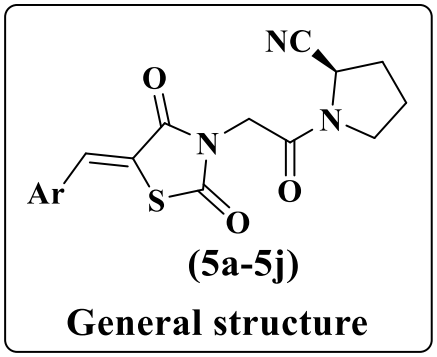


Fig. 38: Pharmacokinetic parameters depicting the peak plasma concentrations of pioglitazone, **5b**, and **5f** at various time intervals, illustrating the drug release profiles from the plasma of experimental animals.

6. *Insilico* studies

6.1. Molecular docking studies

The docking analysis predicted the binding affinity and orientation of ligands (**5a–5j**) within the PPAR-γ receptor binding pocket. The ligands were evaluated based on their energetic scores, including penalties for interactions within the binding domain (**Table 16**). Compounds **5b** and **5f** exhibited superior performance within the series, with glide interaction energies of -45.831 kcal/mol and -45.465 kcal/mol, respectively, compared to the standard pioglitazone, which scored -58.973 kcal/mol. The binding poses of compounds **5b** (**Fig. 39**), **5f** (**Fig. 40**), and pioglitazone (**Fig. 41**) showed stable binding interactions, characterized by hydrophobic contacts and partial polar interactions, with no solvent exposure to the ligands in the PPAR-γ receptor binding domain. Key amino acids involved in eliciting a biological response were identified within the ligand-binding domain, including CYS 285, SER 289, HIS 323, SER 342, HIE 449, and TYR 473, which form hydrogen bonds with the ligands. This information highlights the potential of these ligands to activate the PPAR-γ receptor, promoting its agonist activity.



(5a-5j)

General structure

			PDB ID: 5U5L	H-Bond	
Com.	**Glide Score**	**Glide Energy (kcal/mol)**	**Ligand Atom interactions**	**Amino Acid**	**Bond length**
5a	-6.212	-44.699	-**C=O** of ligand to TYR 473 - **C=O** of ligand to SER 289 **C=O** of ligand to TYR HIE 323	TYR 473 SER 289 HIE 323	2.33 1.86 2.59
5b	-8.591	-45.831	-**CN** of ligand to TYR 473 - **CN** of ligand to HIE 449 -**C=O** of ligand to CYS 285	TYR 473 HIE 449 CYS 285	2.18 2.40 2.27
5c	-6.895	-59.547	-**CN** of ligand to TYR 473 -**C=O** of ligand to TYR 473 -**C=O** of ligand to SER 289	TYR 473 TYR 473 SER 289	2.32 2.53 1.97
5d	-4.643	-52.32	-**C=O** of ligand to GLN 63	GLN 63	1.88
5e	-6.911	-42.595	-**CN** of ligand to TYR 473 - **CN** of ligand to HIE 449 -**C=O** of ligand to CYS 285	TYR 473 HIE 449 CYS 285	2.20 2.40 2.17
5f	-7.91	-45.465	-**C=O** of ligand to CYS 285	CYS 285	2.27
5g	-7.805	-45.968	-**CN** of ligand to TYR 473 - **CN** of ligand to HIE 449 -**C=O** of ligand to CYS 285	TYR 473 HIE 449 CYS 285	2.12 2.41 2.15
5h	-7.91	-48.031	-**CN** of ligand to TYR 473 -**OCH_3** of ligand to SER 342	TYR 473 SER 342	2.54 2.44
5i	-6.453	51.032	-**CN** of ligand to TYR 473 -**C=O** of ligand to CYS 285	TYR 473	2.42
5j	-7.316	-46.630	-**C=O** of ligand to CYS 285	CYS 285 CYS 285	1.97 2.18
Pioglitazone	-11.632	-58.973	-**C=O** of ligand to TYR 473 -**C=O** of ligand to SER 289 -**C=O** of ligand to HIS 323	TYR 473 SER 289 HIS 323	2.09 2.17 1.81

Table. 16: Binding Affinity of Synthesized Compounds (**5a-5j**) within the LBD of PPAR-γ.

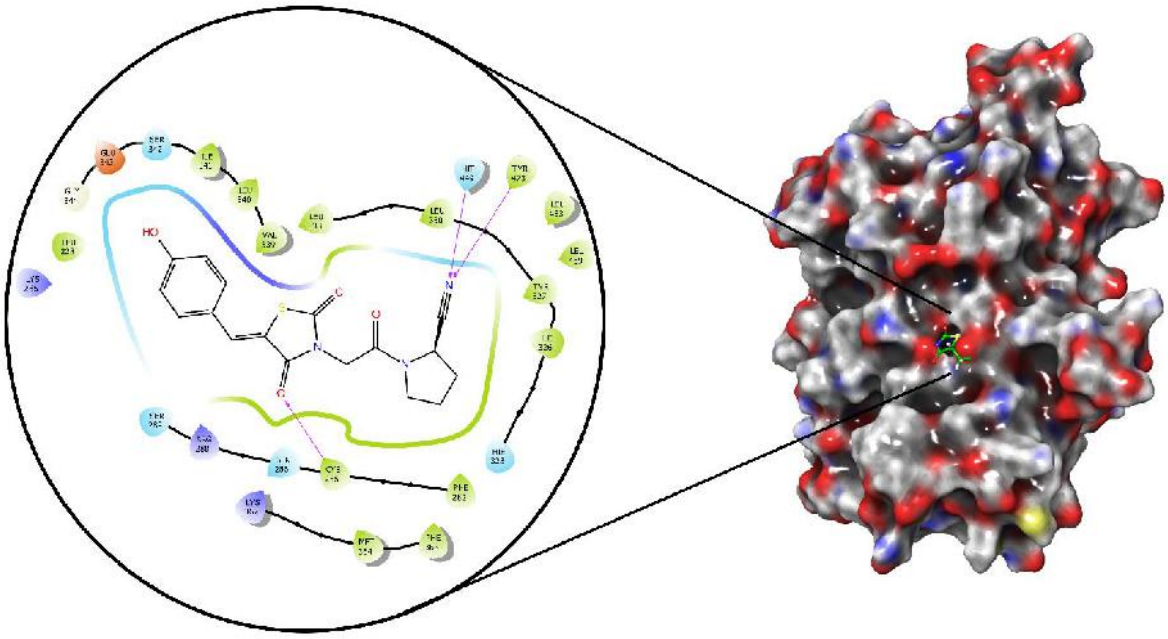


Fig. 39: Binding conformation of compound **5b** within the LBD of PPAR-γ.

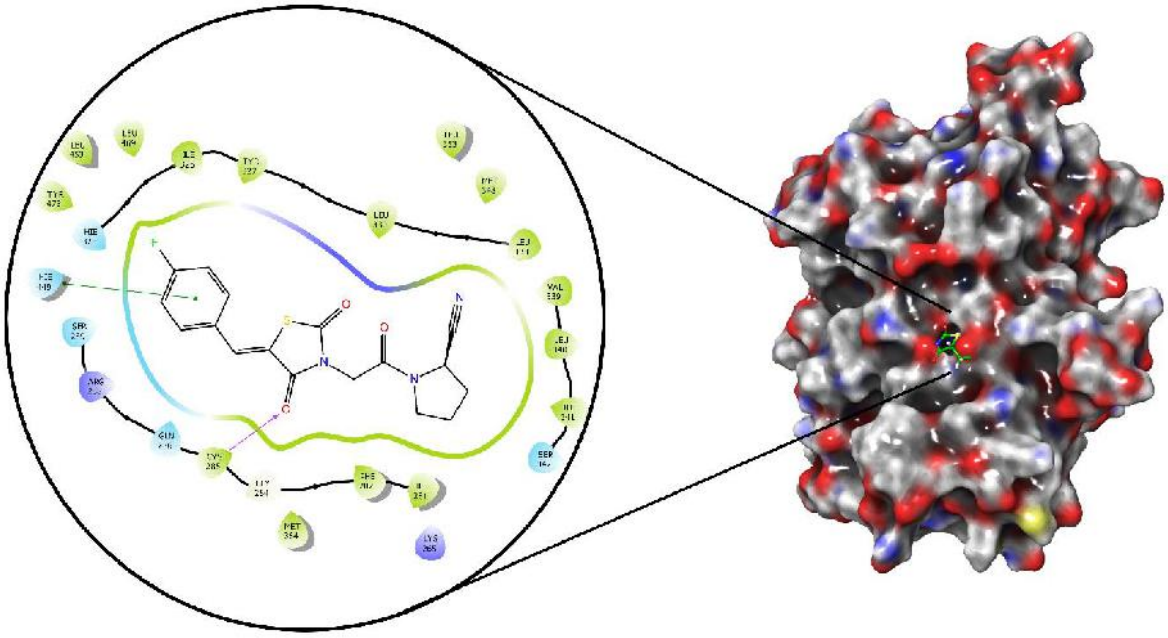


Fig. 40: Binding conformation of compound **5f** within the LBD of PPAR-γ.

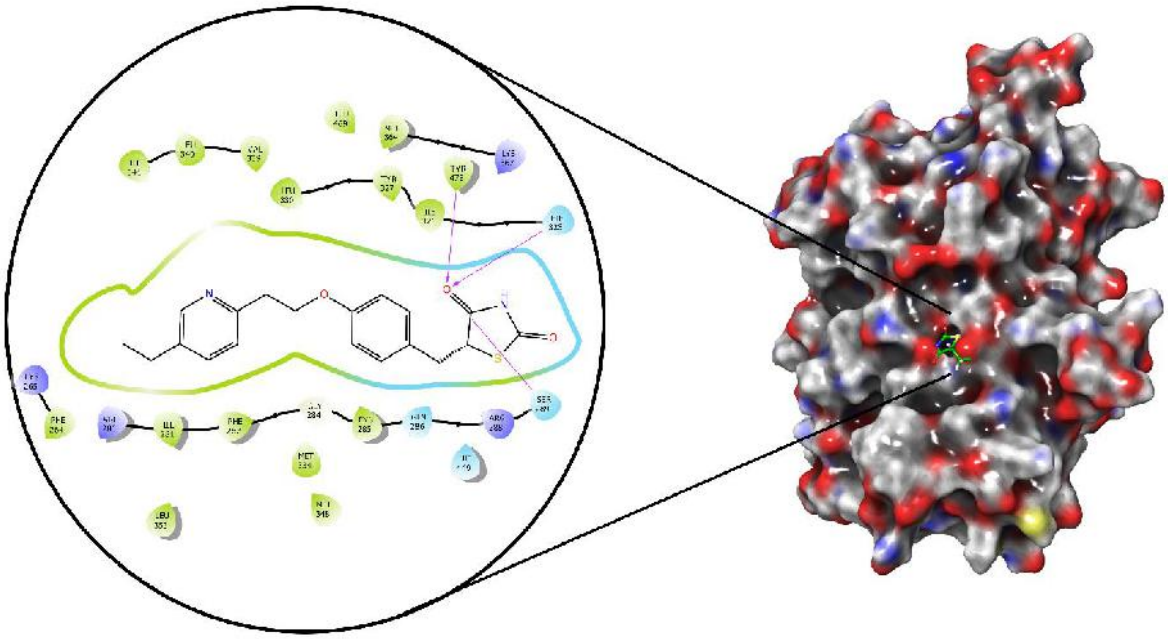


Fig. 41: Binding conformation of compound pioglitazone within the LBD of PPAR-γ.

6.2.Molecular dynamic simulations and MMGBSA

The potential hit compounds, **5b** and **5f**, obtained among the series (**5a-5j**), were subjected to a 500 ns MD simulation in the PPAR-γ LBD using Desmond software. The primary objective of the simulation was to assess the stability of the protein-ligand complex and to analyze their interactions throughout the simulation period. Simulation interaction analysis was performed on the MD trajectory of both complexes, focusing on key parameters such as hydrogen bonding, hydrophobic interactions, RMSD, and RMSF for the protein's Cα atoms, backbone, and ligand. The reference structure for the simulation was set as the starting point, with RMSD used to evaluate the stability and dynamic changes within the protein-ligand complex. Additionally, RMSF was employed to assess the fluctuations of individual amino acid residues, providing insight into the conformational changes in the protein structure, with Frame 0 representing the initial configuration at 0 ns. The interactions of PPAR-γ with **5b** and **5f** are further discussed below.

PPAR-γ – 5b complex: Protein-Ligand : RMSD Analysis: The RMSD analysis of the **PPAR-γ – 5b** complex demonstrated a structurally stable protein-ligand system throughout the 500 ns MD simulation.

The maximum deviations observed for the Cα-RMSD and backbone RMSD were 2.769 Å and 3.029 Å at frames 872 and 873, respectively, indicating minimal structural fluctuations of the protein. Ligand-centric RMSD analysis revealed that the maximum deviation of the ligand's position relative to its reference was 0.636 Å, while the ligand's RMSD relative to the protein structure reached a maximum of 3.153 Å at frame 941. These findings highlight the stability of the protein-ligand complex.

RMSF Analysis: The RMSF analysis provided insights into the flexibility of protein residues and ligand atoms during the simulation. The residue-level fluctuations relative to their reference positions were depicted in the RMSF plot, with the ligand's contact points on the protein highlighted using green bars. The most significant residue fluctuation was observed at GLN 470, which exhibited a variation of 1.151 Å, while fluctuations at other ligand-contacting residues remained below 1.00 Å, signifying stable interactions between the ligand and protein. Analysis of ligand atom mobility, captured through ligand RMSF relative to both the protein and the ligand's reference conformation, showed the highest deviations of 2.154 Å and 1.127 Å, respectively. These fluctuations corresponded to the movement of a carbon atom within the ligand's aromatic ring, further supporting the ligand's stable positioning within the binding pocket.

Protein-Ligand Interaction Map: A detailed analysis of the protein-ligand contact map revealed nine key hydrogen bond interactions with the following residues: CYS 285, GLN 286, ARG 288, SER 289, HIS 323, LEU 340, SER 342, GLU 343, and TYR 473. These interactions persisted consistently throughout the 500 ns MD simulation, underscoring the stability and specificity of the ligand's binding mode. Hydrophobic interactions between the ligand and the protein binding pocket were also sustained over the simulation period, further contributing to the complex's stability. Overall, the RMSD, RMSF, and contact map analyses collectively demonstrate the robust stability of the PPAR-γ – 5b complex during the 500 ns MD simulation, highlighting the strong and persistent interactions that underpin its dynamic behavior. (**Fig. 42**).

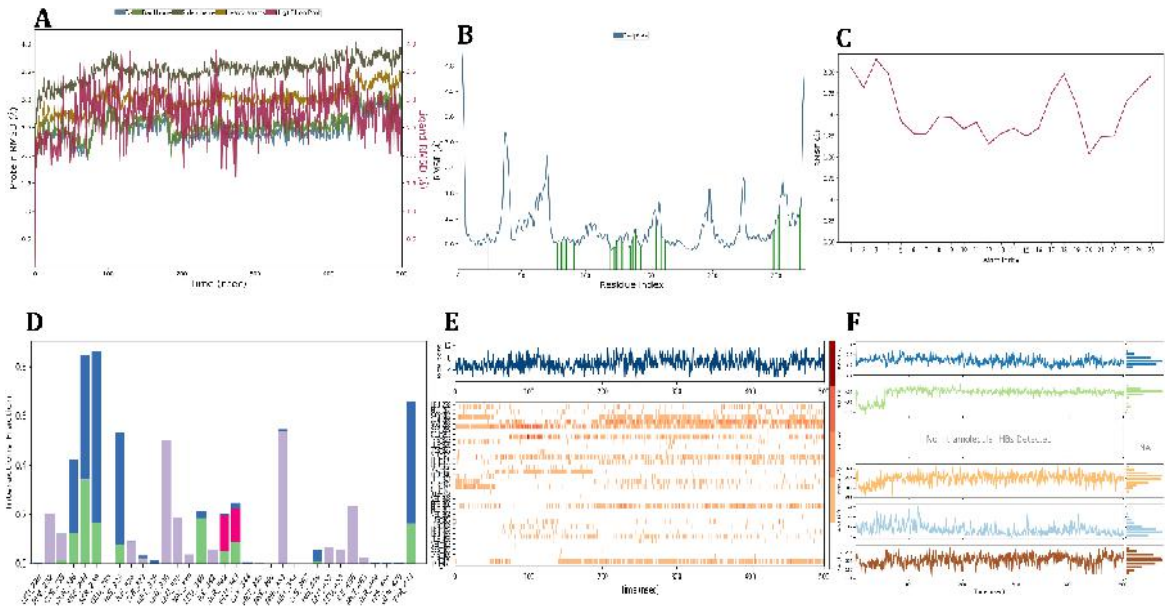


Fig. 42: Compound **5b (a)** Protein Ligand RMSD Plot, (**b**) Protein RMSF Plot, (**c**) Ligand RMSF plot, **(d)** Protein Ligand Contacts Histogram**, (e)** Protein Ligand Contacts timeline, (f) ligand properties**;** over period of 500 ns.

PPAR-γ – 5f complex: RMSD Analysis: The RMSD analysis of the **PPAR-γ–5f** protein-ligand complex revealed maximum deviations of 2.345 Å and 2.533 Å at frames 530 and 507 for protein and ligand RMSD, respectively. These deviations were calculated relative to the ligand aligned on the protein and the ligand aligned on itself, with frame 39 serving as the reference. The observed RMSD values suggest a stable binding orientation with limited structural displacement throughout the trajectory.

RMSF Analysis: The RMSF analysis of the ligand highlighted significant variations at the positions of the chlorine atoms, exhibiting RMSF values of 2.14 Å and 1.23 Å when aligned on the protein and on the ligand, respectively. This indicates differential flexibility at these positions depending on the alignment reference. In terms of protein RMSF, the most pronounced fluctuation was observed at LEU476, where the ligand interaction elicited an RMSF of 3.506 Å. Fluctuations for other protein residues in contact with the ligand were all below 1.00 Å, signifying a high degree of stability in the protein-ligand interactions.

Protein-Ligand Interaction Map: The analysis of protein-ligand contact patterns revealed the formation of hydrogen bonds with CYS285, SER289, and LYS367. Additionally, hydrophobic interactions were identified with several residues, including PHE282, TYR327, VAL339, ILE341, MET348, LEU353, PHE363, HIS449, LEU453, LEU469, TYR473, and LEU476. These contacts, illustrated in **Fig. 42**, underscore the role of both polar and hydrophobic interactions in stabilizing the PPAR-γ–5f complex, contributing to its overall binding affinity and conformational stability.

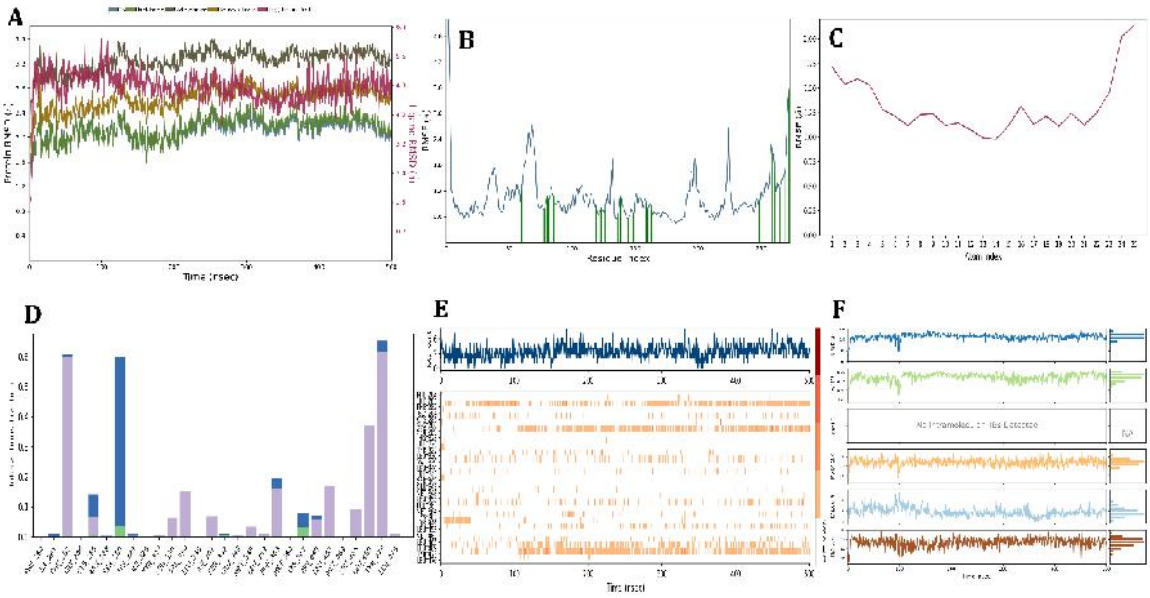


Fig. 43: Compound **5f (a)** Protein Ligand RMSD Plot, (**b**) Protein RMSF Plot, (**c**) Ligand RMSF plot, **(d)** Protein Ligand Contacts Histogram**, (e)** Protein Ligand Contacts timeline, (f) ligand properties**;** over period of 500 ns.

MMGB/SA: The binding free energy, entropy, and overall energetics of the ligand–protein complexes (**5a**–**5j**) were evaluated using MM/GBSA calculations. This analysis provides critical insights into the ligands' binding affinity toward the receptor's active site. Entropy values were derived from quasi-harmonic approximations, which account for molecular vibrational modes, including translational, rotational, and vibrational contributions. The binding free energy (ΔG_{bind}) is a composite parameter consisting of three primary components: the solvation free energy (ΔG_{solv}), the gas-phase interaction energy (ΔG_{gas}), and the entropy contribution (ΔS_{bind}), as described by the following equation:

$\Delta Gbind = \Delta Ggas + \Delta Gsolv - T\Delta Sbind$ Where T denotes temperature.

The ΔGbind values represent the binding affinity of the ligands, reflecting their capacity to interact with the target site. Conversely, the ΔSbind values signify the reduction in conformational entropy, highlighting the restriction of molecular flexibility within the binding pocket. The results of MM/GBSA calculations for the synthesized molecules are presented in **Table 17**. Where pioglitazone showed a ΔGBind value of -57.65 kcal/mol which was less optimised compared to compound **5b** with ΔGBind value of -61.86 kcal/mol, owing to its better interaction with the target receptor.

MM/GBSA Binding free energy (kcal/mol)				
Sr. no	**ΔGBind**	**ΔSbind**	**ΔG BindSolvGB**	**ΔG Bind Hbond**
5a	-52.83	-21.46	24.78	-1.8
5b	-61.86	-14.68	18.32	-1.61
5c	-46.24	-19.32	47.66	-0.99
5d	-46.88	-17.42	22.24	-1.84
5e	-45.16	-23.56	20.77	-0.98
5f	-54.99	-13.11	20.33	-0.18
5g	-56.33	25.97	21.43	-1.69
5h	-55.59	-10.48	22.76	-1.66
5i	-18.03	-18.91	27.6	-1.59
5j	-55.72	-37.67	21.68	-1.12
Pioglitazone	-57.65	-12.65	17.24	-1.38

Table. 17: Binding free energy of synthesized ligands calculated using MM/GBSA analysis.

6.3. Geometric optimization by DFT calculations

To gain deeper insights into the stability, reactivity, and kinetic behavior of the lead molecules **5b** and **5f**, a comprehensive computational analysis was conducted. The molecular geometries of both compounds were optimized, and key ligand electronic properties were calculated. The molecular descriptors, namely the HOMO, the LUMO, and the HOMO-LUMO energy gap (ΔEgap), were evaluated to elucidate the electronic reactivity of the two compounds. The HOMO energy provides a measure of the molecule's electron-donating capability, while the LUMO energy reflects its potential to accept electrons. The energy gap (ΔEgap) between HOMO and LUMO serves as a critical parameter

for assessing molecular reactivity, with a smaller ΔEgap indicating higher reactivity and a greater likelihood of interaction with biological targets. The FMO's for compounds **5b** and **5f** are depicted in **Fig. 44**, offering a visual representation of the electron distribution within these key orbitals. Additionally, **Table 18** presents a comparative analysis of the electronic properties of the two compounds, including the HOMO-LUMO energy gap (ΔEgap), dipole moment (μ), molecular hardness (η), and local softness (σ). Notably, the gas-phase energy of compound **5b** was calculated to be -1519.836 eV, whereas compound **5f** exhibited a slightly lower energy of -1543.853 eV, suggesting differences in their relative stabilities. MEP maps were generated using the B3LYP functional with a 6-31G (d, p**) basis set, based on the optimized geometries of compounds **5b** and **5f**. The MEP illustrates the spatial distribution of electrostatic potential across the molecular surface, highlighting regions of high electron density (negative potential) and low electron density (positive potential). This mapping provides critical insights into the electrophilic and nucleophilic regions of the molecule, which are essential for understanding potential sites of chemical reactivity. The MEP distributions for compounds **5b** and **5f** are displayed in **Fig. 44**, further elucidating the electronic landscape of these molecules.

Compound	Gas Phase Energy (eV)	ΔE_{GAP} (eV)	η (eV)	μ (eV)	ω (eV)	σ (eV)
5b	-1519.836	0.090088	0.045044	22.20051505	-0.13566	0.000414511
5f	-1543.853	0.093843	0.046921	21.31219164	-0.14561	0.000497486

Table. 18: Calculated quantum chemical descriptors of compounds **5b** and **5f**.

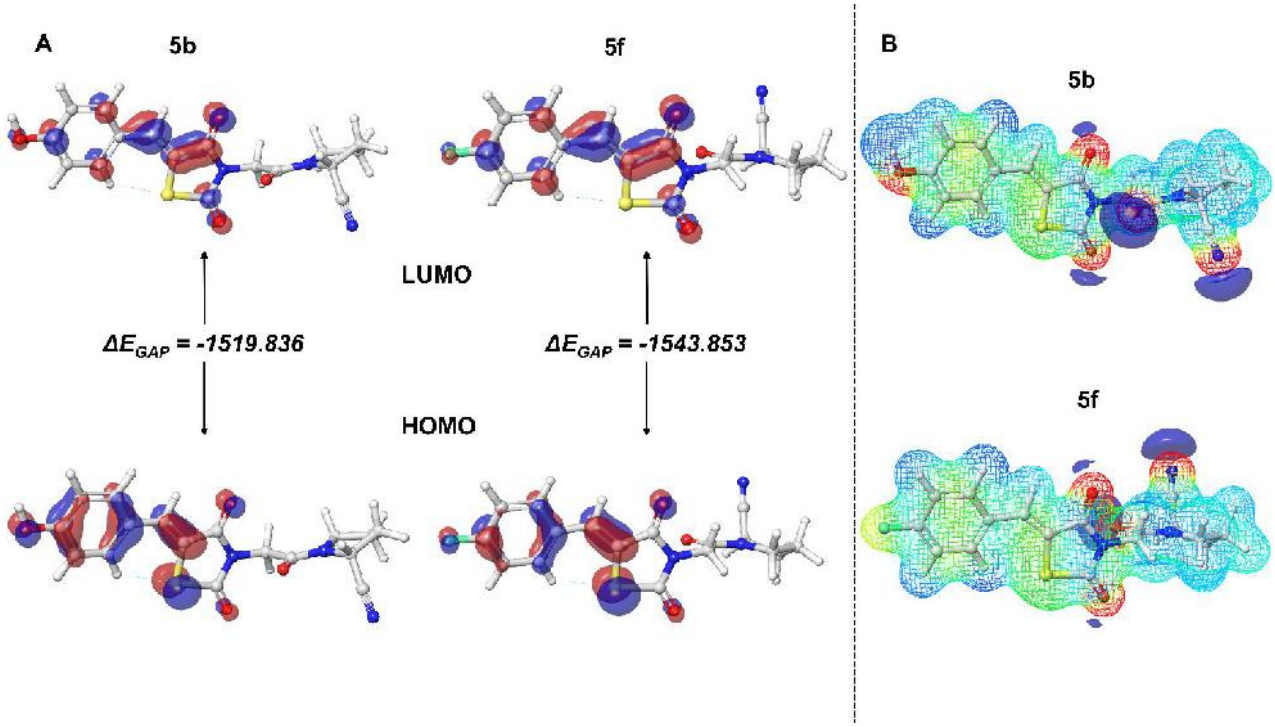


Fig. 44: Representation of compound **5b** and **5f,** (A) HOMO and LUMO orbitals, (B) MEP map.

6.4. ADMET computations

The ADMET properties of the synthesized compounds were predicted using the Schrödinger QikProp program, which evaluates key parameters such as hydrogen bond donors, hydrogen bond acceptors, hydrophilicity, molecular weight, permeability, binding affinity to human serum albumin, and human oral absorption. Violations of Lipinski's ROF and Jorgensen's ROT were assessed and compared to the recommended values, as they are important indicators of oral bioavailability (**Table 19**). Compounds **5b** and **5f** demonstrated a HBD value of 1 each, which is within the acceptable range. The HBA values were 8.5 for 5b and 7.5 for 5f. Log P values were 0.61 for **5b** and 1.26 for **5f**, reflecting favorable partitioning in biological systems. The QPlogS scores for all compounds were suboptimal, falling outside the acceptable range of -6.5 to 0.5. Permeability predictions, based on the MDCK assay, indicated good permeability for all synthesized compounds (**5a-5j**), with values ranging from 36.29 to 39.73. Furthermore, all molecules exhibited favorable Caco-2 permeability, suggesting their potential suitability for oral dosage forms. Additionally, these compounds were predicted to have 100% human

oral absorption. Overall, the ADME predictions from QikProp indicate that the synthesized compounds possess a promising pharmacokinetic profile.

Comp.	MW	DHB	AHB	QPlog Po/w	QP logBB	QPlog HERG	QPP Caco
5a	341.384	0	7.5	1.027	-1.414	-4.042	140.154
5b	357.383	1	8.25	0.671	-2.046	-3.922	42.178
5c	357.383	1	8.25	0.72	-1.946	-3.923	50.964
5d	384.452	0	8.5	1.512	-1.593	-4.114	139.775
5e	355.411	0	7.5	1.345	-1.464	-3.959	140.154
5f	359.374	1	7.5	1.267	-1.315	-3.925	140.154
5g	371.41	0	8.25	1.035	-1.51	-3.893	139.781
5h	401.436	0	9	0.99	-1.6	-3.711	139.781
5i	431.462	0	9.75	1.079	-1.624	-3.634	162.901
5j	331.345	0	8	0.38	-1.357	-3.681	139.781

Comp.	QPP MDCK	QPlogKhsa	%HOA	CNS	ROF	ROT
5a	132.912	-0.864	71.38	-2	0	0
5b	36.296	-0.649	100.00	-2	0	0
5c	44.534	-0.657	100.00	-2	0	0
5d	132.524	-0.702	74.195	-2	0	0
5e	132.912	-0.693	73.241	-2	0	0
5f	239.728	-0.817	100.00	-2	0	0
5g	132.53	-0.91	100.00	-2	0	0
5h	122.656	-0.974	100.00	-2	0	0
5i	142.563	-1.02	100.00	-2	0	0
5j	138.378	-1.164	100.00	-2	0	0

MW: Molecular weight (<500).
DHB: Number of hydrogen bond donors (<5).
AHB: number of hydrogen bond acceptors (<10).
QPlogPo/w: Octanol/ water partition coefficient (<5).
QPlog HERG: IC_{50} value for blockage of HERG K^+ channels (<-5).
QPP Caco: apparent Caco-2 permeability (nm/sec) (<25poor, >500great).
QPP MDCK: apparent MDCK permeability (nm/sec) (<25poor, >500great).
QPlogBB: Prediction of brain/blood partition coefficient (-3.0 to1.2).
%HOA: Percent Human Oral Absorption (>80% is high <25% is poor).
CNS: predicted Central nervous system activity (-2.0 to +2.0).
ROF: Number of violations of Rule of Five.
ROT: Number of violations of Rule of Three.

Table. 19: Computed ADMET properties of synthesised molecules (**5a-5j**).

6.5. Network Pharmacology and gene ontology analysis

The targets for compounds **5b** and **5f** were analyzed for protein-protein interactions using STRING analysis, revealing 15 nodes and 63 edges, with a clustering coefficient of 0.893 (**Fig. 45**). Additionally, gene set enrichment analysis identified 11 pathways associated with the pathogenesis of T2DM that are modulated by the predicted proteins for compounds **5b** and **5f**. Notably, the majority of these proteins influenced the "Adipocytokine signaling pathway," including *PPARGC1A*, *LEP*, *SLC2A4*, *PPARA*, *ADIPOQ*, *CD36*, *SLC2A1*, and *NR1C3*, with a strength score of 2.13 and a false discovery rate (FDR) of 1.83E-11. The second most prominent pathway was 'Insulin resistance,' involving proteins such as *PPARGC1A*, *SLC2A4*, *INS*, *PPARA*, *CD36*, *SLC2A1*, *NR1H2*, and *NR1C3*, with a strength of 1.94 and an FDR of 1.75E-10. The detailed information on the enriched pathways is summarized in **Table 20**. Gene set ontology analysis revealed 284 significantly enriched biological processes. Among these, 'Positive regulation of lipid metabolic processes' exhibited the lowest FDR (4.99E-08), modulating 7 genes from a background of 155 genes, with a strength of 1.77. Similarly, the 'Glucose metabolic process' showed a FDR of 1.86E-07, modulating 6 genes from a background of 116 genes, with a strength of 1.83 (**Fig. 46**). In addition, five molecular functions were significantly enriched. Among these, 'Nuclear receptor activity' showed a FDR of 0.0135, modulating 3 genes from a background of 53 genes, with a strength of 1.87. Furthermore, cellular components analysis identified a single enriched component, the 'Extracellular space,' with a FDR of 0.0410, modulating 10 genes from a background of 3247 genes, with a strength of 0.61. The constructed network consists of 20 nodes, representing 7 pathways, 11 targets, and 2 compounds. Compounds **5b** and **5f** exhibited strong interactions with key proteins such as *INSR*, *ADIPOQ*, *SLC2A4*, and *SLC2A1*, which are implicated in pathways like insulin resistance, adipocytokine signaling, and PPAR signaling (**Fig. 47**).

KEGG ID	Pathway Description	Observed gene/background gene count	Strength	False discovery rate	Genes
hsa04920	Adipocytokine signaling pathway	8/68	2.13	1.83E-11	PPARGC1A, LEP, SLC2A4, PPARA, ADIPOQ, CD36, SLC2A1, NR1C3
hsa04931	Insulin resistance	7/106	1.94	1.75E-10	PPARGC1A, SLC2A4, INS, PPARA, CD36, SLC2A1, NR1H2, NR1C3
hsa04152	AMPK signaling pathway	6/120	1.82	3.23E-08	PPARGC1A, LEP, SLC2A4, INS, ADIPOQ, CD36
hsa03320	PPAR signaling pathway	5/75	1.94	2.37E-07	FABP4, PPARD, PPARA, ADIPOQ, CD36
hsa04932	Non-alcoholic fatty liver disease	4/146	1.56	0.00028	LEP, INS, PPARA, ADIPOQ
hsa04930	Type II diabetes mellitus	3/45	1.94	0.00034	SLC2A4, INS, ADIPOQ
hsa04211	Longevity regulating pathway	3/87	1.66	0.0019	PPARGC1A, INS, ADIPOQ
hsa04922	Glucagon signaling pathway	3/100	1.6	0.0025	PPARGC1A, PPARA, SLC2A1
hsa04910	Insulin signaling pathway	3/132	1.47	0.005	PPARGC1A, SLC2A4, INS
hsa04923	Regulation of lipolysis in adipocytes	2/54	1.69	0.0273	FABP4, INS
hsa04213	Longevity regulating pathway - multiple species	2/61	1.63	0.0314	SOD1, INS

Table. 20: Enrichment analysis of protein regulated by compound **5b** and **5f** by KEGG pathway database.

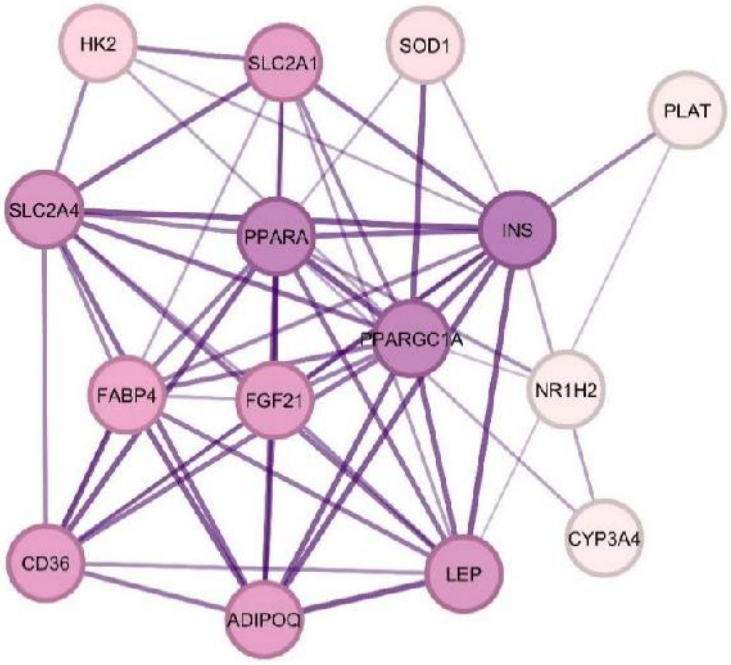


Fig. 45: Protein-protein interactions for compounds **5b** and **5f** were identified through STRING analysis.

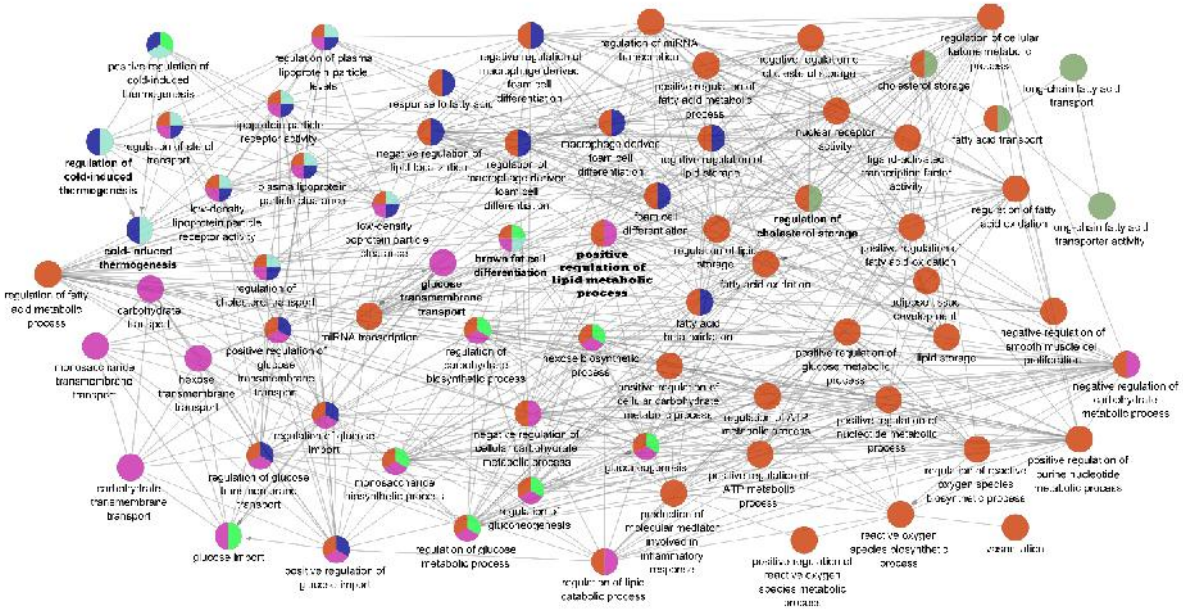


Fig. 46: Significantly enriched Gene ontology 'biological processes' by compound **5b** and **5f**.

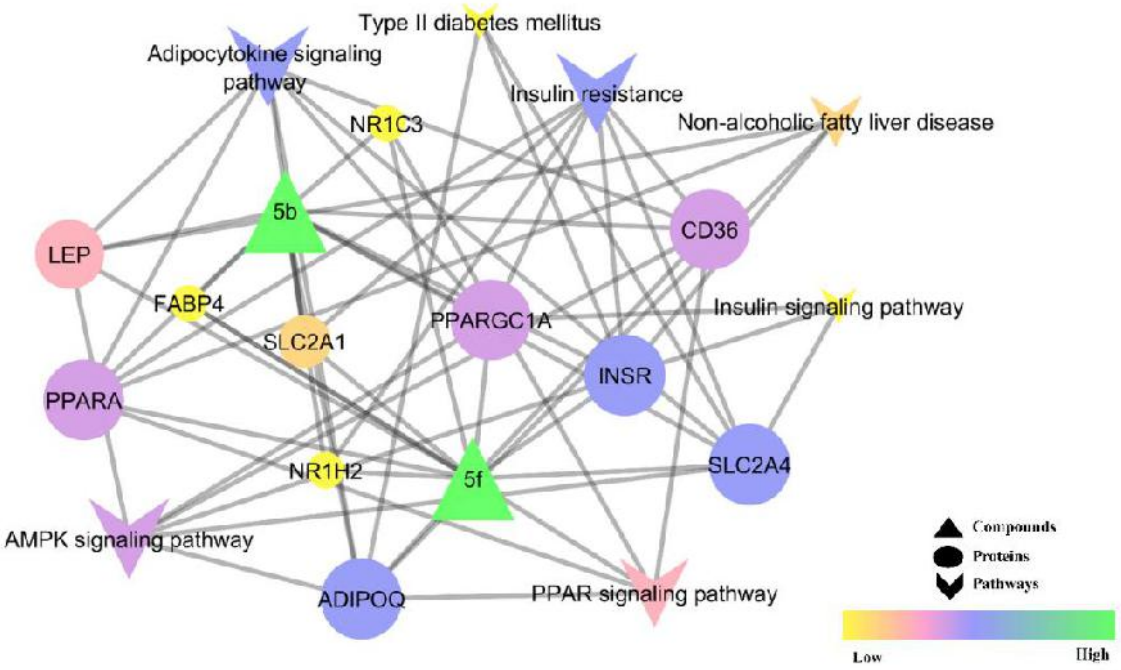


Fig. 47: Interaction of compounds **5b** and **5f** with proteins involved in T2DM and respective pathways.

7. Discussion

In the current study, we synthesized a series of compounds (**5a-5j**) by hybridizing TZD (derived from pioglitazone) with acetyl pyrrolidine (derived from vildagliptin). These ligands were further modified by varying their R-groups to create a diverse compound library. Concurrently, a seven-point pharmacophore model targeting the PPAR-γ ligand-binding domain was developed. The ligand library was then screened using this pharmacophore model to identify potential hits. To validate the screening, a decoy set of 1000 molecules was employed, and enrichment analysis was conducted on the screened ligands. The top 10 compounds were selected for synthesis and spectral characterization. Additionally, the impact of compounds (**5a-5j**) on glucose uptake was evaluated in L6 rat skeletal muscle myotubes, serving as a model for the translocation of GLUT carriers. Results showed that compounds **5b** and **5f** significantly enhanced glucose uptake in L6 cells compared to others in the series. These compounds also displayed superior fitness scores in the pharmacophore analysis. Consequently, the two lead

compounds, **5b** and **5f**, were further tested for their ability to activate the PPAR-γ transcription factor, showing a dose-dependent increase in activity, comparable to the standard pioglitazone.

Fructose-induced insulin resistance is a widely accepted experimental model for evaluating the insulin-sensitizing potential of candidate compounds. Prior studies have demonstrated that prolonged fructose supplementation induces insulin resistance and hyperinsulinemia in Wistar rats. Furthermore, previous reports indicate an inverse relationship between weight gain and fructose-induced insulin resistance in rats.[177-179]

In the present study, fructose supplementation resulted in a reduction in body weight, which may be attributed to diminished appetite, potentially driven by the metabolic effects of fructose. Elevated insulin levels, mild hyperglycemia, and an HOMA-IR index were observed as key indicators of insulin resistance. The pathophysiological mechanisms underlying this condition include enhanced glycogen synthesis, reduced gluconeogenesis, altered glycolytic and glycogenic pathways, and an increased hepatic glucose output. OGTT results confirmed hyperglycemia, as evidenced by an increased AUC for glucose. ITT results revealed elevated insulin levels accompanied by higher HOMA-IR values, further supporting the presence of insulin resistance. Treatment with compounds **5b** and **5f** over a 15-day period mitigated these effects, as evidenced by reductions in both glucose AUC and HOMA-IR values. Additionally, treatment with **5b** and **5f** resulted in a reversal of weight loss, as well as a normalization of food and water intake, compared to the insulin-resistant group. This effect may be mediated by the modulation of adiponectin and leptin activity.[180]

The role of adiponectin in insulin sensitivity and metabolic regulation is well-documented. Balsan *et al*. reported a positive association between adiponectin levels and insulin sensitivity, BMI, body weight, and appetite, highlighting the hormones influence on metabolic homeostasis.[182] These findings suggest that the observed metabolic improvements in the **5b** and **5f** treatment groups may be linked to the regulatory effects of adiponectin and leptin on energy balance and glucose metabolism.

The quantification of glycogen content serves as a crucial biomarker for evaluating glucose utilization through glycogenesis, a process in which glucose is stored as glycogen in the liver and skeletal muscles. Dysregulation of glucose uptake and its subsequent metabolism are critical contributors to the pathophysiology of insulin resistance and T2DM.[183-184] In the current study, two complementary approaches were employed to investigate glucose utilization: (1) analysis of glycogen content and (2) an ex-vivo glucose consumption assay. Fructose supplementation was found to impair glucose utilization, as evidenced by reduced glycogen content in the IR group and diminished glucose uptake by the rat hemidiaphragm from the incubation medium. Notably, treatment with compounds **5b** and **5f** effectively countered these effects. The treated groups exhibited a marked increase in glycogen content and enhanced glucose uptake by the hemidiaphragm relative to the IR group, highlighting the potential of **5b** and **5f** to restore insulin sensitivity and promote glucose utilization

Several studies have demonstrated a significant association between lipid profile alterations and insulin resistance. Elevated triglyceride levels are recognized as a hallmark of progressive insulin resistance, which correlates with an increase in the HOMA-IR index and the area under the curve AUC for glucose, both key indicators of insulin resistance pathogenesis. Additionally, a rise in TG and LDL levels, coupled with a reduction in HDL levels, is a well-established characteristic of dyslipidemia that precedes insulin resistance. In the present study, the IR group exhibited elevated TG and VLDL levels alongside a decline in HDL levels relative to the normal control group. Notably, treatment with compounds **5b** and **5f** effectively countered these lipid abnormalities, underscoring their potential to mitigate insulin resistance and enhance glucose tolerance. This suggests that these compounds may play a therapeutic role in improving metabolic responses to glucose administration.

Furthermore, oxidative stress has been widely implicated in the etiology of insulin resistance, with previous studies documenting significant disruptions in oxidative stress biomarkers. In this study, the IR group showed marked alterations in these biomarkers, whereas treatment with compounds **5b** and **5f** successfully restored them to normal levels. This observation highlights the antioxidant potential of these compounds in mitigating oxidative stress-induced insulin resistance.

The pharmacokinetic evaluation of compounds **5b** and **5f** was conducted using HPLC to estimate their plasma concentrations. Compound **5b** exhibited better pharmacokinetic properties compared to **5f,** with a higher peak plasma concentration (C_{max}), longer time to reach maximum concentration (T_{max}), and a more favorable clearance rate. These findings suggest that **5b** may have enhanced bioavailability and a longer duration of action, supporting its potential as a more effective therapeutic agent for the management of insulin resistance

Sinusoidal congestion, driven by necrosis, inflammation, and hepatocyte apoptosis, serves as a hallmark of hepatic insulin resistance. Insulin resistance promotes the efflux of free fatty acids into the liver, which in turn exacerbates hepatocyte hypertrophy and steatosis. This process results in the compression of sinusoidal lumens, thereby contributing to vascular congestion. Pro-inflammatory cytokines released by immune cells induce endothelial dysfunction, further aggravating vascular congestion. Additionally, heightened hepatic resistance increases portal pressure, compounding sinusoidal congestion. Ballooning degeneration, a key marker of hepatocellular injury, is closely linked to insulin resistance. This phenomenon is attributed to lipotoxicity caused by metabolic stress, which disrupts mitochondrial function, induces cytoplasmic condensation, and triggers cellular swelling. Kupffer cell hyperplasia, often observed in the context of metabolic stress, is another prominent feature associated with insulin resistance. In the present study, treatment with compounds **5b** and **5f** successfully reversed these pathological alterations, highlighting their therapeutic potential in mitigating hepatic insulin resistance.[185-186]

In this study, the molecular structures of compounds **5b** and **5f** were optimized using DFT based quantum chemical calculations. The reactivity, molecular hardness, softness, and surface charge distribution of both compounds were thoroughly analyzed. Results indicated that compound **5b** exhibited superior molecular reactivity compared to **5f**, suggesting enhanced potential for biological interactions. The binding affinity and energy requirements for the interaction of these compounds with the PPAR-γ were further evaluated. Docking analysis revealed that compound **5b** formed a more extensive hydrogen bonding network with key amino acid residues in the PPAR-γ binding pocket,

enhancing its binding strength and optimal positioning, similar to the known PPAR-γ agonist pioglitazone. Conversely, compound **5f** exhibited a distinct binding orientation, resulting in a limited hydrogen bonding network, as confirmed by the PPAR-γ TF assay.

To assess the dynamic behavior and stability of the **5b**-PPAR-γ and **5f**-PPAR-γ complexes, MD simulations were conducted. Key indicators such as RMSD and RMSF revealed that the **5b**-PPAR-γ complex demonstrated reduced deviation and fluctuation compared to the **5f** complex. Notably, amino acid residues that contributed to the hydrogen bonding network exhibited fluctuations of less than 1 Å in the **5b** complex. Both compounds met the ADMET criteria and complied with Lipinski's rule of five, indicating favorable oral bioavailability.

The integration of computational chemistry, pharmacology, bioinformatics, and systems biology has catalyzed a paradigm shift in drug discovery, offering a multitarget approach that significantly reduces development costs. This strategy enables the identification and analysis of complex biological interaction networks in a more systematic and comprehensible manner.

A systems biology approach was utilized to decode the biological targets implicated in the pathogenesis of T2DM associated with the activity of compounds **5b** and **5f**. Proteins and pathways linked to the pathophysiology of T2DM were mapped, and enrichment analysis was performed using STRING and KEGG databases. This analysis identified 11 key pathways modulated by the compounds, with the adipocytokine signaling pathway emerging as the most significantly affected. Proteins within this pathway, including leptin and adiponectin, play essential roles in glucose homeostasis, energy balance, gluconeogenesis, glycogenesis, and GLUT receptor translocation. The modulation of adiponectin levels by **5b** and **5f** suggests an enhancement of insulin sensitivity, which is crucial for managing insulin resistance in T2DM.

Gene expression analysis revealed that treatment with **5b** and **5f** upregulated the ADIPOQ gene, which encodes for adiponectin, a critical factor in improving insulin sensitivity, reducing the AUC for glucose, and lowering circulating insulin levels in treated groups. Additionally, the NR1C3 gene, responsible for encoding the PPAR-γ protein, was upregulated, promoting the PPAR-γ signaling pathway. This

pathway is known to enhance adipogenesis, lipid metabolism, and glucose homeostasis while supporting the expression of genes involved in insulin signaling, such as GLUT transporters. Correspondingly, **5b** and **5f** treatment led to improved glucose uptake and lipid metabolism, contributing to glycemic control in treated groups relative to IR controls. Notably, SLC2A4 (GLUT4), a key regulator of glucose uptake, was modulated by **5b** and **5f**, further supporting their role in glucose homeostasis.

Through an integrated *insilico*, *invitro*, and *invivo* approach, the molecular mechanism of action for compounds **5b** and **5f** in reversing insulin resistance was elucidated. The study proposes a comprehensive molecular model (**Fig. 48**) illustrating how treatment with **5b** and **5f** reestablishes glucose homeostasis. This is achieved by inhibiting gluconeogenesis, enhancing PPAR-γ expression, promoting glucose utilization, and stimulating glycogenesis via pathways such as the adipocytokine signaling pathway, PPAR signaling pathway, AMPK pathway, and insulin signaling pathway. These findings highlight the therapeutic potential of **5b** and **5f** as promising candidates for T2DM management.

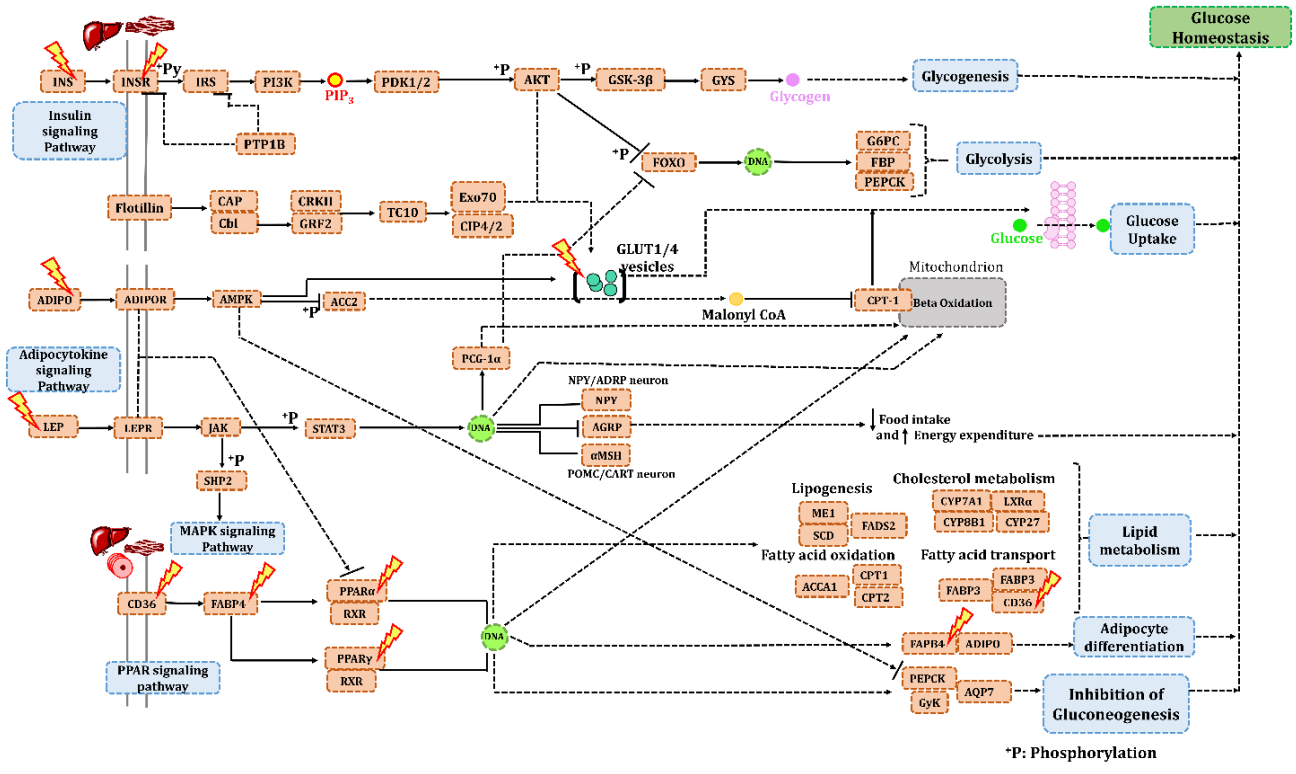
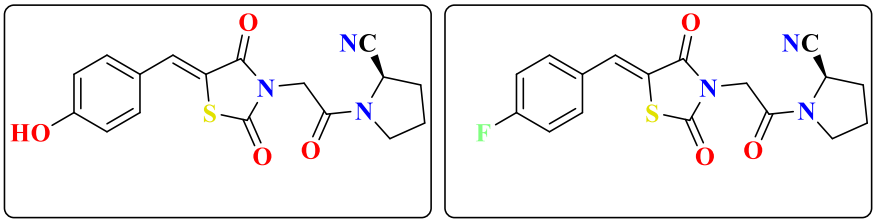


Fig. 48: Proposed possible molecular mechanism of compound **5b** and **5f**, *via* PPAR signaling pathway, Adipocytokine signaling pathway, and insulin signaling pathway, highlighting triggered proteins.

Outcome of scheme.

Identified Hit molecules as Glucose homeostatic agents



(5b) **(5f)**

Chapter 5

Results (Scheme. 3)…

The general depiction of research work carried out for **scheme. 3** is briefly summarized in the following **Fig. 49**.

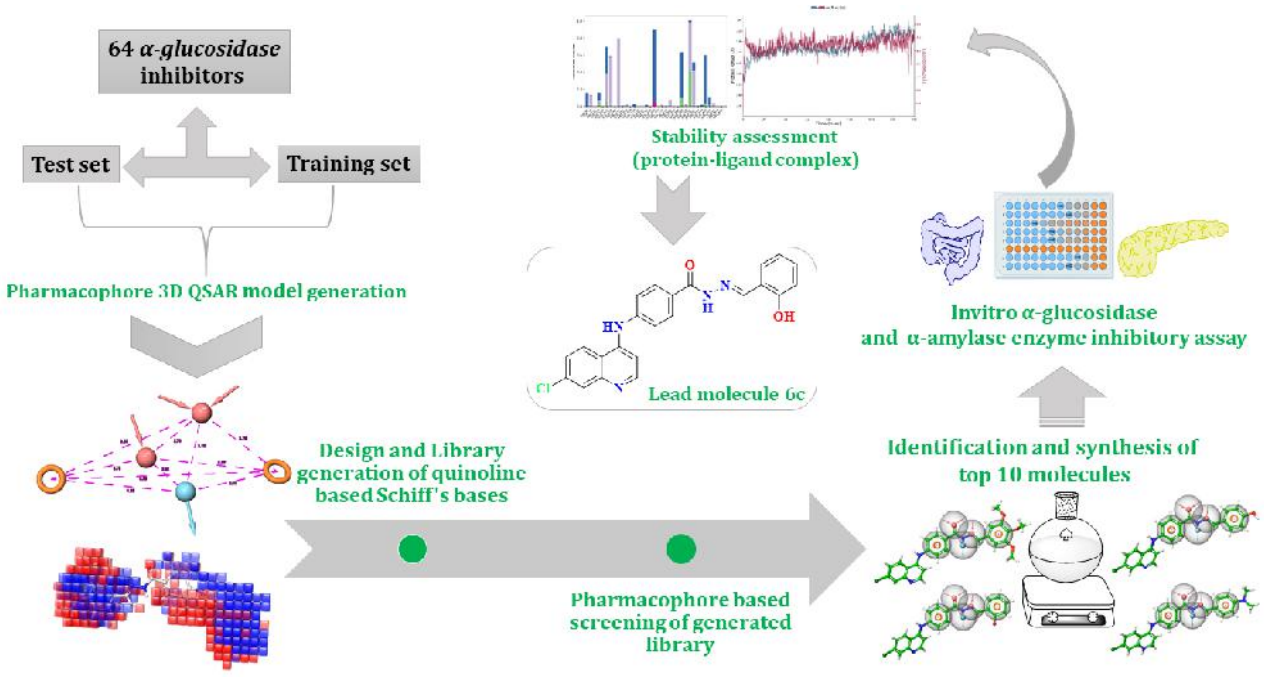


Fig. 49: Study plan of scheme. 3.

1. Design of scheme. 3

Based on the analysis of existing literature, it is evident that the majority of the reported compounds share key structural motifs, including a quinoline core, an imine (C=N) linkage, and a hydrazone unit characteristic of Schiff bases. Additionally, structural modifications have predominantly focused on the strategic variation of hydroxy (OH) group positions on the phenyl ring. Guided by these insights, we have rationally designed a template of quinoline-based benzohydrazide Schiff bases to further explore their structural and functional potential as illustrated in **Fig. 50.**

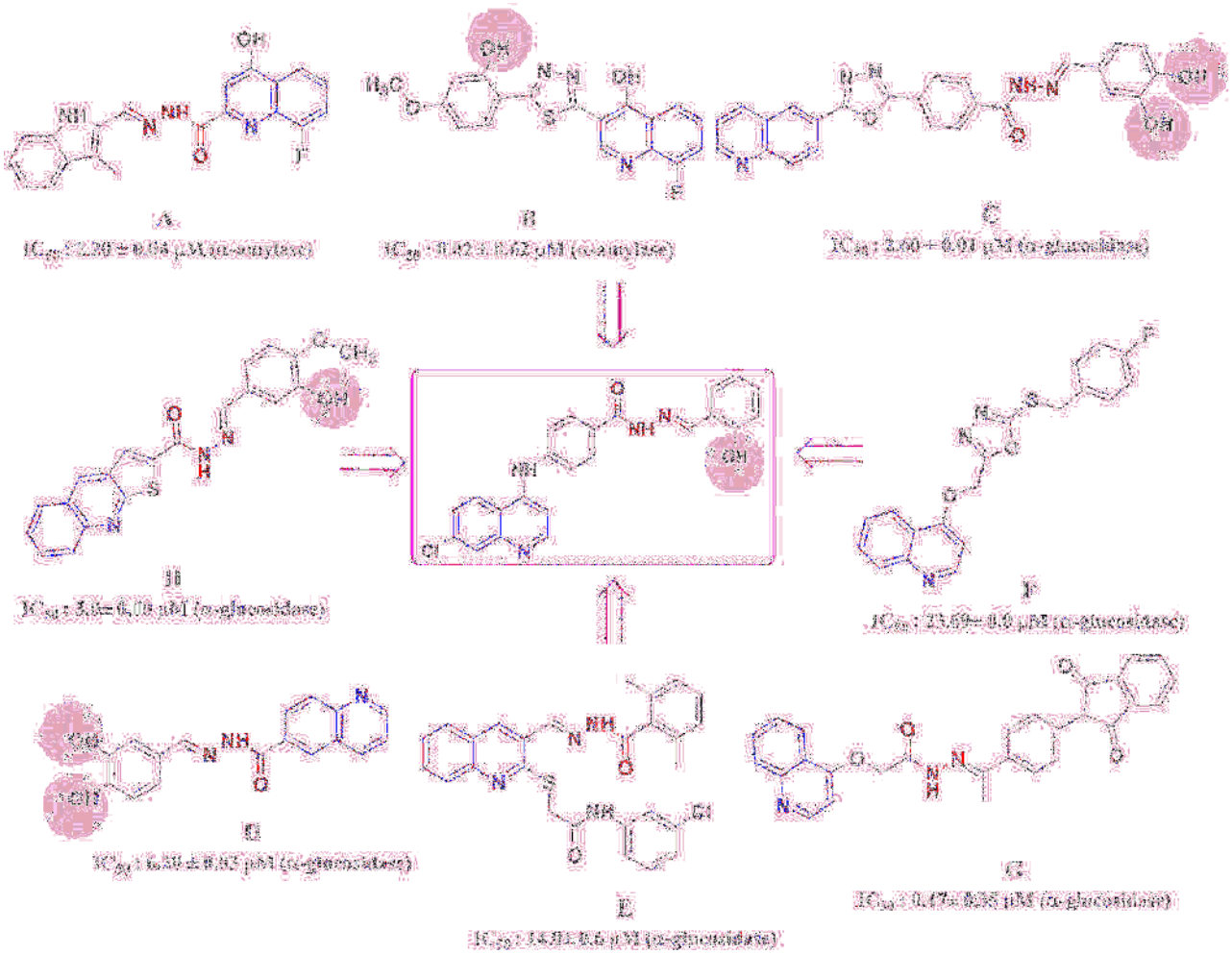
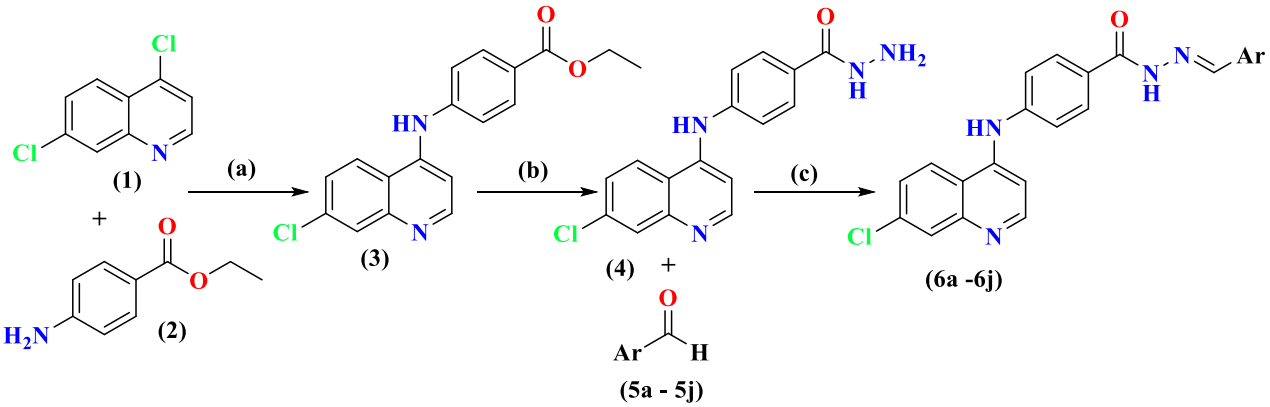


Fig. 50: Design of Quinoline based Schiff's base molecule template.[187-194]

Scheme. 4: Synthesis of quinoline based benzohydrazide based schiffs bases



Reagents and conditions: (a) 2N HCl, reflux; (b) Hydrazine hydrate (80%), reflux; (c) Methanol, Glacial acetic acid, reflux.

2. Structure based pharmacophore and 3D QSAR

The dataset comprising 66 molecules, sourced through a comprehensive literature review, was categorized into active and inactive sets. Pharmacophoric sites were identified for each molecule, leading to the generation of 12 distinct pharmacophore hypotheses. These hypotheses were constructed based on key molecular features, including hydrogen bond acceptors (A), hydrogen bond donors (D), hydrophobic groups (H), aromatic ring groups (R), positively charged groups (P), and negatively charged groups (N). The ability of the model to discriminate between active and inactive molecules was assessed, with the model demonstrating the highest "inactive score" being the most effective in distinguishing between these categories. The "survival score" was used as an indicator of how well the model aligns with active compounds, with higher values signifying superior predictive performance. Hypotheses were ranked according to their statistical parameters, and the top five models are summarized in **Table 21**. The ranking criteria included survival score, inactive score, and vector score. Among the 12 hypotheses, the pharmacophore model designated as AADRR_1 was identified as the best fit, exhibiting a survival score of 5.0697, an inactive score of 2.3579, and a vector score of 0.9552. This model was subsequently selected for further validation. The AADRR_1 model is a five-point pharmacophore hypothesis (**Fig. 51**) comprising two hydrogen bond acceptor sites, one hydrogen bond donor site, and two aromatic ring features. The hydrogen bond acceptors are associated with the nitrogen atom of the Schiff base (-N=CH) and the oxygen atom of a carbonyl group (C=O), while the hydrogen bond donor corresponds to an amino group (NH). The two aromatic ring features are attributed to phenyl ring structures. These pharmacophoric features are critical for the *α-glucosidase* inhibitory activity exhibited by the reported molecules in the dataset.

The AADRR_1 pharmacophoric model was validated through an atom-based 3D QSAR analysis employing PLS regression. The analysis was conducted with a grid spacing of 1.5 Å to ensure precision in the spatial mapping of molecular features. The dataset was randomly divided into a

training set of 8 molecules and a test set of 19 molecules, maintaining uniform structural diversity. The optimal QSAR model was identified at a factor of four, supported by robust statistical parameters. These included a high correlation coefficient (R^2=0.96), a significant cross-validation coefficient (Q^2=0.92), model stability (0.55), and a high F-value (99.8), all of which affirm the reliability of the model. Additionally, the Pearson's correlation coefficient (r=0.9759) highlights a strong predictive capacity. The model's stability was further confirmed by a low standard deviation (SD=0.229) and root mean square error (RMSE=0.29), indicating minimal prediction errors, as summarized in **Table 22**. The 3D QSAR contour plots for the active compound are presented in **Fig. 52**. These plots illustrate the spatial influence of molecular features on *α-glucosidase* inhibitory activity. Positive contributing effects are depicted by blue cubes, while red cubes signify regions where molecular features negatively impact pharmacophoric activity. This visual representation underscores the critical molecular interactions required for *α-glucosidase* inhibition.

Title	Survival Score	Site Score	Vector Score	Volume Score	BEDROC Score	PhaseHypoScore
AADRR_1	5.069738	0.991397	0.955287	0.73662	0.98377	1.287982
AADRR_3	4.905304	0.813427	0.8755	0.715986	0.99262	1.286918
ADRR_2	4.84413	0.995019	0.941394	0.735339	0.987352	1.278046
AADRR_5	4.711901	0.723739	0.815888	0.631069	0.988926	1.271614
AAARR_2	4.739191	0.728928	0.8424	0.635954	0.973156	1.257552
AAADR_2	4.63441	0.823841	0.908019	0.715564	0.97829	1.256364
ADRR_1	4.87274	0.992516	0.944214	0.736519	0.962434	1.254762
AADR_2	4.6006	0.992794	0.952345	0.736964	0.973126	1.249136
AARR_3	4.602119	0.690675	0.957448	0.729225	0.863529	1.139626
AARR_2	4.724841	0.790252	0.964125	0.751729	0.842105	1.125588
ARRR_2	4.674086	0.685647	0.966347	0.716074	0.67823	0.958646

Table. 21: Total number of pharmacophore hypothesis generated.

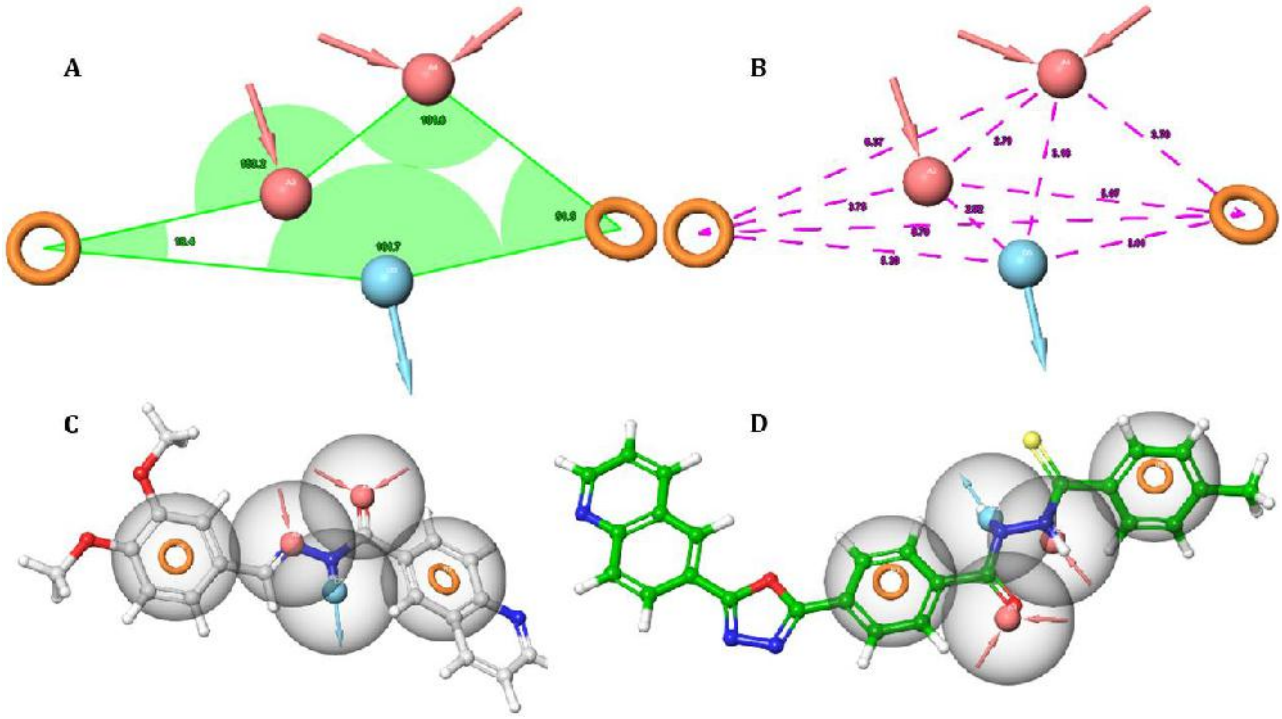


Fig. 51: Representation of the AADRR_1 pharmacophore model illustrating (A) the angles between pharmacophoric sites and (B) the intersite distances in angstroms (Å). The mapping of pharmacophoric sites is shown for (C) an active compound and (D) an inactive compound from the dataset.

ID	PLS Factor	SD	R^2	F	P	RMSE	Q^2	Pearson's r
AADRR1	1	0.067	0.712	42.0	5.62e-06	0.43	0.8430	0.9410
	2	0.3727	0.8979	70.3	1.18e-08	0.34	0.8999	0.9577
	3	0.3366	0.9219	59.0	1.55e-08	0.35	0.8954	0.9522
	4	0.2295	0.9661	99.8	3.99e-10	0.29	0.9294	0.9759

Table. 22: Atom-based 3D QSAR statistics for the selected pharmacophore hypothesis

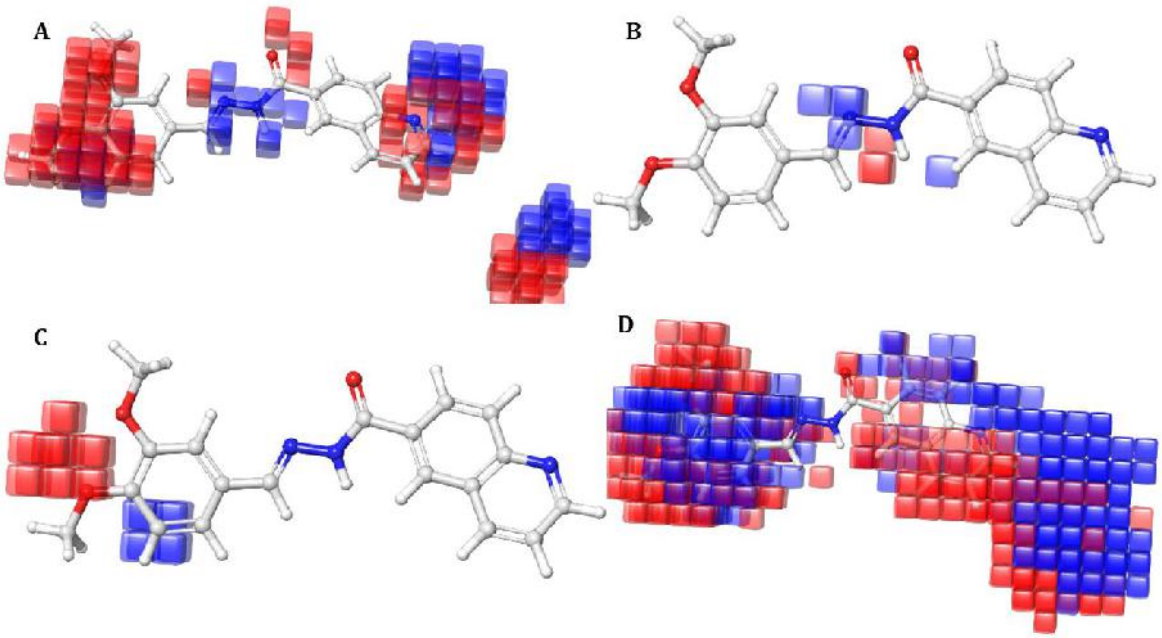


Fig. 52: Contour plot representation for the active compound A5 from the dataset, illustrating the influence of key molecular interactions: (A) Electron-withdrawing effect, (B) Hydrogen bond donor effect, (C) Negative ionic effect, and (D) Positive ionic effect.

2.1. Validation of Pharmacophore model.

The discriminatory performance of the generated pharmacophoric model AADRR_1 was further validated by screening a set of ten designed quinoline-based benzohydrazide Schiff's base molecules alongside a decoy set of 1,000 molecules from Schrodinger's database. The model effectively distinguished the designed molecules from the decoy set. The top hits were identified based on a fitness score above 2, while the decoy molecules showed fitness values below 1.9 (**Table 23**). The performance of the hit list was assessed by the model's AADRR_1 RIE value of 18.14. The Receiver Operating Characteristic (ROC) curve analysis revealed an AUC value of 1, indicating excellent model performance. The enrichment screen plot is presented in (**Fig. 53**). Additionally, the top hits were found to align with the pharmacophoric sites (**Fig. 54**). These promising hits were subsequently synthesized, followed by in vitro evaluation of their inhibitory activity against *α-glucosidase* and α-amylase. Their binding affinities were further assessed using molecular docking, MD simulations, and MM/GBSA analysis.

Title	Fitness
6a	2.593529
6d	2.591902
6c	2.590907
6b	2.587568
6f	2.58324
6h	2.583012
6e	2.575609
6j	2.571411
6i	2.565869
6g	2.565004
schrod_417623	1.983863
schrod_540219	1.980556
schrod_801249	1.980008

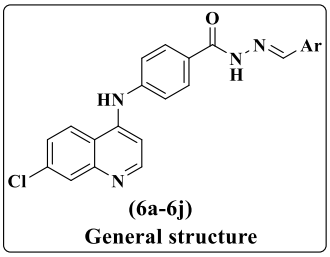


Table. 23: Top 10 molecules identified through pharmacophore-based screening of designed compounds and decoy set ligands.

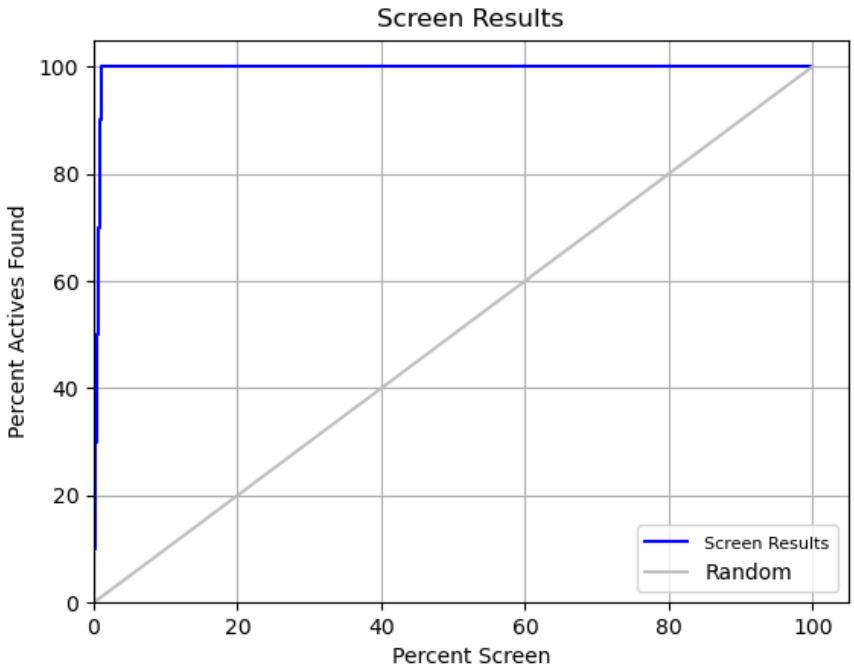


Fig. 53: Enrichment analysis plot of pharmacophore based screening.

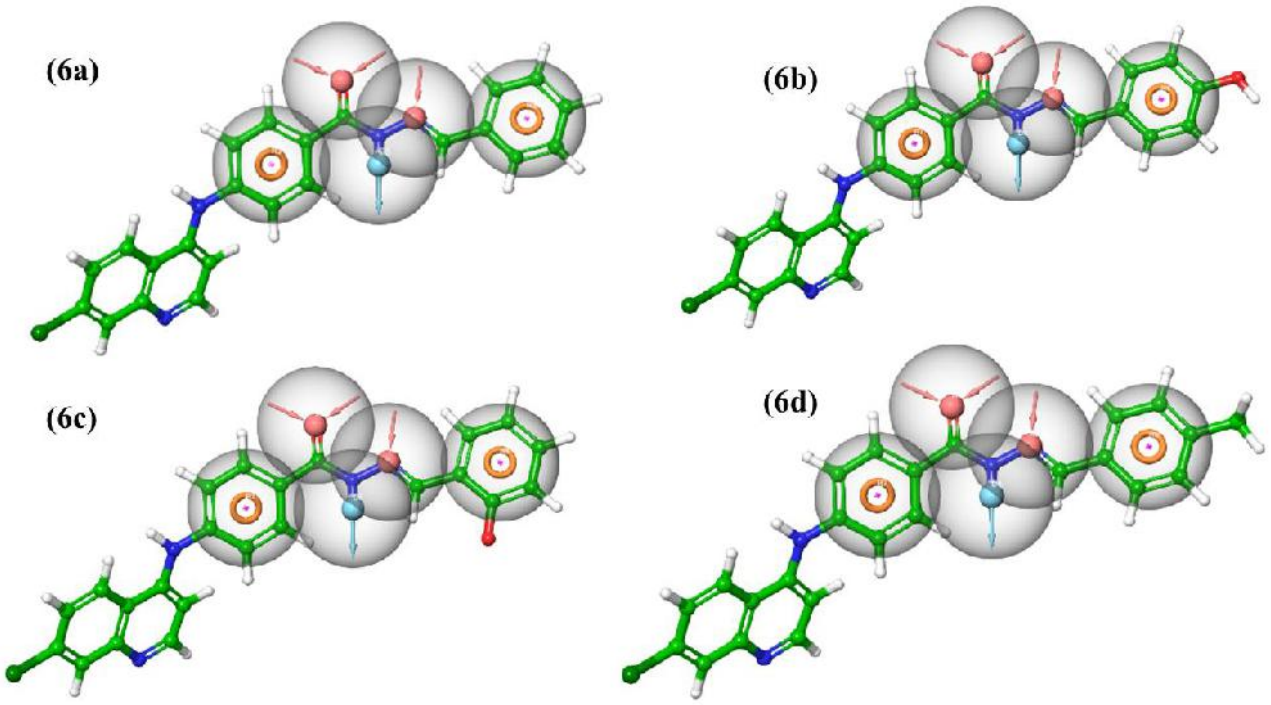


Fig. 54: Illustrates the top-screened active compounds mapped onto the pharmacophoric model AADRR_1.

3. Chemistry

The quinoline-based benzohydrazide Schiff's base derivatives (**6a-6j**) were synthesized according to the procedure outlined in **Scheme 4**. The starting materials, ethyl 4-((7-chloroquinolin-4-yl)amino)benzoate (**3**) and 4-((7-chloroquinolin-4-yl)amino)benzohydrazide (**4**), were synthesized following previously established methods.[195] The substituted benzylidene-4-((7-chloroquinolin-4-yl)amino)benzohydrazide (**6a-6j**) compounds were prepared by reacting equimolar amounts of compound (**4**) with the corresponding aryl aldehydes (**5a-5j**) under reflux conditions, in the presence of a catalytic amount of glacial acetic acid in methanol. The crude products (**6a-6j**) were subsequently recrystallized and dried. The structures of intermediates (**3**) and (**4**) as well as the final compounds (**6a–6j**) were confirmed using FTIR, ^{1}H NMR, ^{13}C NMR, and LCMS spectroscopic techniques. The FTIR spectra of the target compounds (**6a-6t**) exhibited a characteristic absorption band for the amino (NH) group at 3200 cm^{-1}. The ^{1}H NMR spectra of these compounds displayed diagnostic singlet signals at δ 9.00 ppm and δ 11.00 ppm, corresponding to the amino protons of (-

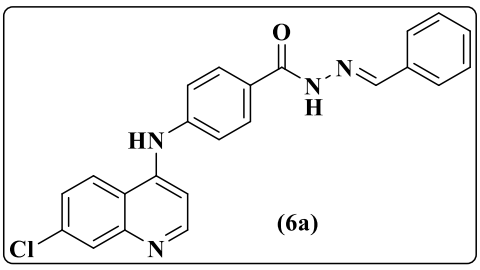
NH-) and (-CONH) groups, respectively. The aromatic protons were observed within the range of δ 6.5-8.5 ppm. The ^{13}C NMR spectra of compounds (**6a-6t**) provided further structural confirmation, with characteristic signals at δ 162 ppm and δ 152 ppm, corresponding to the (-CH=N-) and (C=O) functional groups, respectively. Finally, the molecular structures of the synthesized compounds were corroborated by mass spectrometry, further confirming their identities and molecular compositions.

4. Experimental

General procedure for synthesis of (6a-6j)

To a mixture of compound (**4**),[195] (50 mmol), the appropriate aryl or heteroaryl aldehydes (**5a–5j**), (50 mmol), and methanol (100 mL) containing a catalytic amount of glacial acetic acid was stirred at 75 ºC for 24 h. The progress of the reaction was monitored by thin-layer chromatography (TLC). Upon completion, the reaction mixture was cooled to room temperature, resulting in the precipitation of the crude product. The precipitate was collected by filtration, washed sequentially with water, cold ethanol, and diethyl ether, and subsequently dried to yield the (E)-N'-substituted methylenebenzylidene-4-((7-chloroquinolin-4-yl) amino) benzohydrazide (**6a-6j**).

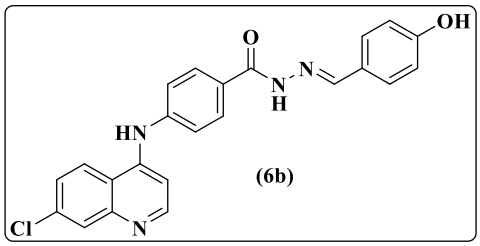
Synthesis of N'-benzylidene-4-((7-chloroquinolin-4-yl) amino) benzohydrazide (6a):



(6a)

Yield: 49.2%; MP: 262-264°C. FTIR (KBr, cm^{-1}), 3179.79 (N-H), 1669.50 (C=O), 1575.91 (C=C), 1558.55 (C=N). ^{1}H NMR [400MHz, δ ppm, DMSO-*d6*]; 7.22-7.20 (d, 1H, *J*=8Hz, Ar-H), 7.49-7.43 (m, 5H, Ar-H), 7.64-7.61 (m, 1H, *J*=9.2 Hz, Ar-H), 7.74-7.72 (d, 2H *J*=8Hz, Ar-H), 7.98-7.95 (m, 3H, Ar-H), 8.47-8.41 (m, 2H, Ar-H). 8.59-8.58 (d, 1H, *J*=4Hz), 9.35 (s, 1H, Ar-NH-Ar), 11.78 (s, 1H, -CONH). ^{13}C NMR [100 MHz, δ ppm, DMSO-*d6*]; 103.90, 118.98, 119.93, 124.56, 125.31, 126.95, 127.73, 128.77, 129.07, 134.05, 134.38, 146.51, 149.62, 152.03. Chemical Formula: $C_{23}H_{17}ClN_4O$; Molecular mass; calculated: 400, LCMS; m/z 401(M+1).

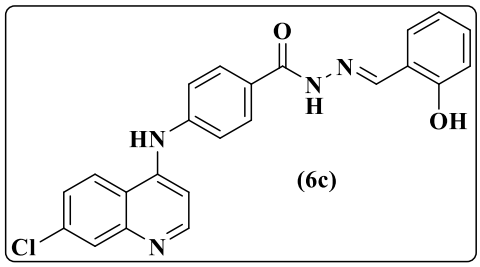
Synthesis of 4-((7-chloroquinolin-4-yl) amino)-N'-(4-hydroxy benzylidene) benzohydrazide (6b):



(6b)

Yield: 88.79%, MP: 280-282°C. FTIR (KBr, cm^{-1}); 3530.85 (O-H), 3272.38 (N-H), 3100.70 (Ar-CH), 1653.07 (C=O), 1574.95 (C=C), 1558.55 (C=N). ^{1}H NMR [400MHz, δ, ppm, DMSO-*d6*]; 6.84-6.82 (d, 2H, *J*=8Hz, Ar-H), 7.19-7.17 (d, 1H, *J*=8 Hz, Ar-H) 7.62-7.43 (m, 5H, Ar-H) 7.95-7.93 (m, 3H, Ar-H), 8.42-8.35 (m, 2H, Ar-H), 8.58-8.56 (d, 1H, *J*= 8 Hz, Ar-H), 9.32 (s, 1H, Ar-NH-Ar), 9.88 (s, 1H, OH), 11.56 (s, 1H, -CONH). ^{13}C NMR [100MHz, δ ppm, DMSO-*d6*]; 103.78, 115.55, 117.45, 119.96, 120.05, 124.57, 125.30, 125.38, 127.74, 128.71, 128.97, 134.05, 146.60, 147.61, 149.63, 152.04. Chemical Formula: $C_{23}H_{17}ClN_4O_2$; Molecular mass; calculated: 416, LCMS; m/z 417(M+1).

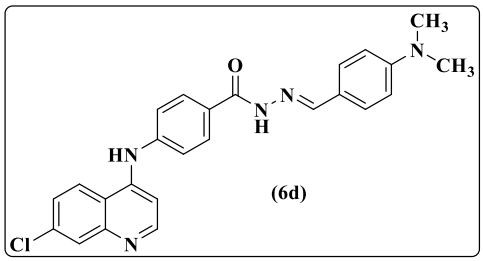
Synthesis of 4-(2-((E)-5-((Z)-4-hydroxybenzylidene)-4-oxo-2-(phenylimino) thiazolidin-3-yl) ethyl) benzenesulfonamide (6c):



(6c)

Yield: 77.2%, MP: 263-265°C. FTIR (KBr, cm^{-1}); 3279.13 (N-H), 3312.88 (O-H), 3015.58 (Ar-CH), 1665.60 (C=O), 1575.91 (C=C), 1532.51 (C=N). ^{1}H NMR [400MHz, δ ppm, DMSO-*d6*]; 6.97-6.93 (m, 2H, Ar-H), 7.34-7.24 (m ,2H, Ar-H), 7.55-7.50 (m, 3H, Ar-H), 7.66-7.64 (m, 1H, Ar-H), 8.00-7.95 (m, 3H, Ar-H), 8,45-8.42 (d, 1H, *J*=8.8Hz, Ar-H), 8.66-8.60 (m, 2H, Ar-H), 9.42 (s, 1H, Ar-NH-Ar), 11.39 (s, 1H, -CONH), 12.06 (s, 1H, -OH). ^{13}C NMR [100MHz, δ ppm, DMSO-*d6*]; 104.61, 116.94, 119.87, 120.43, 125.19, 125.97, 129.73, 137.17, 144.91, 146.97, 148.39, 152.64, 154.34, 157.96, 172.52. Chemical Formula: $C_{23}H_{17}ClN_4O_2$; Molecular mass; calculated: 416, LCMS; m/z 417(M+1)**.**

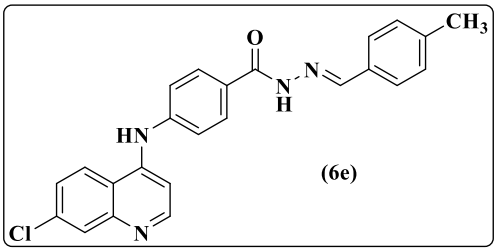
4-((7-chloroquinolin-4-yl) amino)-N'-(4-(dimethyl amino) benzylidene) benzohydrazide (6d):



(6d)

Yield: 78.2 MP: 234-237°C. FTIR (KBr, cm^{-1}); 3298.60 (N-H), 1611.59 (C=O), 1569.15 (C=C), 1525.72 (C=N). ^{1}H NMR [400MHz,δ, ppm, DMSO-*d6*]; 2.99 (s, 6H, N-(CH3)2), 6.78-6.76 (d, 1H, *J*=8Hz, Ar-H), 7.22-7.20 (d, 1H, *J*=5.6Hz, Ar-H), 7.50-7.48 (m, 3H, Ar-H), 7.655-7.651 (m, 2H, Ar-H), 7.98-7.96 (m, 4H, Ar-H), 8.33(s, 1H, Ar-H), 8.45-8.43 (d, 1H, Ar-H), 8.60-8.59 (d, 1H, Ar-H), 9.38 (s, 1H, Ar-NH-Ar), 11.54 (s, 1H, -CO-NH). ^{13}C NMR [100MHz, δ ppm, DMSO-*d6*]; 49.13, 104.23, 112.33, 120.64, 125.15, 125.88, 128.31, 128.90, 129.52, 147.17, 148.70, 150.18, 152.63, 162.59. Chemical Formula: $C_{25}H_{22}ClN_5O$; Molecular mass; calculated: 443, LCMS; m/z 444(M+1).

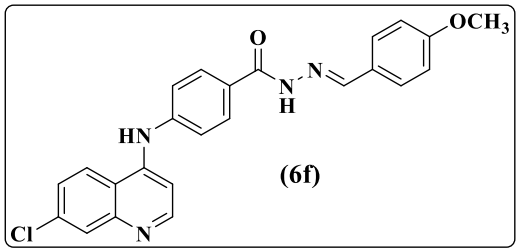
Synthesis of 4-((7-chloroquinolin-4-yl) amino)-N'-(4-methylbenzylidene) benzohydrazide (6e):



(6e)

Yield: 66.6%, MP: 241-243°C. FTIR (KBr, cm^{-1}); 3259.84 (N-H), 1679.11 (C=O), 1573.98 (C=C), 1537.33 (C=N). ^{1}H NMR [400 MHz, δ ppm, DMSO-*d6*]: 2.35 (s, 3H, -CH3), 7.19-7.18 (d, 1H, *J*= 4Hz, Ar-H), 7.28-7.26 (d, 2H, *J*=8Hz, Ar-H), 7.47-7.45 (d, 2H, *J*=8Hz, Ar-H), 7.63-7.60 (m, 4H, Ar-H), 7.95-7.94 (m, 4H, Ar-H), 8.43-8.41 (d, 2H, *J*= 9.2 Hz, Ar-H), 8.58-8.56 (d, 1H, *J*= 5.2 Hz, Ar-H). ^{13}C NMR [100 MHz, δ ppm, DMSO-*d6*]: 20.96, 103.77, 118.94, 119.97, 124.60, 125.25, 126.93, 127.66, 129.05, 129.37, 131.75, 134.03, 139.65, 146.67, 149.60, 151.97. Chemical Formula: $C_{24}H_{19}ClN_4O$; Molecular mass; calculated: 414, LCMS: m/z 411(M+1).

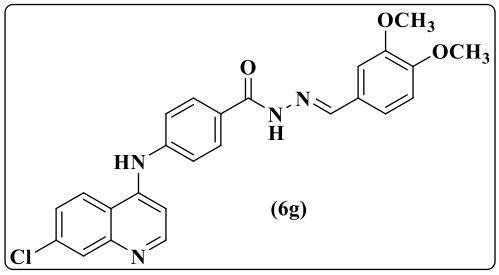
.Synthesis of 4-((7-chloroquinolin-4-yl) amino)-N'-(4-methoxybenzylidene) benzohydrazide (6f):



(6f)

Yield: 78.8%; MP: 233-250°C. FTIR (KBr, cm^{-1}); 3179.79 (N-H), 3060.20 (Ar-CH), 1649.21 (C=O), 1576.87 (C=C), 1529.62 (C=N). ^{1}H NMR [400 MHz, δ ppm, DMSO-*d6*]: 3.80 (s, 3H, -OCH3), 7.03-7.01 (d, 2H, *J*=8.4Hz, Ar-H), 7.19-7.18 (d, 1H, *J*= 5.2 Hz, Ar-H), 7.47-7.45 (d, 2H, *J*=8.4 Hz, Ar-H), 7.69-7.59 (m, 4H, Ar-H), 7.94 (t, 2H, Ar-H), 8.42-8.40 (d, 2H, *J*= 9.2 Hz, Ar-H), 8.58-8.57 (d, 1H, *J*= 5.2, Ar-H), 9.32 (s, 1H, Ar-NH-Ar), 11.64 (s, 1H, -CONH). ^{13}C NMR [100 MHz, δ ppm, DMSO-*d6*]: 55.25, 103.83, 114.30, 118.92, 120.0, 124.57, 125.31, 126.96, 127.73, 128.56, 129.01, 134.05, 146.58, 147.17, 149.63, 152.04, 160.73. Chemical Formula: $C_{24}H_{19}ClN_4O_2$; Molecular mass; calculated: 430, LCMS; m/z 431(M+1).

Synthesis of 4-((7-chloroquinolin-4-yl) amino)-N'-(3, 4-dimethoxy benzylidene) benzohydrazide (6g):

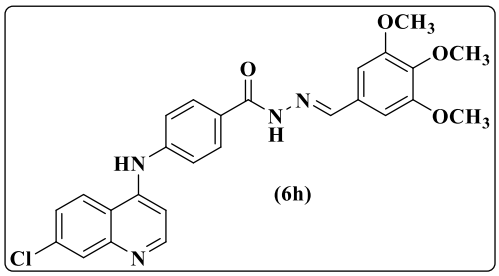


(6g)

Yield: 72.10%, MP: 165-167°C. FTIR (KBr, cm^{-1}); 3275.27 (N-H), 3126.74 (Ar-CH), 1670.43 (C=O), 1572.05 (C=C), 1532.51 (C=N). ^{1}H NMR [400MHz, δ ppm, DMSO-*d6*]; 3.81-3.80 (d, 6H, *J*=4Hz, -OCH3), 7.03-7.01 (d, 1H, *J*=8Hz, Ar-H), 7.13-7.11 (d, 1H, *J*=8Hz, Ar-H), 7.19-7.18 (d, 1H, *J*=4Hz, Ar-H), 7.40-7.34 (m, 2H, Ar-H), 7.49-7.45 (m, 1H, Ar-H), 7.62-7.59 (m, 1H, Ar-H), 7.86-7.84 (d, 1H, *J*=8Hz, Ar-H), 7.96-7.94 (m, 2H, Ar-H), 8.42-8.40 (m, 2H, Ar-H), 8.58-8.56 (m, 1H, Ar-H), 9.33 (s, 1H, Ar-NH-Ar), 11.65 (s, 1H, -CONH). ^{13}C NMR [100MHz, δ ppm, DMSO-*d6*]; 55.56, 103.82, 108.26, 111.51, 118.94, 120.03, 120.24, 121.74, 124.58, 125.33, 127.56, 127.75, 128.31, 129.03, 134.07, 143.94,

146.60, 147.54, 149.06, 149.64, 150.66, 152.04. Chemical Formula: $C_{25}H_{21}ClN_4O_3$; Molecular mass; calculated: 460, LCMS; m/z 461(M+1).

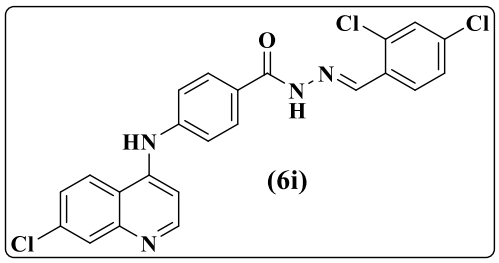
Synthesis of 4-((7-chloroquinolin-4-yl) amino)-N'-(3, 4, 5-trimethoxybenzylidene) benzohydrazide (6h):



(6h)

Yield: 66.2%, MP: 242-245 °C. FTIR (KBr, cm^{-1}); 3179.79 (N-H), 3108.96 (Ar-CH), 1671.39 (C=O), 1576.87 (C=C), 1534.44 (C=N). ^{1}H NMR [400MHz, δ ppm, DMSO-*d6*]; 3.70 (s, 3H, -OCH3), 3.84 (s, 6H, -(OCH3)2), 7.01 (S, 1H, Ar-H), 7.20-7.18 (d, 1H, *J*=5.2Hz, Ar-H), 7.48-7.46 (d, 2H, *J*=8.4Hz, Ar-H), 7.62-7.60 (m, 2H, Ar-H), 7.96-7.94 (m, 2H, Ar-H), 8.42-8.40 (m, 2H, Ar-H), 8.58-8.57 (d, 1H, *J*=5.2Hz, Ar-H), 9.33 (s, 1H, Ar-NH-Ar), 11.76 (s, 1H, -CONH). ^{13}C NMR [100MHz, δ ppm, DMSO-*d6*]; 55.914, 60.066, 103.85, 104.21, 118.92, 119.95, 124.56, 125.31, 127.73, 129.08, 129.90, 146.54, 149.62, 152.02, 153.15. Chemical Formula: $C_{25}H_{21}ClN_4O_3$; Molecular mass; calculated: 490, LCMS; m/z 489(M+1).

Synthesis of 4-((7-chloroquinolin-4-yl) amino)-N'-(2,4-dichloro benzylidene) benzohydrazide (6i):

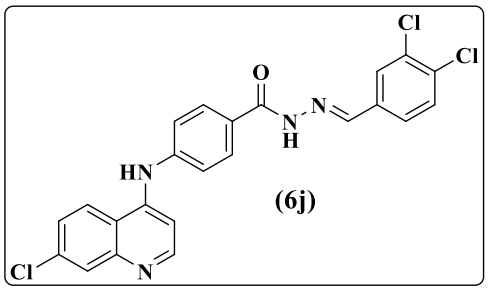


(6i)

Yield: 86.6%, MP: 247-250°C. FTIR (KBr, cm^{-1}); 3099.74 (N-H), 3001.37 (Ar-CH), 1678.14 (C=O), 1575.91 (C=C), 1533.47 (C=N). ^{1}H NMR [400MHz, δ ppm, DMSO-d_6]; 7.25-7.24 (d,1H, *J*=5.2Hz, Ar-H), 7.54-7.50 (m, 3H, Ar-H), 7.66-7.63 (m, 1H, Ar-H), 7.756-7.751 (d, 1H, *J*=2Hz, Ar-H), 8.04-7.98 (m, 4H, Ar-H), 8.44-8.42 (d, 1H, *J*=9.2Hz, Ar-H), 8.62-8.60 (d, 1H, *J*=9.2Hz, Ar-H), 8.84 (s, 1H, Ar-H), 9.41 (s, 1H, Ar-NH-Ar), 12.12 (s, 1H, -CONH). ^{13}C NMR [100MHz, δ ppm, DMSO-d_6]; 104.60, 119.53, 120.16, 125.0, 125.96, 127.30, 128.51, 129.68, 131.25, 134.39, 134.55, 135.48, 142.51, 144.91, 146.95, 150.0,

152.52, 162.81. Chemical Formula: $C_{23}H_{15}Cl_3N_4O$; Molecular mass; calculated: 469, LCMS; *m/z* 470(M+1).

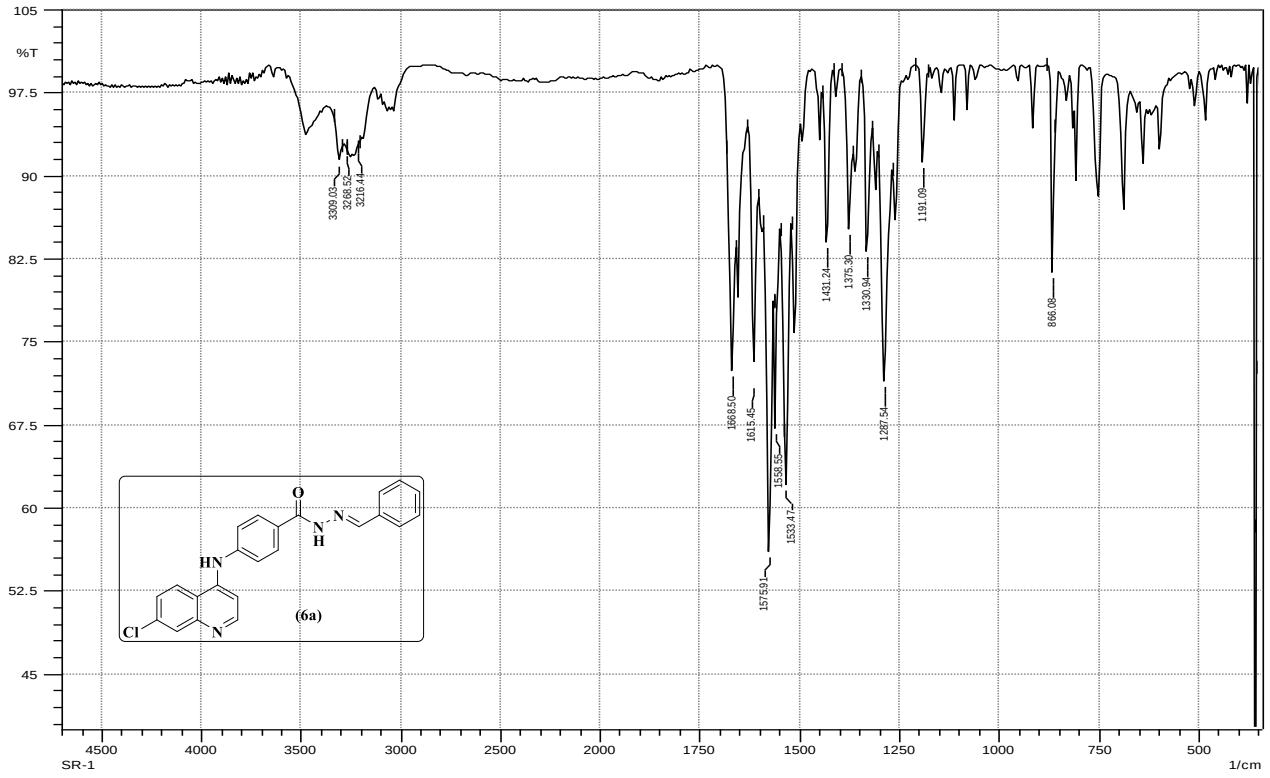
Synthesis of 4-((7-chloroquinolin-4-yl) amino)-N'-(3,4-dichlorobenzylidene) benzohydrazide (6j):



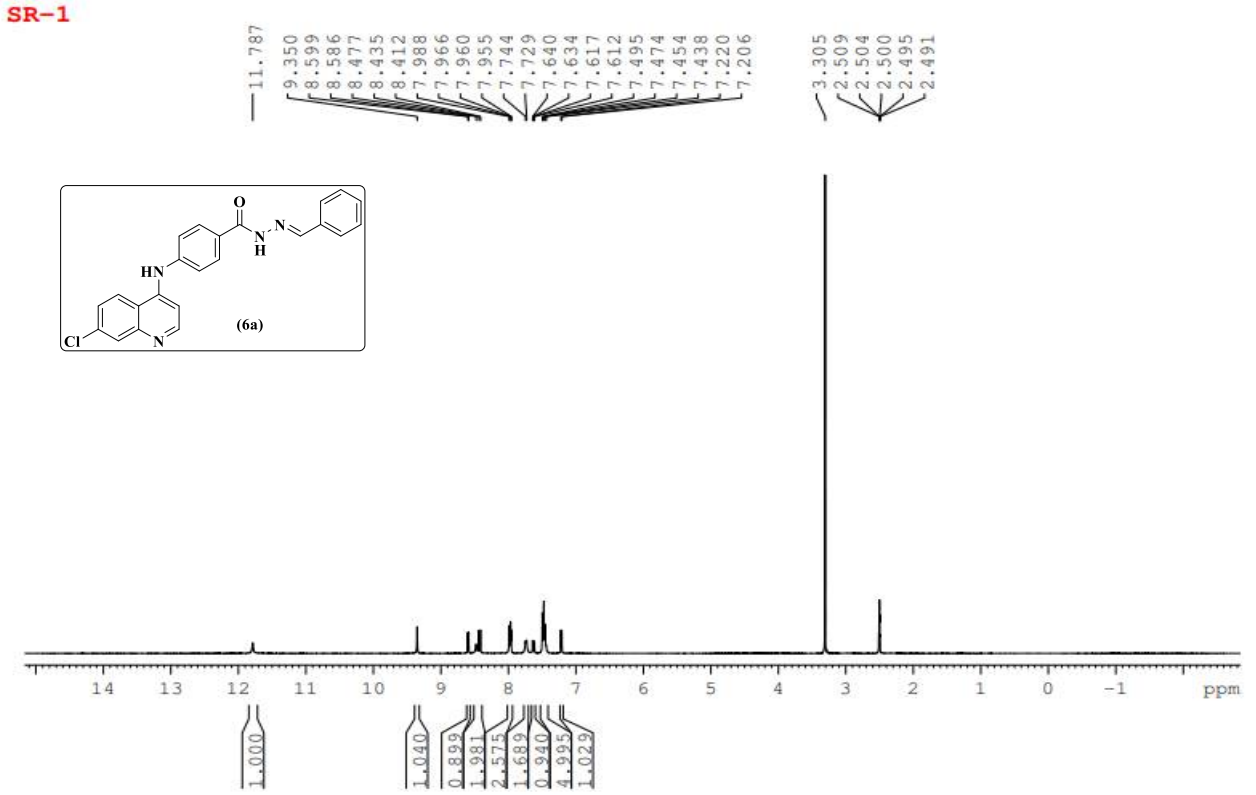
(6j)

Yield: 53.3% MP: 253-256 °C. FTIR (KBr, cm^{-1}); 3250.91 (N-H), 3029.34 (Ar-CH), 1663.07 (C=O), 1575.91 (C=C), 1533.47 (C=N). ^{1}H NMR [400MHz, δ ppm, DMSO-*d6*]; 7.16-7.14 (d, 1H, *J*=8Hz, Ar-H), 7.52-7.24 (d, 1H, Ar-H), 7.43-7.41 (m, 1H), 7.51-7.49 (d, 1H, *J*=8Hz, Ar-H), 7.68-7.61 (m, 2H, Ar-H), 7.89-7.87 (m, 1H, Ar-H), 7.97-7.95 (m, 1H, Ar-H), 8.44-8.41 (m, 1H, Ar-H), 8.57-8.56 (m, 1H, Ar-H), 8.62-8.60 (m, 1H, Ar-H), 9.31 (s, 1H, Ar-H), 9.41 (s, 1H, Ar-NH-Ar), 9.73 (S, 1H), 12.05 (s, 1H, -CO-NH). ^{13}C NMR [100MHz,δ ppm, DMSO-*d6*]; 103.97, 119.35, 120.78, 125.13, 125.83, 128.27, 128.87, 129.79, 134.60, 147.28, 150.15, 152.61, 165.97. Chemical Formula: $C_{23}H_{15}Cl_3N_4O$; Molecular mass; calculated: 469, LCMS; m/z 470(M+1).

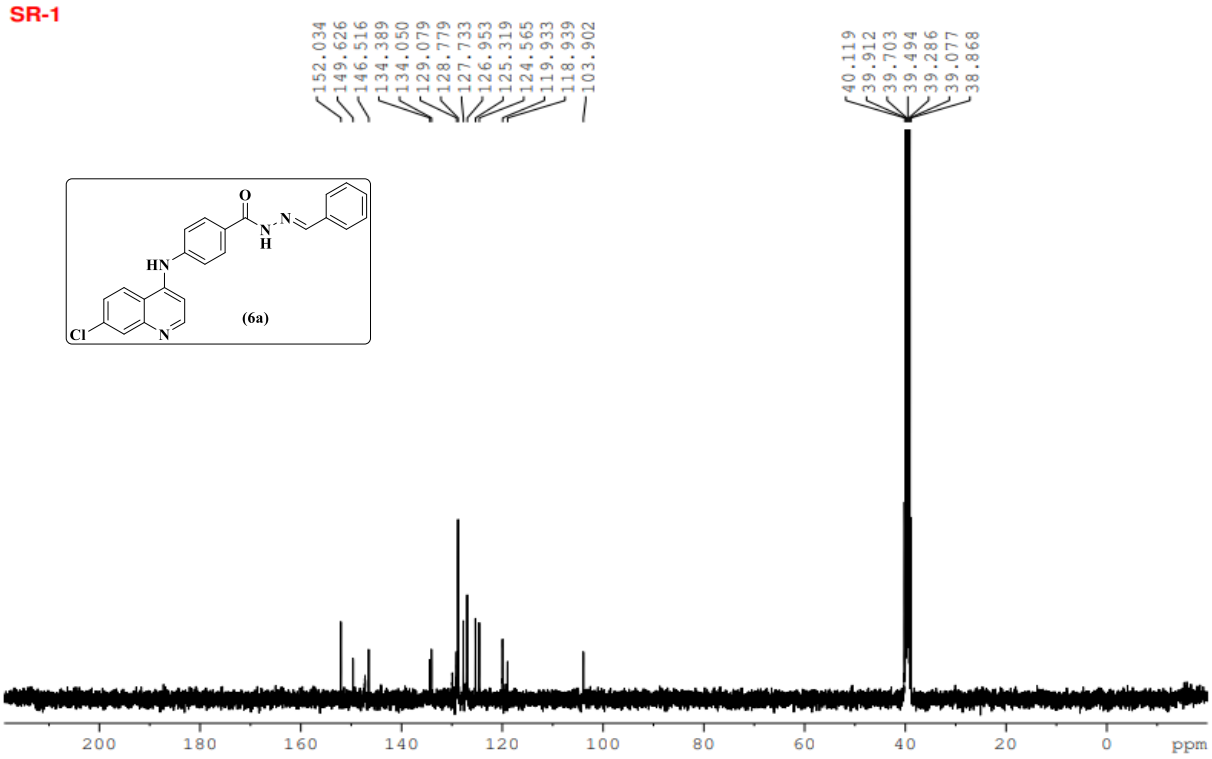
5. Spectral data evaluation



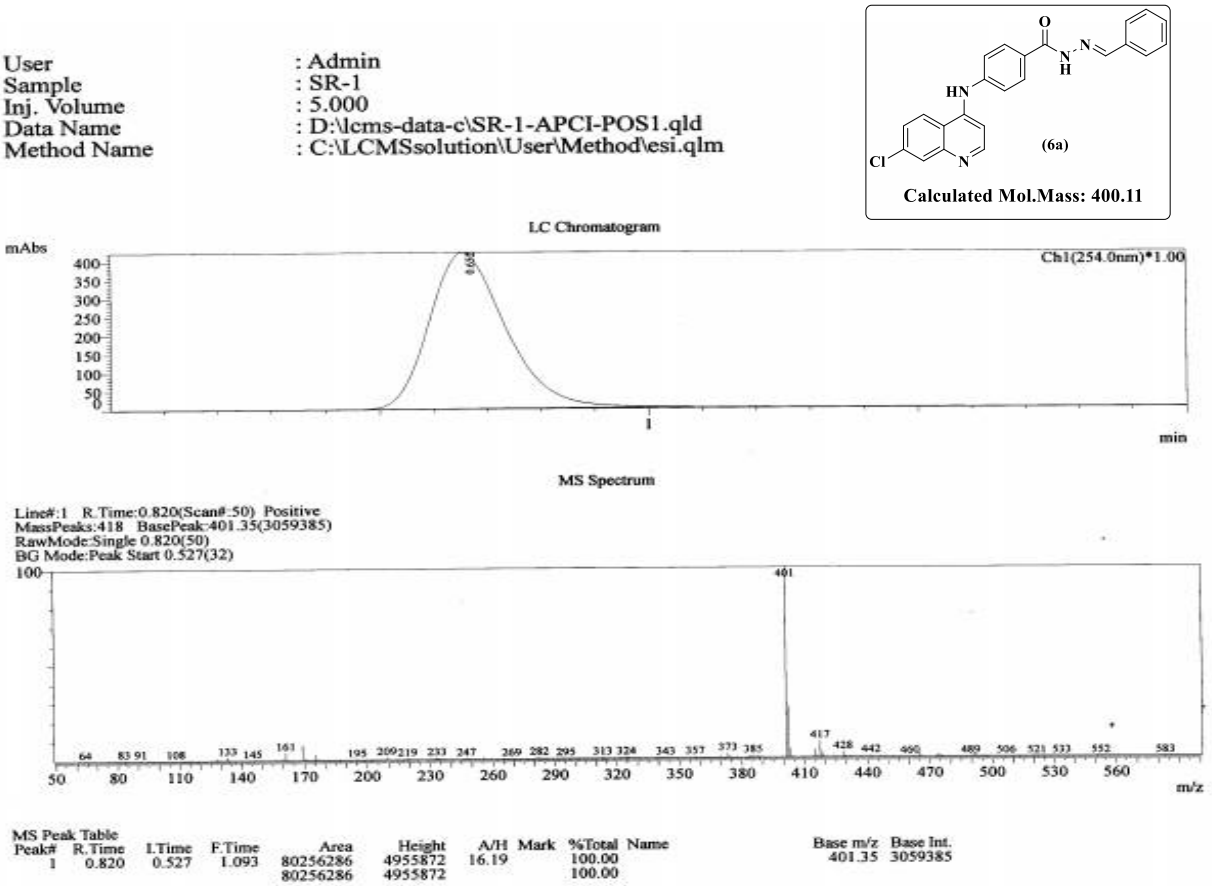
Spectra. 82: FTIR (KBr, cm^{-1}) spectra of compound 6a



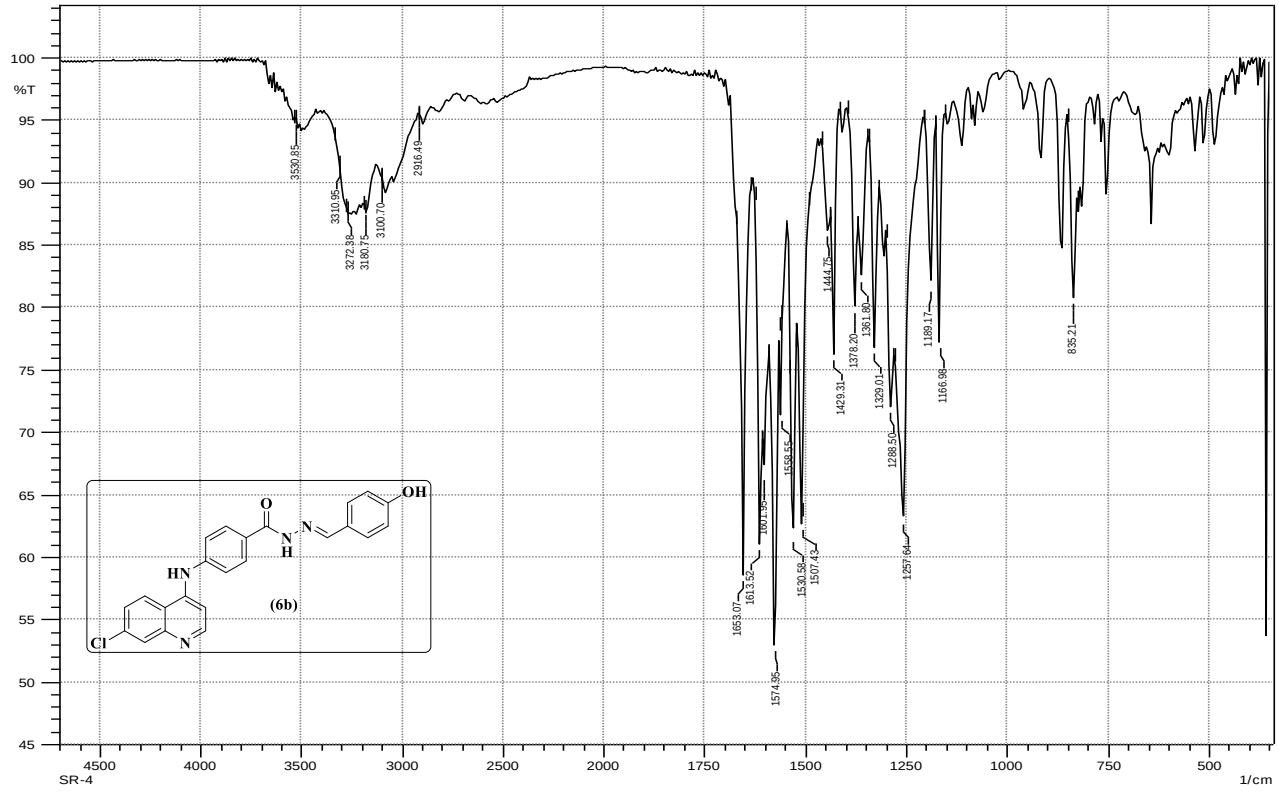
Spectra. 83: ^{1}H NMR (400 MHz, δ, ppm) spectra of compound 6a



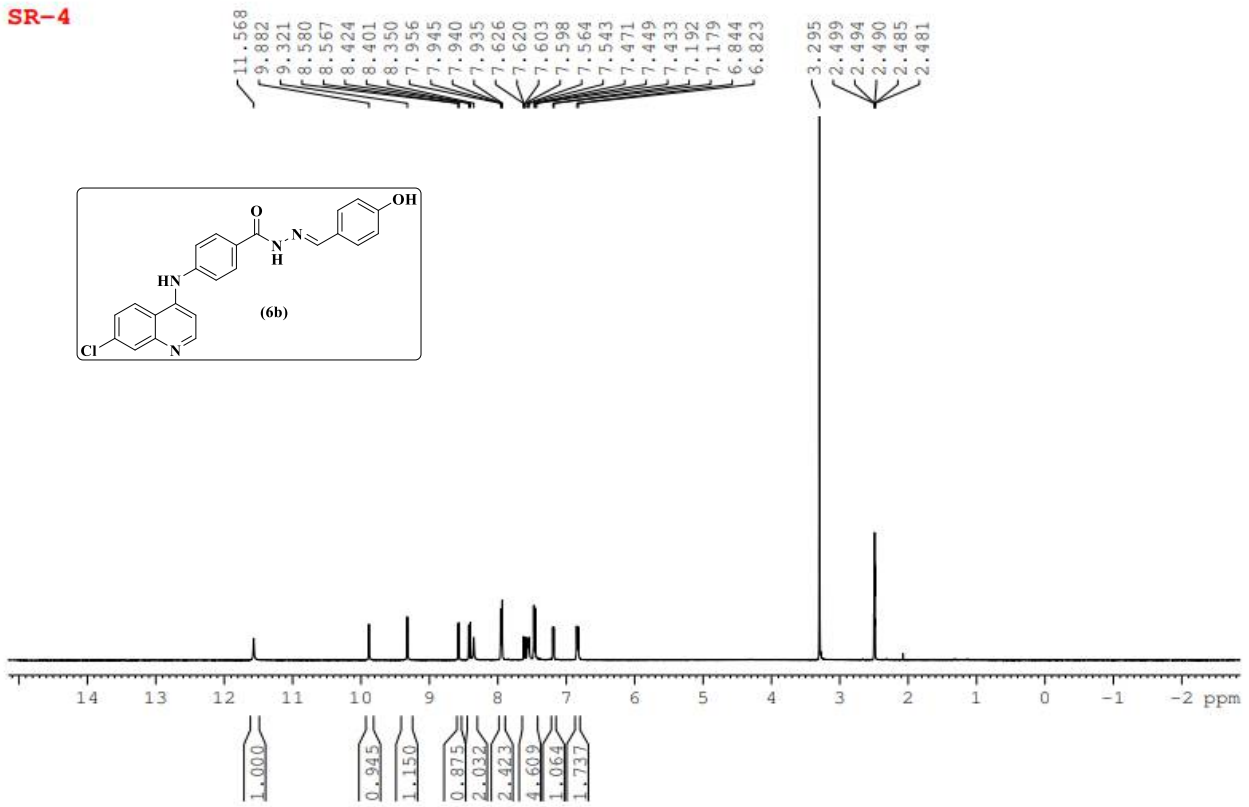
Spectra. 84: ^{13}C NMR (100 MHz, δ, ppm) spectra of compound 6a



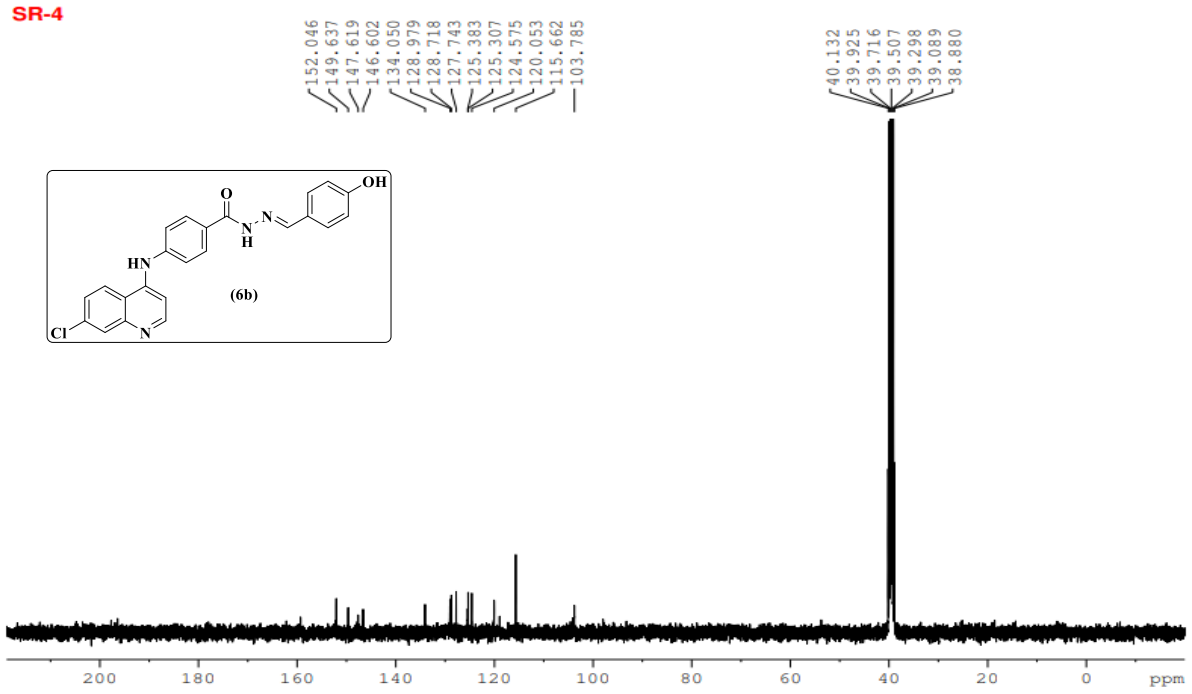
Spectra. 85: LCMS Spectra of compound 6a



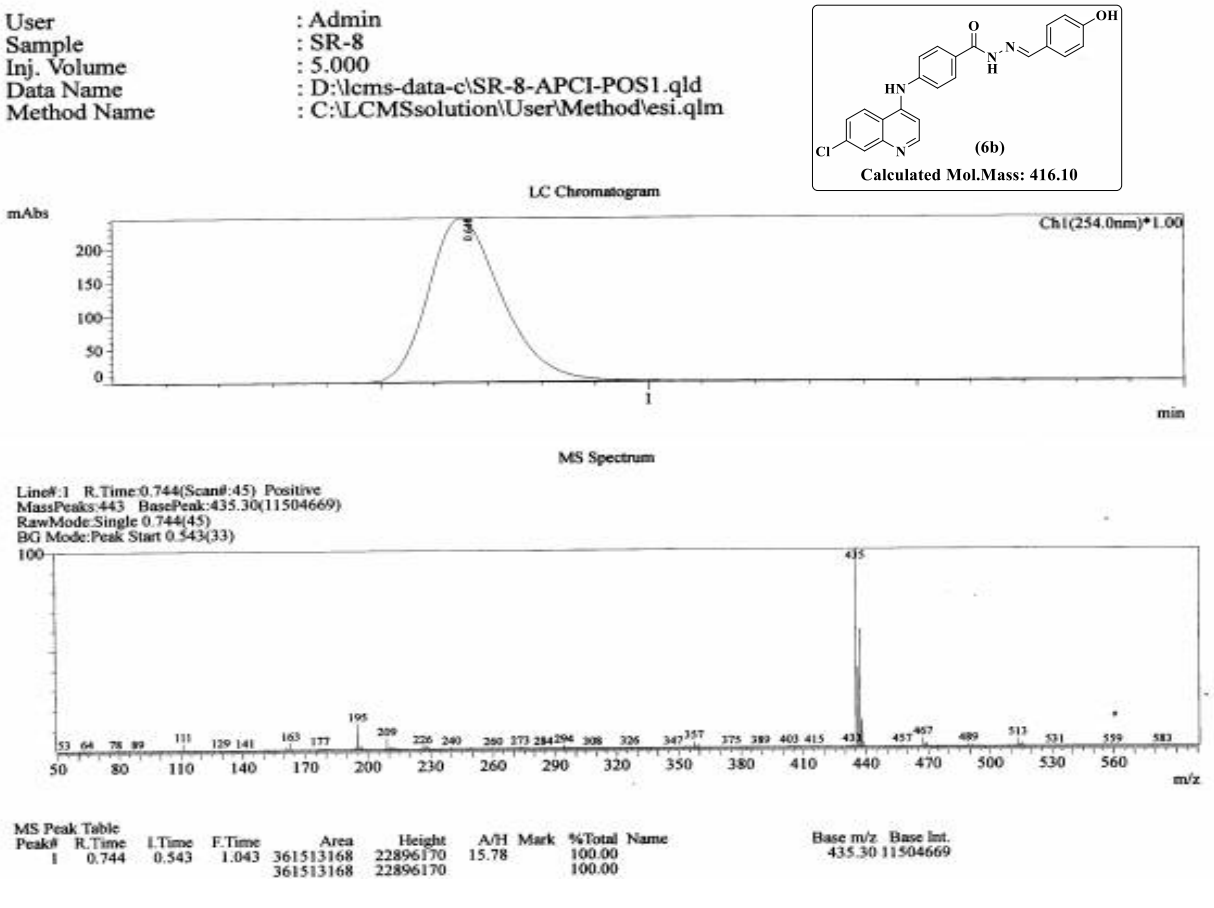
Spectra. 86: FTIR (KBr, cm^{-1}) spectra of compound 6b



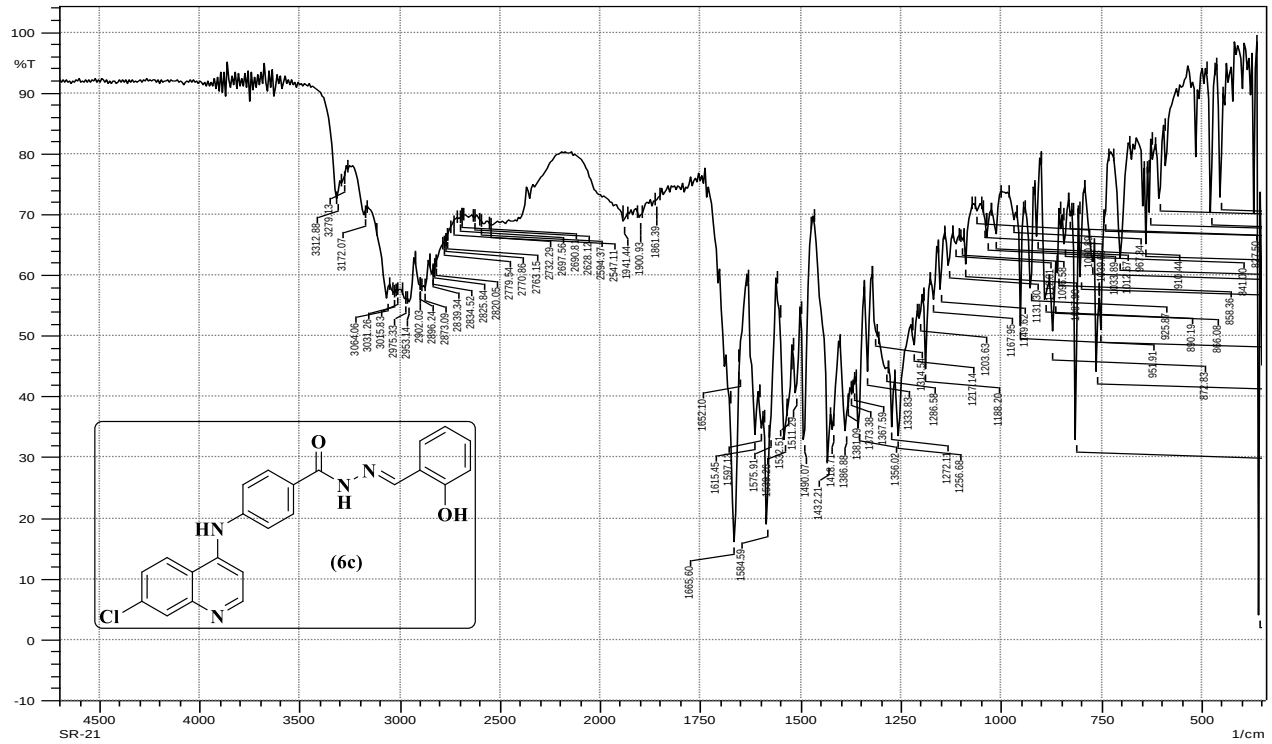
Spectra. 87: ^{1}H NMR (400 MHz, δ, ppm) spectra of compound 6b



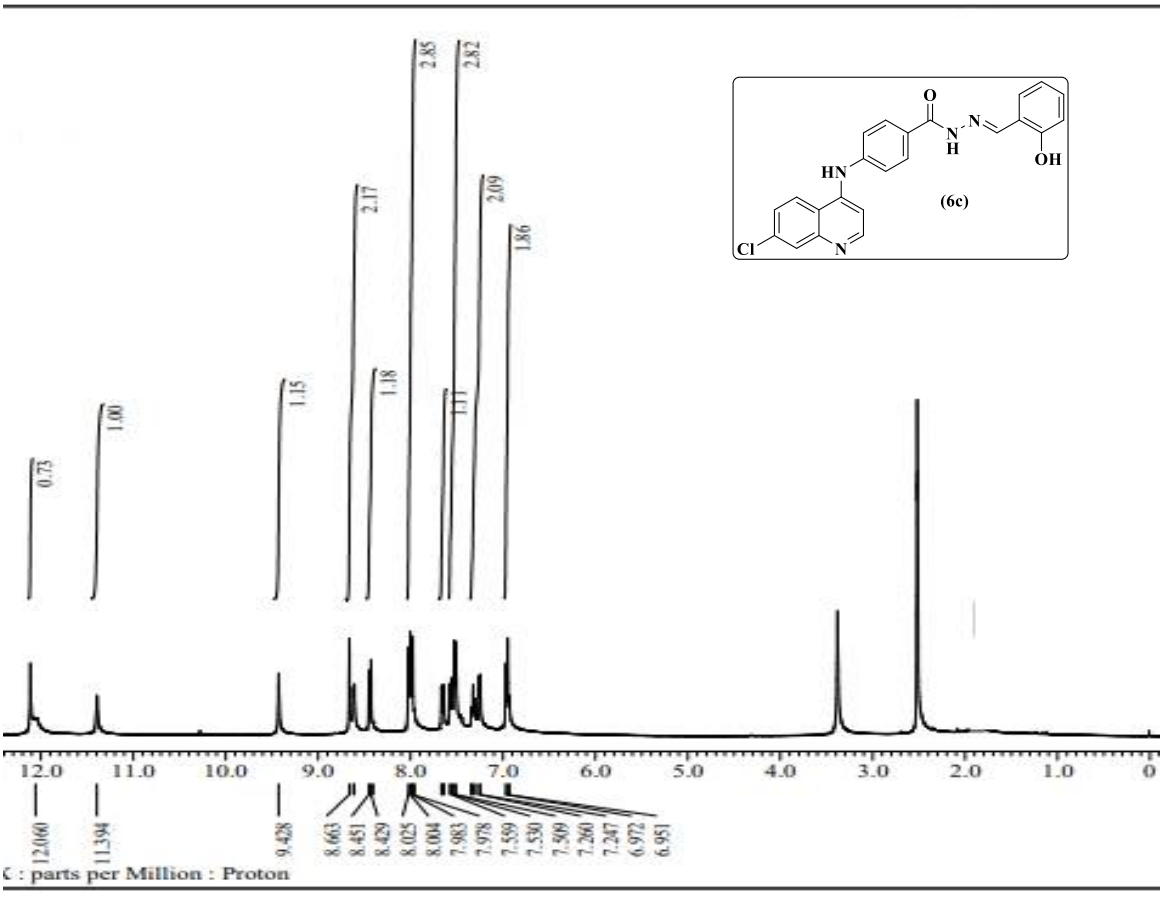
Spectra. 88: ^{13}C NMR (100 MHz, δ, ppm) spectra of compound 6b



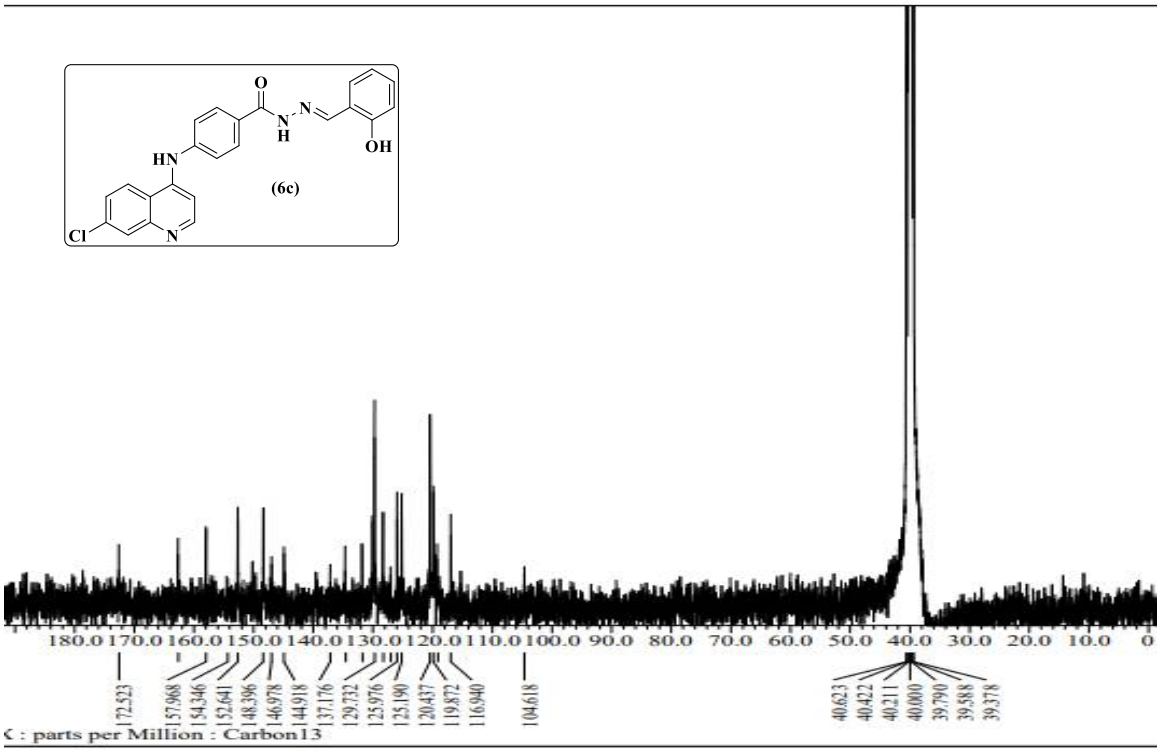
Spectra. 89: LCMS Spectra of compound 6b



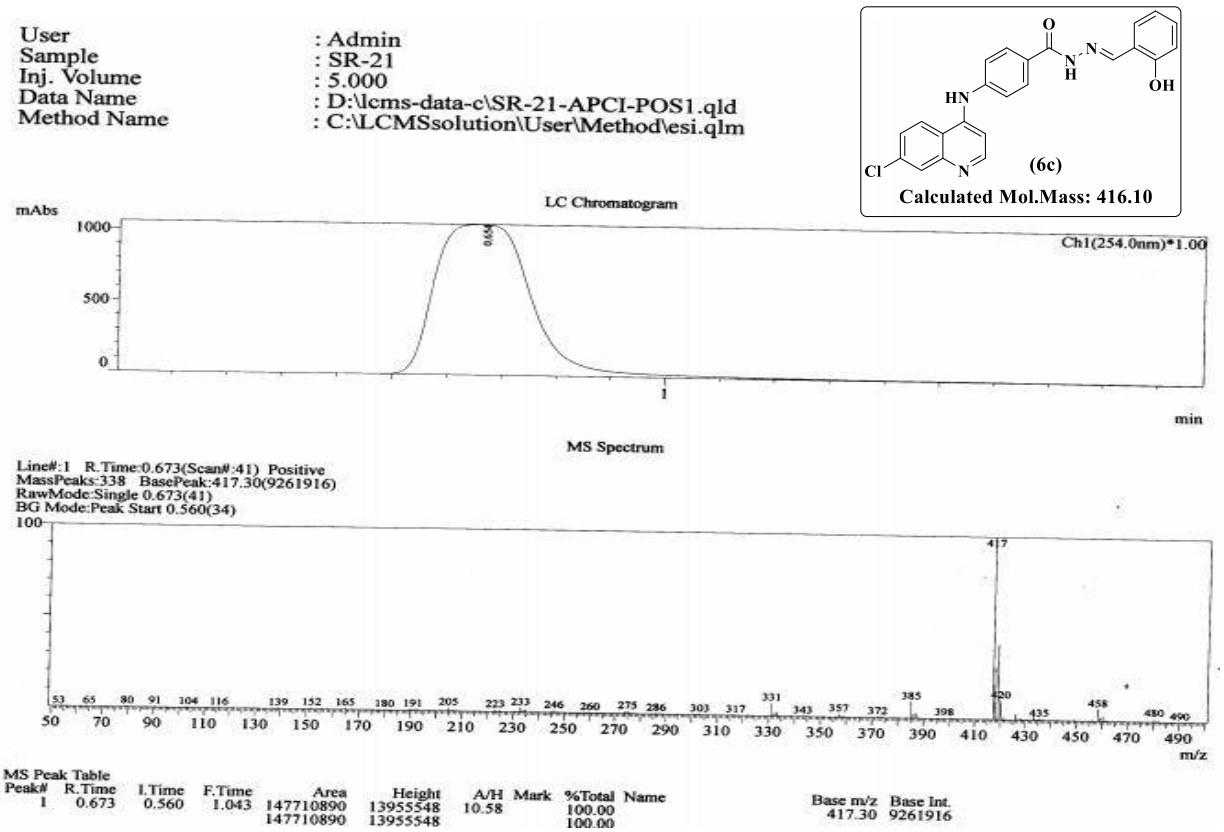
Spectra. 90: FTIR (KBr, cm^{-1}) spectra of compound 6c



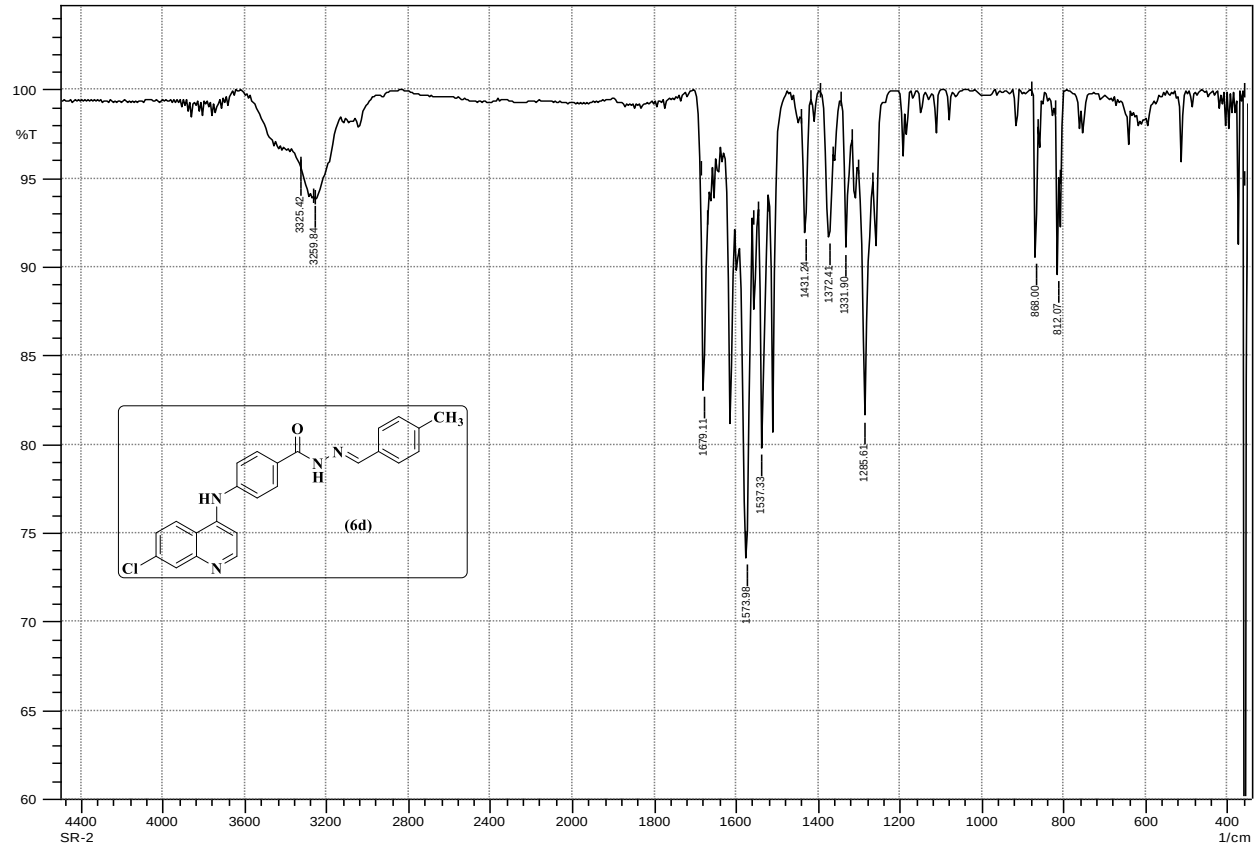
Spectra. 91: ^{1}H NMR (400 MHz, δ, ppm) spectra of compound 6c



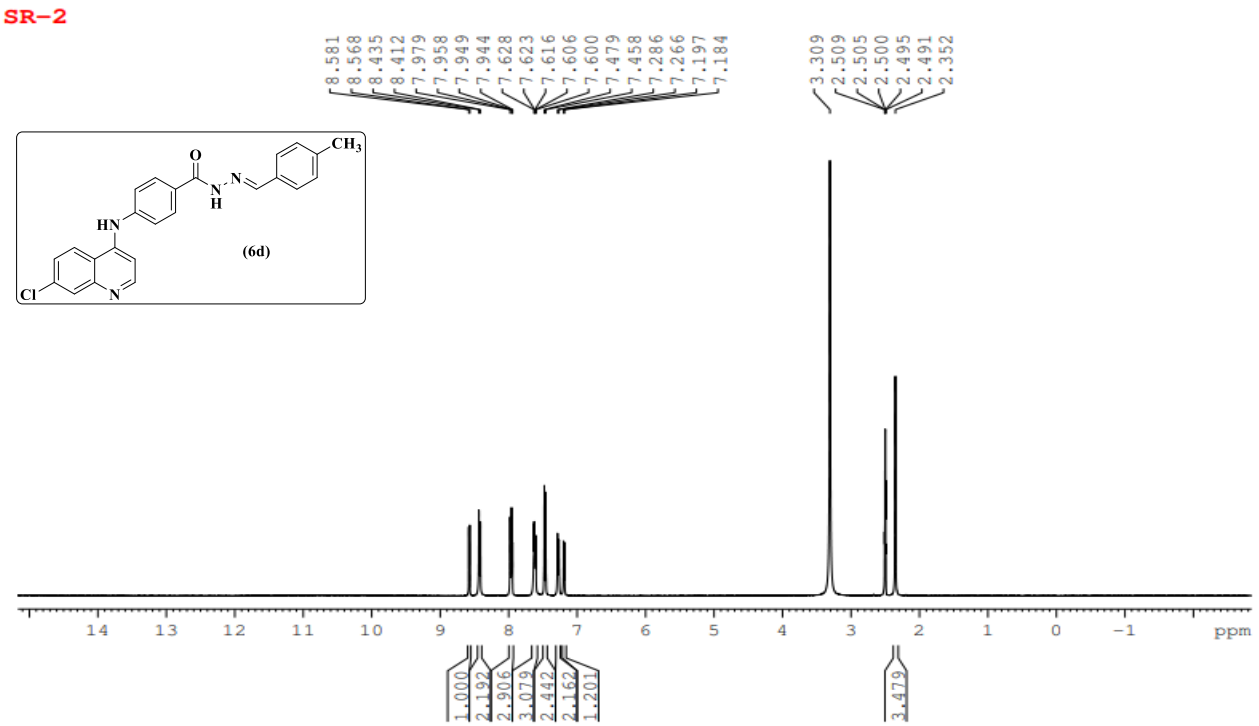
Spectra. 92: ^{13}C NMR (100 MHz, δ, ppm) spectra of compound 6c



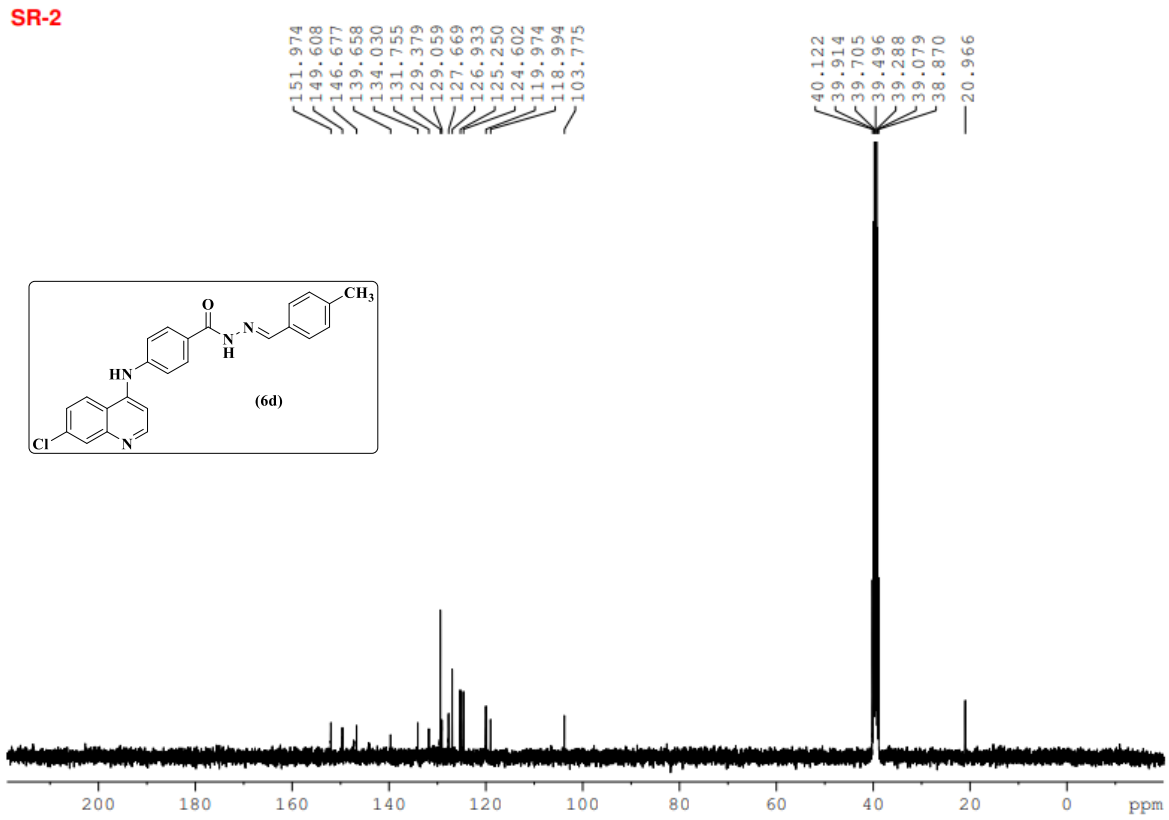
Spectra. 93: LCMS spectra of compound 6c



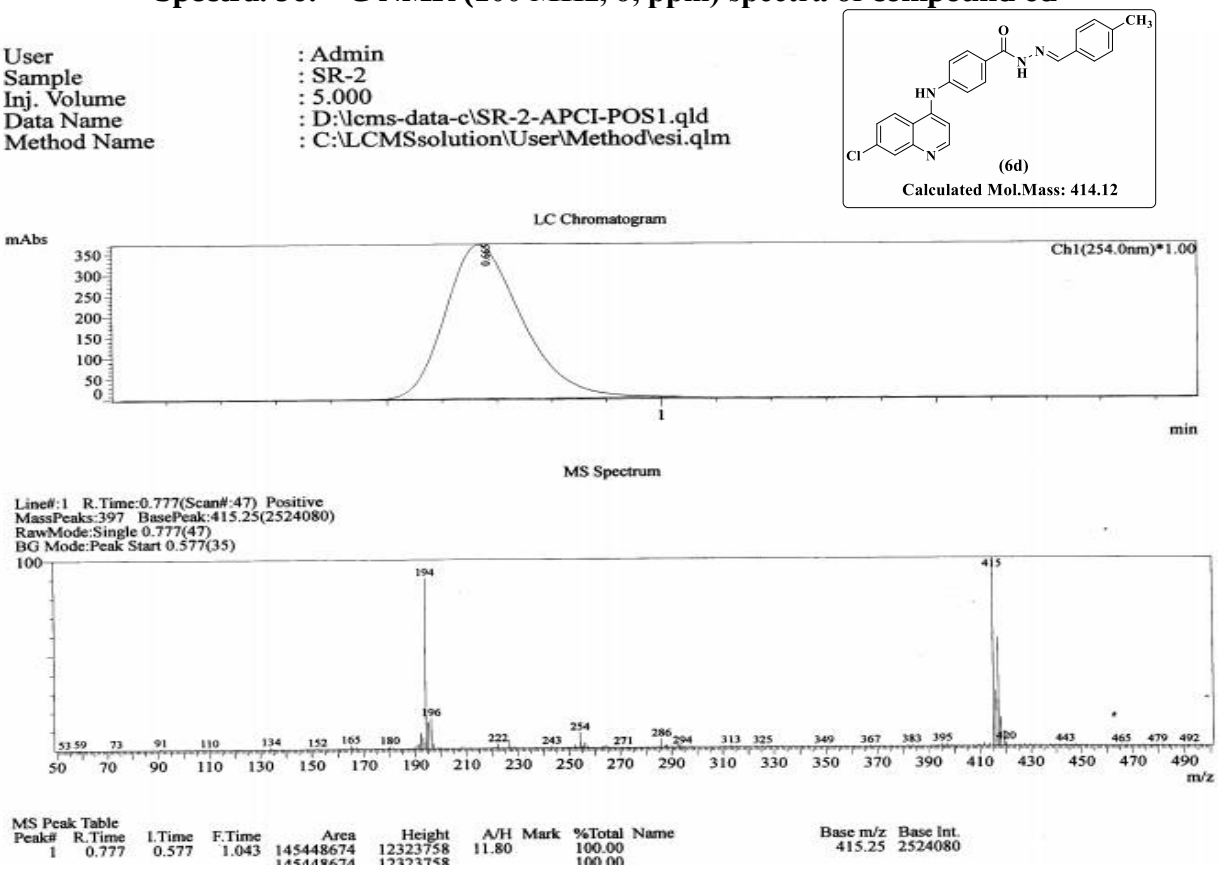
Spectra. 94: FTIR (KBr, cm^{-1}) spectra of compound 6d



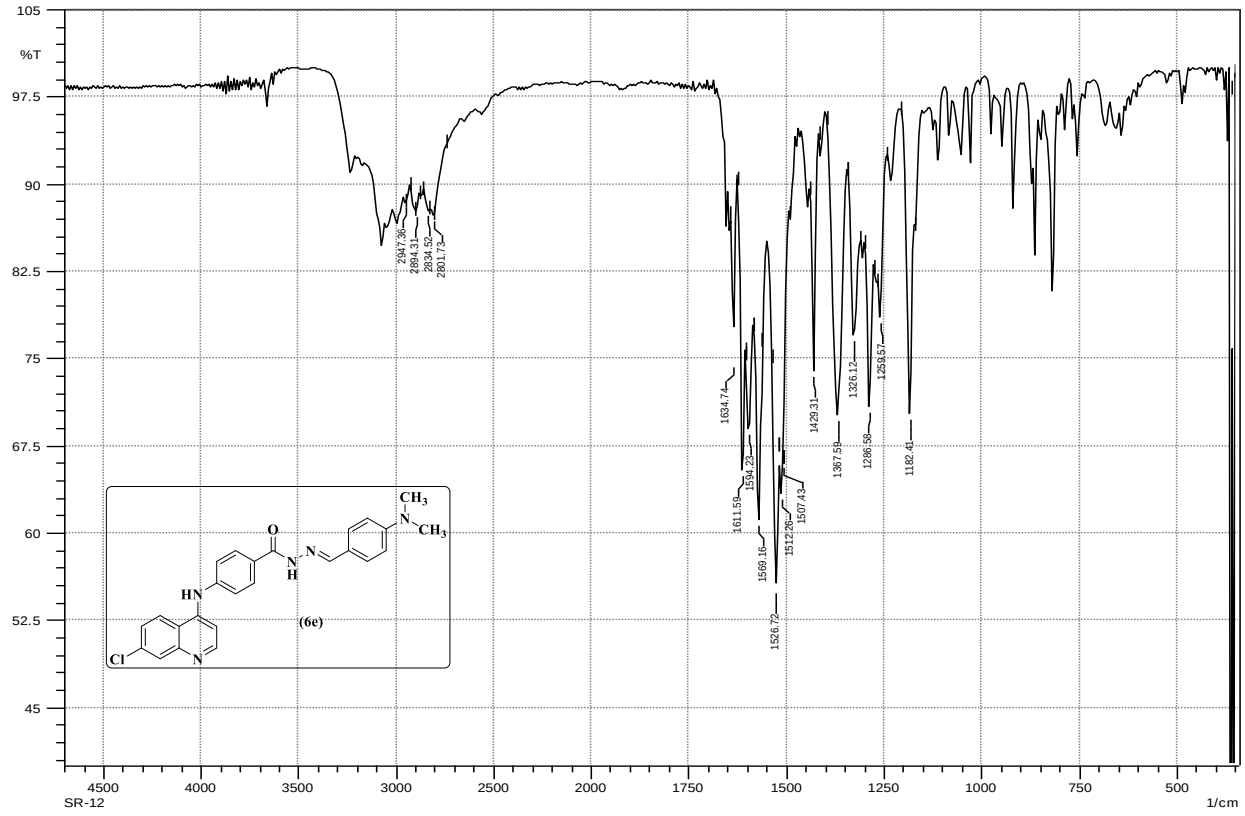
Spectra. 95: ^{1}H NMR (400 MHz, δ, ppm) spectra of compound 6d



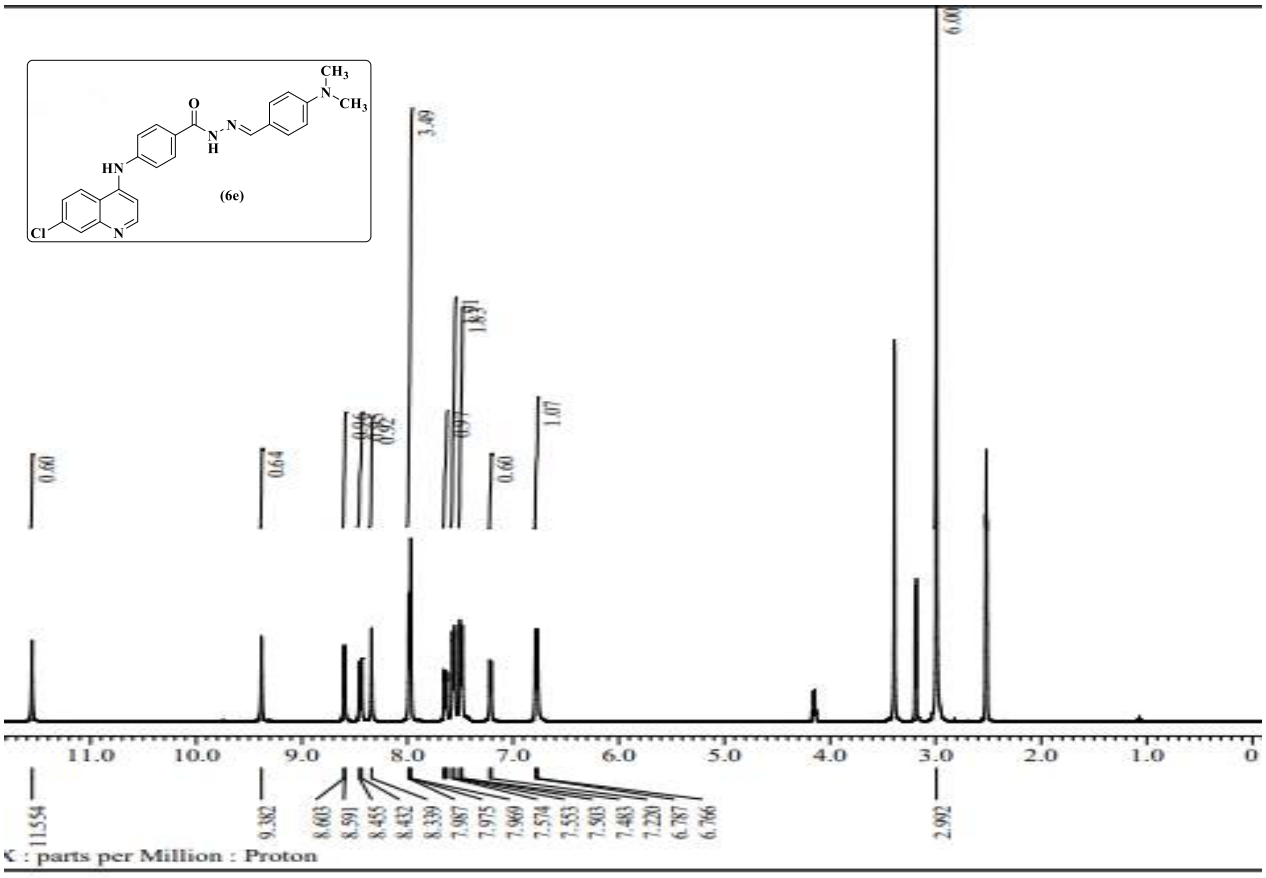
Spectra. 96: ^{13}C NMR (100 MHz, δ, ppm) spectra of compound 6d



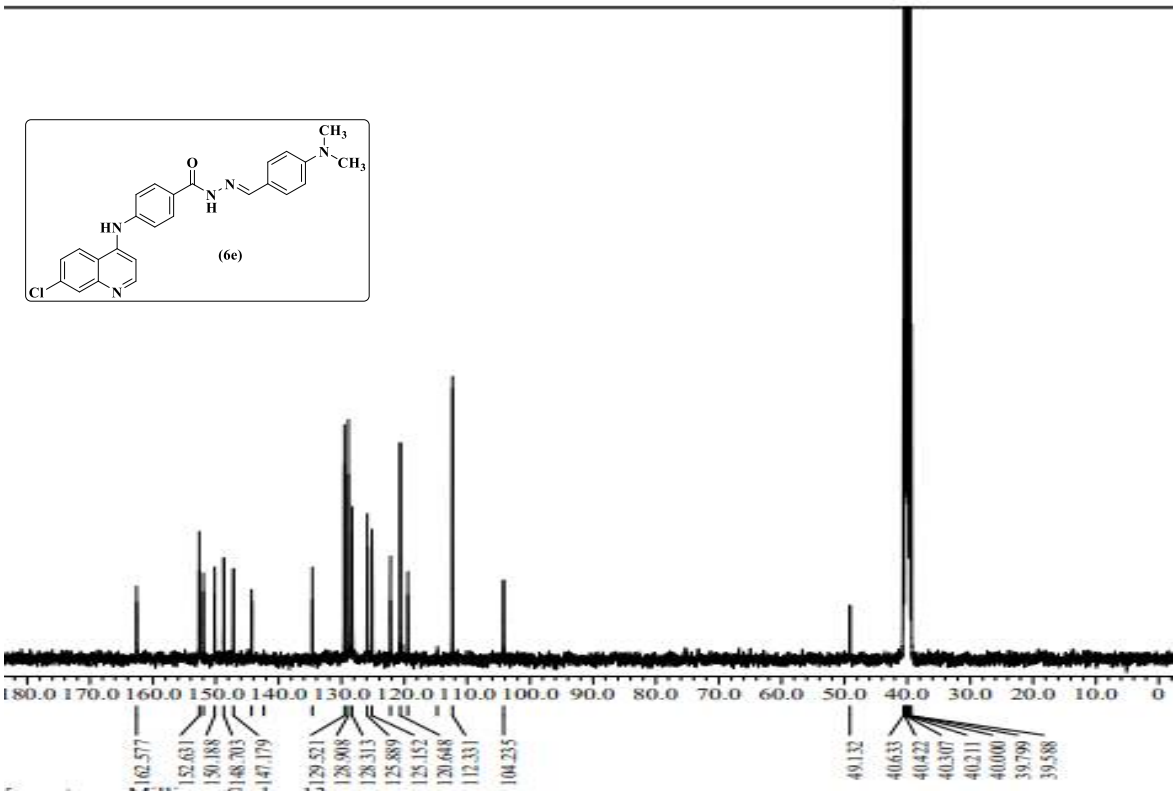
Spectra. 97: LCMS spectra of compound 6d



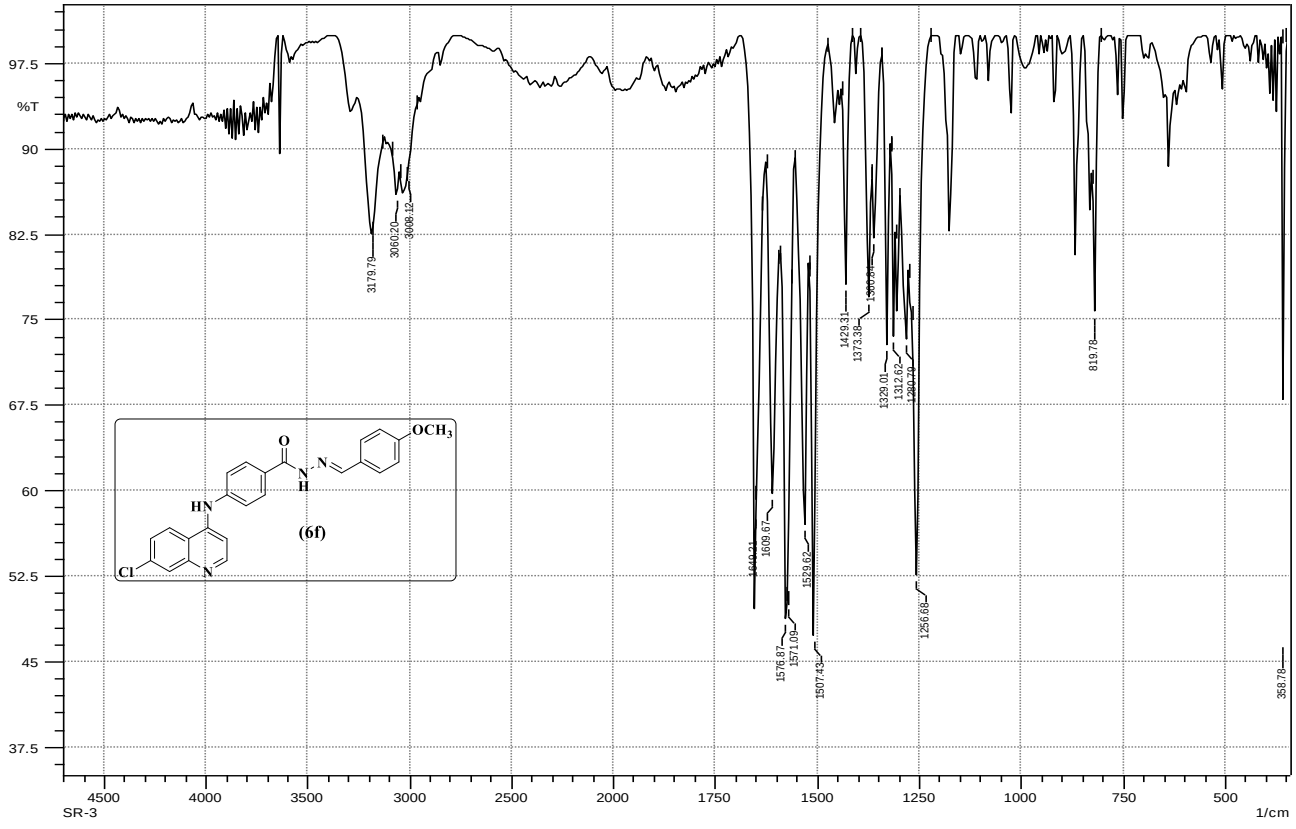
Spectra. 98: FTIR (KBr, cm^{-1}) spectra of compound 6e



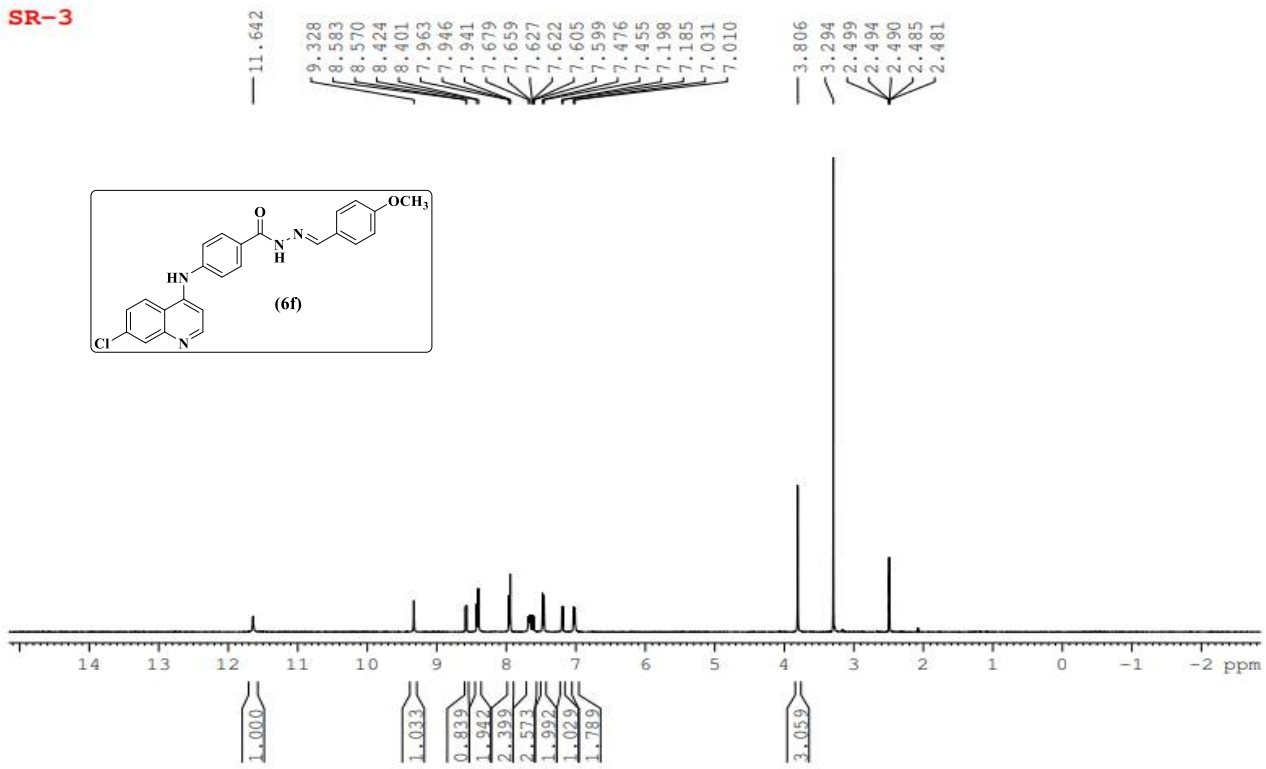
Spectra. 99: ^{1}H NMR (400 MHz, δ, ppm) spectra of compound 6e



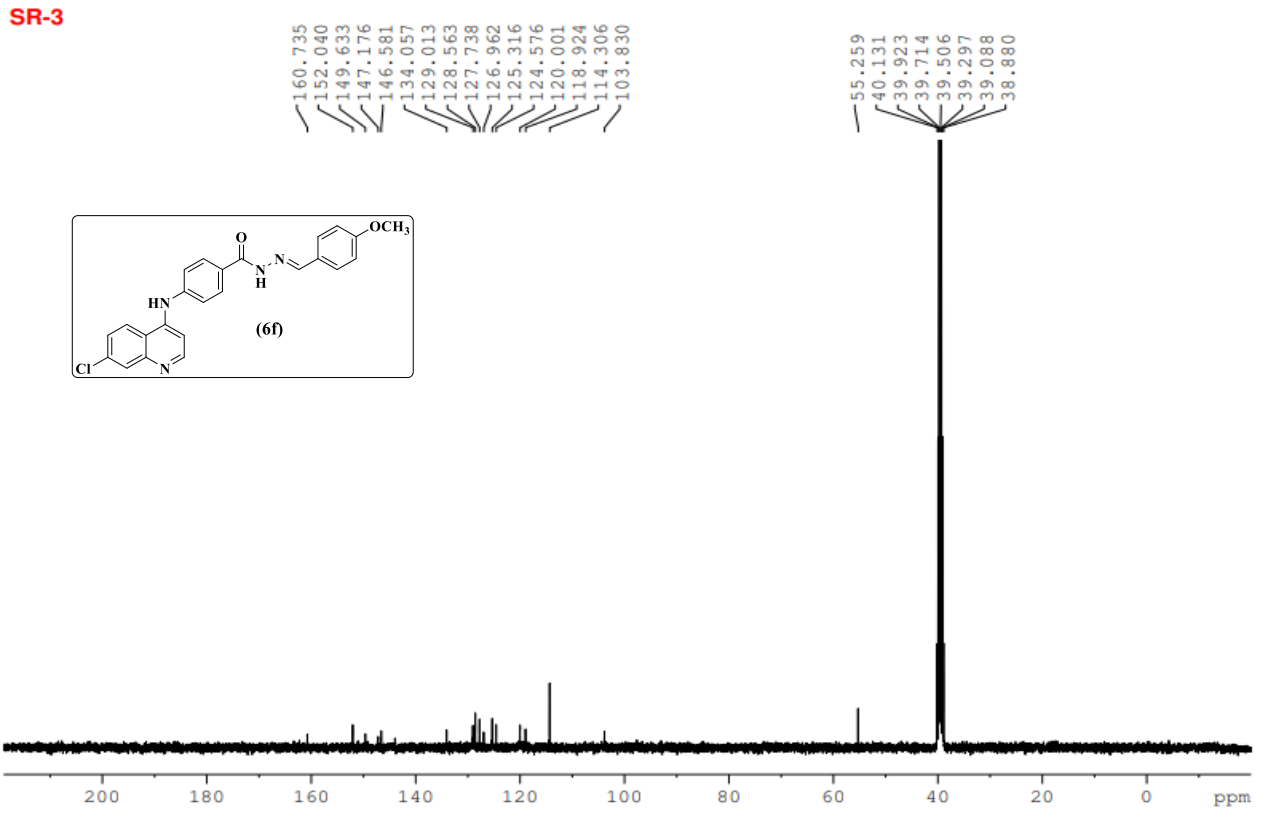
Spectra. 100: ^{13}C NMR (400 MHz, δ, ppm) spectra of compound 6e



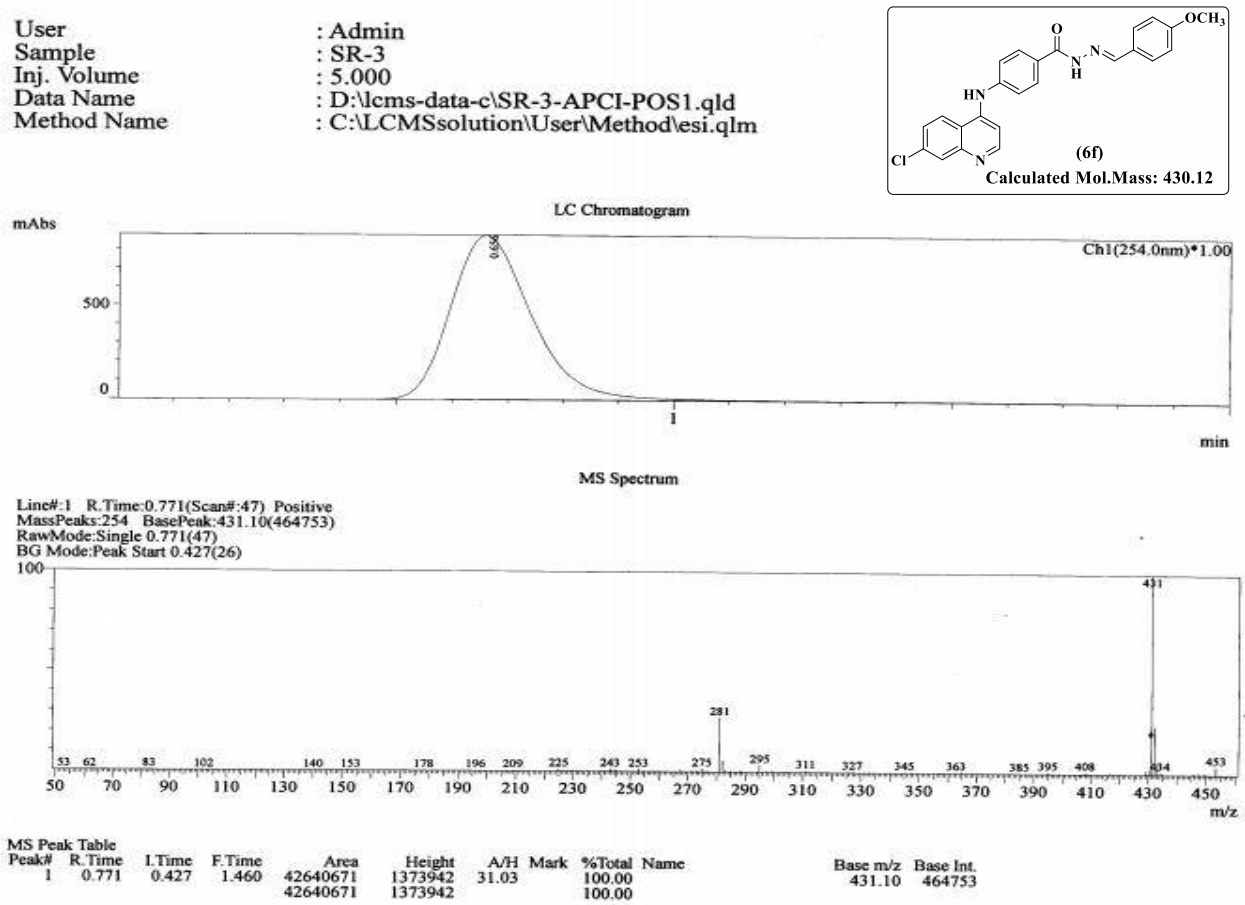
Spectra. 101: FTIR (KBr, cm^{-1}) spectra of compound 6f



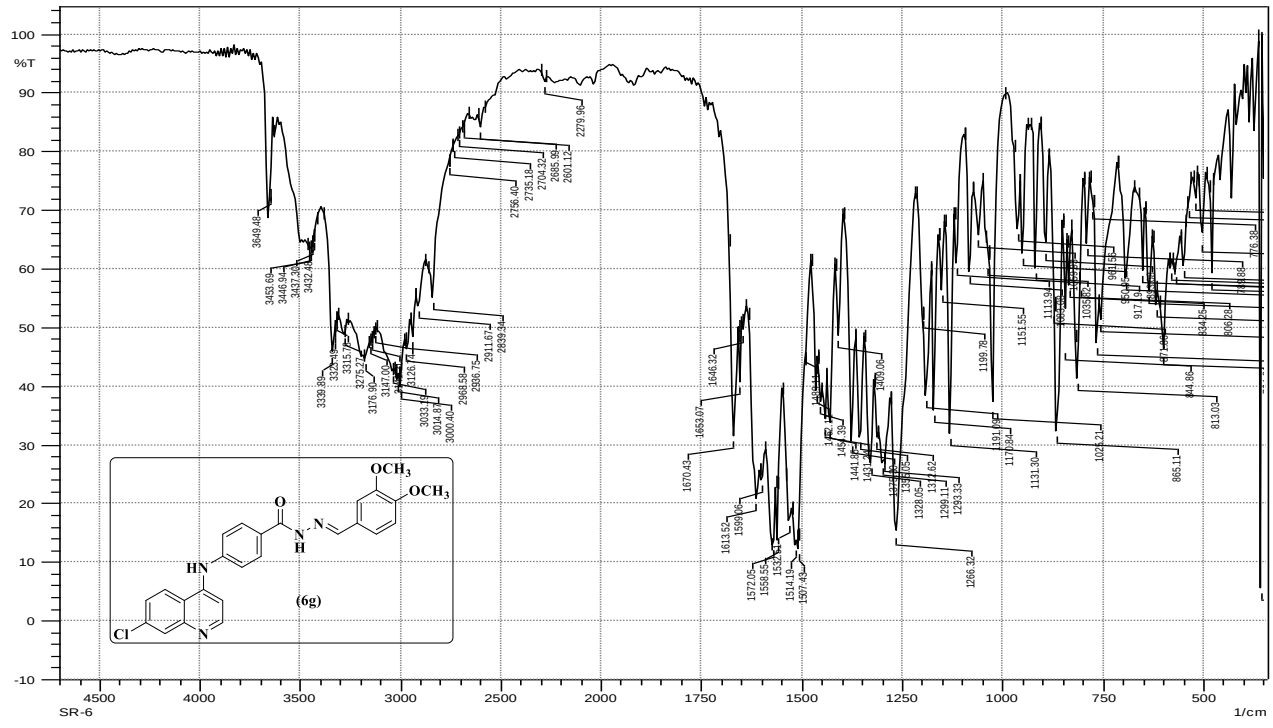
Spectra. 102: ^{1}H NMR (400 MHz, δ, ppm) spectra of compound 6f



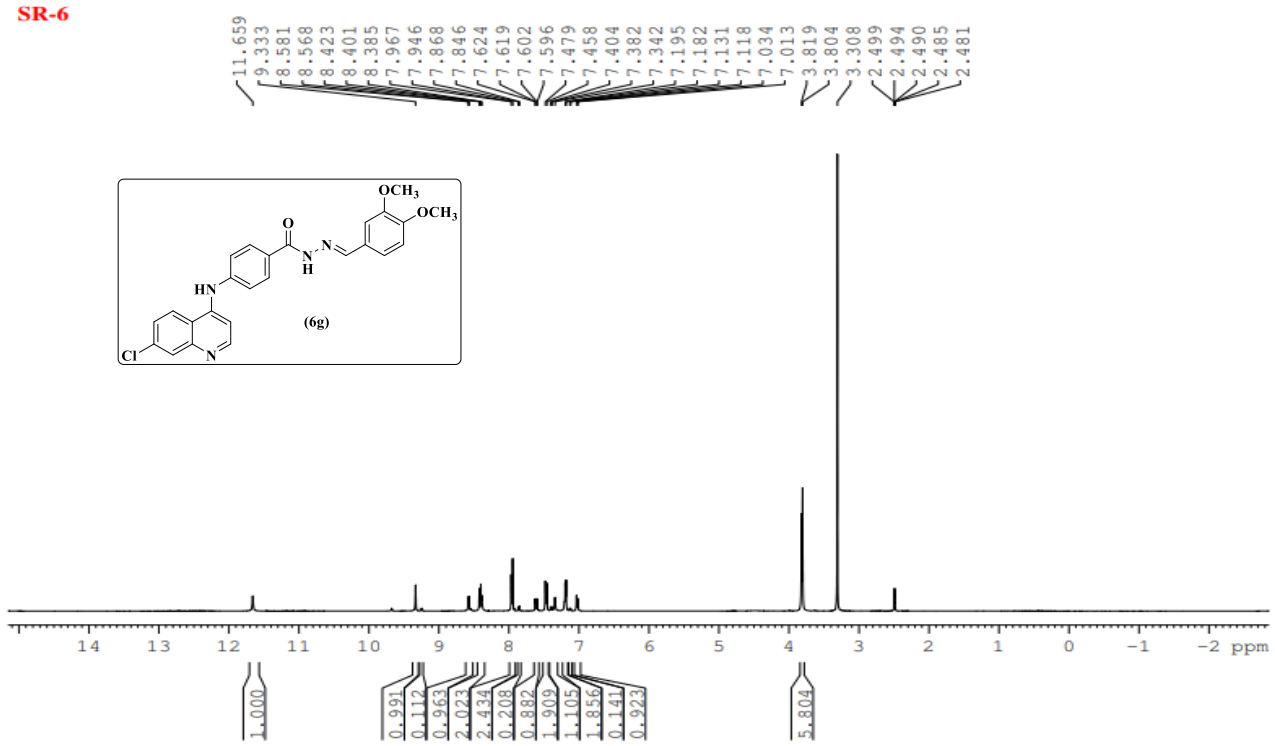
Spectra. 103: ^{13}C NMR (400 MHz, δ, ppm) spectra of compound 6f



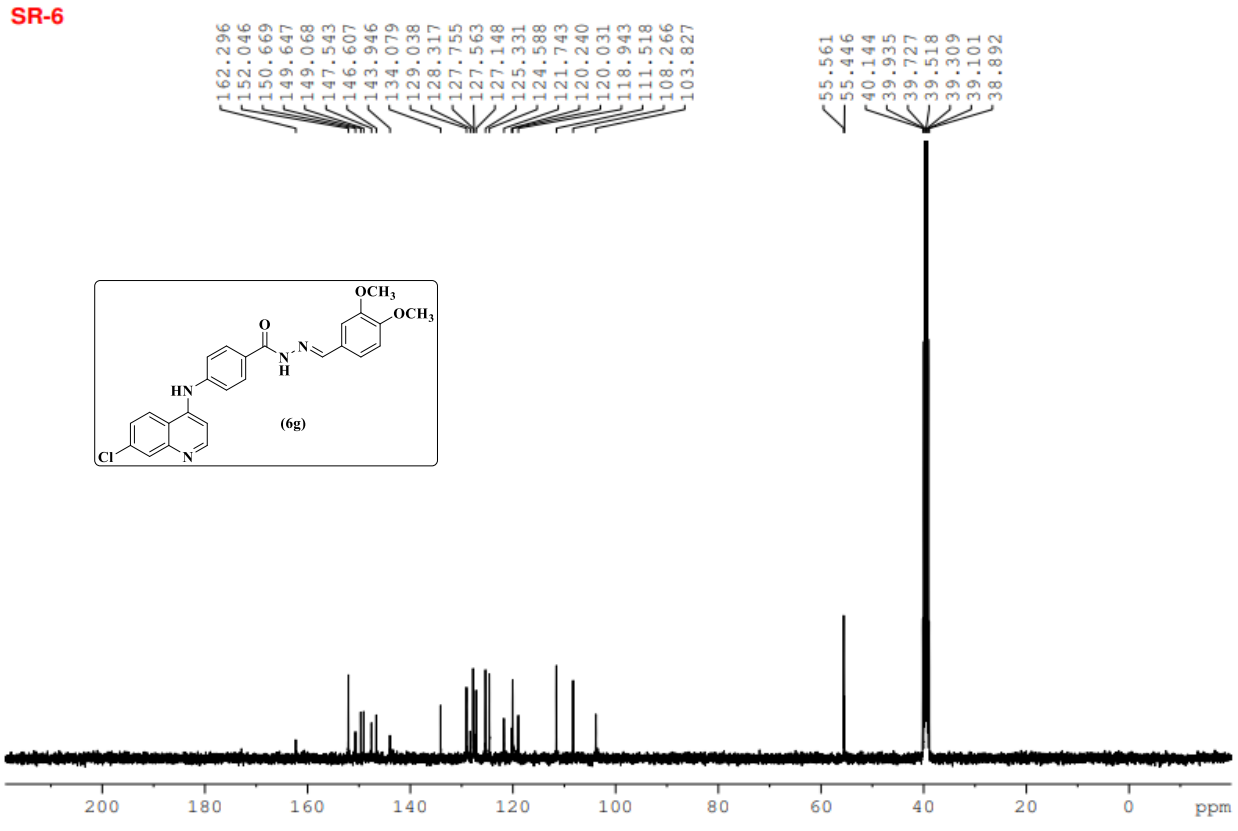
Spectra. 104: LCMS spectra of compound 6f



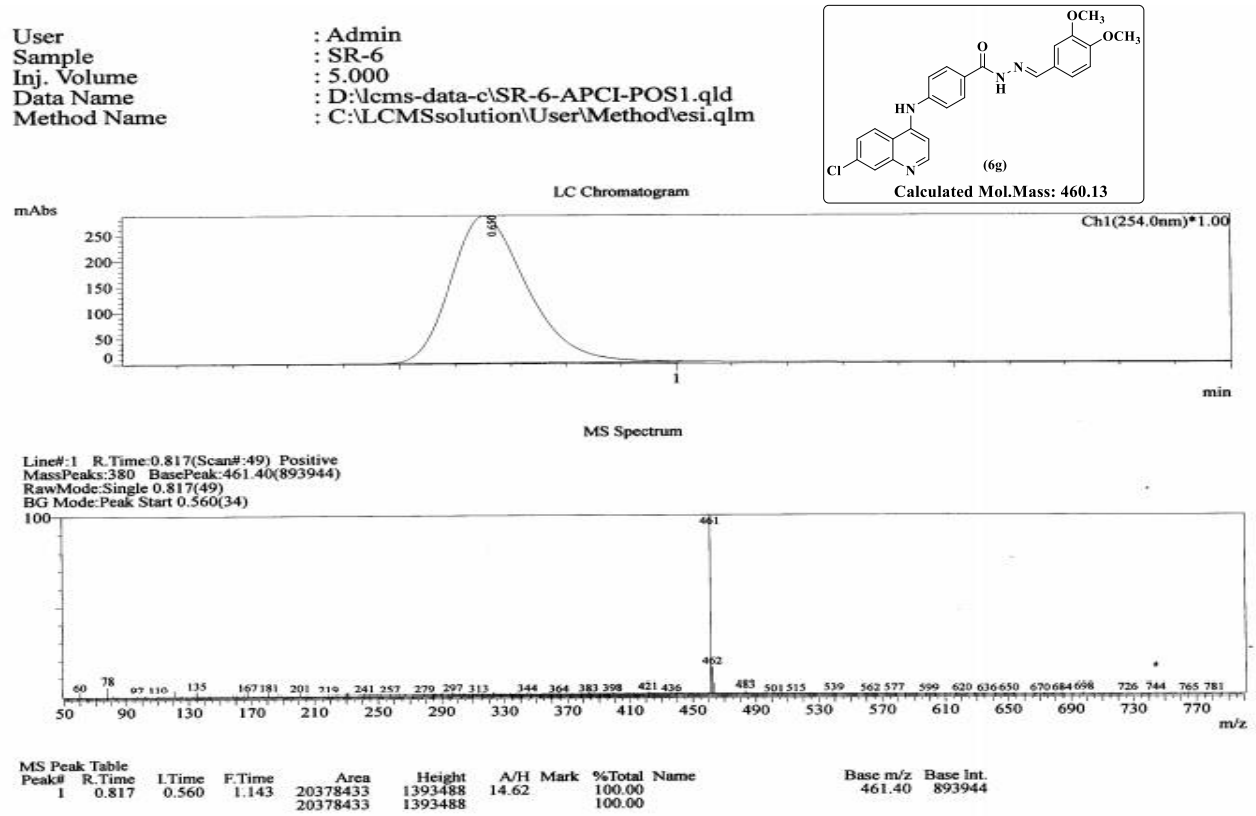
Spectra. 105: FTIR (KBr, cm^{-1}) spectra of compound 6g



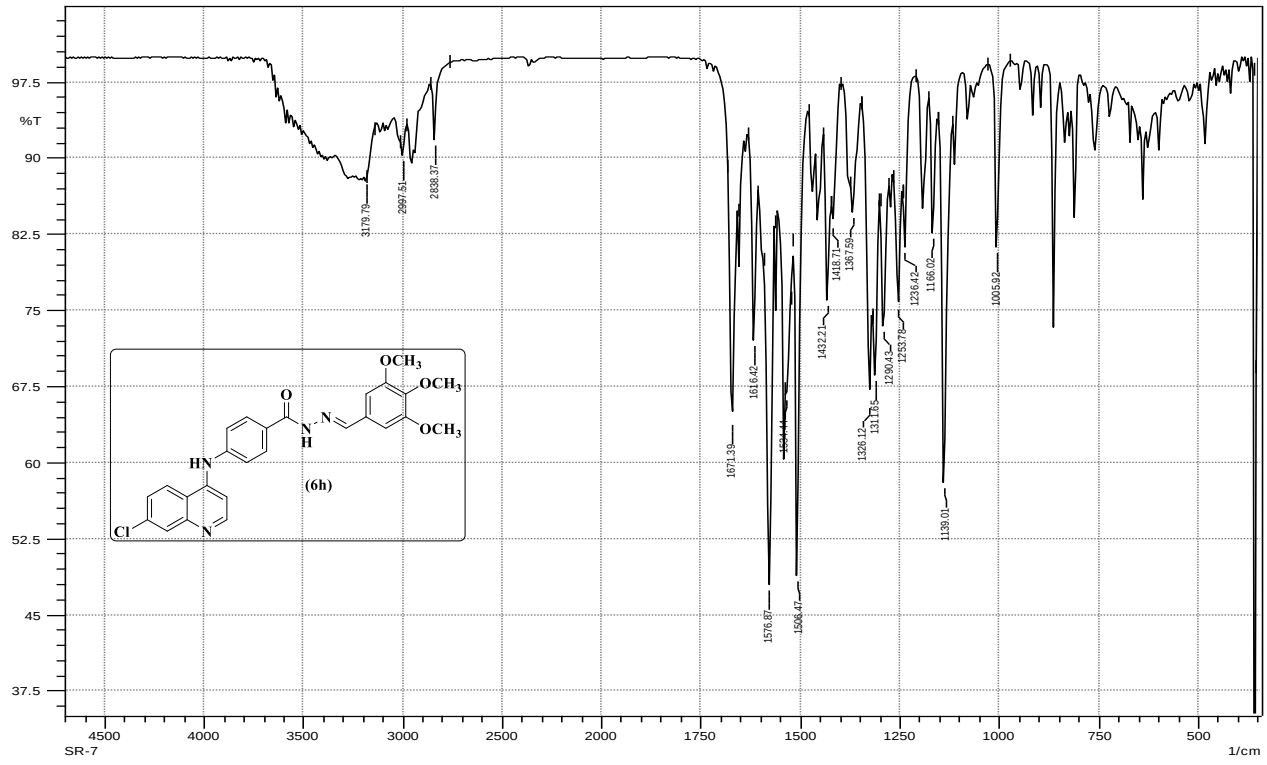
Spectra. 106: ^{1}H NMR (400 MHz, δ, ppm) spectra of compound 6g



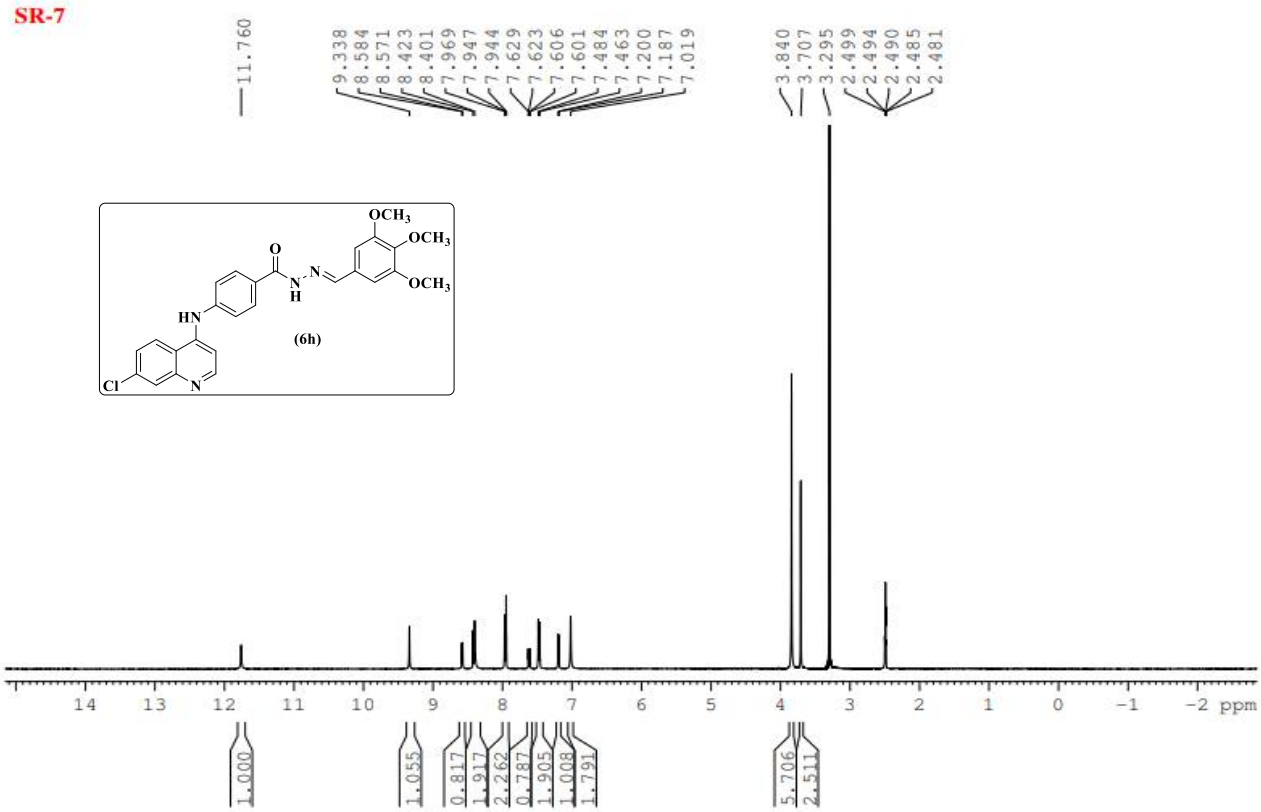
Spectra. 107: ^{13}C NMR (400 MHz, δ, ppm) spectra of compound 6g



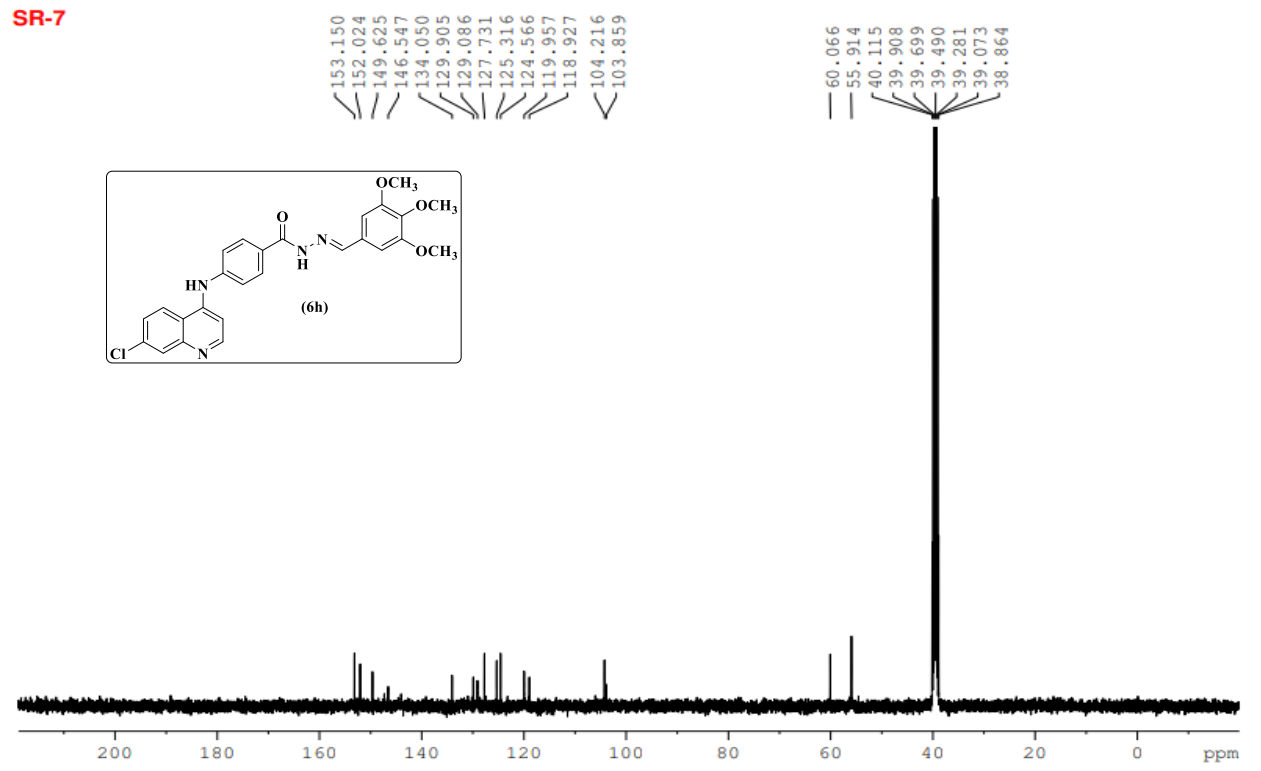
Spectra. 108: LCMS spectra of compound 6g



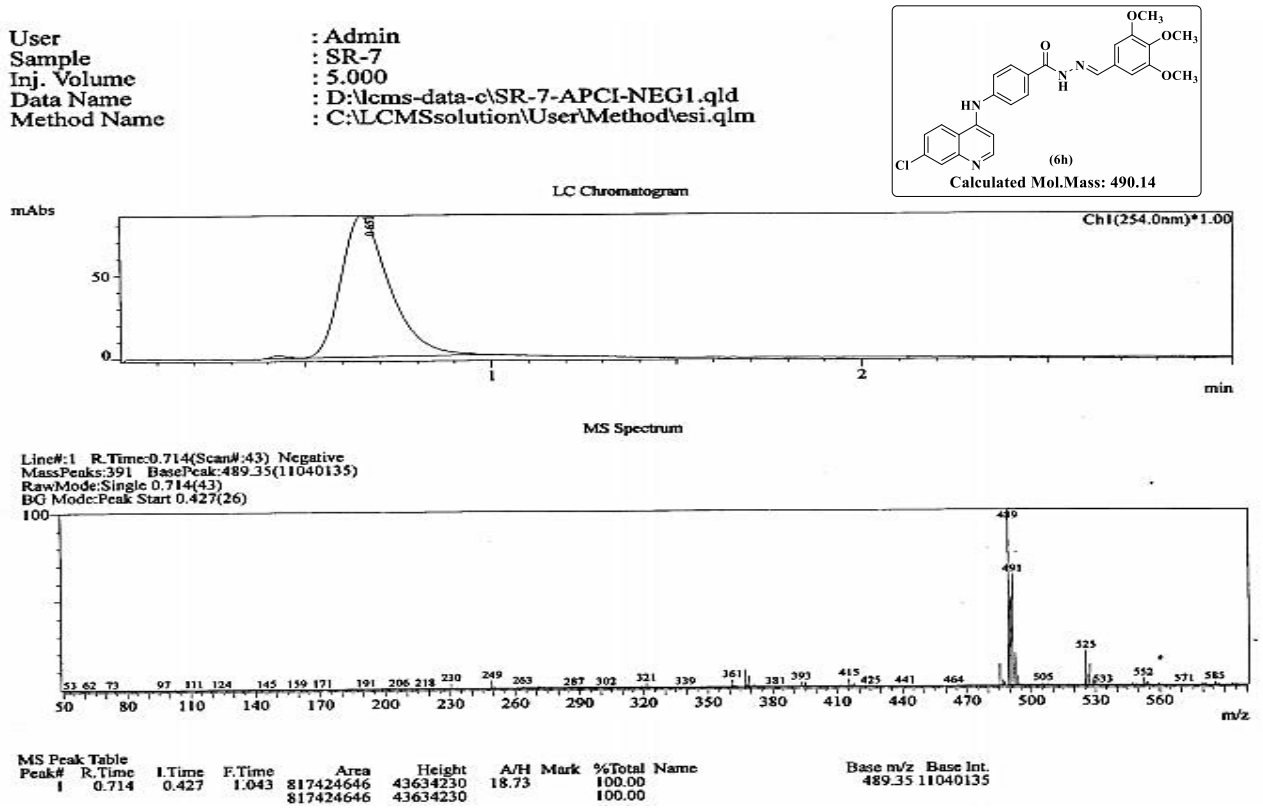
Spectra. 109: FTIR (KBr, cm^{-1}) spectra of compound 6h



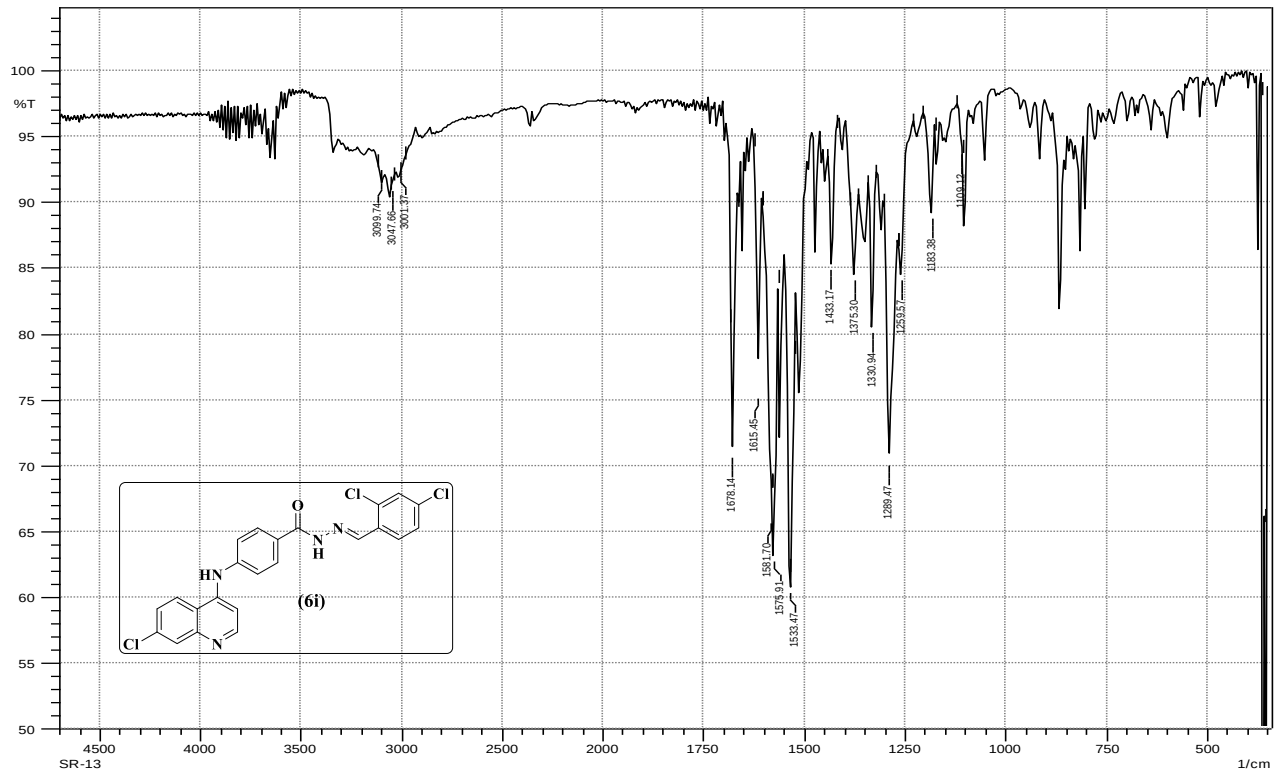
Spectra. 110: ^{1}H NMR (400 MHz, δ, ppm) spectra of compound 6h



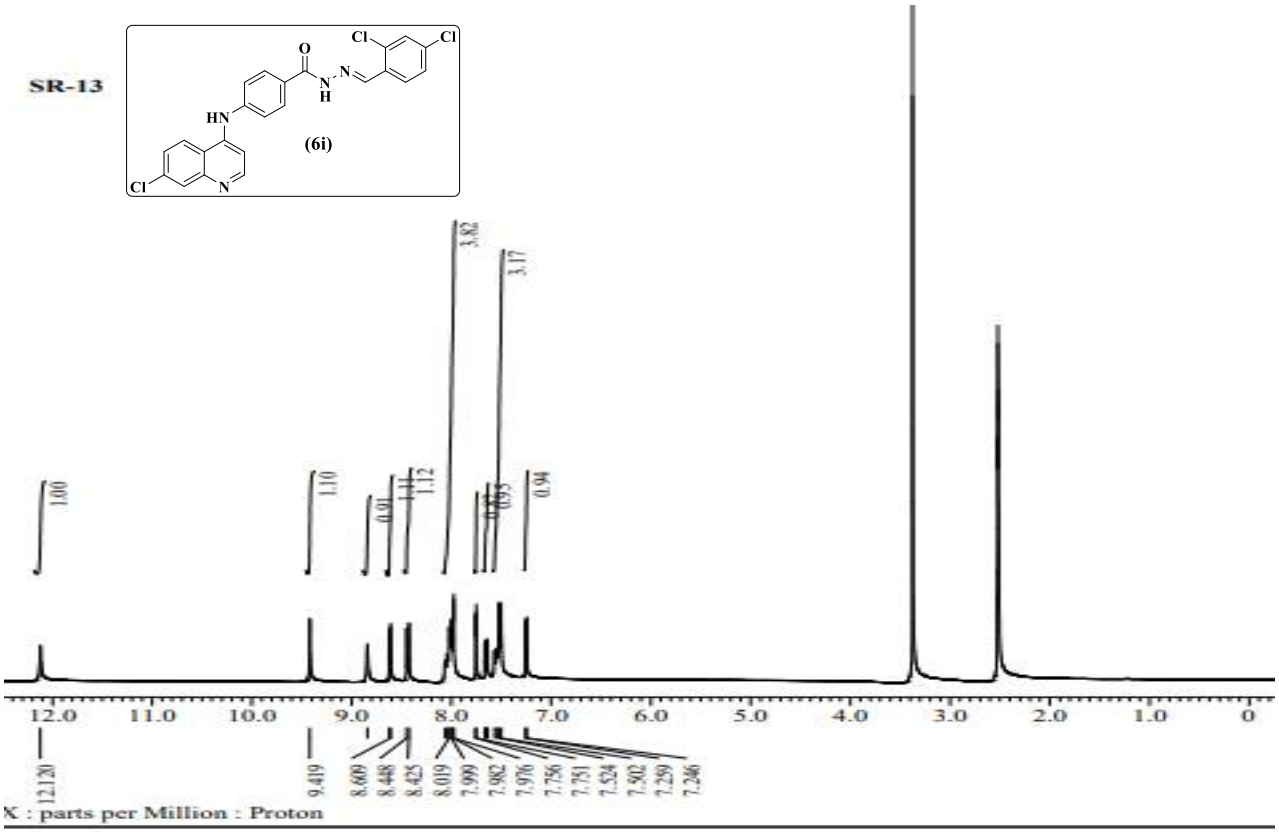
Spectra. 111: ^{13}C NMR (400 MHz, δ, ppm) spectra of compound 6h



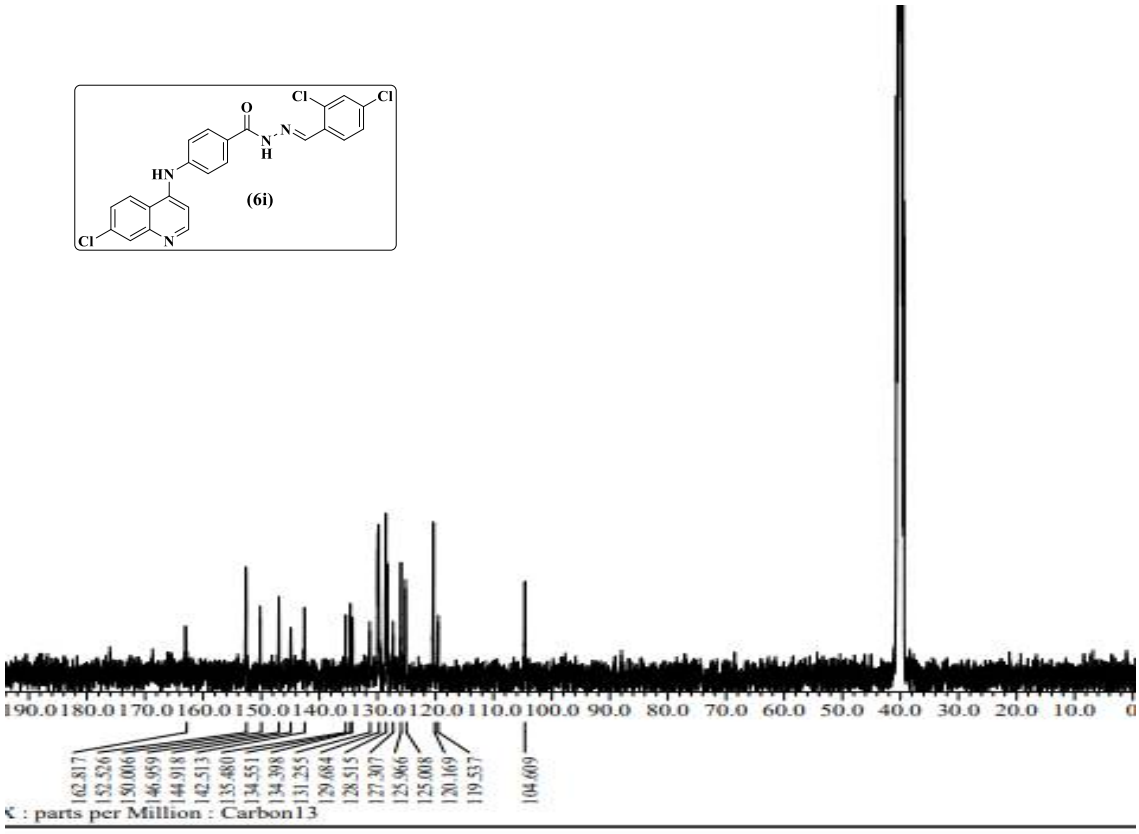
Spectra. 112: HRMS Spectra of compound 6h



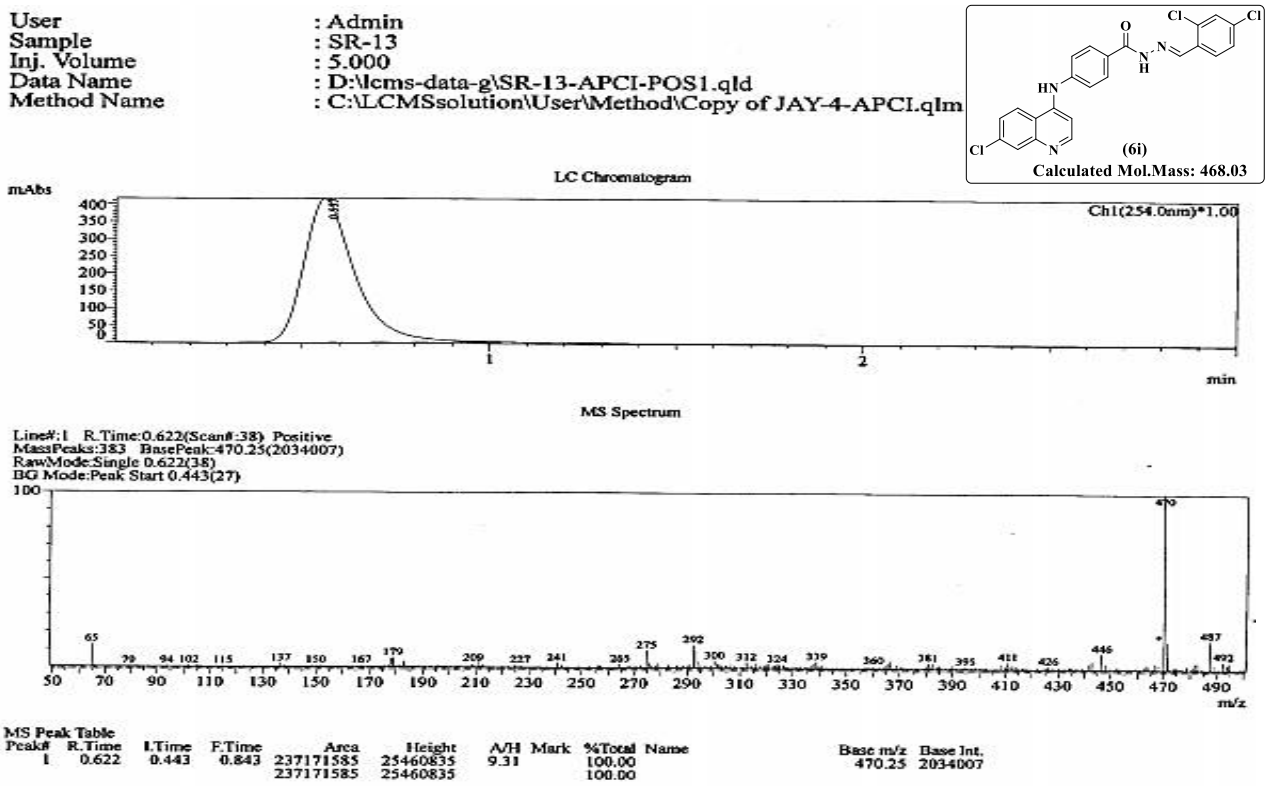
Spectra. 113: FTIR (KBr, cm^{-1}) spectra of compound 6i



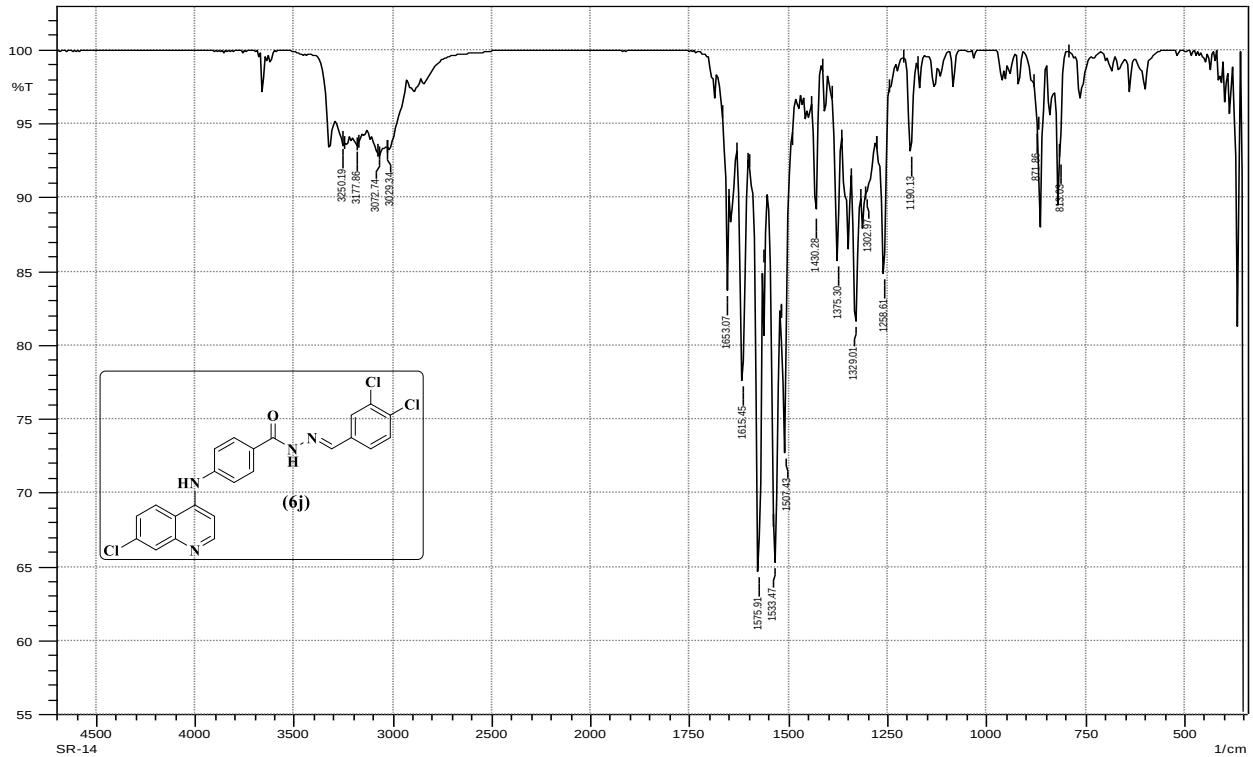
Spectra. 114: ^{1}H NMR (400 MHz, δ, ppm) spectra of compound 6i



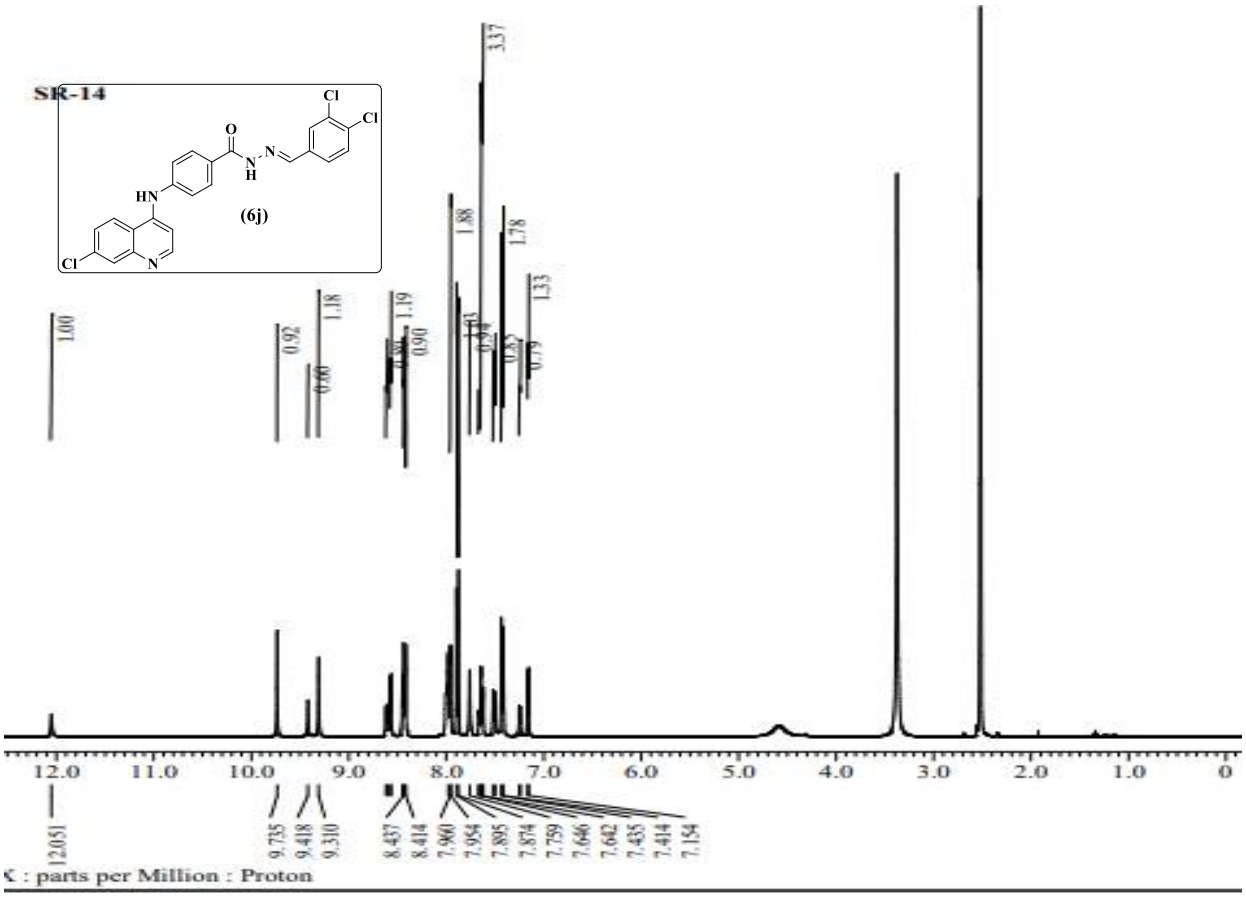
Spectra. 115: ^{13}C NMR (400 MHz, δ, ppm) spectra of compound 6i



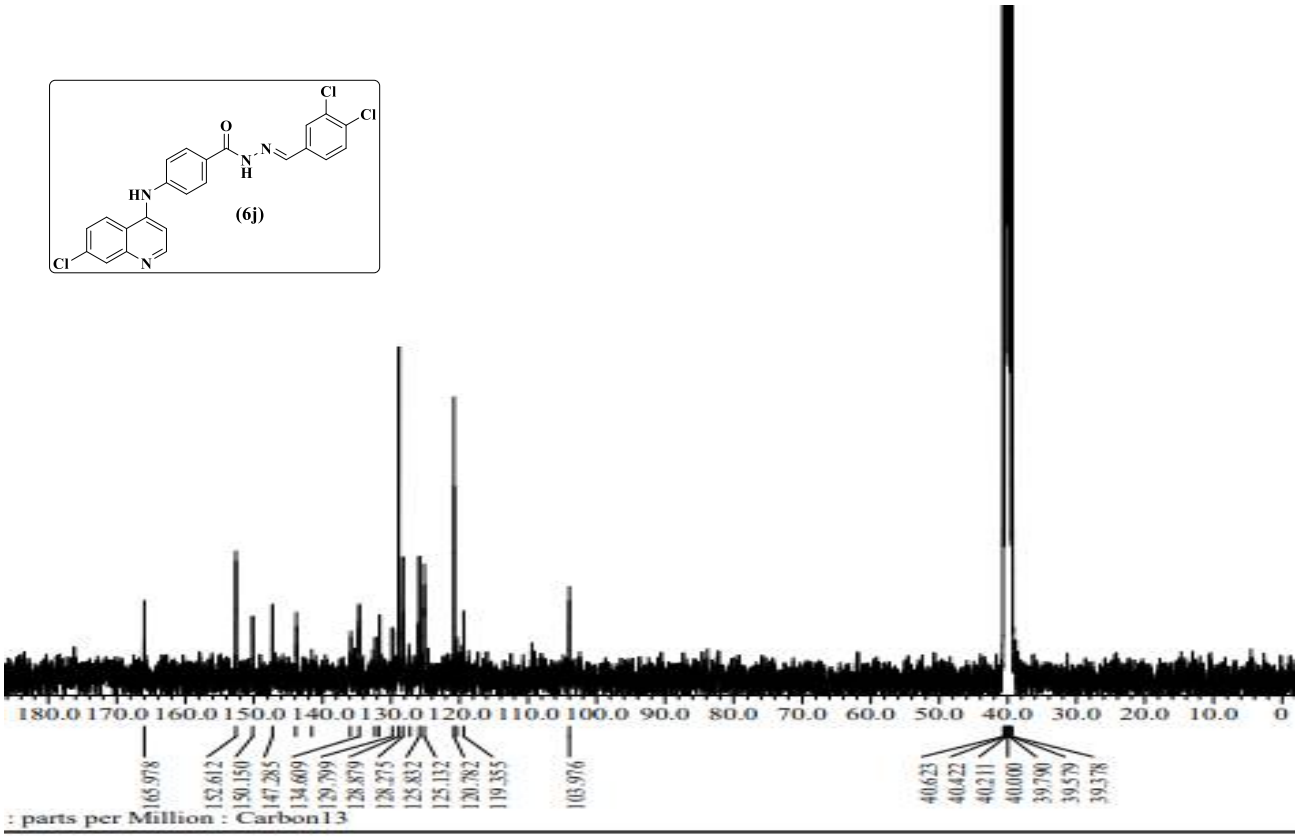
Spectra. 116: LCMS spectra of compound 6i



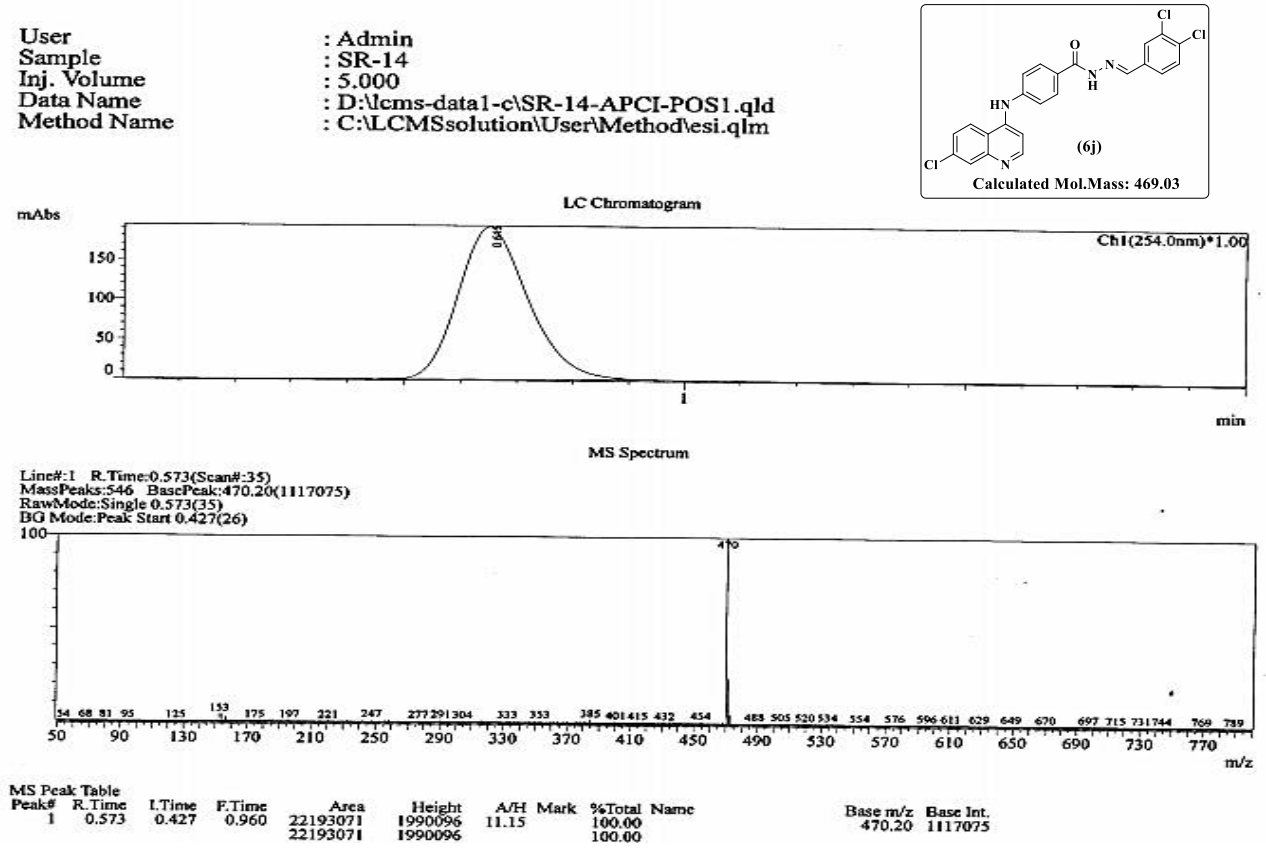
Spectra. 117: FTIR (KBr, cm^{-1}) spectra of compound 6j



Spectra. 118: ^{1}H NMR (400 MHz, δ, ppm) spectra of compound 6j



Spectra. 119: ^{13}C NMR (400 MHz, δ, ppm) spectra of compound 6j

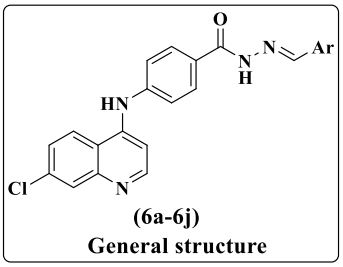


Spectra. 120: LCMS spectra of compound 6j

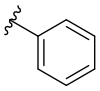
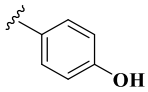
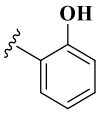
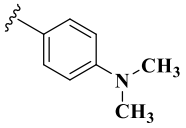
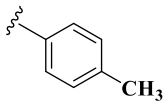
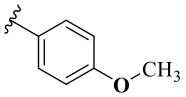
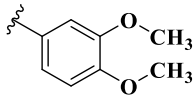
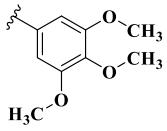
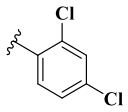
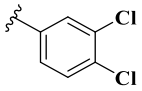
6. Pharmacological evaluation

6.1. *Invitro α-amylase* and *α-glucosidase* inhibition assay

A series of newly synthesized molecules (**6a–6j**) was evaluated for their inhibitory potential against key enzymes implicated in postprandial hyperglycemia. The inhibitory activity of the analogs against *α-glucosidase* exhibited IC_{50} values ranging from 12.95 ± 2.35 μM to 748.35 ± 1.09 μM, relative to the reference inhibitor acarbose (IC_{50} = 25.41 ± 0.16 μM). In parallel, the *α-amylase* inhibitory activity was observed within the IC_{50} range of 29.36 ± 3.24 μM to 78.63 ± 1.35 μM, as compared to acarbose (IC_{50} = 32.63 ± 1.07 μM). Among the tested analogs, compound **6c** demonstrated the most potent inhibition of *α-glucosidase*, with an IC_{50} of 12.95 ± 2.35 μM, followed by compound **6b**, which exhibited an IC_{50} of 19.37 ± 0.96 μM. In the context of *α-amylase* inhibition, compound **6b** displayed superior activity (IC_{50} = 29.36 ± 3.24 μM), with compound **6c** following closely (IC_{50} = 33.04 ± 1.83 μM). A comprehensive summary of the inhibitory profiles of all synthesized compounds (**6a–6j**) is provided in **Table 24.**



(6a-6j)
General structure

Comp.	Ar	IC_{50} values (µM) ±SEM	
		α-glucosidase	*α-amylase*
6a		27.43 ± 1.42	45.62 ± 2.01
6b		19.37 ± 0.96	29.36 ± 3.24
6c		12.95 ± 2.35	33.04 ± 1.83
6d		43.76 ± 4.31	58.74 ± 3.01
6e		31.42 ± 1.67	53. 06 ± 2.06
6f		143.52 ± 2.98	78.63 ± 1.35
6g		302.51 ± 2.12	NI
6h		748.35 ± 1.09	NI
6i		108.56 ± 3.16	65.48 ± 1.16
6j		63.25 ± 0. 23	56.32 ± 3.14
Acarbose		25.41 ± 0.16	32.63 ± 1.07

Note: NI: No inhibition

Table. 24: *Invitro α-glucosidase* and *α-amylase* inhibitory activities of the synthesized derivatives (**6a–6j**).

6.2. Enzyme inhibitory kinetic study

Among the synthesized series of compounds (**6a–6j**), compounds **6b** and **6c** exhibited the most potent *α-glucosidase* inhibitory activity and were further subjected to enzyme kinetic analysis to elucidate their mechanism of inhibition. The Lineweaver–Burk plot for compound **6b** revealed a competitive inhibition mechanism, as evidenced by an unchanged V_{max} and an increase in the Km value. The calculated inhibition constant (Ki) for compound **6b** was determined to be 19.54 µM, as illustrated in **Fig. 55a** & **Fig. 55b.** Similarly, kinetic analysis of compound **6c** indicated a competitive mode of inhibition, with a Ki value of 11.32 µM, as depicted in **Fig. 56a** and **Fig. 56b**.

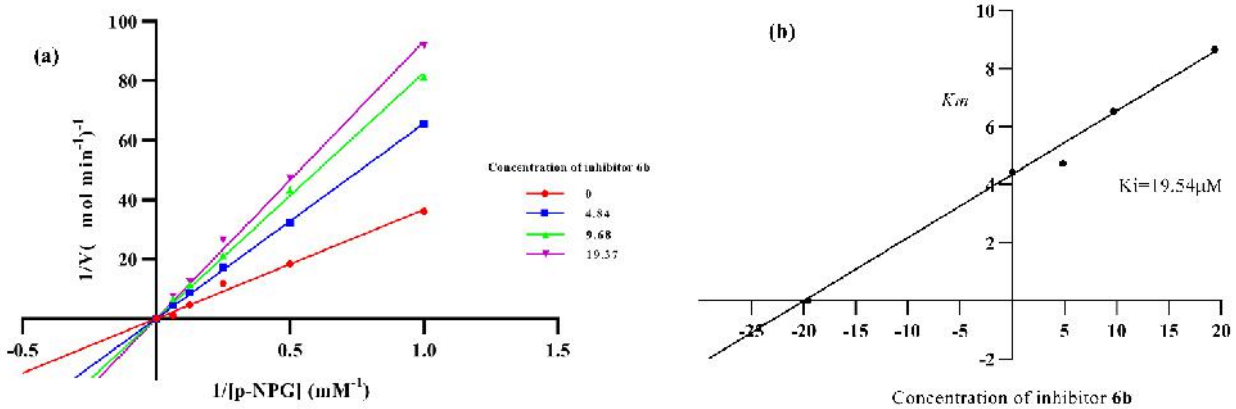


Fig. 55: (**a**) Lineweaver-Burk plot in the presence and absence of various concentration of compound **6b. (b)** Secondary replot between Km and different concentration of inhibitor **6b.**

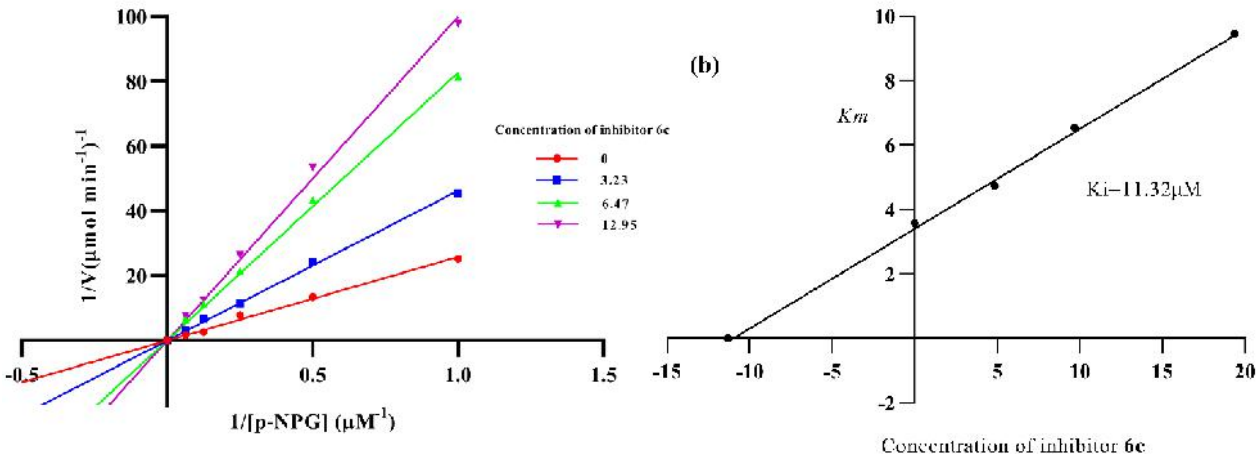


Fig. 56: (**a**) Lineweaver-Burk plot in the presence and absence of various concentration of compound **6c**. (**b**) Secondary replot between Km and different concentrations of inhibitor **6c**.

6.3. Structural activity relationship

A comprehensive review of the literature reveals that numerous quinoline-based compounds have demonstrated significant *α-glucosidase* and *α-amylase* inhibitory activities. Notable examples include quinoline conjugated with dihydropyrano [3,2-c] systems[194] , dihydropyridines[196], 1,3,4-oxadiazoles and 1,2,3-triazoles[192], and quinoline-based Schiff bases[195]. Pharmacophore modeling studies have highlighted that the (CH=N) Schiff base linkage serves as a key structural feature contributing to the biological activity. The selected pharmacophore hypothesis identifies critical features for *α-glucosidase* inhibitory activity, including two aromatic rings, one hydrogen donor group, and two hydrogen acceptor groups. The quinoline-based benzohydrazide Schiff's base analogs (**6a–6j**) were mapped onto the pharmacophore feature sites of the validated model. Notably, compounds **6b** and **6c** exhibited essential interactions at the enzyme's binding site, forming hydrogen bonds that significantly contribute to inhibitory activity. Among the series, **6b** (IC_{50}: 19.37 ± 0.96 µM) and 6c (IC_{50}: 12.95 ± 2.35 µM) demonstrated the highest potency. These active compounds, both of which are quinoline-based benzohydrazide Schiff's base analogs, displayed notable binding interactions within the enzyme's active site.

Molecular docking studies further elucidated the importance of the quinoline scaffold for optimal binding within the enzyme's pocket. The quinoline core facilitated π-π stacking interactions with key amino acid residues, such as PHE 311 and PHE 157 in compound **6b** and TYR 151 in compound 6c. Structural analysis revealed that the hydroxy group's position plays a critical role in modulating electronic effects. Compound **6b** possesses a para-hydroxy substitution, while 6c features an ortho-hydroxy substitution. These positional differences influence the electronic effects of the hydroxy group's electron-donating and electron-withdrawing abilities through resonance and inductive effects, respectively. The SAR analysis revealed that electron-donating substituents, as seen in compounds 6b, 6c, 6d, and 6e, conferred superior inhibitory activity compared to electron-withdrawing substituents present in compounds 6f, 6g, 6h, 6i, and 6j. These findings underscore the

critical influence of hydroxy group substitution on *α-glucosidase* inhibition. The combined evidence from this study and previously published literature highlights the role of hydroxy functional groups in enhancing inhibitory activity. These effects are dependent on the position and electronic nature of substituents, as illustrated in **Fig. 57**, thereby providing valuable insights for the design of more potent *α-glucosidase* inhibitors.

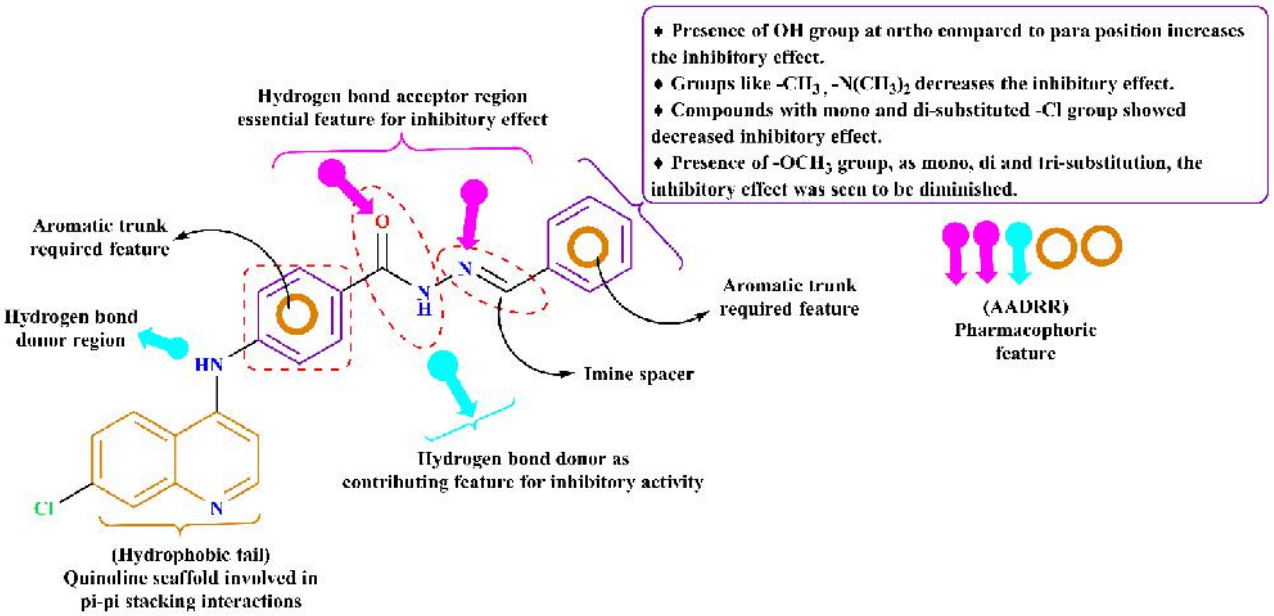
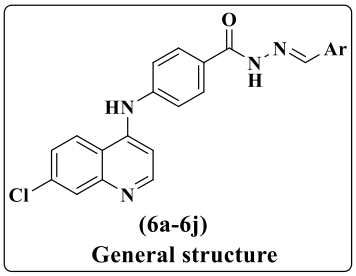


Fig. 57: SAR and Pharmacophoric features required for *α-glucosidase* inhibitory activity.

6.4. Toxicity evaluation

The cytotoxicity of the synthesized molecules (**6a–6j**) was evaluated using the MTT assay on normal mouse fibroblast (L929) cell lines. The results, as presented in **Table 25**, indicate that none of the tested compounds (**6a–6j**) exhibited notable cytotoxic effects, demonstrating their biocompatibility under the experimental conditions.



Comp	Percent survival L929 cell lines	
	125 ug/ml	250 ug/ml
6a	90.28	83.63
6b	89.77	86.29
6c	83.32	79.67
6d	78.31	78.48
6e	92.75	86.42
6f	91.47	85.12
6g	89.95	83.52
6h	87.14	83.06
6i	83.69	75.82
6j	88.17	85.84

Table. 25: Toxicity results of compounds (**6a-6j**) on normal mouse fibroblast L929 cell lines.

7. *Insilico* study

7.1. Molecular docking

The inhibitory potential of the synthesized compounds against *α-glucosidase* and *α-amylase* was evaluated through enzyme inhibition assays. Several of these compounds exhibited significant inhibitory activity in comparison to the standard inhibitor, acarbose. To further substantiate these findings and elucidate the molecular basis of their interactions with the active sites of *α-glucosidase* and α-amylase, molecular docking studies were conducted using the Glide module of Schrödinger's software suite. The docking analysis provided insight into the binding conformations and site-specific interactions of the compounds within the enzyme's active site.

The *α-glucosidase* enzyme structure was modeled using homology modeling techniques. The FASTA sequence (accession ID: P53341) was subjected to BLAST analysis, which identified the crystal structure of isomaltase from Saccharomyces cerevisiae (PDB ID: 3A47) as the closest homolog. This structure was utilized as a template for constructing the *α-glucosidase* model. The structural reliability of the modeled protein was assessed through validation metrics, including Ramachandran plot analysis (**Fig. 58**), ensuring the model's suitability for subsequent docking studies. Among the series of synthesized compounds (**6a–6j**), compounds **6b** and **6c** demonstrated

the highest binding affinities for the *α-glucosidase* active site. Compound **6b** (**Fig. 59**) exhibited a strong binding interaction characterized by multiple key interactions. Specifically, the nitrogen atom of its Schiff base formed a hydrogen bond with the amino acid residue LYS 155. Additionally, the amino (NH) group of the benzohydrazide moiety established a hydrogen bond with ASN 412. Notably, compound **6b** also engaged in three π-π stacking interactions involving its aromatic rings, with one interaction occurring with PHE 311 and two interactions with PHE 157. The calculated glide docking score for compound **6b** was -52.425 kcal/mol, highlighting its strong binding affinity and potential as a potent inhibitor of *α-glucosidase*. The molecular docking analysis of compound **6c** (**Fig. 60**) revealed a hydrogen bond interaction between the nitrogen atom of the Schiff base and the amino acid residue LYS 155. Notably, the same LYS 155 residue was also involved in a pi-cation interaction with the phenyl ring of the compound. Additionally, a pi-pi stacking interaction was observed between the aromatic ring of 6c and the amino acid residues PHE 311 and PHE 157. The quinoline ring's chlorine atom formed a halogen bond with the amino acid residue ASH 214. The calculated glide energy for the obtained binding pose was -45.127 kcal/mol. The docking protocol was validated using Acarbose (**Fig. 61**) as a reference ligand.

The key interacting amino acid residues for all ligands were consistent with the active site residues identified via SiteMap analysis. Among the series of compounds (**6a-6j**), compounds **6b** and **6c** exhibited better binding affinity within the active site of the *α-amylase* enzyme. For compound **6b** (**Fig. 62**), a hydrogen bond was established between the amino (NH) group and the amino acid residue ASP 300. Additionally, hydrogen bonding was observed between the carbonyl group of 6b and the amino acid residue HIE 201, while the hydroxyl (OH) group of **6b** formed a hydrogen bond with GLU 240. The quinoline nucleus's chlorine atom established a halogen bond with the amino acid residue GLN 63. The total glide energy for this docking pose was calculated to be -46.006 kcal/mol. Similarly, compound **6c** (**Fig. 63**) demonstrated a hydrogen bond interaction between its hydroxyl (OH) group and the amino acid residue ILE 235. A pi-pi stacking interaction was also identified between the aromatic ring of 6c and the amino acid residue TYR 151. The total glide

energy for the 6c docking pose was found to be -49.094 kcal/mol. Acarbose (**Fig. 64**) was again used as a reference ligand to validate the docking protocol. The binding interactions of these ligands, including hydrogen bonding, pi-pi stacking, halogen bonding, and pi-cation interactions, within the binding pockets of *α-glucosidase* and *α-amylase* enzymes suggest a plausible binding mechanism that supports the *Invitro* findings. The binding affinities of the complete series of compounds (**6a-6j**) in *α-glucosidase* and *α-amylase* are summarized in **Table 26** and **Table 27**, respectively.

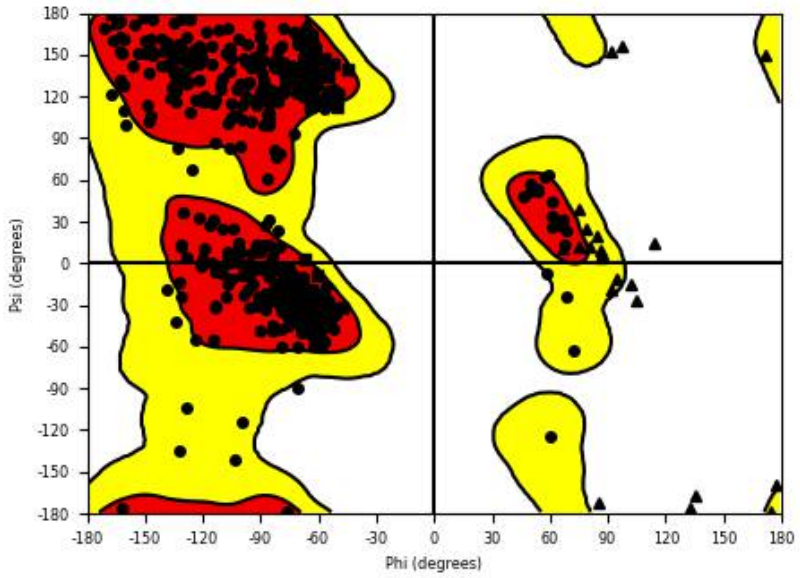


Fig. 58: Ramachandran plot of homology modeled *α-glucosidase* protein.

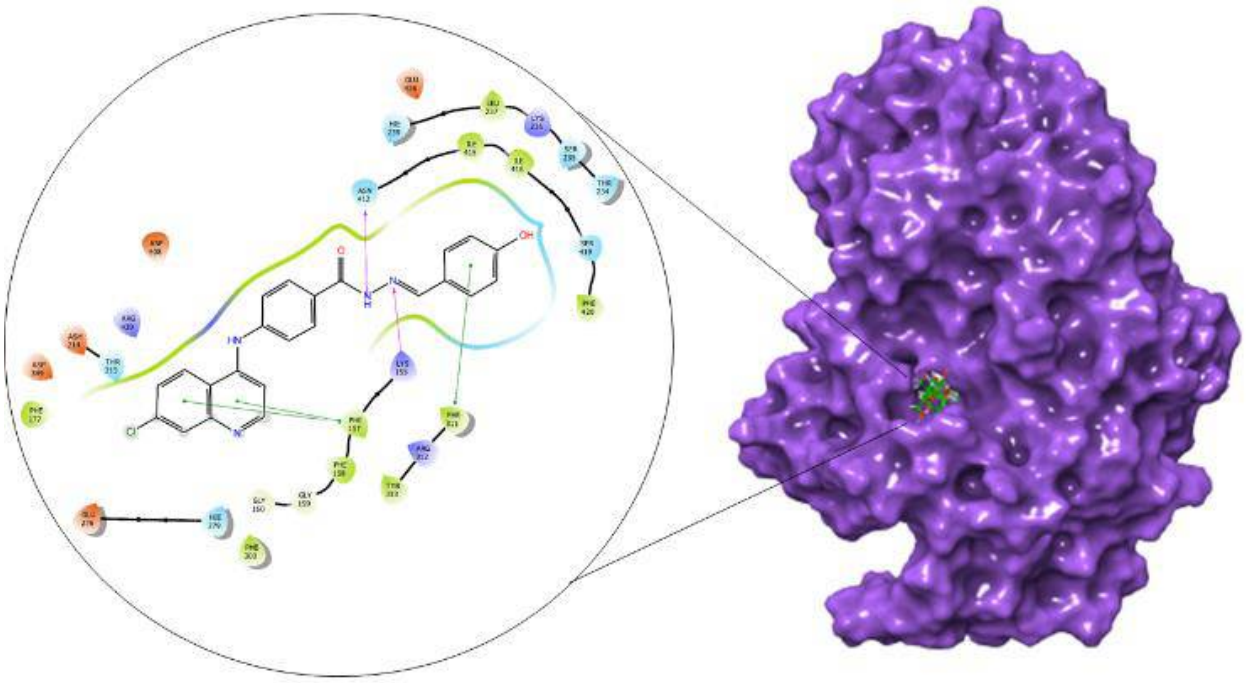


Fig. 59: Represents 2D and surface Binding orientation of compound 6b in the *α-glucosidase* binding pocket.

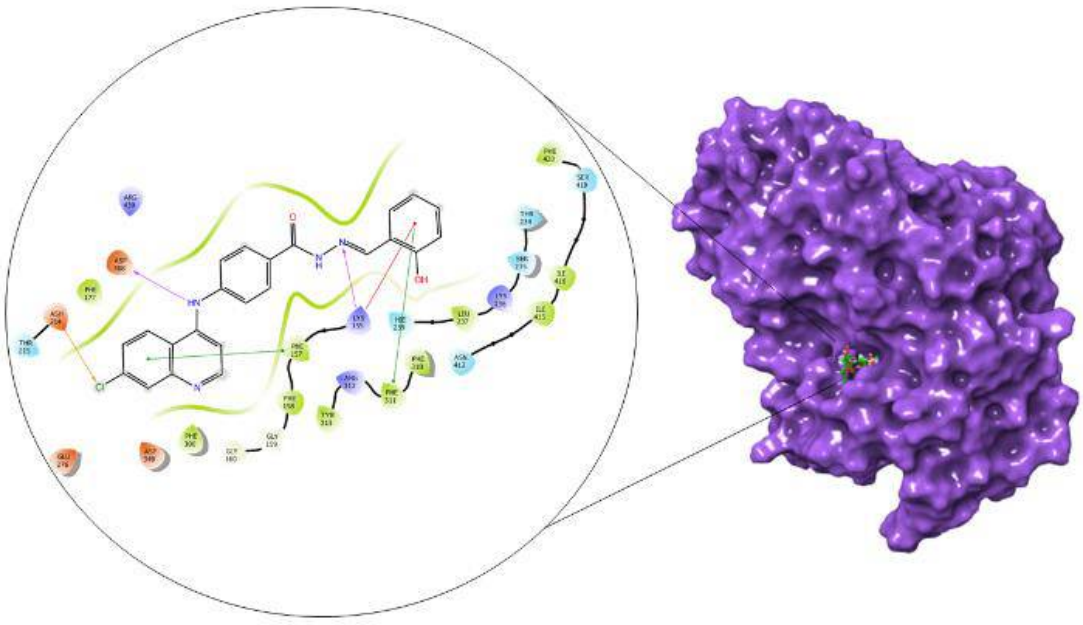


Fig. 60: Represents 2D and surface Binding orientation of compound 6c in *α-glucosidase* binding pocket

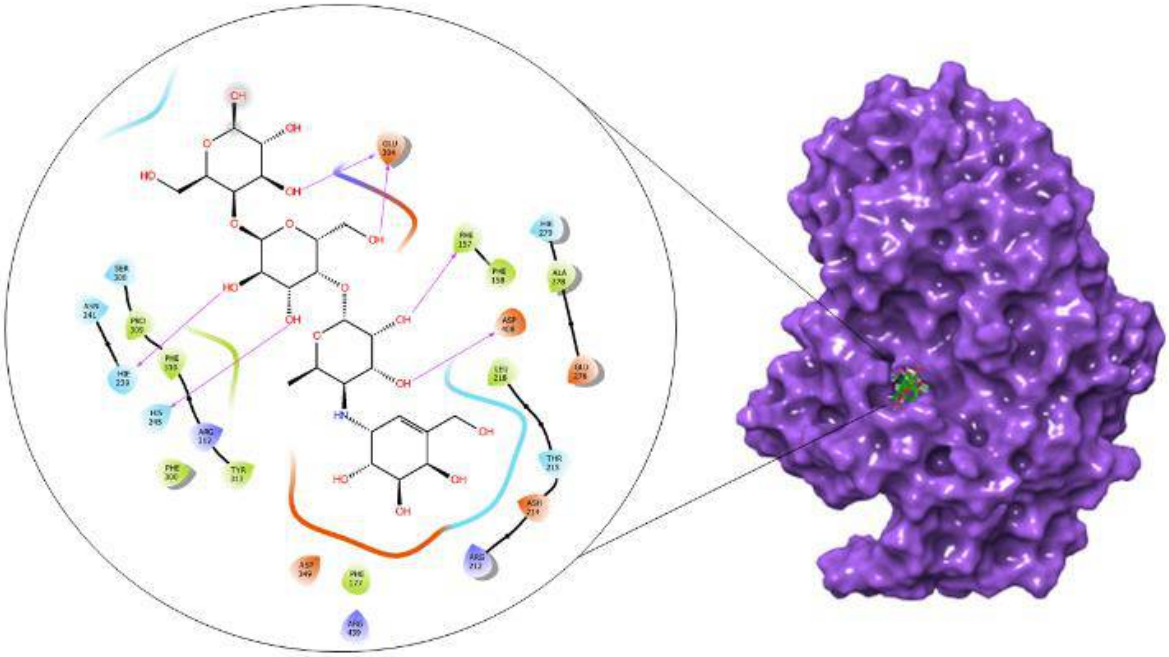


Fig. 61: Represents 2D and surface Binding orientation of compound acarbose in the *α-glucosidase* binding pocket.

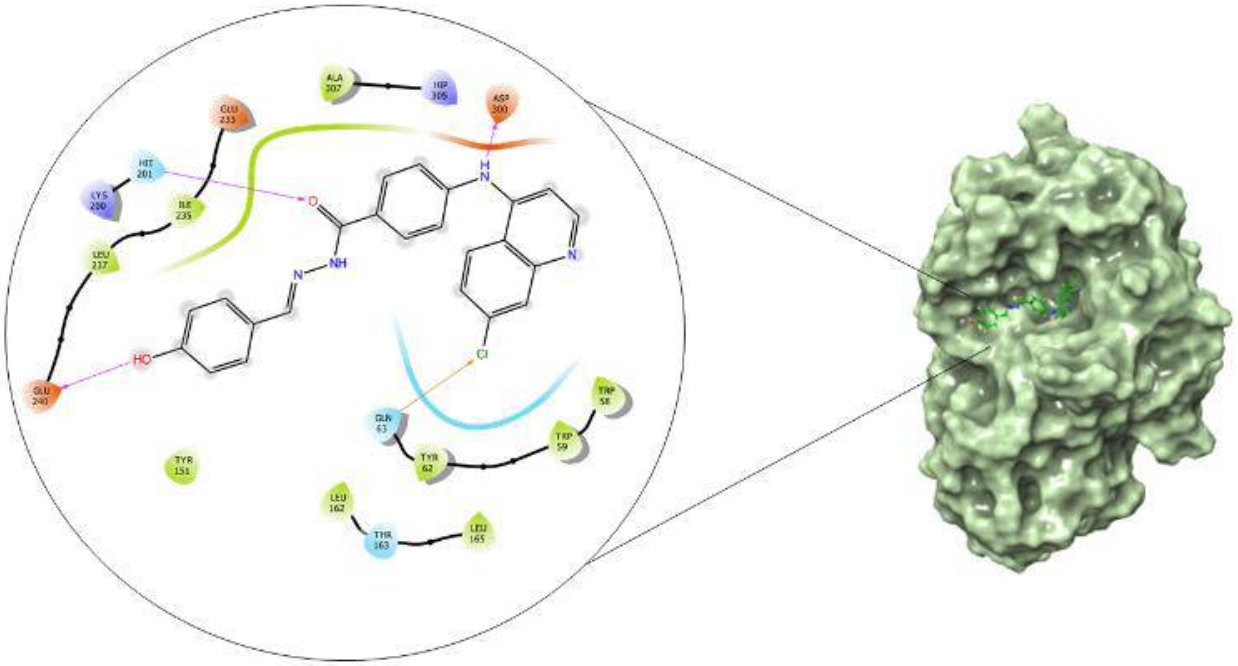


Fig. 62: Represents 2D and surface Binding orientation of compound 6b in *α-amylase* binding pocket.

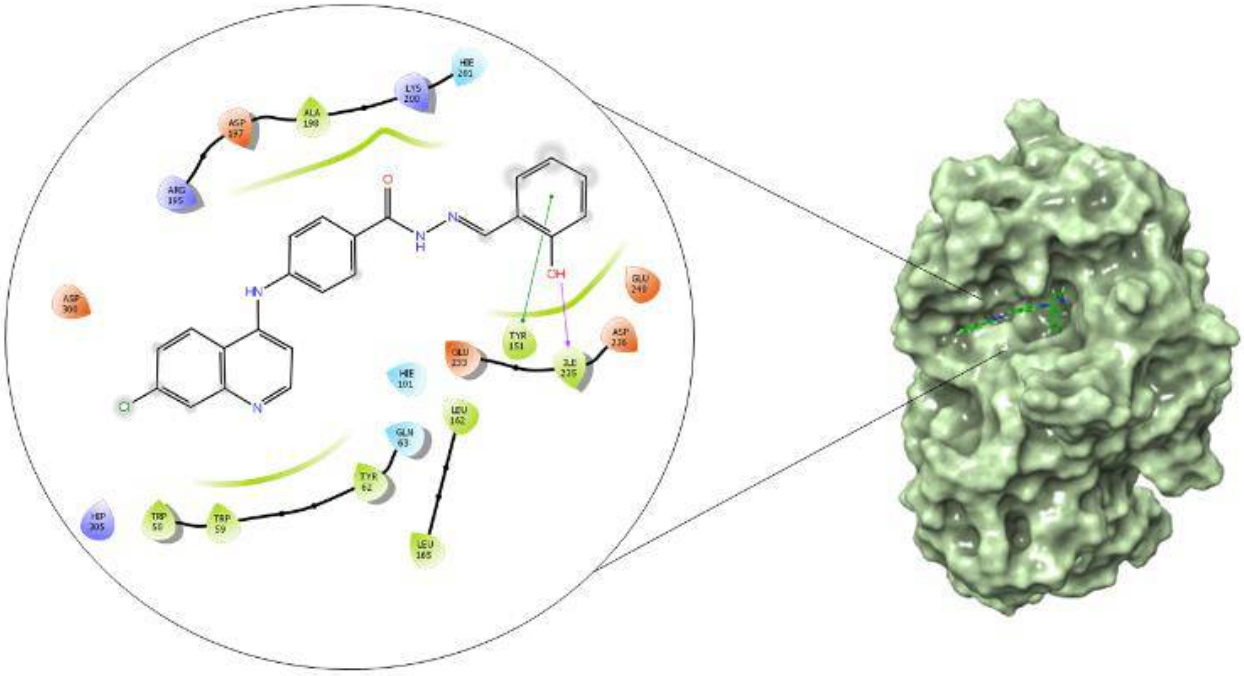


Fig. 63: Represents 2D and surface Binding orientation of compound 6c in *α-amylase* binding pocket.

Reference.

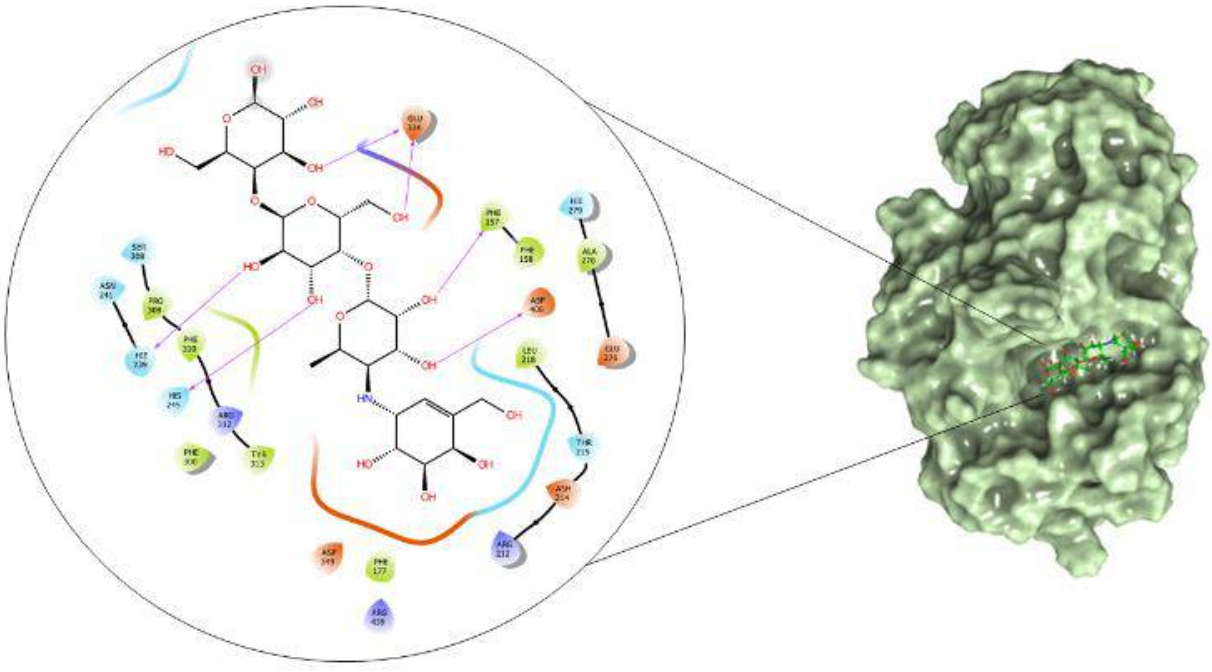


Fig. 64: Represents 2D and surface Binding orientation of compound acarbose in *α-amylase* binding pocket.

Compound	Docking Score	Glide Energy (kcal/mol)	Ligand atom interaction (H-Bond)	Amino Acid residue	Bond length	π-π stacking
6a	-5.133	-53.487	NH of ligand to ASP 408	ASP 408	2.23	-
6b	-6.145	-53.047	NH of ligand to ASN 412	ASN 412	2.01	PHE 311
			N of ligand to LYS 155	LYS 155	2.46	PHE 157
6c	-7.029	-56.784	NH of ligand to ASP 408	ASP 408	2.24	PHE 311
			N of ligand to LYS 155	LYS220	2.27	PHE 157
6d	-5.423	-49.918	N of ligand to GLN 350	GLN 350	2.78	PHE 311
			C=O of ligand to ASN 412	ASN 412	2.08	
6e	-5.068	-50.113	NH of ligand to ASP 408	ASP 408	2.22	-
6f	-5.392	-53.900	NH of ligand to ASP 408	ASP 408	2.13	-
6g	-6.190	-59.221	C=O of ligand to LYS 155	LYS 155	2.53	-
			N of ligand to LYS 155	LYS 155	2.48	
6h	-5.347	-53.043	NH of ligand to ASP 408	ASP 408	2.03	PHE 311
6i	-5.494	-56.111	NH of ligand to ASP 408	ASP 408	1.80	HIE 239
			C=O of ligand to ARG 312	ARG 312	1.86	
6j	-3.90	-7.58	NH of ligand to ASP 408	ASP 408	1.67	PHE 311
Acarbose	-7.199	-51.660	OH of ligand to ASP 408	ASP 408	2.78	
			OH of ligand to GLU 304	GLU 304	1.78	
			OH of ligand to HIE 239	HIE 239	2.63	
			OH of ligand to GLU 304	GLU 304	1.68	
			OH of ligand to HIS 245	HIS245	2.69	
			OH of ligand to PHE 157			

Table. 26: Binding affinity and interactions of compounds (**6a-6j**) in the *α-glucosidase* binding pocket.

Compound	Docking Score	Glide Energy (kcal/mol)	Ligand atom interaction (H-Bond)	Amino Acid residue	Bond length	π-π stacking
6a	-5.133	-53.487	C=O of ligand to HIE 201	HIE 201	2.31	TYR 151 TRP 58
			OH of ligand to GLU 240	GLU 240	1.66	
6b	-6.145	-53.047	C=O of ligand to HIE 201	HIE 201	2.13	-
			NH of ligand to ASP 300	ASP 300	1.74	
6c	-7.029	-56.784	OH of ligand to ILE 235	ILE 235	2.07	TYR 151
6d	-5.423	-49.918	C=O of ligand to TYR 151	TYR 151	2.11	HIE 201
			C=O of ligand to HIE 201	HIE 201	2.01	
			NH of ligand to GLU 233	GLU 233	2.12	
6e	-5.068	-50.113	C=O of ligand to HIE 201	HIE 201	2.28	HIE 201
			C=O of ligand to TYR 151	TYR 151	2.10	TRP 58
6f	-5.392	-53.900	NH of ligand to ASP 197	ASP 197	2.33	TRP 59 HIE 201
6g	-6.190	-59.221	C=O of ligand to HIE 201	HIE 201	1.88	-
6h	-5.347	-53.043	C=O of ligand to HIE 201	HIE 201	2.02	TRP 58
6i	-5.494	-56.111	C=O of ligand to HIE 201	HIE 201	1.95	
6j	-3.90	-7.58	N of ligand to ILE 235	ILE 235	2.40	HIE 201 TRP 59
			OH of ligand to ASP 300	ASP 300	2.63	
			OH of ligand to ASP 300	ASP 300	2.37	
			OH of ligand to ASP 197	ASP 197	1.71	
Acarbose	-7.199	-51.660	OH of ligand to GLU 240	GLU 240	1.74	
			OH of ligand to HIP 205	HIP 205	2.17	
			OH of ligand to HIE 201	HIE 201	2.33	
			OH of ligand to ARG 195	ARG195	1.80	

Table. 27: Binding affinity and interactions of compounds (**6a-6j**) in *α-amylase* binding pocket.

7.2.MD Simulations

The enzyme inhibitory activity of the *α-glucosidase* inhibitors within the **6a–6j** series identified compounds **6b** and **6c** as promising lead candidates. To further evaluate their binding affinity and the stability of the protein-ligand complex, MD simulations were conducted for 200 ns. The analysis of simulation interactions focused on key metrics, including hydrogen bond interactions, RMSD, and RMSF. The RMSD provides insight into the overall structural deviation of atomic positions relative to the initial reference frame (frame 0) throughout the simulation, while the RMSF reveals localized fluctuations in protein regions and shifts in ligand atom positions. The subsequent discussion provides a comprehensive analysis of the behavior and stability of the protein-ligand complexes during the MD simulation.

The ***α-glucosidase*-6b** protein-ligand complex exhibited high structural stability as evidenced by the Protein-Ligand RMSD analysis. The C-alpha and backbone RMSD values remained stable, with maximum deviations recorded at 2.755 Å and 2.754 Å, respectively, at frame 977. Ligand RMSD analysis revealed that, when aligned with the protein, the ligand displayed a maximum deviation of 4.266 Å (frame 989), while alignment with the ligand itself showed a maximum deviation of 1.185 Å (frame 967). These findings suggest a stable ligand orientation within the binding pocket.

The RMSF analysis of the protein highlighted minimal fluctuations in amino acid residues at the binding site, confirming binding site stability. The most pronounced deviation was observed at residue SER 419, with C-alpha and backbone deviations of 2.340 Å and 2.428 Å, respectively (frame 417). Residues in direct contact with the ligand showed negligible fluctuations, further supporting the stability of the ligand-protein interaction. Ligand RMSF analysis, which tracks the movement of ligand atoms during the MD simulation, showed maximum fluctuations of 2.572 Å and 1.225 Å for the carbon atoms of the benzene ring when aligned with the protein and with the ligand,

respectively. No significant deviations were noted in the functional groups, suggesting that the ligand remained stably positioned within the binding pocket throughout the simulation. Hydrogen bonding interactions were analyzed using a protein-ligand contact timeline and a histogram plot. LYS 155

formed a continuous hydrogen bond with the ligand throughout the entire 200 ns MD simulation. Additionally, LYS 155 was observed to form water-bridge-mediated hydrogen bonds with ASP 349 and GLU 276. HIS 239 maintained a hydrogen bond interaction for 100 ns. A stable pi-cation interaction was also observed between the ligand and ARG 312 for the entire simulation period. Further analysis of ligand properties, including the radius of gyration (Rg), SASA, PSA, and the number of intramolecular hydrogen bonds, provided additional insights into ligand stability and conformational behavior within the binding pocket (**Fig. 65**). Collectively, these results underscore the stability of the *α-glucosidase*-6b protein-ligand complex, highlighting the robustness of ligand binding and its interaction dynamics over the course of the 200 ns simulation

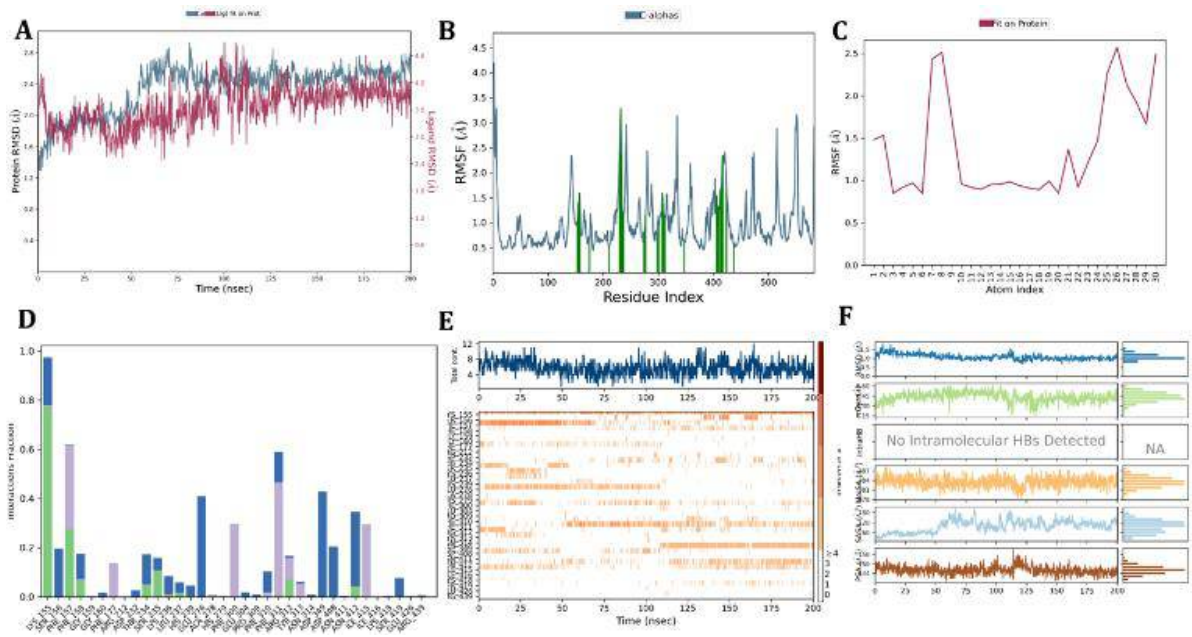


Fig. 65 : simulation interaction diagram of *α-glucosidase*-6b complex A) Represents Protein-ligand RMSD plot, B) Protein RMSF plot, C) ligand RMSF, D) Protein-ligand contact histogram, E) Protein-ligand contact timeline and F) Ligand properties.

The ***α-glucosidase*-6c** complex revealed key insights into its structural stability and ligand interactions. The RMSD analysis of the protein structure relative to the reference C-alpha and backbone atoms indicated maximum deviations of 3.263 Å and 3.254 Å, respectively, observed at frame 999. The ligand stability, assessed using the ligand RMSD relative to alignment on the protein

and self-alignment, demonstrated maximum deviations of 4.985 Å and 1.561 Å, respectively, at frame 15. RMSF analysis of the protein highlighted a notable fluctuation at ASP232 with a peak of 3.023 Å (frame 230), while other ligand-contacting residues exhibited fluctuations below 1.00 Å, suggesting stable interactions within the binding pocket. The ligand RMSF plot confirmed the structural stability of compound **6c**. However, the chlorine atom of the ligand displayed RMS fluctuations of 1.141 Å and 0.695 Å relative to the protein and ligand, respectively. The protein-ligand contact analysis, which included the contact histogram and interaction timeline, revealed critical non-covalent interactions. Hydrogen bonding was observed with PHE311, while water-mediated hydrogen bonds were detected with PRO309, ASP408, and GLU276. Additionally, π-cation interactions with ARG312 and π-π stacking with PHE158 were identified. These interactions collectively highlight the stable and favorable binding mode of compound **6c** within the *α-glucosidase* binding pocket. The ligand's physicochemical properties and binding features are illustrated in **Fig. 66**.

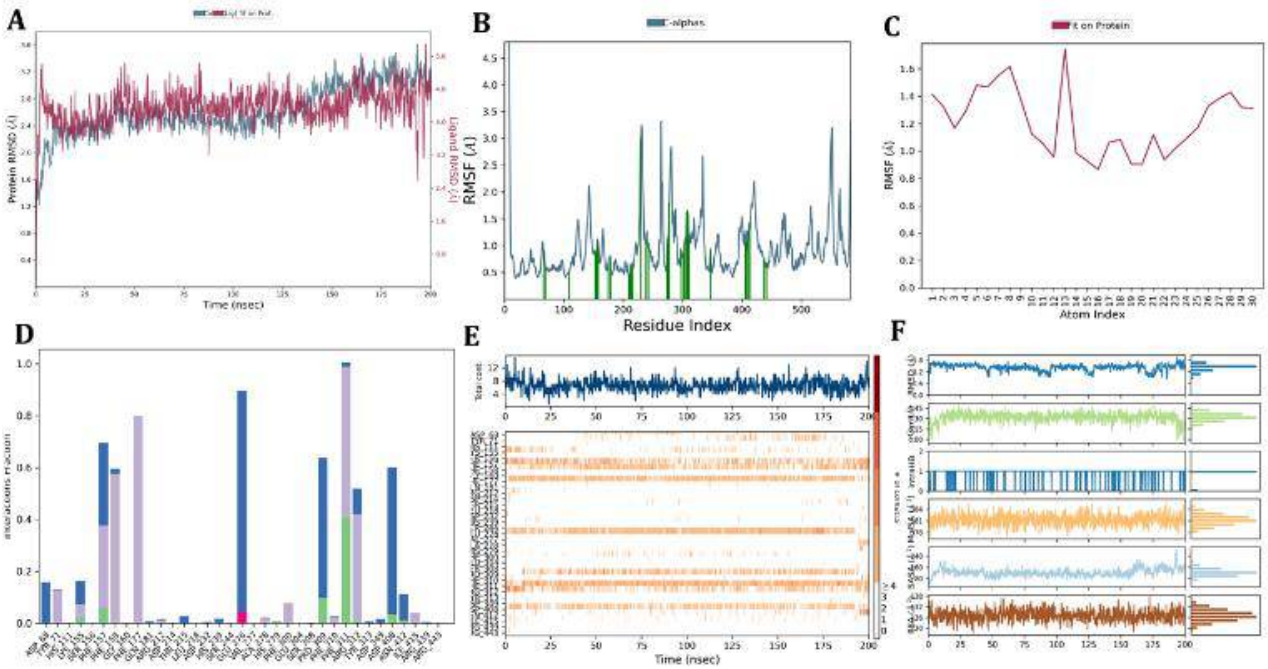


Fig. 66: simulation interaction diagram of *α-glucosidase*-6c complex A) Represents Protein-ligand RMSD plot, B) Protein RMSF plot, C) ligand RMSF, D) Protein-ligand contact histogram, E) Protein-ligand contact timeline and F) Ligand properties.

MMGB/SA: This strategy enables the decomposition of the total binding free energy into distinct components, facilitating a comprehensive analysis of the binding affinity between the ligand and receptor complex. The contributions of key energetic parameters, including van der Waals forces, Coulombic interactions, steric effects, lipophilic interactions, and hydrogen bonding, are systematically summarized in **Table 28**.

Comp.	MMGBSA dG Bind	MMGBSA dG Bind Hbond	MMGBSA dG Bind vdW	MMGBSA dG Bind Coulomb	MMGBSA dG Bind Covalent	MMGBSA dG Bind Solv GB
	Kcal/mol	Kcal/mol	Kcal/mol			
Prime MM/GBSA of *α- glucosidase*						
6a	-40.45	-5.51	-40.7	-44.68	1.26	69.16
6b	-36.6	-0.58	-48.03	-9.04	3.56	41.37
6c	-44.44	-2.16	-34.93	-17.59	7.3	34.71
6d	-43.59	-1.76	-47.37	-22.38	3.97	49.12
6e	-37.76	-0.47	-49.3	-10.25	3.93	45.23
6f	-41.25	-1.89	-51.06	-11.79	9.43	40.65
6g	-43.43	-0.74	-54.6	-9.34	15.87	42.59
6h	-45.14	-0.52	-53.03	-9.68	4.24	43.91
6i	-48.14	-0.74	-50.56	-23.97	5.24	47.6
6j	-37.07	-0.21	-50	-4.32	2.64	35.97
Prime MM/GBSA of *α- amylase*						
6a	-28.72	-1.24	-45.53	-15.34	12.2	54.16
6b	-33.41	-2.23	-45.94	-11.64	13.69	44.7
6c	-39.65	-2.18	-52.01	-15.84	12.38	49.89
6d	-26.24	-0.75	-45.96	-9.03	5.21	57.21
6e	-34.14	-1.26	-53.79	-17.22	13.73	59.35
6f	-32.82	-1.27	-49.86	-12.3	13.1	52.02
6g	-40.7	-1.16	-53.72	-13.61	9.08	54.89
6h	-29.17	-1.37	-53.58	-9.01	14.66	55.01
6i	-25.96	-1.34	-44.3	-14.74	5.87	55.39
6j	-38.29	-1.39	-52.41	-7.47	11.79	47.26

Table. 28: MM/GBSA Calculation of synthesized compounds (**6a-6j).**

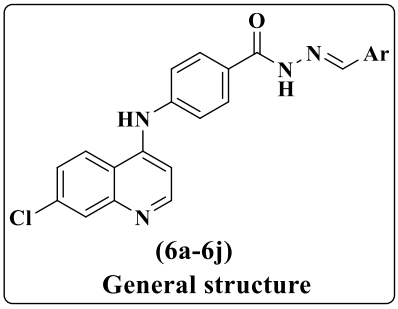
7.3.DFT computations

The optimization of the synthesized molecular structures, particularly their gas-phase energies, is presented in **Table 29**. The analysis of MOs plays a pivotal role in quantum chemistry, as it provides insights into the electronic structure, binding affinity, and reactivity of molecules. Among the key molecular orbitals, the HOMO and the LUMO are of prime importance. These orbitals significantly influence essential chemical properties, including reactivity, stability, and reaction kinetics. The concept of molecular "hardness" (η) serves as a critical indicator of chemical reactivity, with softer molecules generally displaying higher reactivity. The reactivity descriptors, along with the HOMO-LUMO energy gap (ΔE_{GAP}), were calculated using DFT with the B3LYP functional and a 6-31G(d,p**) basis set. The computed values are listed in **Table 30**. The FMO, specifically the HOMO and LUMO, for compounds **6b** and **6c**, are visualized in **Fig. 67**. Notably, a smaller ΔE_{GAP} is often associated with increased molecular reactivity. For compounds **6b** and **6c**, the calculated ΔE_{GAP} values are -0.14006 eV and -0.14059 eV, respectively, highlighting their potential chemical reactivity.

The MEP serves as a vital tool for visualizing the spatial distribution of electric charge within a molecule. It provides critical insights into the nature of electrostatic interactions both within the molecule and between the molecule and a protein's binding pocket. By mapping the MEP onto the molecular surface, regions of high electron density (associated with negative potential) and low electron density (associated with positive potential) can be distinguished. This information aids in predicting potential sites for nucleophilic and electrophilic attack, as well as understanding molecular interactions at a fundamental level.

In this study, MEPs were computed using the B3LYP density functional theory method in conjunction with a 6-31G (d, p**) basis set at the optimized molecular geometry. The MEPs of potential drug candidates **6b** and **6c** are illustrated in **Fig. 68**. The visualization reveals that the size, shape, and spatial orientation of positive (represented by blue regions, corresponding to nucleophilic attack sites), negative (depicted as red regions, corresponding to electrophilic attack sites), and

neutral (green regions) potential zones are significantly influenced by the nature of the substituent functional groups. This variability in the electrostatic potential landscape of drug-like molecules plays a pivotal role in modulating the strength and specificity of drug-receptor interactions at the active site of the target receptor.



(6a-6j)
General structure

Compound	Gas Phase Energy (eV)
6a	-1641.166335
6b	-1716.392044
6c	-1716.389529
6d	-1680.487182
6e	-1775.142601
6f	-1755.69537
6g	-1870.2175
6h	-1984.736796
6i	-2560.346418
6j	-2560.348556

Table. 29: Final Energy of Geometry optimized structures (**6a-6j**).

Quantum chemical parameters	E_{HOMO} (eV)	*ELMO* (eV)	ΔE_{GAP} (eV)	μ (eV)	σ (eV)	η (eV)	ω (eV)
6a	-0.22342	-0.08268	0.14074	-0.15305	14.21060111	0.07037	0.000824
6b	-0.22132	-0.08126	0.14006	-0.15129	14.27959446	0.07003	0.000801
6c	-0.22112	-0.08053	0.14059	-0.150825	14.22576286	0.070295	0.0008
6d	-0.2222	-0.08141	0.14079	-0.151805	14.20555437	0.070395	0.000811
6e	-0.19993	-0.07859	0.12134	-0.13926	16.48261085	0.06067	0.000588
6f	-0.22003	-0.08079	0.13924	-0.15041	14.3636886	0.06962	0.000788
6g	-0.21566	-0.08103	0.13463	-0.148345	14.85552997	0.067315	0.000741
6h	-0.22183	-0.08283	0.139	-0.15233	14.38848921	0.0695	0.000806
6i	-0.22507	-0.08528	0.13979	-0.155175	14.30717505	-0.070096	0.000842

Table. 30: Calculated quantum chemical parameters of synthesized compounds (**6a-6j**).

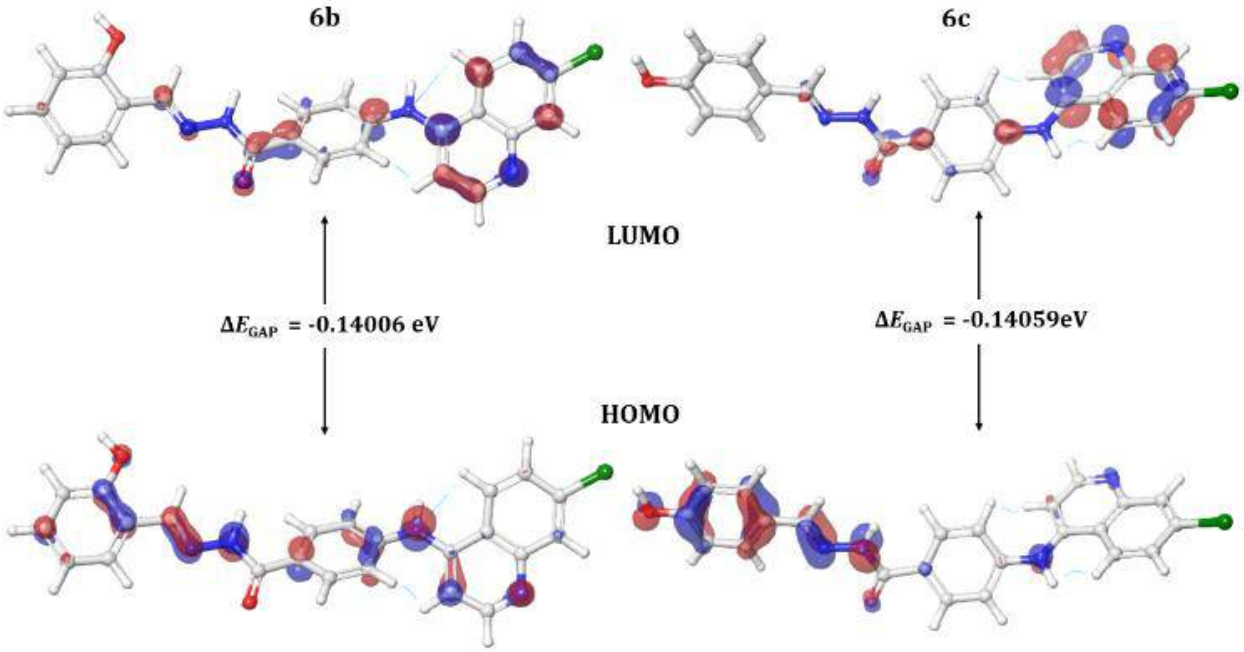


Fig. 67: Represents the HOMO and LUMO orbitals with Energy Gap (ΔEGAP) for the compound **6b** and **6c.**

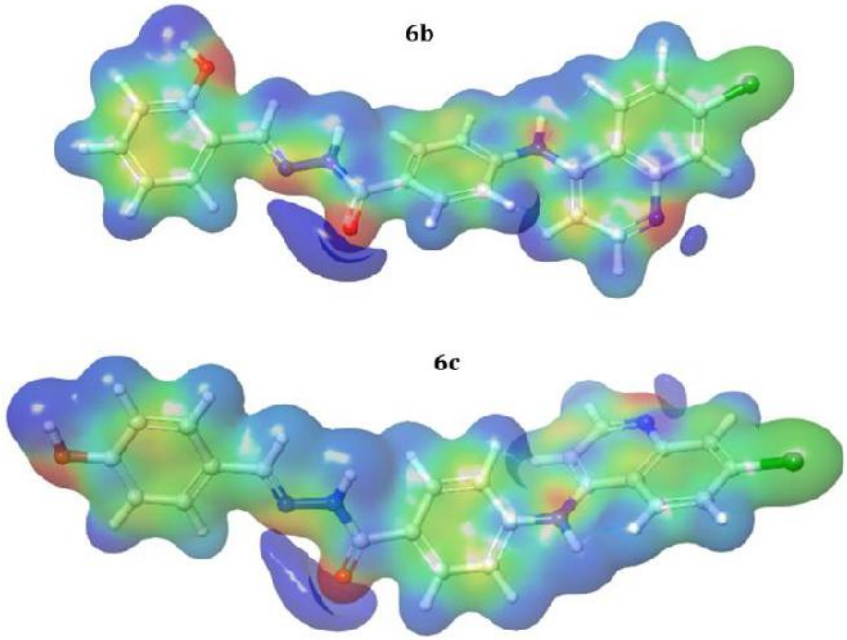


Fig. 68: Represents the Molecular electrostatic potential map for the compounds **6b** and **6c**.

7.4. ADMET predictions

The ADMET (absorption, distribution, metabolism, excretion, and toxicity) properties of the synthesized compounds were computationally predicted using Schrödinger's QikProp module. Key parameters such as hydrogen bond donors, hydrogen bond acceptors, hydrophilicity, molecular weight, permeability, and percent human oral absorption were assessed. Additionally, potential violations of Lipinski's Rule of Five and Jorgensen's Rule of Three were evaluated and compared against established benchmark values, as summarized in **Table 31**. Notably, compounds 6b and 6c adhered fully to Lipinski's Rule of Five, exhibiting no violations, while the remaining compounds displayed at least one deviation from the rule.

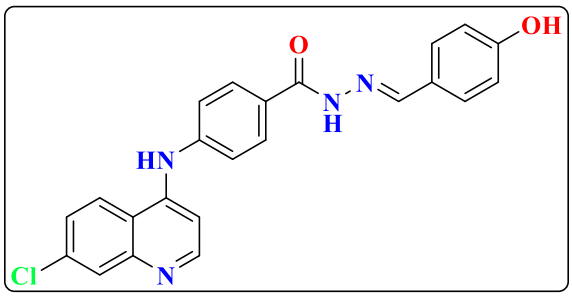
Comp.	MW	DHB	AHB	QPlog Po/w	QP logBB	QPlog HERG	QPP Caco
6a	400.866	2	4	5.529	-0.751	-7.717	1069.586
6b	416.866	3	4.75	4.743	-1.413	-7.632	344.65
6c	416.866	3	4.75	4.862	-1.378	-7.826	393.135
6d	414.893	2	4	5.751	-0.785	-7.585	1053.718
6e	443.935	2	5	5.969	-0.915	-7.672	989.702
6f	430.893	2	4.75	5.658	-0.848	-7.668	1068.846
6g	460.919	2	5.5	5.855	-0.813	-7.665	1348.724
6h	490.945	2	6.25	6.23	-1.101	-8.026	1057.152
6i	469.757	2	4	6.317	-0.492	-7.38	1017.054
6j	469.757	2	4	6.452	-0.506	-7.547	1009.507

Comp.	QPP MDCK	QPlog Khsa	%HOA	CNS	ROF	ROT
6a	1313.383	0.927	100	-1	1	1
6b	386.171	0.704	100	-2	0	1
6c	444.917	0.727	100	-2	0	1
6d	1289.393	1.052	100	-1	1	1
6e	1207.45	1.105	100	-1	1	1
6f	1311.799	0.953	100	-1	1	1
6g	1686.872	0.966	100	-1	1	1
6h	1296.419	1.106	100	-2	1	1
6i	5992.488	1.115	100	0	1	1
6j	6340.43	1.159	100	0	1	1

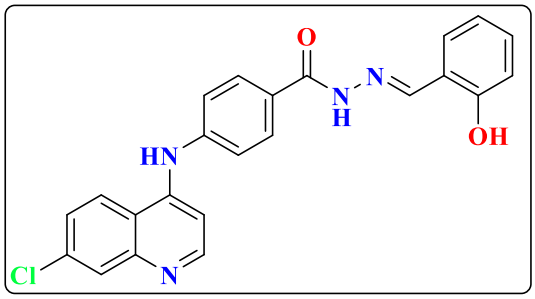
Table. 31: Computed ADMET properties of synthesized molecules (**6a-6j**).

Outcome of scheme.3

Identified Hit molecules as dual targeting *α-amylase* and *α-glucosidase* inhibitor



(6b)



(6c)

Chapter 6

Summary…

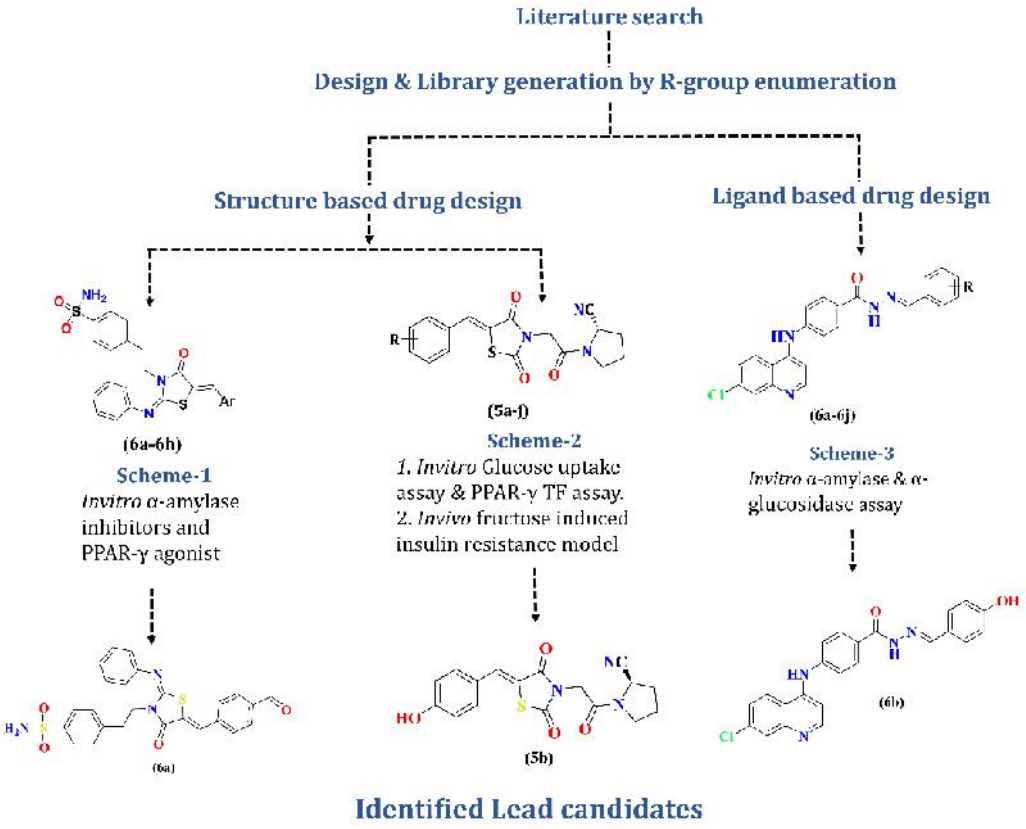


Fig. 69: Summary of the presented work.

In the present study, we utilised a CADD approach **Fig. 68**, to design molecules targeting the proteins involved in the pathogenesis of T2DM. Initially various molecular targets were identified through review of literature, which involved selection of the protein targets like PPAR-γ and postprandial diabetic targets like *α-amylase* and *α-glucosidase* enzyme in our present study. Then, molecular templates containing nitrogen and sulphur in heterocycle system were designed looking at the literature search and pharmacophore present in existing marketed antidiabetic agents. Then a library of molecules were generated by using reaction enumeration and R-group enumeration. The SBDD approach involved, **scheme.1** and **scheme. 2**, where we designed templates which include thiazoldin-4-one clubbed with ethanebenzene sulphonamide moieties for targeting the *α-amylase* enzyme. In **scheme. 2**, we designed molecular template which included TZD clubbed with the pyrrolidine carbonitrile, a motif present in vildagliptin, a DPP-4 inhibitor and assessed its antidiabetic molecular

mechanism. All the molecules (**6a-6h**, **scheme.1 & 5a-5j scheme. 2**) were synthesized and characterized by FTIR, (^{1}H & ^{13}C) NMR, Mass spectral studies. Among the series (**6a-6h**), compound 4-(2-((E)-5-((Z)-2-hydroxybenzylidene)-4-oxo-2-(phenylimino) thiazolidin-3-yl) ethyl) benzenesulfonamide **(6b)** was identified to be the better inhibitor of *α-amylase* enzyme, further the network pharmacology revealed compound **6b**, showed better association with PPAR-γ and GLUT carriers proteins *via* modulation of enriched pathways like PPAR signaling pathway and adipocytokine signaling pathway respectively, hence the same **6b** was evaluated for its PPAR-TF agonist activity, which showed dose-dependent activation of PPAR-γ TF, also the glucose uptake assay in yeast cells confirmed translocation of GLUT carriers by compound **6b**. Moreover compounds **6b** showed better binding dynamics with PPAR- γ LBD *via* docking and dynamic simulation studies.

Similarly, compound **5b** and **5f** were identified to be top hits in pharmacophore mapping at the LBD of PPAR- γ, these compounds showed better glucose uptake in skeletal muscles cells (L6 myotubes) compared to pioglitazone, and also displayed dose depended activation of PPAR- γ. Hence the two compound **5b** and **5f** were considered for the reversal of insulin resistance in fructose induced insulin resistant rat model, to assess their antidiabetic activity. However both the compounds showed amelioration of hyperglycemia and hyperinsulinemia, but compared to **5b** there was significant difference in maintaining the glucose homeostasis in compound **5f** treated group owing to its poor pharmacokinetic properties. Thus the molecular simulation studies displayed a stable binding orientation of compound **5b** in the LBD of PPAR- γ. Network analysis revealed molecular targets like *PPAR-γ, GLUT, INS, INSR, ADIPO, CD36*, and *FAPB4* are, modulated by compound **5b** which is related to glycogenesis, Glycolysis, adipocyte differentiation, lipid metabolism and inhibition of gluconeogenesis and were correlated with *invivo* findings.

Similarly, The LBDD approach involved, primarily selecting a dataset of *α-glucosidase* inhibitors and developing the pharmacophore model, which was validated *via* decoy set and QSAR parameters. Thus the library of molecules were screened over the developed model, we identified

quinoline based schiff base template with better mapping statistics, so the identified ligands were synthesised and evaluated for *invitro α-glucosidase* enzyme inhibition, compound **6b** from the **scheme.3** showed competitive inhibition kinetics. Finally the hypothetical binding mechanism was identified using the docking and MD simulation studies, and based on the obtained insilico and invitro finding and SAR was established for the compound (**6a-6j**).

Chapter 7

Conclusion…

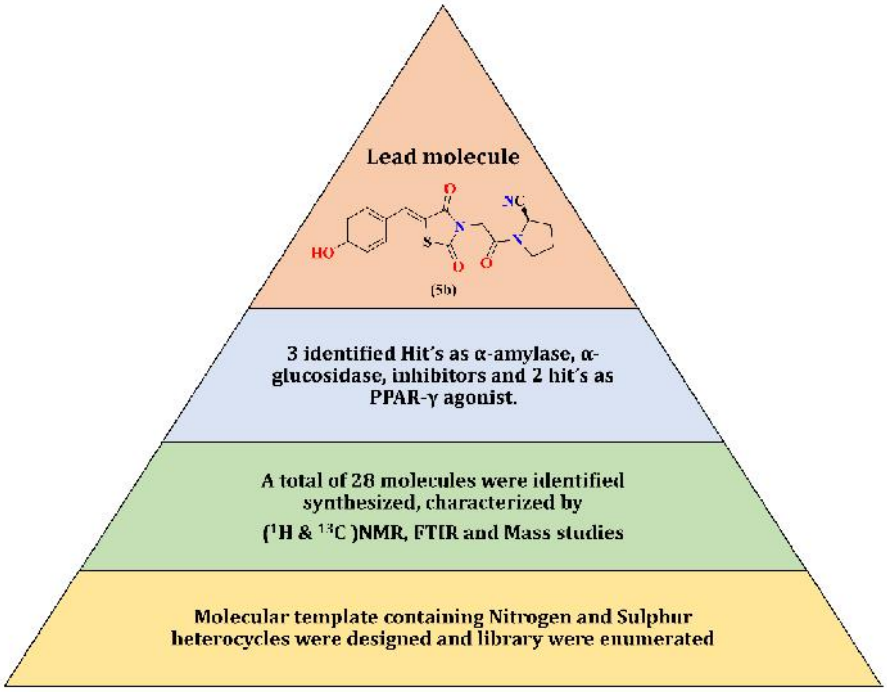


Fig. 70: Outcome of present research work.

The study presented in the thesis work highlights synthesis, characterization, and antidiabetic evaluation of novel nitrogen and sulphur containing heterocyclic agents through a multidisciplinary approach, incorporating CADD techniques followed by *Invitro* and *Invivo* methodologies.

1. Synthesis and biological assessment of benzenesulfonamide-thiazolidinone derivatives The first investigation focuses on the synthesis of nine benzenesulfonamide-thiazolidinone derivatives, which were characterized using FTIR, ^{1}H NMR, ^{13}C NMR, and mass spectrometry. Their antidiabetic efficacy was assessed through *α-amylase* inhibition and glucose uptake in yeast cells. Among the synthesized compounds, **6b** demonstrated the most potent *α-amylase* inhibition, with an IC_{50} of 29.51 ± 1.35 µg/mL, and significantly increased glucose uptake (88.71%). Additionally, compound **6b** activated the LBD and upregulated the expression of the PPAR-γ transcription factor. IFD revealed that **6b** binds to key amino acid residues in the *α-amylase* binding pocket, supporting the *Invitro* inhibition results. DFT calculations confirmed the structural stability of **6b**, and computational pharmacology analysis suggested that it modulates key target proteins such as *PIK3CA*, *EGFR*, *PTEN1*, *PPAR-γ* and *CDK2*, which influence *GLUT4* vesicle translocation and glucose uptake. Further analysis revealed that **6b** also

interacts with *AMY1A*, supporting its *α-amylase* inhibitory activity. These findings offer a mechanistic basis for the potential development of compound **6b** as a promising dual target antidiabetic lead molecule.

2. Investigation of acetyl pyrrolidine-2-carbonitrile-based benzylidene thiazolidine-2,4-Dione hybrids

The second study applies an integrated approach involving *Insilico*, *Invitro*, and *Invivo* techniques to explore the antidiabetic properties of acetyl pyrrolidine-2-carbonitrile-based benzylidene thiazolidine-2, 4-dione hybrids (**5a-5j**). Ten top-hit molecules identified through structure-based pharmacophore screening were synthesized and characterized *via* spectral analysis. *Invitro* glucose uptake assays in L6 myotubes revealed that compounds **5b** and **5f** exhibited significant glucose uptake (79.29 ± 1.02% and 74.58 ± 0.54%, respectively), comparable to pioglitazone (82.36 ± 0.98%). The two compounds also displayed dose-dependent transactivation of PPAR-γ and improved glucose homeostasis, reversing insulin resistance in fructose-induced hyperinsulinemic wistar rats. The OGTT and ITT results confirmed the effectiveness of **5b** and **5f** in mitigating insulin resistance. Their PPAR-γ agonist activity was linked to improvements in lipid metabolism and glucose homeostasis. DFT calculations provided optimized molecular geometries and charge distributions for **5b** and **5f**, while molecular docking and MD simulations demonstrated stable binding with key protein targets. MM/GBSA analysis revealed favorable binding free energies, supporting the potential of these compounds for further development. Network pharmacology analysis suggested that **5b** and **5f** upregulate *ADIPOQ* (adiponectin) and *NR1C3* (PPAR-γ), although further quantification of *LEP* (leptin) and GLP-1 levels is required. These findings identify **5b** as a lead compound for further development of glucose homeostatic agent in antidiabetic drug discovery.

3. Design and Evaluation of Quinoline-Based Benzohydrazide Schiff's Base Derivatives

The third study utilizes LBDD approach to identify potential *α-glucosidase* inhibitors. A molecular library based on a quinoline-benzohydrazide Schiff's base scaffold was constructed, and a ligand based pharmacophore model (AADRR_1) was developed from a dataset of 64 molecules with established *α-glucosidase* inhibitory activity. The top 10 ligands from pharmacophore screening were synthesized and characterized through spectroscopic analysis. *Invitro* evaluations demonstrated that compounds **6b** and **6c** exhibited significant inhibition of *α-glucosidase* (IC_{50} values of 19.37 ± 0.96 µM and 12.95 ± 2.35 µM, respectively) and *α-amylase* (IC_{50} values of 29.36 ± 3.24 µM and 33.04 ± 1.83 µM, respectively). MTT assays on L929 fibroblast cells confirmed the non-toxic nature of synthesized compounds (**6a-6j**). Molecular docking and 200 ns MD simulations revealed stable ligand-enzyme interactions. MM/GBSA calculations provided binding free energy estimates, while DFT analysis confirmed the structural stability and electronic properties of the molecules. Based on these findings, compounds **6b** and **6c** were identified as lead candidates for further optimization and development of postprandial antidiabetic agents.

Limitations and Prospective

- The lead molecules derived from Scheme 1 (**6b**) and Scheme 3 (**6b**) were evaluated for their antidiabetic mechanism through computational modeling and *Invitro* analysis. Further investigation is required, including *Invivo* studies as well as assessments of both acute and chronic toxicity.
- The lead compound **5b**, as outlined in Scheme 2, along with its experimental pharmacological data, was associated with common genes implicated in the pathophysiology of T2DM. However, the network pharmacology analysis was restricted to mapping homologous proteins, which limits its scope. A more precise approach would involve cross-mapping the compound's interactions with specific biomarkers linked to distinct genes, thereby enabling a clearer elucidation of the antidiabetic molecular mechanism of compound **5b**.

Chapter 8

References…

References

1. Stromgaard K, Krogsgaard-Larsen P, Madsen U. Textbook of drug design and discovery. 4th edition, CRC press; 2009 Oct 7, 476p. doi.org/10.1201/9781439882405.
2. Mandal S, Mandal SK. Rational drug design. Eur. J. Pharmacol. 2009 Dec 25;625(1-3):90-100. doi.org/10.1016/j.ejphar.2009.06.065.
3. Zhou SF, Zhong WZ. Drug design and discovery: principles and applications. Molecules. 2017 Feb 13;22(2):279. doi.org/10.3390/molecules22020279.
4. Ban TA. The role of serendipity in drug discovery. Dialogues Clin. Neurosci. 2006 Sep 30; 8(3):335-44. doi.org/10.31887/DCNS.2006.8.3/tban
5. Klebe G. Recent developments in structure-based drug design. J. Mol. Med. 2000 Jul; 78:269-81. doi.org/10.1007/s001090000084.
6. Bacilieri M, Moro S. Ligand-based drug design methodologies in drug discovery process: an overview. Curr. Drug Discov. Technol. 2006 Sep 1;3(3):155-65. doi.org/10.2174/157016306780136781.
7. Lin X, Li X, Lin X. A review on applications of computational methods in drug screening and design. Molecules. 2020 Mar 18; 25(6):1375. doi.org/10.3390/molecules25061375.
8. Khedkar SA, Malde AK, Coutinho EC, Srivastava S. Pharmacophore modeling in drug discovery and development: an overview. Med. Chem. 2007 Mar 1; 3(2):187-97.
9. Hernández-Rodríguez M, C. Rosales-Hernández M, E. Mendieta-Wejebe J, Martínez-Archundia M, Correa Basurto J. Current tools and methods in molecular dynamics (MD) simulations for drug design. Curr. Med. Chem. 2016 Oct 1;23(34):3909-24. doi.org/10.2174/0929867323666160530144742.
10. Blair M. Diabetes mellitus review. Urol. Nurs. 2016 Jan 1;36(1). Doi.org/10.7257/1053-816X.2016.36.1.27.

11. Skyler JS. Diabetes mellitus: pathogenesis and treatment strategies. J. Med. Chem. 2004 Aug 12;47(17):4113-7. doi.org/10.1021/jm0306273.
12. Davies MJ. Insulin secretagogues. Curr. Med. Res. Opin. 2002 Jan 1;18(sup1):s22-30. doi.org/10.1185/030079902125000200.
13. Zhang S, Zhang ZY. PTP1B as a drug target: recent developments in PTP1B inhibitor discovery. Drug Discov. Today. 2007 May 1;12(9-10):373-81. doi.org/10.1016/j.drudis.2007.03.011.
14. Doupis J, Veves A. DPP4 inhibitors: a new approach in diabetes treatment. Adv. Ther. 2008 Jul;25:627-43. doi.org/10.1007/s12325-008-0076-1.
15. White Jr JR. Empagliflozin, an SGLT2 inhibitor for the treatment of type 2 diabetes mellitus: a review of the evidence. Ann. Pharmacother. 2015 May;49(5):582-98. doi.org/10.1177/10600280155735.
16. Wright EM. SGLT2 inhibitors: physiology and pharmacology. K360. 2021 Dec 1;2(12):2027-37. doi.org/10.34067/KID.0002772021.
17. Toeller M. α-Glucosidase inhibitors in diabetes: efficacy in NIDDM subjects. Eur. J. Clin. Investig. 1994 Aug;24(S3):31-5. doi.org/10.1111/j.1365-2362.1994.tb02253.x.
18. Devchand PR, Liu T, Altman RB, FitzGerald GA, Schadt EE. The pioglitazone trek via human PPAR gamma: from discovery to a medicine at the FDA and beyond. Front. pharmacol. 2018 Oct 4; 9:1093. doi.org/10.3389/fphar.2018.01093.
19. Stein SA, Lamos EM, Davis SN. A review of the efficacy and safety of oral antidiabetic drugs. Expert Opin. Drug Saf. 2013 Mar 1;12(2):153-75. doi.org/10.1517/14740338.2013.752813.
20. Hossain MA, Pervin R. Current antidiabetic drugs: review of their efficacy and safety. Nutr. Ther. Interven. Diabetes Metab. Syndr.2018 Jan 1:455-73. doi.org/10.1016/B978-0-12-812019-4.00034-9.
21. Mane PB, Antre RV, Oswal RJ. Antidiabetic drugs: An overview. Int. J. Pharm. Chem. Sci. 2012;1(1):301-6.

22. Grunberger G. Should side effects influence the selection of antidiabetic therapies in type 2 diabetes? Curr. Diabetes Rep. 2017 Apr;17:1-2. doi.org/10.1007/s11892-017-0853-8.
23. Gharge S, Alegaon SG. Recent Studies of Nitrogen and Sulfur Containing Heterocyclic Analogues as Novel Antidiabetic Agents: A Review. Chem. Biodiversity. 2024 Feb;21(2):e202301738. doi.org/10.1002/cbdv.202301738.
24. Khatik GL, Datusalia AK, Ahsan W, Kaur P, Vyas M, Mittal A, Nayak SK. A retrospect study on thiazole derivatives as the potential antidiabetic agents in drug discovery and developments. Curr. Drug Discov. Technol. 2018 Sep 1;15(3):163-77. doi.org/10.2174/1570163814666170915134018.
25. Heydari Z, Mohammadi-Khanaposhtani M, Imanparast S, Faramarzi MA, Mahdavi M, Ranjbar PR, Larijani B. Pyrano [3, 2-c] quinoline derivatives as new class of α-glucosidase inhibitors to treat type 2 diabetes: synthesis, in vitro biological evaluation and kinetic study. Med. Chem. 2019 Feb 1;15(1):8-16. doi.org/10.2174/1573406414666180528110104.
26. Khalifa Z, Upadhyay R, Patel AB. Benzothiazole derivatives as effective α-glucosidase inhibitors: an insight study of structure-activity relationships and molecular targets. Med. Chem. Res. 2024 Sep 23:1-25. doi.org/10.1007/s00044-024-03314-z.
27. Bhatti RS, Shah S, Suresh, Krishan P, Sandhu JS. Recent pharmacological developments on rhodanines and 2, 4-thiazolidinediones. Int. J. Med. Chem. 2013;2013(1):793260. doi.org/10.1155/2013/793260.
28. A Datar P, A Deokule T. Development of thiadiazole as an antidiabetic agent-a review. Mini-Rev. Med. Chem.2014 Feb 1;14(2):136-53.
29. Sahiba N, Sethiya A, Soni J, Agarwal DK, Agarwal S. Saturated five-membered thiazolidines and their derivatives: from synthesis to biological applications. Top. Curr. Chem. 2020 Apr;378(2):34. doi.org/10.1007/s41061-020-0298-4.

30. Long N, Le Gresley A, Wren SP. Thiazolidinediones: an in–depth study of their synthesis and application to medicinal chemistry in the treatment of diabetes mellitus. ChemMedChem. 2021 Jun 7;16(11):1717-36. doi.org/10.1002/cmdc.202100177.
31. Nirwan S, Chahal V, Kakkar R. Thiazolidinones: Synthesis, reactivity, and their biological applications. J. Heterocycl. Chem. 2019 Apr;56(4):1239-53. doi.org/10.1002/jhet.3514.
32. Jain VS, Vora DK, Ramaa CS. Thiazolidine-2, 4-diones: Progress towards multifarious applications. Bioorg. Med. Chem. 2013 Apr 1;21(7):1599-620. doi.org/10.1016/j.bmc.2013.01.029.
33. Jain AK, Vaidya A, Ravichandran V, Kashaw SK, Agrawal RK. Recent developments and biological activities of thiazolidinone derivatives: A review. Bioorg. Med. Chem. 2012 Jun 1;20(11):3378-95. doi.org/10.1016/j.bmc.2012.03.069.
34. Aqlan FM, Al-Bogami AS, Alqahtani NF, Wani MY, Khan SA. Thiazolidinone: A structural motif of great synthetic and biological importance. J. Mol. Struct. 2022 Feb 15;1250:131771. doi.org/10.1016/j.molstruc.2021.131771.
35. Spiegelman BM. PPAR-gamma: adipogenic regulator and thiazolidinedione receptor. Diabetes. 1998 Apr 1;47(4):507-14. doi.org/10.2337/diabetes.47.4.507.
36. Singh R, Sindhu J, Kumar P, Hooda M, Aggarwal R, Lal S, Ahmadi S, Lotfi S, Singh D, Kumar H. α-Amylase Inhibitors Based on Thiazolidinone Skeleton: A Promising Approach in Diabetes Management. ChemistrySelect. 2023 Dec 22; 8(48):e202303852. doi.org/10.1002/slct.202303852.
37. Gharge S, Alegaon SG. Recent Studies of Nitrogen and Sulfur Containing Heterocyclic Analogues as Novel Antidiabetic Agents: A Review. Chem. Biodiversity.2024 Feb;21(2):e202301738. doi.org/10.1002/cbdv.202301738.
38. Gharge S, Alegaon SG, Ranade SD, Khatib NA, Kavalapure RS, Kumar BP, Vinod D, Bavage NB. Design, synthesis of new 2, 4-thiazolidinediones: In-silico, in-vivo anti-diabetic and anti-

inflammatory evaluation. EJMCR. 2024 Aug 1; 11:100151. doi.org/10.1016/j.ejmcr.2024.100151.

39. Gharge S, Alegaon SG, Jadhav S, Ranade SD, Kavalapure RS. Design, synthesis, characterization and antidiabetic evaluation of 3, 5-substituted thiazolidinediones: Evidenced by network pharmacology, Molecular docking, and dynamic simulation, in vitro and in vivo assessment. EJMCR. 2024 Dec 1; 12:100213. doi.org/10.1016/j.ejmcr.2024.100213.
40. Haider S, Shafiq M, Siddiqui AR, Sardar M, Mushtaq M, Shafeeq S, Nur-e-Alam M, Ahmad A, Ul-Haq Z. Uncovering PPAR-γ agonists: An integrated computational approach driven by machine learning. J. Mol. Graph. Model. 2024 Jun 1; 129:108742. doi.org/10.1016/j.jmgm.2024.108742.
41. Naufal M, Hermawati E, Syah YM, Hidayat AT, Hidayat IW, Al-Anshori J. Structure–Activity Relationship Study and Design Strategies of Hydantoin, Thiazolidinedione, and Rhodanine-Based Kinase Inhibitors: A Two-Decade Review. ACS omega. 2024 Jan 19;9(4):4186-209. doi.org/10.1021/acsomega.3c04749.
42. Panten U, Schwanstecher M, Schwanstecher C. Sulfonylurea receptors and mechanism of sulfonylurea action. Exp. Clin. Endocrinol. Diabetes.1996; 104(01):1-9. 10.1055/s-0029-1211414.
43. Mandal S, Chiriki DS, Gurupadayya BM, Chethan IA, Kumar BP. Phenyl glycine incorporated glitazones as promising novel antidiabetic agents through PPARγ agonism: Design, synthesis and preclinical studies. Eur. J. Med Chem. 2022:1; 6:100067. doi.org/10.1016/j.ejmcr.2022.100067.
44. Patchipala SB, Pasupuleti VR, Audipudi AV, babu Bollikolla H. Synthesis, in-vivo anti-diabetic & anticancer activities and molecular modelling studies of tetrahydrobenzo [d] thiazole tethered nicotinohydrazide derivatives. Arab. J. Chem. 2022: 1; 15(2):103546. doi.org/10.1016/j.arabjc.2021.103546.

45. Sameeh MY, Khowdiary MM, Nassar HS, Abdelall MM, Amer HH. Thiazolidinedione Derivatives: In Silico, In Vitro, In Vivo, Antioxidant and Anti-Diabetic Evaluation. Molecules. 2022:27; 27(3):830. doi.org/10.3390/molecules27030830.

46. Prabhakaran S, Nivetha N, Patil SM, Martiz RM, Ramu. One-pot three-component synthesis of novel Phenyl-Pyrano-Thiazol-2-one derivatives and their anti-diabetic activity studies. Results Chem. 2022:12:100439. doi.org/10.1016/j.rechem.2022.100439.

47. Ravikumar D, Subramanyam C, Venkataramaiah C, Rajendra W, Rao KP. Synthesis, spectral characterization and anti-diabetic activity evaluation of phosphoramidate derivatives. Indian J. Chem. 2022:2; 61(1):60-8. Doi.org/10.56042/ijc.v61i1.60061.

48. Huneif MA, Alshehri DB, Alshaibari KS, Dammaj MZ, Mahnashi MH. Design, synthesis and bioevaluation of new vanillin hybrid as multitarget inhibitor of α-glucosidase, α-amylase, PTP-1B and DPP4 for the treatment of type-II diabetes. Biomed & Pharmacotherapy. 2022; 150:113038. doi.org/10.1016/j.biopha.2022.113038.

49. Nidhar M, Khanam S, Sonker P, Gupta P, Mahapatra A. Click inspired novel pyrazole-triazole-persulfonimide & pyrazole-triazole-aryl derivatives; Design, synthesis, DPP-4 inhibitor with potential anti-diabetic agents. Bioorg. Chem. 2022:1; 120:105586. doi.org/10.1016/j.bioorg.2021.105586.

50. Patil S, Alegaon SG, Gharge S, Ranade SD, Khatib NA. Molecular hybridization, synthesis, in vitro α-glucosidase inhibition, in vivo antidiabetic activity and computational studies of isatin based compounds. Bioorg. Chem. 2024:1; 153:107783. doi.org/10.1016/j.bioorg.2024.107783.

51. Bairagi KM, Younis NS, Emeka PM, Venugopala KN, Alwassil OI. Chemistry, anti-diabetic activity and structural analysis of substituted dihydropyrimidine analogues. J. Mol Struct. 2021: 5; 1227:129412. doi.org/10.1016/j.molstruc.2020.129412.

52. Colin-Lozano B, Torres-Gomez H, Hidalgo-Figueroa S, Chávez-Silva F, Estrada-Soto S. Synthesis, in vitro, in vivo and in silico antidiabetic bioassays of 4-nitro (thio)

phenoxyisobutyric acids acting as unexpected PPARγ modulators: an in combo study. Pharmaceuticals. 2022:15; 15(1):102. doi.org/10.3390/ph15010102

53. Nivetha N, Martiz RM, Patil SM, Ramu R, Sreenivasa S. Benzodioxole grafted spirooxindole pyrrolidinyl derivatives: synthesis, characterization, molecular docking and anti-diabetic activity. RSC Adv. 2022; 12(37):24192-207. Doi.org/10.1039/D2RA04452H.
54. Wahid S, Jahangir S, Versiani MA, Khan KM, Sung YY, Iqbal J, Wadood A, Rehman AU, Uzair M, Khan IA, Taha M. Biology-oriented drug synthesis of nitrofurazone derivatives: their α-glucosidase inhibitory activity and molecular docking studies. Arab. J. Chem. 2022:1; 15(6):103806. doi.org/10.1016/j.arabjc.2022.103806.
55. Zhang X, Zheng YY, Hu CM, Wu XZ, Lin J. Synthesis and biological evaluation of coumarin derivatives containing oxime ester as α-glucosidase inhibitors. Arab. J. Chem. 2022:1; 15(9):104072. doi.org/10.1016/j.arabjc.2022.104072.
56. Askarzadeh M, Azizian H, Adib M, Mohammadi-Khanaposhtani M, Mojtabavi S. Design, synthesis, in vitro α-glucosidase inhibition, docking, and molecular dynamics of new phthalimide-benzenesulfonamide hybrids for targeting type 2 diabetes. Sci. Rep. 2022: 22; 12(1):10569. doi.org/10.1038/s41598-022-14896-2.
57. Fan M, Feng Q, He M, Yang W, Peng Z. Synthesis, α-glucosidase inhibition and molecular docking studies of natural product 2-(2-phenyethyl) chromone analogues. Arab. J. Chem. 2022:1; 15(9): 104072. doi.org/10.1016/j.arabjc.2022.104301.
58. El-Zahabi MA, Bamanie FH, Ghareeb S, Alshaeri HK, Alasmari MM. Design, Synthesis, Molecular Modeling and Anti-Hyperglycemic Evaluation of Quinazoline-Sulfonylurea Hybrids as Peroxisome Proliferator-Activated Receptor Gamma (PPARγ) and Sulfonylurea Receptor (SUR) Agonists. Int. J. Mol. Sci. 2022:24; 23(17):9605. doi.org/10.3390/ijms23179605.

59. Madrigal-Angulo JL, Ménez-Guerrero C, Estrada-Soto S, Ramírez-Espinosa JJ, Almanza-Pérez JC. Synthesis, in vitro, in silico and in vivo hypoglycemic and lipid-lowering effects of 4-benzyloxy-5-benzylidene-1, 3-thiazolidine-2, 4-diones mediated by dual PPAR α/γ modulation. Bioorg. Med .Chem .Lett. 2022:128804. doi.org/10.1016/j.bmcl.2022.128804.

60. Kaur R, Kumar R, Dogra N, Yadav AK. Design, synthesis, biological evaluations and in silico studies of sulfonate ester derivatives of 2-(2-benzylidenehydrazono) thiazolidin-4-one as potential α-glucosidase inhibitors. J. Mol Struct. 2022; 1247:131266. doi.org/10.1016/j.molstruc.2021.131266.

61. Bairagi KM, Younis NS, Emeka PM, Venugopala KN, Alwassil OI. Chemistry, anti-diabetic activity and structural analysis of substituted dihydropyrimidine analogues. J. Mol Struct. 2021: 5; 1227:129412. doi.org/10.1016/j.molstruc.2020.129412.

62. Amin S, Sheikh KA, Iqubal A, Khan MA. Synthesis, in-Silico studies and biological evaluation of pyrimidine-based thiazolidinedione derivatives as potential anti-diabetic agent. Bioorg. Chem.2023;1; 134:106449. doi.org/10.1016/j.bioorg.2023.106449.

63. Khan S, Iqbal S, Taha M, Hussain R, Rahim F, Shah M, Awwad NS, Ibrahium HA, Alahmdi MI, Dera AA, Ullah H. Synthesis, in vitro biological assessment, and molecular docking study of benzimidazole-based thiadiazole derivatives as dual inhibitors of α-amylase and α-glucosidase. Front. Chem. 2023:5; 11:1125915. doi.org/10.3389/fchem.2023.1125915.

64. Kumar H, Dhameja M, Kurella S, Uma A, Gupta P. Synthesis, in-vitro α-glucosidase inhibition and molecular docking studies of 1, 3, 4-thiadiazole-5, 6-diphenyl-1, 2, 4-triazine hybrids: Potential leads in the search of new antidiabetic drugs. J. Mol. Struct. 1273:134339. doi.org/10.1016/j.molstruc.2022.134339.

65. Metre TV, Kodasi B, Bayannavar PK, Bheemayya L, Nadoni VB, Hoolageri SR, Shettar AK, Joshi SD, Kumbar VM, Kamble RR. Coumarin-4-yl-1, 2, 3-triazol-4-yl-methyl-thiazolidine-2,

4-diones: Synthesis, glucose uptake activity and cytotoxic evaluation. Bioorg. Chem. 2023:1; 130:106235. doi.org/10.1016/j.bioorg.2022.106235.

66. Huneif MA, Mahnashi MH, Jan MS, Shah M. New Succinimide–Thiazolidinedione Hybrids as Multitarget Antidiabetic Agents: Design, Synthesis, Bio evaluation, and Molecular Modelling studies. Molecules. 2023; 26; 28(3):1207. doi.org/10.3390/molecules28031207.
67. Srinivasa MG, Paithankar JG, Birangal SR, Pai A. Novel hybrids of thiazolidinedione-1, 3, 4-oxadiazole derivatives: synthesis, molecular docking, MD simulations, ADMET study, in vitro, and in vivo anti-diabetic assessment. RSC Adv.2023; 13(3):1567-79. Doi.org/10.1039/D2RA07247E.
68. Kratky M, Sramel P, Bodo P, Prnova MS. Novel rhodanine based inhibitors of aldose reductase of non-acidic nature with phydroxybenzylidene functional group. Eur. J. Med. Chem.2023; 15; 246:114922. doi.org/10.1016/j.ejmech.2022.114922.
69. Gharge S, Alegaon SG, Ranade SD, Kavalapure RS, Kumar BP. Novel rhodanine–thiazole hybrids as potential antidiabetic agents: a structure-based drug design approach. RSC Med.Chem. 2025. doi.org/10.1039/D4MD00689E.
70. Hayat S, Ullah H, Rahim F, Ullah I, Taha M, Iqbal N, Khan F, Khan MS, Shah SA, Wadood A, Sajid M. Synthesis, biological evaluation and molecular docking study of benzimidazole derivatives as α-glucosidase inhibitors and anti-diabetes candidates. J. Mol. Struct. 2023 Mar 15; 1276:134774 doi.org/10.1016/j.molstruc.2022.134774.
71. Wahid S, Jahangir S, Versiani MA, Khan KM, Sung YY, Iqbal J, Wadood A, Rehman AU, Uzair M, Khan IA, Taha M. Biology-oriented drug synthesis of nitrofurazone derivatives: their α-glucosidase inhibitory activity and molecular docking studies. Arab. J. Chem. 2022:1; 15(6):103806. doi.org/10.1016/j.arabjc.2022.103806.

72. Zhang X, Zheng YY, Hu CM, Wu XZ, Lin J. Synthesis and biological evaluation of coumarin derivatives containing oxime ester as α-glucosidase inhibitors. Arab. J. Chem. 2022:1; 15(9):104072. doi.org/10.1016/j.arabjc.2022.104072.

73. Singh G, Singh R, Monga V, Mehan S. 3, 5-Disubstituted-thizolidine-2, 4-dione hybrids as antidiabetic agents: Design, synthesis, in-vitro and In vivo evaluation. Eur. J. Med. Chem. 2024 Jan 12:116139. doi.org/10.1016/j.ejmech.2024.116139.

74. Hu C, Liang B, Sun J, Li J, Xiong Z, Wang SH, Xuetao X. Synthesis and biological evaluation of indole derivatives containing thiazolidine-2, 4-dione as α-glucosidase inhibitors with antidiabetic activity. Eur. J. Med. Chem. 2024 Jan 15; 264:115957.

75. Kamat V, Barretto DA, Poojary B, Kumar A, Patil VB, Hamzad S. In vitro α-amylase and α-glucosidase inhibition study of dihydropyrimidinones synthesized via one-pot Biginelli reaction in the presence of a green catalyst. Bioorg. Chem. 2024 Jan 3:107085. doi.org/10.1016/j.bioorg.2023.107085.

76. Azmi A, Noori M, Ghomi MK, Montazer MN, Iraji A, Dastyafteh N, Oliyaei N, Khoramjouy M, Rezaei Z, Javanshir S, Mojtabavi S. Alpha-glucosidase inhibitory and hypoglycemic effects of imidazole-bearing thioquinoline derivatives with different substituents: In silico, in vitro, and in vivo evaluations. Bioorg. Chem. 2024 Jan 8:107106. doi.org/10.1016/j.bioorg.2024.107106.

77. Zheng Y, Lu L, Li M, Xu D, Zhang L, Xiong Z, Zhou Y, Li J, Xu X, Zhang K, Xu L. New chromone derivatives bearing thiazolidine-2, 4-dione moiety as potent PTP1B inhibitors: Synthesis and biological activity evaluation. Bioorg. Chem. 2024 Feb 1; 143:106985. doi.org/10.1016/j.bioorg.2023.106985.

78. Hassan AS, Morsy NM, Aboulthana WM, Ragab A. Exploring novel derivatives of isatin-based Schiff bases as multi-target agents: design, synthesis, in vitro biological evaluation, and in silico ADMET analysis with molecular modeling simulations. RSC Adv. 2023;13(14):9281-303. Doi.org/10.1039/D3RA00297G.

79. Srinivasa MG, Revanasiddappa BC, Prabhu A, Rani V, Ghate SD, BR PK. Development of novel thiazolidine-2, 4-dione derivatives as PPAR-γ agonists through design, synthesis, computational docking, MD simulation, and comprehensive in vitro and in vivo evaluation. RSC Med. Chem. 2023;14(11):2401-16. doi.org/10.1039/D3MD00273J.

80. Thabet HK, Abusaif MS, Imran M, Helal MH, Alaqel SI, Alshehri A, Mohd AA, Ammar YA, Ragab A. Discovery of novel 6-(piperidin-1-ylsulfonyl)-2H-chromenes targeting α-glucosidase, α-amylase, and PPAR-γ: Design, synthesis, virtual screening, and anti-diabetic activity for type 2 diabetes mellitus. Comp. Bio. Chem. 2024:1; 111:108097. doi.org/10.1016/j.compbiolchem.2024.108097.

81. Ali IH, Hassan RM, El Kerdawy AM, Abo-Elfadl MT, Abdallah HM, Sciandra F, Ghannam IA. Novel thiazolidin-4-one benzenesulfonamide hybrids as PPARγ agonists: Design, synthesis and in vivo anti-diabetic evaluation. Eur. J. Med Chem. 2024:5; 269:116279. doi.org/10.1016/j.ejmech.2024.116279.

82. Thabet HK, Ragab A, Imran M, Helal MH, Alaqel SI, Alshehri A, Mohd AA, Alshammari MR, Abusaif MS, Ammar YA. Discovery of new anti-diabetic potential agents based on paracetamol incorporating sulfa-drugs: Design, synthesis, α-amylase and α-glucosidase inhibitors with docking simulation. Eur. J. Med Chem. 2024: 8:116589. doi.org/10.1016/j.ejmech.2024.116589.

83. Ali Z, Rehman W, Rasheed L, Alzahrani AY, Ali N, Hussain R, Emwas AH, Jaremko M, Abdellattif MH. New 1, 3, 4-Thiadiazole Derivatives as α-Glucosidase Inhibitors: Design, Synthesis, DFT, ADME, and In Vitro Enzymatic Studies. ACS omega. 2024:5; 9(7):7480-90. doi.org/10.1021/acsomega.3c05854.

84. Hussain R, Nabi M, Khan S, Subhan Z, Rahim F, Faisal MS, Hussain A, Ullah H, Khan Y, Bekhit MM, Alnbaheen MS. Design, synthesis and in vitro biological evaluation of new coumarin containing oxazole hybrid derivatives as multitarget inhibitor of α-amylase and α-

glucosidase for the treatment of diabetes. Results Chem. 2024:2:101638. doi.org/10.1016/j.rechem.2024.101638.

85. Punia R, Mor S, Sindhu S, Kumar D, Das PP, Jindal DK, Kumar A, Mohil R, Jakhar K. Design, synthesis, α-amylase and glucose diffusion inhibition, and molecular docking studies of new indenopyrazolones bearing benzothiazole derivatives. Bioorg. Med. Chem Lett. 2024:1; 103:129692. doi.org/10.1016/j.bmcl.2024.129692.
86. Zahid LU, Zaib S, Saeed A, Alharbi HY, Aljohani MS, Alharbi O, Rana N, Khan I, Shabir G, Ahmed A, Saleem A. Synthesis, Glucosidase Inhibition, and In Silico Modeling Analysis of Highly Fluorinated 2-Imino-1, 3-thiazolines in Search of Potent Antidiabetic Agents. ACS omega. 2024: 20; 9(13):15603-14. doi.org/10.1021/acsomega.4c00529.
87. Khan H, Jan F, Shakoor A, Khan A, AlAsmari AF, Alasmari F, Ullah S, Al-Harrasi A, Khan M, Ali S. Design, synthesis, molecular docking study, and α-glucosidase inhibitory evaluation of novel hydrazide–hydrazone derivatives of 3, 4-dihydroxyphenylacetic acid. Sci. Rep. 2024: 18; 14(1):11410. doi.org/10.1038/s41598-024-62034-x.
88. Singh G, Singh R, Monga V, Mehan S. 3, 5-Disubstituted-thiazolidine-2, 4-dione hybrids as antidiabetic agents: Design, synthesis, in-vitro and In vivo evaluation. Eur. J. Med. Chem. 2024; 15; 266:116139. doi.org/10.1016/j.ejmech.2024.116139.
89. Ghasemi M, Iraji A, Dehghan M, Nosood YL, Irajie C, Khouzani NB, Mojtabavi S, Faramarzi MA, Mahdavi M, Al-Harrasi A. Rational design of new quinoline-benzimidazole scaffold bearing piperazine acetamide derivatives as antidiabetic agents. Bioorg. Chem. 2024:1; 153:107908. doi.org/10.1016/j.bioorg.2024.107908.
90. Cele N, Awolade P, Seboletswe P, Khubone L, Olofinsan K, Islam MS, Jordaan A, Warner DF, Singh P. Synthesis, Antidiabetic and Antitubercular Evaluation of Quinoline–pyrazolopyrimidine hybrids and Quinoline-4-Arylamines. ChemistryOpen. 2024 Mar 20:e202400014. doi.org/10.1002/open.202400014.S

91. Azmi A, Noori M, Ghomi MK, Montazer MN, Iraji A, Dastyafteh N, Oliyaei N, Khoramjouy M, Rezaei Z, Javanshir S, Mojtabavi S. Alpha-glucosidase inhibitory and hypoglycemic effects of imidazole-bearing thioquinoline derivatives with different substituents: *In silico*, *invitro*, and invivo evaluations. Bioorg. Chem. 2024:1; 144:107106. doi.org/10.1016/j.bioorg.2024.107106.
92. International Diabetes Federation. IDF Diabetes Atlas, 10th edn. Brussels, Belgium: International Diabetes Federation, 2021.
93. Gassasse Z, Smith D, Finer S, Gallo V. Association between urbanisation and type 2 diabetes: an ecological study. BMJ Glob. Health. 2017 Oct 1; 2(4):e000473. doi.org/10.1136/bmjgh-2017-000473.
94. Pulgaron ER, Delamater AM. Obesity and type 2 diabetes in children: epidemiology and treatment. Curr. Diabetes Rep. 2014 Aug; 14:1-2. doi.org/10.1007/s11892-014-0508-y.
95. Galindo RJ, Trujillo JM, Wang CC, McCoy RG. Advances in the management of type 2 diabetes in adults. BMJ medicine. 2023;2(1). doi.org/10.1136/bmjmed-2022-000372.
96. Galicia-Garcia U, Benito-Vicente A, Jebari S, Larrea-Sebal A, Siddiqi H, Uribe KB, Ostolaza H, Martín C. Pathophysiology of type 2 diabetes mellitus. Int. J. Mol. Sci. 2020 Aug 30;21(17):6275. doi.org/10.3390/ijms21176275.
97. Kapetanovic I. Computer-aided drug discovery and development (CADDD): in silico-chemico-biological approach. Chem. -Biol. Interact. 2008 Jan 30; 171(2):165-76. doi.org/10.1016/j.cbi.2006.12.006.
98. Antar SA, Ashour NA, Sharaky M, Khattab M, Ashour NA, Zaid RT, Roh EJ, Elkamhawy A, Al-Karmalawy AA. Diabetes mellitus: Classification, mediators, and complications; A gate to identify potential targets for the development of new effective treatments. Biomed. Pharmacother. 2023 Dec 1; 168:115734. doi.org/10.1016/j.biopha.2023.115734.
99. Montanari R, Saccoccia F, Scotti E, Crestani M, Godio C, Gilardi F, Loiodice F, Fracchiolla G, Laghezza A, Tortorella P, Lavecchia A. Crystal Structure of PPARgamma Ligand Binding

Domain complexed with a novel Partial Agonist: a new region of the hydrophobic pocket could be exploited for drug design. InAbstract Book 2008 (pp. 1004-1004).

100. Williams LK, Zhang X, Caner S, Tysoe C, Nguyen NT, Wicki J, Williams DE, Coleman J, McNeill JH, Yuen V, Andersen RJ. The amylase inhibitor montbretin A reveals a new glycosidase inhibition motif. Nat. Chem. Biol. 2015 Sep; 11(9):691-6. doi.org/10.1038/nchembio.1865.

101. Madhavi Sastry G, Adzhigirey M, Day T, Annabhimoju R, Sherman W. Protein and ligand preparation: parameters, protocols, and influence on virtual screening enrichments. J. Comput. Aided Mol. Des.2013 Mar; 27:221-34. doi.org/10.1007/s10822-013-9644-8.

102. Bochevarov AD, Harder E, Hughes TF, Greenwood JR, Braden DA, Philipp DM, Rinaldo D, Halls MD, Zhang J, Friesner RA. Jaguar: A high-performance quantum chemistry software program with strengths in life and materials sciences. Int. J. Quantum Chem. 2013 Sep 15; 113(18):2110-42. doi.org/10.1002/qua.24481.

103. Bochevarov AD, Watson MA, Greenwood JR, Philipp DM. Multiconformation, density functional theory-based pKa prediction in application to large, flexible organic molecules with diverse functional groups. J. Chem. Theory Comput. 2016 Dec 13; 12(12):6001-19. doi.org/10.1021/acs.jctc.6b00805.

104. Roos K, Wu C, Damm W, Reboul M, Stevenson JM, Lu C, Dahlgren MK, Mondal S, Chen W, Wang L, Abel R. OPLS3e: Extending force field coverage for drug-like small molecules. J. Chem. Theory Comput. 2019 Feb 15; 15(3):1863-74. doi.org/10.1021/acs.jctc.8b01026.

105. Harder E, Damm W, Maple J, Wu C, Reboul M, Xiang JY, Wang L, Lupyan D, Dahlgren MK, Knight JL, Kaus JW. OPLS3: a force field providing broad coverage of drug-like small molecules and proteins. J. Chem. Theory Comput. 2016 Jan 12;12(1):281-96. doi.org/10.1021/acs.jctc.5b00864.

106. Halgren TA. Identifying and characterizing binding sites and assessing druggability. J. Chem. Inf. Model. 2009 Feb 23; 49(2):377-89. doi.org/10.1021/ci800324m.

107. Halgren T. New method for fast and accurate binding-site identification and analysis. Chem Biol Drug Des. 2007 Feb; 69(2):146-8. doi.org/10.1111/j.1747-0285.2007.00483.x

108. Friesner RA, Murphy RB, Repasky MP, Frye LL, Greenwood JR, Halgren TA, Sanschagrin PC, Mainz DT. Extra precision glide: Docking and scoring incorporating a model of hydrophobic enclosure for protein− ligand complexes. J. Med. Chem. 2006 Oct 19; 49(21):6177-96. doi.org/10.1021/jm051256o.

109. Halgren TA, Murphy RB, Friesner RA, Beard HS, Frye LL, Pollard WT, Banks JL. Glide: a new approach for rapid, accurate docking and scoring. 2. Enrichment factors in database screening. J. Med. Chem. 2004 Mar 25; 47(7):1750-9. doi.org/10.1021/jm030644s.

110. Friesner RA, Banks JL, Murphy RB, Halgren TA, Klicic JJ, Mainz DT, Repasky MP, Knoll EH, Shelley M, Perry JK, Shaw DE. Glide: a new approach for rapid, accurate docking and scoring. 1. Method and assessment of docking accuracy. J. Med. Chem. 2004 Mar 25; 47(7):1739-49. doi.org/10.1021/jm0306430.

111. Yang Y, Yao K, Repasky MP, Leswing K, Abel R, Shoichet BK, Jerome SV. Efficient exploration of chemical space with docking and deep learning. J. Chem. Theory Comput. 2021 Sep 30; 17(11):7106-19. doi.org/10.1021/acs.jctc.1c00810.

112. Sherman W, Day T, Jacobson MP, Friesner RA, Farid R. Novel procedure for modeling ligand/receptor induced fit effects. J. Med. Chem. 2006 Jan 26; 49(2):534-53. doi.org/10.1021/jm050540c.

113. Dixon SL, Smondyrev AM, Rao SN. PHASE: a novel approach to pharmacophore modeling and 3D database searching. Chem Biol Drug Des". 2006 May; 67(5):370-2. doi.org/10.1111/j.1747-0285.2006.00384.x.

114. Sindhu T, Srinivasan P. Identification of potential dual agonists of FXR and TGR5 using e-pharmacophore based virtual screening. Mol. Biosyst. 2015; 11(5):1305-18. doi.org/10.1039/C5MB00137D.

115. Shah BM, Modi P, Trivedi P. Pharmacophore-based virtual screening, 3D-QSAR, molecular docking approach for identification of potential dipeptidyl peptidase IV inhibitors. J. Biomol. Struct. Dyn. 2021 Mar 31;39(6):2021-43. doi.org/10.1080/07391102.2020.1750485.

116. Agrawal R, Jain P, Narayan Dikshit S. Ligand-based pharmacophore detection, screening of potential gliptins and docking studies to get effective antidiabetic agents. Comb. Chem. High Throughput Screen. 2012 Dec 1;15(10):849-76. doi.org/10.2174/138620712803901090.

117. Maurya AK, Mulpuru V, Mishra N. Discovery of novel coumarin analogs against the α-glucosidase protein target of Diabetes mellitus: Pharmacophore-based QSAR, docking, and molecular dynamics simulation studies. ACS omega. 2020 Dec 10; 5(50):32234-49. doi.org/10.1021/acsomega.0c03871.

118. Dixon SL, Smondyrev AM, Knoll EH, Rao SN, Shaw DE, Friesner RA. PHASE: a new engine for pharmacophore perception, 3D QSAR model development, and 3D database screening: 1. Methodology and preliminary results. J. Comput. Aided Mol. Des. 2006 Oct; 20:647-71. doi.org/10.1007/s10822-006-9087-6.

119. Laoud A, Ferkous F, Maccari L, Maccari G, Saihi Y, Kraim K. Identification of novel nt-MGAM inhibitors for potential treatment of type 2 diabetes: Virtual screening, atom based 3D-QSAR model, docking analysis and ADME study. Comput. Biol. Chem. 2018 Feb 1; 72:122-35. doi.org/10.1016/j.compbiolchem.2017.12.003.

120. Gupta MK, Misra K. Atom-based 3D-QSAR, molecular docking and molecular dynamics simulation assessment of inhibitors for thyroid hormone receptor α and β. J. Mol. Model. 2014 Jun; 20:1-9. doi.org/10.1007/s00894-014-2286-5.

121. Bowers KJ, Chow E, Xu H, Dror RO, Eastwood MP, Gregersen BA, Klepeis JL, Kolossvary I, Moraes MA, Sacerdoti FD, Salmon JK. Scalable algorithms for molecular dynamics simulations on commodity clusters. InProceedings of the 2006 ACM/IEEE Conference on Supercomputing 2006 Nov 11 (pp. 84-es). doi.org/10.1145/1188455.1188544.

122. Rashid RS, Temurlu S, Abourajab A, Karsili P, Dinleyici M, Al-Khateeb B, Icil H. Drug Repurposing of FDA Compounds against α-Glucosidase for the Treatment of Type 2 Diabetes: Insights from Molecular Docking and Molecular Dynamics Simulations. Pharmaceuticals. 2023 Apr 6; 16(4):555. doi.org/10.3390/ph16040555.

123. George A, Mondal S, Purnaprajna M, Athri P. Review of electrostatic force calculation methods and their acceleration in molecular dynamics packages using graphics processors. ACS omega. 2022 Sep 8; 7(37):32877-96. doi.org/10.1021/acsomega.2c03189.

124. Schrödinger Release 2024-4: QikProp, Schrödinger, LLC, New York, NY, 2024

125. Shannon P, Markiel A, Ozier O, Baliga NS, Wang JT, Ramage D, Amin N, Schwikowski B, Ideker T. Cytoscape: a software environment for integrated models of biomolecular interaction networks. Genome Res. 2003 Nov 1; 13(11):2498-504. doi.org/10.1101/gr.1239303.

126. Stelzl U, Worm U, Lalowski M, Haenig C, Brembeck FH, Goehler H, Stroedicke M, Zenkner M, Schoenherr A, Koeppen S, Timm J. A human protein-protein interaction network: a resource for annotating the proteome. Cell. 2005 Sep 23; 122(6):957-68. Doi.org/10.1016/j.cell.2005.08.029.

127. Berger SI, Iyengar R. Network analyses in systems pharmacology. Bioinformatics. 2009 Oct 1; 25(19):2466-72. doi.org/10.1093/bioinformatics/btp465.

128. Maslov S, Sneppen K. Specificity and stability in topology of protein networks. Science. 2002 May 3; 296(5569):910-3. doi.org/10.1126/science.1065103.

129. Cirillo VP. Mechanism of glucose transport across the yeast cell membrane. J. Bacteriol. 1962 Sep; 84(3):485-91. doi.org/10.1128/jb.84.3.485-491.1962.

130. Roy A, Dement AD, Cho KH, Kim JH. Assessing glucose uptake through the yeast hexose transporter 1 (Hxt1). PLoS One. 2015 Mar 27; 10(3):e0121985. doi.org/10.1371/journal.pone.0121985.

131. Mirsky N, Berdicevsky I. Effects of insulin and glucose tolerance factor on glucose uptake by yeast cells. Neurosignals. 2004 Dec 21; 3(6):271-7. doi.org/10.1159/000109554.

132. Patil A, Dwivedi PS, Gaonkar SN, Kumbhar V, Shankar Madiwalar V, Khanal P, Patil BM. GLUT-2 mediated glucose uptake analysis of Duranta repens: In-silico and In-vitro approach. J. diabetes metab. disord. 2022 Jun; 21(1):419-27. doi.org/10.1007/s40200-022-00988-3.

133. Khan MF, Maurya CK, Dev K, Arha D, Rai AK, Tamrakar AK, Maurya R. Design and synthesis of lupeol analogues and their glucose uptake stimulatory effect in L6 skeletal muscle cells. Bioorg. Med. Chem. Lett. 2014 Jun 15; 24(12):2674-9. doi.org/10.1016/j.bmcl.2014.04.059.

134. Klip A, Guma A, Ramlal T, Bilan PJ, Lam L, Leiter LA. Stimulation of hexose transport by metformin in L6 muscle cells in culture. Endocrinol. 1992 May 1; 130(5):2535-44. doi.org/10.1210/endo.130.5.1572281.

135. Berg ME, Naams JB, Hautala LC, Tolvanen TA, Ahonen JP, Lehtonen S, Wähälä K. Novel Sulfonanilide Inhibitors of SHIP2 Enhance Glucose Uptake into Cultured Myotubes. ACS omega. 2020 Jan 14;5(3):1430-8. doi.org/10.1021/acsomega.9b02944.

136. Gharge S, Alegaon SG, Ranade SD, Kavalapure RS, Kumar BP, Mhaske PC. Expression of PPAR-γ TF by newly synthesized thiazolidine-2, 4-diones to manage glycemic control: Insights from in silico, in vitro and experimental pharmacology in wistar rats. Bioorg. Chem. 2024 Nov 17:107966. doi.org/10.1016/j.bioorg.2024.107966.

137.Telagari M, Hullatti K. In-vitro α-amylase and α-glucosidase inhibitory activity of Adiantum caudatum Linn. and Celosia argentea Linn. Extracts and fractions. Indian J. Pharmacol. 2015 Jul 1;47(4):425-9. doi.org/10.4103/0253-7613.161270.

138. Wickramaratne MN, Punchihewa JC, Wickramaratne DB. In-vitro alpha amylase inhibitory activity of the leaf extracts of Adenanthera pavonina. BMC complement. med. ther. 2016 Dec;16:1-5. doi.org/10.1186/s12906-016-1452-y.

139. Mehmood R, Mughal EU, Elkaeed EB, Obaid RJ, Nazir Y, Al-Ghulikah HA, Naeem N, Al-Rooqi MM, Ahmed SA, Shah SW, Sadiq A. Synthesis of novel 2, 3-dihydro-1, 5-benzothiazepines as α-glucosidase inhibitors: In vitro, in vivo, kinetic, SAR, molecular

docking, and QSAR studies. ACS omega. 2022 Aug 17; 7(34):30215-32. doi.org/10.1021/acsomega.2c03328.

140. Valentina P, Ilango K, Chander S, Murugesan S. Design, synthesis and α-amylase inhibitory activity of novel chromone derivatives. Bioorg. Chem. 2017 Oct 1; 74:158-65. doi.org/10.1016/j.bioorg.2017.07.018.

141. Ali M, Khan M, Zaman K, Wadood A, Iqbal M, Alam A, Shah S, Rehman AU, Yousaf M, Rafique R, Khan KM. Chalcones: as potent α-amylase enzyme inhibitors; synthesis, in vitro, and in silico studies. Med. Chem. 2021 Oct 1; 17(8):903-12. doi.org/10.2174/1573406416666200611103039.

142. Mosmann T. Rapid colorimetric assay for cellular growth and survival: application to proliferation and cytotoxicity assays. J. Immunol. Methods. 1983 Dec 16; 65(1-2):55-63. doi.org/10.1016/0022-1759 (83)90303-4.

143. Ahangarpour A, Mohammadian M, Dianat M. Antidiabetic effect of hydroalcholic Urtica dioica leaf extract in male rats with fructose-induced insulin resistance. Iran. J. Med. Sci. 2012 Sep;37(3):181.

144. Mamikutty N, Thent ZC, Sapri SR, Sahruddin NN, Mohd Yusof MR, Haji Suhaimi F. The establishment of metabolic syndrome model by induction of fructose drinking water in male Wistar rats. Biomed Res. Int. 2014; 2014(1):263897. doi.org/10.1155/2014/263897.

145. Kumar R, Patel DK, Prasad SK, Sairam K, Hemalatha S. Antidiabetic activity of alcoholic root extract of Caesalpinia digyna in streptozotocin-nicotinamide induced diabetic rats. Asian Pac. J. Trop. Biomed. 2012 Feb 1;2(2):S934-40. doi.org/10.1016/S2221-1691(12)60340-2.

146. Beloff-Chain A, Catanzaro R, Chain EB, Masi I, Pocchiari F, Rossi C. The influence of insulin on carbohydrate metabolism in the isolated diaphragm muscle of normal and alloxan diabetic rats. Proceedings of the Royal Society of London. Series B-Biological Sciences. 143 (1955) 481-503. doi.org/10.1098/rspb.1955.0025. doi.org/10.1098/rspb.1955.0025.

147. Seifter S, Dayton S, Novic B, Muntwyler E. The estimation of glycogen with the anthrone reagent. Arch. Biochem. 25 (1950) 191-200.

148. Nandi A, Chatterjee IB. Scavenging of superoxide radical by ascorbic acid. J. Biosci. 1987 Mar; 11:435-41. doi.org/10.1007/BF02704692.

149. Senthilkumar M, Amaresan N, Sankaranarayanan A, Senthilkumar M, Amaresan N, Sankaranarayanan A. Estimation of malondialdehyde (MDA) by thiobarbituric acid (TBA) assay. doi.org/10.1007/978-1-0716-1080-0_25.

150. Sedlak J, Lindsay RH. Estimation of total, protein-bound, and nonprotein sulfhydryl groups in tissue with Ellman's reagent. Anal. Biochem. 25 (1968) 192-205.

151. Koroliuk MA, Ivanova LI, Maĭorova IG, Tokarev VE. A method of determining catalase activity, Lab. delo. 1 (1988) 16-9.

152. Mandal S, Chiriki DS, Gurupadayya BM, Chethan IA, Kumar BP. Phenyl glycine incorporated glitazones as promising novel antidiabetic agents through PPARγ agonism: design, synthesis and preclinical studies. EJMCR. 2022 Dec 1; 6:100067. doi.org/10.1016/j.ejmcr.2022.100067.

153. Taha M, Shah SA, Imran S, Afifi M, Chigurupati S, Selvaraj M, Rahim F, Ullah H, Zaman K, Vijayabalan S. Synthesis and in vitro study of benzofuran hydrazone derivatives as novel alpha-amylase inhibitor. Bioorg. Chem. 2017 Dec 1; 75:78-85. doi.org/10.1016/j.bioorg.2017.09.002.

154. Nawaz M, Taha M, Qureshi F, Ullah N, Selvaraj M, Shahzad S, Chigurupati S, Waheed A, Almutairi FA. Structural elucidation, molecular docking, α-amylase and α-glucosidase inhibition studies of 5-amino-nicotinic acid derivatives. BMC Chem. 2020 Dec; 14:1-1. doi.org/10.1186/s13065-020-00695-1.

155. Hawash M, Al-Smadi D, Kumar A, Olech B, Dominiak PM, Jaradat N, Antari S, Mohammed S, Nasasrh AA, Abualhasan M, Musa A. Characterization and Investigation of Novel Benzodioxol Derivatives as Antidiabetic Agents: An In Vitro and In Vivo Study in an Animal Model. Biomolecules. 2023 Oct 6; 13(10):1486. doi.org/10.3390/biom13101486.

156.Gummidi L, Kerru N, Ebenezer O, Awolade P, Sanni O, Islam MS, Singh P. Multicomponent reaction for the synthesis of new 1, 3, 4-thiadiazole-thiazolidine-4-one molecular hybrids as promising antidiabetic agents through α-glucosidase and α-amylase inhibition. Bioorg Chem. 2021 Oct 1; 115:105210. doi.org/10.1016/j.bioorg.2021.105210.

157.Kahn BB, Rosen AS, Bak JF, Andersen PH, Damsbo PE, Lund ST, Pedersen OL. Expression of GLUT1 and GLUT4 glucose transporters in skeletal muscle of humans with insulin-dependent diabetes mellitus: regulatory effects of metabolic factors. J. Clin. Endocrinol. Metab. 1992 May 1; 74(5):1101-9. doi.org/10.1210/jcem.74.5.1569156.

158.Brayer GD, Sidhu G, Maurus R, Rydberg EH, Braun C, Wang Y, Nguyen NT, Overall CM, Withers SG. Subsite mapping of the human pancreatic α-amylase active site through structural, kinetic, and mutagenesis techniques. Biochemistry. 2000 Apr 25; 39(16):4778-91. doi.org/10.1021/bi9921182.

159.Manna P, Jain SK. PIP3 but not PIP2 increases GLUT4 surface expression and glucose metabolism mediated by AKT/PKCζ/λ phosphorylation in 3T3L1 adipocytes. Mol. Cell. Biochem. 2013 Sep; 381:291-9. doi.org/10.1007/s11010-013-1714-7.

160.Sano H, Eguez L, Teruel MN, Fukuda M, Chuang TD, Chavez JA, Lienhard GE, McGraw TE. Rab10, a target of the AS160 Rab GAP, is required for insulin-stimulated translocation of GLUT4 to the adipocyte plasma membrane. Cell Metab. 2007 Apr 4; 5(4):293-303. 10.1016/j.cmet.2007.03.001.

161.Thirone AC, Huang C, Klip A. IRS proteins and insulin resistance in humans. Trends Endocrinol. Metab. 2006; 2(17):72-8. doi.org/10.1016%2Fj.tem.2006.01.005.

162.Gustafson TA, He W, Craparo A, Schaub CD, O'Neill TJ. Phosphotyrosine-dependent interaction of SHC and insulin receptor substrate 1 with the NPEY motif of the insulin receptor via a novel non-SH2 domain. Mol. Cell. Biol.1995 May. doi.org/10.1128/MCB.15.5.2500.

163. Sengupta S, Peterson TR, Sabatini DM. Regulation of the mTOR complex 1 pathway by nutrients, growth factors, and stress. Mol. Cell. 2010 Oct 22; 40(2):310-22. doi.org/10.1016/j.molcel.2010.09.026.

164. Saxton RA, Sabatini DM. mTOR signaling in growth, metabolism, and disease. Cell. 2017 Mar 9;168(6):960-76. doi.org/10.1016/j.cell.2017.02.004

165. Laplante M, Sabatini DM. mTOR signaling in growth control and disease. cell. 2012 Apr 13;149(2):274-93. https://doi.org/10.1016/j.cell.2012.03.017.

166. Richter EA, Hargreaves M. Exercise, GLUT4, and skeletal muscle glucose uptake. Physiol. Rev. 2013 Jul 1. doi.org/10.1152/physrev.00038.2012.

167. Chambers MA, Moylan JS, Smith JD, Goodyear LJ, Reid MB. Stretch-stimulated glucose uptake in skeletal muscle is mediated by reactive oxygen species and p38 MAP-kinase. Physiol. J. 2009 Jul 1; 587(13):3363-73. doi.org/10.1113/jphysiol.2008.165639.

168. Bengal E, Aviram S, Hayek T. p38 MAPK in glucose metabolism of skeletal muscle: beneficial or harmful?. Int. J. Mol. Sci. 2020 Sep 4; 21(18):6480. doi.org/10.3390/ijms21186480.

169. Yasmin S, Jayaprakash V. Thiazolidinediones and PPAR orchestra as antidiabetic agents: From past to present, Eur. J. Med. Chem, 126 (2017) 879-93. doi.org/10.1016/j.ejmech.2016.12.020.

170. Gim HJ, Kang B, Jeon R. Synthesis and biological activity of 5-(4-[2-(Methyl-p-substituted phenylamino) ethoxy] benzyl) thiazolidine-2, 4-diones. Arch. Pharmacal Res. 2007 Sep;30:1055-61. doi.org/10.1007/BF02980237.

171. Darwish KM, Salama I, Mostafa S, Gomaa MS, Helal MA. Design, synthesis, and biological evaluation of novel thiazolidinediones as PPARγ/FFAR1 dual agonists, Eur. J. Med. Chem. 109 (2016) 157-72. doi.org/10.1016/j.ejmech.2015.12.049

172. Sun J, Liu HY, Zhang YH, Fang ZY, Lv PC. Design, synthesis and bioactivity evaluation of thiazolidinedione derivatives as partial agonists targeting PPARγ, Bioorg. Chem. 116 (2021) 105342. doi.org/10.1016/j.bioorg.2021.105342.

173. Al Neyadi SS, Adem A, Amir N, Ghattas MA, Abdou IM, Salem AA. Novel Thiazolidinedione and Rhodanine Derivatives Regulate Glucose Metabolism, Improve Insulin Sensitivity, and Activate the Peroxisome Proliferator-Activated γ Receptor. ACS omega. 2024 Jan 25; 9(5):5463-84. doi.org/10.1021/acsomega.3c07149

174. Alagawadi KR, Alegaon SG. Synthesis, characterization and antimicrobial activity evaluation of new 2, 4-Thiazolidinediones bearing imidazo [2, 1-b][1, 3, 4] thiadiazole moiety. Arab. J. Chem. 2011 Oct 1;4(4):465-72. doi.org/10.1016/j.arabjc.2010.07.012.

175. Merz KE, Thurmond DC. Role of skeletal muscle in insulin resistance and glucose uptake. Compr Physiol. 10 (2011) 785-809. doi.org/10.1002/cphy.c190029.

176. Ahmadian M, Suh JM, Hah N, Liddle C, Atkins AR, Downes M, Evans RM. PPARγ signaling and metabolism: the good, the bad and the future, Nat Med. 19 (2013) 557-66. doi.org/10.1038/nm.3159.

177. Khanal P, Patil BM. Reversal of insulin resistance by Ficus benghalensis bark in fructose-induced insulin-resistant rats, J. Ethnopharmacol. 284 (2022) 114761. doi.org/10.1016/j.jep.2021.114761.

178. Dwivedi PS, Rasal VP, Chavan RS, Khanal P, Gaonkar VP. Insulin sensitization by Feronia elephantum in fructose-induced hyperinsulinemic rats: Insights from computational and experimental pharmacology, J. Ethnopharmacol. 316 (2023) 116686. doi.org/10.1016/j.jep.2023.116686.

179. Dai S, McNeill JH. Fructose-induced hypertension in rats is concentration-and duration-dependent, J Pharmacol Toxicol Methods. 33 (1995) 101-7. doi.org/10.1016/1056-8719 (94)00063-A.

180. Iyer SN, Katovich MJ. Vascular reactivity to phenylephrine and angiotensin II in hypertensive rats associated with insulin resistance, Clin. Exp. Hypertens. 18 (1996) 227-42. doi.org/10.3109/10641969609081766.

181. Balsan GA, Vieira JL, Oliveira AM, Portal VL. Relationship between adiponectin, obesity and insulin resistance, Rev. Assoc. Med. Bras. 61 (2015) 72-80. doi.org/10.1590/1806-9282.61.01.072.

182. Adeva-Andany MM, Gonzalez-Lucan M, Donapetry-García C, Fernandez-Fernandez C, Ameneiros-Rodríguez E. Glycogen metabolism in humans, BBA Clin. 5 (2016) 85-100. doi.org/10.1016/j.bbacli.2016.02.001.

183. Friedmann B, Goodman Jr EH, Weinhouse S. Effects of insulin and fatty acids on gluconeogenesis in the rat, JBC. 242 (1967) 3620-7. doi.org/10.1016/S0021-9258(18)95854-0.

184. Pasarín M, Abraldes JG, Liguori E, Kok B, La Mura V. Intrahepatic vascular changes in non-alcoholic fatty liver disease: Potential role of insulin-resistance and endothelial dysfunction. World J Gastroenterol. 23 (2017) 6777. doi:10.3748/wjg.v23.i37.6777.

185. Tabák AG, Herder C, Rathmann W, Brunner EJ, Kivimäki M. Prediabetes: a high-risk state for diabetes development, Lancet. 379 (2012) 2279-90. doi.org/10.1016/S0140-6736(12)60283-9

186. Doycheva I, Loomba R. Effect of metformin on ballooning degeneration in nonalcoholic steatohepatitis (NASH): when to use metformin in nonalcoholic fatty liver disease (NAFLD), Adv. Ther. 31 (2014) 30-43. doi.org/10.1007/s12325-013-0084-6.

187. T, Noreen, M. Taha, S. Imra, S. Chigurupati, F. Rahim, M. Selvaraj, and M. Ali, Synthesis of alpha-amylase inhibitors based on privileged indole scaffold. Bioorg. Chem, 2017, 72, 248-255. doi.org/10.1016/j.bioorg.2017.04.010.

188. M. Taha, M. T. Javid, S. Imran, M. Selvaraj, S. Chigurupati, H. Ullah, and K. M. Khan, Synthesis and study of the *α-amylase* inhibitory potential of thiadiazole quinoline derivatives. Bioorg. Chem, 2017, 74, 179-186. doi.org/10.1016/j.bioorg.2017.08.003.

189.M. Taha, N. H Ismail, S. Imran, A. Wadood, F. Rahim, M. Ali, A. U. Rehman. Novel quinoline derivatives as potent in vitro *α-glucosidase* inhibitors: in silico studies and SAR predictions. MedChemComm, 2015, 6(10), 1826-1836. doi.org/10.1039/C5MD00280J.

190.M. Taha, S. Sultan, S. Imran, F. Rahim, K. Zaman, A. Wadood, and K. M. Khan, Synthesis of quinoline derivatives as diabetic II inhibitors and molecular docking studies. Bioorg. Med. chem, 2019, 27(18), 4081-4088. doi.org/10.1016/j.bmc.2019.07.035.

191.R. Forozan, M. K. Ghomi, A. Iraji, M. N. Montazer, M. Noori, N. Dastyafteh, and M. Mahdavi, Synthesis, in vitro inhibitor screening, structure-activity relationship, and molecular dynamic simulation studies of novel thioquinoline derivatives as potent *α-glucosidase* inhibitors. Sci. Rep, 2023, 13(1), 7819. doi.org/10.1038/s41598-023-35140-5.

192. N. Cele, P. Awolade, P. Seboletswe, K. Olofinsan, M. S. Islam, and P. Singh, *α-glucosidase* and *α-amylase* inhibitory potentials of quinoline–1, 3, 4-oxadiazole conjugates bearing 1, 2, 3-triazole with antioxidant activity, kinetic studies, and computational validation. Pharmaceuticals, 2022, 15(8), 1035. doi.org/10.3390/ph15081035.

193. M. Al-Ghorbani, O. Alharbi, A. B. Al-Odayni, and N. A. Abduh, Quinoline-and Isoindoline-Integrated Polycyclic Compounds as Antioxidant, and Antidiabetic Agents Targeting the Dual Inhibition of α-Glycosidase and *α-amylase* Enzymes. Pharmaceuticals, 2023, 16(9), 1222. doi.org/10.3390/ph16091222.

194. M. Noori, M. Rastak, M. Halimi, M. K Ghomi, M. Mollazadeh, M. Mohammadi-Khanaposhtani, and M. Mahdavi, Design, synthesis, in vitro, and in silico enzymatic evaluations of thieno [2, 3-b] quinoline-hydrazones as novel inhibitors for *α-glucosidase*. Bioorg. Chem, 2022, 127, 105996. doi.org/10.1016/j.bioorg.2022.105996.

195. S. D. Ranade, S. G. Alegaon, U. Venkatasubramanian, A. S. Priya, R. S. Kavalapure, J. Chand, and D. Vinod, Design, synthesis, molecular dynamics simulation, MM/GBSA studies and kinesin spindle protein inhibitory evaluation of some 4-aminoquinoline hybrids. Comput. Biol. Chem, 2023, 105, 107881. doi.org/10.1016/j.compbiolchem.2023.107881.

196. H. Yousuf, S. Shamim, K. M. Khan, S. Chigurupati, S. Hameed, M. N. Khan, and M. Arfeen, Dihydropyridines as potential α-amylase and α-glucosidase inhibitors: synthesis, in vitro and in silico studies. Bioorg Chem, 2020, 96, 103581. doi.org/10.1016/j.bioorg.2020.103581.

Annexure…

The institutional animal ethics committee at the KLE College of Pharmacy in Belagavi examined the animal study protocol (resolution No. KLECOP/CPCSEA-Reg, No.221/Po/Re/S/2000/CPCSEA, Res.34-03/12/2022).

KLE College of Pharmacy
A Constituent Unit of
KLE Academy of Higher Education and Research
(Deemed to be University)
DEPARTMENT OF PHARMACOLOGY
JNMC Campus, Nehru Nagar, Belagavi – 590 010, Karnataka, India
INSTITUTIONAL ANIMAL ETHICS COMMITTEE
Reg.No.221/Po/Re/S/2000/CPCSEA

BELAGAVI

DATE: 03/12/2022

CERTIFICATE

This is to certify that the project proposal no 03 entitled," Synthesis, Characterization, In-silico study and Anti-diabetic Evaluation of Nitrogen and Sulphur containing heterocyclic analogue.", submitted by Dr./ Mr. / Ms. Shriram D Ranade under the guidance of Dr. Shankar G. Alegaon has been approved/recommended by the IAEC of KLE College of Pharmacy, Belagavi, Reg.No.221/Po/Re/S/2000/CPCSEA in its meeting dated 03/12/2022 , resolution No. 34 has been sanctioned .....60..... Rats/ Mice/ Rabbits/Guinea pig (animals) sex ----either---- under this proposal for a duration of next.....months.

You are hereby informed to strictly adhere to the protocol submitted for approval. Further you are required to keep the account of animals used for the project in specified Performa, Form D.

Authorized by	Name	Signature	Date
Member Secretary:	Dr. N.N. Khatib		3/12/22
Main Nominee of CPCSEA:	Dr Vishnu Kangralkar		3/12/22

MEMBER SECRETARY
Institutional Animal Ethics Committee
Reg. No. 221/PO/Rc/S/2000/CPCSEA
KLE College of Pharmacy,
BELAGAVI.

CPCSEA Nominee
Institutional Animal Ethics Committee
Reg. No. 221/PO/Rc/S/2000/CPCSEA
KLE College of Pharmacy,
BELAGAVI.

List of Publications

1. **Ranade SD**, **Alegaon SG, Khatib NA**, Gharge S, Kavalapure RS, Kumar BP. Reversal of insulin resistance to combat type 2 Diabetes mellitus by newer thiazolidinedione's in fructose induced insulin resistant rats. **Eur. J. Med. Chem**. 2024 Dec 15; 280:116939. **Impact factor: 6.0, Cite score: 11.7. Q1**
2. **Ranade SD**, **Alegaon SG, Khatib NA**, Gharge S, Kavalapure RS. Quinoline-based Schiff bases as possible antidiabetic agents: ligand-based pharmacophore modeling, 3D QSAR, docking, and molecular dynamics simulations study. **RSC med chem**. 2024; 15(9):3162-79. **Impact factor: 4.1, Cite score: 5.8. Q1**
3. **Ranade SD**, **Alegaon SG, Khatib NA**, Gharge S, Kavalapure RS, Kumar BP. Design, synthesis, molecular dynamic simulation, DFT analysis, computational pharmacology and decoding the antidiabetic molecular mechanism of sulphonamide-thiazolidin-4-one hybrids. **J. Mol. Struct**. 2024 Sep 5; 1311:138359. **Impact factor: 4.0, Cite score: 7.1. Q2**

Note: The above mentioned impact factor and cite score of the journal are based on the Web of Science and Scopus data respectively are during the year of thesis submission (2025).

List of poster presentation

1. **1st prize:** Thiazolidinedione's as magic bullets: Synthesis and insilico approach as GLUT-4 agonist. International Conference on Innovation and Advances in pharmaceutical sciences, Association of pharmaceutical research, Sri Adichunchanagiri college of pharmacy, Karnataka, India, 11th February 2023.
2. **1st prize:** Exploring molecular mechanism of synthesized thiazolidine-4-one hybrids as antidiabetic agents by integrated *invitro* and system biology approach. Aushadha Vigyan student scientific conference (AVISCON)-2024, JSS College of pharmacy, Mysuru, 2nd March 2024.

European Journal of Medicinal Chemistry 280 (2024) 116939



Contents lists available at ScienceDirect

European Journal of Medicinal Chemistry

journal homepage: www.elsevier.com/locate/ejmech



Research paper



Reversal of insulin resistance to combat type 2 diabetes mellitus by newer thiazolidinedione's in fructose induced insulin resistant rats

Shriram D. Ranade [a], Shankar G. Alegaon [a,*], Nayeem A. Khatib [b], Shankar Gharge [a], Rohini S. Kavalapure [a], B.R. Prashantha Kumar [c]

[a] Department of Pharmaceutical Chemistry, KLE College of Pharmacy, Belagavi, KLE Academy of Higher Education and Research, Belagavi, 590 010, Karnataka, India
[b] Department of Pharmacology, KLE College of Pharmacy, Belagavi, KLE Academy of Higher Education and Research, Belagavi, 590 010, Karnataka, India
[c] Department of Pharmaceutical Chemistry, JSS College of Pharmacy, Mysuru, JSS Academy of Higher Education and Research, Mysuru, 570015, Karnataka, India

ARTICLE INFO

Keywords:
Thiazolidinedione's
Type 2 diabetes mellitus
insulin resistance
Network pharmacology
MD simulations

ABSTRACT

In our pursuit of discovering new antidiabetic agents to manage type 2 diabetes mellitus (T2DM), our approach aimed to identify the bioactive feature/pharmacophore responsible for PPAR-γ expression, as it is accountable for the glucose homeostasis and lipid metabolism. This was achieved by pharmacophore model generation, screening of rationally designed newer thiazolidinedione's library, identifying synthesizing and characterizing the top ten molecules (**5a-5j**) for their (*Invitro* & *invivo*) antidiabetic activity. Preliminary screening of all the ligands by *Invitro* glucose uptake assay in L6 myotubes (skeletal muscle cell line of rats) revealed compound **5b** and **5f** stimulated the glucose uptake with 79.29 ± 1.02 % and 74.58 ± 1.02 % respectively compared to pioglitazone with 82.36 ± 0.98 %. This was validated by PPAR-γ TF expression assay, which highlighted a dose dependent increase in transactivation of PPAR-γ. These compounds **5b** and **5f** were evaluated in fructose induced insulin resistance rat model. Where the treatment with **5b** and **5f** markedly increased the exogenous clearance of glucose and exogenous insulin via OGTT and ITT respectively, also improved the glucose utilization by significantly increasing content of glycogen and uptake of glucose in rat hemidiaphragm and reversed insulin resistance. Likewise a significant decreased in the VLDL and triglyceride levels was seen in **5b** and **5f** treated groups compared to insulin resistant (IR) group. It improved glycogenesis by catabolism of glucose and maintained glycaemic control. Similarly it had marked action on enzymatic oxidative biomarkers. Compound **5b** displayed better, improved $T_{1/2}$ (half-life) of 4.21 h and K_{el} (elimination constant) of 0.381 was noticed in comparison to compound **5f** indicating the pharmacokinetic profile. *Insilico* studies like DFT calculations refined the geometry of **5b** and **5f** ligands, docking and molecular simulation provided the insights in binding affinity, dynamic behaviour and stability of ligands in PPAR-γ ligand binding domain. MM/GBSA provided the energetics of **5b** and **5f** in binding pocket. Finally network pharmacology identified ADIPOQ (adiponectin), NR1C3 (PPAR-γ), SLC2A4 (GLUT4), and LEP (leptin) proteins associate with compound **5b** and **5f** and enriched in Adipocytokine pathway, and PPAR-γ signaling pathway.

1. Introduction

T2DM is a metabolic condition with elevated blood glucose levels, primarily as result of progressive insulin resistance and a relative deficiency in insulin. As T2DM progresses to a chronic stage, it can cause significant damage to multiple organ systems, including the ocular organ, vasculature, kidneys, and the cardiovascular system, it is often associated with conditions such as dyslipidemia and hypertension. Insulin resistance in T2DM is influenced by a combination of factors including physical inactivity, sedentary behaviour, obesity, diets high in sugar, and genetic predisposition [1,2]. According to current estimates, approximately 537 million people globally are living with diabetes. The prevalence of T2DM is rising in all countries, with about 80 % of those affected residing in middle- and low-income nations [3]. The occurrence of T2DM varies based on environmental and lifestyle factors, but there is a well-established link between obesity and the development of T2DM, with approximately 55 % of obesity cases contributing to its onset. Recent genetic research has also identified several genes, such as

* Corresponding author.
E-mail addresses: sgalegaon@klepharm.edu, sgalegaon@gmail.com (S.G. Alegaon).

https://doi.org/10.1016/j.ejmech.2024.116939
Received 22 August 2024; Received in revised form 30 September 2024; Accepted 2 October 2024
Available online 5 October 2024
0223-5234/© 2024 Elsevier Masson SAS. All rights are reserved, including those for text and data mining, AI training, and similar technologies.

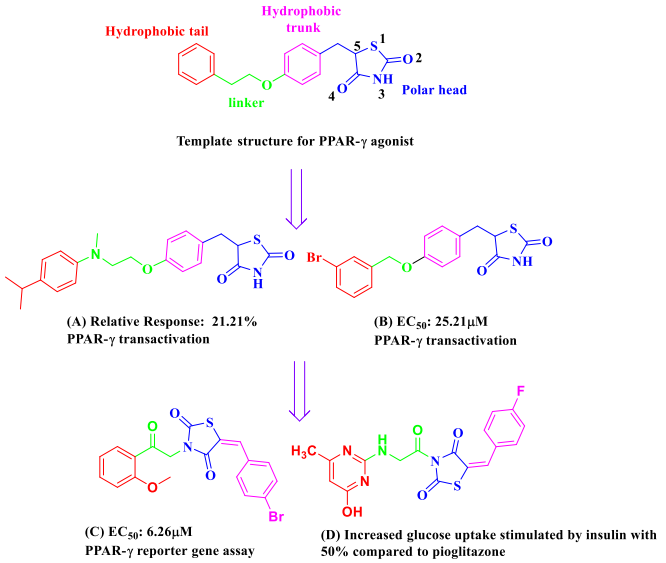


Fig. 1. Development of TZD's over last 3 decades as ligands in the binding domain of PPAR-γ receptor.

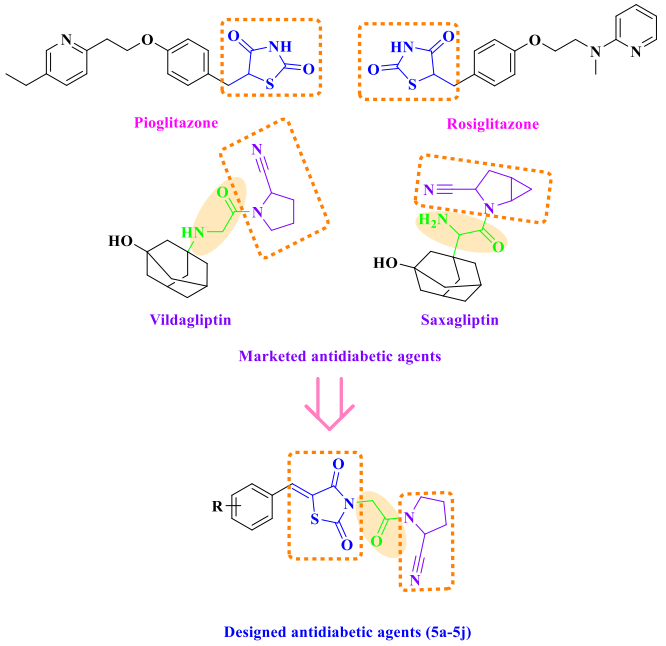


Fig. 2. Design of the acetyl pyrrlodine-2-carbonitrile based substituted benzylidenethiazolidine-2, 4-dione molecules.

NOTCH2, ADIPOQ, LEP, IRS2, TNF-α, and HHEX, that are significantly associated with the progression of T2DM [4,5].

In clinical practice, glucose homeostasis is achieved through pharmacotherapy interventions utilizing various oral antidiabetic agents. These include biguanides like metformin, which act as insulin sensitizers; sulfonylureas such as gliclazide, which function as insulin secretagogues; DPP-4 enzyme inhibitors like vildagliptin; PTP-1B enzyme inhibitors; α-glucosidase inhibitors such as acarbose; and glitazones like pioglitazone, which serve as PPAR-gamma agonists. However, these commonly used medications can have severe side effects, including hypoglycemia, gastrointestinal disturbances, hepatotoxicity, and orthostatic hypotension [6]. Given that diabetes is a complex polygenic condition, it is essential to target the regulation of multiple proteins that operate through various pathways to maintain glucose homeostasis while minimizing side effects [7]. Consequently, there remains a significant need for the development of new antidiabetic agents. Researchers around the globe, way back from the time of ciglitazone (1980s) have carried structural modification on the fifth position of thiazolidinedione (TZD) with branched chain amino acid (BCAA) and carbon chain linkers and have grown the region around the hydrophobic tail resembling the conventional glitazones template, with free TZD as polar head [8], Gim H.J and co-workers (2007) reported compounds **A** (Relative response of 21.21 %) for PPAR- γ agonist activity [9]. Similarly, Khalid M and co-workers (2015) reported compound **B** (EC_{50}: 25.21 μM) as PPAR-γ agonist with substitution at fifth position and keeping the polar head intact [10]. From the last decade researchers explored the substitution on the third position of the TZD head *i.e.* the replacement of amino group (NH) favourably with substituted acetamides, acid chlorides, acetyl chlorides, to explore its potential effect on PPAR- γ activity. Juan. S and co-workers reported compound **C** (EC_{50}: 6.25 μM) as PPAR- γ agonist [11]. Similarly Al Neyadi S.S and Co-workers (2024) reported compound **D** for its glucose utilization and stimulation of PPAR- γ receptor in βTC6 cells [12], depicted in Fig. 1.

From the above literature findings and available marketed antidiabetic agents, including pioglitazone as PPAR- γ agonist and vildagliptin as DPP-4 inhibitor, we carried out structural modification and designed library of acetyl pyrrlodine-2-carbonitrile based substituted benzylidenethiazolidine-2, 4-dione (Fig. 2). Further Identification of top hits by pharmacophore based screening of designed molecules in PPAR-γ ligand binding domain, synthesis, stability, assessment, pharmacokinetic profile, prediction of molecular mechanism and *invivo* antidiabetic evaluation in fructose induced insulin resistance model.

2. Experimental Section

Study plan is presented in Fig. 3.

2.1. Data set preparation

Marketed antidiabetic agents (glitazones) were queried from (https://pubchem.ncbi.nlm.nih.gov/) PubChem. The core molecule of interest was designed as per the previously reported literature, as shown in Fig. 1. A set of 50 congeneric series of molecules were designed, sketched using 2D sketcher in maestro 13.2. All the molecules were energy minimized using OPLS4 force field.

2.1.1. Structure based pharmacophore modelling and validation

The protein structure of PPAR-γ receptor and pioglitazone complex present in its Ligand binding domain was considered for the receptor based pharmacophore modelling, the PDB ID: 5U5L [13] was obtained from the RCSB PDB, the protein preparation wizard panel was utilized, for adding polar hydrogens, fixing the charges, maintaining the ionization state using Epik, considering zero bond order to metals, adding missing amino acids, side chain and filling loop regions using prime module, finally the receptor was minimized via force field (OPLS). The receptor complex was subjected to identify the pharmacophoric feature using "develop pharmacophore hypothesis" via Schrodinger's phase module [14]. The validation of pharmacophore model was carried out by screening the designed 50 molecules and decoy set containing 9820 molecules, followed by enrichment analysis on the screened hypothesis.

2.2. Chemistry

The melting point was obtained with open capillary tubes in a melting point equipment, with no modifications made. The ^{1}H NMR spectra at 400 MHz and ^{13}C NMR spectra at 100 MHz were acquired at room temperature using a Jeol spectrometer. Chemical shifts are measured in ppm (δ), whereas coupling constants (J) are expressed in Hz. High-resolution mass spectra were obtained using an HRMS-impact HD Bruker. IR spectra were collected using a Shimadzu IR Affinity-1

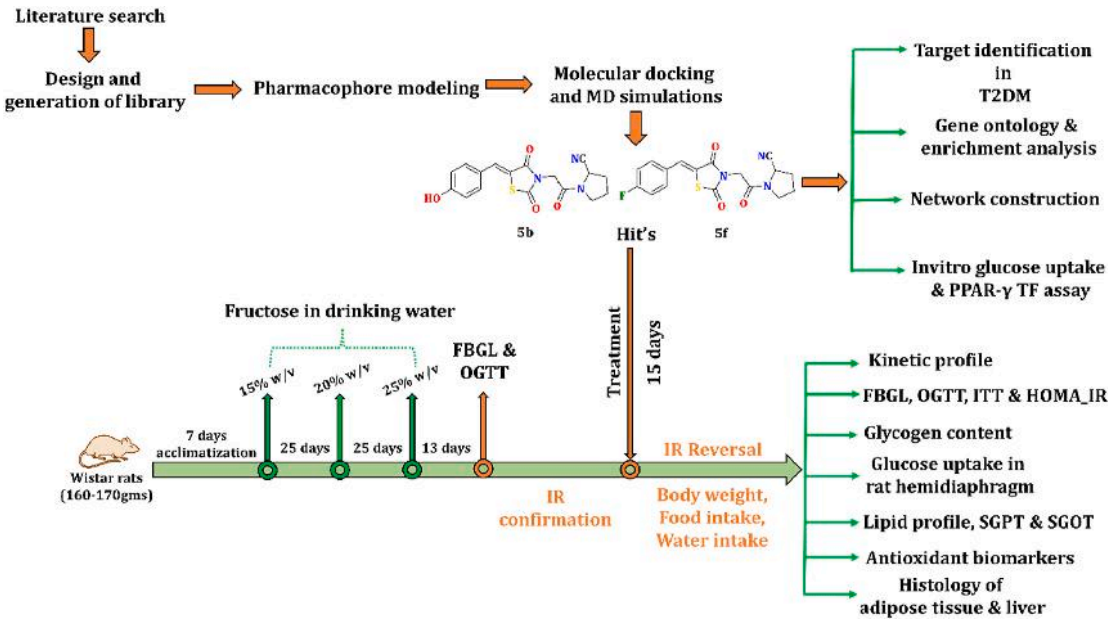


Fig. 3. Plan of study.

spectrophotometer. Commercial solvents and chemical reagents were utilized without further purification. Molecular docking, molecular dynamic simulations, and density functional theory calculations were carried out utilizing Schrödinger's Glide, Prime, Desmond, and Jaguar modules. Maestro was used to visualise interactions, and statistical analysis was done using GraphPad Prism 8.

2.2.1. General procedure for synthesis of 1-(2-(5-substituted-benzylidene-2, 4-dioxothiazolidin-3-yl) acetyl) pyrrolidine-2-carbonitrile (5a-5j)

An equimolar solution of (2-chloroacetyl) pyrrolidine-2-carbonitrile (**4**) and Substituted benzylidenethiazolidine-2, 4-dione (**3a-3j**) in acetonitrile with catalytic amount of triethyl amine was refluxed for 24h. Reaction was monitored with TLC for completion, Reaction mixture was poured on crushed ice to obtain crude product, filtered, washed with cold water, recrystallized from methanol.

2.2.1.1. Synthesis of 1-(2-(5-benzylidene-2, 4-dioxothiazolidin-3-yl) acetyl) pyrrolidine-2-carbonitrile (5a). This compound was prepared as according to the general procedure and it was obtained as white solid; yield: 76.21 %; mp: 211–213 °C; FTIR (KBr, cm^{-1}): 2952.18 (Ar-CH), 2235.59 (CN), 1745.65 (C═O), 1573.02 (C═C). ^{1}H NMR [400 MHz, δ ppm, DMSO-d_6]: 1.90–2.24 (m, 4H, –CH_2 & CH_2), 3.53–3.59 (m, 1H, CH_2), 3.78 (s, 1H, CH_2), 4.52–4.78 (m, 3H, CH_2 & CHCN), 7.56–7.50 (m, 2H, Ar–H), 7.65–7.63 (m, 3H, Ar–H), 7.97 (s, 1H, CH). ^{13}C NMR [100 MHz, δ ppm, DMSO-d_6]: 25.34, 30.00, 43.59, 46.01, 46.99, 119.52, 121.33, 129.96, 130.76, 131.38, 133.32, 134.28, 164.52, 165.69, 167.53; Chemical formula: $C_{17}H_{15}N_3O_3S$; Molecular weight; calculated: 341.39; HRMS; *m/z*: 342.09.

2.2.1.2. Synthesis of 1-(2-(5-(4-hydroxybenzylidene)-2, 4-dioxothiazolidin-3-yl) acetyl) pyrrolidine-2-carbonitrile (5b). This compound was prepared as according to the general procedure and it was obtained as buff white solid; yield: 76.21 %; mp: 168–170 °C; FTIR (KBr, cm^{-1}): 3255.02 (OH), 2957.61 (Ar-CH), 2251.02 (CN), 1749.51 (C═O), 1580.73 (C═C). ^{1}H NMR [400 MHz, δ ppm, DMSO-d_6]: 2.02–2.30 (m, 4H, –CH_2 & CH_2), 3.48–3.60 (m, 1H, CH_2), 3.76–3.80 (m, 1H, CH_2), 4.39–4.86 (m, 3H, CH_2 & CHCN), 6.93–6.95 (m, 2H, Ar–H), 7.51–7.53 (m, 2H, Ar–H), 7.88 (s, 1H, CH), 10.39 (s, 1H, OH). ^{13}C NMR [100 MHz, δ ppm, DMSO-d_6]: 24.75, 29.44, 42.91, 46.28, 45.44, 116.40, 118.93, 123.71, 132.68, 134.10, 160.27, 164.04, 165.30, 167.12; Chemical formula: $C_{17}H_{15}N_3O_4S$; Molecular weight; calculated: 357.38; HRMS; *m/z*: 358.08.

2.2.1.3. Synthesis of 1-(2-(5-(2-hydroxybenzylidene)-2,4-dioxothiazolidin-3-yl)acetyl)pyrrolidine-2-carbonitrile (5c). This compound was prepared as according to the general procedure and it was obtained as yellow solid; yield: 82.32 %; mp: 168–170 °C; FTIR (KBr, cm^{-1}): 3252.12 (OH), 2956.04 (Ar-CH), 2246.20 (CN), 1740.83 (C═O), 1599.06 (C═C). ^{1}H NMR [400 MHz, δ ppm, DMSO-d_6]: 2.01–2.21 (m, 4H, –CH_2 & CH_2), 3.48–3.59 (m, 1H, CH_2), 3.75–3.80 (m, 1H, CH_2), 4.38–4.78 (m, 3H, CH_2 & CHCN), 6.94–6.99 (m, 2H, Ar–H), 7.39–7.32 (m, 2H, Ar–H), 8.15 (s, 1H, CH), 10.64 (s, 1H, OH). ^{13}C NMR [100 MHz, δ ppm, DMSO-d_6]: 25.31, 30.00, 43.50, 46.00, 46.97, 116.76, 119.52, 119.84, 120.23, 120.35, 129.21, 129.56, 133.30, 157.94, 164.59, 165.92, 167.85; Chemical formula: $C_{17}H_{15}N_3O_4S$; Molecular weight; calculated: 357.38; HRMS; *m/z*: 358.08.

2.2.1.4. Synthesis of 1-(2-(5-(4-(dimethylamino) benzylidene)-2, 4-dioxothiazolidin-3-yl) acetyl) pyrrolidine-2-carbonitrile (5d). This compound was prepared as according to the general procedure and it was obtained as yellow solid; yield: 79.63 %; mp: 173–175 °C; FTIR (KBr, cm^{-1}): 2946.39 (Ar-CH), 2249.17 (CN), 1731.19 (C═O), 1569.16 (C═C). ^{1}H NMR [400 MHz, δ ppm, $CDCl_3$-*d6*]: 2.06–2.31 (m, 4H, –CH_2 & CH_2), 3.05 (s, 6H, $N(CH_3)_2$), 3.54–3.60 (m, 1H, CH_2), 3.66–3.74 (m, 1H, CH_2), 4.37–4.81 (m, 3H, CH_2 & CHCN), 6.70–6.72 (m, 2H, Ar–H), 7.40–7.38 (m, 2H, Ar–H), 7.83 (s, 1H, CH). ^{13}C NMR [100 MHz, δ ppm, $CDCl_3$-d_6]: 25.29, 29.98, 40.13, 42.63, 45.82, 46.89, 111.99, 113.77, 117.99, 120.53, 132.75, 135.77, 151.78, 164.16, 166.23, 168.47; Chemical formula: $C_{19}H_{20}N_4O_3S$; Molecular weight; calculated: 383.13; HRMS; *m/z*: 385.13.

2.2.1.5. Synthesis of 1-(2-(5-(4-methylbenzylidene)-2,4-dioxothiazolidin-3-yl)acetyl)pyrrolidine-2-carbonitrile (5e). This compound was prepared as according to the general procedure and it was obtained as buff yellow solid; yield: 84.17 %; mp: 170–172 °C; FTIR (KBr, cm^{-1}): 2947.36 (Ar-CH), 2251.16 (CN), 1738.90 (C═O), 1512.26 (C═C). ^{1}H NMR [400 MHz, δ ppm, $CDCl_3$-d_6]: 1.97–2.29 (m, 4H, –CH_2 & CH_2), 2.37 (s, 3H, CH_3), 3.51–3.57 (m, 1H, CH_2), 3.64–3.73 (m, 1H, CH_2), 4.33–4.74 (m, 3H, CH_2 & CHCN), 7.24–7.26 (m, 2H, Ar–H), 7.36–7.38 (m, 2H, Ar–H), 7.86 (s, 1H, CH). ^{13}C NMR [100 MHz, δ ppm, $CDCl_3$-d_6]: 21.72, 25.28,

29.98, 42.81, 45.84, 46.91, 117.89, 119.87, 130.13, 130.40, 130.46, 134.98, 141.65, 163.85, 165.94, 167.95; Chemical formula: $C_{18}H_{17}N_3O_3S$; Molecular weight; calculated 354.10; HRMS; *m/z*: 356.10.

2.2.1.6. Synthesis of 1-(2-(5-(4-fluorobenzylidene)-2,4-dioxothiazolidin-3-yl)acetyl)pyrrolidine-2-carbonitrile (5f). This compound was prepared as according to the general procedure and it was obtained as yellow solid; yield: 85.32 %; mp: 160–162 °C; FTIR (KBr, cm^{-1}): 2954.11 (Ar-CH), 2241.38 (CN), 1741.80 (C═O), 1596.16 (C═C). ^{1}H NMR [400 MHz, δ ppm, DMSO-d_6]: 2.05–2.32 (m, 4H, –CH_2 & CH_2), 3.49–3.61 (m, 1H, CH_2), 3.77–3.82 (m, 1H, CH_2), 4.41–4.90 (m, 3H, CH_2 & CHCN), 7.38–7.43 (m, 2H, Ar–H), 7.21–7.55 (m, 2H, Ar–H), 8.00 (s, 1H, CH). ^{13}C NMR [100 MHz, δ ppm, DMSO-d_6]: 24.73, 29.40, 43.10, 45.44, 46.30, 116.45, 118.90, 120.52, 129.44, 132.64, 161.81, 163.91, 164.31, 164.90, 164.99, 165.05, 166.80. Chemical formula: $C_{17}H_{14}FN_3O_3S$; Molecular weight; calculated: 358.08; HRMS; *m/z*: 360.08.

2.2.1.7. Synthesis of 1-(2-(5-(4-methoxybenzylidene)-2, 4-dioxothiazolidin-3-yl) acetyl) pyrrolidine-2-carbonitrile (5g). This compound was prepared as according to the general procedure and it was obtained as buff solid; yield: 85.32 %; mp: 167–169 °C; FTIR (KBr, cm^{-1}): 2984.01 (Ar-CH), 2241.38 (CN), 1738.90 (C═O), 1586.52 (C═C). ^{1}H NMR [400 MHz, δ ppm, DMSO-d_6]: 2.02–2.30 (m, 4H, –CH_2 & CH_2), 3.48–3.60 (m, 1H, CH_2), 3.75–3.81 (m, 1H, CH_2), 3.83 (s, 3H, OCH_3), 4.50–4.78 (m, 3H, CH_2 & CHCN), 7.10–7.12 (m, 2H, Ar–H), 7.60–7.62 (m, 2H, Ar–H), 7.92 (s, 1H, CH). ^{13}C NMR [100 MHz, δ ppm, DMSO-d_6]: 25.32, 30.03, 43.53, 46.03, 46.98, 56.07, 115.45, 118.10, 119.47, 125.85, 132.91, 134.24, 161.88, 164.58, 165.78, 167.57. Chemical formula: $C_{18}H_{17}N_3O_4S$; Molecular weight; calculated: 371.41; HRMS; *m/z*: 372.10.

2.2.1.8. Synthesis of 1-(2-(5-(3, 4-dimethoxybenzylidene)-2, 4-dioxothiazolidin-3-yl) acetyl) pyrrolidine-2-carbonitrile (5h). This compound was prepared as according to the general procedure and it was obtained as buff solid; yield: 85.32 %; mp: 171–173 °C; FTIR (KBr, cm^{-1}): 2951.22 (Ar-CH), 2242.34 (CN), 1738.90 (C═O), 1575.91 (C═C). ^{1}H NMR [400 MHz, δ ppm, DMSO-d_6]: 1.90–2.24 (m, 4H, –CH_2 & CH_2), 3.50–3.59 (m, 1H, CH_2), 3.75–3.81 (m, 1H, CH_2), 3.80–3.82 (d, 6H, OCH_3), 4.38–4.88 (m, 3H, CH_2 & CHCN), 7.12–7.14 (m, 2H, Ar–H), 7.22–7.24 (m, 2H, Ar–H), 7.91 (s, 1H, CH). ^{13}C NMR [100 MHz, δ ppm, DMSO-d_6]: 25.34, 30.00, 43.51, 46.00, 46.97, 56.06, 56.23, 112.63, 114.04, 118.16, 119.53, 124.46, 125.97, 134.61, 149.47, 151.65, 164.58, 165.78, 167.62. Chemical formula: $C_{19}H_{19}N_3O_5S$; Molecular weight; calculated: 401.44; HRMS; *m/z*: 402.12.

2.2.1.9. Synthesis of 1-(2-(2, 4-dioxo-5-(3, 4, 5-trimethoxybenzylidene) thiazolidin-3-yl) acetyl) pyrrolidine-2-carbonitrile (5i). This compound was prepared as according to the general procedure and it was obtained as off-white solid; yield: 80.07 %; mp: 164–166 °C; FTIR (KBr, cm^{-1}): 2943.50 (Ar-CH), 2243.31 (CN), 1738.90 (C═O), 1575.91 (C═C). ^{1}H NMR [400 MHz, δ ppm, DMSO-d_6]: 2.01–2.34 (m, 4H, –CH_2 & CH_2), 3.48–3.59 (m, 1H, CH_2), 3.72 (S, 3H, OCH_3), 3.76–3.80 (m, 1H, CH_2), 3.83 (d, 6H, OCH_3), 4.39–4.89 (m, 3H, CH_2 & CHCN), 6.97 (s, 2H, Ar–H), 7.92 (s, 1H, CH). ^{13}C NMR [100 MHz, δ ppm, DMSO-d_6]: 25.34, 30.01, 43.57, 46.00, 46.98, 56.54, 60.75, 108.20, 119.53, 120.30, 128.85, 134.51, 140.17, 153.77, 164.53, 165.64, 167.52. Chemical formula: $C_{20}H_{21}N_3O_6S$; Molecular weight; calculated: 431.46; HRMS; *m/z*: 432.12.

2.2.1.10. Synthesis of 1-(2-(5-(furan-2-ylmethylene)-2, 4-dioxothiazolidin-3-yl) acetyl) pyrrolidine-2-carbonitrile (5j). This compound was prepared as according to the general procedure and it was obtained as buff brown solid; yield: 80.07 %; mp: 178–180 °C; FTIR (KBr, cm^{-1}): 2971.47 (Ar-CH), 2244.27 (CN), 1747.58 (C═O), 1545.05 (C═C). ^{1}H NMR [400 MHz, δ ppm, DMSO-d_6]: 2.06–2.29 (m, 4H, –CH_2 & CH_2), 3.47–3.58 (m, 1H, CH_2), 3.77 (m, 1H, CH_2), 4.37–4.86 (m, 3H, CH_2 & CHCN), 6.76 (s, 1H, Ar–H), 7.16–7.17 (d, 1H, Ar–H), 7.80 (s, 1H, Ar–H), 8.09 (s, 1H, CH). ^{13}C NMR [100 MHz, δ ppm, DMSO-d_6]: 25.34, 29.99, 43.43, 45.99, 46.97, 114.23, 117.84, 119.53, 120.28, 120.61, 148.61, 149.65, 164.11, 164.58, 165.49, 168.26. Chemical formula: $C_{20}H_{21}N_3O_6S$; Molecular weight; calculated: 330.07; HRMS; *m/z*: 332.06.

2.3. Biological evaluation

2.3.1. Invitro glucose uptake in L6 cell lines

L6 cells were nurtured in DMEM with 25 mmol/l D-glucose, 10 % heat-inactivated fetal bovine serum, 10 U/ml penicillin, and 10 mg/ml streptomycin at 37 °C and 5 % CO2. Cells were starved of serum for 24 h. The cells were washed twice with PBS, and the culture medium was replaced with RPMI-1640 containing 11.1 mmol/l glucose and 0.2 % bovine serum albumin. The medium was subsequently treated with pioglitazone (50 mmol/l) or test compounds at equivalent concentrations. DMSO served as a blank control. After 24-h treatment, the amount of glucose in the media was measured using the glucose oxidase (GOD-POD) technique [15]. 10 μl of sample and 1 ml of reagent were incubated at 37 °C for 10 min, finally colorimetric estimation was done at 505 nm, absorbance of test with respect to blank recordings (negative control) was calculated and percentage glucose consumption was calculated using the formula,

$$Glucose\ consumption = \frac{OD\ of\ blank - OD\ of\ test}{OD\ of\ blank}\ X\ 100$$

2.3.2. Invitro PPAR-γ TF assay

This cell-based ELISA technique detects PPAR-γ transcription factor levels in the HepG2 cell line. The Raybio PPAR-γ TF activity evaluation kit was used to conduct this experiment on compounds **5b**, **5f**, and pioglitazone, as instructed by the manufacturer [16].

2.3.3. Experimental pharmacology

2.3.3.1. Ethical approval and procurement of animal. The Male Wistar rats of either sex were procured from the CPCSEA approved vendor from the Invivo Biosciences, Bangalore. The institutional animal ethics committee at the KLE College of Pharmacy in Belagavi examined the animal study protocol (resolution No. KLECOP/CPCSEA-Reg, No.221/Po/Re/S/2000/CPCSEA, Res.34-03/12/2022). Prior to the commencement of the trial, the animals were acclimated for a week to a 12 h light/dark cycle.

2.3.3.2. Acute toxicity study, induction of diabetes through insulin resistance. And grouping of animals. The (OECD) guidelines 423 were referred for the assessment of the acute oral toxicity study of the compounds **5b** and **5e.** Animals weighing between 180 and 200g were fasted overnight. Initially, a dose of 5 mg/kg was administered and observed for the mortality for 48h, and observed for any signs of toxicity following 14 days, since no mortality was seen in this dose group, the dose was increased to 50 mg/kg and observed for signs of mortality and toxicity for 14 days, resulting in no mortality, further the dose was increased to 300 mg/kg, and mortality was observed on 5th and 7th day of administration. Thus 300 mg/kg was considered as LD_{50} and 1/10th of LD_{50} was selected as effective dose for model study.

A 64-day induction phase with high fructose feeding in drinking water was administered, with 15 % w/v fructose during the first 20 days, subsequently 20 % w/v fructose for next 25 days, and 25 % w/v fructose for next 18 days [17,18], followed by 15 days of treatment. Insulin resistance was tested by loading exogenous load of glucose (2 g/kg) of fasting body weight, and the OGTT and AUC for glucose were estimated, for animals with raised blood glucose levels exceeding 120 mg/dl being classified as diabetic. Five group were made containing six animals of either sex each. Group 1 (normal group): Consist of healthy animals feed

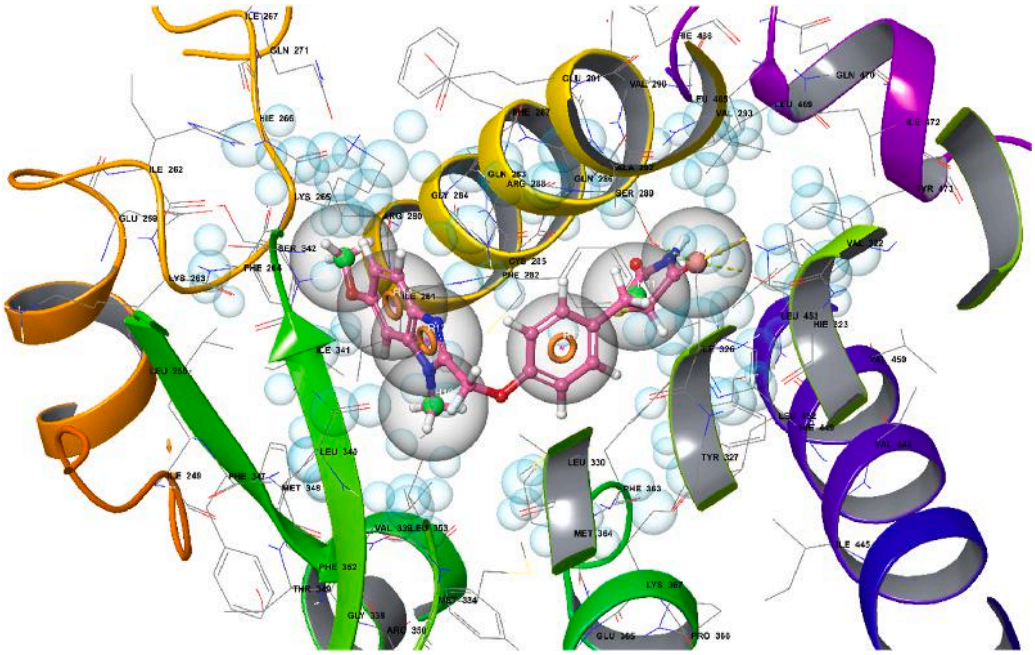


Fig. 4. Generated pharmacophore 7 point hypothesis with reference ligand as pioglitazone in PPAR-γ ligand binding domain.

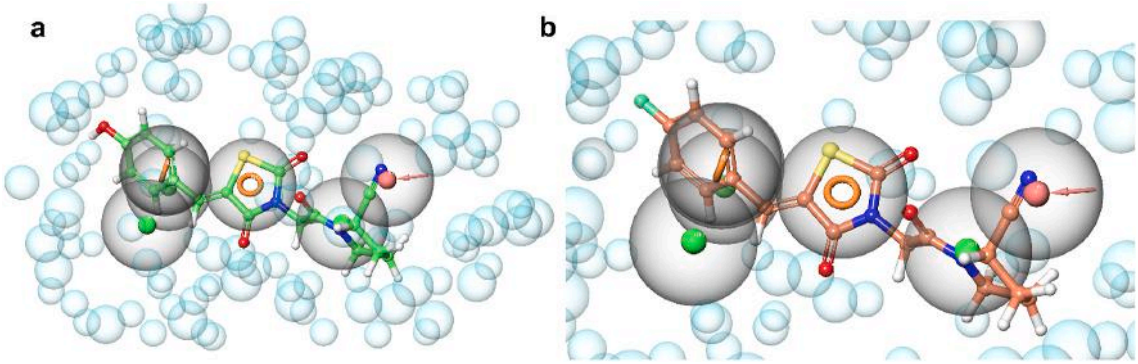
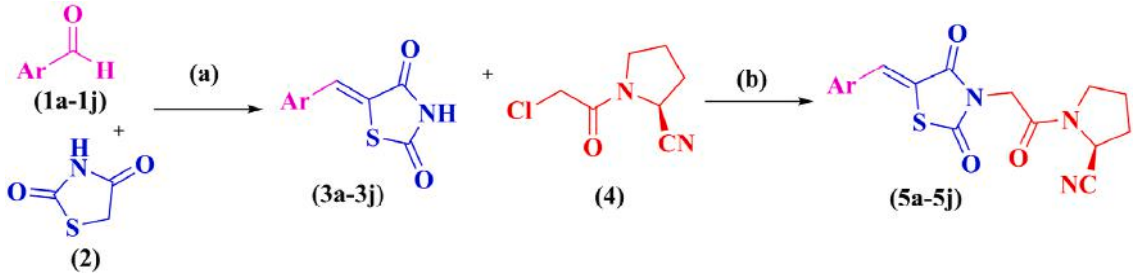


Fig. 5. Alignment of generated sites from the hypothesis with (a) compound **5b** and (b) compound **5f**.



Scheme 1. Reagents and conditions: (a) Piperdine-acetate, toluene, reflux; (b) acetonitrile, triethyamine, reflux.

with normal water and feed; Group 2 is Insulin resistance group (IR): consist of animals receiving fructose in drinking water (63 days) and feed; Group 3 is standard group (Pio10): consist of animals receiving fructose in drinking water (63 days) followed by orally fed pioglitazone 10 mg/kg (0.25 % CMC suspension); Group 4 is treatment group (**5b**): consist of animals receiving fructose in drinking water (63 days) followed by orally fed synthesized compound **5b** at a dose of 30 mg/kg (0.25 % CMC suspension); Group 5 is treatment group (**5e**): consist of animals receiving fructose supplementation in water (63 days) followed by orally fed synthesized compound **5e** with a dose of 30 mg/kg (0.25 % CMC suspension).

2.3.3.3. Estimation of body weight, food intake and water intake. Physical parameters of the individual animals like body weight, food intake, and water intake was measured for three animals per cage, from the day one of induction and every third day from the day one of induction and First day of treatment.

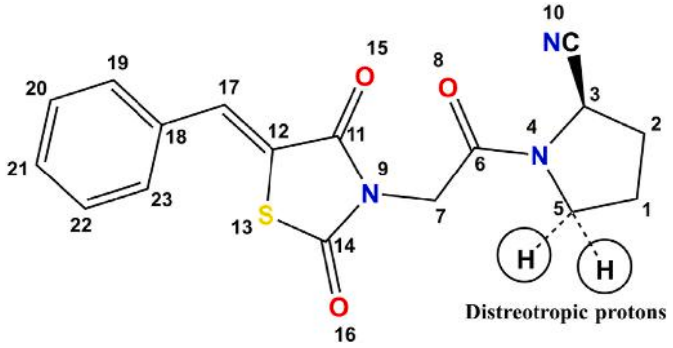


Fig. 6. proton and carbon assignment numbering pattern for NMR interpretation.

2.3.3.4. Estimation of fasting blood glucose level (FBGL) and oral glucose tolerance test (OGTT). All the animals were fasted during the night, and their FBGL were estimated via the glucometer (Janaushadhi, India) by the tail prick method. The insulin sensitivity of whole body was assessed by OGTT and area under curve ($AUC_{0\text{-}120}$) method, where animals were starved over the night, and then given an oral gavage of (2 g/kg) solution of glucose, Blood samples were obtained at (0–120 min) with intervals of 30 min and tested by glucometer [19].

2.3.3.5. Estimation of fasting insulin level, and insulin tolerance test (ITT), and HOMA-IR index. Blood was obtained and examined to estimate levels of insulin using a commercially available kit (GENLISA™ Rat Insulin (INS) ELISA). Subcutaneous insulin (0.75 U/kg) was administered, and blood sugar levels were recorded (0–120 min) with interval of 30 min using a glucometer, the total AUC for glucose was computed for the same [20]. The HOMA-IR index was estimated by the formula,

$$HOMA - IR = \frac{glucose\ mg/dl \times insulin(\mu IU/mL)}{405}$$

2.3.3.6. Collection of blood and visceral organs. At the end of the experiment, the animals were euthanized with an overdose of anaesthetic ether, blood was obtained via cardiac puncture, centrifuged, and plasm was separated, adipose tissue and liver were extracted, rinsed with phosphate buffer to prevent clotting, and preserved in 10 % v/v formalin solution.

2.3.3.7. Lipid profile estimation. Plasma obtained from blood was used to estimate the total cholesterol (TC), triglycerides (TG), high-density lipoprotein (HDL), further the SGPT and SGOT were quantified spectrophotometrically using commercially available kits (GENLISA, and AGD clinipark diagnostic kit) The (LDL) and (VLDL) levels were calculated as follows,

$$VLDL = TG/5$$

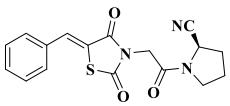
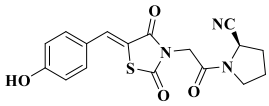
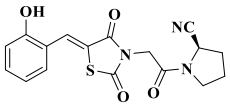
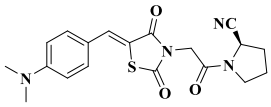
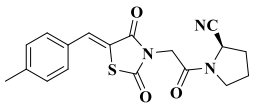
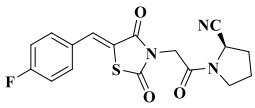
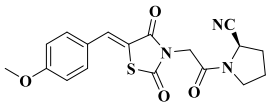
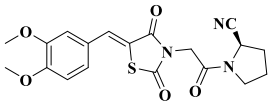
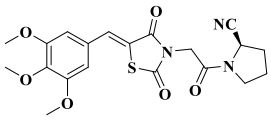
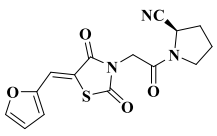
$$LDL = TC - (HDL + VLDL)$$

2.3.3.8. Glucose utilization by rat hemidiaphragm. The glucose consumption capacity was performed in rat hemidiaphragm after the treatment peroid, isolated hemidiaphragm 1 × $1cm^2$ tissue was incubated in (30 mM) glucose solution, and mixed with 0.25U insulin under aeration for 10 min, Following incubation, the percentage variation in the amount of glucose in the incubating mixture was calculated [21]. Thus calculating the difference in concentration as follows,

$$\%\ change\ in\ glucose\ concentration = \frac{Ac - At}{Ac} \times 100$$

Where Ac and At refers to absorbance of concentration of glucose in incubating medium prior later to the incubation of hemidiaphragm tissue respectively in incubating mixture.

Table 1
Invitro percentage glucose uptake of the synthesized compounds (**5a-5j**) in L6 myotubes.

Sr. No	Structure	% glucose uptake in L6 myotubes
5a		63.23 ± 0.02
5b		79.29 ± 1.02
5c		72.86 ± 1.03
5d		64.18 ± 0.31
5e		64.57 ± 0.76
5f		74.58 ± 0.54
5g		58.66 ± 0.31
5h		64.56 ± 0.73
5i		69.74 ± 0.10
5j		57.40 ± 0.07
Pioglitazone	–	82.36 ± 0.98

2.3.3.9. Content of glycogen in liver and skeletal muscles. Both the liver and skeletal muscles were accurately removed during the dissection of the experimental animals, then rinsed with phosphate buffer to eliminate the blood clots, Further, the liver and skeletal muscle tissue were homogenised with 10 % v/v phosphate buffer. The (1 ml) homogenate of liver and skeletal muscle was then incubated with 30 % w/v KOH (2 ml) in a bath of simmering water for 15 min and the volume was makeup to 25 ml with 30 % w/v KOH. Additional ethanol was added, and the

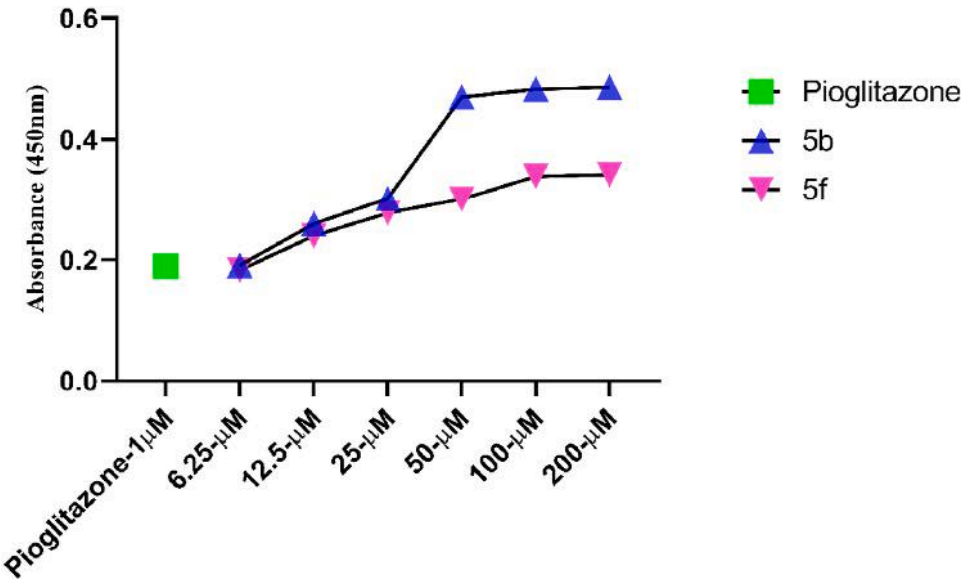


Fig. 7. Expression of PPAR-γ transcription factor by compound **5b, 5f** and pioglitazone.

containt was incubated over night at ambient temperature, resulting in glycogen precipitation. The entire combination was centrifuged at 3000 rpm for 10 min, and the resulting pellet was dissolved in Millipore water, to which 4 ml of anthrone reagent was added and heated for 5 min. The liquid was cooled, and absorbance was measured [22] using a UV spectrophotometer (Shimazdu UV probe 2.4).

2.3.3.10. Oxidative stress markers. The various enzymatic and non-enzymatic oxidative stress parameters in liver tissue like hepatic super oxidase (SOD) [23], malondialdehyde, glutathione [24], and catalase [25], were quantified as per previously established procedure.

2.3.3.11. Histopathology study. The organs tissue like liver and adipose tissue were preserved in 10 % formalin, and subjected to pathological investigations using (H and E) hematoxylin and eosin stain. The liver samples were assessed for, sinusoidal congestion, venous congestion and ballooning degeneration. The adipocytes count and size were estimated from adipose tissue.

2.3.3.12. Instrumentation and chromatographic conditions. Shimadzu Agilent 1220 Infinity II instrument (LC-20AD, Japan) equipped with Quaternary pump with degasser (G7111A), auto-injector (G7129A), PDA detector (G7115A), injecting value with 10 μL loop and CTO-10AS VP column oven. OpenLab CDS software was used for the analytical data interpretation. Phenomenex Luna C18 analytical column (4.6 × 150 mm, 5 μm particle size, Phenomenex Inc., USA) was used for the chromatographic separation. For the sample analysis optimal mobile phase was acetonitrile (ACN): 0.1 % Formic acid (FA) in water with ratio 60:40 v/v and eluted at flow rate of 1 mL/min. Before usage, the mobile phase was filtered through PVDF membrane filter (0.45μ; Millex HV®, Millipore, USA) and degassed ultrasonically. For the sample analysis, the injection volume was kept constant at 10 μL, and the detection wavelength was set for **5b** and **5f** (324 nm), for PIO (273 nm).

2.3.3.13. Preparation stock solution and working standard solution. The primary stock solutions of compounds **5b**, **5f**, and PIO-10 were prepared at a concentration of 1 mg/mL in acetonitrile. To generate working standard solutions, the stock solutions were diluted with the mobile phase to achieve concentrations ranging from 5 to 30 μg/mL. Before performing the HPLC analysis, all standard solutions were maintained at 4 °C in tightly sealed volumetric flasks.

2.3.3.14. Method validation. HPLC method validation, in accordance with ICH guidelines, ensures the reliability and accuracy of analytical results. It encompasses parameters such as linearity, LOD, LOQ, precision, and accuracy. By validating the method, one can ensure its suitability for the intended purpose, providing confidence in the quality and integrity of Bio-analytical data generated using the HPLC technique.

2.3.3.15. Extraction of drugs from plasma followed by Quantification. Fresh blood samples were taken from rats, and plasma was extracted by centrifugation at 12,000 rpm for 10 min at 4 °C. Stock mixtures containing **5b**, **5f**, and PIO-10, of 10 μg/mL concentration, were prepared in acetonitrile. These solutions were used to create a standard calibration curve by spiking various quantities of **5b**, **5f**, and PIO-10 into rat plasma. Aliquots of 500 μL of rat plasma were combined with the standard solutions of **5b**, **5f**, and PIO-10 in separate centrifuge tubes. After thorough mixing, protein precipitation was induced by adding acetonitrile (200 μL). The resulting mixture was finally vortexed and spun at 15,000 rpm for 10 min. The resultant clear supernatant was separated and analyzed with the suggested HPLC method [26].

2.3.3.16. Pharmacokinetic analysis. The synthetic compounds **5b** and **5f** (30 mg/kg), along with the pioglitazone (10 mg/kg), were given orally to three separate groups of six animals each. Blood samples were taken from the retro-orbital sinus for (1–12 h) with 30 min interval. A 0.5 mL of blood was taken out in tubes with EDTA and subjected to centrifugation at 4000 rpm for 10 min at −4 °C. The separated plasma was transferred to Eppendorf tubes and stored at −4 °C for up to 24 h 200 μL of plasma from the Eppendorf tubes, to which acetonitrile to make up volume of 2 mL. This mixture was swirled for 30 s and then spun at 12000 rpm for 10 min. The resulting supernatant was passed via micro syringe and transferred to vials for further analysis [26].

2.3.3.17. Statistical analysis. The data were presented as Mean ± SEM. Statistical analysis was performed using one-way or two-way ANOVA, followed by posthoc tests such as Tukey's or Bonferroni's, and Dunn's test for different parameters, all conducted using GraphPad Prism (version 8). A p-value of less than 0.05 was considered statistically significant. Pharmacokinetic data were analyzed as needed using WinNonlin software (Pharsight Corp., Mountain View, CA). Various parameters, including Cmax (μg/mL), Tmax (h), AUC 0-t (h·μg/mL), AUC 0-inf (h·μg/mL), Kel, and T1/2 (h), were evaluated.

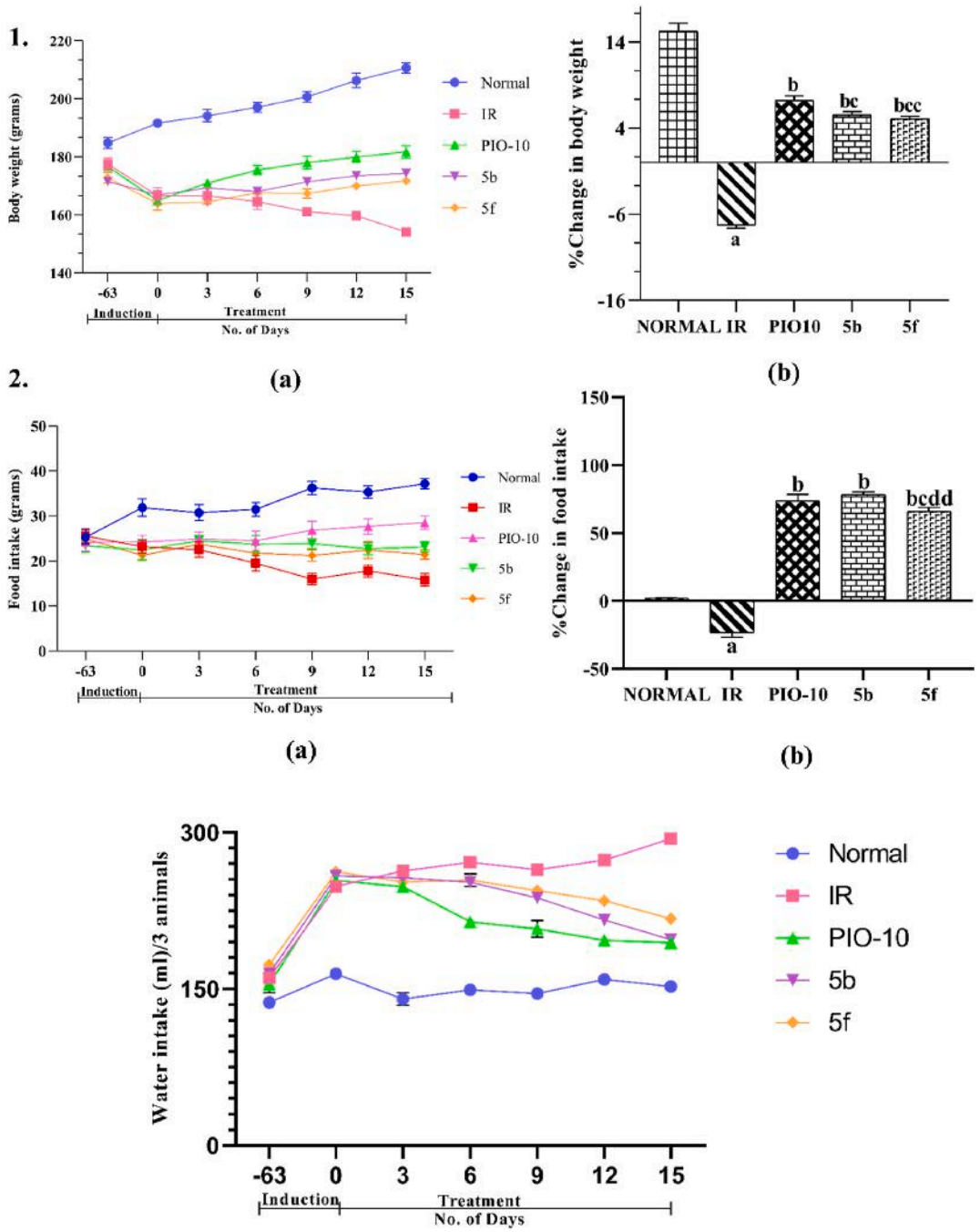


Fig. 8. Effect of compound **5b** and **5f** on food intake, body weight, and water intake. Where, insulin resistance group is **IR**; **PIO-10** is pioglitazone (10 mg/kg) treated group; **5b** is compound **5b** treated group; **5f** is compound **5f** treated group. Data is expressed in Mean ± SEM (n = 6); one-way ANOVA Followed by post Hoc tukey's test was used to analyze percent change in body weight, food intake and water intake; **1.** Body weight: $^{a}P < 0.001$ compared to normal group; $^{b}P < 0.001$ compared to IR; $^{c}P < 0.05$, $^{cc}P < 0.01$ as compared to PIO-10; **2.** Food intake: $^{a}P < 0.001$ compared to normal group; $^{b}P < 0.001$ compared to IR; $^{c}P < 0.05$, as compared to PIO-10; $^{dd}P < 0.01$ as compared to **5b** treated group. **3.** Water intake representation.

2.4. Molecular docking studies

The top 10 ligands obtained by screening the pharmacophoric hypothesis were further assessed for their binding affinity by molecular docking studies using Schrodinger's small molecule suits. The ligands were prepared using the LigPrep panel [27], were the polar hydrogens were assigned, ionization was carried out using Epik, followed by assigning chiral center based on the 3 dimensional geometry and finally all the molecules including standard pioglitazone were energy optimized via an OPLS4 force field.

The crystal structure coordinated of PPAR-γ ligand binding domain (PDB ID: 5U5L) was retrieved, it consist of 1–273 amino acid sequence length. The protein was preprocessed and prepared by adding polar hydrogens, assigning the bond orders and creating zero order bond to metal ions, assigning disulfide bonds, selenomethionines to methionines, deleting water molecules, fixing the missing loops, filling missing side chains, capping the C and N terminals, generating the het states with pH: 7.4 ± 2.0. PROPKA was used for the optimization based on sample water orientations, and finally to obtain stable structure of protein the energy minimization was carried out using an OPLS4 force field via protein preparation workflow panel.

Grid was generated for the prepared protein using receptor grid

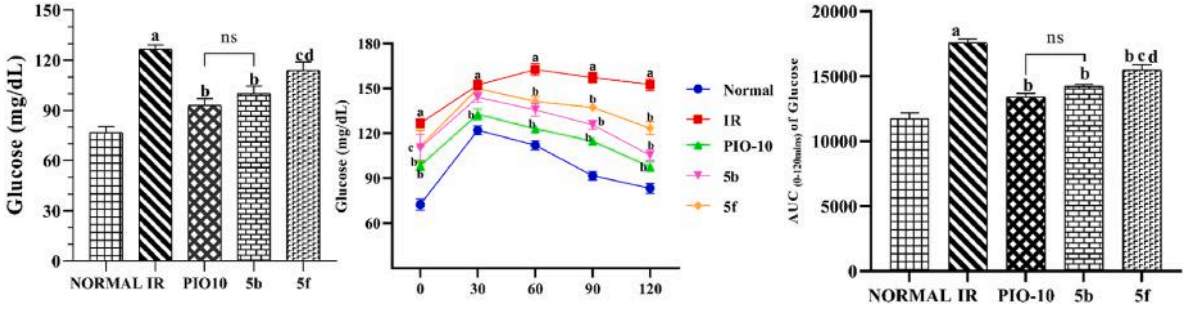


Fig. 9. Effect of compound **5b** and **5f** on FBGL and OGTT. Where, insulin resistance group is IR; PIO-10 is pioglitazone (10 mg/kg) treated group; **5b** is compound **5b** treated group; **5f** is compound **5f** treated group. Data is expressed in Mean ± SEM (n = 6); one-way ANOVA was used to analyze FBGL and AUC for glucose and two-way ANOVA followed by Bonferroni's post hoc test was used to analyze OGTT. [a]P < 0.001 compared to normal; [b]P < 0.001 compared to IR; [c]P < 0.05 compared to PIO-10; [d]P < 0.001 compared to **5b** treated group.

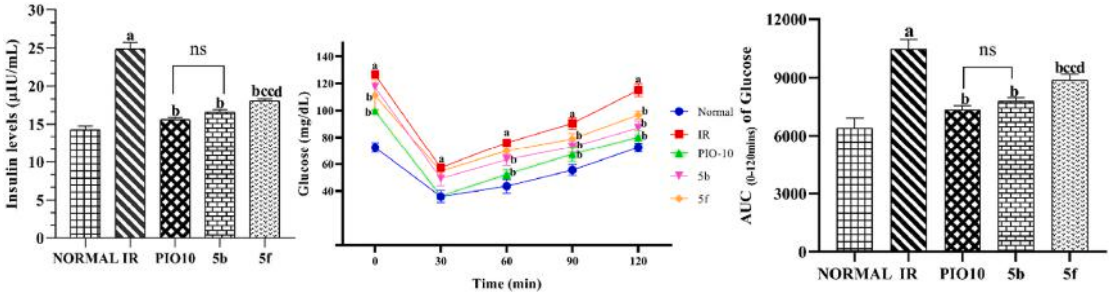


Fig. 10. Effect of compound **5b** and **5f** on insulin levels and OGTT. Where, insulin resistance group is IR; PIO-10 is pioglitazone (10 mg/kg) treated group; **5b** is compound **5b** treated group; **5f** is compound **5f** treated group. Data is expressed in Mean ± SEM (n = 6); one-way ANOVA followed by post Hoc tukeys test was used to analyze insulin levels and AUC for glucose and two-way ANOVA followed by Bonferroni's post hoc test was used to analyze OGTT. [a]P < 0.001 compared to normal; [b]P < 0.001 compared to IR; [c]P < 0.05 compared to PIO-10; [d]P < 0.001 compared to **5b** treated group.

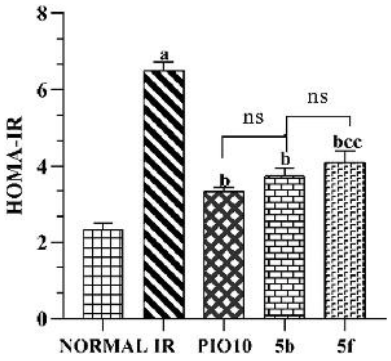


Fig. 11. Effect of compound **5b** and **5f** on HOMO-IR. Where, insulin resistance group is IR; PIO-10 is pioglitazone (10 mg/kg) treated group; **5b** is compound **5b** treated group; **5f** is compound **5f** treated group. Data is expressed in Mean ± SEM (n = 6); HOMA-IR was analyzed by one-way ANOVA followed by post Hoc tukeys test. [a]P < 0.001 compared to normal; [b]P < 0.001 compared to IR; [cc]P < 0.01 compared to PIO-10.

generation panel, the receptor was defined for the van der Waals radius scaling factor of 0.1 and cutoff of partial charges was 0.25. Grid was generated by specifying the cocrystal ligand as centroid. The active site comprise of the coactivator binding surface (AF2) and also being in proximity makes contacts with β-sheet and helix 3 as compared to standard model pioglitazone binding domain. The key residues involved in hydrogen bond network and hydrophobic contacts were identified as HIS 323, SER 289, TYR 473, CYS 285, ILE 281, ILE 341, and MET 348.

Glides extra precision (XP) mode, identifies the binding orientation and affinity of ligands to bind at a specified conformation of PPAR-γ ligand binding domain. It provides wide range of sampling, scoring function was based on water displacement by ligand from hydrophobic region, Hydrogen bonding interaction between protein and ligand with other electrostatic interactions, it takes in account the desolvation effect, due to the restriction of motion of protein and ligand entropic effect is considered, and metal ligand interaction alongside the penalties were assessed and the poses were ranked based on the conformational search sampling, finally post dock minimization was performed for the docked complexes [28,29].

2.5. Molecular dynamic (MD) simulations and MM/GBSA calculations

A 500ns MD Run was executed on Desmond Molecular Dynamics module via maestro (2024-1) release. The **5U5L-5b** and **5U5L-5f** complex was solvated in an orthorhombic box with TIP3P water model with side lengths of 10 Å buffer calculation method, and partial charges from the complex were retained. Long-range electrostatic interactions were efficiently treated using this molecular dynamics simulations that utilizes the Smooth Particle Mesh Ewald (SPME) algorithm to accurately calculate short-range non-bonded interactions with a 9 Å cut-off. To account for the influence of the solvent environment on electrostatic interactions, simulations were conducted in the presence of both solvent and ions. Initial equilibration simulations of 10 ns were performed to validate system suitability. To maintain system electroneutrality, the net charge of the complex was neutralized, and an ionic strength of 0.15 M was achieved by introducing Na^+ and Cl^- ions, finally the whole system was built and subjected for the minimization using OPLS4 force field [30,31].

The (MM/GBSA) calculations was computed via Schrodinger's prime module. This method predicts accurately the free binding energy of the protein ligand complex, hence all the docked complexes were subjected for free energy calculation studies [32].

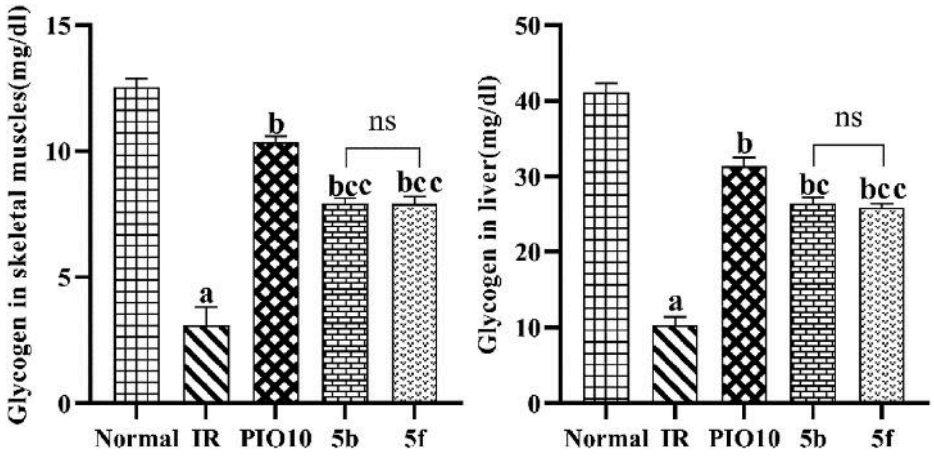


Fig. 12. Effect of Compound **5b** and 5e on glycogen content in skeletal muscles and liver. Where, IR is insulin resistance group; PIO-10 is pioglitazone (10 mg/kg) treated group; **5b** is compound **5b** treated group; **5f** is compound **5f** treated group. Data is expressed in Mean ± SEM (n = 6); one-way ANOVA followed by post Hoc tukeys test was used to analyze glycogen content in skeletal muscles and liver. $^{a}P < 0.001$ compared to normal; $^{b}P < 0.001$ compared to IR; $^{c}P < 0.05$; $^{cc}P < 0.01$ compared to PIO-10.

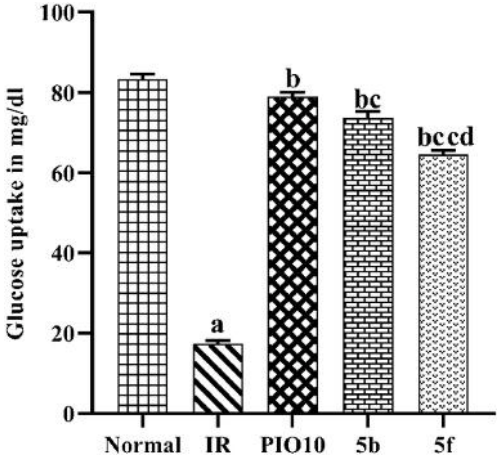


Fig. 13. Effect of Compound **5b** and **5f** on glucose uptake in rat hemi-diaphragm. Where, IR is insulin resistance group; PIO-10 is pioglitazone (10 mg/kg) treated group; **5b** is compound **5b** treated group; **5f** is compound **5f** treated group. Data is expressed in Mean ± SEM (n = 6); one-way ANOVA followed by post Hoc tukeys test was used to analyze glucose uptake. $^{a}P < 0.001$ compared to normal; $^{b}P < 0.001$ compared to IR; $^{c}P < 0.05$ and $^{cc}P < 0.01$ compared to PIO-10; $^{d}P < 0.001$ compared to **5b** group.

2.6. Geometric optimization

The most stable molecular shape can be predicted by minimizing the system's energy, which in turn allows for the calculation of bond lengths, bond angles, and dihedral angles. Density Functional Theory (DFT) is a computational method widely used in quantum chemistry and materials science to explore the electronic structure and properties of molecules. In this study, molecules **5b** and **5f** underwent geometric optimization using the B3LYP and the 6–31G (d, p) basis set, executed via the Schrödinger's Jaguar module. Additionally, an Electrostatic Potential (ESP) map was generated for each synthesized molecule **5b** and **5f**. Quantum chemical parameters, including the energy gap (ΔEGAP), dipole moment (μ), hardness (η), and local softness (σ), were also calculated based on the frontier molecular orbitals [33].

$$\Delta EGAP = ELUMO - EHOMO$$

Table 2
Effect of **5b** and **5f** on lipid profile. Where, IR is insulin resistance group; PIO-10 is pioglitazone (10 mg/kg) treated group; **5b** is compound **5b** treated group; **5f** is compound **5f** treated group. HDL: High Density Lipoproteins, VLDL: Very Low-density Lipoproteins, LDL: Low Density Lipoproteins. Data is expressed in Mean ± SEM (n = 6); one-way ANOVA followed by post Hoc tukeys test was used to analyze the lipid profile. $^{a}P < 0.001$ compared to normal; $^{b}P < 0.001$ compared to IR; $^{c}P < 0.05$ & $^{cc}P < 0.01$ compared to PIO-10 in triglycerides levels, HDL, LDL and total cholesterol levels; $^{c}P < 0.001$ compared to PIO-10 & $^{d}P < 0.001$ compared to **5b** treated group for VLDL levels.

Group	Triglycerides (mg/dL)	Total cholesterol (mg/dL)	HDL (mg/dL)	VLDL (mg/dL)	LDL (mg/dL)
Normal	54.97 ± 1.82	127.98 ± 1.71	65.21 ± 1.01	10.99 ± 0.4	55.77 ± 2.10
IR	140.03 ± 3.55^{a}	93.68 ± 1.68^{a}	25.35 ± 2.03^{a}	28.00 ± 0.28^{a}	40.32 ± 1.08^{a}
PIO-10	63.57 ± 1.83^{b}	122.79 ± 1.83^{b}	60.72 ± 1.20^{b}	12.71 ± 0.24^{b}	49.35 ± 1.12^{b}
5b	76.18 ± 2.24^{bc}	114.79 ± 1.75 ^{bc}	53.25 ± 2.54 ^{bc}	15.23 ± 0.18 ^{bc}	47.81 ± 1.83^{b}
5f	86.15 ± 1.23^{bcc}	112.30 ± 1.83 ^{bc}	51.39 ± 1.34 ^{bcc}	17.23 ± 0.25 ^{bcd}	42.74 ± 1.01

Table 3
Effect of **5b** and **5f** on hepatic markers. Where, IR is insulin resistance group; PIO-10 is pioglitazone (10 mg/kg) treated group; **5b** is compound **5b** treated group; **5f** is compound **5f** treated group. SGOT: serum glutamic oxaloacetic transaminase; SGPT: serum glutamic pyruvate transaminase. Data is expressed in Mean ± SEM (n = 6); one-way ANOVA followed by post Hoc tukeys test was used to analyze SGPT and SGOT levels. $^{a}P < 0.001$ compared to normal; $^{b}P < 0.001$ compared to IR; $^{c}P < 0.05$ & $^{cc}P < 0.01$ as compared to PIO-10.

Group	SGOT (U/L)	SGPT (U/L)
Normal	27.35 ± 1.28	24.19 ± 1.38
IR	59.32 ± 2.09^{a}	56.41 ± 2.09^{a}
PIO-10	32.45 ± 1.83^{b}	29.73 ± 1.33^{b}
5b	41.32 ± 1.23^{bc}	37.12 ± 1.29 ^{bc}
5f	46.36 ± 1.36^{bc}	39.72 ± 1.82 ^{bcc}

Table 4
Effect of **5b** and **5f** on antioxidant biomarkers. Where, IR is insulin resistance group; PIO-10 is pioglitazone (10 mg/kg) treated group; **5b** is compound **5b** treated group; **5f** is compound **5f** treated group. Data is expressed in Mean ± SEM (n = 6); one-way ANOVA followed by post Hoc tukeys test was used to analyze the antioxidant biomarkers. $^{a}P < 0.001$ compared to normal; $^{b}P < 0.001$ compared to IR; $^{c}P < 0.05$ & $^{cc}P < 0.01$ as compared to PIO-10.

Group	SOD (U/ml)	CAT (U/min/mg of protein)	MDA(nM/mg of protein)	GSH (μM/mg of protein)
Normal	29.87 ± 0.98	77.65 ± 0.98	142.65 ± 10.98	110.35 ± 0.86
IR	13.25 ± 1.35^{a}	27.65 ± 1.02^{a}	294.65 ± 11.78^{a}	39.98 ± 1.21^{a}
PIO-10	27.65 ± 1.98^{b}	55.63 ± 0.98^{b}	178.35 ± 8.6^{b}	77.65 ± 1.07^{b}
5b	24.68 ± 1.73^{bc}	52.36 ± 1.32^{b}	197.32 ± 11.74^{b}	61.35 ± .230^{bccc}
5f	20.36 ± 0.98^{bcc}	48.65 ± 1.06^{bcc}	224.65 ± 9.73^{bc}	58.63 ± 1.47^{bccc}

$$\eta = (E_{LUMO} - E_{HOMO}) \ / 2$$

$$\sigma = 1 / \eta$$

$$\mu = (EHOMO + ELUMO)/2$$

$$\omega = \mu^2 \ / \ 2\,\eta$$

2.7. ADMET profile predictions

The synthesized molecules (**5a-5j**) were computed for their Adsorption, distribution, metabolism, excretion and toxological predictions, using Schrodinger's Qikprop module [34].

Table 5
Summary of validation parameters.

Sr. no	Validation parameters	5f	5b	PIO
1	Linearity			
	Linearity range (μg/mL)	5–30	5–30	5.-30
	Slope	24.406x	18.396x	
	Intercept	4.53	8.48	
	Correlation-coefficient	0.9997	0.998	
2	LOD (μg/mL)	0.51	1.33	1.52
	LOQ(μg/mL)	1.57	4.05	4.592
3	Precision			
	Intra-day (%RSD)	0.25	0.71	0.17
	Inter-day (%RSD)	0.39	0.96	0.63
4	Accuracy			
	50 % recovery	97.2	98.5	96.12
	100 % recovery	98.6	99.7	97.87
	150 % recovery	98.1	97.4	99.04

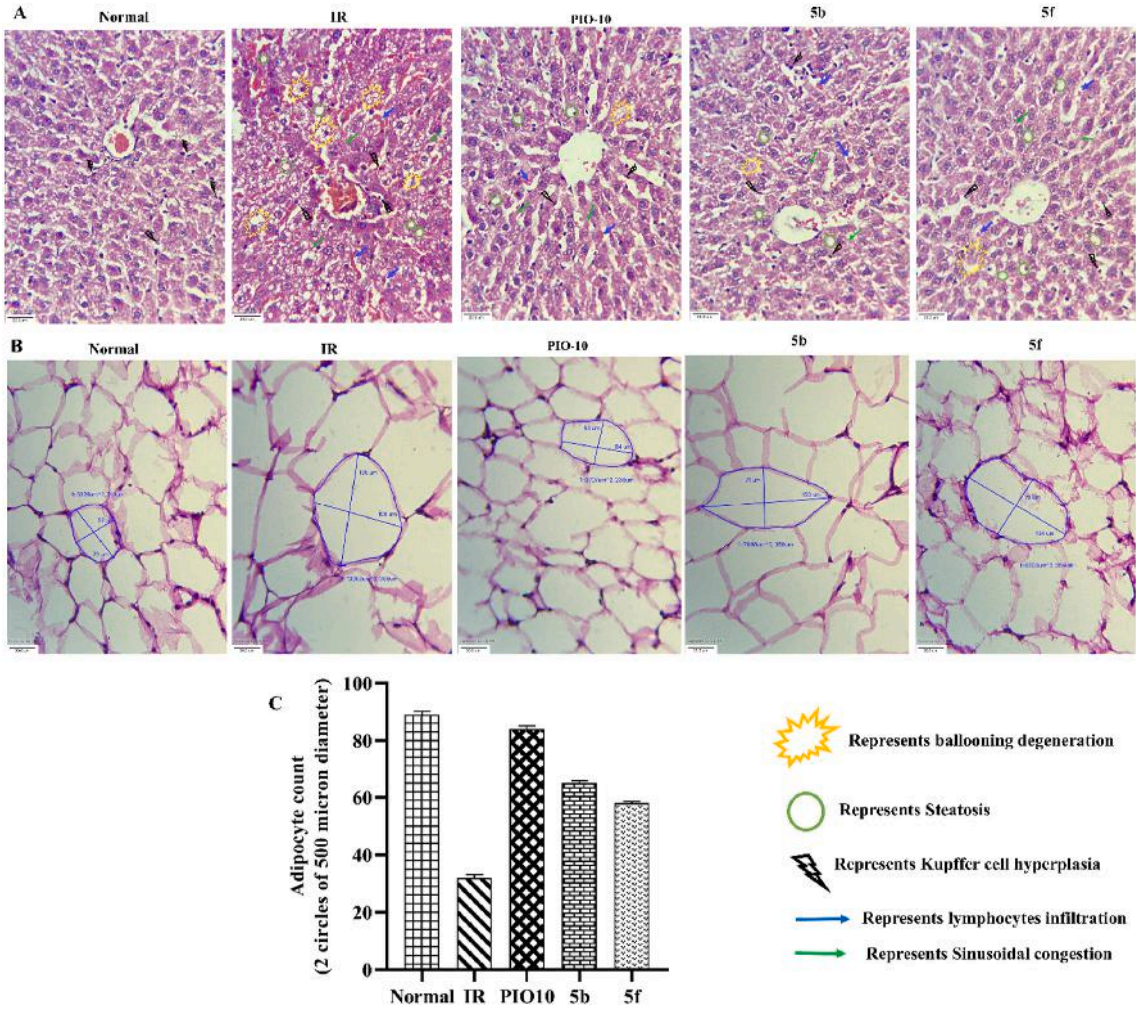


Fig. 14. Effect of compound **5b** and **5f** on; **A**) Liver tissue; **B**) Adipose tissue; **C**) Adipocyte count.

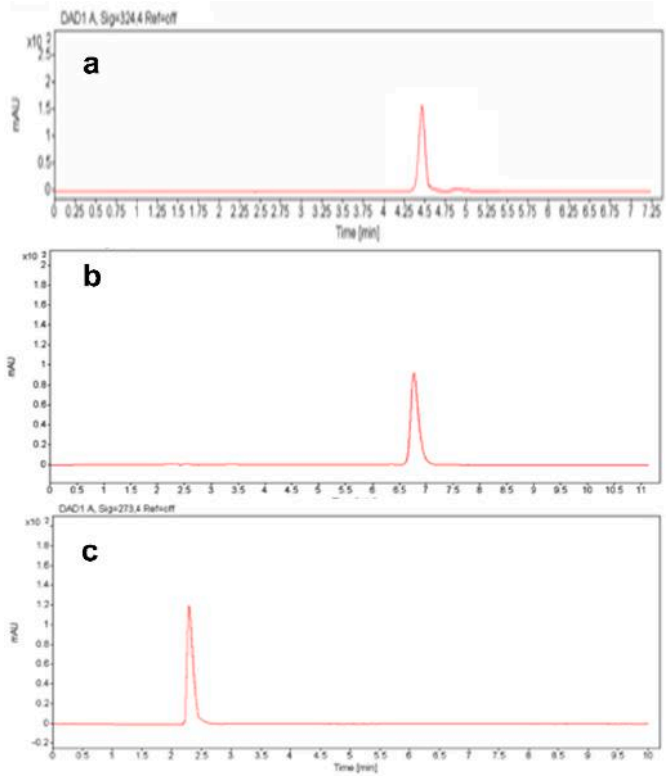


Fig. 15. Hplc chromatogram of (a) **5b**, (b) **5f**, and (c) pioglitazone.

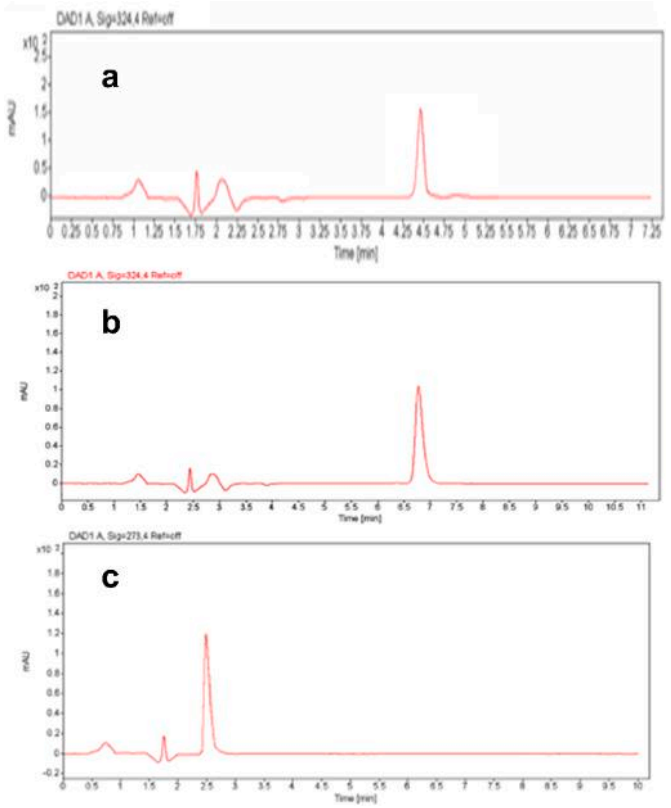


Fig. 16. Hplc chromatogram of (a) **5b**, (b) **5f**, and (c) pioglitazone.

Table 6
Recovery assay of compounds from rat plasma.

Sample	Drug	Excess drug added to analytes (%)	Spiked (μg/ml)	Found (μg/ml)	Recovery (%)
Blood plasma	**5b**	50	15	14.56 ± 0.47	97.1
		100	20	20.20 ± 0.15	101.0
		150	25	24.02 ± 0.74	96.1
	5f	50	15	14.99 ± 0.21	99.96
		100	20	19.91 ± 0.27	99.58
		150	25	24.59 ± 0.34	98.36
	PIO	50	15	14.57 ± 0.54	97.1
		100	20	19.48 ± 0.63	97.4
		150	25	24.51 ± 0.98	98.0

Table 7
Pharmacokinetic parameters of compound **5b**, **5b** and pioglitazone.

Parameters	5f	5b	PIO
C_{max} (μg/mL)	0.9261	1.0261	3.1261
T_{max} (h)	2.0	2.21	2.69
AUC 0-t (h. μg/mL)	5.62	5.98	41.52
AUC 0-inf (h. μg/mL)	6.24	6.62	43.62
K_{el}	0.361	0.387	0.21
$T_{1/2}$ (h)	3.96	4.21	4.92
AUC 0-t (h. μg/mL)	5.62	5.98	41.52

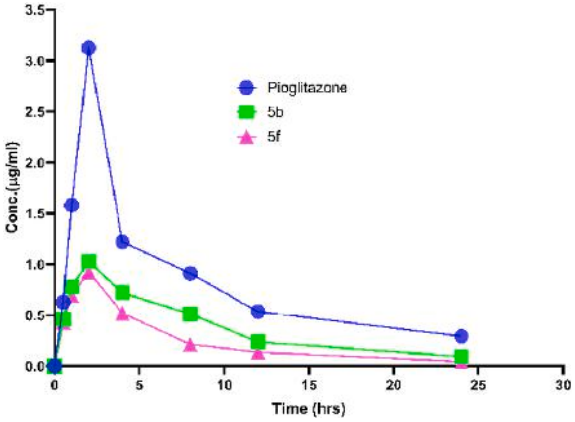


Fig. 17. Pharmacokinetic parameters describing the peak concentration height of pioglitazone, **5b** and **5f** at different time intervals indicating the release of drugs from plasma of experimental animals.

2.8. Target identification, network construction, and gene enrichment analysis

The protein targets for the compounds **5b and 5f** were predicted from DIGEP-Pred and Swiss Target Prediction databases by querying the canonical SMILES. Gene cards was used to obtain the targets associated with T2DM by querying keywords such as 'T2DM and insulin resistance'. Additionally, the targets associated with T2DM were cross referenced with the proteins known to be influenced by compounds **5b** and **5f** using Venny 2.1.0. (https://bioinfogp.cnb.csic.es/tools/venny/). The shared targets were analyzed using the STRING database (https://string-db.org/) to uncover a protein-protein interaction network and identify KEGG enriched pathways by compound **5b** and **5f,** the obtained

Table 8
Binding affinity of synthesized compounds (**5a-5j**) in PPAR-γ ligand binding domain.

	PDB ID: 5U5L		H-Bond		
Com.	Glide Score	Glide Energy (kcal/mol)	Ligand Atom interactions	Amino Acid	Bond length
5a	−6.212	−44.699	-**C=O** of ligand to TYR 473	TYR 473	2.33
			- **C=O** of ligand to SER 289	SER 289	1.86
			C=O of ligand to TYR HIE 323	HIE 323	2.59
5b	−8.591	−45.831	-**CN** of ligand to TYR 473	TYR 473	2.18
			- **CN** of ligand to HIE 449	HIE 449	2.40
			-**C=O** of ligand to CYS 285	CYS 285	2.27
5c	−6.895	−59.547	-**CN** of ligand to TYR 473	TYR 473	2.32
			-**C=O** of ligand to TYR 473	TYR 473	2.53
			-**C=O** of ligand to SER 289	SER 289	1.97
5d	−4.643	−52.32	-**C=O** of ligand to GLN 63	GLN 63	1.88
5e	−6.911	−42.595	-**CN** of ligand to TYR 473	TYR 473	2.20
			- **CN** of ligand to HIE 449	HIE 449	2.40
			-**C=O** of ligand to CYS 285	CYS 285	2.17
5f	−7.91	−45.465	-**C=O** of ligand to CYS 285	CYS 285	2.27
5g	−7.805	−45.968	-**CN** of ligand to TYR 473	TYR 473	2.12
			- **CN** of ligand to HIE 449	HIE 449	2.41
			-**C=O** of ligand to CYS 285	CYS 285	2.15
5h	−7.91	−48.031	-**CN** of ligand to TYR 473	TYR 473	2.54
			-**OCH_3** of ligand to SER 342	SER 342	2.44
5i	−6.453	51.032	-**CN** of ligand to TYR 473	TYR 473	2.42
			-**C=O** of ligand to CYS 285	CYS 285	1.97
5j	−7.316	−46.630	-**C=O** of ligand to CYS 285	CYS 285	2.18
Pioglitazone	−11.632	−58.973	-**C=O** of ligand to TYR 473	TYR 473	2.09
			-**C=O** of ligand to SER 289	SER 289	2.17
			-**C=O** of ligand to HIS 323	HIS 323	1.81

proteins, pathways, and compound **5b** and **5f** were integrated into Cytoscape *ver. 3.9.0* to construct Pathway-Protein interaction. The network analysis was conducted based on "Node degree distribution" and "Betweenness by degree," where parameters such as eccentricity, neighborhood connectivity, in-degree distribution, and out-degree distribution were examined. Gene ontology analysis was carried out using the STRING server to obtain GO terms, including Cellular Component (CC), which helps predict the part of the cell where the molecule may act; Molecular Function (MF), which forecasts the action the molecule might trigger; and Biological Process (BP), which anticipates the cellular response. The integration of these GO terms predicts the effect of the test agent at the cellular level [35,36].

3. Results

3.1. Receptor based pharmacophore modeling

Structure/receptor based pharmacophore hypothesis was generated to identify and understand the structural feature and position required for ligands to elicit biological response. A seven point hypothesis model (AHHHRRR) was generated for the target receptor PPAR-γ ligand binding domain with PDB ID: 5U5l and pioglitazone as reference ligand (Fig. 4). Further the generated library was screened and enrichment analysis (Fig. S1) was performed for the hypothesis along with decoy set of 1000 molecules. The top 10 ligands were considered for synthesis owing to the fitness score in comparison to the reference ligand (Table S1). Pioglitazone showed fitness value of 1.594 with 5 of 7 site matching and align score of 0.808, whereas compound **5b** (A12) and compound **5f** (A3) showed fitness score of 1.081 and 1.026 with 5 of 7 sites matching with align score of 1.126 and 0.085 respectively. Fig. 5 represents alignment of compound **5b** and **5f** on the generated hypothesis.

3.2. Chemistry

The synthesis of top hits (**5a-5j**) from pharmacophore screening is summarized in Scheme 1. The compounds (**2** and **3a-3j**) were synthesized as per previously reported method [37], where appropriate aryl and hetero aryl aldehydes (**1a-1j**) were condensed with thiazolidinedione with a catalytic amount of piperdine-acetate in toulene with a Knoevenagel setup to produce substituted benzylidenethiazolidine-2, 4-dione (**3a-3j**). Further equimolar ratio of intermediate (**3a-3j**) refluxed with 2-chloroacetyl) pyrrolidine-2-carbonitrile (**4**) in acetonitrile and triethylamine, to obtain the target compounds 5-substituted-benzylidene-2, 4-dioxothiazolidin-3-yl) acetyl) pyrrolidine-2-carbonitrile (**5a-5j**).

The hit compound structures (**5a-5j**) were characterized via FTIR, ^{1}H NMR, ^{13}C NMR and HRMS. Further FTIR spectra of compounds 1-(2-(5-substituted-benzylidene-2, 4-dioxothiazolidin-3-yl) acetyl) pyrrolidine-2-carbonitrile (5a-5j) showed nitrile group (CN) absorption peak at 2235.59 to 2251.02 cm^{-1}, carbonyl group (C═O) at 1731.19 to 1749.51 cm^{-1}, Fig. 6 represents proton NMR spectrum of compound (**5a**) produced characteristic relative upfield signal of the pyrrolidine ring with multiplete signal at δ 1.90–2.24 ppm corresponding to methylene protons (4H) from C1 and C2. One methylene proton at δ 3.53–3.59 ppm and 3.78 ppm is due to diastreotropic effect at C5 as per previously reported proton NMR of pyrrolidine ring [38]. Multiplete signal at δ 4.52–4.78 ppm corresponds to proton from the (CHCN) C3 coupled with 2 protons (CH_2) from C7 which was also confirmed by HSQC experiment. Characteristic multiplete signal were observed at δ 7.56–7.50 ppm for 2 aromatic protons and signals at δ 7.65–7.63 ppm for 3 aromatic protons. An indicative (CH) proton of benzylidene was observed at δ 7.97 ppm. The ^{13}C NMR of (**5a**) confirms the presence of characterstic peaks at δ 25.34 (C1), 30.00 (C2), 43.59 (C5), 46.01 (C3), 46.99 (C7) ppm corresponding to pyrrolidine ring, signal at δ 164.52 (C15), 165.69 (C16), 167.53 (C8) corresponds to the carbonyl groups. Further the formation of compound (5a) was evident by the mass spectra. Also the compound (**5b to 5j**) were assigned as per the above criteria.

3.3. Biological evaluation

3.3.1. Invitro glucose consumption assay in L6 cell lines

Skeletal muscles are known as one of the regulators of glucose homeostasis and metabolism, however most of the postprandial glucose is utilized from the circulation by the skeletal muscles, glucose transporters (GLUT's) facilitate glucose uptake by the translocation, mainly GLUT4 and GLUT1, skeletal muscles are abundant of GLUT4 proteins, mainly responsible of glucose uptake in presence of insulin and other

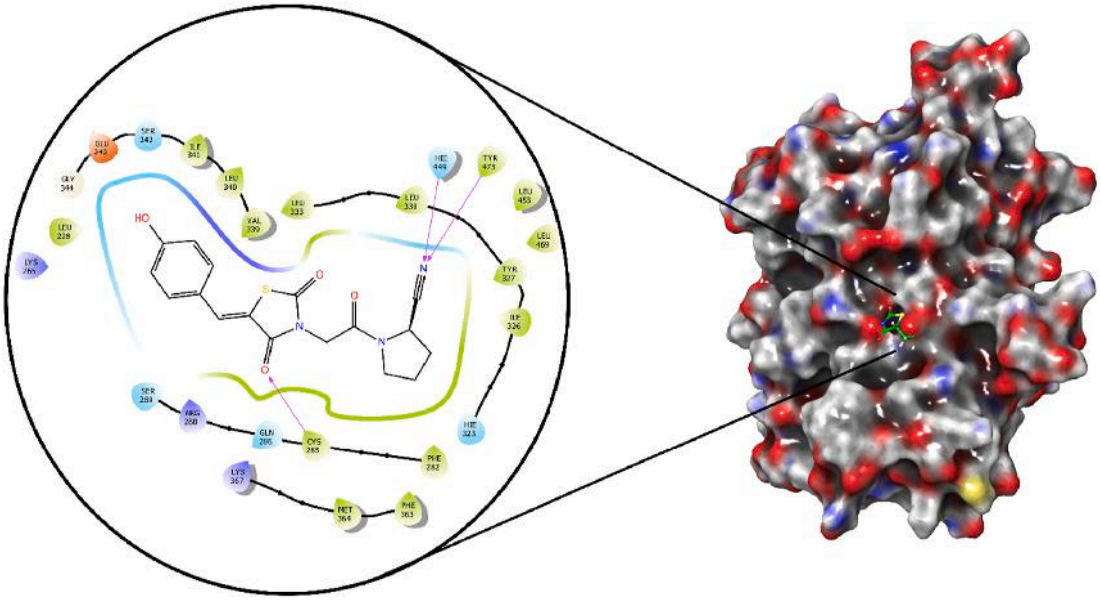


Fig. 18. Binding orientation of compound **5b** in PPAR-γ ligand binding domain.

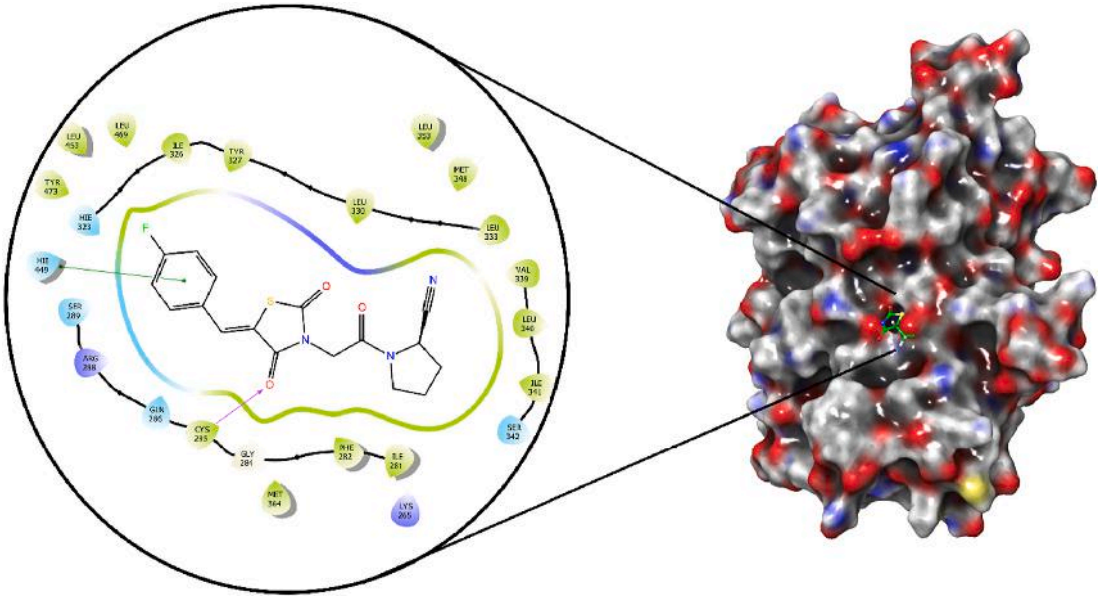


Fig. 19. Binding orientation of compound **5f** in PPAR-γ ligand binding domain.

exogenous stimuli [39]. Hence to assess the glucose uptake capacity of the synthesized compounds (**5a-5j**), glucose consumption assay was performed in L6 myotubes (rat skeletal muscles), the results demonstrated that compounds showed percentage glucose uptake in range of **57.40 ± 0.07 to 79.29 ± 1.02 %.** Among them, compound **5b**, **5c** and **5f** showed moderate to high % glucose uptake of **79.29 ± 1.02, 72.86 ± 1.03** and **74.58 ± 0.54** % respectively, as compared to standard pioglitazone (**82.36 ± 0.98 %**) as depicted in Table .1 These finding indicate the compounds have an ability to either induce translocation of GLUT4 proteins responsible for glucose uptake or have an effect of PPAR- γ transcription factor activity since these PPAR's are also expressed in the skeletal muscles.

3.3.2. Invitro PPAR-γ TF assay

A nuclear receptor, (PPAR- **γ**) is investigated to be the regulator for lipid metabolism and increasing the insulin sensitivity. This PPAR- **γ** transcription factor is known to combine with retinoid X receptor (RXR) and regulates genes associated in lipid and metabolism of glucose. The transcription factor is also been proved to have effect on leptin and TNF-α levels which contributes for the insulin sensitivity, and all these changes are brought by stimulation of PPAR-γ ligand binding domain [40], hence we assessed the agonist activity of hit compounds **5b** and **5f** with pioglitazone as control on PPAR- γ transcription factor assay. The findings suggest, there was effective increase in PPAR- γ transcription factor expression in a dose dependent manner (Fig. 7) with respect to pioglitazone (1 μM) as standard control. Compound **5b** and **5f** were measured at 6.25–50 μM concentration.

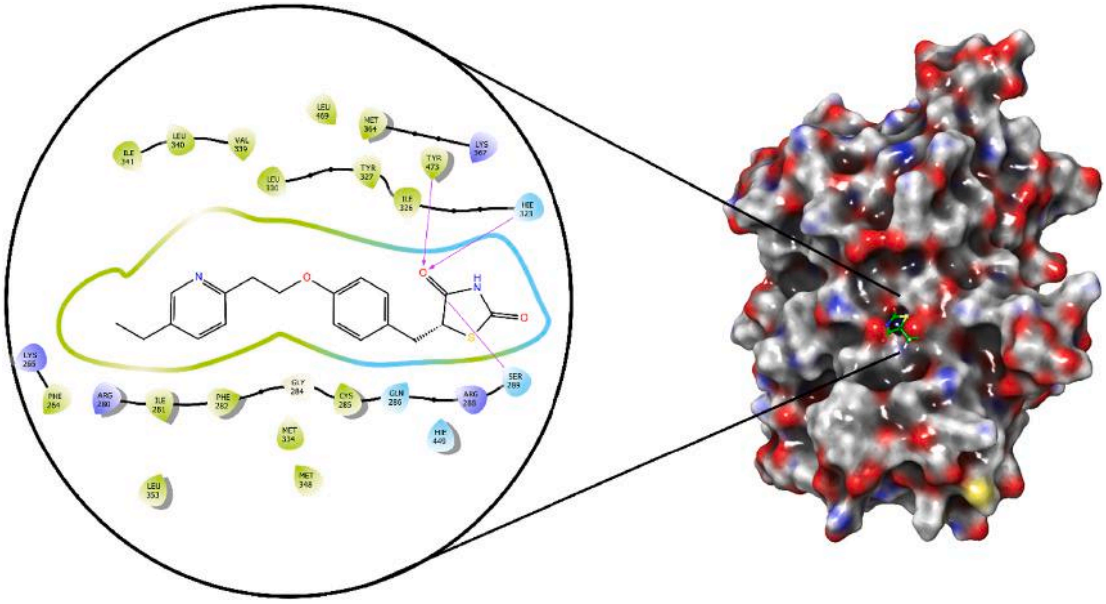


Fig. 20. Binding orientation of pioglitazone in PPAR-γ ligand binding domain.

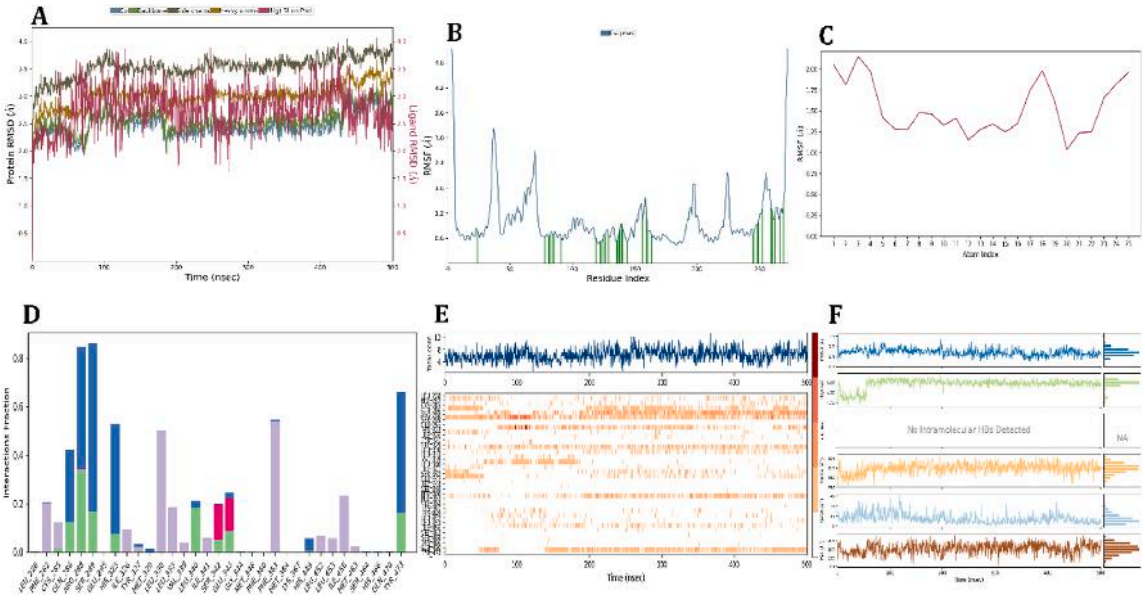


Fig. 21. Compound **5b (a)** Protein Ligand RMSD Plot, (**b**) Protein RMSF Plot, (**c**) Ligand RMSF plot, **(d)** Protein Ligand Contacts Histogram**, (e)** Protein Ligand Contacts timeline, (f) ligand properties**;** over period of 500 ns.

3.4. Experimental pharmacology

3.4.1. Effect of compound 5b and 5f on body weight, food intake and water intake

Compared to the normal group there was marked increase in body weight after induction of insulin resistance, administration of pioglitazone (10 mg/kg) for 15 days, displayed gain in body weight relative to insulin resistance (IR) group. Similarly a significant gain in body weight of compound **5b** and **5f** treated group in contrast to insulin resistance group. Similarly percentage change in body weight was seen significantly reduced in IR group ($p < 0.001$) compared to normal group. A marked increase in percentage change in body weight except for normal group was seen in treatment groups (Fig. 8).

3.4.2. Effect of compound 5b and 5f on fasting blood glucose levels (FBGL) and oral glucose tolerance test (OGTT)

After 15 days of treatment, the IR group showed a significant increase ($p < 0.001$) in FBGL compared to the normal group, while the PIO-10 group, **5b**, and **5f** treated groups showed a significant decrease ($p < 0.001$) in fasting blood glucose levels. There was no significant difference in FBGL levels between the PIO-10 group and the **5b** treated group. In OGTT, the Area under Curve (AUC) was greater in the IR group ($p < 0.001$) compared to the Normal group, whereas the PIO-10 group ($p < 0.001$) had significantly lower AUC values than the IR group. Although there was no significant difference between the **5b** and PIO-10 groups, the **5f** treated group showed a significant rise ($p < 0.01$) in AUC values compared to the **5b** group. (Fig. 9).

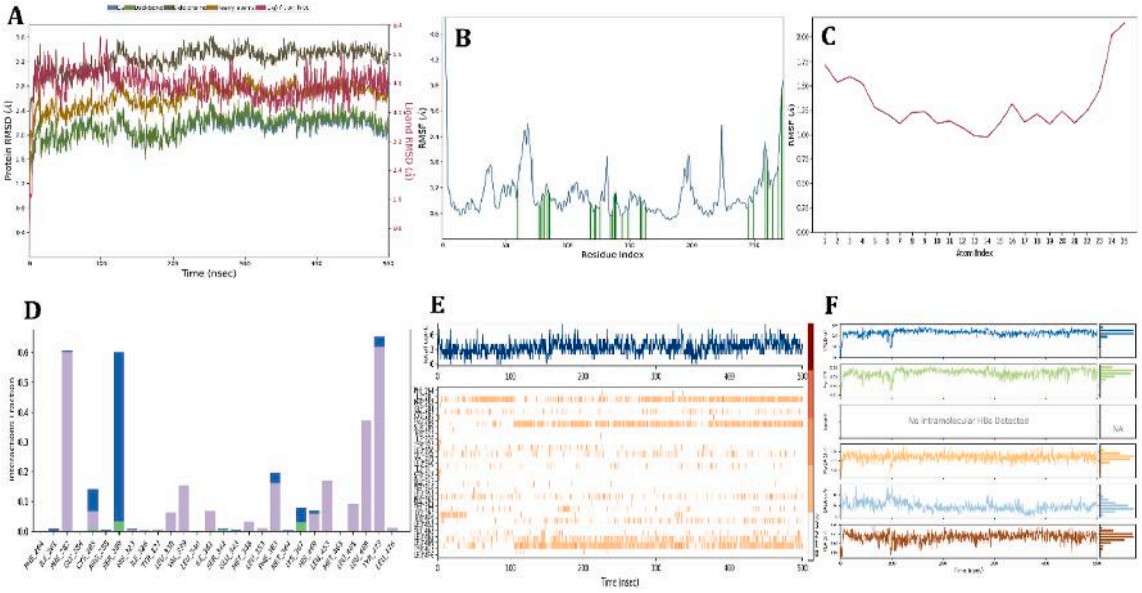


Fig. 22. Compound **5f (a)** Protein Ligand RMSD Plot, (**b**) Protein RMSF Plot, (**c**) Ligand RMSF plot, **(d)** Protein Ligand Contacts Histogram, **(e)** Protein Ligand Contacts timeline, (f) ligand properties; over period of 500 ns.

Table 9
MM/GBSA binding free energy of synthesized ligands.

MM/GBSA Binding free energy				
Sr. no	ΔGBind	ΔSbind	ΔG BindSolvGB	ΔG Bind Hbond
5a	−52.83	−21.46	24.78	−1.8
5b	−61.86	−14.68	18.32	−1.61
5c	−46.24	−19.32	47.66	−0.99
5d	−46.88	−17.42	22.24	−1.84
5e	−45.16	−23.56	20.77	−0.98
5f	−54.99	−13.11	20.33	−0.18
5g	−56.33	25.97	21.43	−1.69
5h	−55.59	−10.48	22.76	−1.66
5i	−18.03	−18.91	27.6	−1.59
5j	−55.72	−37.67	21.68	−1.12
Pioglitazone	−57.65	−12.65	17.24	−1.38

3.4.3. Effect of compound 5b and 5f on insulin levels and insulin tolerance test (ITT)

Fasting insulin levels were significantly higher ($p < 0.001$) in the IR group compared to the normal group. PIO-10 significantly reduced insulin levels ($p < 0.001$) compared to the IR group. Insulin levels decreased significantly ($p < 0.001$) in the compound **5b** and **5f** treatment groups compared to the IR group. There was no significant difference between PIO-10 and **5b** treated groups. However, there was a substantial ($p < 0.01$) difference between PIO-10 and **5f** treated groups. Additionally, compound **5b** showed a significant difference ($p < 0.05$) compared to the **5f** treated group. These findings agreed with the AUC for glucose analysis (Fig. 10).

3.4.4. Effect of compound 5b and 5f on HOMA-IR

HOMO-IR levels increased significantly ($p < 0.001$) in the IR group compared to the normal group, but decreased significantly ($p < 0.001$) in the pioglitazone-treated group. The group treated with **5f** showed a substantial increase ($p < 0.01$) compared to the PIO-10 group, but there was no significant difference between the **5b** and PIO-10 groups (Fig. 11).

3.4.5. Effect of compound 5b and 5f on glycogen content in skeletal muscles and liver

Significant decrease ($p < 0.001$) in glycogen content for skeletal muscles and liver in IR compared to normal group, which was reversed with significant increase ($p < 0.001$) in pioglitazone treatment. Similarly, treatment with **5b** and **5f** showed significant increase ($p < 0.01$ and $p < 0.05$) in glycogen content compared to IR groups. No significant change was seen between the **5b** and **5f** treated groups (Fig. 12).

3.4.6. Effect of compound 5b and 5f on glucose uptake in rat hemidiaphragm

The level of glucose uptake in the IR group decreased significantly ($p < 0.001$) compared to the normal group. The percentage glucose uptake increased significantly ($p < 0.001$) in the PIO-10**,** **5b**, and **5f** treatment groups. A significant reduction ($p < 0.05$ and $p < 0.01$) was seen in the **5b** and **5f** treated groups compared to the PIO-10 group. The **5f** group showed a significant reduction ($p < 0.001$) in glucose uptake compared to the **5b** treatment group (Fig. 13).

3.4.7. Effect of compound 5b and 5f on lipid profile

The IR group had significantly lower levels of HDL, cholesterol, and LDL ($p < 0.001$) and higher levels of triglycerides and VLDL ($p < 0.001$) than the normal group. Pioglitazone, **5b**, and **5f** significantly raised ($p < 0.001$) total cholesterol and HDL levels, whereas **5f** had no significant change in LDL levels compared to the IR group. Similarly, the PIO-10, **5b** and **5f** treated groups showed a substantial drop in triglyceride and VLDL levels (Table 2).

3.4.8. Effect of compound 5b and 5f on SGOT and SGPT levels

The IR group had significantly higher ($p < 0.001$) SGOT and SGPT levels than the normal group, but this was reversed ($p < 0.001$) in the PIO-10, **5b**, and **5f** treated groups. SGOT and SGPT levels increased significantly ($p < 0.05$, $p < 0.01$) in the **5b** and **5f** treatment groups. Similarly, there was no significant change in SGOT or SGPT levels between the **5b** and **5f** treatment groups (Table 3).

3.4.9. Effect of compound 5b and 5f on antioxidant biomarkers

Catalase, GSH, and SOD levels decreased dramatically ($p < 0.001$) in the IR group compared to the normal group, but were significantly reversed ($p < 0.001$) in the Pioglitazone treated group, as well as the **5b** and **5f** treated groups. In contrast, MDA levels increased significantly in the IR group compared to the normal group, but were reversed ($p < 0.001$) in the Pioglitazone and compound **5b** and **5c** treated groups (Table 4).

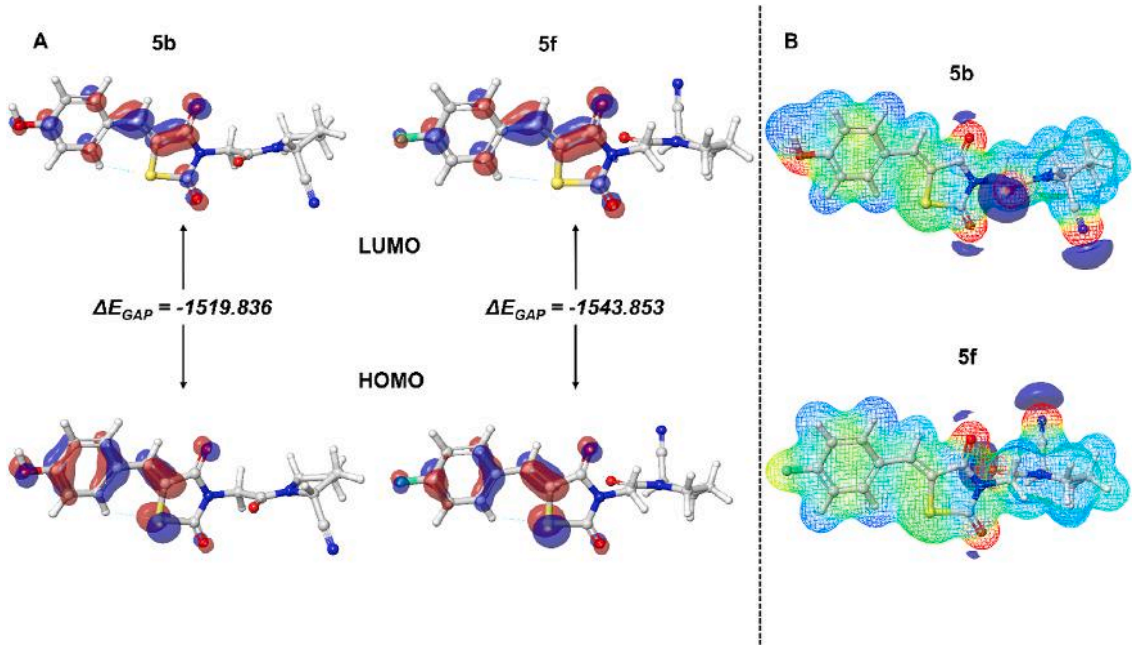


Fig. 23. Representation of compound **5b** and **5f,** (A) HOMO and LUMO orbitals, (B) MEP map.

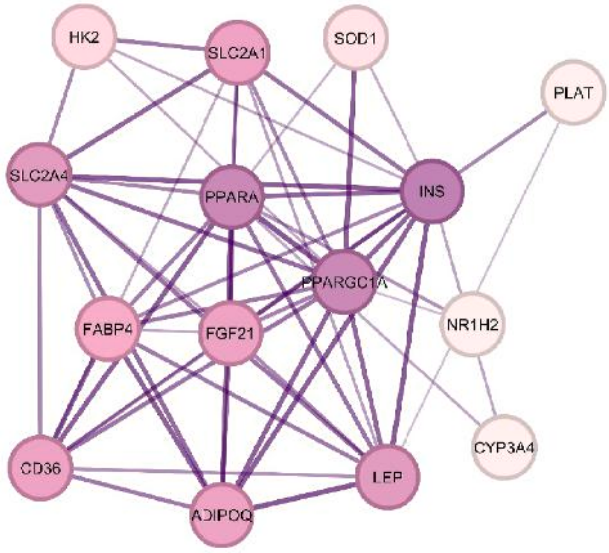


Fig. 24. Protein-protein interaction identified for compound **5b** and **5f** via string.

3.4.10. Histopathology study

Histopathological analysis of adipose and liver tissue, confirmed the resistance due to insulin and reversal of insulin resistance by compound **5b** and **5f** by analysing pathological parameters like, sinusoidal congestion, ballooning degeneration, steatosis, kupffer cell hyperplasia, and lymphocyte infiltration. The IR group shows macrovesicular steatosis characterised by fat vacuoles within the hepatocytes, with nucleus towards cell periphery, likewise ballooning degeneration indicates cell injury, inflammatory response by lymphocyte infiltration was seen, sinusoidal congestion indicating increased pressure within vascular parenchyma, all these factors indicate underlying cause as insulin resistance, which was reversed in the treatment groups (Fig. 14). Similarly histology of adipocyte showed decreased count of adipocytes in IR group contrast to normal group, and was reversed in all the treatment groups as shown in Fig. 14

3.4.11. Bio analytical method development

The retention times (RT) of compound **5b**, **5f**, and pioglitazone were determined using HPLC via a C-18 column. The methodology employed was rigorously validated according to guidelines provided by the USFDA for bioanalytical method development and its validation, ensuring parameters of linearity, sensitivity, precision, and accuracy, all validation parameter mentioned in Table 5. The retention time of compound **5f** was observed at 6.7 min, **5b** at 4.4 min, and the standard pioglitazone at 2.4 min, as depicted in Fig. 15. Further this approach was effectively employed to identify **5b**, **5f**, and Pioglitazone in rat plasma, with six replicate measurements conducted. Results outlined in Table 6 exhibit outstanding recoveries spanning from 96.1 % to 98.6 %. Quantitative estimation revealed distinct peaks for **5b**, **5f**, and Pioglitazone in rat plasma emphasizing the method's exceptional sensitivity, accuracy, and precision. This reaffirms the reliability of the obtained results, vividly depicted in Fig. 16.

3.4.12. In vivo pharmacokinetic parameters determination

The concentrations of pioglitazone, **5b** and **5f** in rat plasma at various time intervals were estimated using an HPLC method. The retention times (RT) obtained from the bioanalytical method were consistent with those of plasma eluents, confirming the existence of the compounds. Kinetic profiling were developed using Phoenix WinNonlin 8.1 software and Agilent Infinity II to identify the plasma level for the three compounds. Pioglitazone demonstrated rapid absorption, achieving a plasma peak (mean) concentration of 3.12 μg/mL at 2.69 h. In comparison, **5f** reached a peak of 0.9261 μg/mL at 2 h, and **5b** reached 1.0261 μg/mL at 2.21 h. The elimination half-lives for **5f**, **5b**, and pioglitazone were identified as 3.96, 4.21, and 4.92 h, respectively. Pioglitazone showed plasma concentration-time curve (AUC) significantly greater than **5f** and **5b**. Despite these differences, when accounting comparable distribution volumes and variations rate constants for elimination, the data obtained from the plasma analysis displayed that the 5b and 5f were similarly absorbed. 0.361 μg/mL for **5f**, 0.387 μg/mL for **5b**, and 0.21 μg/mL for pioglitazone was identified as rate of removal from the body. Further the relative bioavailability was estimated for **5b** and **5f** in comparison to standard pioglitazone using the following formula

Table 10
Enrichment analysis of protein regulated by compound **5b** and **5f** by KEGG pathway database.

KEGG ID	Pathway Description	Observed gene/background gene count	Strength	False discovery rate	Genes
hsa04920	Adipocytokine signaling pathway	8/68	2.13	1.83E-11	PPARGC1A, LEP, SLC2A4, PPARA, ADIPOQ, CD36, SLC2A1, NR1C3
hsa04931	Insulin resistance	7/106	1.94	1.75E-10	PPARGC1A, SLC2A4, INS, PPARA, CD36, SLC2A1, NR1H2, NR1C3
hsa04152	AMPK signaling pathway	6/120	1.82	3.23E-08	PPARGC1A, LEP, SLC2A4, INS, ADIPOQ, CD36
hsa03320	PPAR signaling pathway	5/75	1.94	2.37E-07	FABP4, PPARD, PPARA, ADIPOQ, CD36
hsa04932	Non-alcoholic fatty liver disease	4/146	1.56	0.00028	LEP, INS, PPARA, ADIPOQ
hsa04930	Type II diabetes mellitus	3/45	1.94	0.00034	SLC2A4, INS, ADIPOQ
hsa04211	Longevity regulating pathway	3/87	1.66	0.0019	PPARGC1A, INS, ADIPOQ
hsa04922	Glucagon signaling pathway	3/100	1.6	0.0025	PPARGC1A, PPARA, SLC2A1
hsa04910	Insulin signaling pathway	3/132	1.47	0.005	PPARGC1A, SLC2A4, INS
hsa04923	Regulation of lipolysis in adipocytes	2/54	1.69	0.0273	FABP4, INS
hsa04213	Longevity regulating pathway - multiple species	2/61	1.63	0.0314	SOD1, INS

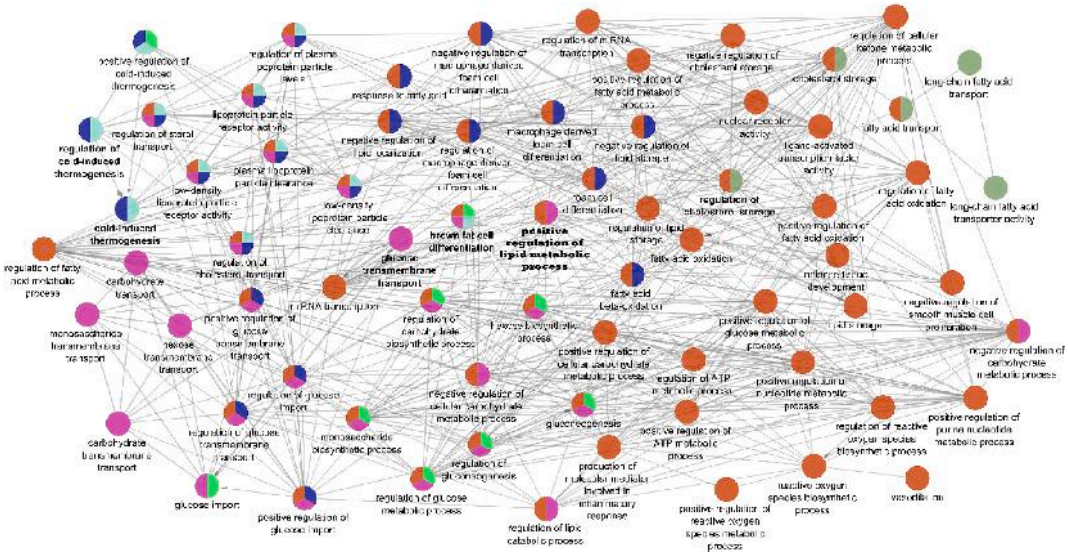


Fig. 25. Significantly enriched Gene ontology 'biological processes' by compound **5b** and **5f**.

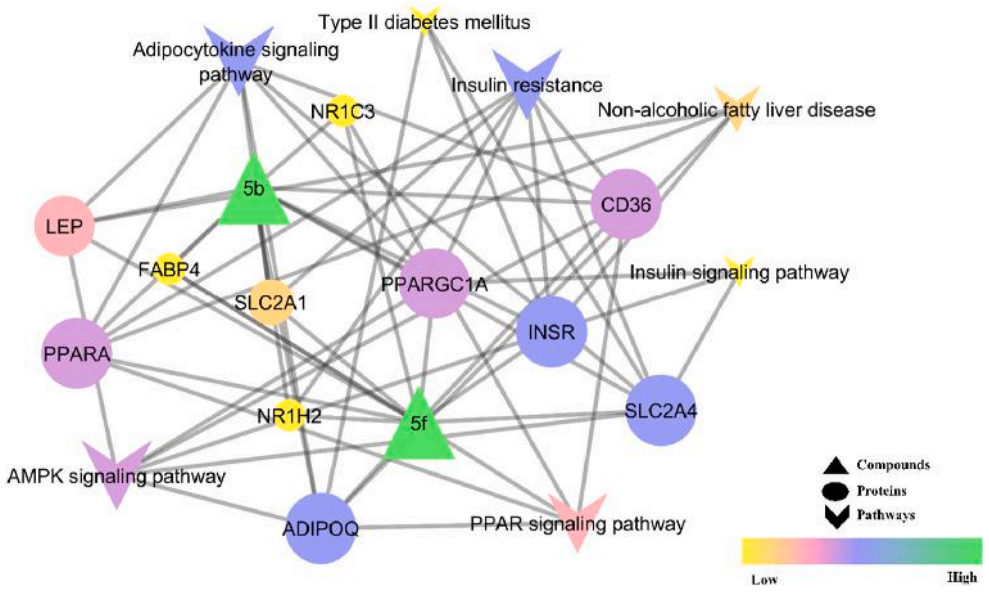


Fig. 26. Interaction of compounds **5b** and **5f** with proteins involved in T2DM and respective pathways.

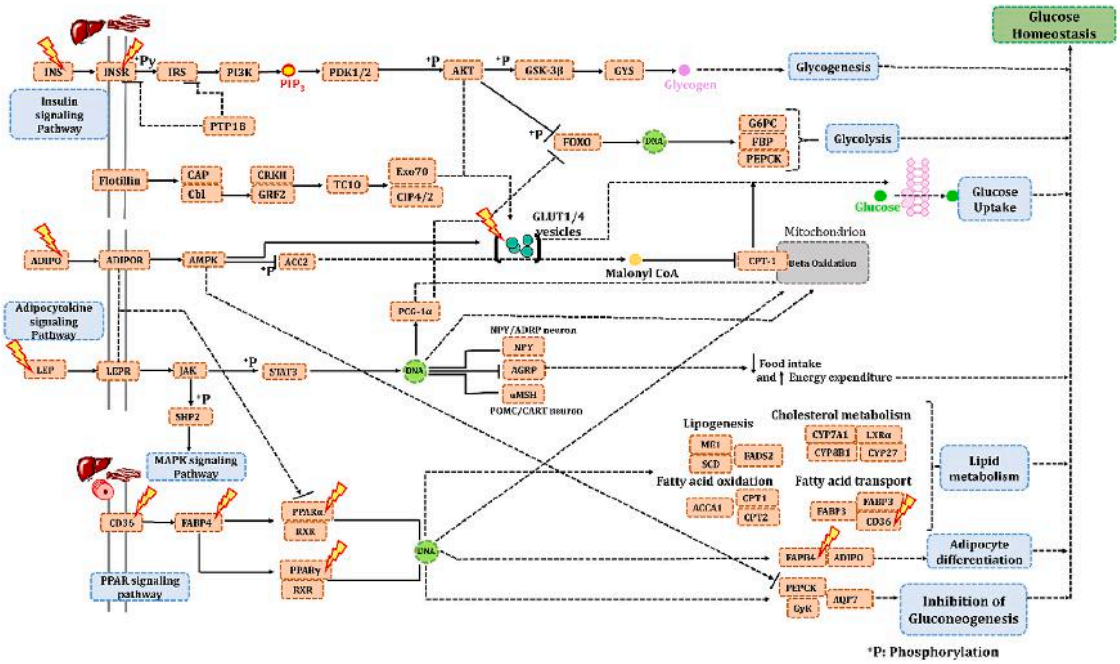


Fig. 27. Proposed possible molecular mechanism of compound **5b** and **5f**, via PPAR signaling pathway, Adipocytokine signaling pathway, and insulin signaling pathway, highlighting triggered proteins.

$$\text{Frel} = \frac{AUC\ Test}{AUC\ Reference} \times 100$$

Where compound 5b and 5f showed relative bioavailability of 13.73 % and 13.54 % respectively.

Where, AUC test is the AUC of the test compounds (**5b** and **5f**) and AUC reference is the AUC of the standard (PIO)

The full kinetic profile is detailed in Table 7 and Fig. 17.

3.5. Molecular docking studies

The docking analysis predicted the binding affinity and orientation of ligands (**5a-5j**) in the PPAR-γ receptor binding pocket. The ligands were scored as per the energetics with inclusion of penalties for the ligands in binding domain (Table 8), which revealed compounds **5b** and **5f** scored better among the series with glide interaction energy of (−45.831 kcal/mol), (−45.465 kcal/mol) respectively, compared to standard pioglitazone (−58.973 kcal/mol). The binding pose of the compound **5b** (Fig. 18), **5f** (Fig. 19) and pioglitazone (Fig. 20) showed intact binding surrounded by hydrophobic and some part of polar contact with no solvent exposure to the ligands in binding domain of PPAR-γ receptor. The amino acids contributing to elicit a biological response were identified in ligand binding domain as CYS 285, SER 289, HIS 323, SER 342, HIE 449, and TYR 473 constituting the hydrogen bonds. This information provides activeness of the ligands to stimulate the PPAR- γ receptor for its agonist activity.

Similarly, the binding affinity of compounds **5b** and **5f** sowed better binding in the SGLT2 binding domain with energy contributions of (−48.789 kcal/mol) and (−49.914 kcal/mol) respectively, compared to standard SGLT2 inhibitor canagliflozin (−45.183 kcal/mol). Canagliflozin showed a network of hydrogen bond interactions with PHE 98, LYS 321, TRP 291, SER 287, and GLN 457 (Fig. S2), likewise compound **5f** demonstrated hydrogen bond interaction with ASN 75, HIE 80, and GLN 457 (Fig. S3), whereas compound **5b** displayed interactions with ASN 57 and GLN 457 (Fig. S4). Thus these results indicate, that the compound **5b** and **5f** is triggering the only amino acid residue GLN 457, which is in common with the interactions of standard canagliflozin.

3.6. Molecular dynamic simulations

The potential hit compounds **5b** and **5f** were considered for an MD simulation run over a period of 500 ns in PPAR-γ ligand binding domain using Desmond software. The MD run focused on the stability assessment of the complex between protein and ligands, and their interactions during the simulation period. The simulation interaction analysis was performed for the MD trajectory of both complexes considering the parameters and statistical relevance such as hydrogen bond contacts, hydrophobic contacts, Root mean square deviation (RMSD), root mean square fluctuations (RMSF) for the protein Cα, protein backbone and ligand complex. Reference structure for the simulation was considered as the initial start point of simulation, RMSD enables to evaluate the extent of stability and dynamic changes within the protein ligand complex. Similarly the individual amino acid residues play important role to understand the conformational changes with respect to the protein structure which is evaluated by the measure of fluctuation of these residues also known as RMSF *i.e*, 0 ns (Frame 0). Description on the PPAR-γ – **5b** and PPAR-γ – **5f** is described below, PPAR-γ – **5b** complex: The Protein-Ligand RMSD Plot of the complex revealed a stable protein structure with C-alpha RMSD and Backbone RMSD having maximum deviations of 2.769 Å and 3.029 Å (Frame 872, 873), respectively. The ligand RMSD aligned on ligand and ligand RMSD aligned on protein exhibited ligand RMSD having maximum deviation of 0.636 Å and 3.153 Å (Frame 941), respectively, suggesting high stability of protein ligand complex over 500 MD run. The RMSF analysis displays the change in each residue with respect to its reference position, as well as ligand interactions with residues shown by green colour bars in the protein RMSF plot. The highest variation was seen with ligand contact with residue GLN 470 in frame 1.151 Å, whereas all other ligand residue contact fluctuations were less than 1.00 Å, indicating stable interactions. Ligand RMSF represents the change in ligand atom mobility during the course of a simulation. Ligand RMSF aligned on protein and ligand revealed highest variation of 2.154 Å and 1.127 Å corresponding to the Carbon atom of aromatic ring, showing stable Ligand inside the binding pocket. A protein-ligand contact map was examined, revealing nine hydrogen bond interactions with residues such as CYS 285, GLN 286, ARG 288, SER 289, HIS 323, LEU 340, SER 342, GLU 343 and TYR 473

over a 500 ns period. Constant hydrophobic interactions of the ligand in the binding pocket were observed. (Fig. 21).

PPAR-γ – **5f** complex**:** The protein-ligand RMSD plot revealed a maximum deviation of 2.345 Å and 2.533 Å (frames 530 & 507) for protein structure RMSD and ligand RMSD with respect to ligand aligned on protein and ligand aligned on ligand, respectively (Frame 39). The ligand RMSF plot revealed a substantial variation of chlorine atoms, with RMSF values of 2.14 Å and 1.23 Å aligned on protein and ligand, respectively. The highest variation in protein RMSF was detected with ligand contact with residue LEU 476 with 3.506 Å, whereas the remainder of the ligand residue contact fluctuations were less than 1.00 Å, indicating stable interactions. The protein-ligand contact plot of (**5f**) revealed hydrogen bond interactions with CYS 285, SER 289, and LYS 367, whereas hydrophobic connections were identified with PHE 282, TYR 327, VAL 339, ILE 341, MET 348, LEU 353, PHE 363, HIS 449, LEU 453, LEU 469, TYR 473, and LEY 476, as shown in (Fig. 22).

MM/GBSA: The determination of binding free energy, entropy and energetics of all the ligand (**5a-5j**) –protein complex were subjected to MM/GBSA calculations. This is an important parameter which highlights the ability of ligand toward the receptor binding domain. The entropy values are obtained based on the transitional-rotational-vibrational entropies, given by the quasi-harmonic estimations which consider oscillatory harmonic as for the molecular vibrations. Here the binding free energy (ΔGbind) is composed of three main parameter, namely, the solvation free energy (ΔGsolv), gas phase interaction energy (ΔGgas) and the contribution of entropy (ΔSbind) as shown in following equation,

$$\Delta Gbind = \Delta Ggas + \Delta Gsolv - T\Delta Sbind,$$

where T denotes temperature.

The ΔGbind values indicate the extent of ligands ability for binding and ΔSbind value indicates reduction in degree of freedom and generation of possible conformations inside the binding pocket. The MM/GBSA calculations for synthesized molecules are summarized in Table 9.

3.7. Geometric optimization by DFT calculations

To further understand the stability, reactivity, and kinetics of the hit molecules 5a and 5f, the molecular geometry was optimized and ligand electronic properties were calculated. The molecular descriptors HOMO, LUMO, and the energy gap between HOMO and LUMO were computed to determine the molecular reactivity of compounds **5b** and **5f**. The ability of molecule to donate electron is indicative of HOMO energy and electron accepting ability is denoted by the LUMO energy, the energy difference between the HOMO and LUMO reactivity, which if lower, suggests higher reactivity and contact with biological targets. The FMO's of the compound **5b** and **5f** are shown in Fig. 23. Table S2 shows the energy gap (ΔEGAP), dipole moment (μ), hardness (η), and local softness (σ). Compound **5b** tends to possess the gas phase energy −1519.836 eV compared to **5f** with energy of −1543.853 eV. Molecular electrostatic potentials (MEP) were computed using the B3LYP approach and a basis set of 6-31G (d, p**) at the optimized geometry; it describes the distribution of electric charges on the molecule, which in turn sheds light on the high electron density (negative potential) and low electron density (positive potential); it helps to anticipate the electrophilic and nucleophilic sites on the molecule, The molecular Electrostatic potential of compound **5b** and **5f** is shown in Fig. 23.

3.8. ADMET profile

ADMET was anticipated using the Schrodinger's Qikprop program, which included hydrogen bond donors, hydrogen bond acceptors, hydrophilicity, molecular weight, permeability, binding to human serum albumin, and human oral absorption. Violations of Lipinski's rule of five and Jorgensen's rule of three were anticipated and compared to suggested values since they are descriptors for oral bioavailability. (Table S3). Compound **5b** and **5f** has Hydrogen bond donor value of one each respectively, which is within the acceptable range, Hydrogen bond acceptor value of 8.5 for **5b** and 7.5 for the compound **5f,** log P value of 0.61 and 1.26 for compound **5b** and **5f** respectively, owing to its better partition coefficient in the biological system. Aqueous solubility (**QPlogS**) scores were poor and lying outside the acceptable range of (−6.5 to 0.5) for all the synthesized molecules. Similarly permeability prediction using madin-darby canine kidney permeability assay (MDCK) showed better permeability for all the synthesized compounds (**5a-5j**) in the range of (36.29–39.728). All the molecules showed better Caco-2 permeability and acceptable for development of oral dosage form. Additionally these molecules were predicted to possess 100 % human oral absorption. Finally, ADME predications using QikProp suggested that synthesized compounds have promising pharmacokinetic profile.

3.9. Network pharmacology and gene ontology analysis

Targets identified for compound **5b** and **5f**, were subjected for protein –protein interaction using string analysis, which identified 15 nodes with 63 edge count having clustering coefficient of 0.893 as shown in Fig. 24. Furthermore gene set enrichment analysis identified 11 pathways involved in pathogenesis of T2DM that are being modulated by the predicted protein identified for the compound **5b** and **5f**. Among them, The majority of the proteins were found to influence the "Adipocytokine signaling pathway." like *PPARGC1A, LEP, SLC2A4, PPARA, ADIPOQ, CD36, SLC2A1* and *NR1C3* with strength of 2.13 and false discovery rate of 1.83E-11, followed by 'insulin resistance' with modulated protein like *PPARGC1A, SLC2A4, INS, PPARA, CD36, SLC2A1, NR1H2,* and *NR1C3* having strength of 1.94 and false discovery rate of 1.75E-10. All the details of the enriched pathways is summarized in Table .10. Gene set ontology analysis predicted 284 biological processes being significantly enriched among them, 'Positive regulation of lipid metabolic processes' scored (4.99e-08) lowest false discovery rate modulating 7 genes with 155 genes at background having strength of 1.77. Likewise 'Glucose metabolic process' was scored (1.86e-07) with low false discovery rate modulating 6 genes with 116 genes ast background with strength of 1.83 (Fig. 25). Likewise 5 molecular functions were significantly enriched. Among them, 'Nuclear receptor activity' scored (0.0135) false discovery rate by modulating of 3 genes with 53 genes at background with strength of 1.87. Moreover, cellular components identified single enriched component as 'Extracellular space' scored (0.0410) a false discovery rate by modulating 10 genes with 3247 genes at background with strength of 0.61. The constructed network represents 20 nodes, which comprise of 7 pathways, 11 targets and 2 compounds. Compound **5b** and **5f** showed high degree of interaction with *INSR, ADIPOQ, SLC2A4*, and *SLC2A1* which are modeled to pathways like insulin resistance, Adipocytokine signaling pathway and PPAR signaling pathway as shown in Fig. 26.

4. Discussion

In the present study, we designed compounds (**5a-5j**) by hybridization of thiazolidinedione (motif from pioglitazone) with acetyl pyrrolidine (motif from vildagliptin). Further these ligands were enumerated by R-group to generate a library. Simultaneous a seven point pharmacophoric hypothesis at the PPAR-γ ligand binding domain was generated. The ligand library was screened for the hit identification on generated pharmacophore model. The screening was validated by means of 1000 molecules as decoy set. The screened ligands were analyzed by enrichment analysis. The top 10 ligands were consider for the synthesis and spectral characterization. Furthermore the effect of compounds (**5a-5j**) was assessed for their ability on translocation of GLUT carriers by *Invitro* glucose consumption capacity in skeletal muscle cell lines of rats (L6 myotubes). Results from the assay demonstrated that the compound **5b** and **5f** enhanced the uptake of glucose in L6 cell lines among the series. Also these compound exhibit good fitness score

from pharmacophore analysis results in comparison to other compounds from the series. Thus the two hit molecules **5b** and **5f** were further evaluated by their ability to agonize PPAR-γ transcription factor in comparison to standard pioglitazone, which indicated a dose dependent increase in activity of transcription factor by **5b** and **5f.**

Fructose-induced insulin resistance is a well-established animal model for evaluating the insulin sensitization capabilities of a test insulin sensitizer. As per the previously published reports, long term supplementation of fructose leads to insulin resistance/hyperinsulinemia in wistar rats [18,20,41,42]. As per the previous published report weight gain is negatively associated with fructose induced insulin resistance rats [18,20,43,44]. In the current study, a decrease in body weight by fructose supplementation was observed this might be due to inadequate appetite as a result of fructose supplementation. The major marker to assess the insulin resistance is surged insulin levels along with mild hyperglycemia and greater HOMA IR index. It is also reported that there is increased synthesis of glycogen and reduction of gluconeogenesis. Also altered glycolysis and glycogenesis followed by increased outflow of the hepatic glucose are indicators of insulin resistance. In present study, OGTT confirmed the hyperglycemia associated with increased AUC for glucose, further more ITT confirmed the elevated insulin levels which was associated with increased HOMA-IR values, indicating insulin resistance, which was ameliorated after the treatment of compound **5b** and **5f** for period of 15 days indicating decreased AUC for glucose and HOMO-IR index. A reversal in weight gain, food intake and water intake was observed in **5b** and **5f** treated groups in contrast to IR group, which might be due to the effect of adiponectin and leptin. Balsan GA. et al.,have reported the correlation between adiponectin, obesity and insulin resistance, where levels of adiponectin are positively associated with insulin sensitivity, BMI, body weight, and appetite [45].

Further estimation of glycogen content is an important parameter to assess the utilization of glucose by the surge of glycogenesis, where glucose is stored in form of glycogen in liver and skeletal muscles, as the disrupted glucose consumption and catabolism are determinants in insulin resistance and T2DM [46,47]. In present study, two attempts were made to understand the glucose consumption. One is glycogen content analysis and other is the ex-vivo glucose consumption assay. Supplementation of fructose led to compromised glucose utilization indicating decreased glycogen content in IR group and there was impaired glucose absorption by rat hemidiaphragm from the incubation media, these effects were reversed in **5b** and **5f** treated groups by surge in glycogen content and glucose consumption by rat hemidiaphragm in contrast to IR group, indicating the ability of compounds **5b** and **5f** to insulin sensitizing effect and enhance the glucose consumption.

Reports have shown that there exist a relationship between lipid profile and insulin resistance [48], where the increased triglyceride levels serve as indicators for the progressive insulin resistance, which was in accordance with significant increase in the HOMO-IR index and AUC for glucose as indicative in pathogenesis of insulin resistance [49]. Similarly increase in triglycerides level and LDL levels, while decrease in HDL is characteristic indicator of dyslipidemia progressive to insulin resistance [50]. In present study, the triglycerides, VLDL levels were increased, and decline in HDL was seen in IR group compared to normal group, which was reversed with **5b a**nd **5f** treated groups. Indicating the ability of compounds to reverse the insulin resistance and ability to improve the response to an administered glucose load. As per the published reports oxidative stress is known to have association with insulin resistance. Abrupt regulation of oxidative stress biomarkers levels where reported in previous studies [51], similarly these changes were reversed by **5b** and **5f** treated groups in contrast to IR group. Further the pharmacokinetic profile of compound **5b** and **5f** were analyzed by estimation of these compounds in plasma by HPLC analysis. Compound **5b** attend better plasma concentration (C_{max}) compared to **5f,** similarly the half-life (T_{max}) and rate of clearance was found to better for **5b** in contrast to **5f.**

The sinusoidal congestion due to necrosis, inflammation, and hepatocyte apoptosis is indicative factor for hepatic insulin resistance, insulin resistance leads to free fatty acids efflux in liver, leading to increased hepatocyte and steatosis, which in return compress the sinusoids by reducing the lumen size. Inflammatory cells like cytokines cause endothelial dysfunction leading to vascular congestion, likewise increased hepatic resistance leads to elevated portal pressure contributing to sinusoidal congestion. Ballooning degeneration an indicator of cell injury is indicator of insulin resistance due to lipotoxicity arising from metabolic stress causing mitochondrial dysfunction, condensation cytoplasm and swelling of cell. Kupffer cell hyperplasia is seen as result of metabolic stress associated with insulin resistance [52–54]. In present study, all these changes were reversed in the treatment group, indicating the effect of compound **5b** and **5f** in amelioration of hepatic insulin resistance.

Emerging progress in computation chemistry, pharmacology bioinformatics, and systems biology in drug discovery has attracted interest as a multitarget strategy to cost-effective medication development., which enables us to identify and analyze the complex biological interaction systems in a simplified manner, In the present study, the geometries of **5b** and **5f** were optimized by quantum chemical calculations with DFT theory, and the energetic with respect to molecular reactivity, hardness, softness and their charge distribution over the surface was analyzed, compound **5b** showed better molecular reactivity for biological interactions compared to **5f**, this was further assessed the binding affinity and energy requirement for the hit compound **5b** and **5f,** where **5b** compound predominantly shared hydrogen bond network with the key amino acid residues, owing to its better binding and positioning in the PPAR-γ binding pocket which is a well know target for the glitazones. Contrary to this compound **5f** lacked the hydrogen bond network owing to its positioning inside the pocket being different from **5b** and pioglitazone**,** which was evident by the finding of PPAR- γ TF assay. The overall dynamic behaviour and stability of the complex was determined by molecular simulation with indicators like RMSD and RMSF, showed lesser deviation and fluctuation for the **5b-PPAR- γ** complex owing to its better hydrogen bond, hydrophobic contact, even the fluctuating amino acid residues contributing in hydrogen bond had less than 1 Å fluctuations as compared to **5f** compound, both the compounds where in acceptance to the ADMET profile and in accordance with Lipinski rule of five making them orally bioavailable. Moreover we decoded the biological targets involved in pathogenesis of T2DM being associated with the hits **5b** and **5f**, which identified the proteins, pathways, their probable effect. The upregulated and downregulated targets associated with the hit compounds were mapped with the proteins associated in T2DM, and enrichment calculation was performed utilizing database like string and KEGG, which identified 11 major pathways modulated by compound **5b** and **5f. "**Adipocytokine pathway" was highly modulated, which include proteins like leptin and adiponectin which play important role in glucose homeostasis, thus balancing appetite and energy requirement, gluconeogenesis, glycogenesis, and translocation of GLUT receptors, which are relatively associated in insulin resistance and T2DM. These adiponectin levels help in insulin sensitization and anti-inflammatory effect. In our study, compound **5b** and **5f** displayed upregulation of *ADIPOQ* gene known for the expression of adiponectin, which might be one of the reason for insulin sensitivity, decreased AUC of glucose leading to glycemic control, decrease in insulin levels in **5b** and **5f** treated groups. The *NR1C3* gene encodes for the PPAR-γ protein was modulated via PPAR signaling pathway was upregulated by the hits **5b** and **5f**, which enhances the adipogenesis, lipid metabolism, maintains glucose homeostasis, and enhance the genes expression involved in insulin signaling pathway like GLUT carriers, this supports the findings in our study, where compound **5b** and **5f** treated groups, showed better glucose uptake, and lipid metabolism leading to control in glycemic level maintaining glucose homeostasis as compared to IR group. Proteins like SLC2A4 (GLUT4) was modulated by compound **5b** and **5f,** which is responsible for glucose uptake and maintain glucose homeostasis. The results from integrated *insilico*, *Invitro* and *invivo*, we propose

a possible molecular mechanism (Fig. 27) that highlights the treatment with compound **5b** and **5f** reversed the insulin resistance and maintained glucose homeostasis by inhibiting gluconeogenesis, enhancing the PPAR-γ expression, and glucose utilization, and stimulating glycogenesis via pathways like Adipocytokine pathway, PPAR signaling pathway, AMPK signaling pathway, insulin signaling pathway.

5. Conclusion

In present study, integrated (*insilico, Invitro* and *invivo*) approach was employed to evaluate the insulin reversal and glucose homeostasis effect of synthesized acetyl pyrrlodine-2-carbonitrile based substituted benzylidenethiazolidine-2, 4-dione hybrids (**5a-5j**). These molecules were identified based on structure based pharmacophore screening, followed by synthesis and characterization by spectral analysis of top ten hits. These hits were screened for their *invitro* glucose uptake capacity in L6 myotubes cell lines, which demonstrated compound **5b** and **5f** showing 79.29 ± 1.02 % and 74.58 ± 0.54 % respectively compared to pioglitazone (82.36 ± 0.98). moreover these molecules were assessed for their *invitro* PPAR-γ TF assay, showing dose dependent increase in transactivation of PPAR- γ, followed by assessment in ameliorating glucose homeostasis and reversal of insulin resistance in fructose induced hyperinsulinemic wistar rats. The efficacy of compound **5b** and **5f** to ameliorate reversing insulin resistance was confirmed by the OGTT and ITT, likewise glucose homeostasis was confirmed by the lipid metabolism via PPAR- γ agonism. Glucose consumption was confirmed by glycogen content and glucose uptake. Moreover antioxidant biomarkers were estimated. *Insilico* prediction like DFT theory provided the optimized geometries with proper charge distribution for the hit molecules, followed by molecular docking and MD simulation studies suggest the better binding and stability, MM/GBSA provided the binding free energy useful for further modification and optimization of the hits **5b** and **5f**, Finally network pharmacology provided *ADIPOQ* (adiponectin) and *NR1C3* (PPAR-γ) upregulated by the hit candidates, also the LEP (leptin), and GLP-1 levels still needed to be quantified and evaluated which remains as the limitation and future scope of the study. Thus these predictions supports the *invitro* and *invivo* findings. Overall the study identifies the compound **5b** as lead for optimization in pursuit of developing newer antidiabetic agents.

CRediT authorship contribution statement

Shriram D. Ranade: Writing – original draft, Validation, Software, Methodology, Investigation, Formal analysis, Data curation. **Shankar G. Alegaon:** Project administration, Methodology, Formal analysis, Data curation, Conceptualization. **Nayeem A. Khatib:** Methodology. **Shankar Gharge:** Methodology. **Rohini S. Kavalapure:** Methodology. **B.R. Prashantha Kumar:** Methodology.

Declaration of competing interest

The authors declare that they have no known competing financial interests or personal relationships that could have appeared to influence the work reported in this paper.

Data availability

No data was used for the research described in the article.

Acknowledgements

This work was supported by Department of Pharmaceutical chemistry, KLE College of Pharmacy, KLE Academy of Higher Education and Research, Belagavi, NMR was carried out in Sophisticated Analytical Instrument facility (SAIF) Karnataka University Dharwad. In addition, we would like to thank Mr. Prarambh S R Dwivedi for assisting in carrying out *Invitro* Glucose uptake assay. Mr. Rahul koli for providing assistance to carry out HPLC, Mr. Sachin Gudasi for assisting in Network pharmacology studies. Praveen Mhaske has assisted in HRMS studies.

Appendix A. Supplementary data

Supplementary data to this article can be found online at https://doi.org/10.1016/j.ejmech.2024.116939.

References

[1] U. Galicia-Garcia, A. Benito-Vicente, S. Jebari, A. Larrea-Sebal, H. Siddiqi, K. B. Uribe, H. Ostolaza, C. Martín, Pathophysiology of type 2 diabetes mellitus, Int. J. Mol. Sci. 21 (2020) 6275, https://doi.org/10.3390/ijms21176275.
[2] L. Dilworth, A. Facey, F. Omoruyi, Diabetes mellitus and its metabolic complications: the role of adipose tissues, Int. J. Mol. Sci. 22 (2021) 7644, https://doi.org/10.3390/ijms22147644.
[3] International Diabetes Federation, IDF diabetes atlas, 10th ed. Brussels, Belgium, https://www.diabetesatlas.org, 2021.
[4] R. Ruze, T. Liu, X. Zou, J. Song, Y. Chen, R. Xu, X. Yin, Q. Xu, Obesity and type 2 diabetes mellitus: connections in epidemiology, pathogenesis, and treatments, Front. Endocrinol. 14 (2023) 1161521, https://doi.org/10.3389/fendo.2023.1161521.
[5] Y. Wu, Y. Ding, Y. Tanaka, W. Zhang, Risk factors contributing to type 2 diabetes and recent advances in the treatment and prevention, Int. J. Mol. Sci. 11 (2014) 1185, https://doi.org/10.7150/ijms.10001.
[6] A. DeMarsilis, N. Reddy, C. Boutari, A. Filippaios, E. Sternthal, N. Katsiki, C. Mantzoros, Pharmacotherapy of type 2 diabetes: an update and future directions, Metabolism 137 (2022) 155332, https://doi.org/10.1016/j.metabol.2022.155332.
[7] W. Li, G. Yuan, Y. Pan, C. Wang, H. Chen, Network pharmacology studies on the bioactive compounds and action mechanisms of natural products for the treatment of diabetes mellitus: a review, Front. Pharmacol. 8 (2017) 74, https://doi.org/10.3389/fphar.2017.00074.
[8] S. Yasmin, V. Jayaprakash, Thiazolidinediones and PPAR orchestra as antidiabetic agents: from past to present, Eur. J. Med. Chem. 126 (2017) 879–893, https://doi.org/10.1016/j.ejmech.2016.12.020.
[9] H.J. Gim, B. Kang, R. Jeon, Synthesis and biological activity of 5-(4-[2-(Methyl-p-substituted phenylamino) ethoxy] benzyl) thiazolidine-2, 4-diones, Arch. Pharmacal Res. 30 (2007) 1055–1061, https://doi.org/10.1007/BF02980237.
[10] K.M. Darwish, I. Salama, S. Mostafa, M.S. Gomaa, M.A. Helal, Design, synthesis, and biological evaluation of novel thiazolidinediones as PPARγ/FFAR1 dual agonists, Eur. J. Med. Chem. 109 (2016) 157–172, https://doi.org/10.1016/j.ejmech.2015.12.049.
[11] J. Sun, H.Y. Liu, Y.H. Zhang, Z.Y. Fang, P.C. Lv, Design, synthesis and bioactivity evaluation of thiazolidinedione derivatives as partial agonists targeting PPARγ, Bioorg. Chem. 116 (2021) 105342 https://doi.org/10.1016/j.bioorg.2021.105342.
[12] S.S. Al Neyadi, A. Adem, N. Amir, M.A. Ghattas, I.M. Abdou, A.A. Salem, Novel thiazolidinedione and rhodanine derivatives regulate glucose metabolism, improve insulin sensitivity, and activate the peroxisome proliferator-activated γ receptor, ACS Omega 9 (2024) 5463–5484, https://doi.org/10.1021/acsomega.3c07149.
[13] H. Rajapaksha, H. Bhatia, K. Wegener, N. Petrovsky, J.B. Bruning, X-ray crystal structure of rivoglitazone bound to PPARγ and PPAR subtype selectivity of TZDs, Biochim. Biophys. Acta (BBA)-General Subjects 1861 (2017) 1981–1991, https://doi.org/10.1016/j.bbagen.2017.05.008.
[14] S.L. Dixon, A.M. Smondyrev, E.H. Knoll, S.N. Rao, D.E. Shaw, R.A. Friesner, PHASE: a new engine for pharmacophore perception, 3D QSAR model development, and 3D database screening: 1. Methodology and preliminary results, J. Comput. Aided Mol. Des. 20 (2006) 647–671, https://doi.org/10.1007/s10822-006-9087-6.
[15] S.P. Mandal, A. Garg, P. Prabitha, A.D. Wadhwani, L. Adhikary, B.P. Kumar, Novel glitazones as PPARγ agonists: molecular design, synthesis, glucose uptake activity and 3D QSAR studies, Chem. Cent. J. 12 (2018) 1–21, https://doi.org/10.1186/s13065-018-0508-0.
[16] S.D. Ranade, S.G. Alegaon, N.A. Khatib, S. Gharge, R.S. Kavalapure, B.P. Kumar, Design, synthesis, molecular dynamic simulation, DFT analysis, computational pharmacology and decoding the antidiabetic molecular mechanism of sulphonamide-thiazolidin-4-one hybrids, J. Mol. Struct. 1311 (2024) 138359, https://doi.org/10.1016/j.molstruc.2024.138359.
[17] N. Mamikutty, Z.C. Thent, S.R. Sapri, N.N. Sahruddin, M.R. Mohd Yusof, F. Haji Suhaimi, The establishment of metabolic syndrome model by induction of fructose drinking water in male Wistar rats, BioMed Res. Int. 1 (2014) 263897, https://doi.org/10.1155/2014/263897.
[18] P. Khanal, B.M. Patil, Reversal of insulin resistance by Ficus benghalensis bark in fructose-induced insulin-resistant rats, J. Ethnopharmacol. 284 (2022) 114761, https://doi.org/10.1016/j.jep.2021.114761.
[19] J. Dupas, A. Feray, C. Goanvec, A. Guernec, N. Samson, P. Bougaran, F. Guerrero, J. Mansourati, Metabolic syndrome and hypertension resulting from fructose enriched diet in Wistar rats, BioMed Res. Int. 1 (2017) 2494067, https://doi.org/10.1155/2017/2494067.
[20] P.S. Dwivedi, V.P. Rasal, R.S. Chavan, P. Khanal, V.P. Gaonkar, Insulin sensitization by Feronia elephantum in fructose-induced hyperinsulinemic rats:

insights from computational and experimental pharmacology, J. Ethnopharmacol. 316 (2023) 116686, https://doi.org/10.1016/j.jep.2023.116686.
[21] A. Beloff-Chain, R. Catanzaro, E.B. Chain, I. Masi, F. Pocchiari, C. Rossi, The influence of insulin on carbohydrate metabolism in the isolated diaphragm muscle of normal and alloxan diabetic rats, Proceedings of the Royal Society of London. Series B-Biological Sciences 143 (1955) 481–503, https://doi.org/10.1098/rspb.1955.0025.
[22] S. Seifter, S. Dayton, B. Novic, E. Muntwyler, The estimation of glycogen with the anthrone reagent, Arch. Biochem. 25 (1950) 191–200.
[23] M.A. Koroliuk, L.I. Ivanova, I.G. Maĭorova, V.E. Tokarev, A method of determining catalase activity, Lab. Delo 1 (1988) 16–19.
[24] J. Sedlak, R.H. Lindsay, Estimation of total, protein-bound, and nonprotein sulfhydryl groups in tissue with Ellman's reagent, Anal. Biochem. 25 (1968) 192–205.
[25] A.L. Claiborne, Catalase activity, in: Handbook Methods for Oxygen Radical Research, CRC press, 2018, pp. 283–284.
[26] S. Mandal, D.S. Chiriki, B.M. Gurupadayya, I.A. Chethan, B.P. Kumar, Phenyl glycine incorporated glitazones as promising novel antidiabetic agents through PPARγ agonism: design, synthesis and preclinical studies, EJMCR 6 (2022) 100067.
[27] Schrödinger Release 2024-3, LigPrep, Schrödinger, LLC, New York, NY, 2024.
[28] R.A. Friesner, R.B. Murphy, M.P. Repasky, L.L. Frye, J.R. Greenwood, T.A. Halgren, P.C. Sanschagrin, D.T. Mainz, Extra precision glide: docking and scoring incorporating a model of hydrophobic enclosure for protein− ligand complexes, J. Med. Chem. 49 (2006) 6177–6196, https://doi.org/10.1021/jm051256o.
[29] T.A. Halgren, R.B. Murphy, R.A. Friesner, H.S. Beard, L.L. Frye, W.T. Pollard, J. L. Banks, Glide: a new approach for rapid, accurate docking and scoring. 2. Enrichment factors in database screening, J. Med. Chem. 47 (2004) 1750–1759, https://doi.org/10.1021/jm030644s.
[30] K.J. Bowers, E. Chow, H. Xu, R.O. Dror, M.P. Eastwood, B.A. Gregersen, J. L. Klepeis, I. Kolossvary, M.A. Moraes, F.D. Sacerdoti, J.K. Salmon, Scalable algorithms for molecular dynamics simulations on commodity clusters, in: Proceedings of the 2006 ACM/IEEE Conference on Supercomputing, 2006, pp. 84–es.
[31] S. Gharge, S.G. Alegaon, S.D. Ranade, N.A. Khatib, R.S. Kavalapure, B.P. Kumar, D. Vinod, N.B. Bavage, Design, synthesis of new 2, 4-thiazolidinediones: in-silico, in-vivo anti-diabetic and anti-inflammatory evaluation, EJMCR 11 (2024) 100151, https://doi.org/10.1016/j.ejmcr.2024.100151.
[32] M.P. Jacobson, D.L. Pincus, C.S. Rapp, T.J. Day, B. Honig, D.E. Shaw, R.A. Friesner, A hierarchical approach to all-atom protein loop prediction, Proteins: Struct., Funct., Bioinf. 55 (2004) 351–367, https://doi.org/10.1002/prot.10613.
[33] S.D. Ranade, S.G. Alegaon, N.A. Khatib, S. Gharge, R.S. Kavalapure, Quinoline-based Schiff's base as possible antidiabetic agents: ligand-based pharmacophore modelling, 3D QSAR, docking and molecular dynamic simulations study, RSC Med. Chem. (2024), https://doi.org/10.1039/D4MD00344F.
[34] Schrödinger Release 2024-3: QikProp, Schrödinger, LLC, New York, NY, 2024.
[35] P.S. Dwivedi, C.S. Shastry, System biology mediated assessment of molecular mechanism for sinapic acid against breast cancer: via network pharmacology and molecular dynamic simulation, Sci. Rep. 13 (2023) 21982, https://doi.org/10.1038/s41598-023-47901-3.
[36] P. Khanal, P.S. Dwivedi, V.S. Patil, A. Shetty, A. Aga, A. Javaid, V.V. Bhandare, Barosmin against postprandial hyperglycemia: outputs from computational prediction to functional responses in vitro, J. Biomol. Struct. Dyn. 42 (2024) 4489–4505, https://doi.org/10.1080/07391102.2023.2233631.
[37] K.R. Alagawadi, S.G. Alegaon, Synthesis, characterization and antimicrobial activity evaluation of new 2, 4-Thiazolidinediones bearing imidazo [2, 1-b][1, 3, 4] thiadiazole moiety, Arab. J. Chem. 4 (2011) 465–472, https://doi.org/10.1016/j.arabjc.2010.07.012.
[38] P. Hemanth Kumar, L. Jyothish Kumar, G. Pavithrra, R. Rajasekaran, V. Vijayakumar, R. Karan, S. Sarveswari, Design, synthesis and exploration of in silico α-amylase and α-glucosidase binding studies of pyrrolidine-appended quinoline-constrained compounds, Res. Chem. Intermed. 46 (2020) 1869–1880, https://doi.org/10.1007/s11164-019-04068-9.
[39] K.E. Merz, D.C. Thurmond, Role of skeletal muscle in insulin resistance and glucose uptake, Compr. Physiol. 10 (2011) 785–809, https://doi.org/10.1002/cphy.c190029.
[40] M. Ahmadian, J.M. Suh, N. Hah, C. Liddle, A.R. Atkins, M. Downes, R.M. Evans, PPARγ signaling and metabolism: the good, the bad and the future, Nat Med 19 (2013) 557–566, https://doi.org/10.1038/nm.3159.
[41] H. Basciano, L. Federico, K. Adeli, Fructose, insulin resistance, and metabolic dyslipidemia, Nutr. Metab. 2 (2005) 1–4, https://doi.org/10.1186/1743-7075-2-5.
[42] A. Ahangarpour, M. Mohammadian, M. Dianat, Antidiabetic effect of hydroalcholic Urtica dioica leaf extract in male rats with fructose-induced insulin resistance, Iran, J. Med. Sci. 37 (2012) 181.
[43] S. Dai, J.H. McNeill, Fructose-induced hypertension in rats is concentration-and duration-dependent, J. Pharmacol. Toxicol. Methods 33 (1995) 101–107, https://doi.org/10.1016/1056-8719(94)00063-A.
[44] S.N. Iyer, M.J. Katovich, Vascular reactivity to phenylephrine and angiotensin II in hypertensive rats associated with insulin resistance, Clin. Exp. Hypertens. 18 (1996) 227–242, https://doi.org/10.3109/10641969609081766.
[45] G.A. Balsan, J.L. Vieira, A.M. Oliveira, V.L. Portal, Relationship between adiponectin, obesity and insulin resistance, Rev. Assoc. Med. Bras. 61 (2015) 72–80, https://doi.org/10.1590/1806-9282.61.01.072.
[46] M.M. Adeva-Andany, M. Gonzalez-Lucan, C. Donapetry-García, C. Fernandez-Fernandez, E. Ameneiros-Rodríguez, Glycogen metabolism in humans, BBA Clin. 5 (2016) 85–100, https://doi.org/10.1016/j.bbacli.2016.02.001.
[47] B. Friedmann, Jr EH. Goodman, S. Weinhouse, Effects of insulin and fatty acids on gluconeogenesis in the rat, JBC 242 (1967) 3620–3627, https://doi.org/10.1016/S0021-9258(18)95854-0.
[48] J. Steinberger, C. Moorehead, V. Katch, A.P. Rocchini, Relationship between insulin resistance and abnormal lipid profile in obese adolescents, J. Pediatr. 126 (1995) 690–695, https://doi.org/10.1016/S0022-3476.(95)70394-2.
[49] J. Jing, J. Li, N. Yan, N. Li, X. Liu, X. Li, J. Zhang, Q. Wang, C. Yang, J. Qiu, X. Liu, Increased TG levels and HOMA-IR score are associated with a high risk of prediabetes: a prospective study, Asia-Pac, J. Public Health 35 (2023) 413–419, https://doi.org/10.1177/10105395231191688.
[50] J.D. Schofield, Y. Liu, P. Rao-Balakrishna, R.A. Malik, H. Soran, Diabetes dyslipidemia, Diabetes Ther 7 (2016) 203–219, https://doi.org/10.1007/s13300-016-0167-x.
[51] P. Codoñer-Franch, A. Navarro-Ruiz, M. Fernández-Ferri, Á. Arilla-Codoñer, E. Ballester-Asensio, V. Valls-Bellés, A matter of fat: insulin resistance and oxidative stress, Pediatr, Diabetes 13 (2012) 392–399, https://doi.org/10.1111/j.1399-5448.2011.00847.x.
[52] M. Pasarín, J.G. Abraldes, E. Liguori, B. Kok, V. La Mura, Intrahepatic vascular changes in non-alcoholic fatty liver disease: potential role of insulin-resistance and endothelial dysfunction, World J. Gastroenterol. 23 (2017) 6777, https://doi.org/10.3748/wjg.v23.i37.6777.
[53] A.G. Tabák, C. Herder, W. Rathmann, E.J. Brunner, M. Kivimäki, Prediabetes: a high-risk state for diabetes development, Lancet 379 (2012) 2279–2290, https://doi.org/10.1016/S0140-6736(12)60283-9.
[54] I. Doycheva, R. Loomba, Effect of metformin on ballooning degeneration in nonalcoholic steatohepatitis (NASH): when to use metformin in nonalcoholic fatty liver disease (NAFLD), Adv. Ther. 31 (2014) 30–43, https://doi.org/10.1007/s12325-013-0084-6.

RSC Medicinal Chemistry

ROYAL SOCIETY OF CHEMISTRY

RESEARCH ARTICLE

Check for updates

Cite this: DOI: 10.1039/d4md00344f

Quinoline-based Schiff bases as possible antidiabetic agents: ligand-based pharmacophore modeling, 3D QSAR, docking, and molecular dynamics simulations study†

Shriram D. Ranade, [a] Shankar G. Alegaon, *[a] Nayeem A. Khatib, [b] Shankar Gharge [a] and Rohini S. Kavalapure [a]

α-Glucosidase enzyme inhibition is a legitimate approach to combat type 2 diabetes mellitus as it manages to control postprandial hyperglycemia. In this pursuit, a literature search identified quinoline-based molecules as potential α-glucosidase inhibitors. Thus our intended approach is to identify pharmacophoric features responsible for the α-glucosidase inhibition. This was achieved by performing, ligand-based pharmacophore modeling, 3D QSAR model development, pharmacophore-based screening of a rationally designed quinoline-based benzohydrazide Schiff base library, identifying, synthesizing and characterizing molecules (**6a–6j**) by IR, (^{1}H and ^{13}C) NMR, and mass studies. Further, these molecules were evaluated for α-glucosidase and α-amylase inhibitory potential. Compound **6c** was found to inhibit α-glucosidase enzyme with an IC_{50} value of 12.95 ± 2.35 μM. Similarly, compound **6b** was found to have an IC_{50} value of 19.37 ± 0.96 μM as compared to acarbose (IC_{50}: 32.63 ± 1.07 μM); the inhibitory kinetics of compounds **6b** and **6c** revealed a competitive type of inhibition; the inhibitory effect can be attributed to its mapped pharmacophoric feature and model validation with a survival score of 5.0697 and vector score of 0.9552. The QSAR model showed a strong correlation with an R^2 value of 0.96. All the compounds (**6a–6j**) showed no toxicity in L929 cell lines by the MTT assay method. Further, the binding orientation and stability of the molecules were assessed using molecular docking studies and MD trajectory analysis. The energy profile of the molecules with protein as a complex and molecules alone was evaluated using MM/GBSA and DFT calculations, respectively; finally, the pharmacokinetic profile was computed using ADMET analysis.

Received 10th May 2024,
Accepted 3rd July 2024

DOI: 10.1039/d4md00344f

rsc.li/medchem

Introduction

Diabetes mellitus type 2 (T2DM) is a chronic metabolic condition characterized by high blood glucose levels caused by insulin resistance and insufficient insulin production. It is a major global health concern, with a rising incidence globally.

T2DM is frequently linked to lifestyle variables such as sedentary lifestyle, obesity, and poor diet, making it a complicated and multifaceted illness.[1–3] Therapeutic targets involved in managing T2DM are the peroxisome proliferator-activated receptor (PPAR-γ), dipeptidyl peptidase-4 inhibitors (DPP-4), protein tyrosine phosphatase inhibitors (PTP1B), sodium-glucose transport protein 2 (SGLT-2) and α-glucosidase and α-amylase inhibitors.[4]

The α-glucosidase enzyme present in the brush border of the small intestine regulates the conversion of oligosaccharides, trisaccharides, and disaccharides into simple monosaccharides like glucose.[5] Similarly, α-amylase present in epithelial cells catalyzes the breaking of oligosaccharides into simple sugars which are then spiked into the bloodstream indicating postprandial hyperglycemia.[6] Thus, targeting these two enzymes provides a therapeutic approach to managing elevated blood glucose levels by delaying digestion and glucose uptake. Presently marketed inhibitors are *N*-heterocyclic carbasugars such as acarbose, miglitol, and voglibose. These molecules at the binding site act as a competitive inhibitor for the substrate. Furthermore, these molecules have been reported to possess gastrointestinal adverse effects such as flatulence, diarrhoea, abdominal discomfort, and sub-optimal efficacy. Thus, to address any of the above conditions there exists a need to develop new α-amylase and α-glucosidase inhibitors.[7–9]

[a] Department of Pharmaceutical Chemistry, KLE College of Pharmacy, Belagavi, KLE Academy of Higher education and Research, Belagavi – 590010, Karnataka, India. E-mail: sgalegaon@gmail.com, sgalegaon@klepharm.edu
[b] Department of Pharmacology, KLE College of Pharmacy, Belagavi, KLE Academy of Higher education and Research, Belagavi – 590010, Karnataka, India

† Electronic supplementary information (ESI) available. See DOI: https://doi.org/10.1039/d4md00344f

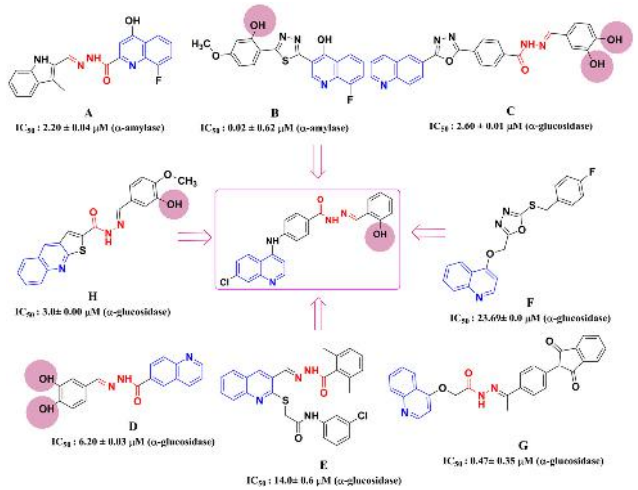


Chart 1 Design of the quinoline-based Schiff base molecule.

The quinoline scaffold is well-known as a building block in medicinal chemistry for its reported broad spectrum of activities which include antimalarial, antitubercular, anticancer, anti-leishmanial, antibacterial, antifungal, antiviral, anti-inflammatory, and antioxidant properties.[10–14] Recently, reported studies also suggest that quinoline-containing scaffolds were evaluated for their antidiabetic properties targeting α-amylase and α-glucosidase. Some examples include, compounds **A** and **B** showing α-amylase inhibitory activity as compared to acarbose with IC_{50} values of 2.20 ± 0.04 μM and 0.02 ± 0.62 μM, respectively.[15,16] Other compounds like compounds **C**, **D**, **E**, **F**, **G**, and **H** displayed α-glucosidase inhibitory activity as compared to standard acarbose with IC_{50} values of 2.60 ± 0.01 μM, 6.20 ± 0.03 μM, 14.01 ± 0.6 μM, 26.69 ± 0.6 μM, 0.47 ± 0.35 μM, and 3.0 ± 0.0 μM, respectively.[17–22] It is observed that most of these reported compounds have common structural features, a quinoline scaffold, an imine (C═N) linkage, hydrazone linkage forming a Schiff base, and also the substitutions were focused by varying the position of hydroxy (OH) groups on the phenyl ring. Considering the above-reported studies, we designed quinoline-based benzohydrazide Schiff bases (Chart 1).

Thus, to expand the inhibitory potential of quinoline as α-glucosidase and α-amylase inhibitors, we have designed and synthesized quinoline-based benzohydrazide Schiff bases.

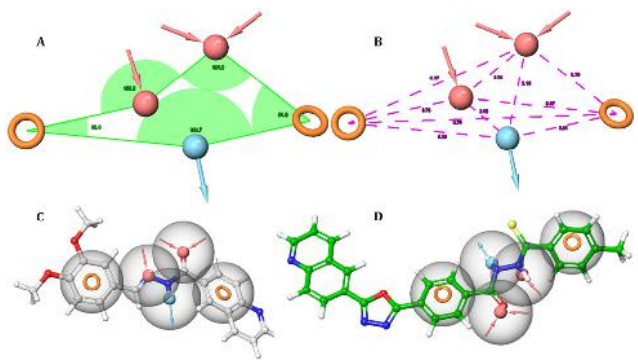


Fig. 1 Representation of pharmacophore model AADRR_1 with respect to (A) angles between pharmacophore sites and (B) intersite distance in Å. Mapping of pharmacophore sites with the (C) active compound and (D) inactive compound from the data set.

Results and discussion

Pharmacophore and 3D QSAR

The data set of 66 molecules obtained from the literature survey was classified into active and inactive sets; the pharmacophoric sites were identified for all the molecules, and a total of 12 hypotheses were generated based on different features namely hydrogen bond acceptor (A), hydrogen bond donor (D), hydrophobic group (H), ring aromatic group (R), positively charged group (P) and negatively charged group (N). The model with the highest inactive score can differentiate between actives and inactive; a higher value of survival score means better mapping of actives with the developed model. The hypotheses were ranked corresponding to their statistical parameters such as survival score, inactive score, and vector score, and the top 5 hypotheses are detailed in Table 1 and S1.† Hypothesis AADRR_1 emerged as the best fit with a favorable survival score of 5.0697, a survival inactive score of 2.3579, and a vector score of 0.9552 and was selected for further validation. The selected model (AADRR_1) has a five-point hypothesis (Fig. 1) which includes two hydrogen bond acceptors; this feature is related to the nitrogen atom of the (–N═CH) Schiff base and oxygen atom of the carbonyl group (C═O); one hydrogen bond donor corresponds to an amino group (NH), and two ring aromatic features are related to the phenyl rings. These chemical features are essential for the α-glucosidase inhibitory activity among the data sets of the reported molecules.

Table 1 Score of different hypothesis models

Sr. no	Hypothesis	Survival score	Inactive score	Vector score	Volume score
1	AADRR_1	5.069738	2.357928	0.955287	0.73662
2	AADRR_3	4.905304	1.982363	0.8755	0.715986
3	ADRR_2	4.84413	2.246359	0.941394	0.735339
4	AADRR_5	4.711901	2.127412	0.815888	0.631069
5	AAARR_2	4.739191	2.172076	0.8424	0.635954
6	AADRR_1	5.069738	2.357928	0.955287	0.73662

This journal is © The Royal Society of Chemistry 2024

Table 2 Atom-based 3D quantitative structural activity relationship (QSAR) results for selected pharmacophore hypothesis

ID	PLS factor	SD	R^2	F	P	RMSE	Q^2	Pearson's r
AADRR1	1	0.067	0.712	42.0	5.62×10^{-06}	0.43	0.8430	0.9410
	2	0.3727	0.8979	70.3	1.18×10^{-08}	0.34	0.8999	0.9577
	3	0.3366	0.9219	59.0	1.55×10^{-08}	0.35	0.8954	0.9522
	4	0.2295	0.9661	99.8	3.99×10^{-10}	0.29	0.9294	0.9759

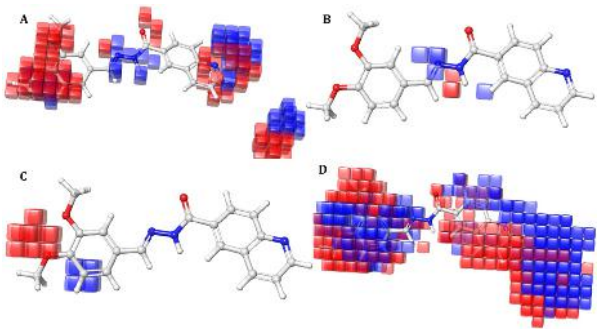


Fig. 2 Representation of contour plots for the active compound A5 from the data set with respect to (A) electron withdrawing effect, (B) hydrogen bond donor effect, (C) negative ionic effect and (D) positive ionic effect.

The AADRR_1 pharmacophoric model was validated by performing atom based 3D QSAR study, using partial least squares (PLS) regression analysis with a grid spacing of 1.5 Å. The data set was divided randomly with uniform structural diversity into test (19 molecules) and training (8 molecules); the best QSAR model was considered as with factor four, based on the parameters such as strong correlation coefficient (R^2), *i.e.* 0.96, cross-correlation coefficient (Q^2), *i.e.* 0.92; the stability of the model was found to be 0.55 and it has the highest F value of 99.8. Pearson's r is 0.9759 indicating the degree of confidence of the model. Moreover, the standard deviation (SD) is 0.229 and RMSE is found to be 0.29 indicating the stability of the model as presented in Table 2. The contour plots of 3D QSAR for the active compound are presented in Fig. 2. Here the blue cubes indicate the positive contributing effects and the red cubes indicate the negative contribution of molecular features for the requirement of the pharmacophore responsible for α-glucosidase inhibitory activity.

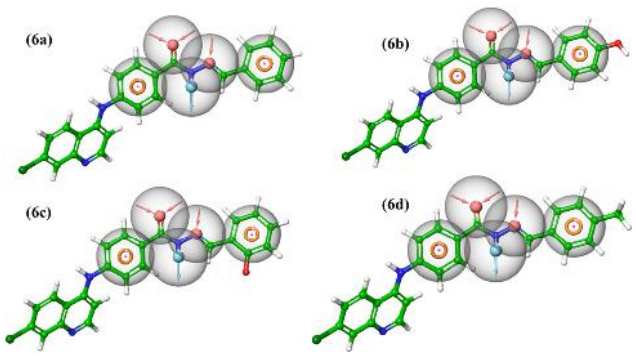


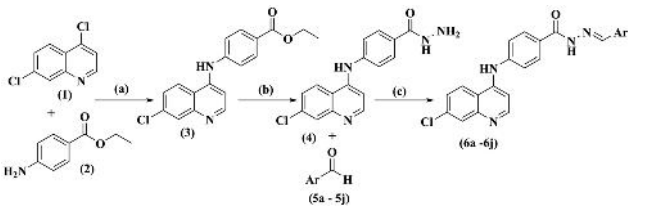
Fig. 3 The top screened actives mapped to the pharmacophoric hypothesis (AADRR_1).

Validation of the pharmacophore model

The generated pharmacophoric model AADRR_1 discriminatory ability was further validated by means of screening a set of ten designed molecules of the quinoline-based benzohydrazide Schiff' base along with a decoy set containing 1000 molecules obtained from the Schrödinger suite. The model successfully identified designed molecules from those of the decoy set molecules. The top hits were identified based on the fitness score ranging above 2. It was seen that the decoy set molecules exhibited fitness values less than 1.9. (Table S2†); the performance of the listed hits was analyzed based on the model AADRR_1 RIE value of 18.14. The area under the curve (AUC) of the ROC displayed a favorable metric for model evaluation value 1 for AADRR_1. The enrichment screen plot is provided in the ESI† (Fig. S1). The top hits were found to be mapped with the pharmacophoric sites (Fig. 3). Thus, these obtained hits were further carried for synthesis, *in vitro* evaluation of α-glucosidase and α-amylase inhibitory assay followed by their binding affinity analysis using molecular docking, MD simulation, and MM/GBSA analysis.

Chemistry

The synthesis of (**6a–6j**) quinoline-based benzohydrazide Schiff' bases was synthesized as shown in Scheme 1. The compound ethyl 4-((7-chloroquinolin-4-yl) amino) benzoate (**3**) and compound (**4**) 4-((7-chloroquinolin-4-yl) amino) benzohydrazide were prepared as per the previously reported method.[23] The substituted benzylidene-4-((7-chloroquinolin-4-yl) amino) benzohydrazide compounds (**6a–6j**) were prepared by using the equimolar ratio of



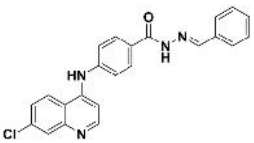
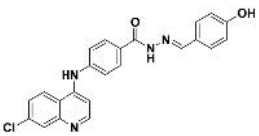
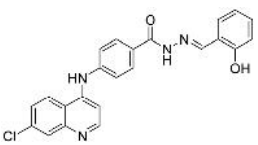
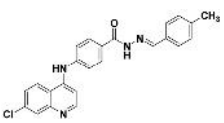
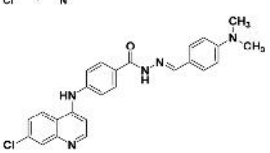
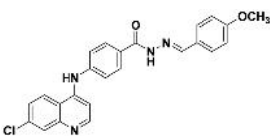
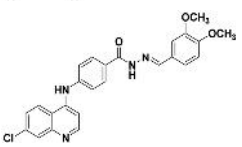
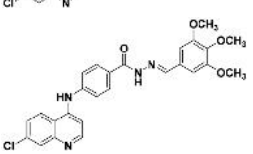
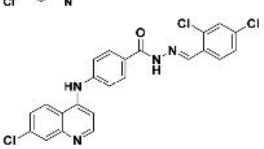
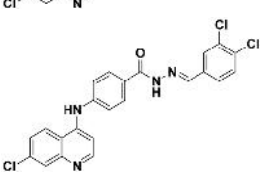
Scheme 1 Reagents and conditions: (a) 2 N HCl, reflux; (b) hydrazine hydrate (80%), reflux; (c) methanol, glacial acetic acid, reflux.

compound (**4**) refluxed with appropriated aryl aldehydes (**5a–5j**) using a catalytic amount of glacial acetic acid in methanol. The final crude compounds (**6a–6j**) were recrystallized and dried.

α-Glucosidase and α-amylase inhibitory assay

The newly synthesized molecules (**6a–6j**) were assessed for their inhibition effect on the enzymes responsible for

Table 3 *In vitro* α-glucosidase and α-amylase inhibitory activity of the synthesized compounds 4-((7-chloroquinolin-4-yl) amino) benzohydrazide Schiff bases (**6a–6j**)

Comp.	Product	IC_{50} values (μM) ± SEM	
		α-Glucosidase	α-Amylase assay
6a		27.43 ± 1.42	45.62 ± 2.01
6b		19.37 ± 0.96	29.36 ± 3.24
6c		12.95 ± 2.35	33.04 ± 1.83
6d		43.76 ± 4.31	58.74 ± 3.01
6e		31.42 ± 1.67	53. 06 ± 2.06
6f		143.52 ± 2.98	78.63 ± 1.35
6g		302.51 ± 2.12	No inhibition
6h		748.35 ± 1.09	No inhibition
6i		108.56 ± 3.16	65.48 ± 1.16
6j		63.25 ± 0. 23	56.32 ± 3.14
Acarbose	—	25.41 ± 0.16	32.63 ± 1.07

This journal is © The Royal Society of Chemistry 2024

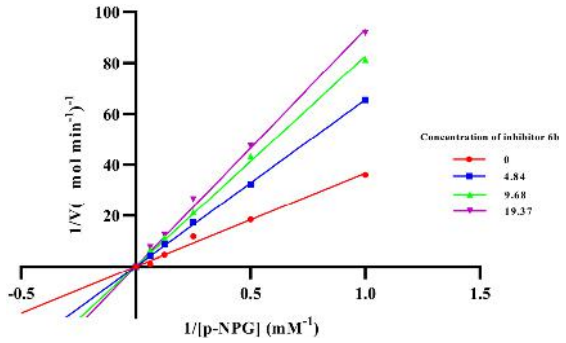


Fig. 4 Lineweaver–Burk plot in the presence and absence of various concentrations of compound **6b**.

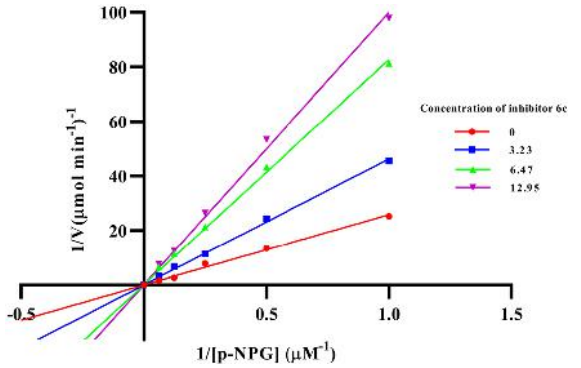


Fig. 6 Lineweaver–Burk plot in the presence and absence of various concentrations of compound **6c**.

postprandial hyperglycemia. Among the series (**6a–6j**), analogs showed a varying degree of inhibitory effect on α-glucosidase with IC_{50} values ranging between (12.95 ± 2.35 μM and 748.35 ± 1.09 μM) compared to standard drug acarbose (25.41 ± 0.16 μM) and α-amylase inhibitory effect in the range of 29.36 ± 3.24 μM and 78.63 ± 1.35 μM as compared to standard drug acarbose (32.63 ± 1.07 μM). The most active inhibitor **6c** from the series displayed significant α-glucosidase inhibition (IC_{50} −12.95 ± 2.35 μM), followed by compound **6b** (IC_{50} −19.37 ± 0.96 μM). The compound **6b** inhibited α-amylase enzyme with IC_{50} −29.36 ± 3.24 μM followed by the compound **6c** (IC_{50} −33.04 ± 1.83 μM). The inhibitory effects of all the compounds are detailed in Table 3.

Enzyme kinetic study

The most potent compounds among the series (**6a–6j**) were compounds **6b** and **6c** which were analyzed for their α-glucosidase inhibitory mechanism by enzyme kinetic study. Compound **6b** was found to be competing with the substrate for the enzyme as evidenced by the Lineweaver–Burk plot, where the V_{max} value was unchanged and increased in the K_m value; the inhibitory constant (K_i) was found to be 19.54 μM and the plot is depicted in Fig. 4 and 5. Similarly, from the Lineweaver–Burk plot, it was observed that the compound **6c** followed a competitive inhibitory pattern; the inhibitory constant (K_i) value was found to be 11.32 μM, as shown in Fig. 6 and 7.

Structural activity relationship

As per the literature search, a number of quinoline-based compounds have been reported to exhibit α-glucosidase and α-amylase inhibitory activity, such as quinoline clubbed with a dihydropyrano[3,2-*c*] system,[24] dihydropyridines,[25] 1,3,4 oxadiazole and a 1,2,3-triazole,[20] quinoline based Schiff base.[15] From the pharmacophore model it was evident that the (CH═N) Schiff base linkage scored as a contributing feature for the biological activity, as it is evident from the selected hypothesis model, the two aromatic rings, one hydrogen donor group, and two hydrogen acceptor group are contributing factors for inhibitory activity of the α-glucosidase enzyme. Compounds (**6a–6j**) were found to be mapped on the pharmacophoric feature sites for the validated model, and these features in the molecules **6b** and **6c** were found to participate in the hydrogen bond interaction in the enzyme's binding site. The active compounds **6b** (IC_{50}: 19.37 ± 0.96) and **6c** (IC_{50}: 12.95 ± 2.35) among the series (**6a–6j**) are structurally quinoline-based

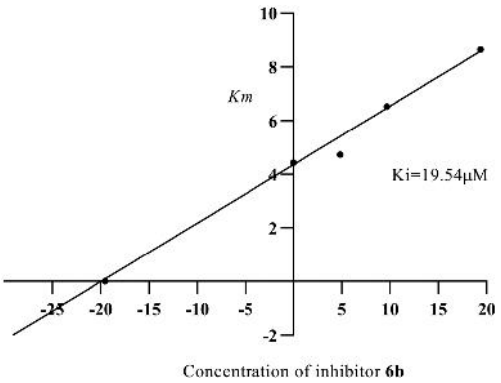


Fig. 5 Secondary replot between K_m and different concentrations of inhibitor **6b**.

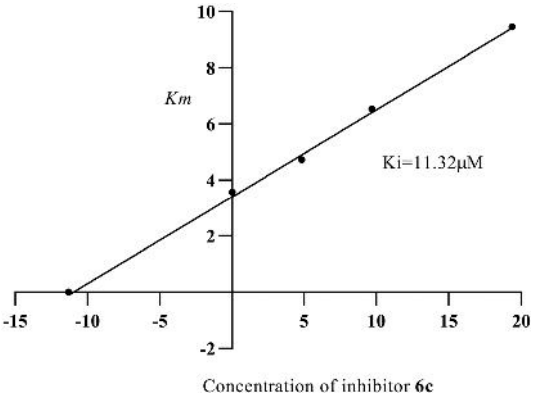


Fig. 7 Secondary replot between K_m and different concentrations of inhibitor **6c**.

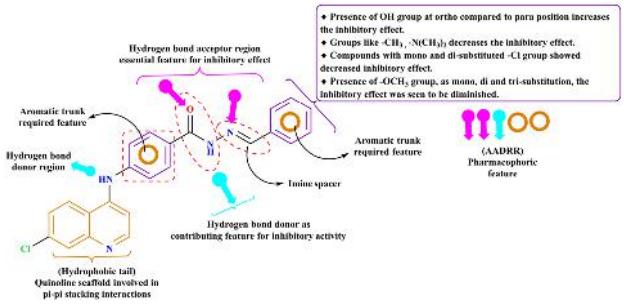


Fig. 8 SAR and pharmacophoric features required for α-glucosidase inhibitory activity.

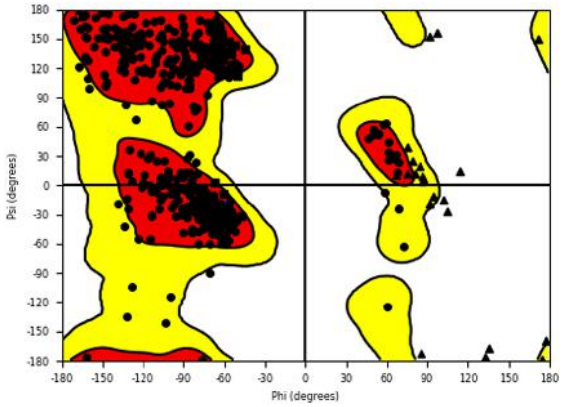


Fig. 9 Ramachandran plot of the homology modeled α-glucosidase protein.

benzohydrazide Schiff base analogs. It is evident from the molecular docking studies that the quinoline scaffold is important for better binding of molecules within the pocket as it forms a pi–pi stacking interaction with PHE 311, PHE 157 in compound **6b**, and TYR 151 in compound **6c**. Both the active compounds exhibit hydroxy group substitution but differ with **6b** having *para* hydroxy substitution and **6c** with *ortho* hydroxy substitution, which implicates the importance of the inductive effect on the hydroxy group's electron-withdrawing ability and resonance effect on its electron-donating ability; the effect of hydroxy and polyhydroxy functional groups depends on the position of substitutions over the molecules to exhibit electron donating and withdrawing effects. It was also seen that the electron-donating substituents like **6b**, **6c**, **6d**, and **6e** showed better activity compared to electron-withdrawing substituents like **6f**, **6g**, **6h**, **6i**, and **6j** within the series (**6a–6j**). Thus from the above findings and previously published literature[18] it is evident that the hydroxy group substitutions have a contributing effect on α-glucosidase inhibitory activity as summarized in Fig. 8.

Cytotoxicity studies

The safety of the synthesized molecules (**6a–6j**) was assessed on the normal mouse fibroblast (L929) cell lines using MTT (3-(4,5-dimethylthiazo-2-yl)-2,5-diphenyl-tetrazolium bromide) assay. The cell toxicity assay results revealed that the compounds (**6a–6j**) displayed no cytotoxic effect as shown in Table 4.

Table 4 Toxicity results on normal mouse fibroblast L929 cell lines

	Percent survival	
	L929 cell lines	
Comp	125 μg ml^{-1}	250 μg ml^{-1}
6a	90.28	83.63
6b	89.77	86.29
6c	83.32	79.67
6d	78.31	78.48
6e	92.75	86.42
6f	91.47	85.12
6g	89.95	83.52
6h	87.14	83.06
6i	83.69	75.82
6j	88.17	85.84

Molecular docking

The α-glucosidase and α-amylase inhibitory assay revealed that several compounds showed noticeable inhibitory effects in comparison to standard inhibitor acarbose. Thus to validate these results and to establish the molecular interactions between the synthesized molecules and the receptor of α-glucosidase and α-amylase enzyme, a molecular docking study was performed using the Glide module of the Schrödinger suite. The binding poses of all the molecules were analyzed to understand the binding site affinity of these molecules. The α-glucosidase protein was constructed using homology modeling using the Fasta sequence (access id: P53341); 'BLAST' results highlighted 'crystal structure of isomaltase from *Saccharomyces cerevisiae*' (PDB ID: 3A47) as the maximum similarity index protein; this was used as the template protein for construction of the model; finally, protein reliability and the Ramachandran plot were analyzed (Fig. 9). Compounds **6b** and **6c** possessed the highest binding affinity among the series (**6a–6j**) in the binding pocket of α-glucosidase enzyme; compound **6b** (Fig. 10) showed

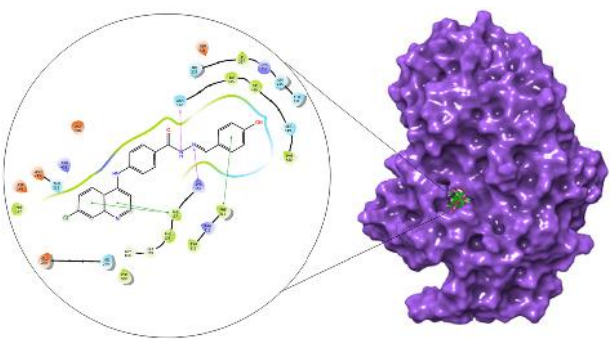


Fig. 10 2D and surface binding orientation of compound **6b** in the α-glucosidase binding pocket.

This journal is © The Royal Society of Chemistry 2024

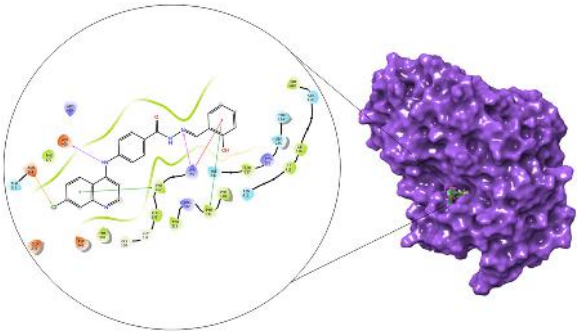


Fig. 11 2D and surface binding orientation of compound **6c** in the α-glucosidase binding pocket.

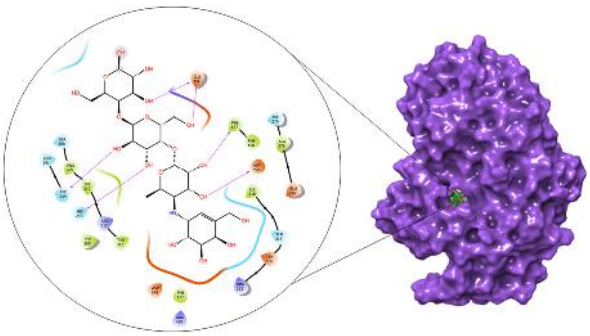


Fig. 12 2D and surface binding orientation of compound acarbose in the α-glucosidase binding pocket.

hydrogen bond interaction between the nitrogen atom of the Schiff base and amino acid residue LYS 155; it also formed a hydrogen bond interaction between the amino (NH) group of the benzohydrazide moiety and ASN 412; furthermore, it displayed three pi–pi stacking interactions with the aromatic rings of the ligand, one with amino acid residue PHE 311 and two bonds with PHE 157; the glide energy was found to be −52.425 kcal mol^{-1}.

Similarly, compound **6c** (Fig. 11) displayed a hydrogen bond interaction between the nitrogen atom of the Schiff base and amino acid residue LYS 155; the same LYS 155 was involved in the formation of a pi–cation interaction with the phenyl ring. Moreover, a pi–pi stacking interaction between the aromatic ring, and amino acid residue PHE 311, and PHE 157 was seen. A halogen bond was formed between the chlorine atom of the quinoline ring and ASH 214 amino acid residue; the glide energy was found to be −45.127 kcal mol^{-1}. Acarbose (Fig. 12) was used as a standard for validating the docking protocol. All the interacting amino acid residues with the ligands matched to the active site key residues obtained from the site map analysis. Similarly, the compounds **6b** and **6c** showed better binding affinity among the series (**6a–6j**) in the α-amylase enzyme binding site, where compound **6b** (Fig. 13) formed a hydrogen bond interaction between the amino (NH) group and ASP 300 amino acid residue; it also formed a hydrogen bond interaction between the carbonyl group and amino acid HIE 201; the hydroxy (OH) group formed a hydrogen bond interaction with GLU 240; moreover a halogen bond was formed between the chlorine atom of the quinoline nucleus and GLN 63 amino acid residue; the overall glide energy for the obtained pose was found to be −46.006 kcal mol^{-1}. Similarly, compound **6c** (Fig. 14) shows a hydrogen bond interaction between the hydroxy (OH) group and amino acid ILE 235; it also formed a pi–pi stacking interaction between the aromatic ring and TYR 151 amino acid residue, with a total glide energy of −49.094 kcal mol^{-1}. Docking validation was carried out using acarbose (Fig. 15) as the standard. Thus the binding

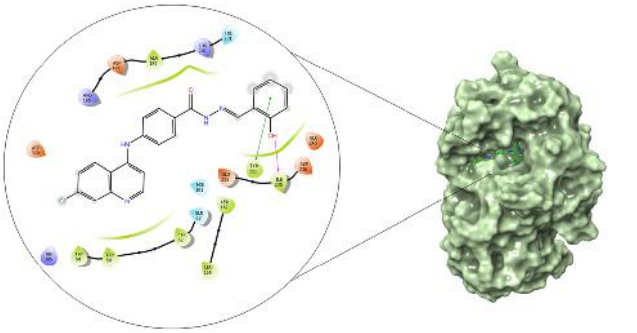


Fig. 14 2D and surface binding orientation of compound **6c** in the α-amylase binding pocket.

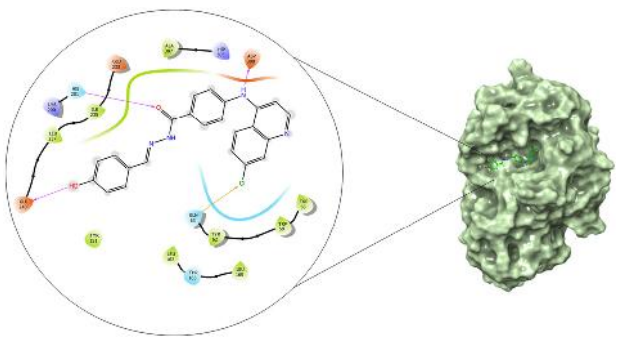


Fig. 13 2D and surface binding orientation of compound **6b** in the α-amylase binding pocket.

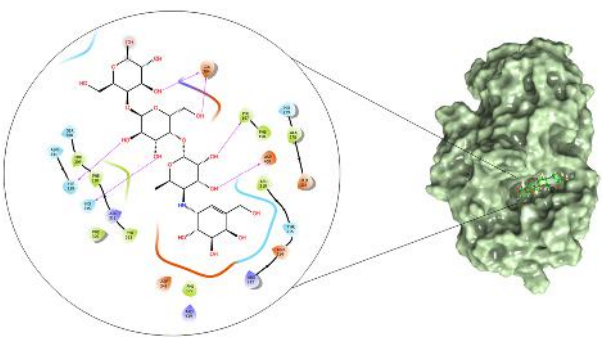


Fig. 15 Represents 2D and surface binding orientation of compound acarbose in the α-amylase binding pocket.

Table 5 Binding affinity and interactions of compounds **6a–6j** in the α-glucosidase binding pocket using the Glide module of the Schrödinger suite

Compound	Docking score	Glide energy (kcal mol^{-1})	Ligand atom interaction (H-bond)	Amino acid residue	Bond length	π–π stacking
6a	−5.133	−53.487	NH of the ligand to ASP 408	ASP 408	2.23	—
6b	−6.145	−53.047	NH of the ligand to ASN 412	ASN 412	2.01	PHE 311
			N of the ligand to LYS 155	LYS 155	2.46	PHE 157
6c	−7.029	−56.784	NH of the ligand to ASP 408	ASP 408	2.24	PHE 311
			N of the ligand to LYS 155	LYS220	2.27	PHE 157
6d	−5.423	−49.918	N of the ligand to GLN 350	GLN 350	2.78	PHE 311
			C═O of the ligand to ASN 412	ASN 412	2.08	
6e	−5.068	−50.113	NH of the ligand to ASP 408	ASP 408	2.22	—
6f	−5.392	−53.900	NH of the ligand to ASP 408	ASP 408	2.13	—
6g	−6.190	−59.221	C═O of the ligand to LYS 155	LYS 155	2.53	—
			N of the ligand to LYS 155	LYS 155	2.48	
6h	−5.347	−53.043	NH of the ligand to ASP 408	ASP 408	2.03	PHE 311
6i	−5.494	−56.111	NH of the ligand to ASP 408	ASP 408	1.80	HIE 239
			C═O of the ligand to ARG 312	ARG 312	1.86	
6j	−3.90	−7.58	NH of the ligand to ASP 408	ASP 408	1.67	PHE 311
Acarbose	−7.199	−51.660	OH of the ligand to ASP 408	ASP 408	2.78	
			OH of the ligand to GLU 304	GLU 304	1.78	
			OH of the ligand to HIE 239	HIE 239	2.63	
			OH of the ligand to GLU 304	GLU 304	1.68	
			OH of the ligand to HIS 245	HIS 245	2.69	
			OH of the ligand to PHE 157			

affinity of these ligands *via* hydrogen bonding, pi–pi stacking, halogen bonding, and pi–cation in the binding pocket of α-glucosidase and α-amylase enzyme indicates the putative binding mode, thus supporting the *in vitro* findings. The detailed binding affinity of compounds **6a–6j** in α-glucosidase (Table 5) and α-amylase (Table 6) is presented. The binding pose of compounds **6a**, **6d**, **6e**, **6f**, **6g**, **6h**, **6i**, and **6j** are presented in the ESI.†

MD simulations

The potential leads **6b** and **6c** against α-glucosidase among the series (**6a–6j**) based on enzyme inhibitory activity were selected for an MD simulation run to assess their affinity towards the binding pocket and the predicted stability of the protein–ligand complex throughout an MD run of 200 ns. Simulation interaction analysis was based on the

Table 6 Binding affinity and interactions of compounds **6a–6j** in the α-amylase binding pocket using Glide module of the Schrödinger suite

Compound	Docking score	Glide energy (kcal mol^{-1})	Ligand atom interaction (H-bond)	Amino acid residue	Bond length	π–π stacking
6a	−5.133	−53.487	C═O of ligand the to HIE 201	HIE 201	2.31	TYR 151
						TRP 58
6b	−6.145	−53.047	OH of the ligand to GLU 240	GLU 240	1.66	—
			C═O of the ligand to HIE 201	HIE 201	2.13	
			NH of the ligand to ASP 300	ASP 300	1.74	
6c	−7.029	−56.784	OH of the ligand to ILE 235	ILE 235	2.07	TYR 151
6d	−5.423	−49.918	C═O of the ligand to TYR 151	TYR 151	2.11	HIE 201
			C═O of the ligand to HIE 201	HIE 201	2.01	
6e	−5.068	−50.113	NH of the ligand to GLU 233	GLU 233	2.12	
			C═O of the ligand to HIE 201	HIE 201	2.28	HIE 201
			C═O of the ligand to TYR 151	TYR 151	2.10	
6f	−5.392	−53.900	NH of the ligand to ASP 197	ASP 197	2.33	TRP 58
						TRP 59
						HIE 201
6g	−6.190	−59.221	C═O of the ligand to HIE 201	HIE 201	1.88	—
6h	−5.347	−53.043	C═O of the ligand to HIE 201	HIE 201	2.02	TRP 58
6i	−5.494	−56.111	C═O of the ligand to HIE 201	HIE 201	1.95	
6j	−3.90	−7.58	N of the ligand to ILE 235	ILE 235	2.40	HIE 201
						TRP 59
Acarbose	−7.199	−51.660	OH of the ligand to ASP 300	ASP 300	2.63	
			OH of the ligand to ASP 300	ASP 300	2.37	
			OH of the ligand to ASP 197	ASP 197	1.71	
			OH of the ligand to GLU 240	GLU 240	1.74	
			OH of the ligand to HIP 205	HIP 205	2.17	
			OH of the ligand to HIE 201	HIE 201	2.33	
			OH of the ligand to ARG 195	ARG 195	1.80	

This journal is © The Royal Society of Chemistry 2024

hydrogen bond contacts, RMSD, and RMSF. The RMSD indicates the average deviation of the selection of atoms for individual frames concerning the reference frame throughout the simulation. RMSF helps to identify the local changes in the protein and changes in the atom position of ligands. Frame 0 was considered as the reference structure. The discussion on the protein–ligand complex is described below:

α-Glucosidase–6b complex. The stability of the protein–ligand complex was determined using the protein–ligand RMSD plot, indicating the stable protein structure concerning the C-alpha RMSD and backbone RMSD having a maximum deviation of 2.755 Å and 2.754 Å (frame 977), respectively. The ligand RMSD was determined by identifying the ligand aligned on a protein and the ligand aligned on a ligand showing a maximum deviation of 4.266 Å (frame 989) and 1.185 Å (frame 967), respectively. The protein RMSF plot indicates the stability of binding site amino acid residues when in contact with a ligand; it was observed that the maximum deviation was found to be with the amino acid residue SER 419 with a deviation of 2.340 Å concerning C-alpha and 2.428 Å for the backbone (frame 417); overall the amino acids involved in the contact with a ligand displayed not much protein RMS fluctuation, while the other fluctuating residues were not involved in the protein–ligand contact, indicating the stability of the ligand in the binding site. The ligand RMSF indicates the change in movement of ligand atoms throughout simulation. The ligand aligned on a protein and the ligand aligned on a ligand showed maximum fluctuations of 2.572 Å and 1.225 Å corresponding to a carbon atom of the benzene ring, and there was no fluctuation of the intact functional groups indicating the stability of the ligand inside the binding pocket. To evaluate the hydrogen bond interactions, the protein–ligand contact timeline and histogram plot were analysed; LYS 155 formed a continuous hydrogen bond interaction for a complete MD run of 200 ns; it also formed a water bridge hydrogen bond interaction with ASP 349 and GLU 276, and HIS 239 formed a hydrogen bond interaction for

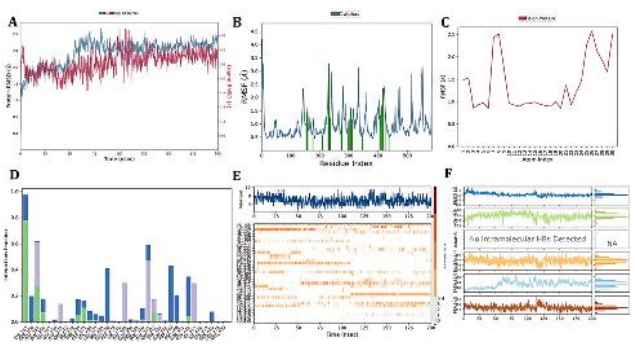


Fig. 16 Simulation interaction diagram of the α-glucosidase–**6b** complex: A) protein–ligand RMSD plot, B) protein RMSF plot, C) ligand RMSF, D) protein–ligand contact histogram, E) protein–ligand contact timeline and F) ligand properties.

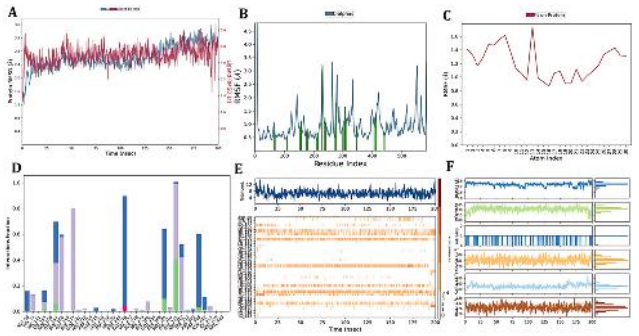


Fig. 17 Simulation interaction diagram of the α-glucosidase–**6c** complex: A) protein–ligand RMSD plot, B) protein RMSF plot, C) ligand RMSF, D) protein–ligand contact histogram, E) protein–ligand contact timeline and F) ligand properties.

100 ns. A pi–cation interaction was seen with ARG 312 throughout the simulation. Also, the ligand properties such as the radius of gyration, SASA, PSA, and intramolecular H bonds were calculated. (Fig. 16).

α-Glucosidase–6c complex. The protein ligand RMSD plot of the α-glucosidase–**6c** complex was presented; the protein structure RMSD concerning the reference C-alpha RMSD and backbone RMSD value showed a maximum deviation of 3.263 Å and 3.254 Å (frame 999), respectively. Ligand stability was evaluated using the ligand RMSD concerning the ligand aligned on a protein and the ligand aligned on a ligand indicating maximum deviations of 4.985 Å and 1.561 Å (frame 15), respectively. ASP 232 showed a fluctuation of 3.023 Å (frame 230), and the rest of the ligand contact residues were found to have less than 1.00 Å RMS fluctuation, indicating stable contact inside the binding pocket. The ligand RMSF plot indicates that compound **6c** is stable, but ligand RMS fluctuations of 1.141 Å and 0.695 Å were seen concerning the protein and ligand, respectively, of the chlorine atom. The protein–ligand contact histogram and timeline were assessed, a hydrogen bond interaction was seen with PHE 311, and water bridge hydrogen bonding was seen with PRO 309, ASP 408, and GLU 276. A pi–cation interaction with ARG 312 and pi–pi stacking with PHE 158 were formed. Finally, the ligand properties were identified (Fig. 17).

Table 7 Final energy of geometry optimized structures

Compound	Gas phase energy (eV)
6a	−1641.166335
6b	−1716.392044
6c	−1716.389529
6d	−1680.487182
6e	−1775.142601
6f	−1755.69537
6g	−1870.2175
6h	−1984.736796
6i	−2560.346418
6j	−2560.348556

Table 8 Calculated quantum chemical parameters of the synthesized compounds (molecular electrostatic potential surface)

Quantum chemical parameters	E_{HOMO} (eV)	E_{LMO} (eV)	ΔE_{GAP} (eV)	μ (eV)	σ (eV)	η (eV)	ω (eV)
6a	−0.22342	−0.08268	0.14074	−0.15305	14.21060111	0.07037	0.000824
6b	−0.22132	−0.08126	0.14006	−0.15129	14.27959446	0.07003	0.000801
6c	−0.22112	−0.08053	0.14059	−0.150825	14.22576286	0.070295	0.0008
6d	−0.2222	−0.08141	0.14079	−0.151805	14.20555437	0.070395	0.000811
6e	−0.19993	−0.07859	0.12134	−0.13926	16.48261085	0.06067	0.000588
6f	−0.22003	−0.08079	0.13924	−0.15041	14.3636886	0.06962	0.000788
6g	−0.21566	−0.08103	0.13463	−0.148345	14.85552997	0.067315	0.000741
6h	−0.22183	−0.08283	0.139	−0.15233	14.38848921	0.0695	0.000806
6i	−0.22507	−0.08528	0.13979	−0.155175	14.30717505	−0.070096	0.000842

Density functional theory (DFT)

Optimization of molecular geometries. The optimization of synthesized molecular structures having gas-phase energy is shown in Table 7. The study of molecular orbitals (MOs) is crucial in quantum chemistry, as it defines chemical behavior and also highlights the binding affinity and reactivity of molecules. The major molecular orbitals of a compound are the highest occupied molecular orbital (HOMO) and the lowest unoccupied molecular orbital (LUMO). Chemical qualities such as reactivity, stability, and kinetics are explained using them. Softer molecules tend to show better reactivity, and the extent to which a molecule is hard or soft is determined by hardness (η). The chemical reactivity descriptors and energy gap are calculated by the DFT/B3LYP/6-31 G (d,p**) method, and the values are mentioned in Table 8. The (FOMOs) HOMO and LUMO orbitals of compounds **6b** and **6c** are depicted in (Fig. 18) A smaller HOMO–LUMO energy gap typically indicates molecular reactivity. Compounds **6b** and **6c** show a ΔE_{GAP} of −0.14006 eV and −0.14059 eV, respectively.

Molecular electrostatic potential (MEP)

The electrostatic potential is a useful tool for determining how electric charge is distributed in a molecule. This sheds light on the electrostatic interactions that occur within the molecule and with the protein when inside the binding pocket. The MEP on a molecular surface can be used to identify areas of high electron density (negative potential) and low electron density (positive potential). The MEP may be used to anticipate electrophilic and nucleophilic attack sites, as well as to examine molecular interactions. Molecular electrostatic potentials were estimated using the B3LYP technique and a basis set of 6-31G (d,p**) at the optimized geometry. The MEP of potential compounds **6b** and **6c** is presented in (Fig. 19). From the graph, it is understood that the size, shape, and orientation of the positive (blue color – nucleophilic attack sites), negative (red color – electrophilic attack sites) and neutral (green color) regions depend on the nature of the substituted functional groups. The variation in mapping this electrostatic potential in drug-like substances is primarily responsible for the extent to which drug-receptor binding happens at the targeted receptor's active site.

ADMET

ADMET properties, including hydrogen bond donors, hydrogen bond acceptors, hydrophilicity, molecular weight, permeability, and percent human oral absorption, were predicted; furthermore predictions regarding violations of Lipinski's rule of five and Jorgensen's rule of three were identified using the Schrödinger Qikprop module and compared with recommended values, as shown in Table 9. Compounds **6b** and **6c** obeyed the Lipinski rule of five without any violations of the rule, whereas the rest of the molecules showed at least 1 violation of the rule of five.

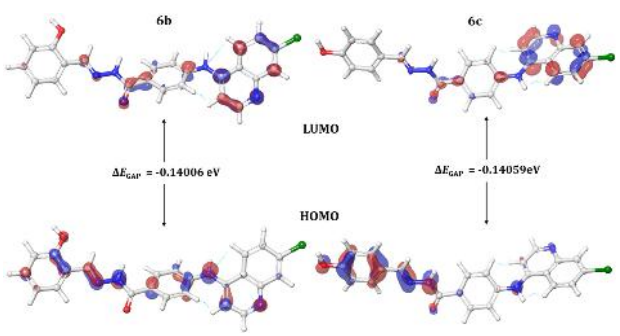


Fig. 18 The HOMO and LUMO orbitals with energy gaps (ΔE_{GAP}) for compounds **6b** and **6c**.

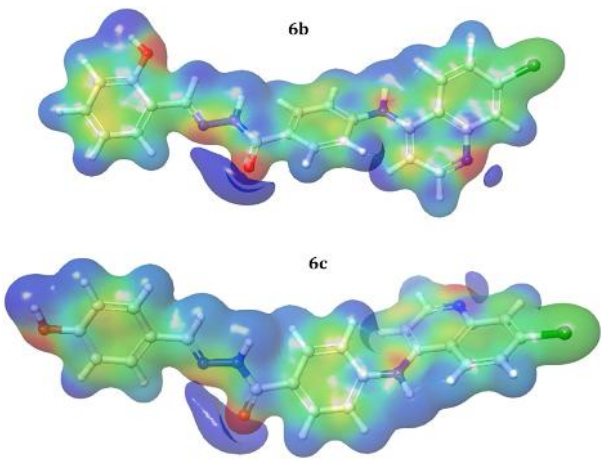


Fig. 19 The molecular electrostatic potential map for compounds **6b** and **6c**.

This journal is © The Royal Society of Chemistry 2024

Table 9 Computed ADMET properties of the synthesized molecules (**6a–6j**)

Comp.	MW	DHB	AHB	QP log $P_{o/w}$	QP log BB	QP log HERG	QP P_{Caco}
6a	400.866	2	4	5.529	−0.751	−7.717	1069.586
6b	416.866	3	4.75	4.743	−1.413	−7.632	344.65
6c	416.866	3	4.75	4.862	−1.378	−7.826	393.135
6d	414.893	2	4	5.751	−0.785	−7.585	1053.718
6e	443.935	2	5	5.969	−0.915	−7.672	989.702
6f	430.893	2	4.75	5.658	−0.848	−7.668	1068.846
6g	460.919	2	5.5	5.855	−0.813	−7.665	1348.724
6h	490.945	2	6.25	6.23	−1.101	−8.026	1057.152
6i	469.757	2	4	6.317	−0.492	−7.38	1017.054
6j	469.757	2	4	6.452	−0.506	−7.547	1009.507

Comp.	QP P_{MDCK}	QP log K_{hsa}	%HOA	CNS	ROF	ROT
6a	1313.383	0.927	100	−1	1	1
6b	386.171	0.704	100	−2	0	1
6c	444.917	0.727	100	−2	0	1
6d	1289.393	1.052	100	−1	1	1
6e	1207.45	1.105	100	−1	1	1
6f	1311.799	0.953	100	−1	1	1
6g	1686.872	0.966	100	−1	1	1
6h	1296.419	1.106	100	−2	1	1
6i	5992.488	1.115	100	0	1	1
6j	6340.43	1.159	100	0	1	1

MM/GBSA

This approach permits resolving the total binding free energy into different components to understand the ligand–receptor complex binding affinity; the contributions of various parameters in the binding free energy are summarized in Table 10, which include van der Waals, coulumbic, steric, lipophilic, and H bond interactions.

Experimental

Molecular dataset: selection and preparation

A diverse dataset of 64 literature reported α-glucosidase inhibitors were selected for ligand-based pharmacophore model generation.[17–22] The reported biological activity IC_{50} value of inhibitors was converted to the negative logarithm of the molar concentration (pIC_{50}) value required to produce

Table 10 MM/GBSA calculation of the synthesized compounds (**6a–6j**)

Comp.	MMGBSA dG bind kcal mol^{-1}	MMGBSA dG bind Hbond kcal mol^{-1}	MMGBSA dG bind vdW kcal mol^{-1}	MMGBSA dG bind coulomb	MMGBSA dG bind covalent	MMGBSA dG bind solv GB
Prime MM/GBSA of α-glucosidase						
6a	−40.45	−5.51	−40.7	−44.68	1.26	69.16
6b	−36.6	−0.58	−48.03	−9.04	3.56	41.37
6c	−44.44	−2.16	−34.93	−17.59	7.3	34.71
6d	−43.59	−1.76	−47.37	−22.38	3.97	49.12
6e	−37.76	−0.47	−49.3	−10.25	3.93	45.23
6f	−41.25	−1.89	−51.06	−11.79	9.43	40.65
6g	−43.43	−0.74	−54.6	−9.34	15.87	42.59
6h	−45.14	−0.52	−53.03	−9.68	4.24	43.91
6i	−48.14	−0.74	−50.56	−23.97	5.24	47.6
6j	−37.07	−0.21	−50	−4.32	2.64	35.97
Prime MM/GBSA of α-amylase						
6a	−28.72	−1.24	−45.53	−15.34	12.2	54.16
6b	−33.41	−2.23	−45.94	−11.64	13.69	44.7
6c	−39.65	−2.18	−52.01	−15.84	12.38	49.89
6d	−26.24	−0.75	−45.96	−9.03	5.21	57.21
6e	−34.14	−1.26	−53.79	−17.22	13.73	59.35
6f	−32.82	−1.27	−49.86	−12.3	13.1	52.02
6g	−40.7	−1.16	−53.72	−13.61	9.08	54.89
6h	−29.17	−1.37	−53.58	−9.01	14.66	55.01
6i	−25.96	−1.34	−44.3	−14.74	5.87	55.39
6j	−38.29	−1.39	−52.41	−7.47	11.79	47.26

50% enzyme inhibition. The dataset was considered over a wide range, *i.e.*, (9.000–6.000); the same enzyme inhibitory experiment was carried out for each molecule to determine the activity (Fig. S1†). Molecules were sketched in the "Maestro" workspace (Maestro 13.2) and converted to 3D and optimization of all molecules was performed using the MacroModel minimization program using the "OPLS4" force field. A screening dataset of quinoline-based benzohydrazide Schiff bases was designed; the OPLS4 force field was used for energy minimization and conformations were generated.

Generation of pharmacophore hypotheses

The "PHASE" module of the Schrödinger suite was utilized for pharmacophore modeling using the energy-optimized molecules *via* the "develop pharmacophore hypothesis" protocol.[26] The data set comprised α-glucosidase inhibitors categorized into active ($pIC_{50} > 8.15$) and inactive ($pIC_{50} < 8.04$) based on the pIC_{50} value. The 4 to 5-point hypothesis model was generated with a minimum of 4 sites and a maximum of 5 site features. Only one alignment per ligand confirmation was retained and flexible ligand superposition using Phase was carried out. Features like hydrogen bond acceptor (A), hydrogen bond donor (D), hydrophobic group (H), ring aromatic group (R), positively charged group (P), and negatively charged group (N) were assigned to molecules using predefined features. A total of 12 pharmacophore hypotheses were generated.

Validation of the pharmacophore model

The Phase module was utilized for the atom-based 3D QSAR validation of the top-ranked pharmacophore hypothesis *via* the partial least squares (PLS) method. The hydrogen bond donor, hydrogen bond acceptor, hydrophobic effect, positive ionic effect, and negative ionic effect were determined using an atom-based QSAR technique, and contour maps were obtained for the above parameters.[27] Phase (v4.0) was employed for the alignment of α-glucosidase inhibitors from the AADRR_1 hypothesis. The data set was randomly divided into a 30% test set and a 70% training set using default setting parameters. The ranking of the generated 3D QSAR model was based on the statistical parameters which include R^2 (training set correlation coefficient), Q^2 (test set correlation coefficient), SD (standard deviation), and Pearson *r* value.

The "hypothesis validation panel" of Phase (v.4.0) was used to perform screening of the designed quinoline-based benzohydrazide Schiff bases along with a decoy set obtained from the Schrödinger suite for the hypothesis AADRR1, and the performance parameters like EF (enrichment factor), BEDROC (Boltzmann enhanced discrimination of receiver operating characteristic), AUC (area under the curve) and ROC (receiver operating characteristics) were calculated to validate the virtual screening accuracy of the developed pharmacophore model.

Chemistry

The melting point was measured in open capillary tubes in the melting point apparatus and was uncorrected. ^{1}H (400 MHz) and ^{13}C NMR (100 MHz) spectra were recorded on Bruker and JEOL spectrometers. All spectra were recorded at room temperature. The chemical shift is quoted in ppm (δ) and coupling constant (J) is reported in Hz. Deuterated dimethyl sulphoxide (DMSO) was used as a solvent for NMR. LCMS spectra were obtained on an LCMS-2010 Shimadzu. IR spectra were recorded on an IR Affinity-1, Shimadzu spectrophotometer. Solvents and chemical reagents that are commercially available were used without further purification. 4,7 Dichloroquinoline was obtained from Acros Organics (New Jersy, USA), and benzocaine and aryl and heteroaryl aldehydes were procured from HiMedia Laboratories Pvt. Ltd. (Mumbai, India). α-Glucosidase assay kit from Biorbyt (Durham, USA) and α-amylase assay kit from Elabscience (USA) were used. Molecular docking and molecular dynamics simulations were performed using Glide, Prime, and Desmond modules of the Schrödinger suite, and Maestro was used for visualizing interactions. GraphPad Prism 8 was used for statistical analysis. Compounds ethyl 4-((7-chloroquinolin-4-yl)amino)benzoate (**3**) and 4-((7-chloroquinolin-4-yl) amino)benzohydrazide (**4**) were synthesized as per the previously reported method.[23]

General procedure for the synthesis of compounds 6a–6j. A mixture of (50 mmol) 4-((7-chloroquinolin-4-yl)amino) benzohydrazide (**4**), appropriate aryl or heteroaryl aldehydes (**5a–5j**) (50 mmol), and 100 ml methanol containing a catalytic amount of glacial acetic acid was stirred at 75 °C for 24 h. The reaction was monitored by TLC for completion. The reaction mixture was cooled to room temperature to obtain the crude product; the precipitate formed was filtered, washed with water, and cold alcohol followed by solvent ether, and dried to obtain (*E*)-*N*′-substituted methylene benzylidene-4-((7-chloroquinolin-4-yl)amino)benzohydrazides (**6a–6j**).

(*E*)-*N*′-Benzylidene-4-((7-chloroquinolin-4-yl)amino)-benzohydrazide (6a). This compound was prepared according to a general procedure and it was obtained as an off-white solid; yield: 49.2%; MP: 262–265 °C. FTIR (KBr, cm^{-1}), 3179.79 (N–H), 2997.51 (Ar–CH), 1669.50 (C═O), 1575.91 (C═C), 1558.55 (C═N). ^{1}H NMR [400 MHz, δ ppm, DMSO-d_6]; 7.22–7.20 (d, 1H, J = 8 Hz, Ar–H), 7.49–7.43 (m, 5H, Ar–H), 7.64–7.61 (m, 1H, J = 9.2 Hz, Ar–H), 7.74–7.72 (d, 2H J = 8 Hz, Ar–H), 7.98–7.95 (m, 3H, Ar–H), 8.47–8.41 (m, 2H, Ar–H). 8.59–8.58 (d, 1H, J = 4 Hz), 9.35 (s, 1H, Ar–NH–Ar), 11.78 (s, 1H, –CONH). ^{13}C NMR [100 MHz, δ ppm, DMSO-d_6]; 103.90, 118.98, 119.93, 124.56, 125.31, 126.95, 127.73, 128.77, 129.07, 134.05, 134.38, 146.51, 149.62, 152.03. Molecular weight; calculated: $C_{23}H_{17}ClN_4O$: 400 found, LCMS; m/z 401(M + 1).

(*E*)-4-((7-Chloroquinolin-4-yl)amino)-*N*′-(4-hydroxy benzylidene)benzohydrazide (6b). This compound was prepared according to a general procedure and it was obtained as an off-white solid; yield: 88.79%, MP: 280–282 °C. FTIR (KBr, cm^{-1});

This journal is © The Royal Society of Chemistry 2024

3530.85 (O–H), 3272.38 (N–H), 2916.49 (Ar–CH), 1653.07 (C═O), 1574.95 (C═C), 1558.55 (C═N). ^{1}H NMR [400 MHz, δ, ppm, DMSO-d_6]; 6.84–6.82 (d, 2H, J = 8 Hz, Ar–H), 7.19–7.17 (d, 1H, J = 8 Hz, Ar–H) 7.62–7.43 (m, 5H, Ar–H) 7.95–7.93 (m, 3H, Ar–H), 8.42–8.35 (m, 2H, Ar–H), 8.58–8.56 (d, 1H, J = 8 Hz, Ar–H), 9.32 (s, 1H, Ar–NH–Ar), 9.88 (s, 1H, OH), 11.56 (s, 1H, –CONH). ^{13}C NMR [100 MHz, δ ppm, DMSO-d_6]; 103.78, 115.55, 117.45, 119.96, 120.05, 124.57, 125.30, 125.38, 127.74, 128.71, 128.97, 134.05, 146.60, 147.61, 149.63, 152.04. Molecular weight; calculated: $C_{23}H_{17}ClN_4O_2$: 416 found, LCMS; m/z 417(M + 1).

(*E*)-4-((7-Chloroquinolin-4-yl)amino)-*N*′-(2-hydroxy benzylidene)benzohydrazide (6c). This compound was prepared according to a general procedure and it was obtained as a white solid; yield: 77.2%, MP: 263–265 °C. FTIR (KBr, cm^{-1}); 3279.13 (N–H), 3312.88 (O–H), 2953.14 (Ar–CH), 1665.60 (C═O), 1575.91 (C═C), 1532.51 (C═N). ^{1}H NMR [400 MHz, δ ppm, DMSO-d_6]; 6.97–6.93 (m, 2H, Ar–H), 7.34–7.24 (m,2H, Ar–H), 7.55–7.50 (m, 3H, Ar–H), 7.66–7.64 (m, 1H, Ar–H), 8.00–7.95 (m, 3H, Ar–H), 8.45–8.42 (d, 1H, J = 8.8 Hz, Ar–H), 8.66–8.60 (m, 2H, Ar–H), 9.42 (s, 1H, Ar–NH–Ar), 11.39 (s, 1H, –CONH), 12.06 (s, 1H, –OH). ^{13}C NMR [100 MHz, δ ppm, DMSO-d_6]; 104.61, 116.94, 119.87, 120.43, 125.19, 125.97, 129.73, 137.17, 144.91, 146.97, 148.39, 152.64, 154.34, 157.96, 172.52. Molecular weight; calculated: $C_{23}H_{17}ClN_4O_2$: 416 found, LCMS; m/z 417(M + 1).

(*E*)-4-((7-chloroquinolin-4-yl)amino)-*N*′-(4-methylbenzylidene)benzohydrazide (6d). This compound was prepared according to a general procedure and it was obtained as a yellow solid; yield: 78.2 MP: 234–237 °C. FTIR (KBr, cm^{-1}); 3298.60 (N–H), 2801.73 (Ar–CH), 1611.59 (C═O), 1569.15 (C═C), 1525.72 (C═N). ^{1}H NMR [400 MHz, δ ppm, DMSO-d_6]; 2.99 (s, 6H, N–$(CH_3)_2$), 6.78–6.76 (d, 1H, J = 8 Hz, Ar–H), 7.22–7.20 (d, 1H, J = 5.6 Hz, Ar–H), 7.50–7.48 (m, 3H, Ar–H), 7.655–7.651 (m, 2H, Ar–H), 7.98–7.96 (m, 4H, Ar–H), 8.33(s, 1H, Ar–H), 8.45–8.43 (d, 1H, Ar–H), 8.60–8.59 (d, 1H, Ar–H), 9.38 (s, 1H, Ar–NH–Ar), 11.54 (s, 1H, –CO–NH). ^{13}C NMR [100 MHz, δ ppm, DMSO-d_6]; 49.13, 104.23, 112.33, 120.64, 125.15, 125.88, 128.31, 128.90, 129.52, 147.17, 148.70, 150.18, 152.63, 162.59. Molecular weight; calculated: $C_{25}H_{22}ClN_5O$: 443 found, LCMS; m/z 444(M + 1).

(*E*)-4-((7-chloroquinolin-4-yl)amino)-*N*′-(4-(dimethylamino)-benzylidene)benzohydrazide (6e). This compound was prepared according to a general procedure and it was obtained as a white solid; yield: 66.6%, MP: 241–243 °C. FTIR (KBr, cm^{-1}); 3259.84 (N–H), 2967.34 (Ar–CH), 1679.11 (C═O), 1573.98 (C═C), 1537.33 (C═N). ^{1}H NMR [400 MHz, δ ppm, DMSO-d_6]: 2.35 (s, 3H, –CH_3), 7.19–7.18 (d, 1H, J = 4 Hz, Ar–H), 7.28–7.26 (d, 2H, J = 8 Hz, Ar–H), 7.47–7.45 (d, 2H, J = 8 Hz, Ar–H), 7.63–7.60 (m, 4H, Ar–H), 7.95–7.94 (m, 4H, Ar–H), 8.43–8.41 (d, 2H, J = 9.2 Hz, Ar–H), 8.58–8.56 (d, 1H, J = 5.2 Hz, Ar–H). ^{13}C NMR [100 MHz, δ ppm, DMSO-d_6]: 20.96, 103.77, 118.94, 119.97, 124.60, 125.25, 126.93, 127.66, 129.05, 129.37, 131.75, 134.03, 139.65, 146.67, 149.60, 151.97. Molecular weight; calculated: $C_{24}H_{19}ClN_4O$: 414 found, LCMS; m/z 411(M + 1).

(*E*)-4-((7-Chloroquinolin-4-yl)amino)-*N*′-(4-methoxybenzylidene)benzohydrazide (6f). This compound was prepared according to a general procedure and it was obtained as an off-white solid; yield: 78.8%; MP: 233–250 °C. FTIR (KBr, cm^{-1}); 3179.79 (N–H), 3060.20 (Ar–CH), 1649.21 (C═O), 1576.87 (C═C), 1529.62 (C═N). ^{1}H NMR [400 MHz, δ ppm, DMSO-d_6]: 3.80 (s, 3H, –OCH_3), 7.03–7.01 (d, 2H, J = 8.4 Hz, Ar–H), 7.19–7.18 (d, 1H, J = 5.2 Hz, Ar–H), 7.47–7.45 (d, 2H, J = 8.4 Hz, Ar–H), 7.69–7.59 (m, 4H, Ar–H), 7.94 (t, 2H, Ar–H), 8.42–8.40 (d, 2H, J = 9.2 Hz, Ar–H), 8.58–8.57 (d, 1H, J = 5.2, Ar–H), 9.32 (s, 1H, Ar–NH–Ar), 11.64 (s, 1H, –CONH). ^{13}C NMR [100 MHz, δ ppm, DMSO-d_6]: 55.25, 103.83, 114.30, 118.92, 120.0, 124.57, 125.31, 126.96, 127.73, 128.56, 129.01, 134.05, 146.58, 147.17, 149.63, 152.04, 160.73. Molecular weight; calculated: $C_{24}H_{19}ClN_4O_2$: 430 found, LCMS; m/z 431(M + 1).

(*E*)-4-((7-Chloroquinolin-4-yl)amino)-*N*′-(3,4-dimethoxy benzylidene)benzohydrazide (6g). This compound was prepared according to a general procedure and it was obtained as an off-white solid; yield: 72.10%, MP: 165–167 °C. FTIR (KBr, cm^{-1}); 3275.27 (N–H), 3126.74 (Ar–CH), 1670.43 (C═O), 1572.05 (C═C), 1532.51 (C═N). ^{1}H NMR [400 MHz, δ ppm, DMSO-d_6]; 3.81–3.80 (d, 6H, J = 4 Hz, –OCH_3), 7.03–7.01 (d, 1H, J = 8 Hz, Ar–H), 7.13–7.11 (d, 1H, J = 8 Hz, Ar–H), 7.19–7.18 (d, 1H, J = 4 Hz, Ar–H), 7.40–7.34 (m, 2H, Ar–H), 7.49–7.45 (m, 1H, Ar–H), 7.62–7.59 (m, 1H, Ar–H), 7.86–7.84 (d, 1H, J = 8 Hz, Ar–H), 7.96–7.94 (m, 2H, Ar–H), 8.42–8.40 (m, 2H, Ar–H), 8.58–8.56 (m, 1H, Ar–H), 9.33 (s, 1H, Ar–NH–Ar), 11.65 (s, 1H, –CONH). ^{13}C NMR [100 MHz, δ ppm, DMSO-d_6]; 55.56, 103.82, 108.26, 111.51, 118.94, 120.03, 120.24, 121.74, 124.58, 125.33, 127.56, 127.75, 128.31, 129.03, 134.07, 143.94, 146.60, 147.54, 149.06, 149.64, 150.66, 152.04. Molecular weight; calculated: $C_{25}H_{21}ClN_4O_3$: 460 found, LCMS; m/z 461(M + 1).

(*E*)-4-((7-Chloroquinolin-4-yl)amino)-*N*′-(3,4,5-trimethoxybenzylidene)benzohydrazide (6h). This compound was prepared according to a general procedure and it was obtained as an off-white solid; yield: 66.2%, MP: 242–245 °C. FTIR (KBr, cm^{-1}); 3179.79 (N–H), 2997.51 (Ar–CH), 1671.39 (C═O), 1576.87 (C═C), 1534.44 (C═N). ^{1}H NMR [400 MHz, δ ppm, DMSO-d_6]; 3.70 (s, 3H, –OCH_3), 3.84 (s, 6H, –$(OCH_3)_2$), 7.01 (S, 1H, Ar–H), 7.20–7.18 (d, 1H, J = 5.2 Hz, Ar–H), 7.48–7.46 (d, 2H, J = 8.4 Hz, Ar–H), 7.62–7.60 (m, 2H, Ar–H), 7.96–7.94 (m, 2H, Ar–H), 8.42–8.40 (m, 2H, Ar–H), 8.58–8.57 (d, 1H, J = 5.2 Hz, Ar–H), 9.33 (s, 1H, Ar–NH–Ar), 11.76 (s, 1H, –CONH). ^{13}C NMR [100 MHz, δ ppm, DMSO-d_6]; 103.85, 104.21, 118.92, 119.95, 124.56, 125.31, 127.73, 129.08, 129.90, 146.54, 149.62, 152.02, 153.15. Molecular weight; calculated: $C_{25}H_{21}ClN_4O_3$: 490 found, LCMS; m/z 489(M + 1).

(*E*)-4-((7-Chloroquinolin-4-yl)amino)-*N*′-(2,4-dichloro benzylidene)benzohydrazide (6i). This compound was prepared according to a general procedure and it was obtained as an off-white solid; yield: 86.6%, MP: 247–250 °C. FTIR (KBr, cm^{-1}); 3099.74 (N–H), 3001.37 (Ar–CH), 1678.14 (C═O), 1575.91 (C═C), 1533.47 (C═N). ^{1}H NMR [400 MHz, δ ppm, DMSO-d_6]; 7.25–7.24 (d,1H, J = 5.2 Hz, Ar–H), 7.54–7.50 (m, 3H, Ar–H), 7.66–7.63 (m, 1H, Ar–H), 7.756–7.751 (d, 1H, J

= 2 Hz, Ar–H), 8.04–7.98 (m, 4H, Ar–H), 8.44–8.42 (d, 1H, J = 9.2 Hz, Ar–H), 8.62–8.60 (d, 1H, J = 9.2 Hz, Ar–H), 8.84 (s, 1H, Ar–H), 9.41 (s, 1H, Ar–NH–Ar), 12.12 (s, 1H, –CONH). ^{13}C NMR [100 MHz, δ ppm, DMSO-d_6]; 104.60, 119.53, 120.16, 125.0, 125.96, 127.30, 128.51, 129.68, 131.25, 134.39, 134.55, 135.48, 142.51, 144.91, 146.95, 150.0, 152.52, 162.81. Molecular weight; calculated: $C_{23}H_{15}C_{l3}N_4O$: 469 found, LCMS; m/z 470(M + 1).

(*E*)-4-((7-Chloroquinolin-4-yl)amino)-*N*′-(3,4-dichlorobenzylidene)benzohydrazide (6j). This compound was prepared according to a general procedure and it was obtained as an off-white solid; yield: 53.3% MP: 253–256 °C. FTIR (KBr, cm^{-1}); 3250.91 (N–H), 3029.34 (Ar–CH), 1663.07 (C═O), 1575.91 (C═C), 1533.47 (C═N). ^{1}H NMR [400 MHz, δ ppm, DMSO-d_6]; 7.16–7.14 (d, 1H, J = 8 Hz, Ar–H), 7.52–7.24 (d, 1H, Ar–H), 7.43–7.41 (m, 1H), 7.51–7.49 (d, 1H, J = 8 Hz, Ar–H), 7.68–7.61 (m, 2H, Ar–H), 7.89–7.87 (m, 1H, Ar–H), 7.97–7.95 (m, 1H, Ar–H), 8.44–8.41 (m, 1H, Ar–H), 8.57–8.56 (m, 1H, Ar–H), 8.62–8.60 (m, 1H, Ar–H), 9.31 (s, 1H, Ar–H), 9.41 (s, 1H, Ar–NH–Ar), 9.73 (S, 1H), 12.05 (s, 1H, –CO–NH). ^{13}C NMR [100 MHz, δ ppm, DMSO-d_6]; 103.97, 119.35, 120.78, 125.13, 125.83, 128.27, 128.87, 129.79, 134.60, 147.28, 150.15, 152.61, 165.97. Molecular weight; calculated: $C_{23}H_{15}Cl_3N_4O$: 469 found, LCMS; m/z 470(M + 1).

α-Glucosidase inhibition assay

The α-glucosidase enzyme inhibitory activity was determined using a previously reported method with little modification.[24] An enzyme solution was prepared in potassium phosphate buffer (pH 6.8), and the synthesized compounds (**6a–6j**) were dissolved in DMSO solution (5 mg mL^{-1}) and were reconstituted in 100 μL of 100 mM potassium phosphate buffer. 10 μL of test sample was added in a 96-well microplate and incubated with 50 μL of α-glucosidase enzyme for 5 min; later a substrate (5 mM, *p*-nitrophenyl-α-D-glucopyranoside in the same potassium phosphate buffer) was added. The spectrophotometrical measurement of released *p*-nitrophenol at 405 nm was analyzed after 5 min incubation with the substrate. DMSO was used as the control and acarbose was used as the standard drug for comparison. The percentage inhibition for each test sample was calculated using the formula,

% inhibition = [(Abs of control − Abs of the test)/Abs Control]

α-Amylase inhibition assay

The α-amylase enzyme inhibitory activity was determined using a previously reported procedure.[15] The reaction mixture consists of the synthesized test compounds **6a–6j** dissolved in DMSO and methanol making up %inhibition = [(Abs of control − Abs of the test)/Abs Control]the remaining volume; acarbose was used as a standard comparative drug and methanol as blank. The reaction mixture was pre-incubated for 15 minutes at 37 degrees Celsius. Then, each tube was filled with a (1%) starch solution and incubated for 25 minutes at 37 degrees Celsius. To stop the reaction, 600 μL of DNSA reagent was added to each tube which was incubated at 100 °C for 8 minutes. The tubes were cooled by immersing them in a cold water bath. Finally, a final dilution (1 mL) was made in each tube to make up the volume using Millipore water.

The absorbance was measured using a 549 nm spectrophotometer. The percentage inhibition was calculated using the formula

% inhibition = [(Abs of control − Abs of the test)/Abs Control]

α-Glucosidase enzyme kinetic study

The most active compounds among the series, compounds **6b** and **6c**, were studied for their inhibitory activity by enzyme kinetic studies against α-glucosidase enzyme; *p*-nitrophenyl-α-D-glucopyranoside with different concentrations (0–16 μM) was used as the substrate in the presence and absence of samples **6b** and **6c** at different concentrations of 0, 4.84, 9.68 and 19.37 and 0, 3.23, 6.47 and 12.95, respectively. The type of inhibition was recognized by plotting the Lineweaver–Burk plot, and the Michaelis–Menten constant (K_m) was obtained using the plot between the reciprocal of (1/[S]) substrate concentrations and reciprocal of the rate of enzyme (1/V) for different concentrations of inhibitors, also the K_m *vs.* the different concentrations of inhibitors **6b** and **6c** was plotted.[28,29]

Cytotoxicity studies

To evaluate the toxicity of a synthesized compound, MTT (3-(4,5-dimethylthiazo-2-yl)-2,5-diphenyl-tetrazolium bromide) assay was performed on a normal mouse L929 cell line as per previously reported literature.[30]

Molecular docking studies

Ligand preparation. All the structure of the synthesized ligands was sketched using Maestro 13.2 (Schrödinger, 2022-4). The LigPrep panel of the Schrödinger suite was used for preparing ligands by adding polar hydrogens, and adding ionization states using the Epik module; torsional flexibility was given to obtain a better complimentary pose. Finally, the optimized potential for liquid simulation (OPLS4) was used for energy minimization.

Homology modeling and protein preparation. The three-dimensional structure (3D) of α-glucosidase for *S. cerevisiae* was built using homology modeling *via* the Prime module of the Schrödinger suite.[31,32] The Fasta sequence was queried from the UniProt protein resource database (**https://www.uniprot.org/**), using the accession code P53341. A similarity search was carried out using BLAST; PDB ID 3A47 was obtained as the template protein structure, and a homology model of α-glucosidase was built and assessed for the protein reliability report and Ramachandran plot. Further, this protein was prepared by adding polar hydrogens, assigning bond orders, creating zero bond orders to metals, creating disulfide bonds, adding terminal oxygen to protein chains, converting

 This journal is © The Royal Society of Chemistry 2024

selenomethionines to methionines, filling missing loops using Prime, filling missing side chains, and capping terminals of the protein and finally the Epik module was used to generate het states at pH 7.4. Further optimization of the protein structure was carried out using sample water orientations; altered hydrogen species within the protein was minimized and finally optimized using the PROPKA module, and lastly, the whole protein structure was energy minimized using the optimized potential for the liquid simulation (OPLS4) force field.[33]

Binding site detection and grid generation

A site map tool was utilized for identifying the binding sites for the prepared α-glucosidase protein, site1 was selected as binding sites based on the site score and volume of the binding pocket, the active site residues obtained were found to be ASN 314, ARG 443, TYR 344, ASP 429, ARG 439, TYR 313, ASN 412, ILE 415, GLU 276, VAL 277, ALA 278, HIE 279, ASP 408, LYS 155, SER 156, PHE 157, PHE 158, GLY 159, GLY 160, ILE 416, LYS 418, SER 419, PHE 420, GLN 238, GLU 426, HIE 239, PHE 298, PHE 300, VAL 303, GLU 304, VAL 305, GLY 306, THR 307, SER 308, PRO 309, PHE 310, PHE 311, ARG 312, TRP 57, VAL 316, PRO 317, PHE 318, GLN 322, ASP 68, MET 69, TYR 71, ALA 326, HIE 111, HIS 245, HIE 348, ASH 214, ASN 347, ASP 349, GLN 350, PHE 117, ARG 212, THR 215, ALA 216, GLY 217, LEU 218, SER 228, PRO 229, PHE 231, ASP 232, THR 234, SER 235, LYS 236, LEU 237, PRO 240, ASN 241, TRP 242, ASN 246. Hence the grid was generated by selecting these amino acid residues as the centroid of the grid using the grid generation panel of the Glide module of the Schrödinger suite. Similarly, the α-amylase protein (PDB ID: 4 W93) was prepared and refined using the protein preparation workflow of the Schrödinger suite. The grid was generated at the cocrystal (montbretin A) site, using a grid generation panel, and was further utilised for the molecular docking studies.

Molecular docking. The extra precision mode (XP) from the Glide module was utilized for docking studies.[34,35] The Glide XP mode can semi-quantitatively rank the ligands that bind to the specific conformation of protein receptors and helps in scoring these ligands considering the penalties which include steric clashes, solvent exposure, *etc.* Here we docked the synthesized compounds (**6a–6j**) into the binding pockets of α-glucosidase and α-amylase. Acarbose was used as a standard for the validation of the docking protocol.

Molecular dynamic (MD) simulations

MD simulation studies were carried out to predict the stability of the overall protein–ligand complex in the binding pocket of α-amylase and α-glucosidase enzyme throughout 200 ns using the Desmond module of the Schrödinger suite.[36] Prior to the setting up of a system for simulation, the protein–ligand complex was minimized using the OPLS4 force field, then the TIP3P solvation model was used, and the box boundary was set up as orthorhombic to specify the shape and size of units repeating for the 10 Å buffer region between the complex atoms and box boundary. Na^+/Cl^- counter ions were used to neutralize the system. Further, the system was subjected to 300 K temperature and pressure of 1.01325 bar for 200 ns using an NPT ensemble. Finally, MD trajectories were recorded and the RMSD, RMSF, hydrogen bonding contacts, and radius of gyration in the protein–ligand complex were analyzed using simulation interaction diagrams.[35]

MM/GBSA calculations

The binding pose of all (**6a–6j**) ligands into the binding pocket of α-amylase and α-glucosidase enzyme were evaluated using the molecular mechanics/generalized Born surface area (MM/GBSA) method developed by Kollman *et al.*;[37] here calculations are based on the sum of the gas-phase molecular mechanics interaction energy between the ligand and protein (ΔE_{MM}), the change in conformational entropy associated with ligand binding ($-T\Delta S$), and the solvation free energy (ΔG_{solv}) as shown in following equation.[38]

$$\Delta G_{bind} = \Delta E_{MM} + \Delta G_{solv} - T\Delta S$$

Density functional theory (DFT) studies

Geometric optimization. The most stable molecular shape can be anticipated by minimizing the system's energy, allowing the calculation of bond lengths, angles, and dihedral angles. Density functional theory (DFT) is a computerized approach used in quantum chemistry and materials science to investigate the electronic structure and characteristics of molecules. All the synthesized molecules were subjected to geometric optimization through the B3LYP (Becke's three-parameter hybrid functional, Lee–Yang–Parr correlation functional) functional and 6-31 G (d,p) basis set, using the Jaguar module of Schrödinger software. Also, an electrostatic potential map (ESP) was generated for all the synthesized molecules; quantum chemical parameters such as the energy gap (ΔE_{GAP}), dipole moment (μ), hardness (η), and local softness (σ) can be calculated using the (frontier molecular orbitals) highest occupied molecular orbital (E_{HOMO}), lowest unoccupied molecular orbital (E_{LUMO}) and following equations.[39,40]

$$\Delta E_{GAP} = E_{LUMO} - E_{HOMO} \quad (1)$$

$$\eta = \frac{E_{LUMO} - E_{HOMO}}{2} \quad (2)$$

$$\sigma = \frac{1}{\eta} \quad (3)$$

$$\mu = \frac{E_{HOMO} - E_{LUMO}}{2} \quad (4)$$

$$\omega = \frac{\mu^2}{2\eta} \quad (5)$$

ADMET predictions

ADMET *i.e.* adsorption, distribution, metabolism, excretion, and toxicity parameters are crucial in the early stage of drug discovery. The ADMET parameters of the synthesized hits were predicted using the Qikprop module of the Schrödinger suite.[41]

Conclusion

This study utilized a combination of computational and rational drug design methods to pinpoint potential α-glucosidase inhibitors for their anti-diabetic properties. Starting with a quinoline-based benzohydrazide Schiff base moiety from the existing literature, we created a molecular library. A pharmacophore model was developed using 64 molecules, split into a training set of 47 and a test set of 17, to identify molecules with defined α-glucosidase inhibitory activity obtained from the literature. Among 12 hypothesis models, the AADRR_1 model was chosen for further screening of our designed ligand library. A 3D QSAR model was then constructed based on the active compounds from the pharmacophore model. The top 10 ligands identified through pharmacophore screening were synthesized and characterized using various spectroscopic methods. These compounds were evaluated for their anti-diabetic effects by inhibiting α-glucosidase and α-amylase enzymes. Compounds **6b** and **6c** showed significant inhibitory effects on α-glucosidase (IC_{50} values of 19.37 ± 0.96 μM and 12.95 ± 2.35 μM, respectively) and α-amylase (IC_{50} values of 29.36 ± 3.24 μM for **6b** and 33.04 ± 1.83 μM for **6c**). MTT assays on normal mouse fibroblast L929 cell lines revealed no toxicity among synthesized compounds (**6a–6j**). Molecular docking and MD simulations over 200 ns were conducted to assess binding affinity and stability. Energetics were evaluated using MM/GBSA and DFT methods. Based on these findings, compounds **6b** and **6c** were identified as lead candidates for further optimization toward developing novel antidiabetic agents.

Data availability

All data are included in the manuscript.

Author contributions

Shankar G. Alegaon: conceptualisation, methodology and supervision; Shriram D. Ranade: synthesis, characterization, computational studies and manuscript writing; Shankar Gharge and Nayeem Khatib: α-amylase and α-glucosidase inhibition assay; Rohini S. Kavalapure: support in biological evaluation.

Conflicts of interest

There are no conflicts to declare.

Acknowledgements

This work was supported by the Department of Pharmaceutical Chemistry, KLE College of Pharmacy, KLE Academy of Higher Education and Research, Belagavi. NMR was carried out at the Sophisticated Analytical Instrument Facility (SAIF) Karnataka University Dharwad.

References

1 U. Galicia-Garcia, A. Benito-Vicente, S. Jebari, A. Larrea-Seba, H. Siddiqi, K. B. Uribe and C. Martin, Pathophysiology of type 2 diabetes mellitus, *Int. J. Mol. Sci.*, 2020, **21**(17), 6275.
2 IDF Diabetes Atlas, International Diabetes Federation, Brussels, Belgium, 10th edn, 2021, **https://www.diabetesatlas.org** (Accessed 2024).
3 S. Padhi, A. K. Nayak and A. Behera, Type II diabetes mellitus: a review on recent drug-based therapeutics, *Biomed. Pharmacother.*, 2020, **131**, 110708.
4 A. Kanwal, N. Kanwar, S. Bharati, P. Srivastava, S. P. Singh and S. Amar, Exploring new drug targets for type 2 diabetes: success, challenges and opportunities, *Biomedicines*, 2022, **10**(2), 331.
5 W. Benalla, S. Bellahcen and M. Bnouham, Antidiabetic medicinal plants as a source of alpha glucosidase inhibitors, *Curr. Diabetes Rev.*, 2010, **6**(4), 247–254.
6 N. Kaur, V. Kumar, S. K. Nayak, P. Wadhwa, P. Kaur and S. K. Sahu, Alpha-amylase as a molecular target for the treatment of diabetes mellitus: A comprehensive review, *Chem. Biol. Drug Des.*, 2021, **98**(4), 539–560.
7 A. S. Dabhi, N. R. Bhatt and M. J. Shah, Voglibose: an alpha glucosidase inhibitor, *J. Clin. Diagn. Res.*, 2013, **7**(12), 3023.
8 H. Sugihara, M. Nagao, T. Harada, Y. Nakajima, K. Tanimura-Inagaki, F. Okajima and S. Oikawa, Comparison of three α-glucosidase inhibitors for glycemic control and body weight reduction in Japanese patients with obese type 2 diabetes, *J. Diabetes Invest.*, 2014, **5**(2), 206–212.
9 S. Roscales and J. Plumet, Biosynthesis and biological activity of carbasugars, *Int. J. Carbohydr. Chem.*, 2016, 4760548.
10 P. Yadav and K. Shah, Quinolines, a perpetual, multipurpose scaffold in medicinal chemistry, *Bioorg. Chem.*, 2021, **109**, 104639.
11 O. F. Elebiju, O. O. Ajani, G. O. Oduselu, T. A. Ogunnupebi and E. Adebiyi, Recent advances in functionalized quinoline scaffolds and hybrids—Exceptional pharmacophore in therapeutic medicine, *Front. Chem.*, 2023, **10**, 1074331.
12 N. Kerru, L. Gummidi, S. Maddila, K. K. Gangu and S. B. Jonnalagadda, A review on recent advances in nitrogen-containing molecules and their biological applications, *Molecules*, 2020, **25**(8), 1909.
13 M. Ilakiyalakshmi and A. A. Napoleon, Review on recent development of quinoline for anticancer activities, *Arabian J. Chem.*, 2022, **15**(11), 104168.
14 L. Kumari, A. Mazumder, D. Pandey, M. S. Yar, R. Kumar, R. Mazumder and S. Gupta, Synthesis and biological potentials

 This journal is © The Royal Society of Chemistry 2024

of quinoline analogs: A review of the literature, *Mini-Rev. Org. Chem.*, 2019, **16**(7), 653–688.
15 T. Noreen, M. Taha, S. Imra, S. Chigurupati, F. Rahim, M. Selvaraj and M. Ali, Synthesis of alpha-amylase inhibitors based on privileged indole scaffold, *Bioorg. Chem.*, 2017, **72**, 248–255.
16 M. Taha, M. T. Javid, S. Imran, M. Selvaraj, S. Chigurupati, H. Ullah and K. M. Khan, Synthesis and study of the α-amylase inhibitory potential of thiadiazole quinoline derivatives, *Bioorg. Chem.*, 2017, **74**, 179–186.
17 M. Taha, N. H. Ismail, S. Imran, A. Wadood, F. Rahim, M. Ali and A. U. Rehman, Novel quinoline derivatives as potent in vitro α-glucosidase inhibitors: in silico studies and SAR predictions, *MedChemComm*, 2015, **6**(10), 1826–1836.
18 M. Taha, S. Sultan, S. Imran, F. Rahim, K. Zaman, A. Wadood and K. M. Khan, Synthesis of quinoline derivatives as diabetic II inhibitors and molecular docking studies, *Bioorg. Med. Chem.*, 2019, **27**(18), 4081–4088.
19 R. Forozan, M. K. Ghomi, A. Iraji, M. N. Montazer, M. Noori, N. Dastyafteh and M. Mahdavi, Synthesis, in vitro inhibitor screening, structure-activity relationship, and molecular dynamic simulation studies of novel thioquinoline derivatives as potent α-glucosidase inhibitors, *Sci. Rep.*, 2023, **13**(1), 7819.
20 N. Cele, P. Awolade, P. Seboletswe, K. Olofinsan, M. S. Islam and P. Singh, α-glucosidase and α-amylase inhibitory potentials of quinoline–1, 3, 4-oxadiazole conjugates bearing 1, 2, 3-triazole with antioxidant activity, kinetic studies, and computational validation, *Pharmaceuticals*, 2022, **15**(8), 1035.
21 M. Al-Ghorbani, O. Alharbi, A. B. Al-Odayni and N. A. Abduh, Quinoline-and Isoindoline-Integrated Polycyclic Compounds as Antioxidant, and Antidiabetic Agents Targeting the Dual Inhibition of α-Glycosidase and α-amylase Enzymes, *Pharmaceuticals*, 2023, **16**(9), 1222.
22 M. Noori, M. Rastak, M. Halimi, M. K. Ghomi, M. Mollazadeh, M. Mohammadi-Khanaposhtani and M. Mahdavi, Design, synthesis, in vitro, and in silico enzymatic evaluations of thieno [2, 3-b] quinoline-hydrazones as novel inhibitors for α-glucosidase, *Bioorg. Chem.*, 2022, **127**, 105996.
23 S. D. Ranade, S. G. Alegaon, U. Venkatasubramanian, A. S. Priya, R. S. Kavalapure, J. Chand and D. Vinod, Design, synthesis, molecular dynamics simulation, MM/GBSA studies and kinesin spindle protein inhibitory evaluation of some 4-aminoquinoline hybrids, *Comput. Biol. Chem.*, 2023, **105**, 107881.
24 H. Yousuf, S. Shamim, K. M. Khan, S. Chigurupati, S. Hameed, M. N. Khan and M. Arfeen, Dihydropyridines as potential α-amylase and α-glucosidase inhibitors: synthesis, in vitro and in silico studies, *Bioorg. Chem.*, 2020, **96**, 103581.
25 S. L. Dixon, A. M. Smondyrev and S. N. Rao, PHASE: a novel approach to pharmacophore modeling and 3D database searching, *Chem. Biol. Drug Des.*, 2006, **67**(5), 370–372.
26 P. Chapdelaine, R. R. Tremblay and J. Y. Dube, P-Nitrophenol-alpha-D-glucopyranoside as a substrate for the measurement of maltase activity in human semen, *Clin. Chem.*, 1978, **24**(2), 208–211.
27 H. Nikookar, M. Mohammadi-Khanaposhtani, S. Imanparast, M. A. Faramarzi, P. R. Ranjbar, M. Mahdavi and B. Larijani, Design, synthesis and in vitro α-glucosidase inhibition of novel dihydropyrano [3, 2-c] quinoline derivatives as potential anti-diabetic agents, *Bioorg. Chem.*, 2018, **77**, 280–286.
28 E. U. Mughal, M. B. Hawsawi, N. Naeem, A. Hassan, M. S. Alluhaibi, S. W. Shah, Y. Nazir, A. Sadiq, H. A. Alrafai and S. A. Ahmed, Exploring Fluorine-Substituted Piperidines as Potential Therapeutics for Diabetes Mellitus and Alzheimer's Diseases, *Eur. J. Med. Chem.*, 2024, **21**, s.
29 R. Mehmood, E. U. Mughal, E. B. Elkaeed, R. J. Obaid, Y. Nazir, H. A. Al-Ghulikah, N. Naeem, M. M. Al-Rooqi, S. A. Ahmed, S. W. Shah and A. Sadiq, Synthesis of novel 2, 3-dihydro-1, 5-benzothiazepines as α-glucosidase inhibitors: In vitro, in vivo, kinetic, SAR, molecular docking, and QSAR studies, *ACS Omega*, 2022, **7**(34), 30215–30232.
30 T. Mosmann, Rapid colorimetric assay for cellular growth and survival: application to proliferation and cytotoxicity assays, *J. Immunol. Methods*, 1983, **65**(1–2), 55–63.
31 M. P. Jacobson, D. L. Pincus, C. S. Rapp, T. J. Day, B. Honig, D. E. Shaw and R. A. Friesner, A hierarchical approach to all-atom protein loop prediction, *Proteins: Struct., Funct., Bioinf.*, 2004, **55**(2), 351–367.
32 M. P. Jacobson, R. A. Friesner, Z. Xiang and B. Honig, On the role of crystal packing forces in determining protein sidechain conformations, *J. Mol. Biol.*, 2002, **320**, 597–608.
33 Y. Yang, Y. Yao, M. P. Repasky, K. Leswing, R. Abel, B. K. Shoichet and S. V. Jerome, Efficient exploration of chemical space with docking and deep learning, *J. Chem. Theory Comput.*, 2021, **17**(11), 7106–7119.
34 T. A. Halgren, R. B. Murphy, R. A. Friesner, H. S. Beard, L. L. Frye, W. T. Pollard and J. L. Banks, Glide: a new approach for rapid, accurate docking and scoring. 2. Enrichment factors in database screening, *J. Med. Chem.*, 2004, **47**(7), 1750–1759.
35 K. J. Bowers, *International Conference for High Performance Computing, Networking, Storage and Analysis, Scalable algorithms for molecular dynamics simulations on commodity clusters*, Tampa Florida, November 2006.
36 W. L. Jorgensen, D. S. Maxwell and J. Tirado-Rives, Development and testing of the OPLS all-atom force field on conformational energetics and properties of organic liquids, *J. Am. Chem. Soc.*, 1996, **118**(45), 11225–11236.
37 W. Wang and P. A. Kollman, Free energy calculations on dimer stability of the HIV protease using molecular dynamics and a continuum solvent model, *J. Mol. Biol.*, 2000, **303**(4), 567–582.
38 E. Wang, H. Sun, J. Wang, Z. Wang, H. Liu, J. Z. Zhang and T. Hou, End-point binding free energy calculation with MM/

PBSA and MM/GBSA: strategies and applications in drug design, *Chem. Rev.*, 2019, **119**(16), 9478–9508.
39 M. Elkolli, N. Chafai, S. Chafaa, I. Kadi, C. Bensouici and A. Hellal, New phosphinic and phosphonic acids: Synthesis, antidiabetic, anti-Alzheimer, antioxidant activity, DFT study, and SARS-CoV-2 inhibition, *J. Mol. Struct.*, 2022, **1268**, 133701.
40 A. Ahmed, A. Saeed, S. A. Ejaz, M. Aziz, M. Z. Hashmi, P. A. Channar and H. R. El-Seedi, Novel adamantyl clubbed iminothiazolidinones as promising elastase inhibitors: design, synthesis, molecular docking, ADMET and DFT studies, *RSC Adv.*, 2022, **12**(19), 11974–11991.
41 *Schrödinger Release 2024-1: QikProp*, Schrödinger, LLC, New York, NY, 2024.

 This journal is © The Royal Society of Chemistry 2024

Journal of Molecular Structure 1311 (2024) 138359

Contents lists available at ScienceDirect

Journal of Molecular Structure

journal homepage: www.elsevier.com/locate/molstr

Design, synthesis, molecular dynamic simulation, DFT analysis, computational pharmacology and decoding the antidiabetic molecular mechanism of sulphonamide-thiazolidin-4-one hybrids

Shriram D. Ranade [a], Shankar G. Alegaon [a,*], Nayeem A. Khatib [b], Shankar Gharge [a], Rohini S. Kavalapure [a], B.R. Prashantha Kumar [c]

[a] Department of Pharmaceutical Chemistry, KLE College of Pharmacy, Belagavi, KLE Academy of Higher education and Research, Belagavi 590 010, Karnataka, India
[b] Department of Pharmacology, KLE College of Pharmacy, Belagavi, KLE Academy of Higher education and Research, Belagavi 590 010, Karnataka, India
[c] Department of Pharmaceutical Chemistry, JSS College of Pharmacy, Mysuru, JSS Academy of Higher Education and Research, Mysuru 570015, Karnataka, India

ARTICLE INFO

Keywords:
Benzenesulphonamide-thiazolidin-4-one hybrids
Network pharmacology
M.D Simulation
Density functional theory
PPAR-γ TF assay

ABSTRACT

In search of novel antidiabetic agents, the study was framed to hybridize and synthesize molecules based on scaffolds of benzenesulfonamide and thiazolidine-4-one, efficiently synthesized (**6a**-6h) and structurally characterized by FTIR, ^{1}H NMR ^{13}C NMR and HRMS spectroscopy. The antidiabetic activity was assessed based on α-amylase inhibition, glucose uptake assay and PPAR-γ transcription factor assay. Compound **6b** (4-(2-((E)-5-((Z)-2-hydroxybenzylidene)-4-oxo-2-(phenylimino) thiazolidin-3-yl) ethyl) benzenesulfonamide) demonstrated promising activity toward α-amylase inhibition having IC_{50} value of **29.51±1.35** μg/ml. A glucose uptake assay was performed for compounds **(6a-**6h**)** to assess the capacity of glucose uptake. Among them, Compound **6b** exhibits notable glucose uptake with 88.71% in the yeast cell line. To support the glucose uptake findings of compound **6b**, expression of PPAR-γ transcription factor was measured of compound **6b** as compared to pioglitazone. Furthermore, induced fit docking was carried out to predict the refined pose of synthesized compounds in the α-amylase binding pocket. MD simulation studies confirmed the stability of compound **6b** in the α-amylase binding pocket. Molecules were geometrically optimized by DFT theory using B3LYP 6–31 G (d, p**) basis set, and electronic properties were studied. Network pharmacology analysis for compound **6b** identified key pathways involved in T2DM and postprandial hyperglycemia like PI3K-Akt pathway, Type II diabetes mellitus pathway metabolic pathway, and digestion of dietary carbohydrates pathway. These findings provide better insights into further developing benzenesulfonamide-based thiazolidin-4-one hybrids as antidiabetic agents.

1. Introduction

Type 2 diabetes mellitus (T2DM) is a long-term metabolic condition characterized by the body's reduced response, to insulin and difficulty in utilizing glucose for energy. This leads to levels of sugar in the blood which can result in health issues including cardiovascular problems and neuropathy. The main focus of treating T2DM is to improve insulin sensitivity enhance the body's ability to take up glucose and maintain blood sugar levels [1]. One of the aspects of diabetes management revolves around identifying therapeutic targets that can effectively modulate glucose homeostasis. To achieve these goals medical interventions target areas like insulin receptor signaling, glucose transporter expression and the function of pancreatic beta cells. Medications such, as metformin, sulfonylureas, SGLT 2 inhibitors and GLP 1 receptor agonists, *α-amylase* and *α-glucosidase* inhibitors are used to address these targets with the aim of managing blood sugar levels and reducing the risk of complications associated with T2DM. A noteworthy focus in this regard is the inhibition of alpha-amylase, an enzyme involved in carbohydrate digestion, particularly targeting postprandial hyperglycemia [2,3].

Acarbose acts as an *α-amylase* inhibitor which slowdowns the metabolism and digestion of carbohydrates causing delayed absorption and eventually results in slow glucose release into blood stream, summing up to postprandial glucose control. These postprandial antidiabetic

* Corresponding author at: Department of Pharmaceutical Chemistry, KLE College of Pharmacy, Belagavi, KLE Academy of Higher education and Research, Belagavi 590 010, Karnataka, India.
E-mail addresses: sgalegaon@klepharm.edu, sgalegaon@gmail.com (S.G. Alegaon).

https://doi.org/10.1016/j.molstruc.2024.138359
Received 1 March 2024; Received in revised form 10 April 2024; Accepted 14 April 2024
Available online 16 April 2024
0022-2860/© 2024 Elsevier B.V. All rights reserved.

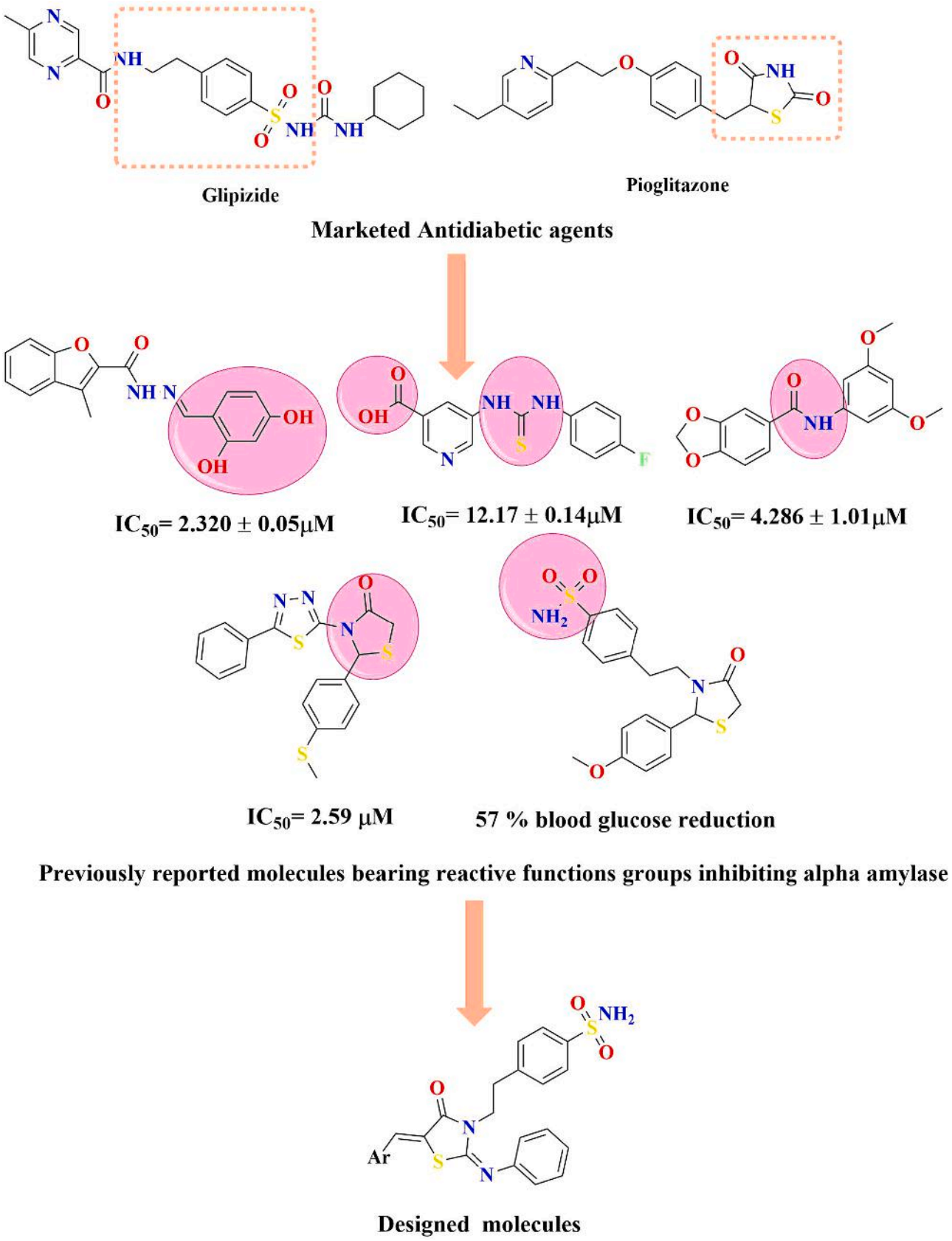


Fig. 1. Design of benzene sulphonamide-thiazolidin-4-one hybrids.

agents in complementary with other antidiabetic medications like metformin, insulin and thiazolidinedione's (TZD's) helps in overall management strategy of T2DM [4].

Recently researchers and academicians around the globe have reported small heterocyclic molecules as inhibitors of *α-amylase* and alpha glucosidase enzyme. TZD's known mainly for their ability to enhance insulin sensitivity have also been reported as inhibitors of *α-amylase* enzyme. This dual action underscores the potential of TZD's past insulin sensitization, by addressing both insulin sensitization and carbohydrate digestion providing newer insights on their therapeutic impact. Many researchers have reported thiazolidinedione's and thaizolidin-4-ones, 1,3 substituted thiazolidinone as *α-amylase* inhibitors such as Rahul Singh and co-workers 2023 reported 2-aryliminothiazolidin-4-one (IC_{60} value: 19.67 ± 0.20 μg/ml) as *α-amylase* inhibitors [5]. Khan and Co-workers 2022 reported thiazolidinone-based indole derivatives (IC_{50} value: 1.80 ± 0.70 μM) as *α-amylase* inhibitors [6]. Saad Fettach and co-workers have 2021 reported benzylidene-thiazolidinediones (IC_{50} value: 18.19 ± 0.11 μM) as *α-amylase* inhibitors [7]. Shoaib Khan and co-workers 2022 reported benzimidazole bearing thiazolidinone derivatives (IC_{50} value: 2.10 ± 0.10 μM) as *α-amylase* inhibitors [8]. The promising *α-amylase* (IC_{50} value: 1.80 ± 0.10 μM) inhibitors were published in 2023 by Aftab et, al [9]. Sulfonylureas are well known for their antidiabetic effect by reducing the elevated blood glucose levels. Marketed molecules like Glipizide, Glimepiride, Gliclazide are basically aryl sulfonylureas majorly differentiated by aryl substitution, where the aryl substitution renders to be lipophilic and urea part shows hydrophilic character. Researchers have explored sulfonylureas by varying substitutions at terminal aryl position [10]. Such as Hassan M. Faidalla 2016 and co-workers 2021 reported fluoropyrazolesulfonylurea derivatives reducing blood plasma glucose levels [11]. Hui-bin Zhang and co-workers 2009 reported substituted benzenesulfonamide derivatives as antidiabetic agents which lowered plasma glucose levels [12]. Ghadeer A. Suaifan and co-workers 2015 reported glycosylated sulfonylureas as antihyperglycemic agents [13]. Ishan I Panchal and co-workers 2018 reported guanidine/sulfonylureas derivatives as antidiabetic agent showing better plasma glucose reduction [14]. Most of the previously reported *α-amylase* inhibitors (Fig. 1) are either class of flavonoids and moieties having poly hydroxy substitutions, terminal carboxylic acid and its isosteres, esters, free primary amine groups, amide linkages [15–18].

Over period of past decade, the rate of drugs failing in the later stage of clinical trials is concurrent, because the assumptions of rational drug design or more selectivity like 'one drug, one gene, one disease' was that, the approach was much safer, selective, more effective drugs arose from designing target selective ligands where undesirable side effects have been removed. However, this hypothesis still facing challenge from last decade. Emerging progress in bioinformatics, polypharmacology, Network Pharmacology in drug discovery has gained attention as multi target approach towards cost effective drug development [19]. Chen, G. and co-workers recently reported synthesis of 1, 3, 4 oxadiazole bearing azaphenols using network pharmacology approach to decipher anticancer activity [20]. Lexian. chen and co-workers reported synthesis and network pharmacology evaluation of 3-(coumarin-3-yl) acrolein derivatives as anticancer agents [21]. Network pharmacology may provide understanding of lead molecule and their interactions with targets, providing better insights in developing antidiabetic agents.

From the above literature review and findings, it is necessary to render structural modifications by altering molecular framework of compounds to attain pharmacological response. Herein we carried out hybridization of benzene sulphonamide moiety with an isostere of carboxylic acid knows as 1, 3 substituted thiazolidinone. (Fig. 1)

2. Experimental

2.1. Method and materials

Melting point was measured in open capillary tubes in melting point apparatus and were uncorrected. 400 MHz- ^{1}H and 100 MHz- ^{13}C NMR spectra were recorder Jeol spectrometer. All spectra were recorded at room temperature. Chemical shift is quoted in ppm (δ) and coupling constant (*J*) are reported in Hz. Mass spectra were obtained on a HRMS-impact HD Bruker. IR spectra were recorded on IR Affinity-1, Shimadzu spectrophotometer Solvents and Chemical reagents that are commercially available were used without further purification. 4-(2-Amino Ethyl) Benzene Sulfonamide form Chemscene (New Jersy, USA), derivatives of aldehydes were procured from HiMedia laboratories Pvt. Ltd. (Mumbai, India). Molecular docking, Molecular Dynamic simulations, Density functional theory calculations were performed using Glide, Prime, Desmond and Jaguar module of Schrodinger's, Maestro was used for visualising interactions. GraphPad prism 8 was used for statistical analysis.

2.2. Synthesis of 4-(2-(3-phenylthioureido) ethyl) benzenesulfonamide: (3)

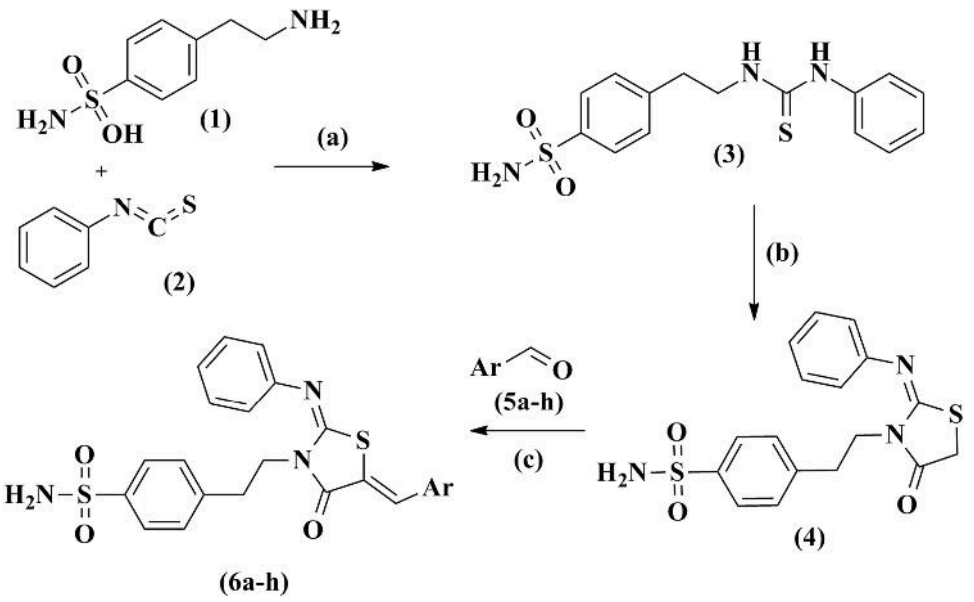
A solution of 4-(2-Amino Ethyl) Benzene Sulfonamide **(1)** (9.9 mmol) and phenylisothiocynate **(2)** (9.9 mmol) in 15 mL of dimethylformamide with catalytic amount of triethylamine was stirred at room temperature for 6h. The reaction was monitored by TLC for completion. Reaction mixture was poured on crushed ice to form crude product, the precipitate formed was filtered, washed with water followed by recrystallization with ethanol to obtain 4-(2-(3-phenylthioureido) ethyl) benzenesulfonamide (**3**) as white colour solid. Yield: 94 %; mp: 179–181 °C. FTIR (KBr, cm^{-1}): 3187.51 (NH_2), 3038.98 (Ar-CH), 1539.26 (C=C). ^{1}H NMR [400 MHz, δ ppm, DMSO-d_6]: 2.96–2.92 (t, 2H, CH_2), 3.719–3.710 (t, 2H, CH_2), 7.112–7.082 (m, 1H, *J* = 7.2 Hz, Ar-H), 7.301–7.291 (m, 5H, Ar-H), 7.320 (s, 2H, NH_2), 7.44–7.42 (m, 2H, *J* = 8 Hz, Ar-H), 7.77–7.75 (m, 2H, *J* = 8 Hz, Ar-H), 9.57 (s, 1H, NH). 13C NMR [100 MHz, δ ppm, DMSO-*d6*]: 34.69, 45.46, 123.61, 124.71, 126.30, 129.24, 129.71, 139.48, 142.65, 144.10, 180.77. Molecular formula: $C_{15}H_{17}N_3O_2S_2$; Molecular Mass; calculated: 335.08; HRMS; *m/z* 336. 08

2.3. Synthesis of 4-(2-(4-oxo-2-(phenylimino) thiazolidin-3-yl) ethyl) benzenesulfonamide: (4)

To an equimolar mixture of (**3**), chloroacetic acid, sodium acetate in 95 % ethanol was refluxed for 12 h. Reaction was monitored by TLC for completion of reaction. Reaction mixture was cooled, poured into crushed ice to obtain crude product, filtered washed with water and recrystallized from ethanol to obtain 4-(2-(4-oxo-2-(phenylimino) thiazolidin-3-yl) ethyl) benzenesulfonamide (4) as White colour solid. Yield: 87 %; mp: 143–145 °C. FTIR (KBr, cm^{-1}): 3266.59 (NH_2), 3032.23 (Ar-CH), 1708.04 (C=O), 1592.31 (C=C). ^{1}H NMR [400 MHz, δ ppm, DMSO-*d6*]: 3.03–3.00 (t, 2H, CH2), 3.95 (s, 2H, S-CH_2), 3.98 (t, 2H, CH_2) 6.81–6.79 (m, 2H, *J* = 7.6hz, Ar-H), 7.117–7.083 (m, 1H, Ar-H), 7.325–7304 (s, 2H, *J* = 8.4 Hz Ar-H), 7.341 (m, 2H, NH_2), 7.42–7.40 (m, 2H, *J* = 7.6hz, Ar-H), 7.75–7.73 (m ,2H, *J* = 7.6hz, Ar-H). ^{13}C NMR [100 MHz, δ ppm, DMSO-*d6*]: 32.71, 32.94, 43.47, 121.35, 124.76, 126.26, 129.79, 129.87, 142.94, 148.59, 155.41, 172.32. Molecular formula: $C_{17}H_{17}N_3O_3S_2$; Molecular Mass; calculated: 375.07; HRMS; *m/z*: 376.07.

2.4. General procedure for synthesis of (6a-6h)

An equimolar mixture of (**4**) and appropriate aryl aldehydes (**5a-**5 h) in 15 ml methanol was refluxed for 24 h with catalytic amount of piperdine. Reaction was monitored by TLC. Reaction mixture was cooled



Scheme 1. Reagents and conditions: (a) Dimethylformamide, triethylamine, rt; (b) Chloroacetic acid, sodium acetate, 95 % ethanol, reflux; (c) Methanol, piperdine, reflux.

to room temperature and obtained crude product was filtered and recrystallized using methanol.

2.4.1. Synthesis of 4-(2-((E)-5-((Z)-4-formylbenzylidene)-4-oxo-2-(phenylimino) thiazolidin-3-yl) ethyl) benzenesulfonamide (6a)

This compound was prepared according to general procedure and it was obtained as buff white solid; yield: 78.16 %; mp: 176–178 °C; FTIR (KBr, cm^{-1}): 3409.33 (NH_2), 3093.95 (Ar-CH), 1663.68 (C=O), 1581.70 (C=C). ^{1}H NMR [400 MHz, δ ppm, DMSO-*d6*]: 3.123–3.019 (t, 2H, CH_2), 4.172–4.140 (t, 2H, CH_2), 6.877–6.857 (d, 2H, Ar-H), 7.193–7.156 (m, 1H, Ar-H), 7.433–7.413 (m, 2H, *J* = 8 Hz, Ar-H), 7.390–7.352(m, 4H, Ar-H), 7.563 (s, 2H, NH_2), 7.664 (s, 1H, CH), 7.753–7.733 (d, 2H, *J* = 8 Hz, Ar-H). 9.982 (s, 1H, CHO). ^{13}C NMR [100 MHz, δ ppm, DMSO-*d6*]: 32.910, 44.063, 121.424, 122.986, 125.429, 126.282, 129.578, 129.875, 130.038, 131.063, 134.819, 142.858, 142.983, 148.099, 149.632, 166.017; molecular formula: $C_{25}H_{21}N_3O_4S_2$; Molecular mass; calculated: 491.10; HRMS: *m/z* 492.10 found

2.4.2. Synthesis of 4-(2-((E)-5-((Z)-2-hydroxybenzylidene)-4-oxo-2-(phenylimino) thiazolidin-3-yl) ethyl) benzenesulfonamide (6b)

This compound was prepared according to general procedure and it was obtained as yellow solid; yield: 78.32 %; mp: 143–145 °C. FTIR (KBr, cm^{-1}): 3274.31 (NH_2), 3504.81 (OH), 1639.56 (C=O), 3060.55 (Ar-CH). ^{1}H NMR [400 MHz, δ ppm, DMSO-*d6*]: 3.11 (t, 2H, CH_2), 4.15 (s, 2H, CH_2), 6.869–6.854 (d, 2H, *J* = 6hz, Ar-H), 6.926–6.907 (d, 2H, *J* = 7.6hz Ar-H), 7.230–7.156 (m, 2H, Ar-H), 7.34 (s, 2H, NH_2), 7.442–7.426 (m ,4H, *J* = 6.4 Hz, Ar-H), 7.765–7.748 (m, 2H, *J* = 6.8 Hz, Ar-H), 7.95 (s, 1H, CH), 10.46 (s, 1H, OH) ^{13}C NMR [100 MHz, δ ppm, DMSO-*d6*]: 32.93, 43.84, 116.52, 119.92, 120.16, 120.70, 121.46, 125.24, 126.06, 126.28, 128.81, 129.89, 129.98, 132.39, 142.95, 148.41, 150.44, 157.47, 166.36; molecular formula: $C_{24}H_{21}N_3O_4S_2$; Molecular mass; calculated: 479.10; HRMS: *m/z*: 480.10.

2.4.3. Synthesis of 4-(2-((E)-5-((Z)-4-hydroxybenzylidene)-4-oxo-2-(phenylimino) thiazolidin-3-yl) ethyl) benzenesulfonamide: (6c)

This compound was prepared according to general procedure and it was obtained as yellow solid; yield: 81.46 %; mp: 163–165 °C. FTIR (KBr, cm^{-1}): 3428.54 (O—H), 1648.73 (C=O), 2921.16 (Ar-CH), 1592.31 (C=C). ^{1}H NMR [400 MHz, δ ppm, DMSO-*d6*]: 3.106–3.166 (t, 2H, CH_2), 4.12–4.16 (t, 2H, CH_2), 6.794–6.773 (m, 2H, *J* = 8.4 Hz Ar-H), 6.883–6.864 (m, 2H, *J* = 7.6 Hz, Ar-H), 7.176–7.140 (m, 1H, Ar-H), 7.312–7.291 (d, 2H, *J* = 8 Hz, Ar-H), 7.37 (s, 2H, NH_2), 7.43–7.41 (d, 2H, *J* = 8 Hz, Ar-H) 7.595 (s, 1H, CH), 7.76–7.74 (m, 2H, *J* = 8 Hz Ar-H), 9.67 (s, 1H, OH); ^{13}C NMR [100 MHz, δ ppm, DMSO-*d6*]: 32.95, 43.74, 115.67, 117.26, 121.35, 121.50, 123.42, 125.16, 126.27, 129.86, 129.98, 131.65, 132.78, 142.96, 148.54, 150.46, 150.46, 162.12, 166.44; molecular formula: $C_{24}H_{21}N_3O_4S_2$; Molecular mass; calculated: 479.57; HRMS: *m/z*: 480.10.

2.4.4. Synthesis of 4-(2-((E)-5-((Z)-4-methoxybenzylidene)-4-oxo-2-(phenylimino) thiazolidin-3-yl) ethyl) benzenesulfonamide: (6d)

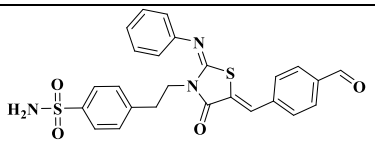
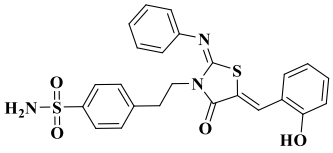
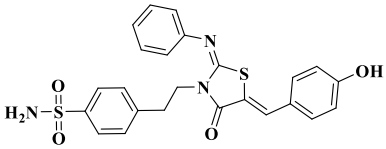
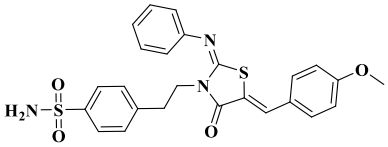
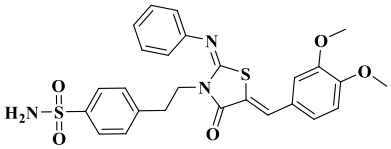
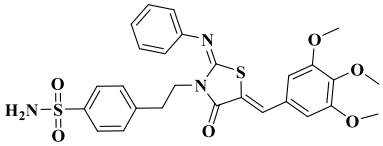
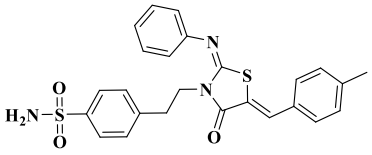
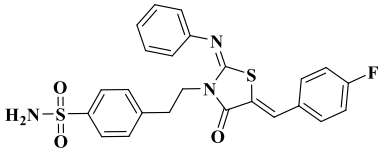
This compound was prepared according to general procedure and it was obtained as buff white solid; yield: 75.12 %; mp: 149–151 °C. FTIR (KBr, cm^{-1}): 3272.38 (NH_2), 1623.17 (C=O), 1590.06 (C=C); ^{1}H NMR [400 MHz, δ ppm, $CDCl_3$-*d6*]: 3.196–3.159 (t, 2H, CH_2), 3.82 (s, 3H, –OCH_3), 4.26–4.23 (t, 2H, CH_2), 4.91 (s, 2H, NH_2), 6.925–6.890 (m, 4H, Ar-H), 7.206–7.170 (m, 1H, Ar-H), 7.401–7.362 (m, 4H, Ar-H.), 7.45–7.43 (m, 2H, *J* = 8 Hz Ar-H), 7.68 (s, 1H, CH), 7.86–7.84 (d, 2H, *J* = 8 Hz Ar-H). ^{13}C NMR [100 MHz, δ ppm, $CDCl_3$-*d6*]: 33.47, 43.63, 55.53, 114.66, 118.31, 121.18, 124.98, 126.31, 126.76, 129.50, 129.94, 131.20, 132.04, 140.30, 143.89, 148.13, 150.42, 161.01, 166.94; molecular formula: $C_{24}H_{21}N_3O_4S_2$; Molecular mass; calculated: 493.11; HRMS: *m/z*: 494.12.

2.4.5. Synthesis of 4-(2-((E)-5-((Z)-3, 4-dimethoxybenzylidene)-4-oxo-2-(phenylimino) thiazolidin-3-yl) ethyl) benzenesulfonamide (6e)

This compound was prepared according to general procedure and it was obtained as buff white solid; yield: 75.12 %; mp: 167–169 °C

FTIR (KBr, cm^{-1}): 3247.30 (NH_2), 3068.88 (Ar-CH), 1699.36 (C=O), 1593.27 (C=C). ^{1}H NMR [400 MHz, δ ppm, DMSO-*d6*]: 3.112 (t, 2H, CH_2), 3.754–3.72 (d, 6H, –OCH_3), 4.157 (t, 2H, CH_2), 6.895–6.877 (d, 2H, *J* = 7.2 Hz, Ar-H), 7.065–6.992 (q, 2H, Ar-H), 7.172 (s, 2H, Ar-H), 7.345 (s, 2H, NH_2) 7.438–7.420 (m, 2H, *J* = 7.2 Hz, Ar-H), 7.393–7.375 (m, 2H, *J* = 7.2 Hz, Ar-H), 7.667 (s, 1H, CH), 7.756–7.737 (d, 2H, *J* = 7.6 Hz Ar-H). ^{13}C NMR [100 MHz, δ ppm, DMSO-*d6*]: 32.929, 43.852, 56.069, 56.117, 112.60, 114.84, 118.59, 121.511, 122.871, 125.305, 126.263, 126.512, 129.894, 129.961, 131.226, 142.935, 148.358, 149.326, 150.246, 150.964, 166.228; molecular formula: $C_{26}H_{25}N_3O_5S_2$; Molecular weight; calculated: 523.12; HRMS; *m/z*: 524.13.

Table 1
IC_{50} values of Compounds (6a-6h) for α-amylase inhibition.

Code	Structure	IC_{50} ± SEM[a] (μg/ml)
6a		**47.56 ±0.165**
6b		**29.51±1.35**
6c		**35.70±0.21**
6d		**31.19±0.104**
6e		**36.77±0.263**
6f		**47.79±0.05**
6g		**>50**
6h		**47.70±0.183**
Acarbose		**26.89±0.116**

[a]Standard Error Mean.

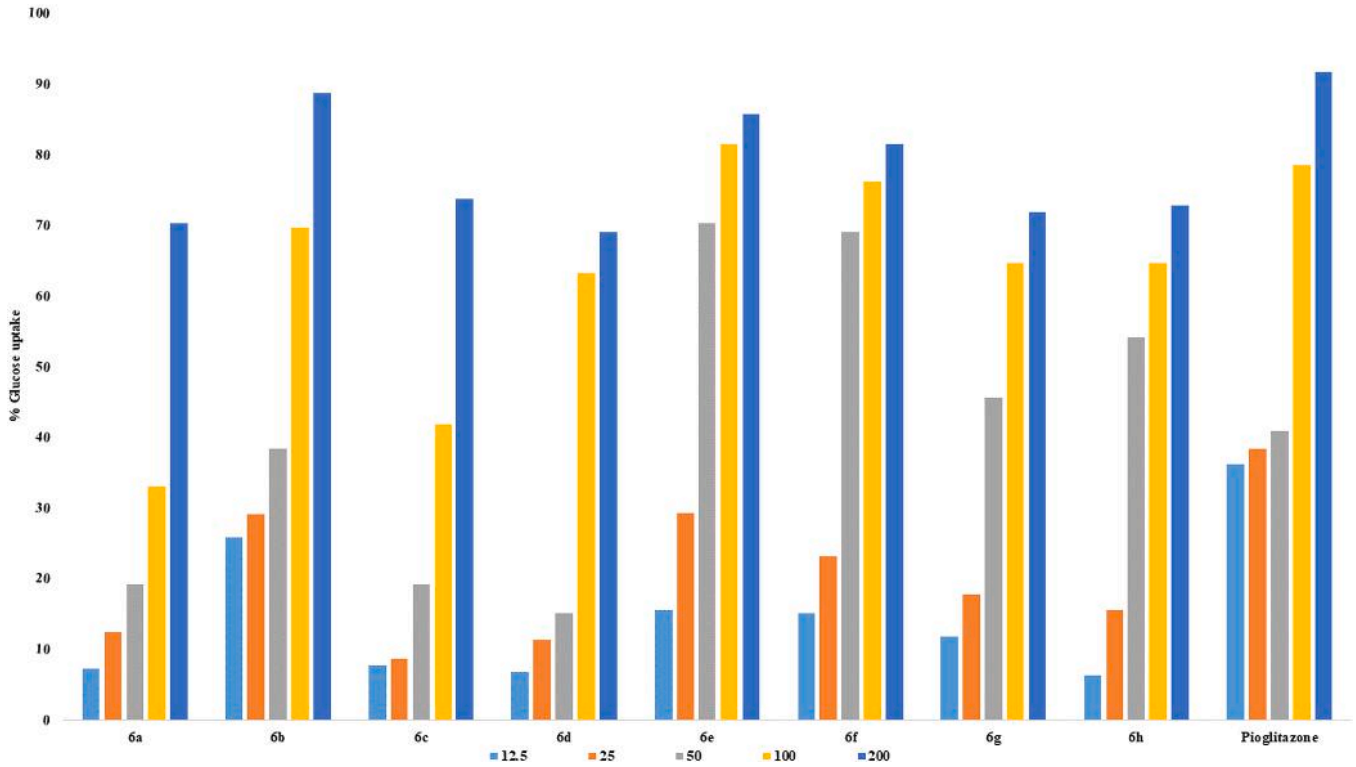


Fig. 2. Glucose uptake capacity of synthesised compounds **(6a-**6h**)** in yeast cells.

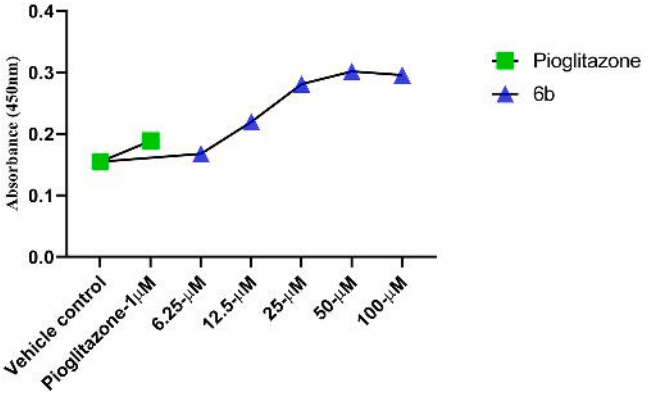


Fig. 3. Expression of PPAR-γ transcription factor of compound **6b and pioglitazone**.

2.4.6. Synthesis of 4-(2-((E)-4-oxo-2-(phenylimino)-5-((Z)-3,4,5-trimethoxybenzylidene) thiazolidin-3-yl) ethyl) benzenesulfonamide (6f)

This compound was prepared according to general procedure and it was obtained as buff white solid; yield: 83.12 %; mp: 173–175 °C; FTIR (KBr, cm^{-1}): 3247.30 (NH_2), 3085.27 (Ar-CH), 1701.29, (C=O).^{1}H NMR [400 MHz, δ ppm, DMSO-*d6*]: 3.115 (t, 2H, CH_2), 3.710–3.673 (d, 9H, –OCH_3), 4.162 (t, 2H, CH_2), 6.801 (s, 2H, Ar-H), 6.910–6.892 (d, 2H, J = 7.2 Hz, Ar-H), 7.183–7.166 (m, 1H, J = 6.8 Hz, Ar-H), 7.440–7.421 (m, 2H, J = 7.6hz, Ar-H), 7.352 (m 3H, Ar-H, NH_2), 7.657 (s, 1H, CH), 7.758–7.740 (d, 2H, J = 7.2 Hz Ar-H). ^{13}C NMR [100 MHz, δ ppm, DMSO-*d6*]: 32.910, 43.938, 56.509, 60.716, 108.028, 120.485, 121.530, 125.429, 126.273, 129.904, 131.169, 139.725, 142.897, 142.964, 148.032, 149.735, 153.628, 166.017. Molecular formula: $C_{27}H_{27}N_3O_6S_2$; Molecular mass; calculated: 553.13; HRMS: *m/z* 554.14.

2.4.7. Synthesis of 4-(2-((E)-5-((Z)-4-methylbenzylidene)-4-oxo-2-(phenylimino) thiazolidin-3-yl) ethyl) benzenesulfonamide (6 g)

This compound was prepared according to general procedure and it was obtained as buff white solid; yield: 80.52 %; mp: 151–153 °C FTIR (KBr, cm^{-1}): 3273.34 (NH_2), 3124.82 (C—H), 1711.90 (C=O), ^{1}H NMR [400 MHz, δ ppm, $CDCl_3$-*d6*]: 2.363 (s, 3H, -CH_3), 3.203–3.168 (t, 2H, CH_2), 4.277–4.240 (t, 2H, CH_2), 4.814 (s, 2H, -NH_2), 6.910–6.890 (d, 2H, J = 8 Hz, Ar-H), 7.216–7.196 (m, 2H, J = 8 Hz, Ar-H), 7.344–7.324 (m, 2H, J = 8 Hz, Ar-H), 7.405–7.367(m, 2H, Ar-H), 7.462–7.440 (m, 2H, J = 8.8 Hz, Ar-H), 7.711 (s, 1H, CH), 7.872–7.852 (d, 2H, J = 8 Hz, Ar-H). ^{13}C NMR [100 MHz, δ ppm, $CDCl_3$-*d6*]: 21.652, 33.475, 43.651, 120.045, 121.166, 125.037, 126.790, 129.511, 129.894, 129.952, 130.163, 130.862, 131.447, 140.281, 140.769, 143.887, 148.042, 150.313, 166.882. Molecular formula: $C_{25}H_{23}N_3O_3S_2$; Molecular mass; calculated: 477.12; HRMS: *m/z* 478.12.

2.4.8. Synthesis of 4-(2-((E)-5-((Z)-4-fluorobenzylidene)-4-oxo-2-(phenylimino) thiazolidin-3-yl) ethyl) benzenesulfonamide (6h)

This compound was prepared according to general procedure and it was obtained as buff white solid; yield: 78.16 %; mp: 147–149 °C; FTIR (KBr, cm^{-1}): 3274.31 (NH_2), 2938.69 (Ar-CH), 1710.93 (C=O), 1596.16 (C=C). ^{1}H NMR [400 MHz, δ ppm, DMSO-*d6*]: 3.133–3.100 (t, 2H, CH_2), 4.184–4151 (t, 2H, CH_2), 6.881–6.862 (d, 2H, J = 7.6 Hz, Ar-H), 7.193–7.156 (m, 1H, Ar-H), 7.398–7.7.289 (m, 6H, Ar-H, -NH_2), 7.442–7.422 (d, 2H, J = 8 Hz, Ar-H), 7.584–7.550 (m, 2H, Ar-H), 7.757–7.736 (m, 2H, J = 8.4 Hz, Ar-H), 7.757 (s, 1H, CH). ^{13}C NMR [100 MHz, δ ppm, DMSO-*d6*]: 32.900, 43.996, 116.864, 117.084, 121.166, 121.415, 125.401, 126.273, 129.770, 129.904, 130.038, 130.402, 132.750, 132.836, 142.877, 142.973, 148.253, 149.853, 161.868, 164.350, 166.084; molecular formula: $C_{24}H_{20}FN_3O_3S_2$; Molecular mass; calculated: 481.09; HRMS: *m/z* 482.10.

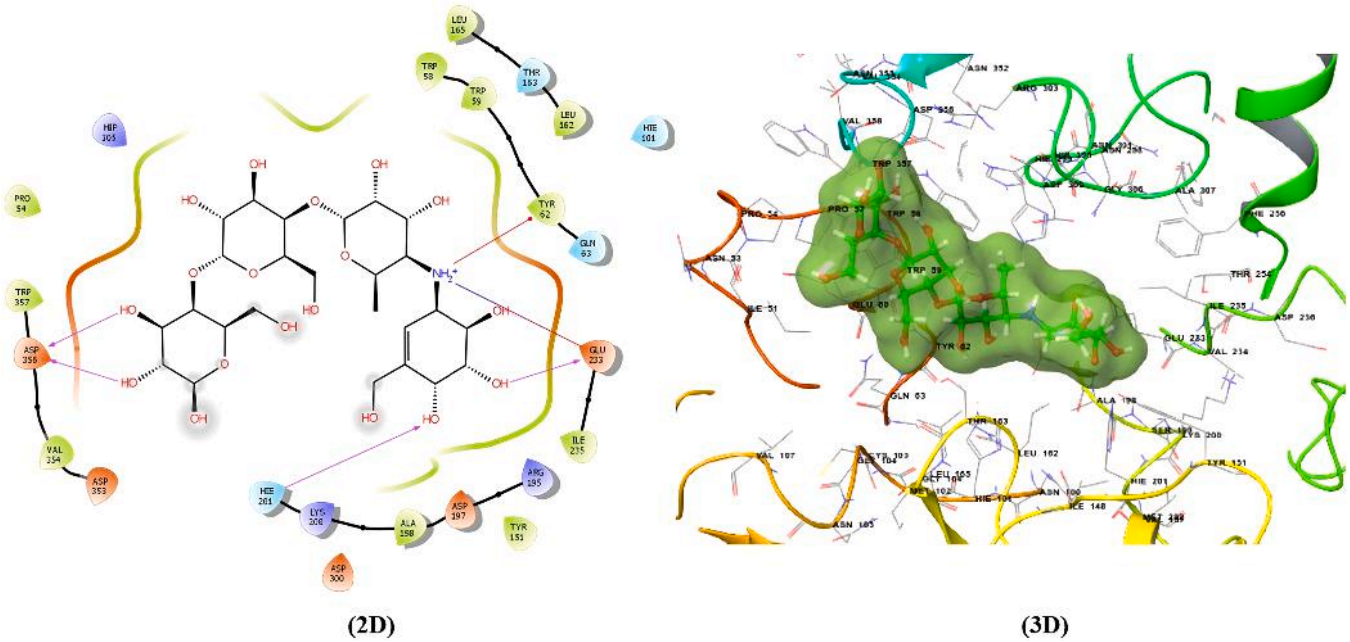


Fig. 4. 2D and 3D Binding orientation of **Acarbose** in 4W93 binding pocket.

2.5. Biological evaluation

2.5.1. Invitro α-amylase inhibition assay

The *α-amylase* inhibitory activity was carried out with modification as per previously reported procedure [22–25]. The reaction mixture comprised of 200 μL of synthesized molecules dissolved in methanol, control as phosphate buffer, acarbose was used as positive control, methanol as negative control at different concentrations, 200 μL (pH=6.9) phosphate buffer and 200 μL of the *α-amylase* enzyme solution. At 37 °C for 15 min reaction mixture was pre-incubated. Followed by addition of (1 %) starch solution to each tube and it was then incubated for 25 min at 37 °C. to cease the reaction, DNSA reagent (600 μL) was added and then all the tubes were incubated at 100 °C for 8 min, followed by cooling it by immersion of tubes in cold water bath, final dilution (1 mL) in each tube was made up to make up the volume using Millipore water. The absorbance was measured at 549 nm [23,24].

The formula used to calculate the inhibition percentage (%) is given below:

$$\text{Inhibition percentage activity } (\%) = \frac{(\text{ODcontrol 540nm} - \text{ODcontrol blank 540nm}) - (\text{OD sample 540 nm} - \text{OD sample blank})}{\text{OD control 540nm} - \text{OD control blank 540 nm}} \times 100$$

2.5.2. Glucose uptake assay in yeast cells

The yeast cells were used to perform glucose uptake assay as previously reported by Cirillo [26]. Percentage glucose uptake by synthesised compounds in yeast cells was measured and compared with standard pioglitazone. 1% w/v yeast cell suspension was prepared and soaked overnight followed by (4200 rpm, 5 min) centrifugation, supernatant (10 mL) was separated and 90 mL Millipore water was added, concentrations of synthesised compounds (**6a-**6h) and pioglitazone were suspended in 500 ng/mL glucose solution at 37 °C for 10 min. 2 mL of 3, 5-dinitro-salicylic acid reagent was added along with Millipore water to make up the volume. Later incubated at 37 °C for 60 min, centrifuged at 3800 rpm for 10 min. UV spectrophotometer was used to record the absorbance at 520 nm and% glucose uptake was calculated as

$$\%\ \textit{Glucose uptake} = \left(\frac{1 - At}{Ac}\right) \times 100$$

Where "At" and "Ac" represent test and control absorbance respectively.

2.5.3. Human PPAR-γ transcription factor assay

It is a cell-based ELISA method to detect the PPAR-γ transcription factor DNA binding affinity. This assay was formed on compound **6b** following the instructions provided by the manufacturer (Raybio PPAR-**γ** TF activity assay kit).

2.6. Insilico study

2.6.1. Induced fit docking

IFD module of Schrodinger software (Schrodinger. 2022) was considered for docking study to identify the binding mode and interaction in *α-amylase* binding pocket. The LigPrep panel was used to generate all possible enantiomers, specifying chirality, and protonation states of all synthesised molecules at physiological pH were generated, OPLS force field was utilised for energy minimization of ligands. Extra precision mode of glide module was used as fitness function for the docking based on cutting-edge score with wide range of flexible sampling, penalties were considers alongside scoring functions, best poses were ranked by conformational search sampling and various interactions, finally post dock minimization was carried out for the ligand receptor complex [27].

Protein Preparation was carried out on the crystal structure of

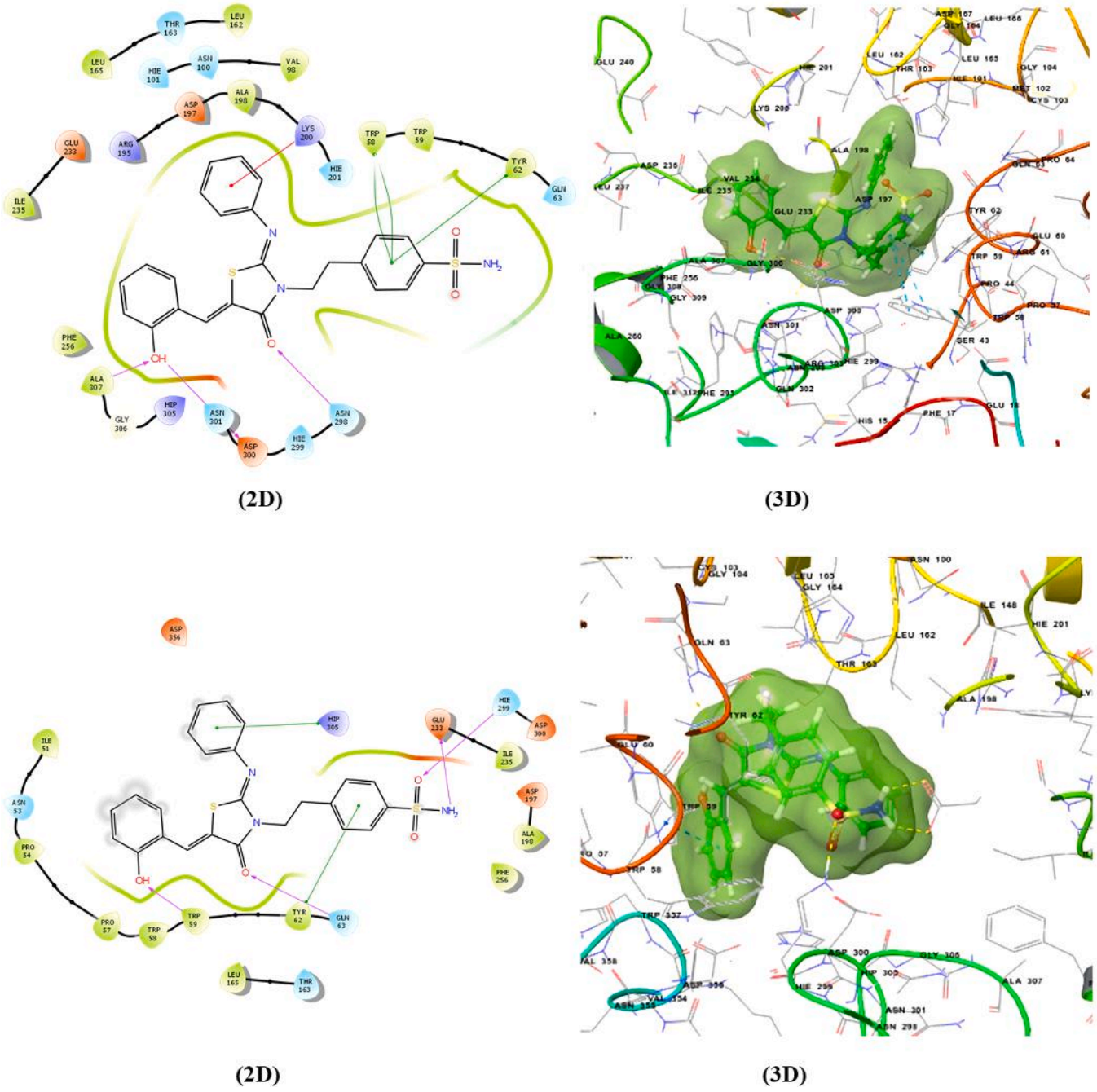


Fig. 5. (a) 2D and 3D Binding orientation of **6b** in 4W93 binding pocket. **(b)** 2D and 3D Binding orientation of **6b** in 4W93 binding pocket.

Human pancreatic alpha-amylase (PDB ID: 4W93) by retrieving it into the protein preparation workflow panel from protein data bank (https://www.rcsb.org). It consists 1–496 amino acid sequence length, Ca^{+2} and Cl^{-} ions.

The protein was pre-processed by removing water molecules and ligands from pdb file and keeping Ca^{+2} and Cl^{-} ion intact, assigning bond orders, and generating PKa values at PH 7 ± 2. The protein was further optimized by energy minimization using OPLS3e force field to obtain stable structure for further studies. Human pancreatic alpha-amylase has Domain A, B, and C. Active site residues are Asp197, Glu233, and Asp300 located in Domain A along with Ca^{+2} binding site in Domain B and also includes ARG 195, HIE 299, ALA 198, GLN 63. Hence the binding affinity of synthesised inhibitors was evaluated at Domain A active binding site by generating grid using a grid generation panel [28].

2.6.2. Molecular dynamic simulations

Gromacs (https://www.gromacs.org/) ver. 2021. 6, was used to perform MD simulation of compound **6b-4w93** complex. The preparation of complex was carried out by the removal of hetero atoms complex. CHARMM 36 all atom force field generation of protein topology [29], also the ligand topology file was genetrated using CHARMM general force field (CGenFF) server (https://cgenff.umaryland.edu/). Avogadro program was used to fill Hydrogen wherever required. editconf module of Gromacs was utilised for building the intermediate complex. System was solvated using a three-point water model in a dodecahedron with dimensions of 1 mm on all sides. Na^{+} and Cl^{-} ions counter ions were used for neutralizing the system as per the need. Steepest gradient integrator with verlet cutoff scheme for maximum of 50,000 steps with adding restrains was employed in energy minimization. Canonical (NVT) and isobaric (NPT) equilibrators for 1 ns for two coupling groups i.e.,

Table 2
The Induced fit docking results of selected compounds in 4W93 binding pocket.

Com.	PDB ID:4W93		H-Bond		
	IFD Score	Glide Energy (kcal/mol)	Ligand Atom interactions	Amino Acid	Bond length
6a	−1159.02	−53.02	-NH_2 of ligand to HIP 305	HIP 305	1.92
			-C=O of ligand to SER 43	SER 43	1.83
6b	−1162.77	−54.56	-OH, of ligand to ALA 307, ASP 300	ALA 307, ASP300	2.29
			-C=O of ligand to ASN 298	ASN 298	2.02
			-NH_2 of ligand to GLU233	GLU 233	1.98
			-C=O of ligand to GLN 63	GLN 63	2.02
6c	−1173.41	−69.32	-OH, of ligand to GLU 233	GLU 233	1.08
6d	−1165.25	−52.32	-C=O of ligand to GLN 63	GLN 63	1.80
6e	−1163.86	−60.99	-*S* = *O* of ligand to ARG195	ARG195	1.88
			-*S* = *O* of ligand to HIE299	HIE299	1.90
			-NH_2 of ligand to GLU 233	GLU 233	2.26
			-NH_2 of ligand to ASP 197	ASP 197	2.02
6f	−1160.82	−59.79	-S=O of ligand to ASN 352	ASN 352	1.79
			-NH_2 of ligand to VAL 351	VAL 351	1.90
			NH_2 of ligand to ASP 356	ASP 356	2.10
			–OCH_3 of ligand to HIE 201	HIE 201	1.62
6 g	−1163.00	−57.44	-NH_2 of ligand to ASP 197	ASP 197	1.68
			-C=O of ligand to ARD 195	ARG 195	1.68
			-NH_2 of ligand to GLU 233	GLU 233	2.02
6h	−1165.10	−58.87	-C=O of ligand to GLN 63	GLN 63	2.07
			-S=O of ligand to HIE299	HIE299	1.97
			-NH_2 of ligand to GLU 233	GLU 233	2.17
Acarbose	−577.22	−52.034	-OH, of ligand to GLU 233	GLU 233	2.16
			-OH, of ligand to ASP 356	ASP 356	1.67
			-OH, of ligand to ASP 356	ASP 356	1.73
			-OH, of ligand to HIE 201	HIE 201	2.13

protein-ligand and water-ions were used for equilibration of the whole system. Constant volume and temperature at 300 K were employed by Berendsen thermostat (V-rescale), also pressure coupling algorithm (C-rescale) was employed to maintain constant pressure at 1 bar. Computations of long range electrostatic, coulomb and Vander Waals with cut off of 1.2 nm was calculated using Particle mesh Ewald (PME). Constraints in bond length was employed using the LINCS algorithm. Finally, the **6b-4W93** complex was subjected to a MD run for 100 ns. The coordinates and energies were saved at every 20 picoseconds to acquire 10,000 frames. The inbuilt Gromacs utilities were used to analyse the trajectories. Root mean square deviation (RMSD), root mean square fluctuation (RMSF), radius of gyration (RoG), solvent accessible surface area (SASA) and number of hydrogen bonds were measured for a time span of 100 ns using QtGrace visualizer.

2.6.3. Molecular mechanics poisson-Boltzmann surface area (MMPBSA) analysis

The gmx_MMPBSA module was employed, run was performed for 100 frames, an internal PBSA solver in a sander was employed for poison Boltzmann calculation run [30]. The results obtained from gmx_MMPBSA run were visualised by the MMPBSA_ana module. The energy contribution parameters like electrostatic and Vander Waals molecular mechanics, polar contribution to solvation, non-polar contribution to attractive solute-solvent interactions to the solvation, total gas phase molecular mechanics, total solvation, relative binding and total energy contribution per residue was measured.

2.6.4. Geometric optimization

Geometric optimization calculation of the title compounds was carried out with the Jaguar module of Schrodinger's material science suit [31] Using density functional theory by becke's three-parameter hybrid functional correlation with Lee, Yang, and Paar (B3LYP) was employed with 6–31G** basis set for calculation in the gas phase. Properties such as Highest occupied molecular orbital (HOMO), lowest unoccupied molecular orbital (LUMO), energy gap (ΔE_{GAP}), dipole moment (μ), hardness (η), local softness (σ) can be calculated using the FMO (Frontiers molecular orbitals) and following equations [32–34].

$$\Delta E_{GAP=} E_{LUMO} - E_{HOMO}$$

$$\eta = (\mathrm{ELUMO} - E\mathrm{HOMO})\ /2$$

$$\sigma = 1/\eta$$

$$\mu = (EHOMO + ELUMO)/2$$

$$\omega = \mu^2/2\eta$$

2.6.5. ADMET predictions

ADMET properties of title compounds was calculated using Qikprop module of Schrodinger's suit [35].

2.7. Computational pharmacology

2.7.1. Target identification, network construction and cluster analysis

The targets for the **6b** were predicted from DIGEP-Pred (https://www.way2drug.com/ge/) and SwissTargetPrediction (http://www.swisstargetprediction.ch/) databases by subjecting the canonical SMILES. The targets for type 2 diabetes mellitus (T2DM) were retrieved from the DisGeNET database using the keywords "Diabetes Mellitus, α-amylase, Non-Insulin-Dependent; CUI: C0011860". The targets identified to be involved in T2DM and α-amylase were matched with the proteins known to be regulated by **6b** using Venny 2.1.0 (https://bioinfogp.cnb.csic.es/tools/venny/). The targets in common were subjected to STRING *ver. 11.5* (https://string-db.org/) [36] to construct a protein-protein interaction network along with KEGG-enriched pathways. Moreover, KEGG pathway analysis was executed to identify T2DM and α-amylase associated pathways regulated by **6b**; further integrated into Cytoscape *ver. 3.9.0* to acquire Pathway-Protein interaction [37]. The network analysis was performed on the basis of "*Node degree distribution*" and "*Betweenness by degree*" where parameters like eccentricity, neighbourhood connectivity, in-degree distribution, and out degree distribution were analysed. Cluster analysis was performed using the K-means clustering module of STRING with a clustering coefficient of five clusters.

2.7.2. Gene ontology analysis

Gene Ontology analysis was performed using the STRING server to obtain GO terms i.e. Cellular component (CC); helps to predict the component of cell where the molecule may act, Molecular function (MF); predicts the operation that may be initiated by the molecule, and

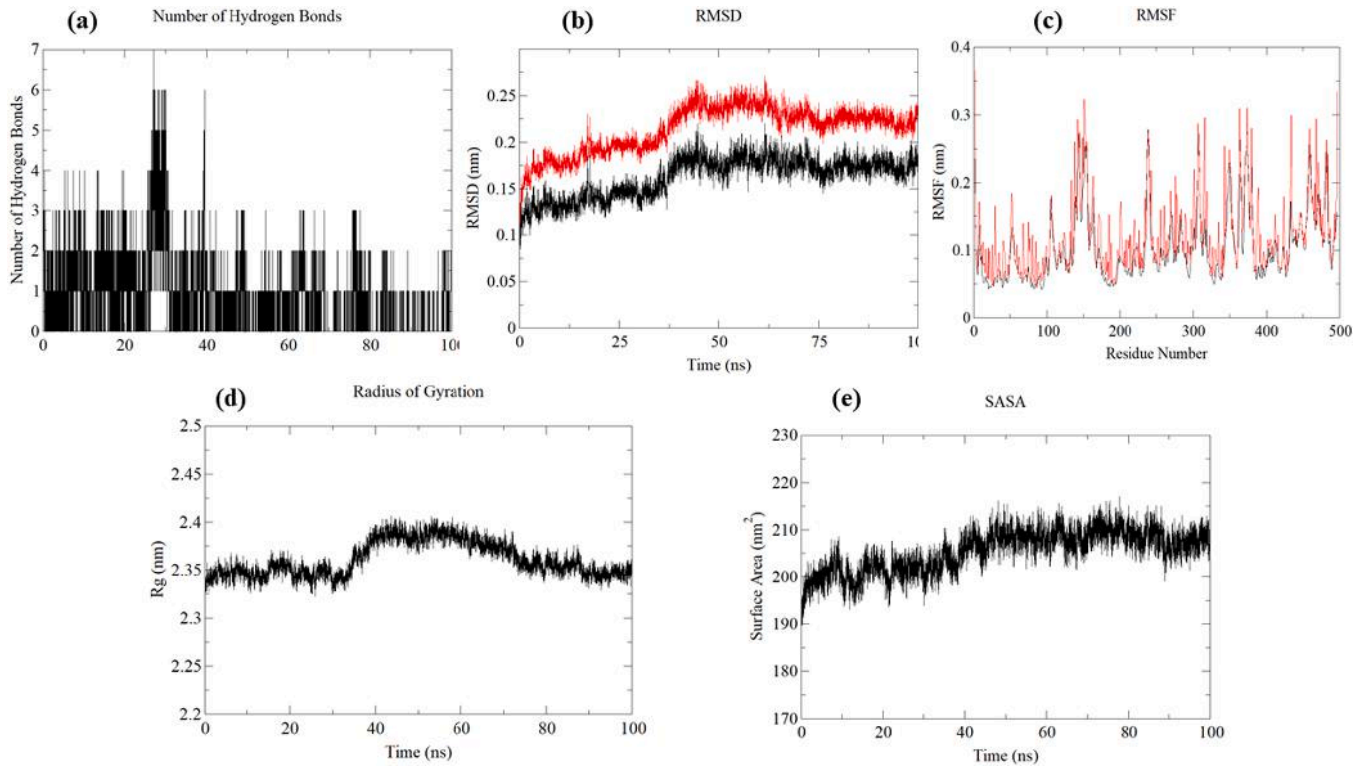


Fig. 6. Parameters describing stability of compound **6b** and **4w93** complex, where **(a)** Number of hydrogen bonds between protein and ligand; **(b)** RMSD of backbone (black) and complex (red); **(c)** RMSF of complex (black) and RMSF of c-alpha atom (red); **(d)** Radius of gyration; **(e)** Solvent Assessable Surface area (SASA); .

Table 3
Final energy of geometry optimized structures.

Compound	Gas Phase Energy (eV)
6a	−2226.816209
6b	−2141.384249
6c	−2165.395209
6d	−2228.020846
6e	−2342.540483
6f	−2457.057217
6 g	−2152.815555
6h	−2212.725562

biological process (BP); predicts the response the cell may deliver. Integration of GO terms predict the effect of test agent on cellular level.

3. Results and discussions

3.1. Chemistry

The synthesis of new 4-(2-((E)-5-(substituted-benzylidene)-4-oxo-2-(phenylimino) thiazolidin-3-yl) ethyl) benzenesulfonamide **(6a-**6h**)** has been described in Scheme 1. 4-(2-(3-phenylthioureido) ethyl) benzenesulfonamide **(3)** was obtained reaction between 4-(2-Amino Ethyl) Benzene Sulfonamide **(1)** and phenylisothiocynate in presence of catalytic amount of triethylamine. Compound 4-(2-(4-oxo-2-(phenylimino) thiazolidin-3-yl) ethyl) benzenesulfonamide **(4)** was formed by refluxing thiourea derivative compound **(3)** with chloroacetic acid and anhydrous sodium acetate. The target compounds **(6a-**6h**)** were prepared by Knoevenagel condensation type reaction between appropriate aryl aldehyde and compound **(4)** in presence of methanol containing catalytic amount of piperdine.

The compounds **(3), (4)**, and all the target compound structures **(6a-**6h**)** were characterised by FTIR, ^{1}H NMR, ^{13}C NMR and HRMS. The FTIR

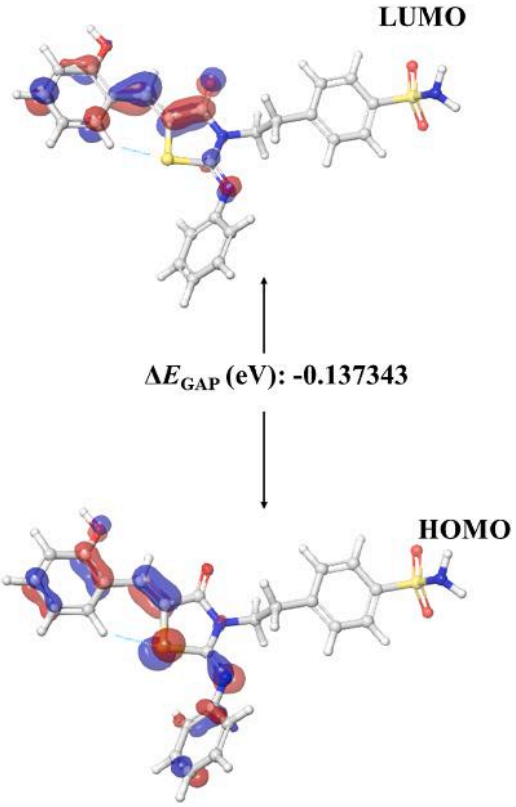


Fig. 7. Contours of HOMO and LUMO of compound **6b**.

Table 4
Calculated quantum chemical parameters of synthesized compounds.

Quantum chemical parameters	E_{HOMO} (eV)	E_{LUMO} (eV)	ΔE_{GAP} (eV)	μ (eV)	σ (eV)	η (eV)
6a	−0.230245	−0.101432	−0.128813	−0.1658385	−15.5263832	−0.064406
6b	−0.19179	−0.054447	−0.137343	−0.1231185	−14.5620818	−0.068671
6c	−0.194667	−0.057394	−0.137273	−0.0686365	−14.5695074	−0.126030
6d	−0.210492	−0.072777	−0.137715	−0.1416345	−14.5227462	−0.068857
6e	−0.204323	−0.071377	−0.132946	−0.13785	−15.0437019	−0.066473
6f	−0.208655	−0.075328	−0.133327	−0.0666635	−15.0007125	−0.141991
6 g	−0.216732	−0.076572	−0.14016	−0.146652	−14.2694063	−0.07008
6h	−0.220833	−0.080641	−0.140192	−0.150737	−14.2661492	−0.070096

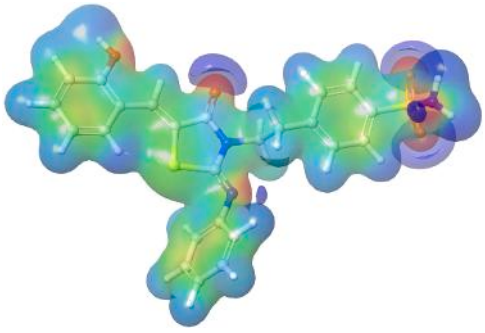


Fig. 8. MEP map of compound **6b**.

spectra of compound 4-(2-(3-phenylthioureido) ethyl) benzenesulfonamide **(3)** showed primary amine **(NH_2)** absorption peak at 3187 cm^{-1}, proton NMR spectrum **(3)** produced characteristic amino **(NH_2)** group signal at δ value 7.32 ppm, the two signals of **(CH_2)** group around δ value 2.947 ppm (triplet) and 3.719, secondary amino **(NH)** group signal at δ value 9.570 ppm, and the mass spectrum showed confirmative peak. (Supplementary document) The 4-(2-(4-oxo-2-(phenylimino) thiazolidin-3-yl) ethyl) benzenesulfonamide **(4)** showed primary amine **(NH_2)** absorption band around 3266 cm^{-1} ^{1}H NMR spectrum showed amino group **(NH_2)** signal at δ 7.34 ppm, characteristic methylene protons **(CH_2)** indicative of cyclization appeared at δ 3.986 ppm, the two signals of **(CH_2)** group at δ value 3.019 ppm (triplet) and 3.959 ppm, IR spectra of target compounds **(6a-6h)** showed characteristic absorption band of amino **(NH_2)** group at around 3100–3400 cm^{-1} The ^{1}H NMR of compounds **(6a-6h)** reveals the presence of indicative singlets at δ value around 7 ppm attributed to amino protons **(NH_2)**, δ value around 3 and 4 ppm attributes to the two **(CH_2)** signals respectively. Further, 4-(2-((E)-5-(substituted-benzylidene)-4-oxo-2-(phenylimino) thiazolidin-3-yl) ethyl) benzenesulfonamide **(6a-6h)** were confirmed by HRMS spectral studies.

3.2. Biological evaluation

3.2.1. Invitro α-amylase inhibition assay

In continuation of our investigation on enzyme inhibitions [35,38]. All the synthesised title compounds were evaluated against α-amylase inhibition assay few compounds showed *α-amylase* enzyme inhibition. All compounds showed varying enzymatic activity with IC_{50} value

Table 5
ADEMT parameters of synthesised inhibitors.

Comp.	MW	DHB	AHB	QPlog Pw	QPlog Po/w	QP logS	QPlog HERG	QPP Caco
6a	491.579	2	10.5	17.713	2.782	−5.802	−7.705	35.837
6b	479.568	3	9.25	17.809	3.077	−5.688	−7.627	68.105
6c	479.568	3	9.25	17.813	3.018	−5.734	−7.607	55.68
6d	493.594	2	9.25	15.981	3.879	−6.273	−7.708	194.292
6e	523.621	2	10	16.228	3.967	−6.516	−7.612	194.263
6f	553.647	2	10.75	16.459	4.058	−6.313	−7.208	193.624
6 g	477.595	2	8.5	15.449	4.091	−6.615	−7.717	193.748
6h	481.559	2	8.5	15.528	4.02	−6.414	−7.696	193.865
Comp.	**QPP MDCK**	**QPlogBB**	**%HOA**	**CNS**	**ROF**	**ROT**		
6a	33.49	−2.581	77.77	−2	0	1		
6b	26.944	−2.697	75.863	−2	0	0		
6c	104.019	−2.092	90.616	−2	0	1		
6d	104.009	−2.208	78.174	−2	1	1		
6e	100.958	−2.213	78.682	−2	1	1		
6f	30.917	−2.77	64.873	−2	1	1		
6g	187.455	−1.885	91.423	−2	0	1		
6h	16.728	−2.998	71.056	−2	0	1		

MW: Molecular weight (<500).
DHB: Number of hydrogen bond donors (<5).
AHB: number of hydrogen bond acceptors (<10).
QPlogPw: water/gas partition coefficient.
QPlogPo/w: Octanol/ water partition coefficient (<5).
QPlogS: Aqueous solubility (−6.5 to0.5).
QPlog HERG: IC_{50} value for blockage of HERG K^+channels (<−5).
QPP Caco: apparent Caco-2 permeability (nm/*sec*) (<25poor, >500great).
QPP MDCK: apparent MDCK permeability (nm/*sec*) (<25poor, >500great).
QPlogBB: Prediction of brain/blood partition coefficient (−3.0 to1.2).
%HOA: Percent Human Oral Absorption (>80 % is high <25 % is poor).
CNS: predicted Central nervous system activity (−2.0 to +2.0).
ROF: Number of violations of Rule of Five.
ROT: Number of violations of Rule of Three.

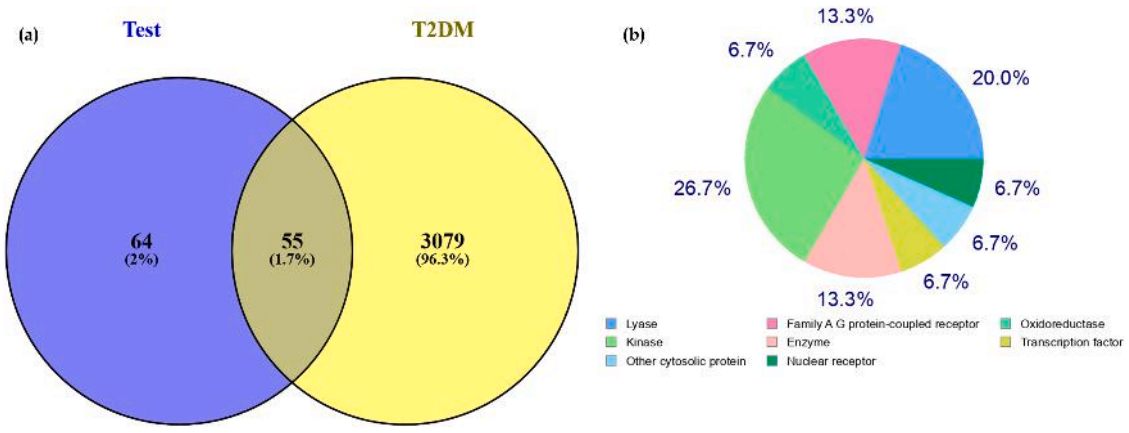


Fig. 9. (a) The Venn diagram representation of common genes between test agent and type 2 diabetes mellitus; **(b)** The categorical representation of genes modulated by compound identified via SwissTargetPrediction.

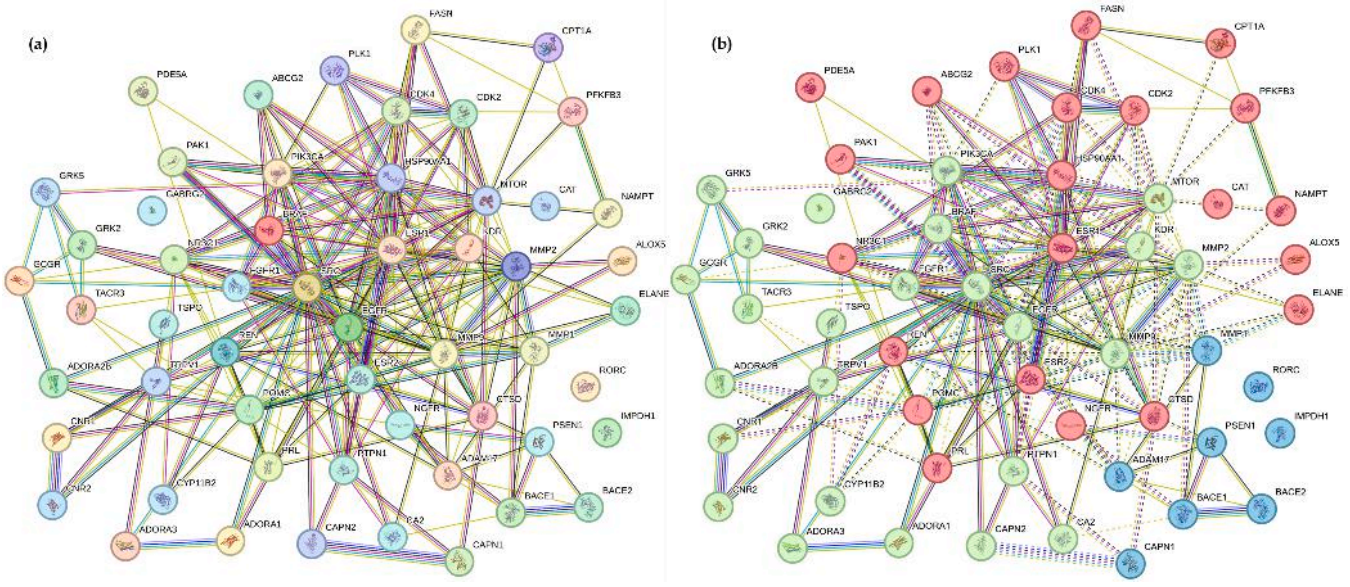


Fig. 10. (a) STRING identified Protein-protein interaction for compound **6b, and (b)** The cluster analysis where cluster 1: red; cluster 2: green; cluster 3: blue.

ranging from 29.51±1.35 μg/ml to 58.73±0.476 μg/ml (Table 1). Among them, compound **6b** showed better inhibitory effect in the series with the IC_{50} value of 29.51±1.35 μg/ml compared to standard acarbose with the IC_{50} value of 26.89±0.116 μg/ml. other analogs such as **6c, 6d** and **6e** displayed inhibitory effect with IC_{50} value of 35.70±0.21 μg/ml, 31.19±0.104 μg/ml and 36.77±0.263 μg/ml. **6b** being the promising lead for inhibition of the *α-amylase* enzyme has a polar substitution (OH) at *ortho* position on phenyl ring, second most potent lead molecule **6d** bears substitution (–OCH_3) at *para* position on phenyl moiety. Similarly, the activity decreases as we increase the non-polar substitution like 2, 4-dimethoxy and 3,4,5-trimethoxy group on phenyl ring. Acarbose molecule being polyhydroxy compound acts as electron Donor, **6b** resembles the electron donating property as results of polar hydroxy group substitution at *ortho* position.

Structural reactivity for the given set of compounds can be identified and correlated to its biological activity, herein polar groups with electron donating ability have shown better inhibitory effect as seen in compound **6b** and **6c** as compared structure of acarbose bearing polyhydroxy substitution is a polar electron donating molecule. Whereas the substitution of non-polar electron donating group in the compound 6 g, decreased the inhibitory activity. Further the inhibitory effect of the compounds **6a, 6d, 6e, 6f** and 6h having electron withdrawing groups was seen to be decreasing.

3.2.2. *Glucose uptake assay in yeast cells*

Further, synthesized compounds **(6a-**6h**)** were subjected to glucose uptake assay in yeast cells. In human body 80 % of glucose is taken up by skeletal muscle as a result of sensitization by insulin, any impairment in insulin secretion or resistance on skeletal muscles and adipose tissue leads to decreased glucose uptake. Clearance of glucose from the blood is carried out by (GLUT's) such as GLUT1 and GLUT4 which are actively present in plasma membrane. GLUT4 dominantly promotes the uptake of glucose [36]. In this regard, we aimed to study role of synthesised compounds **(6a-**6h**)** on GLUT modulation in the yeast cell lines. Compounds **(6a-**6h**)** were screened for their glucose uptake activity at varying concentrations of 12.5 μg/ml, 25 μg/ml, 50 μg/ml, 100 μg/ml and 200 μg/ml (Fig. 2) Compounds **6b, 6e**, and **6f** promoted better glucose uptake with 88.71%, 85.79% and 81.43 % at 200 μg/ml respectively, when compared to standard pioglitazone (91.64% at 200 μg/ml). Compounds **6a, 6c, 6d**, 6 g, and 6h displayed moderate percent glucose uptake with 70.21 %, 73.67 %, 69.05 %, 71.84 %, 72.79 % and 68.63 % respectively at 200 μg/ml.

Table 6
KEGG Pathway analysis of compound **6b**.

Pathway (KEGG ID)	OGC/BGC	Strength	FDR	Proteins
Adherens junction (hsa04520)	0.05797	1.32	0.00052	EGFR, PTPN1, SRC, FGFR1
Adipocytokine signaling pathway (hsa04920)	0.0441	1.2	0.0062	CPT1A, MTOR, POMC
AGE-RAGE signaling pathway in diabetic complications (hsa04933)	0.0312	1.05	0.0129	MMP2, CDK4, PIK3CA
AMPK signaling pathway (hsa04152)	0.041667	1.17	0.00034	PIK3CA, CPT1A, FASN, MTOR, PFKFB3
FoxO signaling pathway (hsa04068)	0.0476	1.23	3.94E-05	CAT, PIK3CA, CDK2, EGFR, PLK1, BRAF
Insulin resistance (hsa04931)	0.037736	1.13	0.002	PIK3CA, CPT1A, MTOR, PTPN1
Insulin signaling pathway (hsa04910)	0.0378	1.13	0.00047	PIK3CA, FASN, MTOR, PTPN1, BRAF
JAK-STAT signaling pathway (hsa04630)	0.0253	0.96	0.0064	PIK3CA, EGFR, PRL, MTOR
Longevity regulating pathway (hsa04211)	0.0344	1.09	0.0111	CAT, PIK3CA, MTOR
Longevity regulating pathway - multiple species (hsa04213)	0.0447	1.25	0.0049	CAT, PIK3CA, MTOR
MAPK signaling pathway (hsa04010)	0.0209	0.88	0.0013	NGFR, KDR, EGFR, PAK1, FGFR1, BRAF
mTOR signaling pathway (hsa04150)	0.02	0.86	0.0348	PIK3CA, MTOR, BRAF
Neurotrophin signaling pathway (hsa04722)	0.0357	1.11	0.0024	NGFR, PIK3CA, PSEN1, BRAF
Notch signaling pathway (hsa04330)	0.0384	1.14	0.0383	ADAM17, PSEN1
PI3K-Akt signaling pathway (hsa04151)	0.0286	1.01	1.65E-06	NGFR, CDK4, KDR, PIK3CA, CDK2, EGFR, PRL, HSP90AA1, MTOR, FGFR1
Progesterone-mediated oocyte maturation (hsa04914)	0.0526	1.28	0.00012	PIK3CA, CDK2, PLK1, HSP90AA1, BRAF
T cell receptor signaling pathway (hsa04660)	0.03	1.03	0.014	CDK4, PIK3CA, PAK1
Type II diabetes mellitus (hsa04930)	0.0444	1.2	0.0307	PIK3CA, MTOR



Low **High**

Where, OGC: Observed gene count, BGC: Background gene count, FDR: False discovery rate.

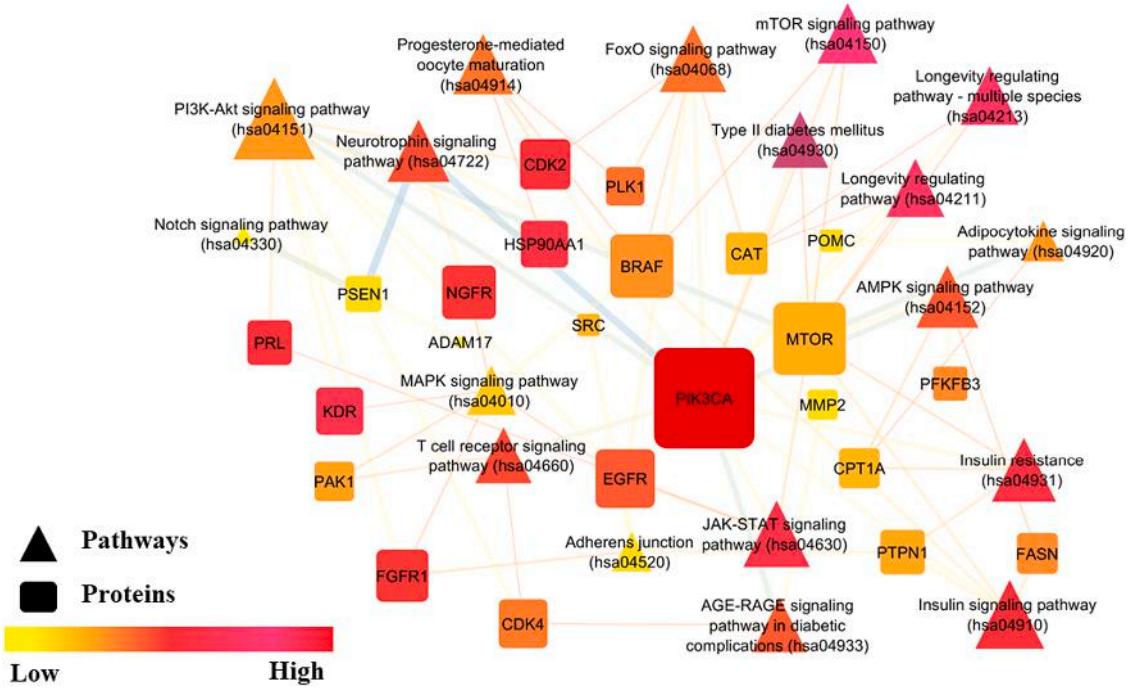


Fig. 11. The protein-pathway interaction modulated by compound **6b**.

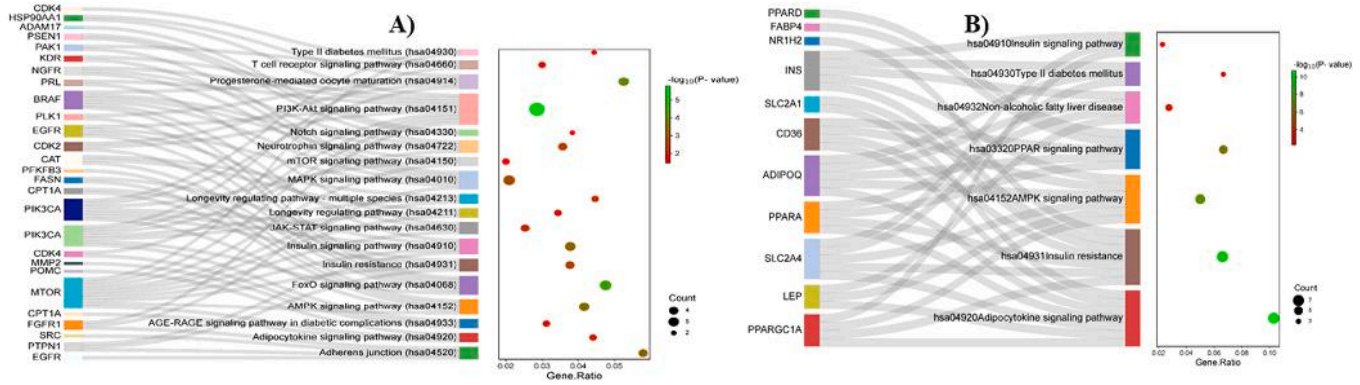


Fig. 12. Connections between pathways and its protein enrichment analysis **A)** Type II DM, **B**) alpha amylase.

3.2.3. *Human PPAR-γ transcription factor assay*

Ligand dependent transcription in Peroxisome proliferator-activated receptor plays an important role in adipogenesis and glucose homeostasis. In this method, immobilization of peroxisome proliferator response element (PPRE) to the bottom of 96 well ELISA plate. Subsequently horse-radish peroxidase attached linked to a secondary antibody was added to the above wells, which was measured by calorimetry at 450 nm. Pioglitazone serves as positive control at 1 μM, compound **6b** was measured at concentration range of 6.25–100 μM. (Fig. 3) Results demonstrate that there was a dose dependent increase in PPAR-γ expression of compound **6b** as compared to standard pioglitazone.

3.4. *Insilico study*

3.4.1. *Induced fit docking*

The α-amylase inhibition results demonstrated that few of the synthesised compounds have prominent antidiabetic effect, hence to support the above finding we carried out hypothetical binding interactions of these synthesised ligands **(6a-**6h**)** via inducing flexibility at binding site of α-amylase enzyme and refining the poses of ligand receptor complex by induced fit docking using IFD module of Schrodinger's suits version 2022–2. The compounds **(6a-**6h**)** and Acarbose were docked in binding pocket of (PDB ID: 4W93) Human pancreatic alpha-amylase. Standard sampling protocol was utilised for docking, which includes simultaneous prime refinement and glide docking for accurate ligand receptor binding mode prediction. As previously reported by Brayer, G. D., et al., [27] key amino acids residues present in the domain A binding site of α-amylase enzyme, responsible for eliciting biological response are Asp197, Glu233, and Asp300, ARG 195, HIE 299, ALA 198, TYR 62 and GLN 63. Acarbose displayed three hydrogen bond networks with GLU 233, ASP 356, among which hydroxy group formed bond with GLU233, in addition it also formed a salt bridge between amino groups in its quaternary state to GLU 233. pi-cation interaction was seen between TYR 62 and quaternary state amino group as seen in (Fig. 4), compound **6b** also possess orientation where the *ortho* substituted OH group form a hydrogen bond with ALA 307 and ASP 300, the carbonyl group of thiazolidin-4-one part forms a hydrogen bond with ASN 289, three pi-pi stacking interactions are seen with TRP 58 and TYR 62, as depicted in (Fig. 5a). (Fig. 5b) represents two hydrogen bonds between NH_2 group of the ligand and GLU 233 amino acid residue, one hydrogen between Oxygen atom of SO_2 group of the ligand and HIE 299 residue. It also forms pi-pi stacking interaction with TRP 59. Docking scores and

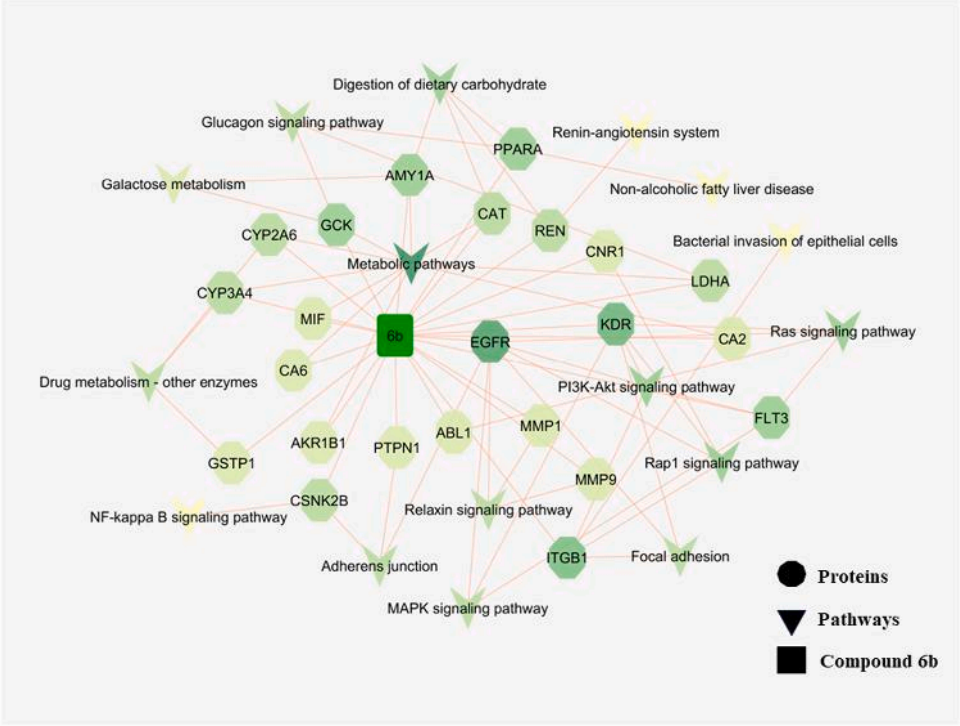


Fig. 13. Protein-pathway interaction modulated by compound **6b**.

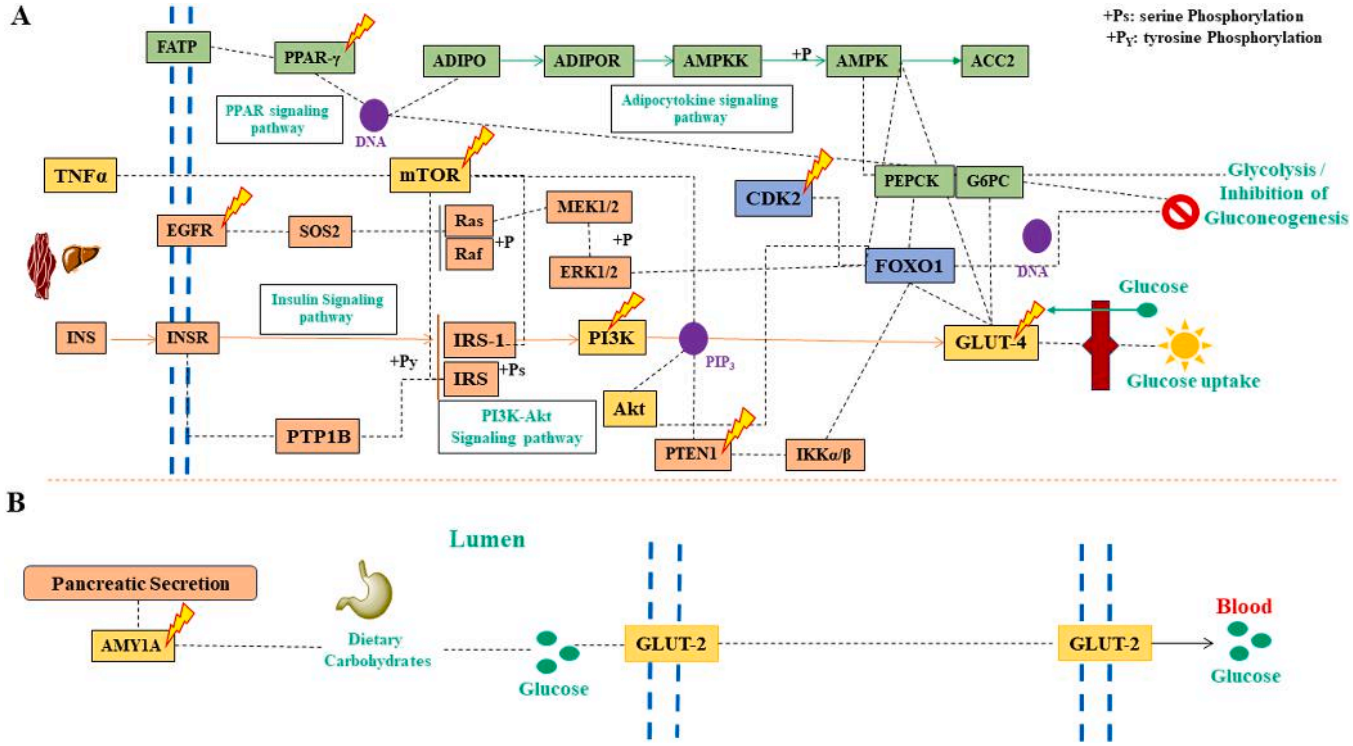


Fig. 14. Probable molecular mechanism of compound **6b** in **A)** Glucose uptake (hsa04930, hsa04151, map03320). **B**) *α-amylase* inhibition. (map04973) represents checkpoints affected by the compound **6b** .

hydrogen bond interactions of synthesised compounds **(6a-**6h**)** are given in Table 2, and all the binding orientations of Compounds **6a, 6c, 6d, 6e, 6f,** 6g**,** 6h**, 6i** are provided in SI (**Supplementary index**)

3.4.2. Complex stability analysis using MD simulations

The **6b-4W93** (ligand -protein) complex was studied for their stability for a period of 100 ns employing Molecular dynamic simulation using Gromacs package. The complex displayed an RMSD fluctuations of less than 2.5 Å for initial 50 ns of simulation. Thereafter the RMSD

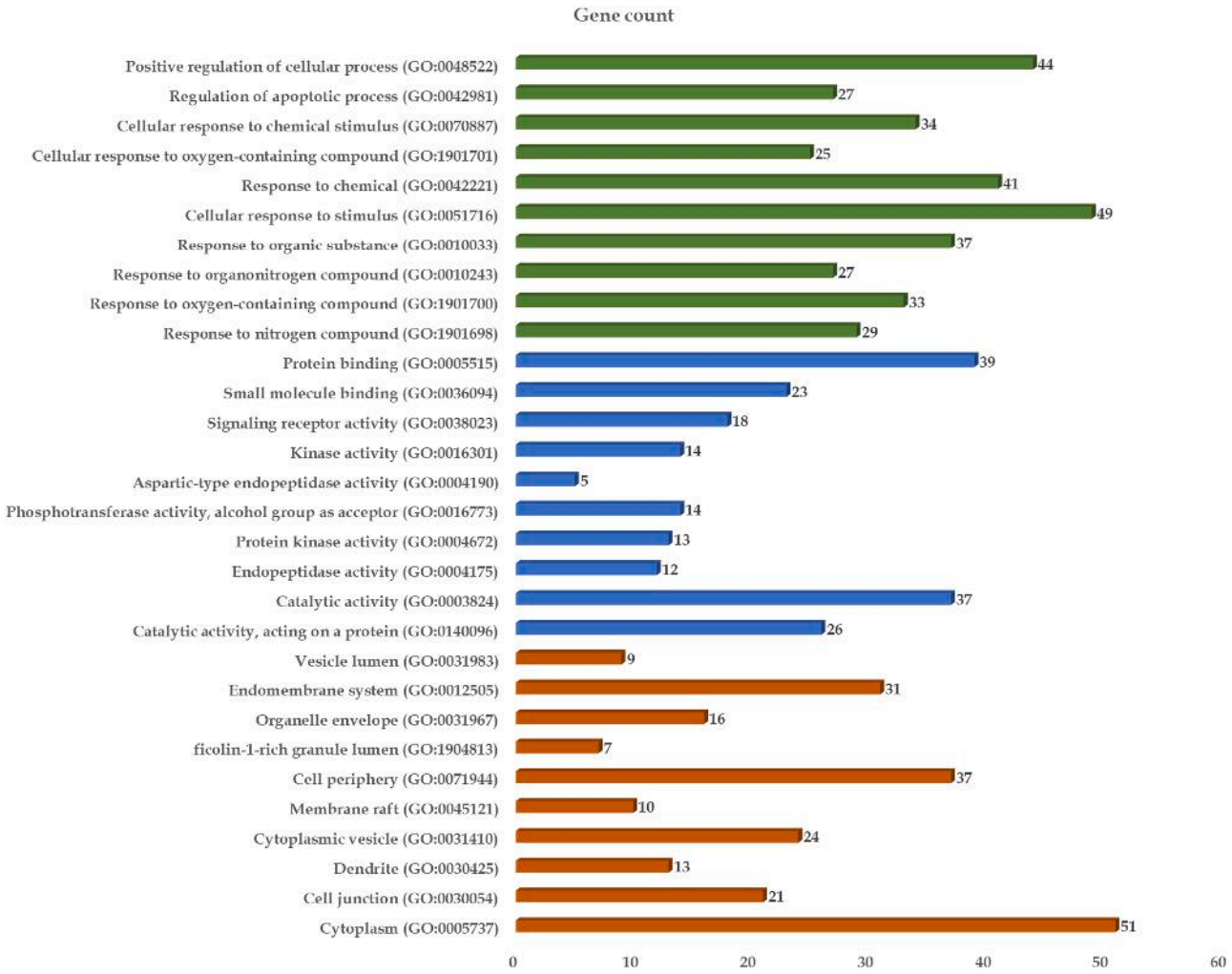


Fig. 15. The Gene ontology for the top 10 Biological processes (green), Molecular function (blue), and cellular component (orange).

fluctuation was seen between 56 ns to 58 ns ranging from 2.5 Å to 2.6 Å, however the complex showed stability over complete 100 ns run. The backbone RMSD fluctuation was seen to be less than 2 Å till first 50 ns of run, further fluctuation was noticed at 57, 61, and 67 ns of 2.01 Å each, and however the RMSD for both backbone and complex was intact for 100 ns run. The RMSF of complex showed fluctuation in range of 1 Å to 3 Å. The hydrogen bonded residues ASN 298, ASP 300, ALA 307 displayed fluctuation of 0.9 Å, 0.9 Å, 2.0 Å respectively. Residue number 549 showed maximum fluctuation with 2.5 Å, which does not fall in binding pocket. The RoG displayed maximum fluctuation of 2 Å, the gyration value had high peaks at around 40 ns and 60 ns of MD run. The SASA value displayed fluctuation between 178. 813 to 215.411 nm^2 A maximum of 4 hydrogen bonds were visible; initially, 1–4 hydrogen bonds were visible till 30 ns, and there after there was increase in hydrogen bond to 6 in the span of 31 ns to 46 ns, further the 3 hydrogen bonds were prominent up to 80 ns and thereafter 2 hydrogen bonds which were stable throughout 100 ns MD run. The Vander Waals energy contribution assessment by MMPBSA displayed residue ASN 298 to possess an energy contribution of −7.71 kcal/mol followed by ASP 300 and ALA 307 with energy contribution of −5.15 and −2.24 kcal/mol. (Fig. 6)

3.4.3. *Molecular mechanics poison-Boltzmann surface area (MMPBSA) analysis*

MMPBSA analysis was carried out for 100 ns run for the compound **6b-4w93** complex, where it possessed the least Vander Waals mechanics energy of (−34.53 ± 0.06 Kcal/mol), non-polar contribution of solute-solvent interaction to the solvation energy (−22.79± 0.08 Kcal/mol), and total gas phase molecular mechanics energy (18.01 ± 0.13 Kcal/mol).

3.4.3. *DFT analysis*

All the synthesised title compounds **(6a-**6h**)** were subjected to the geometric optimization using DFT theory calculation. Gas phase energy of optimised molecular structure have been tabulated in Table 3 The frontiers molecular orbital (FMO) orbitals mainly constitute Highest Occupied molecular orbital (HOMO) and lowest unoccupied molecular orbital (LUMO). HOMO energy relates to the ionization potential and LUMO energy related to electron affinity. FMO orbitals describe the chemical qualities such as reactivity, stability and kinetics. The FMO orbitals of synthesised compounds **6b** is depicted in the (Fig. 7) the chemical reactivity descriptors are calculated by DFT/B3LYP/6–31 G (d, p**) method and their values are tabulated in Table 4 molecular reactivity is indicated by the energy gap between HOMO-LUMO orbitals, smaller the energy gap, more the reactivity. Results reveal that compound has energy level of the HOMO is equal to −0.19179 eV, and the energy levels in LUMO is −0.054447 eV. The electrochemical potential μ = −0.1231185 eV, the chemical hardness was found to be −0.068671 eV and the chemical softness of molecules was found to be −14.5620818 eV.

3.4.4. Molecular electrostatic potential surface

The electrostatic potential is a valuable tool for determining how electric charge is distributed in a molecule. It sheds light on the electrostatic interactions that occur within the molecule and with its surroundings. The ESP on a molecular surface can be used to distinguish between areas with high electron density (negative potential) and those with low electron density (positive potential). The ESP may be used to predict electrophilic and nucleophilic attack sites and to investigate molecular interactions. Molecular electrostatic potentials were calculated at the optimised geometry using the B3LYP approach and a basis set of 6–31 G (d, p**). The MEP of the Compound **6b** is depicted in (Fig. 8)

3.4.5. ADMET prediction

Hydrogen bond donors, hydrogen bond acceptors, hydrophilicity, molecular weight, permeability, binding to human serum albumin, human oral absorption was predicted for ADMET using Qikprop module of Schrodinger's software. Violations for Lipinski rule of five and Jorgensen's rule of three were predicted and compared with recommended values as shown in Table 5

3.4.6. Target identification, network construction and cluster analysis

The network pharmacology is multidisciplinary approach that integrates concepts from pharmacology and systems biology, it involves the use of network analysis to study the complex interaction between bioactive molecules and their pathways [39]. In regards to above context, network pharmacology approach was utilised to identify potential targets associated and underlying molecular mechanism of compound **6b** for glucose uptake and α-amylase inhibition.

A total of 3134 targets were identified to be involved in the pathogenesis of T2DM *via* the DisGeNet database. Similarly, a total of 119 targets were predicted to be modulated by compound **6b** from which 46.22% of identified targets from the DIGEP-Pred and SwissTargetPrediction database were found to be in common with T2DM. 46.22% of targets were found to be in common by modulating 55 proteins (Fig. 9a). The categorical classification of matched proteins between compound **6b** and T2DM revealed top three categories to be affiliated as kinases (26.7 %), enzymes (13.3%), and G-protein coupled receptor (13.3%) (Fig. 9b). STRING was used to assess protein-protein interaction by subjecting the matched targets (Fig. 10a). The recognized pathways were assessed for their involvement in T2DM which revealed 18 pathways to be involved in T2DM Table 6. A Protein-pathway interaction (Fig. 11) was constructed using cytoscape which revealed PI3KCA, MTOR, and BRAF were identified to possess the highest edge count of 14, 10, and 6 respectively **(Supplementary Index (node table)).** The PI3K-Akt signaling pathway (hsa04151) was identified to be the major pathway modulated by the compound with a false discovery rate of 1.65E-06, strength of 1.01, and gene ratio of 0.0286 (Fig. 10b). Cluster analysis revealed 3 clusters with cluster 2 to possess the maximum number of genes *i.e.*25 (*ADORA1, ADORA2B, ADORA3, BRAF, CA2, CAPN2, CNR1, CNR2, CYP11B2, EGFR, FGFR1, GABRG2, GCGR, GRK2, GRK5, KDR, MMP2, MMP9, MTOR, PIK3CA, PTPN1, SRC, TACR3, TRPV1*, and *TSPO*). **(Supplementary Index (Cluster**)).

PI3K-Akt signaling pathway being modulated based on gene count *NGFR, CDK4, KDR, PIK3CA, CDK2, EGFR, PRL, HSP90AA1, MTOR, and FGFR1*. PI3K-Akt pathways initiates with the binding of IRS protein to subunits of Phosphatidyl inositol 3-kinase (PI3k). this in turn leads to the activation of Akt kinase, further Akt catalysis the translocation of GLUT present in cytoplasmic vesicles on the surface of cell membrane and thereby increases glucose transport across the cell in presence of insulin, besides this Akt is involved in the many intracellular metabolic processes [40,41].

IRS consist of six proteins IRS1–6, among them IRS-1 and IRS-2 play a vital role in transduction of insulin signals. IRS-2 and IRS-2 are expressed in almost all the tissues like muscle, liver, fat, and pancreatic islets. Mainly IRS-1 and IRS-2 play major role in adipose tissue and hepatocytes respectively [42,43]. mTOR exist in two types of complexes with different proteins and down streaming substrates, mTOR complex 1 and mTOR complex 2. In skeletal muscles, the activation of mTORC1 results in phosphorylation of IRS-1, which directly activate PI3K-Akt downstream signals leading to accumulation of the glycogen and glucose uptake effect [44,45].

Glucose uptake is facilitated by the GLUT family belonging to membrane transporters, mainly GLUT 1, GLUT 2 and GLUT 4, here in GLUT 1 helps in basal glucose uptake, moreover glucose uptake is facilitated by the GLUT 4 vesicles present besides the plasma membrane of muscle fibres. Various molecular mechanisms are responsible for GLUT 4 translocation. Among them, the proteins like p38-mitogen activated protein kinase. Glucose uptake is majorly initiated under conditions of exercise, AMP-activated kinase is primary sensor for the demand for energy in contracting state of muscles, inducing a downstream signaling cascade of events leading to the GLUT-4 translocation activity [46–49].

Similarly, network was constructed for compound **6b** to identify proteins involved in postprandial hyperglycaemia using DIGEP-Pred, the targets for postprandial hyperglycaemia were identified from gene card database. Proteins modulated by the compound **6b** were screened for proteins involved in postprandial hyperglycaemia. STRING was utilised to enrich the protein involved in various pathways; pathways involved in postprandial hyperglycaemia were identified using KEGG database. The metabolic pathway was identified to be modulated by the greater number of proteins. It predicted that Compound **6b,** modulated total of 193 targets, among them *EGFR, AMY1A, KDR, ITGB1, FLT3, CAT, REN, CSNK2B, GCK* were highly modulated. Metabolic pathway was found to be highly enriched pathway, represented in the (Fig. 12). The compound **6b**-protein-pathway network was constructed using cytoscape tool depicted in the (Fig. 13)

Thus, the *Invitro* Glucose uptake capacity and *α-amylase* inhibition of compound **6b** is evident by the predicted possible interaction with proteins-pathways involved in progression of type II diabetes mellitus and its complications, by network pharmacology, enrichment analysis. (Fig. 14) Represent the proposed plausible molecular mechanism of compound **6b** as **(A)** GLUT modulators **(B)** *α-amylase* inhibitors.

3.4.7. Gene ontology analysis

The GO analysis identified 59 CC in which Cytoplasm (GO:0,005,737) scored the lowest false discovery rate of 2.62E-05 *via* the modulation of 51 observed genes i.e. *NGFR, MMP2, NAMPT, NR3C1, CTSD, CAT, CDK4, KDR, PIK3CA, CPT1A, CDK2, REN, EGFR, PAK1, CA2, CAPN2, PLK1, PRL, TACR3, FASN, ADAM17, GRK2, BACE1, CYP11B2, PSEN1, BACE2, HSP90AA1, ESR2, IMPDH1, PDE5A, MTOR, ADORA1, CNR1, PTPN1, MMP9, SRC, ALOX5, CNR2, GRK5, TSPO, GCGR, POMC, FGFR1, ESR1, GABRG2, BRAF, CAPN1, TRPV1, ELANE, PFKFB3*, and *ABCG2* against 12,056 background genes at a strength of 0.18. Similarly, 46 MF were identified in which Catalytic activity, acting on a protein (GO:0,140,096) scored the lowest false discovery rate of 2.82E-07 *via* the modulation of 26 observed genes i.e. *MMP2, CTSD, CDK4, KDR, PIK3CA, CDK2, REN, EGFR, PAK1, CAPN2, PLK1, ADAM17, GRK2, BACE1, MMP1, PSEN1, BACE2, MTOR, PTPN1, MMP9, SRC, GRK5, FGFR1, BRAF, CAPN1,* and *ELANE* against 2279 background genes at a strength of 0.61. Moreover, 480 BP were identified where, Response to nitrogen compound (GO:1,901,698) scored the lowest false discovery rate of 1.65E-18 *via* the modulation of 29 observed genes i.e. *NGFR, MMP2, CAT, CDK4, PIK3CA, CPT1A, CDK2, REN, EGFR, CA2, CAPN2, TACR3, GRK2, BACE1, CYP11B2, PSEN1, HSP90AA1, MTOR, ADORA1, CNR1, PTPN1, MMP9, SRC, CNR2, TSPO, GCGR, POMC, GABRG2*, and *TRPV1* against 1058 background gene count with a strength of 0.99. The GO of the top 5 CC, MF, and BP has been represented in the form of bar graph (Fig. 15).

4. Conclusion

In summary, the study encloses the synthesis of nine benzenesulphonamide-thiazolidne-4one derivatives, characterised by FTIR, ^{1}H NMR, ^{13}C NMR and Mass studies. The antidiabetic evaluation was carried out by inhibiting the α-*amylase* enzyme and performing the glucose uptake capacity in yeast cells. It was found that compound **6b** exhibits prominent α-*amylase* enzyme inhibition with IC_{50} value of **29.51±1.35** μg/ml, the same compound also promotes the glucose uptake in yeast cells with **88.71**% and has ability to activate ligand binding domain and expression of PPAR-γ transcription factor. Computational calculation such as Induced fit docking studies suggest binding of **6b** to key amino acid residues present in the binding pocket of the α-*amylase* enzyme play contributing factor to support the *Invitro* α-*amylase* inhibition studies. quantum chemical parameter of the molecule using DFT theory support the stability of compound **6b,** furthermore computational pharmacology approach suggests the key target proteins being modulated by the compound **6b** are PIK3CA, EGFR, PTEN1, CDK2 leading to regulation of GLUT 4 vesicles responsible for the uptake of glucose as observed in yeast cells. PI3K-Akt pathway and Type II diabetes mellitus pathway were highly being modulated. Similarly, **6b** targeted AMY1A, responsible for α-*amylase* enzyme activity. Thus, the above *invitro* and *insilico* findings provide insights on probable mechanism of action of compound **6b.** Furthermore, these findings provide a frame work for further optimization of compound **6b** as lead molecule to carter the need for developing newer antidiabetic agents.

CRediT authorship contribution statement

Shriram D. Ranade: Writing – original draft, Validation, Software, Investigation, Data curation. **Shankar G. Alegaon:** Writing – original draft, Supervision, Methodology, Data curation, Conceptualization. **Nayeem A. Khatib:** Methodology. **Shankar Gharge:** Methodology. **Rohini S. Kavalapure:** Methodology. **B.R. Prashantha Kumar:** Methodology.

Declaration of competing interest

The authors declare that they have no known competing, financial interests or personal relationship that could have appeared to influence the work reported in this paper.

Data availability

No data was used for the research described in the article.

Acknowledgements

This work was supported by Department of Pharmaceutical chemistry, KLE College of Pharmacy, KLE Academy of Higher Education and Research, Belagavi, NMR was carried out in Sophisticated Analytical Instrument facility (SAIF) Karnataka University Dharwad. In addition, we would like to thank Mr. Prarambh S R Dwivedi for MD Simulation studies and network pharmacology. Mr. Sachin Gudasi for their support in Network pharmacology studies.

Supplementary materials

Supplementary material associated with this article can be found, in the online version, at doi:10.1016/j.molstruc.2024.138359.

References

[1] U. Galicia-Garcia, A. Benito-Vicente, S. Jebari, A. Larrea-Sebal, H. Siddiqi, K. B. Uribe, H. Ostolaza, C. Martín, Pathophysiology of type 2 diabetes mellitus, Int J Mol Sci 21 (17) (2020) 6275, https://doi.org/10.3390/ijms21176275.
[2] T.M. Belete, A recent achievement in the discovery and development of novel targets for the treatment of type-2 diabetes mellitus, J. Exp. Pharmacol. (2020) 1–5, https://doi.org/10.2147/JEP.S226113.
[3] S. Dhankhar, S. Chauhan, D.K. Mehta, Saini K Nitika, M. Saini, R. Das, S. Gupta, V Gautam, Novel targets for potential therapeutic use in diabetes mellitus, Diabetol. Metab. Syndr. 15 (1) (2023) 17, https://doi.org/10.1186/s13098-023-00983-5.
[4] M. Altay, Acarbose is again on the stage, World J. Diabetes. 13 (1) (2022) 1, 10.4239%2Fwjd.v13.i1.1.
[5] R. Singh, P. Kumar, J. Sindhu, M. Devi, A. Kumar, S. Lal, D. Singh, Parsing structural fragments of thiazolidin-4-one based α-amylase inhibitors: a combined approach employing in vitro colorimetric screening and GA-MLR based QSAR modelling supported by molecular docking, molecular dynamics simulation and ADMET studies, Comput. Biol. Med. 157 (2023) 106776, https://doi.org/10.1016/j.compbiomed.2023.106776.
[6] S. Khan, S. Iqbal, F. Rahim, M. Shah, R. Hussain, H. Alrbyawi, W. Rehman, A. A. Dera, L. Rasheed, H.H. Somaily, R.A. Pashameah, New biologically hybrid pharmacophore thiazolidinone-based indole derivatives: synthesis, in vitro alpha-amylase and alpha-glucosidase along with molecular docking investigations, Molecules. 27 (19) (2022) 6564, https://doi.org/10.3390/molecules27196564.
[7] S. Fettach, F.Z. Thari, Z. Hafidi, H. Tachallait, K. Karrouchi, M. El Achouri, Y. Cherrah, H. Sefrioui, K. Bougrin, M.E. Faouzi, Synthesis, α-glucosidase and α-amylase inhibitory activities, acute toxicity and molecular docking studies of thiazolidine-2, 4-diones derivatives, J. Biomol. Struct. Dyn. 40 (18) (2022) 8340–8351, https://doi.org/10.1080/07391102.2021.1911854.
[8] S. Khan, H. Ullah, F. Rahim, M. Nawaz, R. Hussain, L. Rasheed, Synthesis, in vitro α-amylase, α-glucosidase activities and molecular docking study of new benzimidazole bearing thiazolidinone derivatives, J. Mol. Struct. 1269 (2022) 133812, https://doi.org/10.1016/j.molstruc.2022.133812.
[9] A.A. Khan, H. Ullah, F. Rahim, M. Taha, F. Khan, W. Rehman, A. Wadood, K. M. Khan, Synthesis, in vitro α-glucosidase and α-amylase activities, and an in silico molecular docking study of triazinoindole-thiazolidinone hybrid derivatives, Chem. Data Collect. 45 (2023) 101035, https://doi.org/10.1016/j.cdc.2023.101035.
[10] A.K. Singh, R. Singh, Is gliclazide a sulfonylurea with difference? A review in 2016, Expert. Rev. Clin. Pharmacol. 9 (6) (2016) 839–851, https://doi.org/10.1586/17512433.2016.1159512.
[11] H.M. Faidallah, M.M. Al-Mohammadi, K.A. Alamry, K.A. Khan, Synthesis and biological evaluation of fluoropyrazolesulfonylurea and thiourea derivatives as possible antidiabetic agents, J. Enzyme Inhib. Med. Chem. 31 (sup1) (2016) 157–163, https://doi.org/10.1080/14756366.2016.1180594.
[12] H.B. Zhang, Y.A. Zhang, G.Z. Wu, J.P. Zhou, W.L. Huang, X.W. Hu, Synthesis and biological evaluation of sulfonylurea and thiourea derivatives substituted with benzenesulfonamide groups as potential hypoglycemic agents, Bioorg. Med. Chem. Lett. 19 (6) (2009) 1740–1744, https://doi.org/10.1016/j.bmcl.2009.01.082.
[13] G.A. Suaifan, M.B. Shehadeh, R.M. Darwish, H. Al-Ijel, V. Abbate, Design, synthesis and in vivo evaluation of novel glycosylated sulfonylureas as antihyperglycemic agents, Molecules. 20 (11) (2015) 20063–20078, https://doi.org/10.3390/molecules201119676.
[14] I.I. Panchal, D.J. Sen, A.D. Patel, U. Shah, M. Patel, A. Navale, V. Bhavsar, Molecular docking, synthesis and biological evaluation of sulphonylureas/guanidine derivatives as promising antidiabetic agent, Curr. Drug Discov. Technol. 15 (4) (2018) 315–325, https://doi.org/10.2174/1570163814666171002102904.
[15] M. Taha, T. Noreen, S. Imran, F. Nawaz, S. Chigurupati, M. Selvaraj, F. Rahim, N. Hadiani Ismail, A. Kumar, A. Mosaddik, A.M Alghamdi, Synthesis, α-amylase inhibition and molecular docking study of bisindolylmethane sulfonamide derivatives, Med. Chem. Res. 28 (2019) 2010–2022, https://doi.org/10.1007/s00044-019-02431-4.
[16] M. Nawaz, M. Taha, F. Qureshi, N. Ullah, M. Selvaraj, S. Shahzad, S. Chigurupati, A. Waheed, F.A. Almutairi, Structural elucidation, molecular docking, α-amylase and α-glucosidase inhibition studies of 5-amino-nicotinic acid derivatives, BMC. Chem. 14 (1) (2020), https://doi.org/10.1186/s13065-020-00695-1, 1-1.
[17] M. Hawash, N. Jaradat, S. Shekfeh, M. Abualhasan, A.M. Eid, L. Issa, Molecular docking, chemo-informatic properties, alpha-amylase, and lipase inhibition studies of benzodioxol derivatives, BMC. Chem. 15 (1) (2021) 40, https://doi.org/10.1186/s13065-021-00766-x.
[18] L. Gummidi, N. Kerru, O. Ebenezer, P. Awolade, O. Sanni, M.S. Islam, P. Singh, Multicomponent reaction for the synthesis of new 1, 3, 4-thiadiazole-thiazolidine-4-one molecular hybrids as promising antidiabetic agents through α-glucosidase and α-amylase inhibition, Bioorg. Chem. 115 (2021) 105210, https://doi.org/10.1016/j.bioorg.2021.105210.
[19] L.I. Shao, B. Zhang, Traditional Chinese medicine network pharmacology: theory, methodology and application, Chin. J. Nat. Med. 11 (2) (2013) 110–120, https://doi.org/10.1016/S1875-5364(13)60037-0.
[20] G. Chen, M. Zhang, Y. Chen, Y. Zhang, G. Luo, Y. Long, W. Yang, X. Yu, Synthesis, biological evaluation and network pharmacology based studies of 1, 3, 4-oxadiazole bearing azaphenols as anticancer agents, Arab. J. Chem. 17 (1) (2024) 105386, https://doi.org/10.1016/j.arabjc.2023.105386.
[21] L. Chen, Q. Lv, J. Cai, J. Liang, Z. Liang, J. Lin, Y. Xiao, R. Chen, Z. Zhang, Y. Hong, H. Ji, Design, synthesis and anticancer activity studies of 3-(coumarin-3-yl)-acrolein derivatives: evidenced by integrating network pharmacology and vitro

assay, Front. Pharmacol. 14 (2023) 1141121, https://doi.org/10.3389/fphar.2023.1141121.
[22] S.P. Loh, O. Hadira, In vitro inhibitory potential of selected Malaysian plants against key enzymes involved in hyperglycemia and hypertension, Malays. J. Nutr. 17 (1) (2011) 77–86.
[23] İ. Şahin, M. Çeşme, F.B. Özgeriş, Ö. Güngör, F. Tümer, Design and synthesis of 1, 4-disubstituted 1, 2, 3-triazoles: biological evaluation, in silico molecular docking and ADME screening, J. Mol. Struct. 1247 (2022) 131344, https://doi.org/10.1016/j.molstruc.2021.131344.
[24] İ. Şahin, M. Çeşme, F.B. Özgeriş, F. Tümer, Triazole based novel molecules as potential therapeutic agents: synthesis, characterization, biological evaluation, in-silico ADME profiling and molecular docking studies, Chem. Biol. Interact. 370 (2023) 110312, https://doi.org/10.1016/j.cbi.2022.110312.
[25] İ. Şahin, M. Çeşme, N. Yüce, F. Tümer, Discovery of new 1, 4-disubstituted 1, 2, 3-triazoles: in silico ADME profiling, molecular docking and biological evaluation studies, J. Biomol. Struct. Dyn. 41 (5) (2023) 1988–2001, https://doi.org/10.1080/07391102.2022.2025905.
[26] T. Noreen, M. Taha, S. Imran, S. Chigurupati, F. Rahim, M. Selvaraj, N.H. Ismail, J. I. Mohammad, H. Ullah, F. Nawaz, M. Irshad, Synthesis of alpha amylase inhibitors based on privileged indole scaffold, Bioorg. Chem. 72 (2017) 248–255, https://doi.org/10.1016/j.bioorg.2017.04.010.
[27] L.K. Williams, X. Zhang, S. Caner, C. Tysoe, N.T. Nguyen, J. Wicki, D.E. Williams, J. Coleman, J.H. McNeill, V. Yuen, R.J. Andersen, The amylase inhibitor montbretin A reveals a new glycosidase inhibition motif, Nat. Chem. Biol. 11 (9) (2015) 691–696, https://doi.org/10.1038/nchembio.1865.
[28] V.P. Cirillo, Mechanism of glucose transport across the yeast cell membrane, J. Bacteriol. 84 (3) (1962) 485–491, https://doi.org/10.1128/jb.84.3.485-491.1962.
[29] S. Release, 4: Induced Fit Docking Protocol, Glide, Schrödinger, LLC, New York, NY, 2018.
[30] G.D. Brayer, G. Sidhu, R. Maurus, E.H. Rydberg, C. Braun, Y. Wang, N.T. Nguyen, C.M. Overall, S.G. Withers, Subsite mapping of the human pancreatic α-amylase active site through structural, kinetic, and mutagenesis techniques, Biochemistry 39 (16) (2000) 4778–4791, https://doi.org/10.1021/bi9921182.
[31] K. Vanommeslaeghe, E. Hatcher, C. Acharya, S. Kundu, S. Zhong, J. Shim, E. Darian, O. Guvench, P. Lopes, I. Vorobyov, A.D. Mackerell Jr, CHARMM general force field: a force field for drug-like molecules compatible with the CHARMM all-atom additive biological force fields, J. Comput. Chem. 31 (4) (2010) 671–690, https://doi.org/10.1002/jcc.21367.
[32] M.S. Valdés-Tresanco, M.E. Valdés-Tresanco, P.A. Valiente, E. Moreno, gmx_MMPBSA: a new tool to perform end-state free energy calculations with GROMACS, J. Chem. Theory. Comput. 17 (10) (2021) 6281–6291, https://doi.org/10.1021/acs.jctc.1c00645.
[33] A.D. Bochevarov, E. Harder, T.F. Hughes, J.R. Greenwood, D.A. Braden, D. M. Philipp, D. Rinaldo, M.D. Halls, J. Zhang, R.A Friesner, Jaguar: a high-performance quantum chemistry software program with strengths in life and materials sciences, Int. J. Quantum. Chem. 113 (18) (2013) 2110–2142, https://doi.org/10.1002/qua.24481.
[34] Y.S. Mary, P.B. Miniyar, Y.S. Mary, K.S. Resmi, C.Y. Panicker, S. Armaković, S. J. Armaković, R. Thomas, B. Sureshkumar, Synthesis and spectroscopic study of three new oxadiazole derivatives with detailed computational evaluation of their reactivity and pharmaceutical potential, J. Mol. Struct. 1173 (2018) 469–480, https://doi.org/10.1016/j.molstruc.2018.07.026.
[35] R. Gupta, R.P. Chaudhary, X-ray, NMR and DFT studies on benzo [h] thiazolo [2, 3-b] quinazoline derivatives, J. Mol. Struct. 1049 (2013) 189–197, https://doi.org/10.1016/j.molstruc.2013.06.038.
[36] S.S. Hamdani, B.A. Khan, M.N. Ahmed, S. Hameed, K. Akhter, K. Ayub, T. Mahmood, Synthesis, crystal structures, computational studies and α-amylase inhibition of three novel 1, 3, 4-oxadiazole derivatives, J. Mol. Struct. 1200 (2020) 127085, https://doi.org/10.1016/j.molstruc.2019.127085.
[37] S.D. Ranade, S.G. Alegaon, U. Venkatasubramanian, A.S. Priya, R.S. Kavalapure, J. Chand, S.S. Jalalpure, D. Vinod, Design, synthesis, molecular dynamics simulation, MM/GBSA studies and kinesin spindle protein inhibitory evaluation of some 4-aminoquinoline hybrids, Comput. Biol. Chem. 105 (2023) 107881, https://doi.org/10.1016/j.compbiolchem.2023.107881.
[38] K.E. Merz, D.C. Thurmond, Role of skeletal muscle in insulin resistance and glucose uptake, Compr. Physiol. 10 (3) (2011) 785–809, https://doi.org/10.1002/cphy.c190029.
[39] P. Shannon, A. Markiel, O. Ozier, N.S. Baliga, J.T. Wang, D. Ramage, N. Amin, B. Schwikowski, T. Ideker, Cytoscape: a software environment for integrated models of biomolecular interaction networks, Genome Res. 13 (11) (2003) 2498–2504, https://doi.org/10.1101/gr.1239303.
[40] R.S. Kavalapure, S.G. Alegaon, U. Venkatasubramanian, A.S. Priya, S.D. Ranade, P. Khanal, S. Mishra, D. Patil, P.S. Salve, S.S. Jalalpure, Design, synthesis, and molecular docking study of some 2-((7-chloroquinolin-4-yl) amino) benzohydrazide Schiff bases as potential Eg5 inhibitory agents, Bioorg. Chem. 116 (2021) 105381, https://doi.org/10.1016/j.bioorg.2021.105381.
[41] U. Chandran, N. Mehendale, S. Patil, R. Chaguturu, B. Patwardhan, Network pharmacology. Innovative Approaches in Drug Discovery, 2017, p. 127, 10.1016%2FB978-0-12-801814-9.00005-2.
[42] P. Manna, S.K. Jain, PIP3 but not PIP2 increases GLUT4 surface expression and glucose metabolism mediated by AKT/PKCζ/λ phosphorylation in 3T3L1 adipocytes, Mol. Cell. Biochem. 381 (2013) 291–299, https://doi.org/10.1007/s11010-013-1714-7.
[43] H. Sano, L. Eguez, M.N. Teruel, M. Fukuda, T.D. Chuang, J.A. Chavez, G. E. Lienhard, T.E. McGraw, Rab10, a target of the AS160 Rab GAP, is required for insulin-stimulated translocation of GLUT4 to the adipocyte plasma membrane, Cell Metab. 5 (4) (2007) 293–303.
[44] A.C. Thirone, C. Huang, A. Klip, IRS proteins and insulin resistance in humans, Trends Endocrinol. Metabol. 2 (17) (2006) 72–78, 10.1016%2Fj.tem.2006.01.005.
[45] T.A. Gustafson, W. He, A. Craparo, C.D. Schaub, T.J O'Neill, Phosphotyrosine-dependent interaction of SHC and insulin receptor substrate 1 with the NPEY motif of the insulin receptor via a novel non-SH2 domain, Mol. Cell. Biol. (1995), https://doi.org/10.1128/MCB.15.5.2500.
[46] S.H. Um, F. Frigerio, M. Watanabe, F. Picard, M. Joaquin, M. Sticker, S. Fumagalli, P.R. Allegrini, S.C. Kozma, J. Auwerx, G Thomas, Absence of S6K1 protects against age-and diet-induced obesity while enhancing insulin sensitivity, Nature 431 (7005) (2004) 200–205, https://doi.org/10.1038/nature02866.
[47] M. Laplante, D.M. Sabatini, mTOR signaling in growth control and disease, Cell 149 (2) (2012) 274–293, https://doi.org/10.1016/j.cell.2012.03.017.
[48] M.A. Chambers, J.S. Moylan, J.D. Smith, L.J. Goodyear, M.B. Reid, Stretch-stimulated glucose uptake in skeletal muscle is mediated by reactive oxygen species and p38 MAP-kinase, J. Physiol. (Lond.) 587 (13) (2009) 3363–3373, https://doi.org/10.1113/jphysiol.2008.165639.
[49] E. Bengal, S. Aviram, T. Hayek, p38 MAPK in glucose metabolism of skeletal muscle: beneficial or harmful? Int. J. Mol. Sci. 21 (18) (2020) 6480, https://doi.org/10.3390/ijms21186480.